

100
392
THS



PH.D.



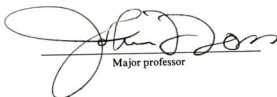


This is to certify that the
dissertation entitled
INSTABILITY PHENOMENA IN A TWO-DIMENSIONAL
SLIT-JET FLOW FIELD

presented by
SYED KHURSHED ALI

has been accepted towards fulfillment
of the requirements for

PH.D. degree in MECHANICAL ENGINEERING



Major professor

Date 5/15/91

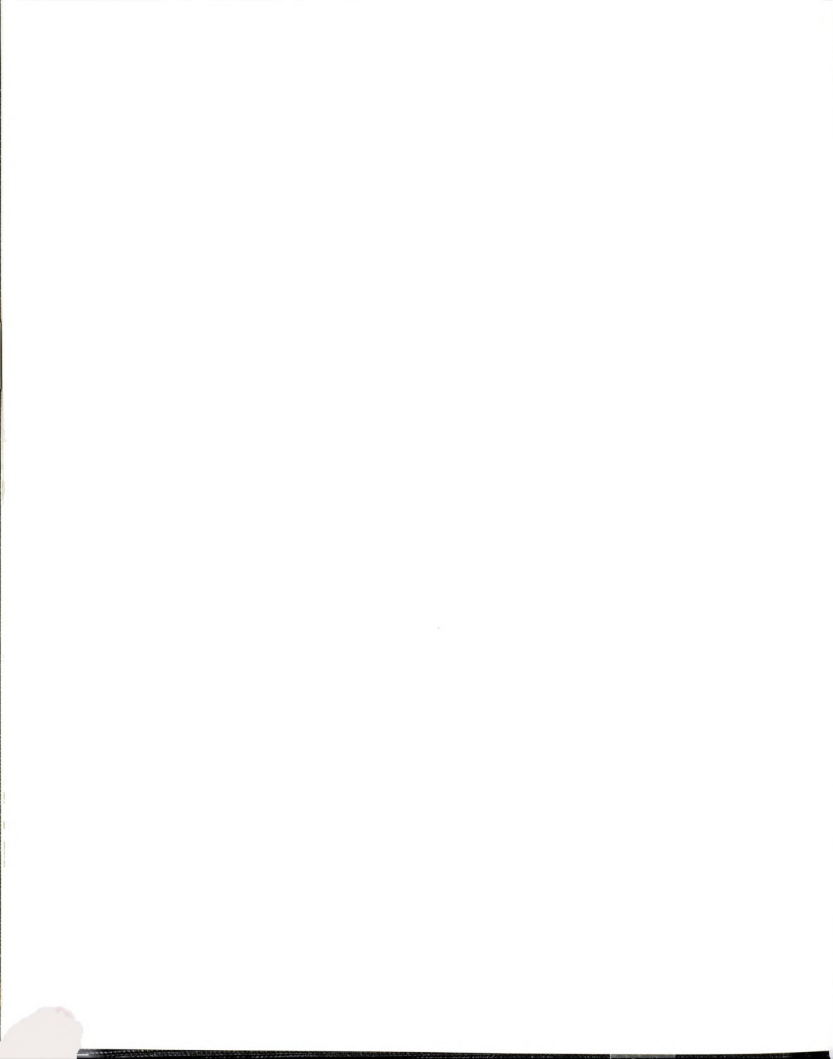
LIBRARY
Michigan State
University

PLACE IN RETURN BOX to remove this checkout from your record.
TO AVOID FINES return on or before date due.

DATE DUE	DATE DUE	DATE DUE
_____	_____	_____
_____	_____	_____
_____	_____	_____
_____	_____	_____
_____	_____	_____
_____	_____	_____
_____	_____	_____
_____	_____	_____

MSU Is An Affirmative Action/Equal Opportunity Institution

c:\cric\date due.pm3-p.1



INSTABILITY PHENOMENA IN A
TWO-DIMENSIONAL SLIT-JET FLOW FIELD

Volume I

By

Syed Khurshed Ali

A DISSERTATION

Submitted to
Michigan State University
in partial fulfillment of the requirements
for the degree of

DOCTOR OF PHILOSOPHY

Department of Mechanical Engineering

1991

65X-2064

ABSTRACT

INSTABILITY PHENOMENA IN A TWO-DIMENSIONAL SLIT-JET FLOW FIELD

By

Syed Khurshed Ali

The instability phenomena in an unexcited, isothermal, submerged, two-dimensional slit-jet flow field have been investigated using experimental and analytical techniques. Dye flow visualization and laser Doppler anemometry were used over a wide range of Reynolds numbers: $100 \leq \frac{\langle U \rangle w}{\nu} \leq 3500$. The linearized, inviscid equations of motion were used together with the measured velocity profiles to predict the type of solution and the characteristics of the maximally amplified spatial disturbances. In addition, the discharge coefficient of the slit-jet, C_D , was also measured over a wide range or Re .

The instability of the slit-jet results in the formation of a symmetric vortex street. The results of this study are in general agreement with previous studies. However, it has been found that the process of vortex formation is more complex than that identified previously. The results of flow visualization show that: i) contrary to prior observations the vortex motions form even beyond $Re=1500$, ii) the Re over the range of 0-3500 can be subdivided into four regimes,

and iii) the formation of a large scale motion is preceded by a sequence of well defined events.

Strouhal number (St_F), convection speed (u_c^*) and wavelength (λ^*) have been determined from the flow visualization data. The St_F and λ^* distributions as a function of Reynolds number show considerable scatter. Similar scatter was also reported earlier.

The Strouhal number based upon the dominant frequency of the velocity fluctuations, St_V , also shows some scatter. It is observed that for similar values of Re and the same x/w locations, St_F is nominally twice the value of St_V . No explanation for this difference in the two Strouhal numbers has been found.

The intensity of the velocity fluctuations, $\tilde{u}(x/w)/U_0$, exhibits exponential growth at nominally the same rate over the entire Re range: 500-3000. The average value of the growth rate, $d[\log(\tilde{u}(x)/U_0)]/dx$, was found to be 0.54.

Velocity surveys across the jet exhibit a top-hat velocity profile at $x/w=1$ and a rounded jet at $x/w=2.4$. The solution of the linearized, inviscid equations of motion for the top-hat velocity profile predicts a symmetric vortex street with Strouhal number, $St_I=0.66$, which compares very well with the average value of $St_V=0.70$ at $x/w=1$. Also, the predicted and the measured convection speeds



compare quite well. However, the predicted value of λ/w is larger than the value found from the flow visualization data.



I dedicate this thesis to

Mr. Syed Mohammad Hosain

my father and mentor



ACKNOWLEDGMENTS

Thanks are due first and foremost to Almighty Allah for His un-
blessings and kindness which made the completion of this thesis
e.

Next, I would like to express my sincere appreciation to
F. Foss for his continual support and guidance throughout
and other studies. Appreciation is also extended to
V. Beck, Dr. M. M. Koochesfahani, Dr. M. C. Potter, and
Y. Wang for serving as members of the Guidance Committee.

In addition, I would like to express my gratitude and acknowledge
contribution of the following people in making this dissertation
e:

Richard Haw for developing the software to drive the stepper
under computer control;

Robert Rose of the Mechanical Engineering Department for his
the experimental set up, specially with the electrical cir-
eeded for this work;

Steve Southward for modifying the computer code so that



aneous flow visualization/LDA measurements could be
ished;

fellow graduate and undergraduate students at the Turbulent
Flows Lab I, in particular: Matt Boerma, Larry Cameron, Alan
, Ron Focia, John Joyce, Steve Larson, Irwin Lawson, Tim McCau-
y Mondol, Bob Mitchell, Chris Pung and Zai-Chun Yang;

. C. Petty for letting me use his laser Doppler anemometer and
r system for velocity measurements;

friends Dr. S. Shakir and Dr. M. Usman for providing both
al and social support over the long duration of stay in East

the financial support provided by the Mechanical Engineering
ent, the Department of Mathematics, the National Science Foun-
United Technologies Research Center, Krebbs Engineers, and MSU
ion during the course of this study are deeply appreciated.

nally, I wish to acknowledge the support and sacrifice of my
, the encouragement of my brothers and sisters, and the pati-
nd support of my wife, Fatima, and children during the pursuit
er education.



TABLE OF CONTENTS

	Page
OF TABLES	xvii
OF FIGURES	xviii
NCLATURE	xlvi
TER 1 HISTORICAL PERSPECTIVE AND PLAN OF STUDY	1
1.1 Introduction	1
1.2 Historical Perspective	3
1.2.1 Instability of the Slit-Jet Flow Field -	
Experimental Studies	3
1.2.2 Instability of 2D Jets Issuing from Contoured	
Nozzles	5
1.2.3 Theoretical Investigation of Instability of 2D	
Jets	8
1.2.3.1 Solution of Orr-Sommerfeld Equation	9
1.2.3.2 Numerical Solution of Full Navier-Stokes	
Equation	13
1.2.3.3 Simulation of Vortex Street	14
1.3 Objectives of the Present Study	15
1.4 Contents of the Thesis	17
ER 2 ANALYTICAL CONSIDERATIONS	19
2.1 Introduction	19
2.2 Inviscid Flow Pattern in the Slit-Jet Flow Field.	20



2.2.1	Introduction	20
2.2.2	Inviscid Flow Analysis	21
2.2.2.1	Details of Conformal Transformations	22
2.2.2.2	Equation of Separating Streamline	25
2.2.2.3	Contraction Ratio	28
2.2.2.4	Equation of Streamline in z-plane	29
2.2.2.5	Equations of Velocity and Pressure Fields on Nozzle Plate	32
2.2.3	Comparison Between Jets from Finite and Infinite Plenums	35
2.2.3.1	Pressure Field Along the Nozzle Plate	35
2.2.3.2	Trajectory of Separating Streamline	36
2.3	Determination of Boundary Layer Parameters	36
2.3.1	Momentum Thickness θ	38
2.3.2	Displacement Thickness δ_d	40
2.4	Stability Calculations of the Slit-Jet Flow Field	42
2.5	Model for Growth of Pressure Fluctuations Along the Centerline	46
2.5.1	Introduction	46
2.5.2	Derivation of Equation for Pressure Fluctuations	47
2.5.3	Discussion	50
3	EXPERIMENTAL FACILITY AND PROCEDURES	51
3.1	Introduction	51
3.2	Experimental Facility	52



3.2.1	Volume Flow Sensor	53
3.2.2	Filling Device	54
3.2.3	Working Liquid	55
3.2.4	Operating Principle	55
3.3	Flow Modelling	56
3.4	Computer Facility for Data Acquisition and Control	60
3.5	Software to Control the Bleed Valve	61
3.5.1	Program CLAWSN	62
3.5.2	Program ZVALVE	63
3.6	Operating Procedure / Start of Experimental Run	63
3.7	Calibration of Sensors	65
3.7.1	Checking Operation of the LDA System	65
3.7.2	Calibration of Volume Flow Sensor	67
3.7.2.1	Calibration of Pressure Transducer	67
3.7.2.2	Calibration of LVDT	68
3.7.2.3	Data Acquisition and Processing	68
3.8	Methods of Flow Visualization	69
3.8.1	Schlieren	70
3.8.2	Hydrogen Bubble Technique	71
3.8.3	Dye Injection	72
3.9	Data Acquisition	73
3.9.1	Flow Visualization	74
3.9.2	Velocity Measurement using LDA	75
3.9.3	Combined Flow Visualization and LDA	

Velocity-Sensing	77
4 FLOW VISUALIZATION: QUALITATIVE RESULTS & DISCUSSION . 78	
4.1 Introduction	78
4.2 Width Evaluation of the Dye Streak	81
4.3 Common Patterns of the Flow Field	81
4.3.1 Starting Vortex Pair	82
4.3.2 Bulges with Overriding Unit Vortices at Low Re . . 84	
4.3.3 Bulges on Jet Boundary with Large Scale Vortex Formations	84
4.3.4 Formation of Unit Vortices at High Re Values . . . 84	
4.4 Various Regimes Based on Reynolds Number	85
4.4.1 $Re < 157$	86
4.4.2 $157 \leq Re \leq 210$	86
4.4.3 $268 \leq Re \leq 1700$	87
4.4.3.1 Formation of Symmetric Motions	87
4.4.3.2 Some Exceptions to the Common Observations . . . 89	
4.4.4 $Re > 2300$	90
4.5 Interactions Between Symmetric Motions	92
4.6 Loss of Symmetry in Vortex Street	94
5 ALGORITHMS FOR PROCESSING THE PHOTOGRAPHIC DATA 97	
5.1 Introduction	97
5.2 Creation of Data Base for Flow Visualization Experiments	98
5.2.1 Computation of Spatially/Temporally Averaged Velocity of Jet	98



5.2.2	Picture Timings or Beginning and End Time for LDA Data	100
5.2.3	Digitization on PRIME 750 Computer System. . . .	100
5.2.4	Combining Information: Time, $\langle U \rangle$ and Position of Vortex Pairs	102
5.3	Algorithms for Processing Photographic Database . .	102
5.3.1	Algorithms for Geometric/Kinematic Properties of the Jet Flow Fields	103
5.3.1.1	Space-Time ($x^* - t^*$) Plots of Vortices	103
5.3.1.2	Lateral Spacing Between Vortices of Individual Pairs	103
5.3.1.3	Difference in Axial Location of the Two Vortices of a Pair	104
5.3.2	Algorithms to Compute Vortex Street Parameters .	104
5.3.2.1	Strouhal Number $St_F(x/w)$	105
5.3.2.2	Translation Speed $c_k(x/w)$ of Vortex Pairs . . .	106
5.3.2.3	Passage Time t_k^p	109
5.3.2.4	Longitudinal Spacing Between Vortex Pairs . . .	110
5.3.2.5	A Statistical Method to Compute Estimates of u_c and λ :	111
5.4	Example Calculations	114
5.4.1	Geometric/Kinematic Properties	114
5.4.2	Parameters of the Vortex Street	115
5.4.2.1	Choice of Control Parameters T_p and T_w	115
5.4.2.2	Discussion of Results	120



6 QUANTITATIVE RESULTS USING PROCESSED DIGITIZED DATA . 122

6.1 Synopsis 122

6.2 Geometric/Kinematic Properties of the Jet Flow

Fields 124

6.2.1 Space-Time (x^* , t^*) Plots of Vortices 125

6.2.2 Lateral Spacing Between Vortices of Individual

Pairs 126

6.2.3 Difference in Axial Locations of the Vortices

of a Pair 128

6.3 Stability Characteristics of the Slit-Jet Flow

field 130

6.3.1 Distribution of Strouhal No. $St_F(x^*)$ 130

6.3.1.1 Examination of the Possible Sources of

variation in $St_F(x^*)$ 131

6.3.1.2 Conclusion 134

6.3.2 Convection Velocities u_c^* of the Vortex Motions . 135

6.3.3 Distribution of Wavelength $\lambda^*(x^*)$ 136

6.4 Conclusions 138

7 VELOCITY MEASUREMENTS USING LASER DOPPLER ANEMOMETRY 142

7.1 Introduction 142

7.2 Discharge Coefficient C_D of the Slit-Jet 143

7.3 Velocity Field Information 146

7.3.1 Longitudinal Surveys 146

7.3.1.1 Introduction 146

7.3.1.2 Velocity Time Histories at Selected Locations . 148



7.3.1.3	Mean and Rms Velocity Distributions	149
7.3.2	Lateral Surveys	152
7.3.2.1	Introduction	152
7.3.2.2	Velocity Time Histories at Selected Locations .	153
7.3.2.3	Mean and Rms Velocity Distributions Across the Jet	154
7.3.2.3.1	Velocity Distributions at $x/w=1$	155
7.3.2.3.2	Velocity Distributions at $x/w=2.4$	155
7.3.2.4	Analytical Models of the Mean Velocity Profile	156
7.3.2.4.1	Velocity Profile at $x/w = 1$	157
7.3.2.4.2	Velocity Profile at $x/w=2.4$	158
7.4	Autospectrum - Definition, Examples and Uses . . .	160
7.4.1	Power Spectral Density Function	160
7.4.2	Examples and Uses.	161
7.5	Identification of Background Disturbances Using the Autospectra	162
7.5.1	Influence of Disturbances Induced by Two Different Filling Processes	163
7.5.2	Background Disturbances in the Plenum	165
7.6	Determination of Strouhal Number St_V from the Autospectra	166
7.6.1	Distribution of $St_V(x^*, Re)$	167
7.6.2	Distribution of $\tilde{u}(St_V, Re, x^*)/\tilde{u}(Re, x^*)$	169
7.6.3	Strouhal No. from the Combined LDA-Flow	



Visualization Experiments	172
8 STABILITY OF THE SLIT-JETS - INFERENCES, RESULTS AND REGION	175
8.1 Introduction	175
8.2 Inferences from the Autospectra of $u(x, y=0, t)$. . .	176
8.2.1 Region of "Non-Selective" Growth of Disturbances	176
8.2.2 Region of "Selective" Growth of Disturbances . .	177
8.2.3 Influence of Pairing of Vortices on $St_v(x^*)$. . .	177
8.2.4 Quasiperiodicity in an Unexcited jet	178
8.3 Stability Calculations Using the Lateral Mean Velocity Profiles	178
8.3.1 Computations at $x/w = 1$	179
8.3.2 Computations at $x/w = 2.4$	180
8.4 Growth of Pressure Fluctuations Along the Jet Centerline	182
8.4.1 Choice of Parameters and Results	184
8.4.2 Discussion	186
9 CONCLUSIONS AND RECOMMENDATIONS	187
9.1 Introduction	187
9.2 Conclusions	187
9.2.1 General Properties of the Slit-Jet	188
9.2.2 Stability Characteristics	190
9.3 Recommendations	197



IX A	DESIGN OF FLOW FACILITY	399
A.1	General Requirements and Constraints	399
A.2	Proposed Facility and Additional Constraints	401
A.3	Design Strategies to Meet the Requirements	402
A.3.1	Dimensions and Range of Parameters	402
A.3.2	Control of Flow Rate	403
A.3.3	Control of Disturbance Level	403
IX B	SELECTION OF A REGRESSION MODEL FOR $E_T(T)$ DATA	405
B.1	Introduction	405
B.2	Example	406
IX C	DETAILS OF EXPERIMENTAL RUNS AND SPACE-TIME PLOTS.	408
C.1	Introduction	408
C.2	Details of Experimental Runs	408
C.3	Space-Time Plots	410
F	REFERENCES	452

Table

1 - F

2 - V

3 - I

4 - S

.

5 - E

8.1

0.1

LIST OF TABLES

le	Page
Fiducial Points of Various Planes	23
V_b/V_s at $Re = 980$	83
Influence of T_p, T_w on St_F, u_c and λ	116
St_F and St_V from the Combined LDA-Flow Visualization Experiments	173
Eigenvalues at maximum growth rate	181
- Sum of squares and F ratio	407
- Details of Experimental Runs	409

Figure

1 - So

2 - A

3 - So

ch

tr

pl

4 - So

pl

5 - So

6 - So

7 - So

8 - So

9 - St

fi

pl

10 - T

i

11 - N

f

12 - N

LIST OF FIGURES

Figure	Page
Schematic representation of the two-dimensional slit-jet.	201
A Jet Pump.	202
Schematic representation of a slit-jet issuing from a finite, channel-like plenum. The boundaries of the plenum and the trajectories of the separating streamline define the complex plane: $z=(x_1+ix_2)$	203
Schematic representation of a slit-jet issuing from an infinite plenum.	203
Schematic representation of ζ plane.	204
Schematic representation of ζ' plane.	204
Schematic representation of t plane.	205
Schematic representation of w plane.	205
Streamline pattern upstream of a slit-jet issuing from a) a finite, channel-like plenum with $m = 20$, and b) an infinite plenum.	206
Influence of m on the ratio of slit widths w/w_∞ and the proximity ratio H/w	207
Normalized pressure distribution on the nozzle plate for a finite ($m=20$) and an infinite plenum.	208
Normalized pressure distribution on an expanded pressure axis.	209

13 - C

(

14 - S

v

n

15 - D

t

s

16 - S

f

17 - S

f

18 - S

s

E

19 - Sc

v

d

20 - S

m

i

.

21 - S

f

22 - S

Comparison of the widths of the jets issuing from a finite ($m = 20$) and an infinite plenum.	210
Schematic representation of the separating streamline with velocity U_0 and the limits of integration for flow on the nozzle plate.	211
Definition sketch for the stability analysis. The flow along the center streamline between "o" and "n" is modelled as steady flow.	212
Schematic representation of the gravity driven, steady state, finite duration liquid flow facility.	213
Schematic representation of the operational features of the flow facility.	214
Schematic representation of the Filling Device (FD). A: Pla- stic tube, B: Rubber gasket, C: Styrofoam base, D: String, E: Handle to maneuver the device.	215
Schematic representation of the formation of two-dimensional vortices in the plenum. A: Glass tank, B: Plenum, C: Two- dimensional vortices, D: Receiver, E: To vacuum tank. . .	216
Schematic representation of the use of FD to prevent the for- mation of vortices in the plenum. A: String, B: Nozzle hous- ing, C: Filling device (FD), D: FD parked during experiment.	216
Schlieren visualization of vortex formation during the filling process.	217
Schematic representation of the four control volumes CV_1 used	

in 1

23 - Sche

PNH

assu

24 - Flow

. . .

25 - Sche

pres

thrc

26 - Conl

27 - Sche

perl

28 - Comp

tach

29 - Norr

30 - Sche

Volu

C: v

step

(LVI

31 - Sche

Trat

32 - Cali

. . .

33 - Cali

in flow modelling.	218
Schematic representation of the time histories of q ($=C_D U_0 A_j$), P_{NH} , and A_v . A step change in the jet velocity at $t=0$ is assumed in the analysis.	219
Flow chart of the "tight wait loop" to jog the stepper motor.	220
Schematic representation of the time histories of the cavity pressure, P_{NH} , and the rate of flow of air into the cavity through the bleed valve, q_b	221
Configuration of the single channel LDA system.	222
Schematic representation of the arrangement to check the performance of the LDA system.	223
Comparison of disk velocity measured by the LDA and the tachometer.	224
Normalized rms of the disk velocity.	225
Schematic representation of the arrangement for calibrating the Volume Flow Sensor (VFS). A: Glass tank with liquid, B: VFS, C: Vertical traversing mechanism, D: Computer controlled stepper motor, E: Linear Variable Differential Transformer (LVDT), F: Tripod with support arm.	226
Schematic representation of the Linear Variable Differential Transformer (LVDT).	227
Calibration data for the pressure transducer used in the VFS.	228
Calibration data for the LVDT used in the calibration of VFS.	

Se

34 - FI

35 - Re

cl

36 - Sc

fl

37 - FI

us

38 - Sc

or

ti

ir

39 - SJ

. . .

40 - Sc

41 - Sc

Ap

42 - Sc

L

43 - Sc

li

44 - Ve

45 - Je

Tr

ti

See Figure 30 for the experimental configuration.	229
- Flow chart for calibrating the VFS.	230
- Rate of pressure rise in the cup as a function of its velocity.	231
- Schematic representation of the ray diagram for the schlieren flow visualization.	232
- Flow visualization photographs of the slit-jet flow field using the schlieren technique: $Re=1400$ and $w=2.63$ cm. . .	233
- Schematic representation of the arrangement for injecting dye on the nozzle plates. A: Stand, B: Bottle with dye, C: Plastic tubing, D: Header, E: Nozzle plate, F: Jet of dye spreading on the nozzle plates.	234
- Side view of the flow facility with incoming/outgoing signals.	235
- Schematic representation of the comparator circuit. . . .	236
- Schematic representation of the switching circuit for the Apple IIe computer.	237
- Schematic representation of the configuration for combined LDA-flow visualization experiments.	238
- Schematic representation of the corner eddies in a channel-like plenum under steady flow conditions.	239
- Variation of δ_d/w as a function of Re	240
- Jet development at $Re = 87$, $V_b/V_s = 0.68$ and $w = 1.99$ cm. The nondimensional times are a) 11.8 and b) 18.1. Up to this time the bulge behind the SVP remains undeformed.	241

46 - Je

no

-

in

co

47 - Je

Th

t

th

of

48 - Ra

te

tr

49 - Je

Th

In

ev

is

ge

rt

50 - Je

si

f)

de

fo

- Jet development at $Re = 105$, $V_b/V_s = 0.7$ and $w = 1.99$ cm. The nondimensional times are a) 14.2, b) 18.1 and c) 22.4. By $t^* = 22.4$ the bulge has evolved into a kink. Note the increased inward displacement of the separating streamline position as compared to that in Figure 45. 242
- Jet development at $Re = 129$, $V_b/V_s = 0.72$ and $w = 1.99$ cm. The nondimensional times are a) 16.9, b) 22.5 and c) 27.0. By $t^* = 22.5$ the bulge has evolved into a kink and by $t^* = 27.0$ the kink has evolved into a foldover. Note the development of the vena contracta. 243
- Ratio of bulge velocity to the velocity of the starting vortex pair as a function of Re . The figure also shows the distribution of $V_b/\langle U \rangle$ and $V_s/\langle U \rangle$ as functions of Re 244
- Jet development at $Re = 156$, $V_b/V_s = 1.04$ and $w = 1.99$ cm. The nondimensional times are a) 22.7, b) 24.1 and c) 26.8. In (a) a bulge has evolved into a kink; in (b) the kink has evolved into a foldover. Since $V_b/V_s > 1$, the foldover in (c) is passing into the SVP. Note the development of another bulge behind the SVP. This was the smallest Re at which unit vortices were first observed on the jet column. 245
- Jet development at $Re = 980$ and $w = 2.63$ cm. The nondimensional times are a) 10.9, b) 12.0, c) 13.1, d) 14.1, e) 15.2, f) 16.3, g) 17.3, h) 18.4, i) 19.5 and j) 20.5. The SVP is designated by 1. The indices 2, 3, ... designate the newly forming distinctive motions. Bulges 2 and 3 merge with the

SV

ev

51 - Je

Th

d'

th

in

fo

co

52 - Fr

w

ol

53 - Fr

w

9

2

54 - Je

cr

an

55 - Th

d

ti

ti

m

56 - S

- SVP without evolving into rollovers. However the bulge No. 4 evolves into a vortex pair before coalescing with the SVP. 246
- 1 - Jet development at $Re = 207$, $w = 2.63$ cm and $V_b/V_s = 1.07$. The nondimensional times are a) 12.5, b) 15.1, c) 17.7 and d) 20.2. A number of dark spots in the SVP in (a) indicate the mergers of kinks/foldovers with the SVP. The foldover in (a) is approaching the SVP in (b) and another bulge has formed with overriding unit vortices. In (d) three bulges can be identified. 247
- 2 - Formation of bulges and large scale vortex motions at two values of Re : a) 510 and b) 1200. Nominally similar features are observed over the Reynolds number range of 269-1700. . . . 248
- 3 - Formation of unit vortices in the slit-jet flow field along with the large scale vortex motions. Re , w and t^* are a) 980, 2.63 cm and 24.8; b) 1044, 1.40 cm and 36.8; c) 2949, 2.57 cm and 14.2. 249
- 4 - Jet development at three values of Re with $V_b/V_s < 1$, $w = 1.99$ cm and $t^* \approx 18.1$. Re and V_b/V_s are a) 86, 0.68 b) 105, 0.70 and c) 129, 0.72. 250
- 5 - The slit-jet flow field of Figure 49 at later times. The nondimensional times are a) 28.2, b) 30.2 and c) 32.3. In (a) the first bulge is passing into the SVP, whereas, in (c) as the second bulge is approaching the SVP more bulges have formed on the jet column. 251
- Sequence of photographs at $Re = 281$ and $w = 1.51$ cm exhibiting

the form

times ar

g) 49.1.

tex no.

the grow

ing phot

jet exhl

57 - Process

nondimen

e) 18.1

can be t

is begin

of spots

58 - Process

The nono

15.0. N

ices dow

interact

interact

70 prese

59 - Schemati

in the m

identifi

the formation two dimensional vortex pairs. The nondimensional times are a) 42.3, b) 43.4, c) 44.5, d) 45.7, e) 46.8, f) 47.9, g) 49.1, h) 50.2 and i) 51.3. Note: i) the formation of vortex no. 8 in (h) can be traced back to the bulge in (b). ii) the growth of bulge no. 7 stopped around $t^* \approx 46$; in the remaining photographs it simply appears as a mark of dye. iii) the jet exhibits development of sinuous mode beyond $x^* \approx 8$. . . 252

Process of vortex formation at $Re = 1063$ and $w = 2.57$ cm. The nondimensional times are a) 17.0, b) 17.3, c) 17.5, d) 17.8, e) 18.1 and f) 18.4. The formation of vortex no. 14 in (f) can be traced back to the bulge in (b). In (e) bulge no. 15 is beginning to form. Note in (f) the symmetric accumulation of spots of dye as the bulge no. 15 is evolving into a kink.

. 253

Process of formation of symmetric vortex street at $Re = 1580$. The nondimensional times are a) 13.8, b) 14.2, c) 14.6 and d) 15.0. Note the two spots of dye which appear to be unit vortices downstream of the kink no. 15. Also note the symmetric interaction between 10 and 11 in (a) and somewhat asymmetric interaction between (10,11) and (12) in (c) and (d). Figure 70 presents a continuation of this sequence up to $t^* = 16.2$.

. 254

Schematic representation of the process of vortex formation in the near-field of the slit-jet flow. Various features are identified as: A: Formation of veena contracta, B: Inflexion

point in

E. Foldo

60 - Jet deve

ional ti

f) 29.5

rked by

time. 7

ame part

61 - Jet deve

onal tir

no. 14

formatio

the inte

and comp

62 - Jet deve

ional t

tias 12

kink in

before

which i

10. A

63 - Jet deve

and t *

39.3, at

tex not

point in the dye streak, C: Bulge, D: Kink in the dye streak,
E: Foldover, F: Rollover and G: Fully formed vortex pair. 255

Jet development at $Re = 362$ and $w = 2.63$ cm. The nondimens-
ional times are a) 25.5, b) 26.3, c) 27.1, d) 27.9, e) 28.7,
f) 29.5 and g) 30.3. Note that the growth of the features ma-
rked by the indices 11, 13, 14 and 16 stopped at some point of
time. These features then simply became a mark of dye or bec-
ame part of another vortex pair. 256

Jet development at $Re = 1685$ and $w = 2.57$ cm. The nondimensi-
onal times are a) 15.5, b) 15.9, c) 16.3 and d) 16.8. Vortex
no. 14 in contrast to no. 13 has formed without an apparent
formation of a bulge; in (d) bulge no. 15 has formed. Note
the interaction between the vortices 11 and 12 strating in (b)
and completing in (d). 257

Jet development at $Re = 1697$ and $w = 2.57$ cm. The nondimens-
ional times are a) 14.9, b) 15.3, c) 15.7 and d) 16.1. Enti-
ties 12 an 14 appear as accumulations of dye and produce a
kink in the jet boundary. Kink No. 12 grows into a foldover
before disintegrating and becoming a part of vortex No. 11
which is itself in the process of coalescing with vortex No.
10. Also note the interaction between vortices 8 and 9. 258

Jet development at $Re \approx 280$ in three different jets. Re , w
and t^* are: a) 281, 2.63 cm and 29.7, b) 276, 1.99 cm and
39.3, and c) 280, 1.51 cm and 39.3. Note the pattern of vor-
tex motions in the three jets. 259

64 - Jet develop

and t^* are

38.7, c) 4

65 - Jet develop

sional time

the format

ates from

66 - Unit vortici

w 2.57 cm.

c) 22.1. 1

ces number

67 - Process of

The nondim

d) 16.7. 1

vortex No.

process de

between (7

(10,11) and

that in c)

68 - Jet develop

sional time

unit vortici

vortex No.

growth of

- Jet development at $Re = 420$ in three different jets. Re , w and t^* are: a) 408, 2.63 cm and 38.9, b) 426, 1.99 cm and 38.7, c) 426, 1.99 cm and 57.0, and d) 421, 1.51 cm and 57.0. 260
- Jet development at $Re = 2299$ and $w = 2.57$ cm. The nondimensional times are a) 18.1, b) 18.6, c) 19.1 and d) 19.7. Note the formation of unit vortex motions as the dye streak separates from the nozzle plates. 261
- Unit vortices in the near-field of a slit-jet at $Re = 3401$ and $w = 2.57$ cm. The nondimensional times are a) 20.5, b) 21.3 and c) 22.1. Note the absence of a bulge as large scale vortices number 19 and 20 form. 262
- Process of vortex formation at $Re = 3389$ and $w = 2.57$ cm. The nondimensional times are a) 14.4, b) 15.2, c) 16.0 and d) 16.7. Note: i) asymmetry in the process of formation of vortex No. 13. ii) formation of vortex No. 15 resembles the process described for Re range < 1700 . iii) interaction between (7,8) and 9 in a), between 10 and 11 in a), between (10,11) and 12 in b) and between 13 and 14 in d). Also note that in c) vortex No. 12 has passed through (10,11). . . 263
- Jet development at $Re = 3469$ and $w = 2.57$ cm. The nondimensional times are a) 10.4, b) 11.2 and c) 12.0. Note: i) the unit vortices in the nearfield. ii) the absence of bulge as vortex No. 4 forms in b). iii) bulge formation precedes the growth of vortices 3, 5 and 6. 264

69 - Interaction

$w = 1.99$ cm

c) 52.5, d)

ces 7 and 8

over, (7,8)

the large 1

(6,7,8) and

served in a

ich formed

sintegrated

70 - Continuation

re 58. The

16.2. Note

(10,11) and

interaction

71 - One sided p

1001 and w

b) 10.6, c)

72 - Simultaneous

The nondime

73 - First stage

nondimensio

27.5. Note

joined by 2

Also, 28 an

Interaction between symmetric vortex motions at $Re = 678$ and $w = 1.99$ cm. The nondimensional times are a) 50.2, b) 51.3, c) 52.5, d) 53.6, e) 54.8 and f) 55.9. Starting in b) vortices 7 and 8 began to interact and before the pairing was over, (7,8) started to interact with vortex No. 6 in d). Note the large longitudinal spacing in f) between the conglomerate (6,7,8) and the vortex No. 9; similar spacing can also be observed in a). The figure also shows that the bulge No. 10 which formed in b) did not become a vortex pair; rather, it disintegrated into a mark of dye by $t^* = 54.8$ in f). 265

Continuation of the sequence of photographs presented in Figure 58. The nondimensional times are a) 15.4, b) 15.8 and c) 16.2. Note the asymmetry during the interaction between (10,11) and 12 in a) and the return of symmetry in c) as the interaction is completed. 266

One sided pairing event between pairs (3,4) and (5,6) at $Re = 1001$ and $w = 2.57$ cm. The nondimensional times are: a) 10.0, b) 10.6, c) 11.1 and d) 11.6. 267

Simultaneous coalescence of three vortex pairs at $Re = 3401$. The nondimensional times are a) 22.1, b) 22.9 and c) 23.6. 268

First stage of formation of five pairings at $Re = 3401$. The nondimensional times are a) 25.2, b) 26.0, c) 26.7 and d) 27.5. Note that vortex pairs 24 and 25 pair and they are joined by 26 in b) and by 27 at some time between c) and d). Also, 28 and 29 are undergoing pairing in d). 269

74 - Second stage

$w = 2.57$ cm

c) 29.8 and

conglomerat

med which c

75 - Loss of sym

$= 2.57$ cm.

c) 15.2 and

are beginnin

vortices 11

of the cent

erved in d)

in c) and c

centerline.

76 - Loss of sym

instability

1571 and th

c) 10.7 and

tric, two-c

77 - Reorganizat

sional time

ex pair num

a) and b) t

cence and b

dimensional

Second stage of formation of five pairings at $Re = 3401$ and $w = 2.57$ cm. The nondimensional times are a) 28.3, b) 29.1, c) 29.8 and d) 30.6. The pair (28,29) begins to approach the conglomerate (24-27) in a) and by d) a new pair has been formed which comprises of five pairings.	270
Loss of symmetry due to asymmetric pairing at $Re = 1004$ and $w = 2.57$ cm. The nondimensional times are a) 13.7, b) 14.5, c) 15.2 and d) 16.0. In a) the vortices of the pair (8-10) are beginning to displace with respect to one another, while, vortices 11 and 12 are about to pair on the right hand side of the centerline. Similarly, asymmetric pairing can be observed in d). Note, however, that the newly forming vortices in c) and d) are symmetrically located with respect to the centerline.	271
Loss of symmetric vortex street due to the three dimensional instability of the two-dimensional vortex cores. Flow $Re = 1571$ and the nondimensional times are a) 8.5, b) 9.6, c) 10.7 and d) 11.8. Note the reestablishment of the symmetric, two-dimensional vortex pattern in d).	272
Reorganization of vortex motions at $Re = 1027$. The nondimensional times are a) 11.0, b) 11.9, c) 12.7 and d) 13.6. Vortex pair numbers (7,8) and 9 have been tilted in a). Between a) and b) the pairs (7,8), 9 and 10 begin to undergo coalescence and by d) they appear to have regained the two-dimensional character.	273

78 - A represent

enter durin

$E_{NM}(t)$ are

The output

mes at whic

79 - A typical

digitized.

esced pair:

coma as 9,

80 - Schematic

pair in the

start of th

81 - Four possi

respect to

ne. The i

82 - Scheme for

with respec

$(k+1)$. Th

The curly

in determin

indicates

83 - Schematic

overall es

independent

slope of th

A representative sample of the data recorded by the A/D converter during a flow visualization experiment. $E_I(t)$ and $E_{NH}(t)$ are the voltages corresponding to $p_I(t)$ and $p_{NH}(t)$. The output, $C(t)$, of the comparator circuit represents the times at which photographs were taken. 274

A typical representation of the photographs that have been digitized. Each vortex pair is marked by a number. The coalesced pairs are designated by two numbers separated by a comma as 9,10 in this photograph. 275

Schematic representation of the location of the k th vortex pair in the j th photograph which is at time t_j after the start of the experiment. 276

Four possible cases of positions of the k th vortex pair with respect to the plane of observation at x_0 from the exit plane. The index j denotes the picture number at time t_j . . 277

Scheme for determining the spacing L_k of the k th vortex pair with respect to the neighboring vortex pairs: $(k-1)$ and $(k+1)$. The index j denotes the photograph number at time t_j . The curly bracket indicates the vortex pairs which are used in determining L_k . The solid line at x_0 from the exit plane indicates the plane of observation. 278

Schematic representation of the technique used to find the overall estimates of λ^* and u_c^* from the measured St_F and the independent estimates of L_k^* and c_k^* of each vortex pair. The slope of the line OC is equal to St_F 279

84 - Space-ti

run. Up

over 10

ces is 1

85 - Streamw

control

.05, 0.1

86 - Distribu

C_K^* of τ

0.05 +, 2

are repre

indicate

87 - Streamw

T_W See

88 - Distribu

upon St.

89 - Distribu

L_K^* betw

For lege

90 - Streamw

T_W For

91 - Residual

combinat

92 - Comparis

differer

Space-time plot of vortices from the start of the experimental run. Up to 5 vortices merge with the starting vortex pair over $10 < t^* < 18$. Around $t^* = 35$, a large cluster of vortices is formed due to 3 sequential pairings. 280

Streamwise distribution of St_F for five combinations of the control parameters T_p, T_w : 0.05, .05 + ; 0.1, 0.1 * ; .05, 0.1 x; 0.1, 0.05 o, and 0.1, 0.2 v. 281

Distribution of mean and rms values of convection velocity, c_k^* , of vortices for three combinations of T_p and T_w : 0.05, 0.05 +, z ; 0.1 , 0.1 *, s and 0.1, 0.2 v, w. The mean values are represented by the first symbol, whereas the second symbol indicates the standard deviation from the mean value. . . 282

Streamwise distribution of u_c^* for five combinations of T_p and T_w . See Figure 85 for legend. 283

Distribution of the estimate of longitudinal spacing L^* based upon St_F and \bar{c}^* . See Figure 85 for legend. 284

Distribution of mean and rms values of longitudinal spacing, L_k^* , between vortices for three combinations of T_p and T_w . For legend see Figure 86. 285

Streamwise distribution of λ^* for five combinations of T_p and T_w . For legend see Figure 85. 286

Residual of the regression of St_F through c_k^* and L_k^* for five combinations of T_p and T_w . For legend see Figure 85. . . 287

Comparison of St_F with local Strouhal number based upon the difference in the passage time, δt_k , between two vortex pairs.

c: Strouhal nu

connects the va

93 - Space-time plot

94 - Space-time plot

95 - Space-time plot

96 - Space-time plot

97 - Space-time plot

98 - Normalized late

over the Re ran

tions, the midd

plotted at 1 st

99 - Normalized late

over the Re ra

100 - Normalized lat

over the Re ra

101 - Normalized lat

over the Re ra

102 - Normalized lat

over the Re ra

.....

103 - Normalized lat

over the Re ra

.....

104 - Normalized lat

over the Re ra

c: Strouhal number based upon δt_k , X: St_F . The solid line connects the values of St_F 288

Space-time plot of vortices at $Re = 269$ and $w = 1.99$ cm. . 289

Space-time plot of vortices at $Re = 696$ and $w = 2.63$ cm. . 290

Space-time plot of vortices at $Re = 1269$ and $w = 1.40$ cm. 291

Space-time plot of voritces at $Re = 1697$ and $w = 2.57$ cm. 292

Space-time plot of voritces at $Re = 3401$ and $w = 2.57$ cm. 293

Normalized lateral spreading between vortices of given pairs over the Re range of 269-285. At selective streamwise locations, the middle x represents \bar{d}^* and the outer x's have been plotted at 1 standard deviation form the mean value. . . . 294

Normalized lateral spreading between vortices of given pairs over the Re range of 362-525. See Figure 98 for details. 295

Normalized lateral spreading between vortices of given pairs over the Re range of 640-698. See Figure 98 for details. 296

Normalized lateral spreading between vortices of given pairs over the Re range of 930-1074. See Figure 98 for details. 297

Normalized lateral spreading between vortices of given pairs over the Re range of 1257-1272. See Figure 98 for details. 298

Normalized lateral spreading between vortices of given pairs over the Re range of 1571-1697. See Figure 98 for details. 299

Normalized lateral spreading between vortices of given pairs over the Re range of 2949-3469. See Figure 98 for details.

.....

105 - Statistical det

the Re range 26

x/w value; *:

square fit to t

106 - Statistical det

the Re range of

107 - Statistical det

the Re range of

108 - Statistical det

the Re range of

109 - Statistical det

the Re range of

110 - Statistical det

the Re range of

111 - Statistical det

the Re range of

112 - Normalized asyn

et in the Re r

.....

113 - Normalized asyn

et in the Re r

.....

114 - Normalized asyn

et in the Re r

.....	300
Statistical details of the lateral spreading of vortices in the Re range 269-285. +: The rms of the population at each x/w value; *: the ratio of the residual of the least square fit to the rms of the population denoted by +.	301
Statistical details of the lateral spreading of vortices in the Re range of 362-525. For legend see Figure 105.	302
Statistical details of the lateral spreading of vortices in the Re range of 640-698. For legend see Figure 105.	303
Statistical details of the lateral spreading of vortices in the Re range of 930-1074. For legend see Figure 105.	304
Statistical details of the lateral spreading of vortices in the Re range of 1257-1272. For legend see Figure 105.	305
Statistical details of the lateral spreading of vortices in the Re range of 1571-1697. For legend see Figure 105.	306
Statistical details of the lateral spreading of vortices in the Re range of 2949-3469. For legend see Figure 105.	307
Normalized asymmetry estimate of the "symmetric" vortex street in the Re range of 269-285. See Figure 98 for details.	308
Normalized asymmetry estimate of the "symmetric" vortex street in the Re range of 362-525. See Figure 98 for details.	309
Normalized asymmetry estimate of the "symmetric" vortex street in the Re range of 640-698. See Figure 98 for details.	

.....
115 - Normalized asy

 eet in the Re

.....
116 - Normalized asy

 eet in the Re

.....
117 - Normalized asy

 eet in the Re

.....
118 - Normalized asy

 eet in the Re

.....
119 - Statistical de

 street over th

 details. .

.....
120 - Statistical de

 street over th

 details. .

.....
121 - Statistical de

 street over th

 details. .

.....
122 - Statistical de

 street over th

 details. .

Normalized asymmetry estimate of the "symmetric" vortex street in the Re range of 930-1074. See Figure 98 for details.	310
Normalized asymmetry estimate of the "symmetric" vortex street in the Re range of 1257-1272. See Figure 98 for details.	311
Normalized asymmetry estimate of the "symmetric" vortex street in the Re range of 1571-1697. See Figure 98 for details.	312
Normalized asymmetry estimate of the "symmetric" vortex street in the Re range of 2949-3469. See Figure 98 for details.	313
Statistical details of the symmetry of the "symmetric" vortex street over the Re range of 269-285. See Figure 105 for details.	314
Statistical details of the symmetry of the "symmetric" vortex street over the Re range of 362-525. See Figure 105 for details.	315
Statistical details of the symmetry of the "symmetric" vortex street over the Re range of 640-698. See Figure 105 for details.	316
Statistical details of the symmetry of the "symmetric" vortex street over the Re range of 930-1074. See Figure 105 for details.	317
Statistical details of the symmetry of the "symmetric" vortex street over the Re range of 930-1074. See Figure 105 for details.	318

123 - Statistical de
street over th
details. .

124 - Statistical de
street over th
details. .

125 - Statistical de
street over th
details. .

126 - Distribution o
sugar mixture
and the jet wi
b: 276, 1.99;

127 - Distribution o
sugar mixture
ignated by h.
f: 362, 2.63;
j: 408, 2.63;
n: 426, 1.99.

128 - Distribution o
used as the wo
widths in cm a

129 - Distribution o
used as the wo
symbols q, r a

Statistical details of the symmetry of the "symmetric" vortex street over the Re range of 1257-1272. See Figure 105 for details.	319
Statistical details of the symmetry of the "symmetric" vortex street over the Re range of 1571-1697. See Figure 105 for details.	320
Statistical details of the symmetry of the "symmetric" vortex street over the Re range of 2949-3469. See Figure 105 for details.	321
Distribution of St_F in the Re range of 269-285. A water-sugar mixture was used in all these cases. The Re values and the jet widths in cm are 0: 269, 1.99; a: 269, 1.99; b: 276, 1.99; c: 277, 1.51; d: 280, 1.51; e: 285, 2.63.	322
Distribution of St_F in the Re range of 362-426. A water-sugar mixture was used in all cases except for the case designated by h. The Re values and the jet widths in cm are: f: 362, 2.63; g: 373, 2.63; h: 396, 1.4; i: 407, 1.51; j: 408, 2.63; k: 412, 1.51; l: 421, 1.51; m: 423, 1.99; n: 426, 1.99.	323
Distribution of St_F in the Re range of 510-525. Water was used as the working fluid. The Re values and the jet widths in cm are: o: 525, 1.4; p: 510, 1.4.	324
Distribution of St_F in the Re range of 640-700. Water was used as the working fluid for the cases designated by the symbols q, r and s. For the cases designated by t, u and v	

a water-sugar

widths in cm a

t: 679, 1.99;

130 - Distribution o

was used as th

case designate

cm are: w: 93

2.57; B: 1004

1074, 2.57.

131 - Distribution o

was used as th

widths in cm a

1272, 1.4.

132 - Distribution o

was used as th

widths in cm a

2.57 and L: 16

133 - Distribution o

was used as th

widths in cm a

2.57, P: 3401,

134 - Distribution o

ratio, B/w, as

were derived f

135 - Distribution o

a water-sugar mixture was used. The Re values and the jet widths in cm are: q: 640, 1.4; r: 640, 1.4; s: 640, 1.4; t: 679, 1.99; u: 696, 2.63 and v: 698, 1.99. 325

Distribution of St_F in the Re range of 930-1074. Water was used as the working fluid in all cases except in the case designated by x. The Re values and the jet width in cm are: w: 930, 1.4; x: 980, 2.63; y: 1044, 1.4; A: 1001, 2.57; B: 1004, 2.57; C: 1027, 2.57; D: 1063, 2.57 and E: 1074, 2.57. 326

Distribution of St_F in the Re range of 1257-1272. Water was used as the working fluid. The Re values and the jet widths in cm are: F: 1257, 1.4; G: 1269, 1.4 and H: 1272, 1.4. 327

Distribution of St_F in the Re range of 1570-1700. Water was used as the working fluid. The Re values and the jet widths in cm are: I: 1571, 2.57; J: 1580, 2.57; K: 1685, 2.57 and L: 1697, 2.57. 328

Distribution of St_F in the Re range of 2949-3400. Water was used as the working fluid. The Re values and the jet widths in cm are: M: 2949, 2.57; N: 2964, 2.57; O: 3389, 2.57, P: 3401, 2.57 and Q: 3469, 2.57. 329

Distribution of St_F as a function of Re with the aspect ratio, B/w, as a parameter. Note that these St_F values were derived from the rate of formation of bulges. . . . 330

Distribution of St_θ as a function of Re with B/w as a

parameter. θ

the rate of f

136 - Distribution o

parameter. Th

137 - Distribution o

parameter. Th

138 - Distribution o

B/w as a paran

Beavers and W

139 - Distribution o

end see Figure

of all sizes.

140 - Distribution o

end see Figure

141 - Distribution o

end see Figure

142 - Distribution o

end see Figure

143 - Distribution o

end see Figure

144 - Distribution o

gend see Figure

145 - Distribution o

gend see Figure

146 - Distribution o

parameter. θ_0 and U_0 have been used to nondimensionalize the rate of formation of bulges.	331
6 - Distribution of St_F as a function of Re with B/w as a parameter. These values of St_F were recorded at $x/w=2.2$	332
7 - Distribution of St_F as a function of Re with B/w as a parameter. These values of St_F were recorded at $x/w=2.7$	333
8 - Distribution of Strouhal number as a function of Re with B/w as a parameter. This figure is a reproduction of Beavers and Wilson (1970) data.	334
9 - Distribution of $u_c^*(x^*)$ in the Re range of 269-285. For legend see Figure 126. Note the good collapse of data for jets of all sizes.	335
0 - Distribution of $u_c^*(x^*)$ in the Re range of 362-426. For legend see Figure 127.	336
1 - Distribution of $u_c^*(x^*)$ in the Re range of 510-525. For legend see Figure 128.	337
2 - Distribution of $u_c^*(x^*)$ in the Re range of 640-700. For legend see Figure 129.	338
3 - Distribution of $u_c^*(x^*)$ in the Re range of 930-1074. For legend see Figure 130.	339
4 - Distribution of $u_c^*(x^*)$ in the Re range of 1257-1272. For legend see Figure 131.	340
5 - Distribution of $u_c^*(x^*)$ in the Re range of 1570-1700. For legend see Figure 132.	341
6 - Distribution of $u_c^*(x^*)$ in the Re range of 2949-3469. For legend see Figure 133.	342

- gend see Figure
- 147 - Distribution
end see Figure
of various si.
(shown in Figure
- 148 - Distribution
end see Figure
- 149 - Distribution
end see Figure
- 150 - Distribution
end see Figure
- 151 - Distribution
end see Figure
- 152 - Distribution
legend see Figure
- 153 - Distribution
legend see Figure
- 154 - Distribution
legend see Figure
- 155 - Slopes of the
ction of Re.
as were used in
- 156 - Intercepts of
of Re.
- 157 - Distribution of

gend see Figure 133.	342
- Distribution of $\lambda^*(x^*)$ in the Re range of 269-285. For legend see Figure 126. Note that the variations in λ^* for jets of various sizes are consistent with the variations in St_F (shown in Figure 126) and u_c^* (shown in Figure 139). . . .	343
- Distribution of $\lambda^*(x^*)$ in the Re range of 362-426. For legend see Figure 127.	344
- Distribution of $\lambda^*(x^*)$ in the Re range of 510-525. For legend see Figure 128.	345
- Distribution of $\lambda^*(x^*)$ in the Re range of 640-700. For legend see Figure 129.	346
- Distribution of $\lambda^*(x^*)$ in the Re range of 930-1074. For legend see Figure 130.	347
Distribution of $\lambda^*(x^*)$ in the Re range of 1257-1272. For legend see Figure 131.	348
- Distribution of $\lambda^*(x^*)$ in the Re range of 1570-1700. For legend see Figure 132.	349
- Distribution of $\lambda^*(x^*)$ in the Re range of 2949-3469. For legend see Figure 133.	350
Slopes of the streamwise distribution of $\lambda^*(x^*)$ as a function of Re. The data have been grouped in the same ranges as were used in the plots St_F , u_c^* and λ^*	351
Intercepts of streamwise distribution of λ^* as a function of Re.	352
Distribution of the estimate of nondimensional location of	

the formation

158 - Distribution

of Re in jets

mbols represe

21.7 ($\tau_N/w =$

with $B/w = 10$

C_D for an inv

159 - Schematic rep

ersals. For

raised or low

veys the flow

160 - Nondimensiona

of the jet at

161 - Nondimensiona

of the jet at

162 - Nondimensiona

of the jet at

163 - Nondimensiona

of the jet at

164 - Nondimensiona

of the jet at

165 - Nondimensiona

of the jet at

166 - Nondimensiona

of the jet at

the formation of bulges as a function of Re.	353
- Distribution of discharge coefficient, C_D , as a function of of Re in jets with two different slit widths. The closed sy- mbols represent the measurements made in a jet with $B/w =$ 21.7 ($t_N/w = 1$) and the open symbols represent the case with $B/w = 10.8$ ($t_N/w \approx 0.5$). The solid line represents C_D for an inviscid jet.	354
- Schematic representation of the mechanism for velocity trav- ersals. For longitudinal surveys the base of the LDA was raised or lowered using plastic blocks. For lateral sur- veys the flow facility was traversed across the LDA. . .	355
- Nondimensional velocity time histories along the centerline of the jet at $Re = 509$ and $w = 1.27$ cm.	356
- Nondimensional velocity time histories along the centerline of the jet at $Re = 1011$ and $w = 2.57$ cm.	357
- Nondimensional velocity time histories along the centerline of the jet at $Re = 1021$ and $w = 2.57$ cm.	358
- Nondimensional velocity time histories along the centerline of the jet at $Re = 1293$ and $w = 2.57$ cm.	359
- Nondimensional velocity time histories along the centerline of the jet at $Re = 1328$ and $w = 2.57$ cm.	360
- Nondimensional velocity time histories along the centerline of the jet at $Re = 1527$ and $w = 2.57$ cm.	361
- Nondimensional velocity time histories along the centerline of the jet at $Re = 2308$ and $w = 2.57$ cm.	362

167 - Nondimensional

of the jet at

168 - Normalized me

of the jet.

city distribu

169 - Schematic rep

jectory of the

sents the pat

170 - Distribution

tuations along

ithmic plot.

171 - Dependence of

$\log(\tilde{u}(x,y=0)/$

the distribut

172 - Nondimensional

$x/w=1$ and $Re=$

173 - Nondimensional

jet at $x/w=2.4$

174 - Nondimensional

jet at $x/w=1$ a

175 - Nondimensional

jet at $x/w=2.4$

176 - Samples of vel

locations: $(x$

were inferred

- Nondimensional velocity time histories along the centerline of the jet at $Re = 2854$ and $w = 2.57$ cm.	363
- Normalized mean velocity distribution along the centerline of the jet. The solid line represents the inviscid velocity distribution.	364
- Schematic representation of the influence of Re on the trajectory of the separating streamline. The curve 1-2 represents the path of integration normal to the streamlines.	365
- Distribution of the intensity of streamwise velocity fluctuations along the centerline of the jet on a logarithmic plot.	366
- Dependence of the slope of streamwise distribution of $\log(\bar{u}(x,y=0)/U_0)$ on Reynolds number. Figure 170 presents the distribution at each value of Re	367
- Nondimensional velocity time histories across the jet at $x/w=1$ and $Re=1600$	368
- Nondimensional velocity time histories across the jet at jet at $x/w=2.4$ and $Re=1600$	369
- Nondimensional velocity time histories across the jet at jet at $x/w=1$ and $Re=3000$	370
- Nondimensional velocity time histories across the jet at jet at $x/w=2.4$ and $Re=3000$	371
Samples of velocity time histories at $Re=1600$ and from two locations: $(x/w,y/w)=(1,\pm 0.58)$, at which flow reversals were inferred to have taken place.	372

177 - Mean velocity

values of Re.

reversals tool

178 - Distribution

tions across

179 - Mean velocity

values of Re.

reversals tool

180 - Distribution

tions across

181 - Normalized mea

represents The

data. The dat

termining the

182 - Normalized mea

represents The

data. The dat

termining the

183 - Normalized mea

represents The

The data in cl

ing the param

184 - Power spectral

$(x/w, y/w) = (0.8$

185 - Power spectral

- Mean velocity distribution across the jet at $x/w=1$ and two values of Re . The data from the regions where velocity reversals took place are not included here.	373
- Distribution of the intensity of streamwise velocity fluctuations across the jet at $x/w=1$ and two values of Re	374
- Mean velocity distribution across the jet at $x/w=2.4$ and two values of Re . The data from the regions where velocity reversals took place are not included here.	375
- Distribution of the intensity of streamwise velocity fluctuations across the jet at $x/w=2.4$ and two values of Re	376
- Normalized mean velocity profile at $x/w=1$. The solid line represents The Montgomery profile fitted to the measured data. The data in closed symbols were not included in determining the two parameters of the Montgomery profile. . . .	377
- Normalized mean velocity profile at $x/w=2.4$. The solid line represents The Montgomery profile fitted to the measured data. The data in closed symbols were not included in determining the two parameters of the Montgomery profile. . . .	378
- Normalized mean velocity profile at $x/w=2.4$. The solid line represents The Bickley profile fitted to the measured data. The data in closed symbols were not included in determining the parameter.	379
Power spectral density function of streamwise velocity at $(x/w, y/w)=(0.86, 0)$ and $Re \approx 1260$	380
Power spectral density function of streamwise velocity at	

$$(x/w, y/w) = (1,$$

186 - A comparison

streamwise ve

two different

represents th

and NF indica

not used.

187 - A comparison

streamwise ve

two different

details.

188 - A comparison

nant fluctuat

ions. The cl

filling devic

filling devic

189 - A comparison

filling condi

190 - A comparison

two different

ails.

191 - Plots of dist

velocity fluc

and over a wi

192 - Distribution

($x/w, y/w$)=(1,0) and $Re \approx 1640$	381
- A comparison of the power spectral density function of the streamwise velocity at $Re \approx 960$ and at ($x/w, y/w$)=(2.2,0) for two different filling conditions. The curve marked with F represents the case in which the filling device was used and NF indicates the case in which the filling device was not used.	382
- A comparison of the power spectral density function of the streamwise velocity at $Re \approx 2000$ and at ($x/w, y/w$)=(2.2,0) for two different filling conditions. See Figure 186 for details.	383
- A comparison of the Re dependence of the frequency of dominant fluctuations in $u(t)$ for two different filling conditions. The closed symbols represent the case in which the filling device was used and the open symbols in which the filling device was not used.	384
- A comparison of the Re dependence of C_D for two different filling conditions. See Figure 188 for details.	385
- A comparison of the Re dependence of intensity of $u(t)$ for two different filling conditions. See Figure 188 for details.	386
- Plots of distribution of normalized intensity of streamwise velocity fluctuations as a function of frequency at $x/w=1$ and over a wide range of Re	387
Distribution of St_V as a function of Re at $x/w=1$. The das-	

hed line rep

193 - Distribution
dashed line

194 - A comparison
nant fluctuat
widths at x/y

195 - Streamwise d
uations at R

196 - Streamwise d
uations at R

197 - Streamwise d
uations at R

198 - Autospectra
the transiti
ion of mutua
 $St_v = 0.37$ at
199 - Eigenvalues
represent th
eigenvalue p

200 - Eigenvalues
Figure 199 f

201 - Eigenvalues
199 for deta

202 - Normalized p
streamwise l

- hed line represents the average value of $St_V=0.70$ 388
- Distribution of St_V as a function of Re at $x/w=2.2$. The dashed line represents the average value of $St_V=0.52$. . . 389
- A comparison of the Re dependence of the frequency of dominant fluctuations of $u(t)$ for two jets with different slit widths at $x/w=2.2$ 390
- Streamwise distribution of the intensity of velocity fluctuations at $Re=1000$ and at three different values of St_V . 391
- Streamwise distribution of the intensity of velocity fluctuations at $Re=1300$ and at three different values of St_V . 392
- Streamwise distribution of the intensity of velocity fluctuations at $Re=2300$ and at three different values of St_V . 393
- Autospectra of $u(t)$ in a jet with $w=1.27$ cm and $Re=510$. Note the transition in the neighborhood of $x/w=1.34$ - the "region of mutual interaction" - from $St_V=0.71$ at $x/w=0.9$ to $St_V=0.37$ at $x/w=2.12$ 394
- Eigenvalues for the Montgomery profile at $x/w=1$. A and B represent the symmetric and asymmetric solutions of the eigenvalue problem. 395
- Eigenvalues of the Montgomery profile at $x/w=2.4$. See Figure 199 for details. 396
- Eigenvalues of the Bickley profile at $x/w=2.4$. See Figure 199 for details. 397
- Normalized pressure and velocity fluctuations at three streamwise locations: $s=0.5, 1.0$ and 1.5 with $-\alpha_1=3.5$,

$$\alpha = 10.4, \omega = 4$$

A.1 - Details of the

B.1 - Time histories

.....

B.2 - An illustration

$E_1(t)$, and the

C.1 - Space-time plots

.....

C.2 - Space-time plots

.....

C.3 - Space-time plots

.....

C.4 - Space-time plots

.....

C.5 - Space-time plots

.....

C.6 - Space-time plots

.....

C.7 - Space-time plots

.....

C.8 - Space-time plots

.....

C.9 - Space-time plots

.....

C.10 - Space-time plots

$\alpha_r=10.4$, $\omega=4.4$ and $u_a=6.2\times 10^{-4}$.	398
- Details of the mechanism for actuating the bleed valve.	411
- Time histories of the voltages recorded during an experiment.	412
- An illustration of the regression of the measured voltage, $E_I(t)$, and the corresponding residual.	413
- Space-time plot of vortices (R040F) at $Re=269$ and $w=1.99$ cm.	414
- Space-time plot of vortices (R040A) at $Re=276$ and $w=1.99$ cm.	415
- Space-time plot of vortices (R040D) at $Re=277$ and $w=1.51$ cm.	416
- Space-time plot of vortices (R040B) at $Re=280$ and $w=1.51$ cm.	417
- Space-time plot of vortices (R040I) at $Re=285$ and $w=2.63$ cm.	418
- Space-time plot of vortices (R060I) at $Re=361$ and $w=2.63$ cm.	419
- Space-time plot of vortices (R060H) at $Re=373$ and $w=2.63$ cm.	420
- Space-time plot of vortices (R090P) at $Re=396$ and $w=1.40$ cm.	421
- Space-time plot of vortices (R060E) at $Re=407$ and $w=1.51$ cm.	422
- Space-time plot of vortices (R060G) at $Re=408$ and $w=2.63$ cm.	

.....
C.11 - Space-time p

.....
C.12 - Space-time p

.....
C.13 - Space-time p

.....
C.14 - Space-time p

.....
C.15 - Space-time p

.....
C.16 - Space-time p

.....
C.17 - Space-time p

.....
C.18 - Space-time p

.....
C.19 - Space-time p

.....
C.20 - Space-time p

.....
C.21 - Space-time p

.....
C.22 - Space-time p

.....	423
11 - Space-time plot of vortices (R060B) at $Re=412$ and $w=1.51$ cm.	424
.....	425
12 - Space-time plot of vortices (R060D) at $Re=421$ and $w=1.51$ cm.	426
.....	427
13 - Space-time plot of vortices (R060A) at $Re=423$ and $w=1.99$ cm.	428
.....	429
14 - Space-time plot of vortices (R060F) at $Re=426$ and $w=1.99$ cm.	430
.....	431
15 - Space-time plot of vortices (R090V) at $Re=510$ and $w=1.40$ cm.	432
.....	433
16 - Space-time plot of vortices (R090U) at $Re=525$ and $w=1.40$ cm.	434
.....	435
17 - Space-time plot of vortices (R090R) at $Re=640$ and $w=1.40$ cm.	436
.....	437
18 - Space-time plot of vortices (R090S) at $Re=640$ and $w=1.40$ cm.	438
.....	439
19 - Space-time plot of vortices (R090T) at $Re=640$ and $w=1.40$ cm.	440
.....	441
20 - Space-time plot of vortices (R100C) at $Re=679$ and $w=1.99$ cm.	442
.....	443
1 - Space-time plot of vortices (R100D) at $Re=698$ and $w=1.99$ cm.	444
.....	445
2 - Space-time plot of vortices (R180E) at $Re=930$ and $w=1.40$ cm.	446
.....	447

C.23 - Space-time p

w=2.57 cm.

C.24 - Space-time p

w=2.57 cm.

C.25 - Space-time p

w=2.57 cm.

C.26 - Space-time p

w=1.40 cm.

C.27 - Space-time p

w=2.57 cm.

C.28 - Space-time p

w=2.57 cm.

C.29 - Space-time p

w=1.40 cm.

C.30 - Space-time p

w=1.40 cm.

C.31 - Space-time p

w=2.57 cm.

C.32 - Space-time p

w=2.57 cm.

C.33 - Space-time p

w=2.57 cm.

C.34 - Space-time p

w=2.57 cm.

C.35 - Space-time p

23 - Space-time plot of vortices (U090A000) at Re=1001 and w=2.57 cm.	436
24 - Space-time plot of vortices (U090A001) at Re=1004 and w=2.57 cm.	437
25 - Space-time plot of vortices (U090C002) at Re=1027 and w=2.57 cm.	438
26 - Space-time plot of vortices (R180D) at Re=1044 and w=1.40 cm.	439
27 - Space-time plot of vortices (U090C000) at Re=1063 and w=2.57 cm.	440
28 - Space-time plot of vortices (U090C001) at Re=1074 and w=2.57 cm.	441
29 - Space-time plot of vortices (R180C) at Re=1257 and w=1.40 cm.	442
30 - Space-time plot of vortices (R180A) at Re=1272 and w=1.40 cm.	443
31 - Space-time plot of vortices (U150K001) at Re=1571 and w=2.57 cm.	444
32 - Space-time plot of vortices (U150K000) at Re=1580 and w=2.57 cm.	445
33 - Space-time plot of vortices (U150L000) at Re=1685 and w=2.57 cm.	446
34 - Space-time plot of vortices (U220C000) at Re=2299 and w=2.57 cm.	447
35 - Space-time plot of vortices (U300I001) at Re=2949 and	

w=2.57 cm.

C.36 - Space-time p

w=2.57 cm.

C.37 - Space-time p

w=2.57 cm.

C.38 - Space-time p

w=2.57 cm.

w=2.57 cm.	448
C.36 - Space-time plot of vortices (U300I002) at Re=2964 and	
w=2.57 cm.	449
C.37 - Space-time plot of vortices (U300G002) at Re=3389 and	
w=2.57 cm.	450
C.38 - Space-time plot of vortices (U300G000) at Re=3469 and	
w=2.57 cm.	451

A_j	area of
A_{NH}	area of
A_r	area of
A_v	time depe
a_k	differenc
a	parameter
b	parameter
b	half width
B	length of
C_D	Discharge
C_{Dv}	Discharge
c	complex p
c_k	measured
\bar{c}	mean cor
	perimenta
D	material
D	partial d
d_k	time dep
	kth pair
f	frequency
f_k	kth freq
	time seri
f_T	passage
	on counti

Nomenclature

A_j	area of slit jet = Bw
A_{NH}	area of nozzle housing = BH
A_r	area of receiver
A_v	time dependent area of the bleed valve
A_k	difference in axial location of the two vortices of a pair
α	parameter in the equation for the Bickley jet
β	parameter in the equation for the Bickley jet
b	half width of the jet
L	length of nozzle
C_d	Discharge coefficient of the slit-jet
C_{dv}	Discharge coefficient of the bleed valve
c	complex phase speed; $c = c_r + ic_i$
c_k	measured convection speed of k th vortex motion
\bar{c}	mean convection speed of vortex motions for a given experimental run
d/dt	material derivative
$\partial/\partial y$	partial derivative in the y direction
Δy_k	time dependent lateral spacing between the vortices of the k th pair
ω	frequency or rate of rotation
ω_k	k th frequency component of the autospectrum of a discrete time series
ω_x	passage frequency of vortex motions at a given x and based on counting from a sequential photographic data

f_i	frequency
	instabil:
f_T	frequency
	autospect
$\tilde{G}(f_k)$	estimate
g	accelerat
H	distance
$H(\lambda)$	shape fac
h	sampling
h_{NH}	time depe
h_r	time depe
h_{eq}	liquid le
h_p	time depe
i,j,k	unit vect
i	$\sqrt{-1}$
j	$\sqrt{-1}$
k	location
L	estimate
L_k	measured
	vortex pa
\bar{L}	mean valu
n	ratio of
N_i	mass of a
N	total num
N	total num
n	distance

- f_I frequency of the most unstable disturbance predicted by the instability calculations
- f_F frequency of the dominant fluctuation determined from the autospectrum of the measured velocity $u(t)$
- $\bar{G}(f_k)$ estimate of power spectral density function at frequency f_k
- g acceleration due to gravity
- H distance between the walls of the channel-like plenum
- $H(\lambda)$ shape factor as a function of $\lambda = \frac{\theta^2 U_1'}{\nu}$; used by White (1974)
- h sampling time interval in seconds
- h_{NH} time dependent head of liquid in the nozzle housing
- h_r time dependent head of liquid in the receiver
- h_{eq} liquid level in the system before the plenum is charged
- h_p time dependent height of piston from the reference location
- i, j, k unit vectors in the x, y and z directions
- $\sqrt{-1}$
- $\sqrt{-1}$
- location of half source in the t-plane; see equation (11)
- estimate of spacing between vortex motions based on \bar{c} and f_F
- measured spacing between vortices at x_0 around the kth vortex pair
- mean value of spacing at x_0 for a given experimental run
- ratio of H to the width of jet at vana contracta
- mass of air in the deformable control volume CV_2
- total number of vortices in a given experimental run
- total number of data points in a time series
- distance normal to s in the streamwise coordinate system

n	time dep
n	index of
p	pressure
p_0	pressure
p'	disturba
$p_k(y)$	function
p_k	kinetic
\bar{p}_k	time ave
p'_k	fluctuat
p_l	pressure
p_{NH}	pressure liquid
p_{atm}	atmosphe
p_{amb}	ambient
Q	magnitud
q	flow rat
q_0	time dep
r	radius
r	ratio of
Re	Reynolds
Re_0	Reynolds
Re_ϕ	Reynolds
s	streamwi
S	sum of s
St	Strouhal

n	time dependent index of the number of motor steps
n	index of refraction
p	pressure
p_0	pressure at vena contracta where $u_1 = U_0$
p'	disturbance pressure function
$p_a(y)$	function describing y dependence of $p'(x,y,z)$
p_k	kinetic pressure; $p_k = p + \rho gh$
\bar{p}_k	time average value of p_k
p'_k	fluctuating component of p_k
p_I	pressure in the cup of the volume flow sensor (VFS)
p_{NH}	pressure in the nozzle housing above the surface of the liquid
p_{atm}	atmospheric pressure
p_{amb}	ambient pressure
Q	magnitude of velocity $V = u_1 + iu_2$
q	flow rate through the slit-jet
q_b	time dependent flow rate through the bleed valve
r	radius
r	ratio of widths of two jets
Re	Reynolds number based on w and $\langle U \rangle$
Re_0	Reynolds number based on w and U_0
Re_θ	Reynolds number based on θ
s	streamwise distance in the streamwise coordinate system
t	sum of squares of δ_k
St	Strouhal number; $St = fw / \langle U \rangle$

St_F	Strouhal
St_I	Strouhal
St_V	Strouhal
St_0	Strouhal
St_y	Strouhal
T	time per velocity
T_d	total da
T_v	tolerance a vortex
T_p	tolerance whether
t	time in
t_k	kth time
t_k^p	passage
t	transform
t_w	thickness
U_1	freestream
$\langle \rangle$	spatial/
U_0	$\bar{u}(x, y, z)$ case m
U_v	time dep valve
u_1, u_2	velocities
\bar{u}	time mean
\tilde{u}	rms of the
u_c	convective

St_F	Strouhal number based on f_F
St_I	Strouhal number based on f_I
St_V	Strouhal number based on f_V
St_0	Strouhal number based upon f_I and U_0
St_θ	Strouhal number based upon f_F , θ and U_0
T	time period of the dominant fluctuation in the measured velocity
T_d	total data acquisition time for $u(t)$ measurement using LDA
T_w	tolerance around the plane of observation to decide whether a vortex is "far" from the plane of observation
T_P	tolerance on spacing between two vortex motions to decide whether they have paired
t	time in seconds
t_k	kth time step for computing the area of the bleed valve
t_k^P	passage time of the kth vortex motion past x_0
t	transformed ζ' -plane
t_N	thickness of the nozzle plate
U_1	freestream velocity in the x_1 direction
$\langle U \rangle$	spatial/temporal average velocity of the jet
U_0	$\bar{u}(x \geq x_m, y=0)$; $x_m \approx w$ for a real fluid and $x_m \rightarrow \infty$ in an inviscid case
U_v	time dependent velocity at the vena contracta of the bleed valve
u_1, u_2	velocities in the x_1 and x_2 directions, respectively
\bar{u}	time mean of the longitudinal velocity
i	rms of the longitudinal velocity
U_c	convection velocity of vortex motions

w'	disturban
w'	streamwis
$u_a(y)$	vector d
v	complex v
v	magnitide
\vec{v}	velocity
\vec{v}_3	velocity
\vec{v}_r	relative
v_i	volume of
v_b	velocity
v_s	velocity
v_{cup}	velocity tank
w	slit widt
w_e	slit widt
w	transforr
$w(x)$	width of finite pl
$w_k(x)$	width of
w_{ave}	average w
x	streamwis
x_k	time dep the exit
x_k^j	streamwis jth photo
x_0	streamwis
x_1, x_2	streamwis flow anal

disturbance velocity vector; $\vec{u}' = iu' + jv'$

streamwise disturbance velocity

vector defining y dependence of \vec{u}'

complex velocity = $u_1 + iu_2$

magnitude of velocity in the s direction

velocity vector

velocity of the boundary of the deformable control volume

relative velocity of the fluid crossing the control surface

volume of the ith control volume

velocity of bulge

velocity of starting vortex pair (SVP)

velocity of cup of the VFS relative to the liquid in the tank

slit width

slit width for a jet issuing from an infinite plenum

transformed t-plane; $w = \phi + i\psi$

width of a jet at a distance x from the exit plane of a finite plenum

width of a jet at x in the case of an infinite plenum

average width of the dye streak

streamwise coordinate

time dependent average distance of the kth vortex pair from the exit plane; see equation (129)

streamwise distance of the kth vortex (left or right) in the jth photograph

streamwise location of the plane of observation

streamwise and lateral coordinates used in the potential flow analysis of the slit-jet flow field

X_L, X_U	upper and
x_n	discrete
X_D	normaliz of bulge
X_k	discrete
y	lateral
y_k^j	lateral jth photo
y_0	parameter
z	transverse
z	$z = x_1$ the flow
z	position

GREEK SYMBOLS

α	angle be
α	complex
β	parameter
β_1, β_2	parameter
δ_d	boundary
δ_k	estimate the kth
ζ	transform
ζ'	transform
ζ_k	weightin (141)
η	estimator model
θ	momentum

x_L, x_U upper and lower limits of integration in the x_1 direction
 x_n discrete time series
 x_b normalized estimate of the average location of the formation of bulges from the exit plane
 x_k discrete Fourier transform of x_n
 y lateral coordinate
 y_k^j lateral distance of the k th vortex (left or right) in the j th photograph
 y_0 parameter in the equation for the Montgomery profile
 z transverse coordinate
 $z = x_1 + ix_2$; this complex plane defines the geometry of the flow field
 Z position of core of LVDT with respect to its body

GREEK SYMBOLS

α angle between the x_1 -axis and the direction of flow
 α complex wavenumber; $\alpha = \alpha_r + i\alpha_i$
 α_1 parameter in the equation for the Montgomery profile
 β_1, β_2 parameters in the model for linear regression
 δ boundary layer displacement thickness
 δ_k estimate of deviation of nondimensional passage frequency of the k th vortex pair from St_F ; see equation (145)
 ζ transformed z -plane; see equation (6)
 ζ transformed ζ -plane; see equation (7)
 w_k weighting function of the k th vortex pair; see equation (141)
 \hat{y} estimator of the dependent variable in a linear regression model
 θ momentum deficit thickness or angular position

p_0	momentum
λ	wavelength
λ_1	wavelength
v	kinematic
ρ	density
ρ_w	density
ρ_2	time dependent
ρ_v	density
σ	estimate
σ_b	normalization of
$\sigma_i \sigma_j$	rms of output
τ_w	shear stress
ϕ	function
ψ	disturbance
ψ'	disturbance
u	complex function

SPECIAL SYMBOLS

$\langle \cdot \rangle$	time average
$\langle \cdot \rangle$	rms of the
$\langle \cdot \rangle$	spatial average

ABBREVIATIONS

CV _i	ith contrast
A/D	analog to
FD	filling device

momentum deficit thickness at separation

wavelength or streamwise spacing between vortex motions

wavelength corresponding to f_I

kinematic viscosity

density

density of working liquid

time dependent density of air in the control volume CV_2

density of air at the vena contracta of the bleed valve

estimate of the standard error

normalized estimate of the standard deviation in the location of the formation of bulges from the exit plane

rms of output and input signals of LVDT

shear stress at the wall

function describing the y dependence of ψ'

disturbance stream function

disturbance vorticity function

complex frequency; $\omega = \omega_r + i\omega_i$

SPECIAL SYMBOLS

) time average of the quantity ()

) rms of the fluctuating quantity ()

>) spatial average of the quantity ()

BREVIATIONS

i ith control volume

) analog to digital converter

filling device

LDA	laser Do
LSB	least si
LUDF	Linear V
NH	nozzle h
STP	starting
VFS	volume f

LDA	laser Doppler anemometer
LSB	least significant bit
LVDT	Linear Variable Differential Transformer
NH	nozzle housing
SVP	starting vortex pair
VFS	volume flow sensor

1.1 Introduction

This study is naturally occurring slit-jet flow field slit-jet geometry. (Beavers and Wills slot" (Valentine (field.) As the flow of a jet, a vena contracta case of an infinite streamlines become the case of a rectangular jet width) forms within exit plane. In jet, symmetric vortices significant contribution

HISTORICAL PERSPECTIVE AND PLAN OF STUDY

1.1 Introduction

This study is concerned with the instability characteristics of naturally occurring disturbances in a submerged, two-dimensional slit-jet flow field. Figure 1 is a schematic representation of the slit-jet geometry. (Note that "sharp-edged two-dimensional slit" [Beavers and Wilson (1970), hereinafter referred to as BW] or "plane jet" [Vallentine (1967)] are alternative designations for this flow field.) As the fluid from the plenum enters the receiver in the form of a jet, a vena contracta is formed downstream of the exit plane. In the case of an ideal fluid, the jet width continues to decrease and the streamlines become asymptotically parallel [Vallentine (1967)]. In the case of a real fluid, however, the vena contracta (the minimum jet width) forms within nominally 1.5 slit widths downstream of the exit plane. In addition, depending upon the Reynolds number of the jet, symmetric vortex motions form and develop. These motions make a significant contribution to the spread of the jet [BW, Clark and Kit

(1980), Foss and K

this work, the Rey

$$Re = \frac{w \langle U \rangle}{\nu}$$

where w is the w

of the jet and ν i

The use of $\langle U \rangle$ a

use by BW in the

slit-jet.

The simple ge

to produce a flow

derstanding of th

serve as a building

free boundary layer

and growth of symme

analyses and numeri

The results o

from a technologica

slit-jet flow fil

application is rela

shown schematicall

which entrains th

therefore, depend u

1980), Foss and Korschelt (1983), hereinafter referred to as FK]. In this work, the Reynolds number of the jet is defined as

$$Re = \frac{w\langle U \rangle}{\nu} \quad (1)$$

where w is the width of the jet, $\langle U \rangle$ is the spatial average velocity of the jet and ν is the kinematic viscosity of the working liquid. The use of $\langle U \rangle$ as the characteristic velocity is consistent with its use by BW in the first investigation of the instability of the slit-jet.

The simple geometry of the slit-jet nozzle (Figure 1) is expected to produce a flow field which is universal in nature. Hence, an understanding of the instability of the two-dimensional slit-jet will serve as a building block in unraveling the stability phenomena of free boundary layer flows. Also, the results related to the formation and growth of symmetric vortex patterns can serve as a bench mark for analyses and numerical experimentation.

The results of this investigation are also expected to be useful from a technological point of view. The characteristics of the slit-jet flow field can be exploited in a number of ways. One such application is related to the performance of a jet pump. A jet pump, shown schematically in Figure 2, consists of an inner high speed jet which entrains the outer fluid. The pumping efficiency will, therefore, depend upon the stability characteristics of the high speed

jet which will com
secondary fluid.
three subsections
statement of the
of this thesis.

1.2 Historical Pe

The studies
two-dimensional jet

i) experimen

ii) experimen
contoured

iii) theoretic
two-dimer

1.2.1 Instability

The instabili
itself in the forma
Kit (1980)]. The
notions can be expr

jet which will control its ability to induce streamwise motion in the secondary fluid. The balance of chapter 1 has been subdivided into three subsections which deal with (i) a review of literature, (ii) a statement of the objectives of this study, and (iii) the organization of this thesis.

1.2 Historical Perspective

The studies investigating the stability of an unexcited, two-dimensional jet will be categorized as:

- i) experimental studies of the instability of the slit-jet;
- ii) experimental studies of the instability of jets issuing from contoured nozzles;
- iii) theoretical investigations of the stability of two-dimensional jets.

2.1 Instability of the Slit-Jet Flow Field - Experimental Studies

The instability phenomena of the slit-jet flow field manifests itself in the formation of a symmetric vortex street [BW, Clark and t (1980)]. The nondimensional frequency of the naturally occurring vortices can be expressed as a Strouhal number, St ,

$$St = \frac{Fw}{\langle \dot{D} \rangle}$$

BW found that S
250-1500. This wa
observed. A bre
is reported by BW
(1980) show consta
dence on w. As
paratus dependent
830-1160.¹ In addi
1.2 w, and the con
their Re range.
the slit-jet flow
than a length s
momentum thickness
jet issuing from a
by parallel stream
Sakao (1964), Ro
Antonia, Browne, Ra

¹Note that FK rep
upon the measure
is the inferred S
 $c_0 = \langle \dot{D} \rangle / U_0 = 0.7$
present study.

$$St = \frac{fw}{\langle U \rangle} \quad (2)$$

BW found that St was independent of Re ($St \approx 0.43$) over the range 250-1500. This was the same range over which symmetric motions were observed. A breakdown in the formation of symmetric coherent motions is reported by BW for Re values greater than 1500. Clark and Kit (1980) show constancy of St with Re , but, their St shows direct dependence on w . As interpreted by Foss (1980), this suggests an apparatus dependent condition. FK found $St=0.61$ over their Re range of 830-1160.¹ In addition, FK found the spacing between the vortices, $\lambda = 1.2 w$, and the convection velocity of the vortices, $u_c = 0.51 U_0$, over their Re range. These results show that the instability phenomena of the slit-jet flow field depend upon a geometric length scale w , rather than a length scale of the separating boundary layer (e.g., the momentum thickness θ). This makes the slit-jet flow different from a jet issuing from a contoured nozzle. The latter flow is characterized by parallel streamlines at the exit plane. [Sato (1960), Sato and Sakao (1964), Rockwell and Niccolls (1972), Husain and Clark (1977), Antonia, Browne, Rajgopalan and Chambers (1983), Namer and Otugen

¹Note that FK reported a St value of 0.43. This value was based upon the measured centerline velocity U_0 . The value, $St = 0.61$, is the inferred Strouhal number using the discharge coefficient, $C_D = \langle U \rangle / U_0 = 0.71$, that was computed using the data from the present study.

(1988)].

The breakdown and reported by BK begins with pair the centerline of the investigated the 1 vortices. FK have stabilities response their subsequent b the shed boundary from the instabilities which were of the second instability vortex motions in instability causes the lack of experimental rate, etc., in the with the preexisting

1.2.2 Instability

The growth of stively investigated vortex street pattern Rockwell and Niccol vortex pattern was

(1988)].

The breakdown of the symmetric vortex motions has been observed and reported by BW and Clark and Kit (1980). The process of breakdown begins with pairing and coalescence of vortices on the same side of the centerline of the jet. Clark and Kit (1980) have also investigated the lateral distortion and interaction of the cylindrical vortices. FK have hypothesized the existence of three different instabilities responsible for the formation of the vortex motion and their subsequent breakdown. According to them, the "rolling up" of the shed boundary layer into "unit" vortex motions can be inferred from the instability of similar curved shear layers. The vortex motions which were observed by BW have been hypothesized to be caused by the second instability which results in an agglomeration of the "unit" vortex motions into large scale coherent motions. Finally, the third instability causes the breakdown of the vortex motions. Because of the lack of experimental data related to velocity profile, growth rate, etc., in the slit-jet flow field, no comparisons can be made with the preexisting results based upon theoretical considerations.

1.2.2 Instability of 2D Jets Issuing from Contoured Nozzles

The growth of natural disturbances in a jet has been more extensively investigated for a contoured nozzle than for a slit-jet. The vortex street pattern has been found to be Re dependent [see, e.g., Lockwell and Niccolls (1972)]. According to this study, a symmetric vortex pattern was observed at lower values of $Re = 1860$. At values

of Re beyond 5000
metric and an asym
number reported in
jet in this stu
streamlines is inf
and Hussain (198
pattern has been f
file at the exi
profile (underdeve
was observed. H
(fully-developed p
This seems to b
that study, two mo
two-dimensional je
centerline of the
velocity distribut
of an asymmetric v
city distribution,
which imply the for
studies (Antonia,
Goldschmidt (1986)
fore the end of
metric mode, but
dominant.

of Re beyond 5000 the vortex pattern was found to cycle between a symmetric and an asymmetric vortex street. The highest value of Reynolds number reported in this study was 10,800. From the photographs of the jet in this study, a top-hat type of velocity profile with parallel streamlines is inferred at the exit plane. In other studies [Husain and Hussain (1983), Chambers, Antonia and Browne (1985)], the vortex pattern has been found to depend upon the shape of the velocity profile at the exit plane of the jet. For a top-hat type of velocity profile (underdeveloped velocity profile) a symmetric vortex pattern was observed. However, in the case of a parabolic velocity profile (fully-developed profile) an asymmetric vortex street was observed. This seems to be in agreement with the findings of Sato (1960). In that study, two modes of fluctuations were found in the flow field of two-dimensional jets, one symmetric and the other asymmetric about the centerline of the jet. The asymmetric fluctuations prevailed when the velocity distribution was nearly parabolic which implies the formation of an asymmetric vortex street. However, for a top-hat type of velocity distribution, symmetrical velocity fluctuations were observed which imply the formation of a symmetric vortex street. Some recent studies [Antonia, Browne, Rajgopalan and Chambers (1983), Thomas and Oldschmidt (1986)] have shown that the near-field of a plane jet before the end of the potential core exhibits the presence of a symmetric mode, but farther downstream the asymmetric mode becomes dominant.

A large variation in the number (Chambers and others) of values of St in the literature, that, whereas, St varies with the frequency of sinusoidal oscillation with wind speed" in the range, 100-2000, St varied as, $f \propto St$ reported St , based on the increasing momentum thickness of the frequency of oscillation be independent of St . (1972) found St proportional to length and velocity. It has been found to exist (1968)].

Unlike the slotted jet the contoured jet theoretical prediction is in addition to the wavelength of the oscillation (1972) to be dependent on a fully-developed periodic flow.

A large variation exists in the reported values of Strouhal number [Chambers and Goldschmidt (1982)]. Based upon the reported values of St in the plane and circular jets Schweiger (1983) concluded that, whereas, St is independent of Re for a given nozzle configuration, it varies with the width w . According to Sato (1960), "the frequency of sinusoidal fluctuations in the jet has no simple relation with wind speed". Sato and Sakao (1964) found that over the low Re range, 100-2000, the frequency, f , of the naturally occurring motions varied as, $f \propto U_j^2$, where U_j is the jet exit speed. Sato (1960) reported St , based upon w and U_j , to be constant over Re 1500-8000 and then increasing dramatically. However, for the same data when the momentum thickness θ was used as the length scale in nondimensionalizing the frequency ($N_j = \frac{f\theta}{U_j}$) and in defining $Re_\theta = \frac{U_j\theta}{\nu}$, N_j was found to be independent of Re_θ for $80 \geq Re_\theta \geq 500$. Rockwell and Niccolis (1972) found $St = 0.012 Re^{0.5}$. Here w and $\langle U \rangle$ have been used as the length and velocity scales, respectively. A similar relationship has been found to exist in circular jets as well [Becker and Massaro (1968)].

Unlike the slit-jet flow field, enough data have been acquired in the contoured jet to compare the experimental findings with the theoretical predictions based upon the linearized stability theory. In addition to the passage frequency of the vortical motions, the wavelength of these motions has been found by Rockwell and Niccolis (1972) to be Re dependent: $\frac{\lambda}{w} = 0.44 Re^{-0.5}$. For the laminar jet with fully-developed profile, the lowest Reynolds number at which the jet

has been found to
confirmed by the
the presence of p
around $Re \approx 10$.
periodic velocity
beyond $x = 20\omega$
ponent of velocity
of the jet, with
velocity profile
agreement between
tions.

1.2.3 Theoretical

Various approaches
stability of two-

i) a solution

Rayleigh
disturbance

ii) a solution
methods

iii) a simulation

The first technique

has been found to become unstable is 10 [Andrade 1939]. This has been confirmed by the measurements of Sato and Sakao (1964) who observed the presence of periodic velocity fluctuations in the jet beginning around $Re \approx 10$. Their investigation also showed that for $Re \geq 50$ the periodic velocity fluctuations of the near-field became irregular beyond $x \approx 20w$. The growth of disturbances in the streamwise component of velocity has been found to be exponential in the near-field of the jet, with the rate of growth dependent upon the shape of the velocity profile [Sato (1960)]. In the same study Sato has shown good agreement between his experimental results and theoretical predictions.

1.2.3 Theoretical Investigation of Instability of 2D Jets

Various approaches have been used to analytically investigate the stability of two-dimensional jets. Three of these are:

- i) a solution of the (viscous) Orr-Sommerfeld or the (inviscid) Rayleigh equation for temporal or spatial growth of disturbances;
- ii) a solution of full Navier Stokes equation using numerical methods;
- iii) a simulation of the vortex street using point vortices.

the first technique is the most commonly utilized.

1.2.3.1 Solution

Common practice
tions of the inst

i) The stability
to be sensitive to
ponent [Savic (19
and Criminale (197
least two solutions

Whereas, the symme
tion, the asymmet
linearized stability
Criminale (1971)].

ii) The stability
investigated under
tely large distance
turbation conditions
centerline of the
or the lateral.
Researchers, in ge
dition of the u or
and Criminale (19
designate the symm
(1960) and Ikeda
hences based upon
designation by the

1.2.3.1 Solution of Orr-Sommerfeld Equation

Common practices and major results of the theoretical investigations of the instability of the jet are:

i) The stability of the symmetric profile of a jet has been found to be sensitive to two modes of disturbances in a given velocity component [Savic (1941), Savic and Murphy (1943), Sato (1960), Mattingly and Criminale (1971) and Ikeda (1977)]. That is, there exists at least two solutions to the eigenvalue problem [Koochesfahani (1989)]. Whereas, the symmetric arrangement of vortices represents one solution, the asymmetric arrangement represents the other solution of the linearized stability equation [Savic and Murphy (1943), Mattingly and Criminale (1971)].

ii) The stability of a given velocity profile (the basic flow) is investigated under the constraint of vanishing fluctuations at infinitely large distance from the centerline of the jet. In addition, perturbation conditions (symmetric or asymmetric with respect to the centerline of the jet) are also specified: either the streamwise, u' , or the lateral, v' , component of disturbance velocity is used. Researchers, in general, do not agree in designating the symmetry condition of the u or v component of velocity. For example, Mattingly and Criminale (1971) used the v component of velocity fluctuations to designate the symmetry condition of the disturbances, whereas, Sato (1960) and Ikeda (1977) defined the symmetry condition of the disturbances based upon the u component of the velocity fluctuations. The designation by the latter authors will be used in this study:

a) Symmetr

distribu

and ω'

b) Asymmetr

distribu

and ω'

where ψ' and ω

vorticity, respect

metric vortex pat

(Mattingly and Cr

iii) The m

basic flow state

shapes have been

specified as,

$$U(y) = b \text{ sech}$$

has been common

(1956), Tatsumi a

tingly and Crimin

the above equation

tribution. Montg

profile given by

- a) Symmetric disturbance condition: the u' disturbances are distributed symmetrically with respect to y whereas v' , ψ' and ω' are asymmetrically distributed.
- b) Asymmetric disturbance condition: the u' disturbances are distributed asymmetrically with respect to y whereas v' , ψ' and ω' are symmetrically distributed.

where ψ' and ω' are the disturbance stream function and disturbance vorticity, respectively. It is to be noted that (a) results in a symmetric vortex pattern, and (b) results in an asymmetric vortex pattern [Mattingly and Criminale (1971)].

iii) The mean velocity profile of the jet flow serves as the basic flow state in the stability equation. Various velocity profile shapes have been used. The Bickley jet [Bickley (1937)] which is specified as,

$$U(y) = b \operatorname{sech}^2\left(\frac{y}{a}\right) \quad a, b \text{ are constants} \quad (3)$$

has been commonly used [Savic (1941), Savic and Murphy (1943), Curle (1956), Tatsumi and Kakutani (1958), Sato and Sakao (1964) and Mattingly and Criminale (1971)]. Sato (1960) has used a modified form of the above equation. Ikeda (1977) has used a parabolic velocity distribution. Montgomery (1985) has specified a top-hat type of velocity profile given by

$$u(y) = \begin{cases} 1 \\ \text{cc} \end{cases}$$

iv) As expected stability
ferent stability
Criminale (1971)
higher growth rates
found the same
Montgomery (1985)
file the symmetric
asymmetric disturbance
be represented
vortex street, which
metric vortex street

v) For the
found to be 4 [C]

The results
the instability of
ity phenomena. I

i) The value
has not been expected
ment of Sato and

ii) Sato (1985)
with maximum amplitude

$$u(y) = \begin{cases} 1 & |y| \leq y_0 \\ \cosh\left[\frac{|y| - y_0}{\beta}\right] \exp\left[-0.5\left\{\frac{|y| - y_0}{\beta}\right\}^2\right] & |y| \geq y_0 \end{cases} \quad (4)$$

iv) As expected, different velocity profile shapes predict different stability characteristics. For the Bickley jet, Mattingly and Criminale (1971) have found the asymmetric disturbances to have a higher growth rate than the symmetric disturbances. Ikeda (1977) found the same to be true for a parabolic velocity profile. Montgomery (1985), however, found that for the top-hat velocity profile the symmetric disturbances exhibit higher growth rate than the asymmetric disturbances. Hence, if the velocity profile of a jet can be represented by equation (4) the jet should exhibit a symmetric vortex street, whereas, for the profile given by equation (3) an asymmetric vortex street should be expected.

v) For the Bickley jet, the critical Reynolds number has been found to be 4 [Curle (1956), Tatsumi and Kakutani (1958)].

The results of the experimental and theoretical investigations of the instability of the jet agree only in some aspects with the stability phenomena. For example, some of the disagreements are:

i) The value of the critical Reynolds number for the Bickley jet has not been experimentally confirmed in the well controlled experiment of Sato and Sakao (1964).

ii) Sato (1960) reports that for the Bickley jet the frequency of maximum amplification rate does not agree with the experimentally

observed frequency

parabolic jet good

theoretical results

iii) The theoretical
calculation, $\frac{\alpha c_i}{c_r}$, based
on the assumption that the jet
does not agree with the
observed frequency

(1960).

A probable
prediction and
parallel flow in
not be parallel
(1958), Sato and

Considering
jectured that a
will require taking
i) the curvature
plane of the jet
profile in the stream
ii) the viscous

observed frequency. However, when the calculations are based upon the parabolic jet good agreement is achieved between the experimental and theoretical results.

iii) The theoretical predictions of the spatial rate of amplification, $\frac{\alpha_i}{c_r}$, based upon the Bickley profile and the parabolic profile do not agree with the experimentally determined values found by Sato (1960).

A probable cause for the disagreement between the theoretical predictions and experiment is considered to be the assumption of parallel flow in the former. That is, the streamlines are observed to not be parallel especially at low Re values [Tatsumi and Kakutani (1958), Sato and Sakao (1964)].

Considering the state of the art of stability theory, it is conjectured that a modelling of the slit-jet stability characteristics will require taking into account:

i) the curvature of the streamlines in the vicinity of the exit of the jet which results in a rapidly changing mean velocity profile in the streamwise direction;

ii) the viscous effects (especially at low Re values).

Numerical solutions of the primitive variables $v(x,y,z,t)$, etc. are obtained by applying this technique to two-dimensional problems. Their calculations show formation of a two-dimensional pass through the jet width, which is in agreement with the experimental observations [Sato (1964)]. It has been found to be in good agreement with the stream.

Flow visualization is a field based upon experimental work. It is in good agreement:

- 1) The flow visualization studies seem to be satisfactory, but, for the distance of about 10 cm, the graphic data from

1.2.3.2 Numerical Solution of Full Navier-Stokes Equation

Numerical solution of the full Navier-Stokes equation in the primitive variables can provide sufficient data $\{u(x,y,z,t), v(x,y,z,t), \text{ etc.}\}$ in a given physical domain to investigate the stability characteristics of a given flow field. Shimizu and Wada (1985) applied this technique to study the vortex growth process in a two-dimensional jet with a potential core. The outflow boundary in their calculations terminated at 7 jet widths. The streakline plots show formation of symmetric vortex motions for $Re > 800$. The non-dimensional passage frequency, based upon the centerline velocity and the jet width, was found to be 0.22. This value compares quite well with the experimentally determined value of 0.23 for symmetrical formations [Sato (1960)]. In this numerical study the disturbances have been found to grow exponentially up to about 4.2 slit-width downstream.

Flow visualization observation of the development of the flow field based upon the numerical work of Shimizu and Wada (1985) and the experimental work of BW in a slit-jet flow field shows some qualitative agreement:

i) The formation of the large scale symmetric motions in both studies seems to begin with symmetric disturbances on the jet boundary, but, for the numerical work the symmetric disturbances form at a distance of about 3 slit-widths downstream; in comparison, the photographic data from BW show the presence of these disturbances within a

distance of 1 sl:

ii) The num

for Re values les

shows the growth

= 250.

iii) The nu

of fully develop

Clark and Kit (19

1.2.3.3 Simulati

Some of the
have also been in
growth and devel
is represented by
tance apart. Per
respect to each o
calized disturba
tern. Their comp
for both the s
street; i.e., sym
disturbances. Th
to check the agree
nined values.

Aref and Sigge
down of an asymm

distance of 1 slit-width downstream.

ii) The numerical work does not exhibit symmetric vortex motions for Re values less than 800. The experimental data on the other hand, shows the growth and development of symmetric motions beginning at $Re \approx 250$.

iii) The numerical work does not show the process of coalescence of fully developed vortices which was commonly observed by BW and Clark and Kit (1980).

1.2.3.3 Simulation of Vortex Street

Some of the instability characteristics of a two-dimensional jet have also been investigated by using point vortices to simulate the growth and development of the vortex street. In this method, the jet is represented by two rows of point vortices which are a certain distance apart. Perturbations are introduced by displacing the rows with respect to each other symmetrically or asymmetrically. BW imposed localized disturbances on the row of vortices to study the growth pattern. Their computations show that a symmetric vortex street results from both the symmetric and asymmetric perturbation of the vortex street; i.e., symmetric disturbances should dominate the asymmetric disturbances. They did not calculate any other instability parameters to check the agreement with the corresponding experimentally determined values.

Aref and Siggia (1981) studied in detail the evolution and break-up of an asymmetric vortex street. As a special case, they

investigated the
turbation to res
metric vortex s
represent vortex
However, at lat
mode and nearest
street is maintai

1.3 Objectives o

The object
analytically inve
isothermal, two-
numbers ranging f
using the followi

i) Detailed
field o
tained.

ii) Using th
a) hyp
the sym
b) check
only up
more lin
c) dete

investigated the evolution of two vortex sheets with an initial perturbation to resemble a plane jet. The two sheets evolved into a symmetric vortex street. The calculations show that the spirals which present vortex motions become fuzzy with the passage of time. However, at later times the "vortices become unstable to a pairing and nearest neighbors merge". The symmetric character of vortex street is maintained at all times.

3 Objectives of the Present Study

The objective of this study was to experimentally and analytically investigate the instability phenomena of a submerged, thermal, two-dimensional slit-jet flow field at low Reynolds numbers ranging from 100-4000. This objective has been addressed by using the following experimental techniques:

- i) Detailed flow visualization pictures of the slit-jet flow field over much of the desired range of Re have been obtained.
- ii) Using the data base of (i):
 - a) hypothesize the process which leads to the formation of the symmetric vortex street;
 - b) check whether the symmetric coherent motions are observed only up to $Re = 1500$ as reported by BW. Note that FK in a more limited investigation, supported the observation of BW;
 - c) determine the Reynolds number dependence, if any, of the

qualite
the sym
d) che
vortex
first o

iii) Measure
the Bic
best f
eigenva
for the

iv) Measure
centerl
turbanc
in (iii

v) Determin
using th
velocity
numbers.
(regardi
provide
field.
with the
through

qualitative features of the growth and breakdown process of the symmetric vortex motions;

d) check FK's hypothesis that the agglomeration of unit vortex motions results in "large" scale motions which were first observed by BW.

iii) Measure the $\bar{u}(x=c, y)$ velocity profiles and determine whether the Bickley (equation 3) or Montgomery (equation 4) profile best fits the data. Use the fitted profile and compute the eigenvalues of the inviscid, linearized stability equation for the spatially growing disturbances.

iv) Measure the longitudinal velocity distribution along the centerline of the jet to determine the growth rate of disturbances and compare it with the computed values as found in (iii).

v) Determine the discharge coefficient of the slit-jet flow, using the measured centerline (U_0) and spatial average ($\langle U \rangle$) velocity values as $C_D = \frac{\langle U \rangle}{U_0}$, over a wide range of Reynolds numbers. Note that these data are of intrinsic interest (regarding the nozzle shapes used in this study) and they provide valuable diagnostic information about this flow-field. Specifically, the measured C_D values can be compared with the value of 0.611 which characterizes an inviscid flow through the slit-jet nozzles.

1.4 Contents of

Chapter 2

Investigation:

i) Potenti.

upstream and down

The purpose of th

plenum which will

jet.

ii) Thwaite

velocity distribu

boundary layer pa

iii) Linear

growth of disturb

equation of motio

Chapter 3 de

data acquisition s

of the experiment

Chapter 4 d

flow visualization

lead to the for

upon the patterns

sidered.

Contents of the Thesis

Chapter 2 presents three analytical aspects of this investigation:

- i) Potential flow methods have been used to map the flow field upstream and downstream of the nozzle plates which form the slit-jet. The purpose of this analysis was to determine the size of the smallest jet which will not influence the free streamline of the exiting jet.
- ii) Thwaites integral method has been used together with the velocity distribution computed from inviscid analysis to determine the boundary layer parameters δ_d and θ^* .
- iii) Linear and nonlinear stability analyses for the spatial growth of disturbances have been carried out using the inviscid Euler equations of motion.

Chapter 3 describes the experimental facility, modelling of flow, data acquisition system, flow visualization techniques and the details of the experimental procedures.

Chapter 4 describes the qualitative results obtained from the flow visualization pictures and presents the sequence of events that lead to the formation of the symmetric vortex street. Also, based on the patterns of the flow field, various flow regimes are considered.

Chapter 5

cessing the info
ments.

Chapter 6 pr

algorithms of Cha

Chapter 7 p

tudinal velocity
the estimates of

Chapter 8

flow field using
velocity data pre

Chapter 9 su

recommendations f

Chapter 5 presents the details of the algorithms used for processing the information gathered from the flow visualization experiments.

Chapter 6 presents the quantitative results obtained by using the algorithms of Chapter 5 and the flow visualization data base.

Chapter 7 presents the results based upon the lateral and longitudinal velocity surveys in the slit-jet flow field. It also presents estimates of the discharge coefficient of the slit-jet.

Chapter 8 presents the results of the stability of the slit-jet flow field using the analyses presented in Chapter 2 and the measured velocity data presented in Chapter 7.

Chapter 9 summarizes the findings of this investigation and makes recommendations for future work.

2.1 Introduction

This chapter
ferent aspects of
analysis to deter-
the jet issuing f-
2.3 the Thwaites
parameters using
briefly presents
analysis which wi-
disturbances in
developed for the
the streamwise co-
a model for the ve-
analysis will be a

ANALYTICAL CONSIDERATIONS

Introduction

This chapter presents mathematical analyses related to four different aspects of the slit-jet flow field. Section 2.2 presents the analysis to determine the flow pattern in the channel-like plenum and jet issuing from it using the potential flow methods. In Section 2.3 the Thwaites method is applied to estimate the boundary layer thicknesses using the results of the previous section. Section 2.4 presents the formulations of the linear inviscid instability analysis which will be applied in Chapter 8 to predict the growth of disturbances in the slit-jet flow field. In Section 2.5 a model is developed for the pressure fluctuations along the jet centerline using the streamwise component of the unsteady Euler (Euler-s) equation and model for the velocity fluctuations. Again, the results of this analysis will be applied in Chapter 8.

2.2 Inviscid Flow

2.2.1 Introduction

Figure 3 is a schematic diagram of a flow field in a plenum which has a rectangular cross-section. In general, the flow is considered to be an idealized case where the flow is finite ($H/w \rightarrow \infty$) and the ratio, $B/w \geq 10.4$, is large enough to make the flow two-dimensional.

This section discusses the flow field in a width slit-jet flow. The objective of this section is to study the potential flow field.

- i) Compare the flow field in a plenum with the flow field in a parison. The plenum flow is characterized by a finite H/w , hence the investigation is limited to a finite H/w .

- ii) Obtain the flow field on the

Inviscid Flow Pattern in the Slit-Jet Flow Field.

1 Introduction

Figure 3 is a schematic representation of a finite, channel-like plenum which has been used in the test facility of this investigation. In general, the flow field in this case will be different from the idealized case when the (infinite aspect ratio) jet is fed from an infinite ($H/w \rightarrow \infty$) plenum; see Figure 4. The value of the aspect ratio, $B/w \geq 10.4$, for the present facility is such that the flow is two-dimensional in nature.

This section presents an inviscid analysis of the finite plenum with a slit-jet flow field to determine the streamline pattern. The objective of the analysis is to use the velocity field determined by potential flow methods to:

- i) Compare the flow fields of the jet issuing from a finite plenum with that issuing from an infinite plenum. The comparison will be used to determine how small can the ratio of the plenum width to the jet width, H/w , be without significantly influencing the flow field. (Note that the ratio, H/w , has been referred to as the "proximity ratio" in this investigation.)
- ii) Obtain an estimate of (a) the integral of potential velocity on the nozzle plate, and, (b) the streamwise gradient of the

potent:

used in

the two

2.2.2 Inviscid

Use of pot

slit-jets, one in

finite plenum, is

i) The v

the two

keeps

ii) Since

where

and the

When these

general, can be

0 and $\vec{v} \times \vec{u} = 0$.

(Bernoulli equati

One of the

Theory as outline

the determinatio

flow; it is u

potential velocity on the nozzle plate. These estimates are used in an integral method, the Thwaites method, to compute the two boundary layer parameters θ and δ_d .

2 Inviscid Flow Analysis

Use of potential flow methods to compare the flow fields of two jets, one issuing from a finite plenum and the other from an infinite plenum, is justified because:

- i) The viscous effects are confined to the boundary layers on the two nozzle plates. The favourable pressure gradient keeps the boundary layers thin.
- ii) Since the experiment begins from rest, i.e. $\vec{\omega} = 0$ everywhere in the liquid, the majority of the flow in the plenum and the jet core (i.e. $x \approx 3w$) remains irrotational.

When these conditions are satisfied the velocity field, in all, can be determined from the kinematic conditions alone: $\vec{\nabla} \cdot \vec{u} = \vec{\nabla} \times \vec{u} = 0$. Once the velocity field is established, the momentum (Euler equation) can be used to determine the pressure field.

One of the potential flow methods, the method of Free Streamline as outlined in the text by Vallentine (1967), is suitable for determination of the velocity and pressure fields in the subject. It is used herein for this purpose. A series of

transformations

ix_2) pattern (s

tern. The comp

the complex conj

$$\frac{\partial v}{\partial z} = \frac{\partial \phi}{\partial x_1} +$$

[Valentine (1967

2.2.2.1 Details

In Figure 3

center of the sli

Without loss of g

"-s, the dimensi

approach channel

The dimensionless

gle α is defined

of flow.

Table 1 li

points. The flow

only one side is

transformations are employed to express the z -plane (i.e., $z = x_1 + iy_1$) pattern (see Figure 3) in terms of the w -plane ($w = \phi + i\psi$) pattern. The complex velocity field ($v = u_1 + iu_2$) is determined from the complex conjugate of $\frac{dw}{dz}$:

$$\frac{dw}{dz} = \frac{\partial \phi}{\partial x_1} + i \frac{\partial \psi}{\partial x_1} = \frac{1}{i} \left(\frac{\partial \phi}{\partial x_2} + i \frac{\partial \psi}{\partial x_2} \right) = u_1 - iu_2 \quad (5)$$

[Mentz (1967), equation 5.15, p 146].

2.1 Details of Conformal Transformations

In Figure 3 the z -plane is the physical plane with origin at the center of the slit. The dimensionless flow rate is assumed to be π . Without loss of generality, when the streamlines become parallel at x_2 the dimensionless jet width is assumed to be π as well. The channel width is assumed to be " m " times the jet width at $x_2 = -\infty$. The dimensionless approach velocity is therefore equal to $\frac{1}{m}$. The angle is defined to be the angle between the x_1 -axis and the direction of flow.

Table 1 lists the angle and velocity at each of the significant points. The flow is symmetrical with respect to I'-I, and therefore, only one side is considered in the analysis.

Tab

Point z

I' $\alpha = -\pi/2$; $V =$

A $-\pi/2, -\pi; 0$

B $-\pi; 1$

I $-\pi/2; 1$

The following
ties in Table 1:

a) z-plane t

The z-plane

$$\zeta = \frac{1}{|V|} e^{i\alpha}$$

where $|V|$ is the
angle defined ear
rations and Figur

Table 1 - Fiducial Points of Various Planes

Point	Plane				
	z	ζ	ζ'	t	w
$\alpha = -\pi/2$; $V=1/m$		$me^{-i\pi/2}$	$\ln(m) - i\pi/2$	$-\frac{m+1}{2m} - k$	$-\infty$
$-\pi/2, -\pi$; 0		$\infty e^{-i\pi/2}$; $\infty e^{-i\pi}$	$\infty - i\pi/2$; $\infty - i\pi$	$-\infty, \infty$	0
$-\pi$; 1		$1 e^{-i\pi}$	$0 - i\pi$	1	$\log(\frac{m^2+1}{2m})$
$-\pi/2$; 1		$1 e^{-i\pi/2}$	$0 - i\pi/2$	-1	∞

The following transformations are used to determine the quantities in Table 1:

z-plane to ζ plane:

The z-plane is first transformed into the ζ plane defined by

$$\zeta = \frac{1}{|V|} e^{i\alpha} \quad (6)$$

where $|V|$ is the magnitude of the resultant velocity and α is the flow angle defined earlier. Table 1 includes the details of the transformations and Figure 5 shows the ζ -plane.

b) ζ -plane to

Taking the n

$$\zeta' = \ln \zeta$$

or,

$$\zeta' = \ln \left(\frac{1}{|V|} \right)$$

Again, Table 1 an

c) ζ' -plane

Using the
tern is transform

$$t = \cosh \left(\frac{\pi}{l} \right)$$

Referring to Fig.

$$t = \cosh 2(\zeta)$$

The location
stituting the ζ'
Figure 7 shows

b) ζ -plane to ζ' -plane

Taking the natural log of the ζ -plane gives the ζ' -plane:

$$\zeta' = \ln \zeta \quad (7)$$

$$\zeta' = \ln \left\{ \frac{1}{|V|} \right\} + i\alpha \quad (8)$$

Table 1 and Figure 6 contain the pointwise detail.

c) ζ' -plane to t -plane

Using the Schwarz-Christoffel transformation, the ζ' -plane pattern is transformed to the t -plane as (see Figure 7)

$$t = \cosh \left\{ \frac{\pi}{l} (\zeta' - \zeta'_1) \right\} \quad (9)$$

From Figure 6, $l = \frac{\pi}{2}$ and $\zeta'_1 = -i\pi$, which gives

$$t = \cosh 2(\zeta' + i\pi) \quad (10)$$

The location of various points on the t plane is obtained by substituting the ζ' coordinates in (10) which are listed in Table 1.

Figure 7 shows the t plane. From the half source at $I' = -\frac{(m^4 + 1)}{2m^2}$

the fluid reaches
ing through other

d) t-plane t

The w-plane
source of strengt
the same strength

$$w = \frac{\pi}{2\pi} \ln(t)$$

or, equivalently,

$$w = \ln\left(\frac{t+1}{t-1}\right)$$

Table 1 and Figure

2.2.2.2 Equation

Along a fr
velocity $|V|$ is

$$\zeta' = ia$$

where a varies
streamline in the

Fluid reaches a half sink at $I = -1$ both directly and after pass-
through other points.

d) t -plane to w -plane

The w -plane transformation is obtained by superimposing the half
strength of $-\frac{\pi}{2}$, at $t = -\frac{m^4 + 1}{2m^2} = -k$ (say) and half sink of
same strength at $t = -1$. Thus,

$$w = \frac{\pi}{2\pi} \ln(t + k) - \frac{\pi}{2\pi} \ln(t + 1) \quad (11)$$

equivalently,

$$w = \ln \left(\frac{t + k}{t + 1} \right)^{\frac{1}{2}} \quad (12)$$

1 and Figure 8 present the pointwise detail.

2. Equation of Separating Streamline

Along a free streamline $a'g'c'$ (see Figure 3) the magnitude of
velocity $|V|$ is equal to 1. Equation (8) thus becomes

$$\psi' = i\alpha \quad (13)$$

α varies from 0 to $-\frac{\pi}{2}$. Using (10) the equation of the free
line in the t plane becomes

$$t = \cos 2\alpha$$

Since, along a st

$$dw = d\phi = \frac{d\phi}{ds}$$

With V equal to v

$$dw = ds$$

Differentiating

$$ds = \frac{1}{2} \left(\frac{1}{t+1} \right)$$

From (14),

$$dt = -2\sin 2\alpha$$

Substituting for

(17) becomes

$$ds = - \left(\frac{1}{k+1} \right)$$

Since, $dx_1 = ds$

$$t = \cos 2\alpha \quad (14)$$

along a streamline $d\psi = 0$,

$$dw = d\phi = \frac{d\phi}{ds} ds = V ds \quad (15)$$

equal to unity along the free streamline,

$$w = ds \quad (16)$$

differentiating (12) and setting $dw = ds$,

$$s = \frac{1}{2} \left\{ \frac{1}{t+k} - \frac{1}{t+1} \right\} dt \quad (17)$$

(14),

$$= -2 \sin 2\alpha d\alpha \quad (18)$$

Substituting for t and dt by (14) and (18), respectively, equation (17) comes

$$= - \left\{ \frac{1}{k + \cos 2\alpha} - \frac{1}{1 + \cos 2\alpha} \right\} \sin 2\alpha d\alpha \quad (19)$$

$$dx_1 = ds \cos \alpha$$

$$dx_1 = -\cos\alpha$$

$$\text{and } dx_2 = ds \sin\alpha$$

$$dx_2 = -\sin\alpha$$

The above equations
stitutions to yield

$$x_1 = \frac{\sqrt{k}}{\sqrt{2}}$$

$$x_2 = -\frac{1}{2} \frac{\sqrt{k}}{\sqrt{2}}$$

The integration
streamline on the
width of the jet

$$C_1 = \frac{\pi}{2}$$

At $x_2 = 0$, $\alpha = 0$
fore

$$C_2 = 0$$

Therefore the equation

$$dx_1 = -\cos\alpha \sin 2\alpha \left\{ \frac{1}{k + \cos 2\alpha} - \frac{1}{1 + \cos 2\alpha} \right\} d\alpha \quad (20)$$

$$x_2 = ds \sin\alpha, \text{ or}$$

$$dx_2 = -\sin\alpha \sin 2\alpha \left\{ \frac{1}{k + \cos 2\alpha} - \frac{1}{1 + \cos 2\alpha} \right\} d\alpha \quad (21)$$

These equations have been integrated using some trigonometric substitutions to yield,

$$x_1 = -\frac{\sqrt{k-1}}{\sqrt{2}} \tan^{-1} \left\{ \frac{\sqrt{2}}{\sqrt{k-1}} \cos\alpha \right\} + C_1 \quad (22)$$

$$x_2 = -\frac{1}{2} \frac{\sqrt{k+1}}{\sqrt{2}} \ln \left\{ \frac{\sqrt{k+1} + \sqrt{2} \sin\alpha}{\sqrt{k+1} - \sqrt{2} \sin\alpha} \right\} + \ln(\tan\alpha + \sec\alpha) + C_2 \quad (23)$$

Integration constants C_1 and C_2 are determined for the free streamline on the left hand side of the centerline. At $x_1 = -\frac{\pi}{2}$ (half of the jet at $x_2 = -\infty$), $\alpha = -\frac{\pi}{2}$, therefore

$$x_1 = -\frac{\pi}{2}$$

$\alpha = 0$, $\alpha = 0$ (at the lip of nozzle plate on left hand side) there-

$$x_2 = 0$$

where the equation for the separating streamline will become

$$x_1 = \frac{\sqrt{k}}{\sqrt{2}}$$

$$x_2 = \frac{1}{2} \frac{\sqrt{k}}{\sqrt{2}}$$

The corres
the jet from an
k = \pi:

$$x_1 = \frac{\pi}{2} \cdot c$$

$$x_2 = \ln(\tan$$

2.2.2.3 Contra

The contra
jet width after
the exit plane.
a channel-like p
and $x_1 = \frac{w}{2}$ in e

$$w = \pi + 2 \sqrt{}$$

The contraction

$$C_D = \frac{1}{\pi + 2}$$

$$x_1 = -\frac{\sqrt{k-1}}{\sqrt{2}} \tan^{-1} \left\{ \frac{\sqrt{2}}{\sqrt{k-1}} \cos \alpha \right\} - \frac{\pi}{2} \quad (24)$$

$$x_2 = -\frac{1}{2} \frac{\sqrt{k+1}}{\sqrt{2}} \ln \left\{ \frac{\sqrt{k+1} + \sqrt{2} \sin \alpha}{\sqrt{k+1} - \sqrt{2} \sin \alpha} \right\} + \ln(\tan \alpha + \sec \alpha) \quad (25)$$

The corresponding expressions for the separating streamline for jet from an infinite plenum (see Figure 4) are obtained by letting $\alpha = 0$:

$$x_1 = -\frac{\pi}{2} - \cos \alpha \quad (26)$$

$$x_2 = \ln(\tan \alpha + \sec \alpha) - \sin \alpha \quad (27)$$

2.3 Contraction Ratio

The contraction ratio for a jet is defined as the ratio of the width after the formation of the vena contracta to its width at exit plane. The width of the jet at the exit plane, issuing from channel-like plenum, can be obtained by setting the flow angle $\alpha = 0$

$w_1 = \frac{w}{2}$ in equation (24). This gives,

$$w = \pi + 2 \sqrt{\frac{k-1}{2}} \tan^{-1} \sqrt{\frac{2}{k-1}} \quad (28)$$

Contraction ratio then becomes

$$C_D = \frac{\pi}{\pi + 2 \sqrt{\frac{k-1}{2}} \tan^{-1} \sqrt{\frac{2}{k-1}}} \quad (29)$$

As k becomes

finite plenum:

$$C_D = \frac{\pi}{\pi + 2}$$

See Vallentine (

2.2.2.4 Equation

The transf

potential functi

(12). In orde

plane, $z = x_1 +$

$$\frac{dz}{dt} = \frac{dz}{dw} \times \frac{dw}{dt}$$

where z is expre

$$\frac{dw}{dt} = \frac{1}{2} \left(\tau + \right)$$

Equation (10) is

$$f' = \ln f' =$$

or,

becomes large the value of C_D approaches the value for an infinite plenum:

$$C_D = \frac{\pi}{\pi + 2} \quad (30)$$

allentine (1967) page 214.

4 Equation of Streamline in z-plane

The transformations applied in Sec 2.2.2.1 relate the complex potential function $w = \phi + i\psi$ to the complex t plane; see equation

In order to obtain the streamline pattern in the physical $z = x_1 + ix_2$ is expressed in terms of t . Using the chain rule:

$$\frac{dz}{dt} = \frac{dz}{dw} \times \frac{dw}{dt}, \quad (31)$$

z is expressed in terms of t . Differentiating (12),

$$\frac{dw}{dt} = \frac{1}{2} \frac{(1 - k)}{(t + k)(t + 1)} \quad (32)$$

Equation (10) is manipulated to obtain $\frac{dz}{dw}$ as,

$$- \ln \zeta = \frac{1}{2} \cosh^{-1} t - i\pi \quad (33)$$

$$\ln\left(\frac{dz}{dw}\right) = \ln$$

or,

$$\frac{dz}{dw} = -\left(t + \right.$$

therefore,

$$\frac{dz}{dt} = \frac{k-1}{2} \left(t \right.$$

A closed form
contained functi
were found. T
be different fro
the literature
(1912) which has

$$\sqrt{t+1} \pm \sqrt{t}$$

Using (37), equa

$$\frac{dz}{dt} = \frac{1}{\sqrt{2}} \left(\sqrt{t} \right.$$

The above equati

$$\ln\left(\frac{dz}{dw}\right) = \ln\left\{t + \sqrt{t^2 - 1}\right\}^{\frac{1}{2}} - i\pi \quad (34)$$

$$\frac{dz}{dw} = -\left\{t + \sqrt{t^2 - 1}\right\}^{\frac{1}{2}} \quad (35)$$

Therefore,

$$\frac{dz}{dt} = \frac{k-1}{2} \frac{\left\{t + \sqrt{t^2 - 1}\right\}^{\frac{1}{2}}}{(t+k)(t+1)} \quad (36)$$

Closed form integration of (36) was sought. Tables of integrals of functions similar to (36) but no corresponding relationships were found. The presence of $\sqrt{t^2 - 1}$ in the numerator caused (36) to differ from those functions which were tabulated. A survey of the literature related to potential methods led to a paper by Page (1962) which has used the relationship

$$\sqrt{t+1} \pm \sqrt{t-1} = \sqrt{2} \left\{t \pm \sqrt{t^2 - 1}\right\}^{\frac{1}{2}} \quad (37)$$

Thus, (37), equation (36) can be expressed as,

$$\frac{dz}{dt} = \frac{1}{\sqrt{2}} \left\{ \frac{\sqrt{t+1} + \sqrt{t-1}}{t+1} - \frac{\sqrt{t+1} + \sqrt{t-1}}{t+k} \right\} \quad (38)$$

The above equation when integrated yields $z = f(t)$, namely,

$$z = -\tan^{-1} \frac{1}{\dots}$$

The constant C
t-plane: when t
of the jet, w
this condition,

$$z = -\tan^{-1} \frac{1}{\dots}$$

Equations
pattern upstream
comparison, this
issuing from an
finite plenum ca

$$w = -\ln t$$

$$z = t + \sqrt{t^2}$$

which can be der

The ratio
vena contracta,
behavior of th

$$z = -\tan^{-1}\sqrt{\frac{t-1}{2}} + \sqrt{\frac{k-1}{2}} \tan^{-1}\sqrt{\frac{t+1}{k-1}} + \sqrt{\frac{k+1}{2}} \tan^{-1}\sqrt{\frac{t-1}{k+1}} + C \quad (39)$$

constant C is evaluated by applying the boundary condition in the exit plane: when $t = 1$, $z = 0.5w$. For the channel-like plenum the width of the jet, w at the exit plane, is given by equation (28). Using this condition, $C = \frac{\pi}{2}$. Therefore,

$$z = -\tan^{-1}\sqrt{\frac{t-1}{2}} + \sqrt{\frac{k-1}{2}} \tan^{-1}\sqrt{\frac{t+1}{k-1}} + \sqrt{\frac{k+1}{2}} \tan^{-1}\sqrt{\frac{t-1}{k+1}} + \frac{\pi}{2} \quad (40)$$

Equations (12) and (40) have been used to plot the streamline pattern upstream of the exit plane of the jet. See Figure 9. For comparison, this figure also exhibits the streamline pattern for a jet issuing from an infinite plenum. The corresponding equations for infinite plenum case are (see text by Vallentine (1967) pp. 211-214)

$$w = -\ln t \quad (41)$$

$$z = t + \sqrt{t^2 - 1} - \cos^{-1}\left\{\frac{1}{t}\right\} + \frac{\pi}{2} \quad (42)$$

can be derived in the same way as (40).

The ratio of the width of the finite plenum to the jet width at contracta, m , influences the slit width which in turn affects the behavior of the jet. Figure 10 shows the variation of the ratio of

slit widths of
(H/w) as a function of
the width of the slit
(5.1416).

2.2.2.5 Equations

In the case of a
where u_1 and u_2
respectively.
channel-like plenum

$$\frac{dv}{dz} = \frac{1}{\sqrt{t + \dots}}$$

An expression for the
finite plenum jet
the integral and
The derivation of

Along AB or
and, therefore,

$$s' = \ln \left| \frac{1}{v} \right|$$

Substituting in

widths of finite to infinite plenum (w/w_∞) and proximity ratio (w) as a function of m . Note that as m becomes large w approaches the width of the jet for an infinite plenum, i.e., $w_\infty = \pi + 2$ (= 1416).

2.2.5 Equations of Velocity and Pressure Fields on Nozzle Plate

In the complex plane, $z = x_1 + ix_2$, the derivative $\frac{dw}{dz} = u_1 - iu_2$ where u_1 and u_2 are the velocities in the x_1 and x_2 directions, respectively. From equation (35) for a jet issuing from the channel-like plenum,

$$\frac{dw}{dz} = \frac{-\sqrt{2}}{\sqrt{t+1} + \sqrt{t-1}} \quad (43)$$

An expression for the velocity field on the nozzle plate of a finite plenum jet is first derived to evaluate the pressure field and integral and the differential of the potential velocity along x_1 . The derivation is carried out as follows.

Along AB on the nozzle plate (see Figure 3) the flow angle $\alpha = -\pi$ therefore, ζ' in (8) becomes

$$\zeta' = \ln\left|\frac{1}{v}\right| - i\pi \quad (44)$$

Substituting in (10),

$$t = \cosh 2(\dots)$$

Replacing $\left(\frac{1}{V}\right)$ by

$$t = \cosh(1 \dots)$$

or,

$$q^4 - 2q^2 t$$

Solving for q ,

$$q = \pm \left\{ t \pm \dots \right\}$$

The inner and the

i) Inner:
negative sign.

ii) Outer
tive.

Therefore,

$$t = \cosh 2(\ln |\frac{1}{V}|) \quad (45)$$

Replacing $|\frac{1}{V}|$ by $\frac{1}{q}$ and noting $\cosh(-\gamma) = \cosh(\gamma)$, (45) becomes

$$t = \cosh(\ln q^2) \quad (46)$$

$$q^4 - 2q^2 t + 1 = 0 \quad (47)$$

solving for q ,

$$q = \pm \left\{ t \pm \sqrt{t^2 - 1} \right\}^{\frac{1}{2}} \quad (48)$$

Inner and the outer signs are determined as:

i) Inner: At A (Figure 3) $t \rightarrow \infty$ and $q \rightarrow 0$, which suggests a negative sign.

ii) Outer: Being magnitude of velocity $|V|$, q cannot be nega-

therefore,

$$q = \left(t - \sqrt{t^2 - 1} \right)$$

Using the relat

$$q = \frac{\sqrt{t+1}}{t+1}$$

The Berno

two points for

flow field.

pressure p_0 and

(x_1, x_2) in the

$$p = p_0 + \frac{\rho}{2}$$

Using (50), t

plate for the f

$$\frac{p - p_0}{\frac{\rho}{2}} = 1$$

For an infinite

$$\frac{p - p_0}{\frac{\rho}{2}} = 1$$

At the lip, t

t (the corner i

$$q = \left\{ t - \sqrt{t^2 - 1} \right\}^{\frac{1}{2}} \quad (49)$$

g the relation given by (37)

$$q = \frac{\sqrt{t+1} - \sqrt{t-1}}{\sqrt{2}} \quad (50)$$

The Bernoulli equation relates the pressure difference between points for an inviscid, incompressible, irrotational and steady field. Using the vena contracta as the reference location with pressure p_0 and velocity magnitude $|\vec{V}| = 1$, the pressure at any point (x_2) in the flow field is given by

$$p = p_0 + \frac{\rho}{2}(1 - |\vec{V}|^2) \quad (51)$$

; (50), the normalized pressure distribution along the nozzle for the finite plenum becomes

$$\frac{p - p_0}{\frac{\rho}{2}} = 1 - \frac{(\sqrt{t+1} - \sqrt{t-1})^2}{2} \quad (52)$$

in infinite plenum the pressure drop is found to be

$$\frac{p - p_0}{\frac{\rho}{2}} = 1 - \frac{(\sqrt{t+1} - \sqrt{t-1})^4}{4} \quad (53)$$

the lip, $t = 1$ and pressure drop becomes zero. At large values of corner in case of finite plenum) the pressure drop approaches

the maximum val

2.2.3 Comparis

The invisc
two jets were s
parison between

i) varia

ii) traje

2.2.3.1 Pressu

Equations

Δp^+ , due to acc

illustrates the p

The value of m

a proximity re

sure change bec

both jets occ

expanded pressu

distribution

values of x. A

flow fields

exit planes of

maximum value of 1.

3 Comparison Between Jets from Finite and Infinite Plenums

The inviscid streamline pattern upstream of the exit plane of the jets were shown in Figure 9. Using the inviscid analysis, a comparison between the two flow fields can also be made based upon:

- i) variation of pressure field along the nozzle plate;
- ii) trajectory of separating streamline.

3.1 Pressure Field Along the Nozzle Plate

Equations (52) and (53) express the normalized pressure change, due to acceleration along the nozzle plate. Figure 11 illustrates the pressure change over the nozzle plate for both the jets. The value of m for the finite plenum is equal to 20; this results in a proximity ratio, $H/w = 12.2$. At the lip of the two jets, the pressure change becomes zero. More than 95% of the pressure change in the jets occur within one slit width of the separating lip. On an extended pressure change axis, Figure 12 shows the difference in the distribution of the pressure change between the two jets for larger values of x . Again, for $m = 20$, the pressure changes and hence the flow fields of the two jets become identical in the vicinity of the exit planes of the jets.

2.2.3.2 Trajectories

The normal trajectories of the two jets provide the exit plane. The separating streamlines

Parametric trajectories of the plenum slit-jet flow as a function of the ratio of the plenum to the jet area, A_p/A_j , are shown in Figure 10. Both of the plenum walls move forward as A_p/A_j increases. Hence, the lower limit of the plenum thickness, t_p , is a function of A_p/A_j and t_j .

2.3 Determination of the

Two boundary conditions are used to determine the plenum thickness: the plenum thickness at the exit of the jet and the plenum thickness at the exit of the jet. The stability calculation

3.2 Trajectory of Separating Streamline

The normalized change in pressure along the nozzle plate of the jets provided a comparison of the two flow fields upstream of the exit plane. Downstream of the exit plane, the trajectories of the separating streamline are used for comparison.

Parametric equations (24), (25) and (26), (27) express the trajectories of the separating streamline for the finite and the infinite plenum slit-jets, respectively. Figure 13 illustrates the variation of the ratio of the width, $w(x_2)$, of the jet issuing from a finite plenum to the width, $w_\infty(x_2)$, of the jet from an infinite plenum, as a function of $-x_2/w_\infty$. Plots for four values of m are included. Figure 13 shows the variation of the ratio $w(0)/w_\infty(0)$ as a function of m . From the plots show that as m becomes large, that is the two plenum jets move farther apart, the finite and infinite plenum jets become kinematically similar. Hence, $m = 20$ (proximity ratio, $H/w = 12.2$) can be taken as the lower limit of wall separation for which the two jets are kinematically and dynamically similar.

Determination of Boundary Layer Parameters

Two boundary layer parameters momentum thickness θ and displacement thickness δ_d need to be determined. The Thwaites integral method has been used to get an estimate of these parameters. The value of θ at the exit of the jet is traditionally used as a length scale in similarity calculations. The value of δ_d will be used to check whether

all the vortices
marked by the d

The Thwaites
integral equation

$$\tau_w = -\rho \frac{d\theta}{dx_1}$$

The text
integral method
momentum thickness

$$\theta^2 = \frac{0.45}{U_1^6}$$

The displacement

$$\delta_d = \theta H(\lambda)$$

where $H(\lambda)$ is
of $\lambda = \theta^2 U_1^6 / \nu$

The evaluation
free stream (p
num, except for
inviscid and

the vortical fluid at the separating lip on the nozzle plate was tracked by the dye or not.

The Thwaites method is based upon the x_1 component of momentum integral equation for a steady, constant density flow:

$$\tau_w = -\delta \frac{dp}{dx_1} - \frac{d}{dx_1} \int_0^\delta \rho u_1^2 dx_2 + U_1 \frac{d}{dx_1} \int_0^\delta \rho u_1 dx_2 \quad (54)$$

The text, "Viscous Flow", by White (1974) has described all the integral methods in detail including the Thwaites method. The momentum thickness θ is given by

$$\theta^2 = \frac{0.45\nu}{U_1^6} \int U_1^5 dx_1 \quad (55)$$

displacement thickness δ_d is expressed in terms of θ as

$$\delta_d = \theta H(\lambda) \quad (56)$$

where $H(\lambda)$ is called the shape factor and is expressed as a function of $\lambda = \theta^2 U_1' / \nu$.

The evaluation of θ and δ_d depends upon the known distribution of stream (potential) velocity $U_1(x_1)$. Because the flow in the plate boundary layer, except for the thin boundary layers on the nozzle plates, remains laminar and irrotational the expressions developed in Section 2.2.2.5

have been used
on the nozzle
2.2.2.5 have
the derivative
t-plane.

2.3.1 Momentum

Equation
the velocity U
the width of t

$$\left\{ \frac{\partial}{\partial y} \right\}^2 = \frac{C}{Re}$$

where Re_0 is
contracta; Re
viscid separa
 $U_1^* = 1$; equal

$$\left\{ \frac{\partial}{\partial y} \right\}^2 = \frac{0.4}{Re}$$

where, x_U^* an
 x_1 direction
channel-like
in the t plan
of the veloci
Therefore,

ave been used to represent the variation of the free stream velocity in the nozzle plates. Because the equations for velocities in Section 2.2.5 have been developed in the t -plane, the integral in (55) and the derivative $\frac{dU_1}{dx_1}$ will be transformed before evaluation to the z -plane.

3.1 Momentum Thickness θ

Equation (55) has been used to estimate θ . Non-dimensionalizing the velocity U_1 by the velocity $U_0 = U_2(x_2 \rightarrow -\infty)$, and the length x_1 by the width of the jet w , equation (55) becomes,

$$\left\{ \frac{\theta}{w} \right\}^2 = \frac{0.45}{Re_0 U_1^{*6}} \int_0^{x_1^*} U_1^{*5} dx_1^* \quad (57)$$

where Re_0 is Reynolds number based upon the velocity at vena contracta: $Re_0 = \frac{U_0 w}{\nu}$. At the lip of the jet (see Figure 14), the inviscid separating streamline expands to the ambient pressure, so that $x_1^* = 1$; equation (57) thus becomes,

$$\theta^2 = \frac{0.45}{Re_0} \int_{x_L^*}^{x_U^*} U_1^{*5} dx_1^* \quad (58)$$

where, x_U^* and x_L^* are the upper and lower limits of integration in the z direction (i.e., the lip of the nozzle plate and the corner of the channel-like plenum), respectively. The integral in (58) is evaluated in the t plane: equation (50) is used which expresses the magnitude of the velocity on the nozzle plate where $x_2 = 0$, $u_2 = 0$ and $dx_1 = dz$. Therefore,

$$u_1^* = -q$$

and,

$$dx_1^* = \frac{k-}{2}$$

and when,

Using these,

$$\int_{x_L^*}^{x_U^*} u_1^* dx$$

This integral
to 0.0565. T

$$\theta^* = \frac{0.1}{\sqrt{}}$$

In this inv
city. Since
(62) becomes

$$\theta^* = 0.1$$

$$u_1^* = -q = -\frac{\sqrt{t+1} - \sqrt{t-1}}{\sqrt{2}} \quad (59)$$

nd,

$$dx_1^* = \frac{k-1}{2} \frac{\sqrt{t+1} + \sqrt{t-1}}{\sqrt{2}(t+k)(t+1)} dt \quad (60)$$

nd when,

$$x_U^* = 0.5, \quad t = 1$$

$$x_L^* = \frac{\pi\pi}{2w}, \quad t = \infty$$

sing these,

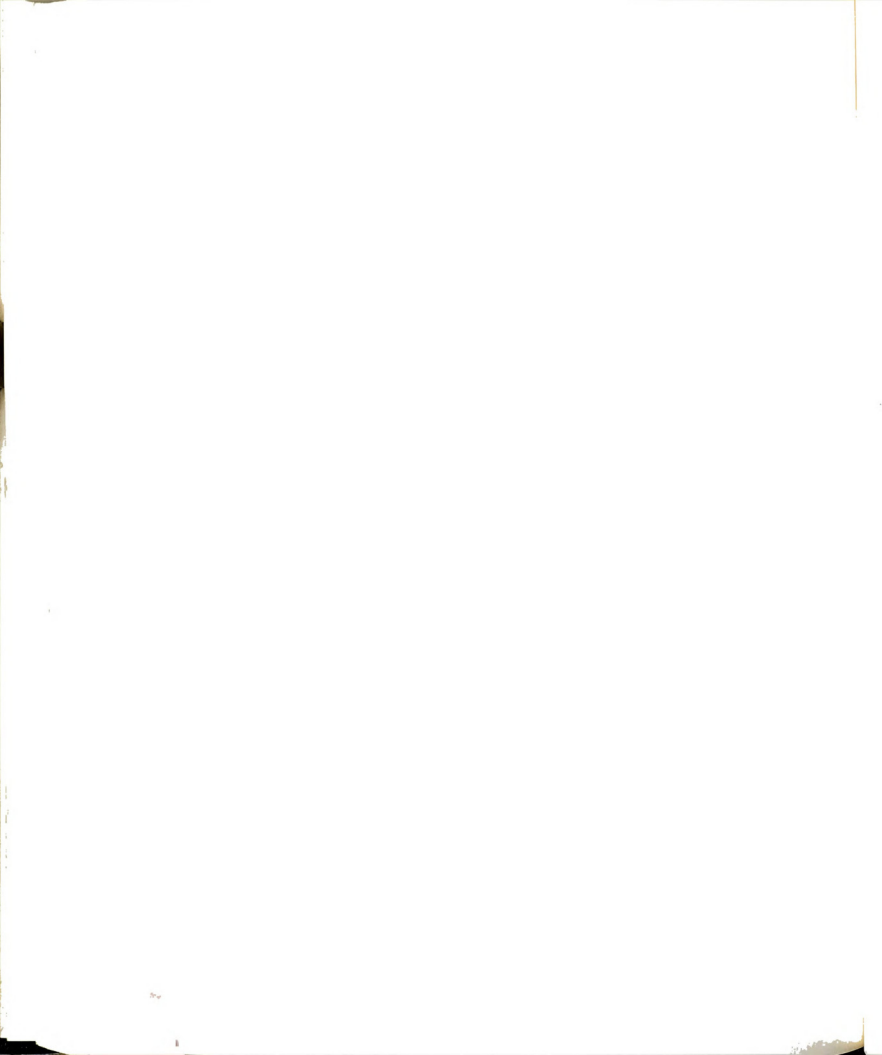
$$\int_{x_L^*}^{x_U^*} U_1^{*5} dx_1^* = \frac{k-1}{2} \int_1^{\infty} \left\{ \frac{\sqrt{t+1} - \sqrt{t-1}}{\sqrt{2}} \right\}^5 \frac{\sqrt{t+1} + \sqrt{t-1}}{\sqrt{2}(t+k)(t+1)} dt \quad (61)$$

this integral has been evaluated numerically and was found to be equal to 0.0565. Taking the square root of (58)

$$\theta^* = \frac{0.15945}{\sqrt{Re_0}} \quad (62)$$

this investigation, $\langle U \rangle$ has been used as the characteristic velocity. Since $\langle U \rangle = C_D U_0$, $Re = C_D Re_0$. Hence, in terms of $\langle U \rangle$, equation 2) becomes

$$\theta^* = 0.15945 \frac{\sqrt{C_D}}{\sqrt{Re}} \quad (63)$$



2.3.2 Displacement Thickness δ_d

In order to evaluate δ_d , $\lambda = \frac{\delta^2 U'}{\nu}$ has to be found so that $H(\lambda)$ can be obtained from the Table 4-8 in the text by White (1974). Again, nondimensionalizing the length by w and the velocity by U_0 ,

$$\frac{du_1}{dx_1} = \frac{U_0}{w} \frac{du_1^*}{dx_1^*} \quad (64)$$

On the nozzle plate $x_2 = 0$, $u_2 = 0$ and therefore,

$$\frac{dw}{dz} = \frac{dw}{dx_1} = u_1 \quad (65)$$

Equation (64) thus becomes

$$\frac{du_1}{dx_1} = \frac{U_0}{w} \frac{d^2 w}{dz^2} \quad (66)$$

Differentiating (43) with respect to z yields

$$\frac{d^2 w}{dz^2} = \frac{(\sqrt{t-1} + \sqrt{t+1}) (t+k) (t+1)}{\sqrt{2(k-1)} \sqrt{t^2-1} (t + \sqrt{t^2-1})^{3/2}} \quad (67)$$

at $(x_1, x_2) = (w/2, 0)$, $t = 1$ and the above expression becomes indeterminate. Applying L'Hospital's rule,

$$\lim_{t \rightarrow 1} \frac{d^2 w}{dz^2} = \frac{k+1}{k-1} \quad (68)$$

where $k = \frac{m}{2m} + \frac{1}{2}$. As m becomes large k becomes large, that is,



$$\text{Limit}_{k \rightarrow \infty} \frac{d^2 w}{dz^2} = \text{Limit}_{k \rightarrow \infty} \frac{k+1}{k-1} = 1 \quad (69)$$

For $m = 20$, $k = 200.00125$ and $(k+1)/(k-1) = 1.01005$. Equation (66) thus gives,

$$\frac{du_1}{dx_1} = \frac{U_0}{w} \quad (70)$$

The parameter λ then becomes,

$$\lambda = \frac{\theta^2 U_0}{\nu w} \quad (71)$$

Using (55), normalizing as before and setting $u_1(x_1 = w/2, x_2 = 0) = U_0$ (see Figure 14),

$$\lambda = 0.45 \int_{x_L^*}^{x_U^*} U_1^{*5} dx_1^* \quad (72)$$

with the value of the integral found in Section 2.3.1,

$$\lambda = 0.02542$$

From Table (4-8) in White (1974), $H(\lambda=0.02542) = 2.515$. Equation (56) thus gives,

$$\delta_d = 2.515\theta \quad (73)$$

or,



$$\delta_d^* = \frac{0.401}{\sqrt{Re_0}} \quad (74)$$

In terms of $\langle U \rangle$,

$$\delta_d^* = 0.401 \frac{\sqrt{C_D}}{\sqrt{Re}} \quad (75)$$

2.4 Stability Calculations of the Slit-Jet Flow Field

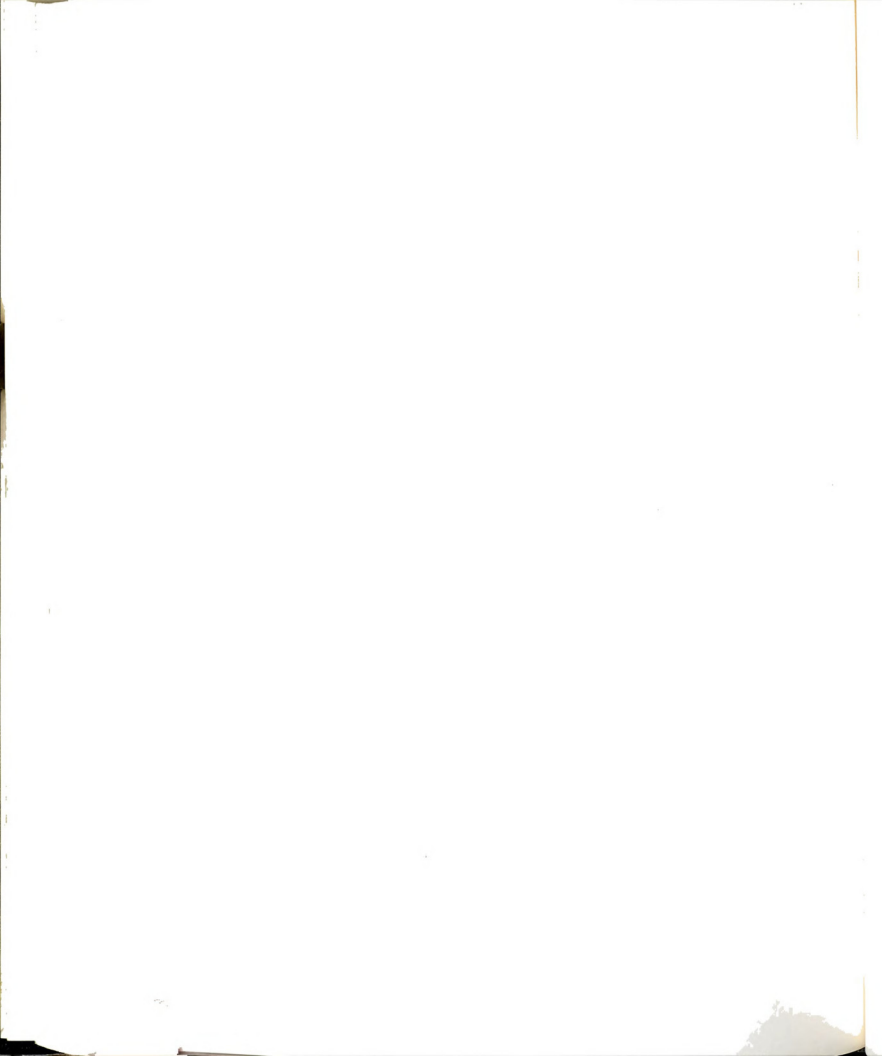
The inviscid stability of the slit-jet flow field was studied by investigating the spatial growth of arbitrary infinitesimal perturbations. The coordinate system that has been used is shown in Figure 15; u and v are the velocities in the x and y directions, respectively. The slit width, w , and the centerline velocity, U_0 , have been used as the characteristic length and velocity scales, respectively. The velocity U_0 is the maximum average velocity of the jet which occurs around $x/w \approx 1$. The time, t , is nondimensionalized by w/U_0 and the pressure by ρU_0^2 . The nondimensional Euler equation

$$\frac{D\vec{u}}{Dt} = -\vec{\nabla} p \quad (76)$$

and the continuity equation for incompressible flow

$$\vec{\nabla} \cdot \vec{u} = 0 \quad (77)$$

were used to develop the model equation to investigate the instability of the jet. The asterisks will be omitted in the following equations for convenience. The mean flow velocity \bar{u} was assumed to depend only



upon the lateral dimension y (parallel flow), but, the perturbations in the velocity \vec{u}' and pressure p' depended on x and y . The linearized, nondimensional equations of motion are expressed as

$$\frac{\partial u'}{\partial t} + \bar{u} \frac{\partial u'}{\partial x} + v' \frac{\partial \bar{u}}{\partial y} = -\frac{\partial p'}{\partial x} \quad (78)$$

$$\frac{\partial v'}{\partial t} + \bar{u} \frac{\partial v'}{\partial x} = -\frac{\partial p'}{\partial y} \quad (79)$$

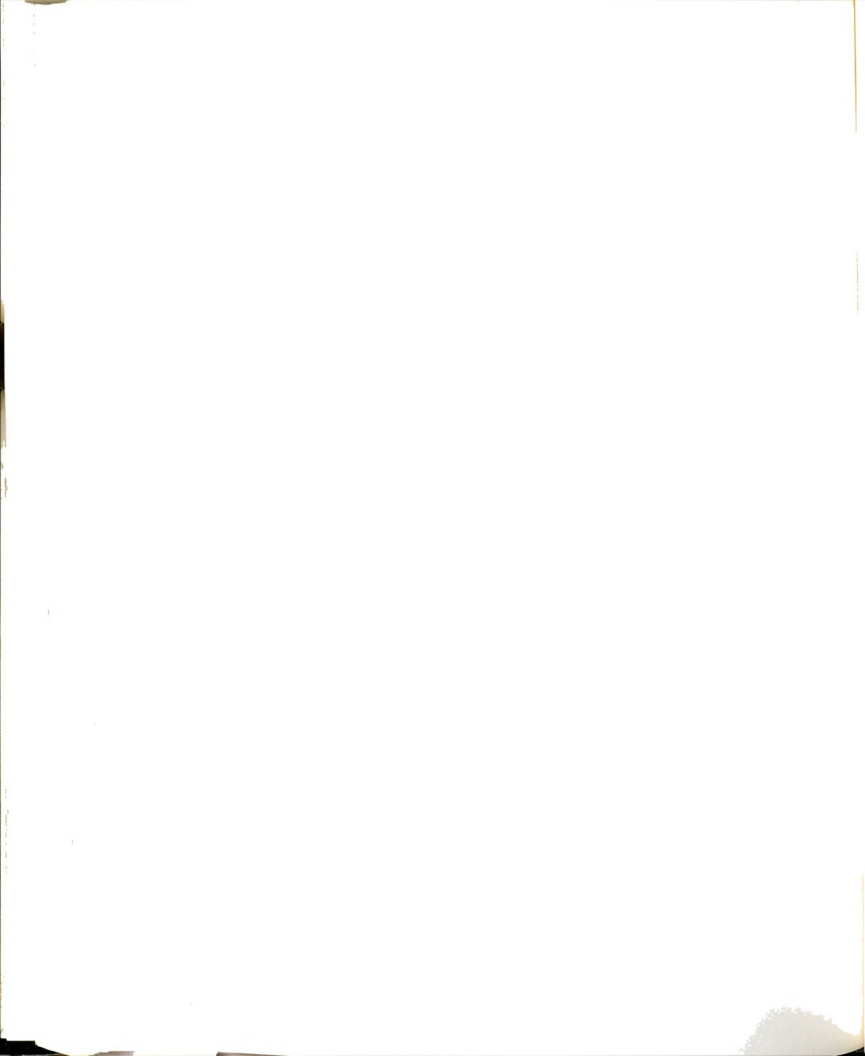
$$\frac{\partial u'}{\partial x} + \frac{\partial v'}{\partial y} = 0 \quad (80)$$

Following the usual assumption that the perturbations are composed of independent wave-like components,

$$\vec{u}' = \vec{u}_a(y) \exp[i(\alpha x - \omega t)] \quad (81)$$

$$p' = p_a(y) \exp[i(\alpha x - \omega t)] \quad (82)$$

the partial differential equations (78) through (80) reduce to ordinary differential equations. In equations (81) and (82) $\alpha = \alpha_r + i\alpha_i$ is the complex nondimensional wave-number and $\omega = \omega_r + i\omega_i$ is the complex nondimensional frequency. For spatial growth of disturbances $\omega_i = 0$; $\vec{u}_a(y)$ and $p_a(y)$ depend only on y . Further simplification is achieved by expressing the velocities (u', v') in terms of disturbance stream function ψ



$$\psi(x, y, t) = \phi(y) \exp[i(\alpha x - \omega t)] \quad (83)$$

$$u' = \frac{\partial \psi'}{\partial y} \quad v' = -\frac{\partial \psi'}{\partial x} \quad (84)$$

From equations (83) and (84) u_a and v_a can be expressed as

$$u_a = \frac{\partial \phi}{\partial y} \quad (85)$$

$$v_a = -i\alpha\phi \quad (86)$$

Using the symbol D for $\frac{\partial}{\partial y}$,

$$u_a = D\phi \quad (87)$$

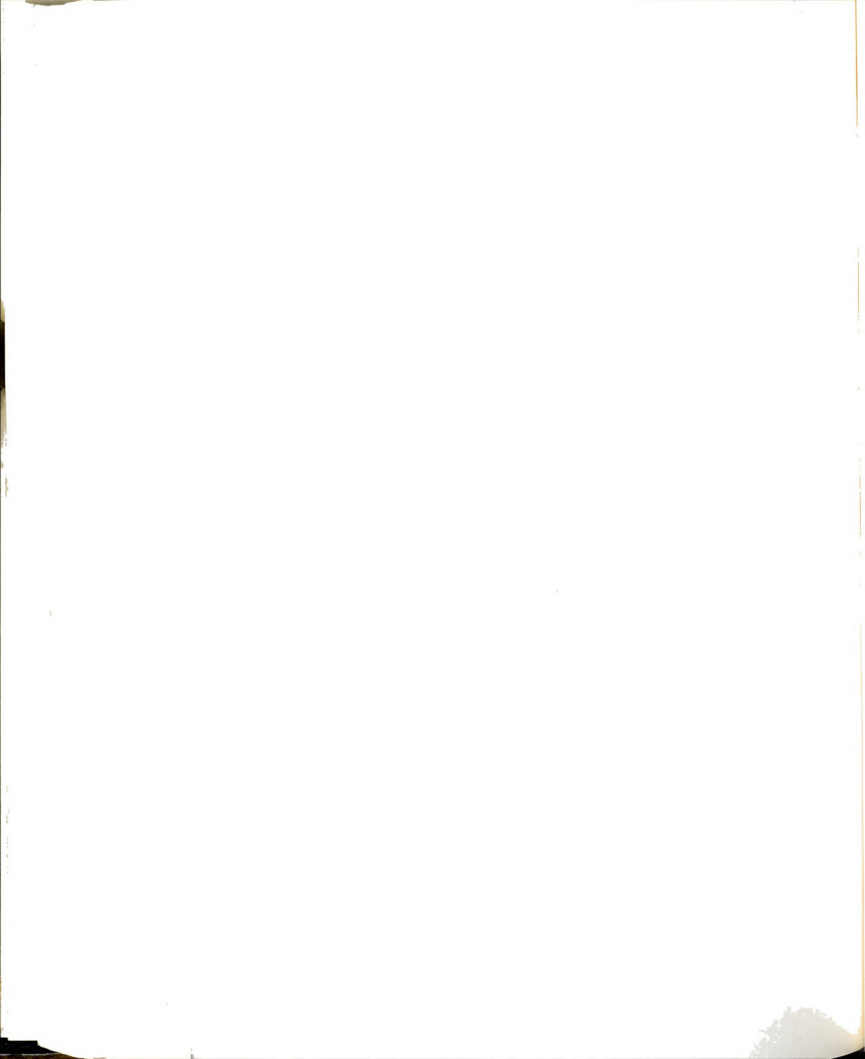
Inserting (81) and (82) in (78) and replacing u_a and v_a by (87) and (86), respectively, p_a can be expressed as

$$p_a = \phi D\bar{u} - (\bar{u} - \frac{\omega}{\alpha}) D\phi \quad (88)$$

Similarly, inserting (81), (82), (86), (87), and (88) in equation (79) yields

$$(\bar{u} - \frac{\omega}{\alpha}) (D^2 - \alpha^2)\phi - (D^2\bar{u})\phi = 0 \quad (89)$$

or



$$D^2\phi - \left[\frac{D^2\bar{u}}{u-\omega/\alpha} + \alpha \right] \phi = 0 \quad (90)$$

This equation can be integrated with boundary conditions

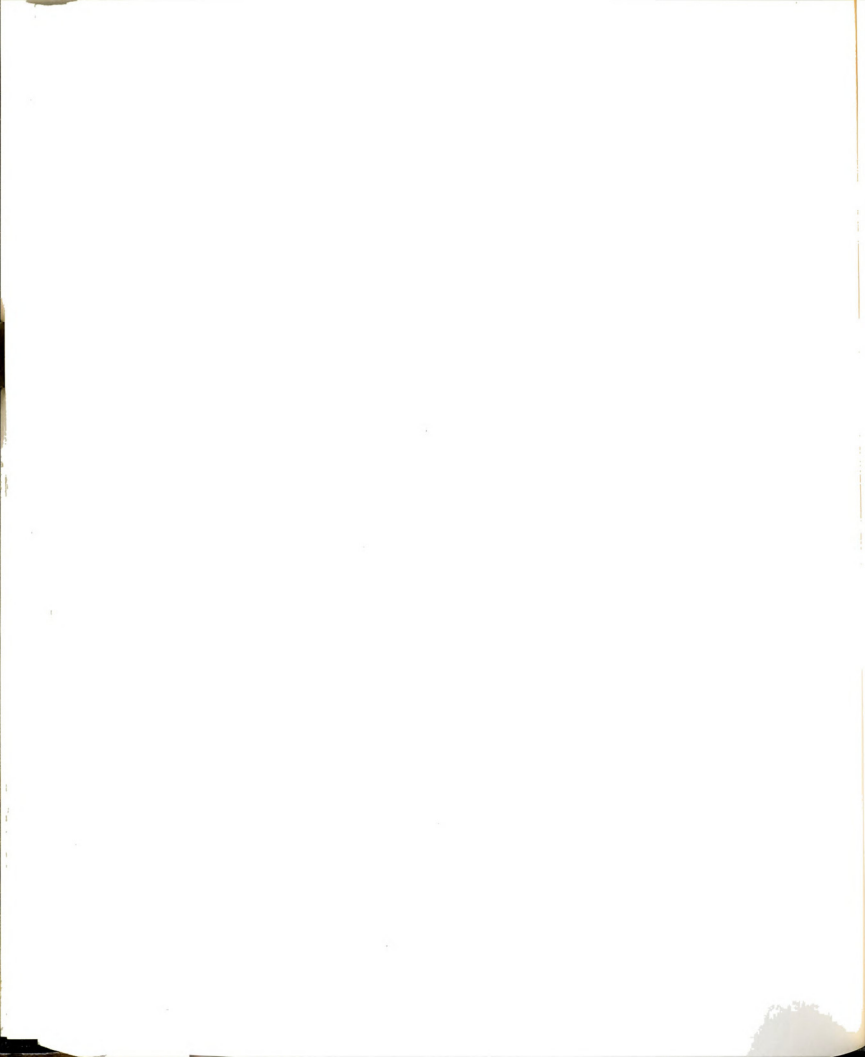
$$\phi(y \rightarrow \pm\infty) = e^{\mp\alpha y} \quad (91)$$

A computer program [developed by Koochesfahani (1989)] was used to solve equation (90) subject to (91). The program uses a "shooting" technique and integrates equation (90) from both sides of the jet towards $y = 0$ where the values of ϕ and ϕ' are checked from the two sides, respectively. If the values match within a tolerance (e.g., 0.0001), the eigenvalues α_r and $-\alpha_i$ are accepted as wave-number and spatial growth rate of unstable disturbances for a given frequency ω . The calculations are repeated for another value of ω , and, in this way α_r and $-\alpha_i$ are found for all frequencies ω . The value of ω for which $-\alpha_i$ has the maximum value predicts the most unstable disturbance.

The frequency ω and the corresponding eigenvalues α_r and α_i are related to the following experimentally determinable quantities [Freymuth (1966)]:

$$\omega = 2\pi St_0 = 2\pi \frac{f_I w}{U_0} \quad (92)$$

$$\alpha_r = 2\pi \frac{w}{\lambda_I} \text{ at } \omega \quad (93)$$



$$-\alpha_I = \text{Growth rate at } \omega \quad (94)$$

where λ_I and f_I are the predicted values of the wavelength and frequency, respectively. Since, the spatial average velocity, $\langle U \rangle$, has been used as the characteristic velocity in this investigation, ω in terms of $\langle U \rangle$ will become

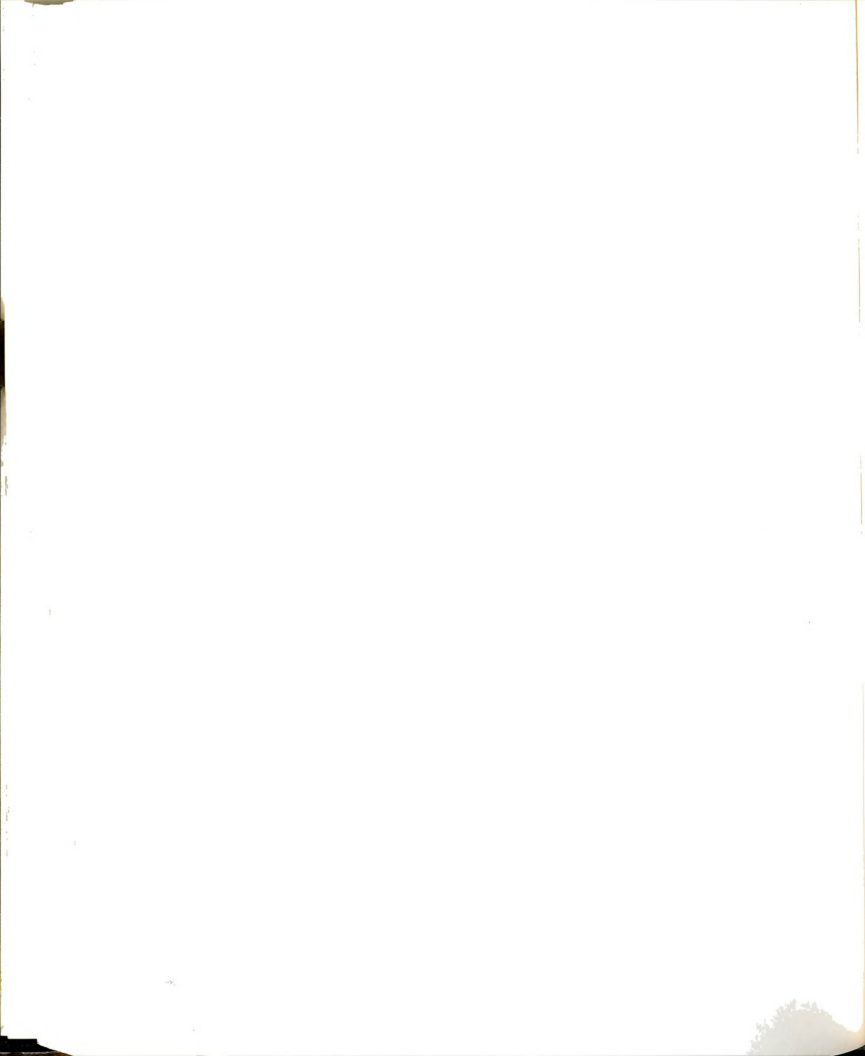
$$\omega = 2\pi f_I \frac{C_D}{\langle U \rangle} = 2\pi C_D St_I \quad (95)$$

where C_D is the discharge coefficient of the jet and St_I is the predicted value of Strouhal number at the maximum growth rate. Similarly, the quantity $\omega/\alpha_I C_D$ yields the phase speed, c_I , in terms of $\langle U \rangle$. These quantities will be determined in Chapter 8.

2.5 Model for Growth of Pressure Fluctuations Along the Centerline

2.5.1 Introduction

In the previous section the pressure fluctuations were modelled, in accordance with the conventional linear analysis, to grow at the same rate and to fluctuate at the same frequency as the velocity fluctuations. In this section, an equation will be derived for the pressure fluctuations along the center streamline using the unsteady Euler's equation and a similar model for the velocity fluctuations which was used in Section 2.4. It will be shown that for large growth rates the pressure fluctuations can grow spatially not only at twice the rate of velocity fluctuations but also oscillate at twice the



frequency. The use of this model would be justified only if it can be shown that the slit-jet flow field remains inviscid in the vicinity of the exit plane. From the considerations of Sections 2.2 and 2.3 it is recognized that the shear effects upstream of the exit plane of the jet remain confined to thin boundary layers on the nozzle plates. Similarly, the core fluid of the jet issuing from the slit should remain inviscid and have a top-hat velocity profile until the shear effects propagate to the centerline.

2.5.2 Derivation of Equation for Pressure Fluctuations

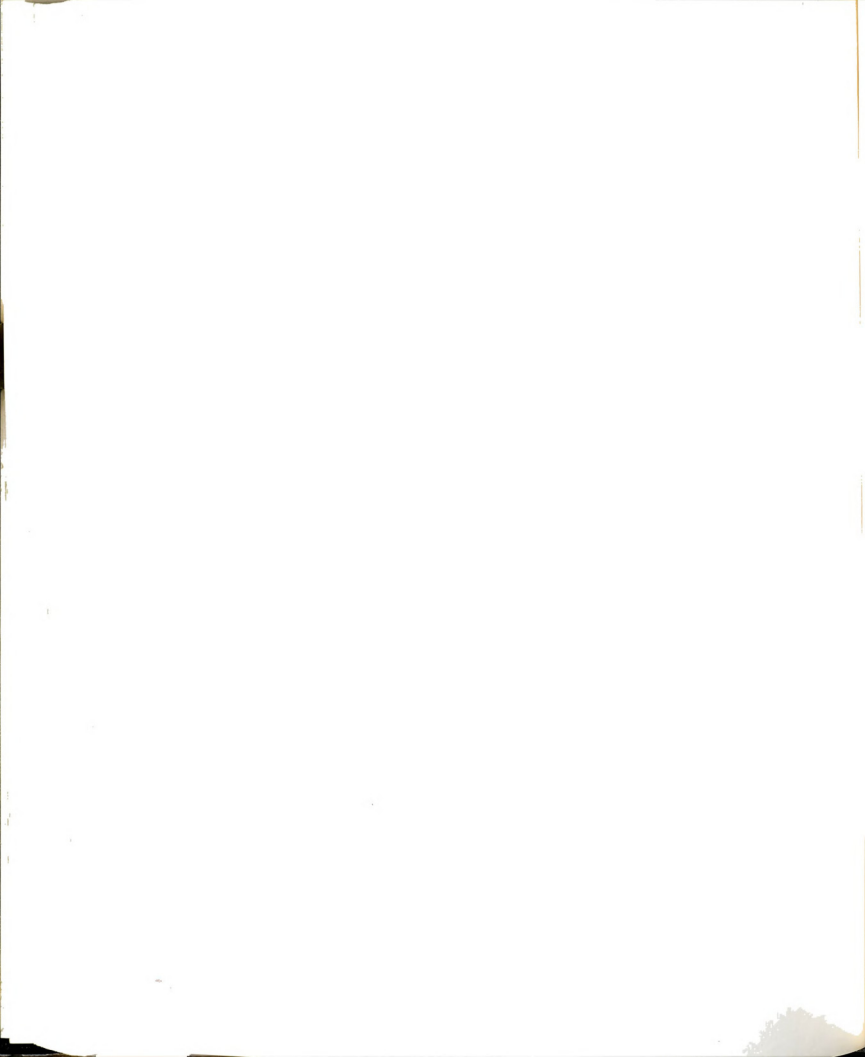
The unsteady Euler equation along a streamline, s , is written as (see Potter and Foss p 357)

$$\frac{\partial V}{\partial t} + V \frac{\partial V}{\partial s} = -\frac{1}{\rho} \frac{\partial p_k}{\partial s} \quad (96)$$

where V is the component of velocity in the s direction and $p_k = p + \rho gh$. Integrating along a streamline passing through the center of the jet (see Figure 15)

$$\int_1^2 \frac{\partial V}{\partial t} ds + \left[\frac{V^2}{2} + \frac{p_k}{\rho} \right]_1^2 = 0 \quad (97)$$

In the plenum (upstream of the nozzle plates) no oscillations are expected to develop, and if the location of (1) is such that oscillations are negligibly small the first term in equation (97) will be zero, so that



$$\frac{v^2}{2} + \frac{p_k}{\rho} = \text{Constant} \quad (98)$$

Treating (n) as the terminal nodal point (i.e., $s=0$) where velocity fluctuations at the instability frequency begin to grow, equation (97) can be written as

$$\int_0^s \frac{\partial v}{\partial t} ds + \left[\frac{v^2}{2} + \frac{p_k}{\rho} \right]_s = C \quad (99)$$

As before (Section 2.4), to nondimensionalize (99) w and U_0 are used as the characteristic length and velocity scales. Equation (99) becomes

$$\int_0^s \frac{\partial v^*}{\partial t^*} ds^* + \left[\frac{v^{*2}}{2} + p_k^* \right]_s = C' \quad (100)$$

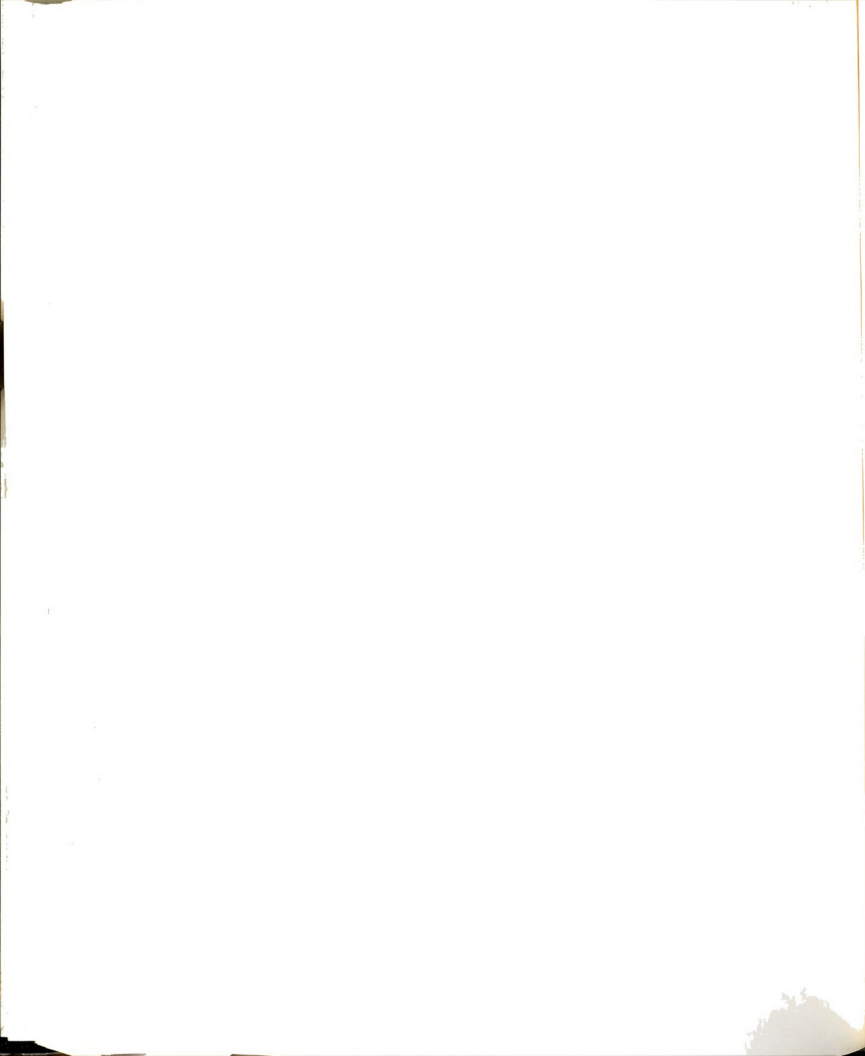
The asterisks will be omitted in the following equations for convenience.

The velocity V and pressure p_k are decomposed into time average and fluctuating quantities as

$$V(s,t) = \bar{U}(s) + u'(s,t) \quad (101)$$

$$p_k(s,t) = \bar{p}_k(s) + p_k'(s,t) \quad (102)$$

The same model is proposed for the fluctuating velocity $u'(s,t)$ as was



used in the previous section, however, $u'(s,t)$ is now restricted along s , giving

$$u'(s,t) = u_a \exp[i(\alpha s - \omega t)] \quad (103)$$

where, as before, α is complex and ω is real. Using equation (103) for the integration of the first term in equation (100) and taking the real part of the integral, the following equation results

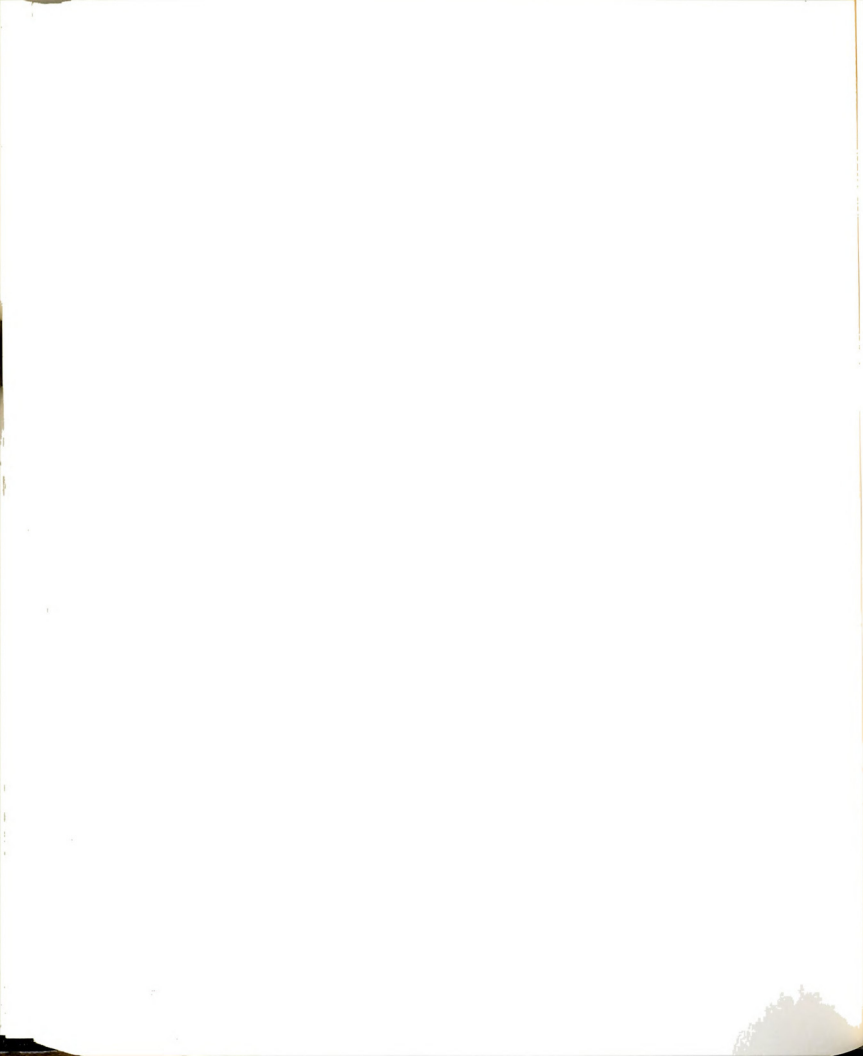
$$\left[-\frac{u_a \omega}{\alpha_r^2 + \alpha_i^2} \right] \exp(-\alpha_i s) [\alpha_r \cos(\alpha_r s - \omega t) + \alpha_i \sin(\alpha_r s - \omega t)] + (\bar{p}_k + p'_k) + \frac{1}{2} [\bar{u} + u']^2 = C' \quad (104)$$

Taking time average of equation (104) over a complete cycle of (ωt) from 0 to 2π radians, the time average equation is found to be

$$\bar{p}_k + \frac{1}{2} [\bar{u}^2(s) + \frac{u_a^2 \exp(-2\alpha_i s)}{2}] = C' \quad (105)$$

Subtracting this from equation (104) the equation for p'_k is obtained:

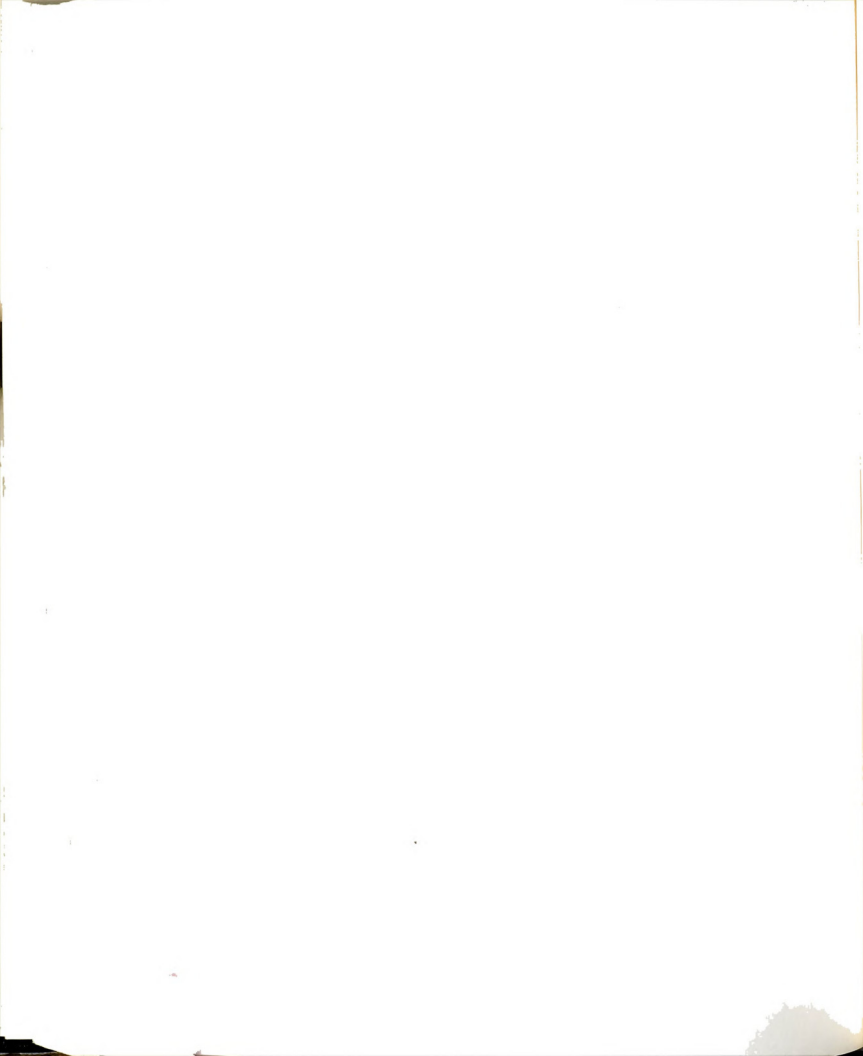
$$p'_k(s,t) = \left[-\frac{u_a \omega}{\alpha_r^2 + \alpha_i^2} \right] \exp(-\alpha_i s) [\alpha_r \cos(\alpha_r s - \omega t) + \alpha_i \sin(\alpha_r s - \omega t)] - \bar{u}(s) u_a \exp(-\alpha_i s) \cos(\alpha_r s - \omega t) - \frac{u_a^2}{4} \exp(-2\alpha_i s) \cos 2(\alpha_r s - \omega t) \quad (106)$$



2.5.3 Discussion

The equation for the fluctuating pressure, p'_k , is comprised of three terms. The growth rate for the last term is twice as large as the growth rate of the fluctuating velocity (see equation (103)) and of the first two terms. Also, the frequency of oscillation of the last term is twice the frequency of the velocity fluctuations and of the first two terms. Hence, the pressure fluctuations p'_k have the potential of not only growing spatially at twice the rate of u' , but, also oscillating at twice the frequency of u' . This will happen if $(-\alpha_i)$ is large so that the last term becomes the dominant term in equation (106).

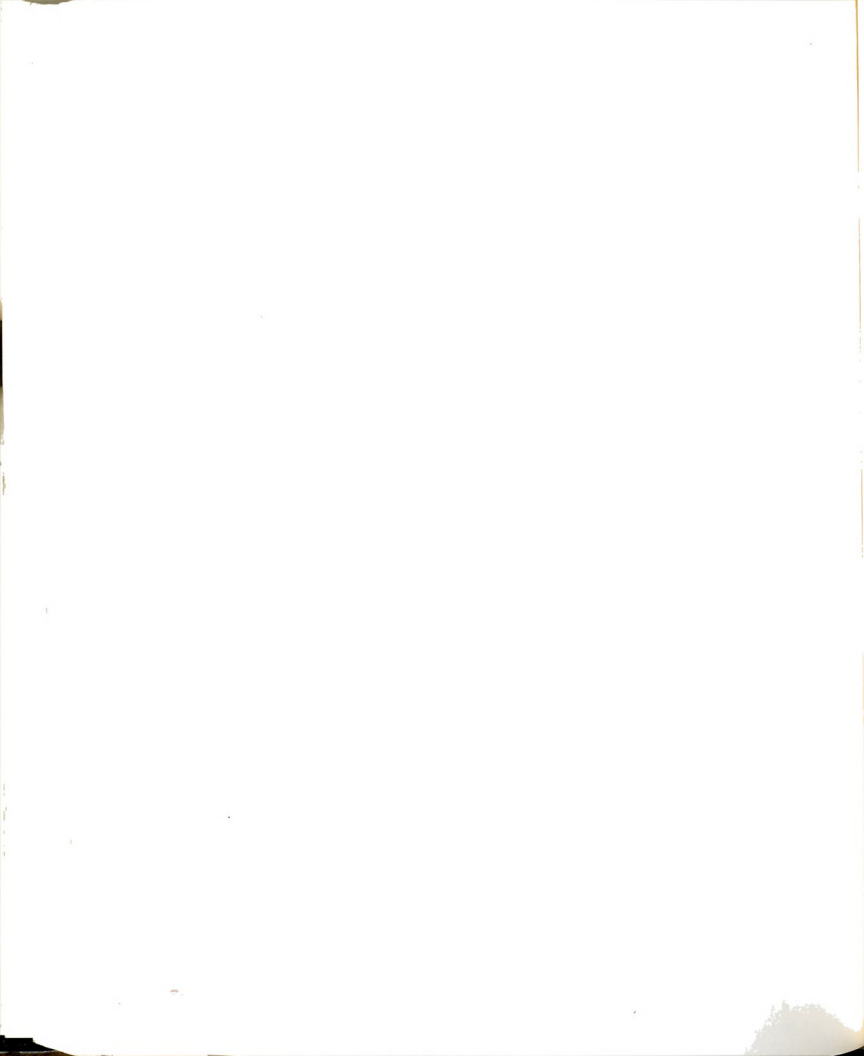
In Chapter 8, $p'_k(s,t)$ will be determined for the experimentally determined values of α_r , α_i , ω and u_a .



EXPERIMENTAL FACILITY AND PROCEDURES

3.1 Introduction

A novel flow facility has been designed (see Appendix A for design details) and fabricated to study the stability characteristics of the slit-jet flow field. A schematic representation of this gravity driven, steady state, finite duration liquid flow facility is presented in Figure 16. The data acquisition comprised of flow visualization using dye, and single channel laser Doppler anemometry. This chapter describes the flow facility, operating principle, modeling of flow, operating procedure, calibration of sensors, flow visualization techniques and details of data acquisition.

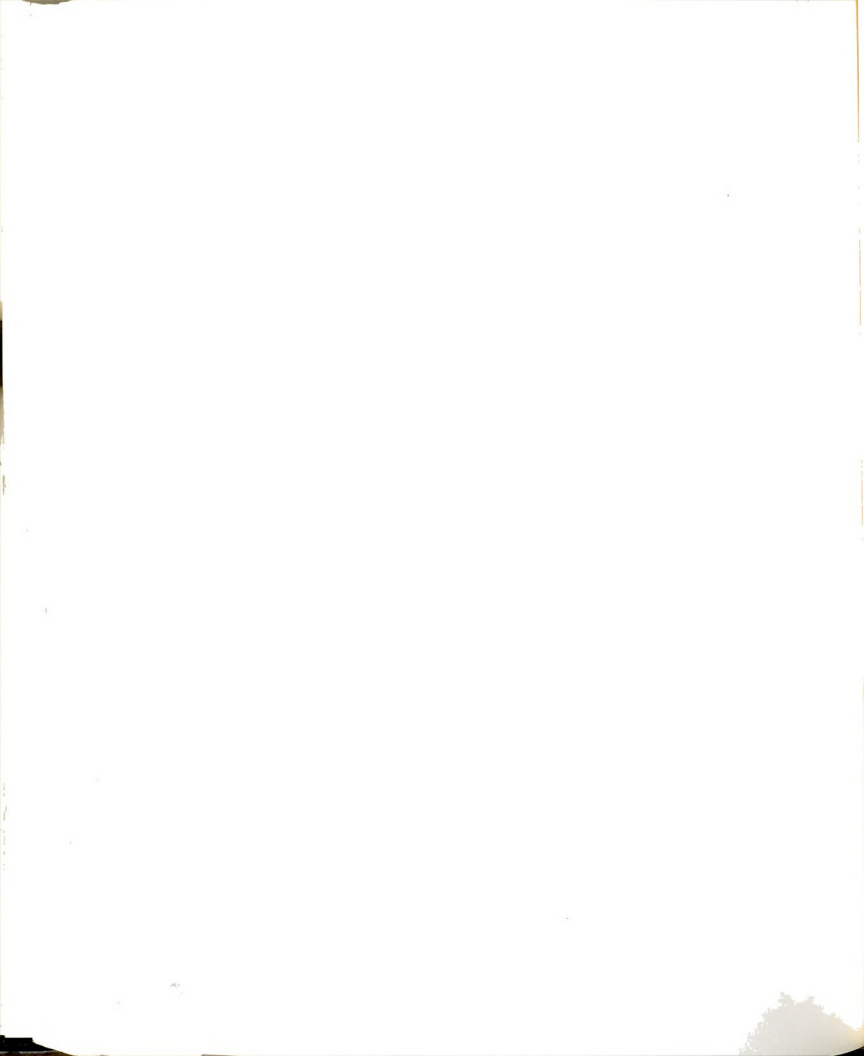


3.2 Experimental Facility

As shown in Figure 16, the flow facility is comprised of two major units: i) a glass tank, and ii) a clear plastic structure called the Nozzle Housing (NH). The two nozzle plates with knife edges are supported at right angles to the jet-axis by the NH, thus forming the two-dimensional slit-jet. These plates are provided with a number of taps which are used to inject the dye for flow visualization.

The tank is filled with a suitable working liquid such that its level is above the nozzle plates under the conditions of static equilibrium. The NH has partially open sides and an air tight cover plate which supports a bleed valve and has two additional openings: i) a pressure tap connected to a Validyne DP15-26 with an operating range of 35.6 cm water column, and ii) vacuum tank connection. The latter is used to raise the liquid head. This establishes the condition to start the jet flow when the cavity is pressurized. The liquid-filled space above the nozzle plates is designated as "the plenum"; the space below is called "the receiver".

Two additional devices, which are part of the experimental configuration, are the i) Volume flow sensor, and ii) Filling device.



3.2.1 Volume Flow Sensor

Figure 17 is a schematic representation of the operational features of the flow facility. The volume flow sensor (hereinafter referred to as VFS), drawn on the left hand side of the NH, is comprised of an "inverted cup" and a pressure transducer (12.7 cm water column, Validyne DP15-22 pressure sensor). As the plenum fluid discharges into the receiver the liquid level rises causing a pressure rise in the cup. This pressure, $p_I(t)$, is related to the volume flow of the jet as shown in the following analysis.

In general, the pressure $p_I(t)$ can be expressed as

$$p_I(t) = p_I(o) + at + bt^2 + ct^3 + \dots \quad (107)$$

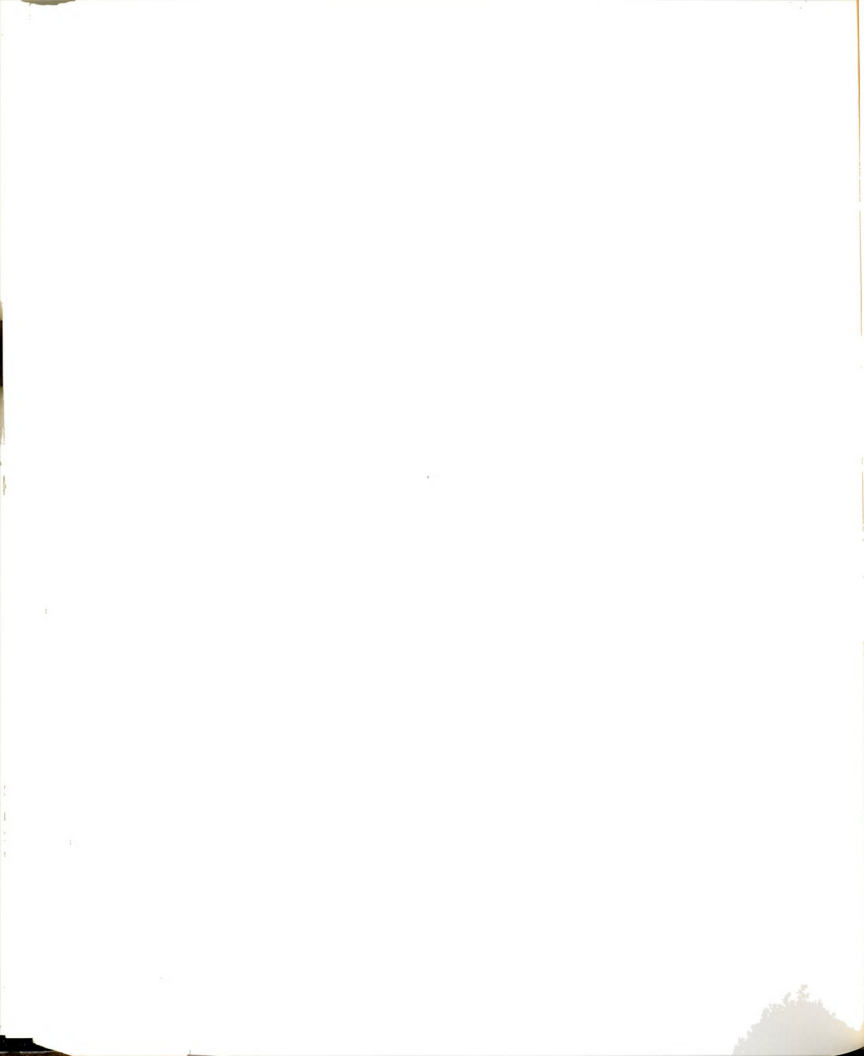
and,

$$\frac{dp_I}{dt} = a + 2bt + 3ct^2 + \dots \quad (108)$$

If the pressure rises linearly with time (for a constant velocity jet), $b = c = 0$, and

$$\frac{dp_I}{dt} = a \quad (109)$$

The rate of rise of $p_I(t)$, i.e., $\frac{dp_I}{dt}$, is proportional to the rate of rise of water column in the receiver. Therefore,



$$\text{Volume flow rate} \propto \frac{dp_I}{dt} \times \text{Area of receiver.} \quad (110)$$

and, since this flow is coming through the jet of area $A_j = Bw$, with spatially averaged velocity $\langle U \rangle = \frac{1}{A_j} \int \vec{V} \cdot \hat{i} \, dA$,

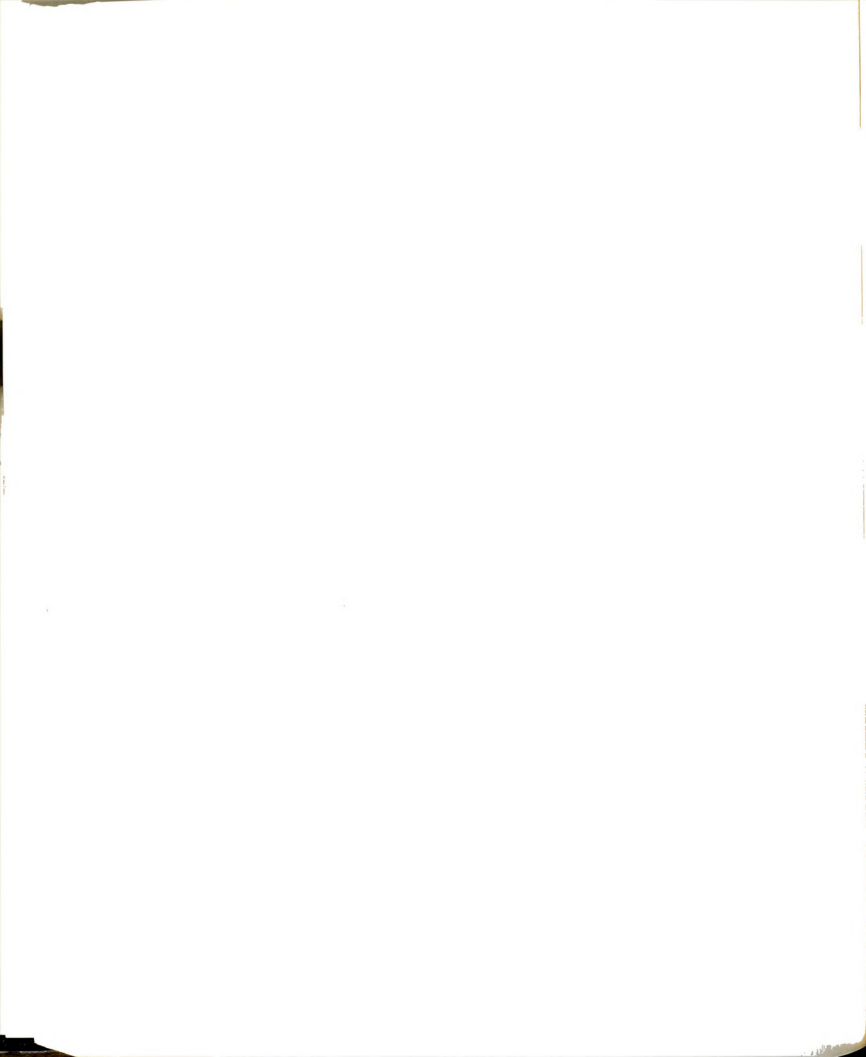
$$A_j \langle U \rangle \propto \frac{dp_I}{dt} \times \text{Area of receiver} \quad (111)$$

Using the above, $\langle U \rangle$ can be determined from the $p_I(t)$ data. (Section 3.7.2 describes the details of calibration of the volume flow sensor to determine the spatially averaged velocity of the jet).

3.2.2 Filling Device

Figure 18 shows a device called the Filling Device (hereinafter referred to as FD) which is made from six or more plastic tubes, supported by a buoyant styrofoam base and a pair of strings. It is used to prevent the formation of two-dimensional vortices (see Figure 19) during the filling process. The use of the FD is shown in Figure 20. The formation of symmetric vortex motions was visualized using the schlieren method; see Figure 21.

The two large counter rotating eddies and the symmetric vortex motions, as shown in Figure 19, possess two-dimensional coherence, and as reported by Gutmark and Ho (1983), such motions can influence the behavior of the jet. It is expected that the use of the FD would help randomize the background disturbances. Experiments have been conducted with and without the FD to determine the influence of the



background disturbance (initial condition) on the behavior of the jet. The results of these experiments have been presented in Section 7.5.

3.2.3 Working Liquid

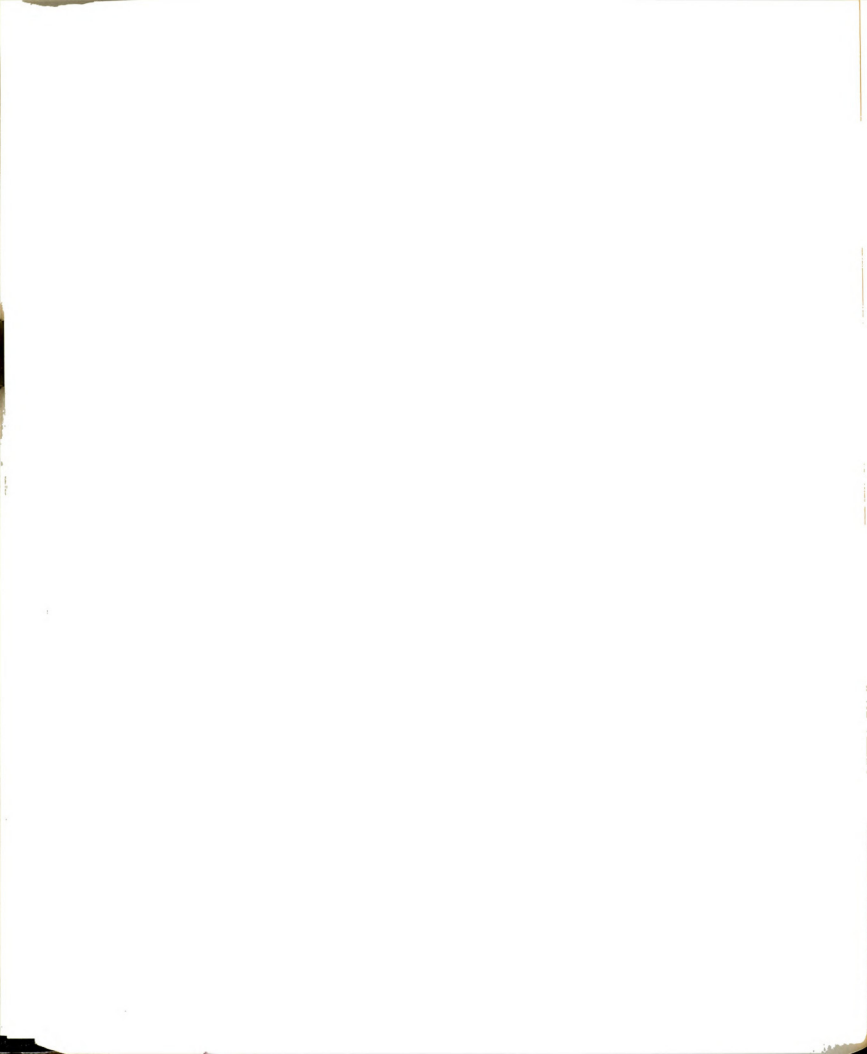
Any Newtonian liquid, with known density ρ and kinematic viscosity ν , can be used to execute the experiment. In this study, three different liquids were used: water, water-sugar and water-glycerol mixtures. Water was used for the relatively high Re runs (400-8000), whereas, a water-sugar or a water-glycerol mixture was used for lower Re runs (75-1000). Note that the latter mixtures have relatively large kinematic viscosity values which permit low Re values to be studied with adequately large velocity values. A sufficiently large velocity ($\langle U \rangle \geq 1$ cm/s) is required for the control system to properly function.

3.2.4 Operating Principle

The "steady state" operation of this finite duration, gravity driven flow facility is achieved by a controlled pressurization of the cavity in the NH such that

$$\frac{\partial p_k}{\partial t} - \frac{\partial}{\partial t}(p + \rho gh) = 0 \quad (112)$$

For this condition, $\vec{V}(x,y)$ in the plenum and receiver is constant during the duration of the experiment.



3.3 Flow Modelling

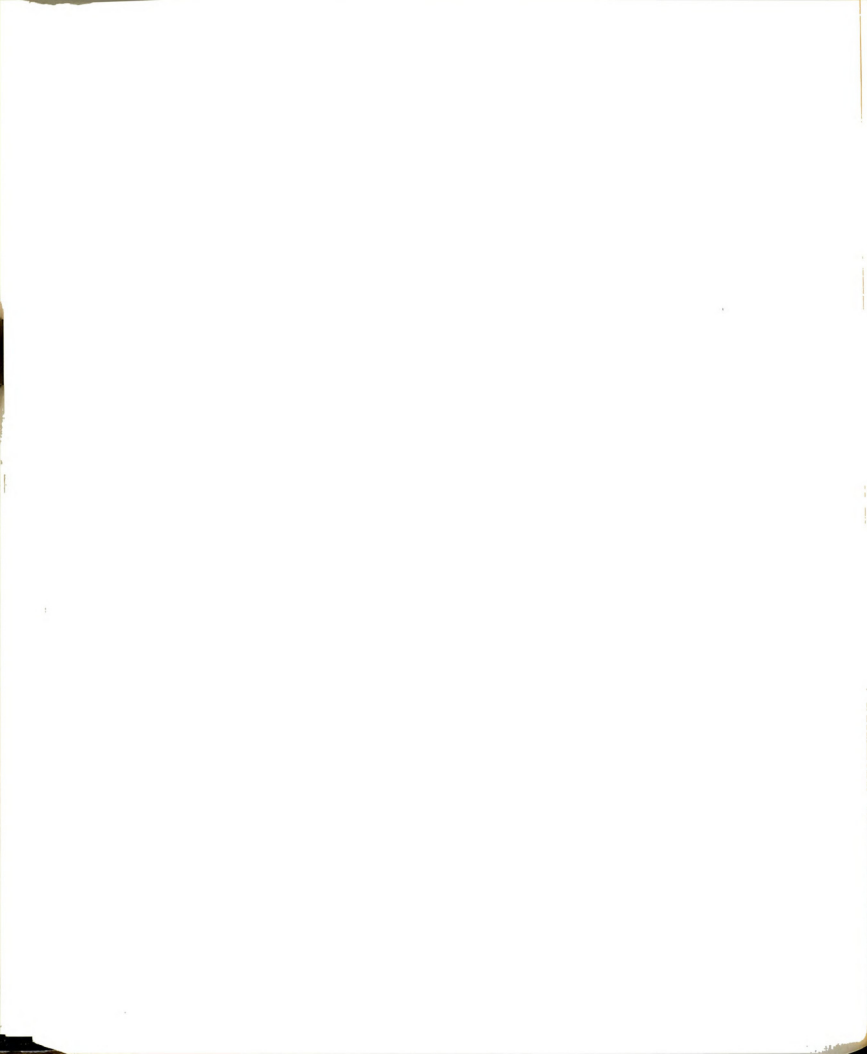
A control volume approach [Potter and Foss (1982)] has been used to model the two flows: i) liquid from the NH to the receiver, and ii) air from the ambient to the NH through the computer controlled bleed valve in the cover plate. The objective of this analysis is to determine the rate of opening of the bleed valve $A_v(t)$ such that a constant velocity liquid jet is obtained.

For simplicity, and because it has proven to be satisfactory a posteriori, the initial transient condition (wherein $\frac{\partial U_0}{\partial t} > 0$) is not considered in this analysis. Note that this restriction permits the use of the Bernoulli equation for the description of the unsheared regions of the flow. The velocity U_0 for the following analysis is given in terms of the desired Reynolds number (Re) as

$$U_0 = \frac{\nu}{w} \frac{Re}{C_D} = \text{constant} \quad (113)$$

where ν is kinematic viscosity of the working liquid, w is slit width and C_D is discharge coefficient of the jet.

Four control volumes CV_i , $i = 1, \dots, 4$, are used in the modelling; see Figure 22. This figure also describes the symbols used. The conservation of mass equation for a deformable control volume [Potter and Foss (1982)],



$$\int_c \frac{\partial \rho}{\partial t} dV + \int_{cs} \rho_B \vec{V}_B \cdot \hat{n} dA + \int_{cs} \rho_I \vec{V}_I \cdot \hat{n} dA = 0 \quad (114)$$

together with the Bernoulli equation are applied to CV_1 resulting in

$$h_{NH}(t) = h_{NH}(0) - \frac{A_j}{A_{NH}} C_D U_0 t \quad (115)$$

and

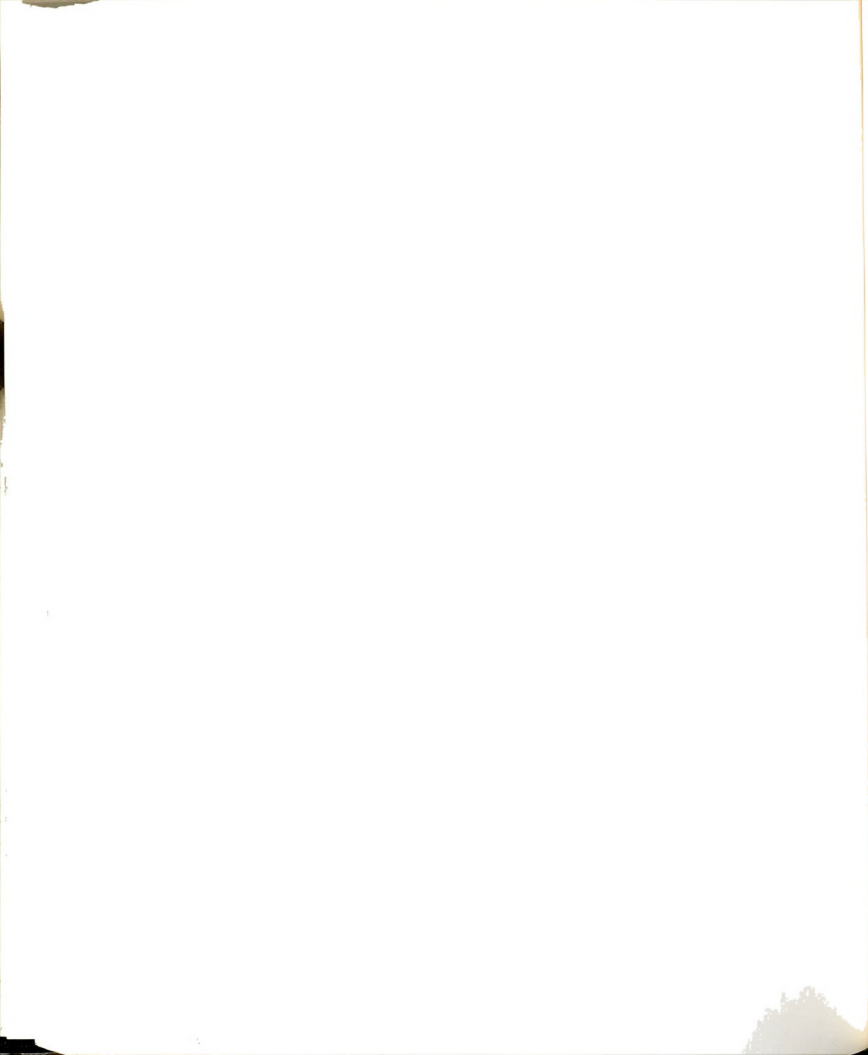
$$P_{NH}(t) = 0.5 \rho_w U_0^2 \left[1 - \left\{ \frac{A_j}{A_{NH}} C_D \right\}^2 \right] + \rho_w g [h_r(t) - h_{NH}(t)] + p_{atm} \quad (116)$$

Considering the conservation of mass in the entire system, equation (116) becomes

$$P_{NH}(t) = \rho_w g A_j C_D U_0 \left[\frac{A_r + A_{NH}}{A_r \times A_{NH}} \right] t + 0.5 \rho_w U_0^2 \left[1 - \left\{ \frac{A_j}{A_{NH}} C_D \right\}^2 \right] + \rho_w g \left[\frac{A_r + A_{NH}}{A_r} \right] [h_{eq} - h_{NH}(0)] + p_{atm} \quad (117)$$

With $U_0 = c$ equation (117) shows that $P_{NH}(t)$ should increase linearly with time.

The space between the deformable control surface of CV_1 and the top cover plate is divided into two control volumes, CV_2 and CV_3 which are separated by a fictitious, massless piston which moves with velocity $\dot{h}_p(t)$. This piston simplifies the thermodynamic description of the air in the cavity as noted below; note that the pressures are equal within the two control volumes to $P_{NH}(t)$.



The constant mass of air, M_2 , below the piston is assumed to undergo an isentropic compression. Under this condition and using equation (114), the position of the massless piston is found to be

$$h_p(t) = h_{NH}(0^-) + \frac{M_2}{A_{NH}\rho_2(0^-)} \left\{ \frac{p_{NH}(0^-)}{p_{NH}(t)} \right\}^{\frac{1}{\gamma}} - \frac{A_1}{A_{NH}} C_D U_0 t \quad (118)$$

The time dependent volume (V_3) of, and the pressure within, CV_3 are in terms of the above information. The pressurization of CV_3 is caused by the influx of atmospheric air through the bleed valve. The compression of air in CV_3 is assumed to undergo a polytropic process with exponent n . With this assumption, equation (114) yields the time dependent area of the bleed valve, $A_v(t)$,

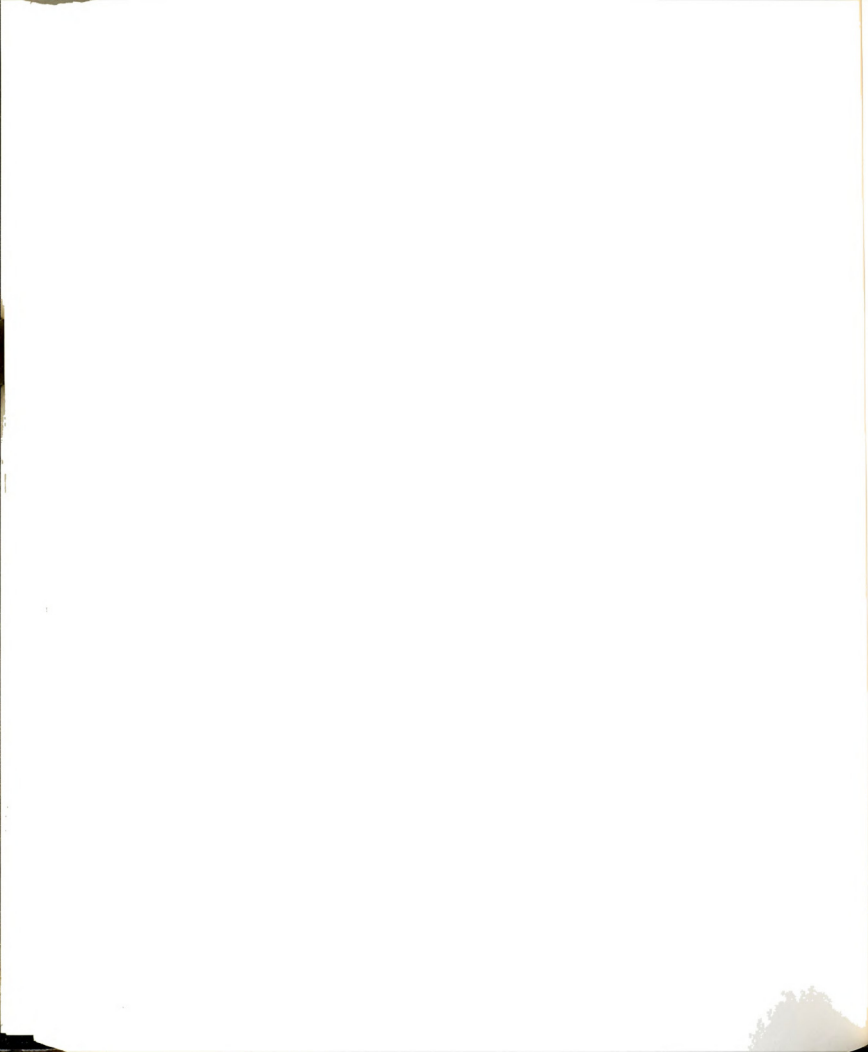
$$A_v(t) = \frac{K \dot{p}_{NH} (p_{NH})^{\frac{1-n}{n}} V_3(t) - n K (p_{NH})^{\frac{1}{n}} A_{NH} \dot{h}_p(t)}{n \rho_v C_{Dv} U_v(t)} \quad (119)$$

where

$$K = [\rho (p_{NH})^{\frac{-1}{n}}]_{t=0}$$

C_{Dv} = discharge coefficient of the bleed valve

ρ_v = density of air at the vena contracta of the bleed valve =
 ρ_{atm}



$U_v(t)$ = the unsteady inviscid velocity at the vena contracta of the bleed valve.

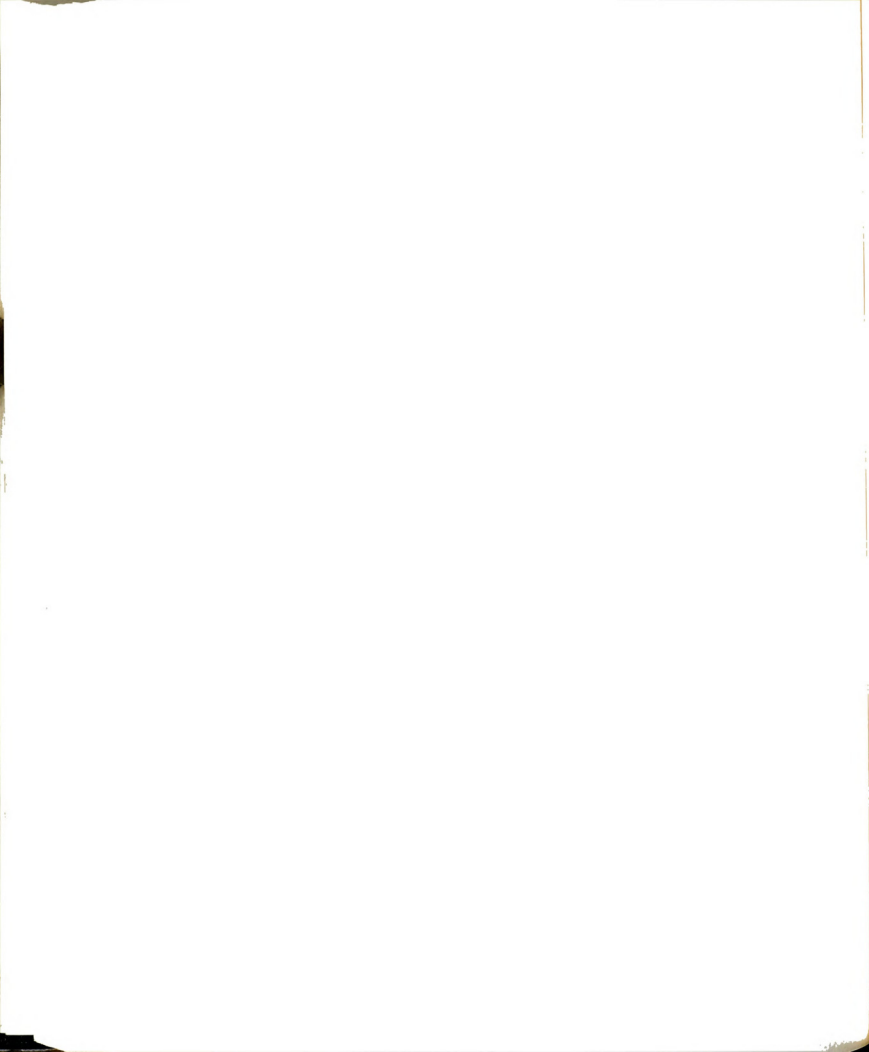
The velocity $U_v(t)$ is obtained by applying the Bernoulli equation to the control volume CV_4 :

$$U_v(t) = \left[\frac{2(p_{\text{atm}} - p_{\text{NH}}(t))}{\rho_{\text{atm}}} \right]^{0.5} \quad (120)$$

The expression (119) for the opening of the bleed valve, $A_v(t)$, is valid for any time t after the start of the experiment. Since the experiment is of finite duration, the modelling of its starting procedure becomes important and warrants some discussion. Figure 23 is the schematic representation of the time histories of three quantities of interest: the liquid jet velocity at vena contracta U_0 , the pressure of the nozzle housing p_{NH} , and the area of the bleed valve A_v . The discussion is focused at times $t = 0^-$, 0 and 0^+ ; $t = f$ indicates the time when $p_{\text{NH}}(t)$ becomes atmospheric and the jet stops.

For $t \leq 0^-$ the system is at rest with $U_0 = 0$, a hydrostatic condition for p_{NH} (i.e., $p_{\text{NH}}(0^-) = \rho g[h_r(0^-) - h_{\text{NH}}(0^-)]$) and $A_v = 0$. At $t = 0$, the jet velocity at the vena contracta is modelled to change to U_0 as a step function. For this to happen the model requires the pressure $p_{\text{NH}}(0^-)$ to rise by the dynamic head $= \frac{0.5\rho_w U_0^2}{U_0^2}$, i.e.,

$$p_{\text{NH}}(0) = p_{\text{NH}}(0^-) + \frac{\rho_w U_0^2}{2} \quad (121)$$

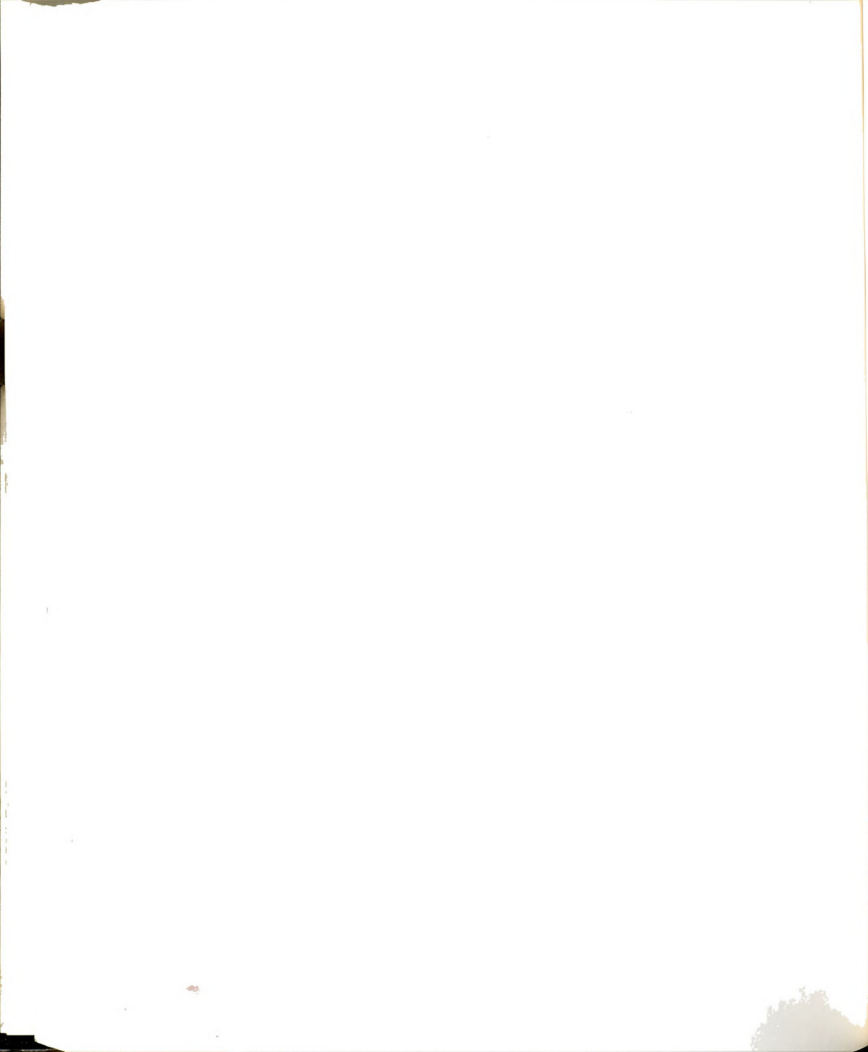


Since the pressurization of the NH is caused by the influx of atmospheric air, the model requires a simultaneous compression of the air in CV_2 and the opening of the bleed valve to allow a finite mass of air in CV_3 . At $t = 0^+$, the model allows the pressure p_{NH} to begin its linear variation with time as A_v is made to open following equation (119). For these conditions, $U_0(t < 0) = 0$ and $U_0(0 \leq t < f) = 0$. At $t = f$, $p_{NH} = p_{atm}$ and $U_0 = 0$. The effect of the transient at $t = 0$ can be minimized by drawing a relatively large head $h_{NH}(0^-)$: This can be seen from the equations (117) and (119). For the same value of Re (i.e., U_0), the absolute value of the ratio $0.5\rho_w U_0^2 / (p_{NH}(0^-) - p_{atm})$ decreases as $h_{NH}(0^-)$ increases. As a result at $t = 0$, the massless piston and the bleed valve are required to move by a small amount.

3.4 Computer Facility for Data Acquisition and Control

A PDP 11/73 computer system using RSX 11M+ operating system was used i) to run the experiment, and ii) to acquire data. This section describes the computer facility and the characteristics of the A/D converter.

The PDP 11/73 computer system is networked to other computing facilities in the College of Engineering using the EGRNET. Its node name is EOWYN. The system has 4 megabyte of resident memory, two hard disk drives each with a storage capacity of 70 megabytes and a tape drive TK50.



The computer has two A/D converters:

i) TSI's 12 bit, 10 channel A/D converter (IFA200). Its input range is limited to 0-5 volts with the least significant bit (LSB) = 1.25 mV.

ii) DEC's 12 bit, 8 channel A/D converter (AXV11C) with LSB = 5 mV.

In addition the system is equipped with an interface, the DRV11 board, which is used for running the stepper motor and to control other peripheral devices.

3.5 Software to Control the Bleed Valve

The bleed valve is activated by a stepper motor which in turn can be run by sending pulses from the computer. This provided the basis of running the experiment under software control. This section describes the computer programs which were developed to run the experiments.

Two Fortran programs were developed to run on the laboratory's PDP 11/73 computer system: i) CLAWSN to generate a time series for the stepper motor. This series was stored in the computer. (ii) ZVALVE to run the stepper motor in accordance with the time series generated by CLAWSN.

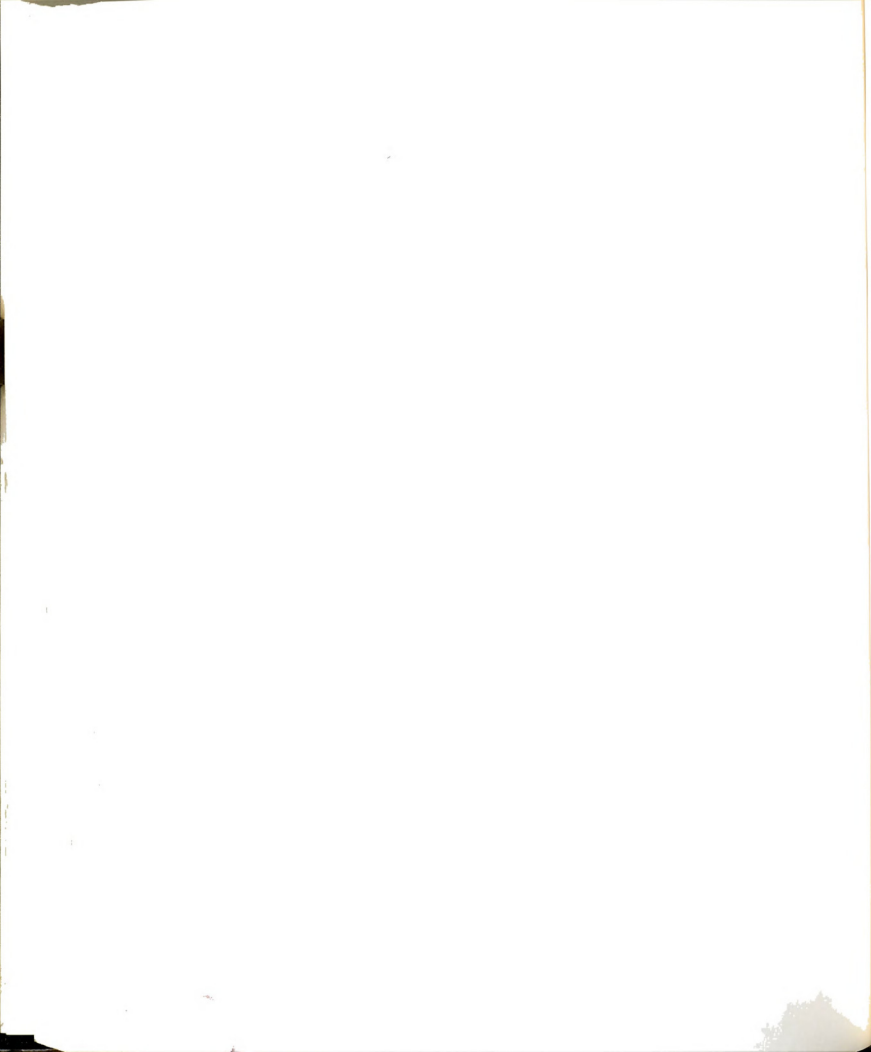


3.5.1 Program CLAWSN

The user provides the program with the value of the desired Reynolds number (Re), the width of the jet (w), the kinematic viscosity of the working liquid (ν), the head of the liquid filled in the tank under equilibrium conditions (h_{eq}), and the level to which the liquid would be raised ($h_{NH}(0^+)$). Based upon this information and using equation (119) the program computes the area of the bleed valve $A_v(t_k)$, where $t_k = k\delta t$ and δt ranges over $10^{-5} \leq \delta t \leq 10^{-2}$ sec. Since the valve opens in steps of $\Delta A_v = 8.59384 \times 10^{-8} \text{ m}^2/\text{step}$, the ratio of $A_v(t_k)$ and ΔA_v yields the n th step of the motor to be taken at t_k time. For the initial part of the experimental run the valve opens slowly allowing larger values of δt in the computation; towards the end of the run the valve opens at a much faster rate requiring very small values of δt . The program automatically adjusts the value of δt so that the time required for the n th step could be found. The area of the valve at time t is given by

$$A_v(t) = A_v(0) + n(t)\Delta A_v \quad (122)$$

where $n = 0, 1, 2, \dots$ are the number of motor steps. The minimum time allowed between two consecutive steps is = 1 msec.

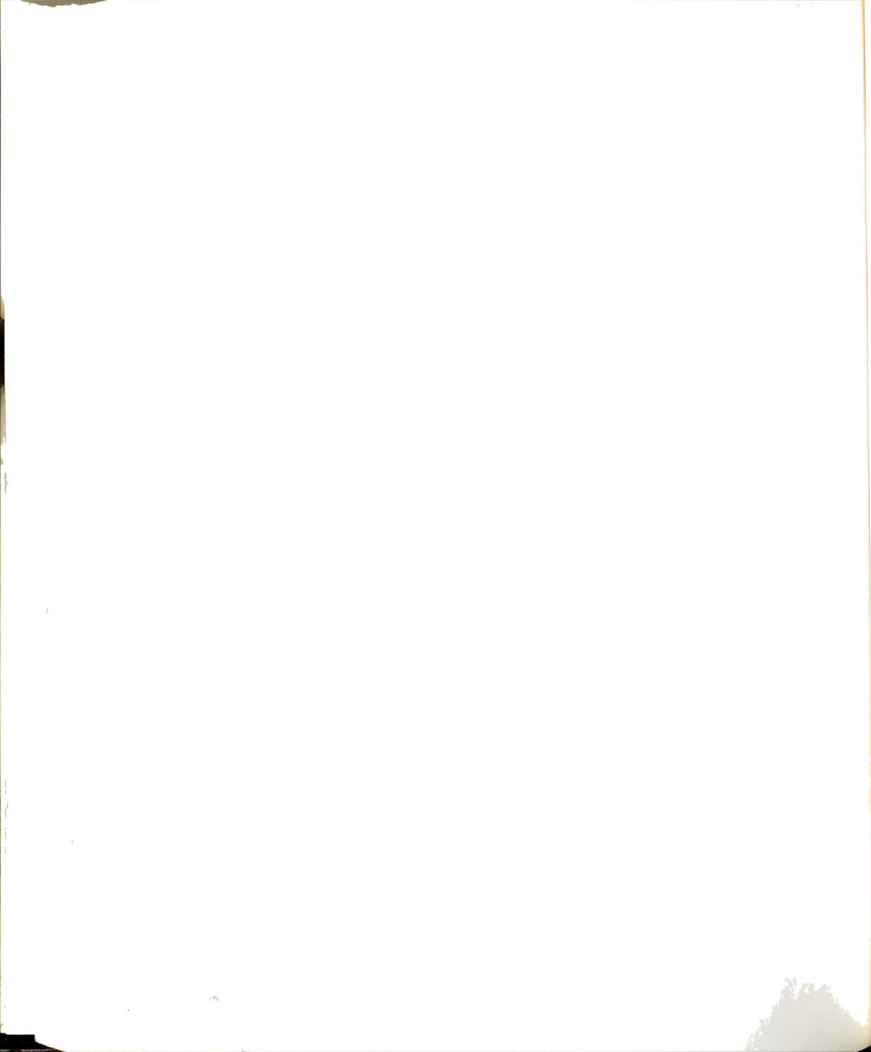


3.5.2 Program ZVALVE

This program performs two functions: i) run the experiment under a tight wait loop, and ii) acquire data. (See Section 3.9 for details of data acquisition.) When this program is started, it first reads the file stored by the program CLAWSN. In addition to the timings of the stepper motor other data are also read. Figure 24 presents the flow chart of the tight wait loop which jogs the stepper motor. The time required to execute a step is indicated on the right hand side. Using the interrupt control system of the computer and the real time clock a signal is sent to the motor to take a step at the designated time. From the estimates of the time for each operation it is noted that it takes 3.1 μ sec in the wait loop while 8 μ sec are required to send a pulse to the motor. In case of some delay, one or more pulses are sent to the motor in quick succession to conform the rest of the run to the time array t. Since a task running at a higher priority can interrupt the signal sequence, it was necessary to ensure that there was no other user on this multiuser system when the experiment was run.

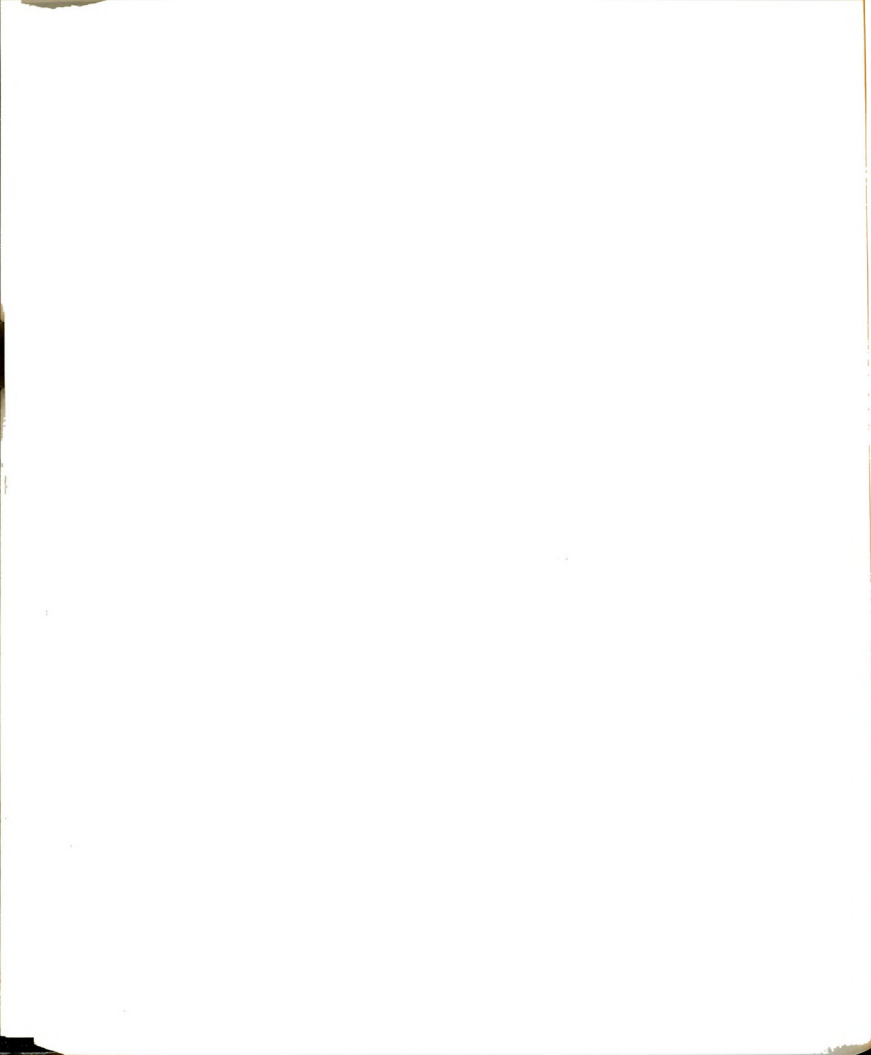
3.6 Operating Procedure / Start of Experimental Run

The glass tank was filled with about 0.2 cubic meter (50-55 gallons) of an appropriate working liquid (see Section 3.2.3.). With the cover plate of the NH in place, the air cavity underneath it was evacuated slowly to fill the plenum. Two different protocols were used for filling the plenum: i) filling by inducing the recharge flow



from the receiver to the upper plenum through the slit-jet opening, and ii) by using the FD as shown in Figure 20. The liquid surface was thus raised to a level which was slightly above a predetermined level equal to $h_{NH}(0^-)$, for a given Reynolds number. After waiting for the "filling disturbances" to decay to a sufficiently low level, the suction-flow-which had compensated for the air leakage was turned off. The continuing leakage permitted the cavity pressure p_{NH} to increase slowly. During the time period required for the decay of the disturbances in the plenum the program ZVALVE (see Section 3.5.2. for detail) was run on the laboratory's PDP 11/73 system to initiate the experiment and acquire data.

Using the DEC A/D converter, the program monitors the rise in the cavity pressure p_{NH} . When the cavity pressure became equal to $p_{NH}(0^-)$ the computer opened the bleed valve at the fastest rate possible (= 666 steps per second) to simulate a step change in the jet velocity, U_0 . After opening the bleed valve, the DEC A/D converter again monitored the cavity pressure to check whether the pressure had risen by $0.5\rho_w U_0^2$. As this pressure was reached the computer began i) opening the bleed valve such that $p_{NH}(t)$ varied linearly, and (ii) acquiring data at a user specified rate using the TSI IFA200 A/D converter. Figure 25 provides a schematic representation of the time histories of the cavity pressure p_{NH} and the rate of flow q_b of the atmospheric air to the cavity.



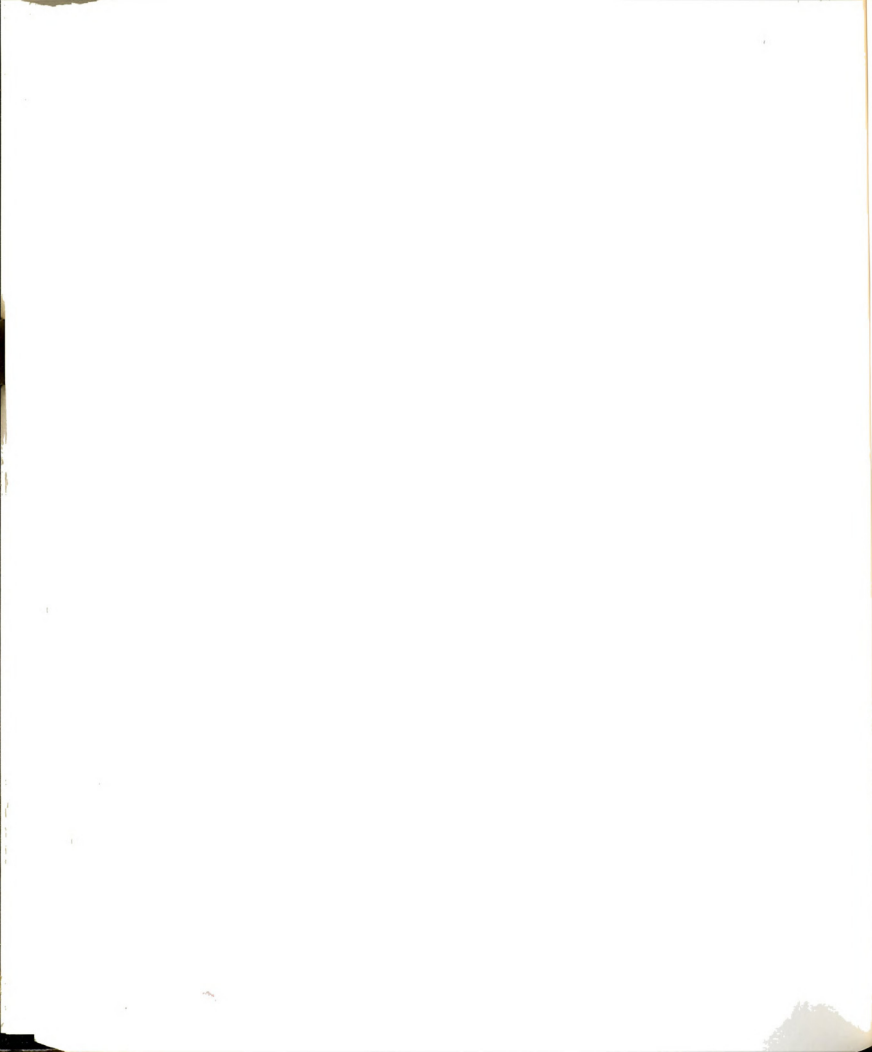
3.7 Calibration of Sensors

Two sensors were used to determine the jet velocities: i) a single channel laser Doppler anemometer (LDA), and ii) a volume flow sensor. The LDA was used to obtain pointwise measure of the longitudinal component of velocity $u(x,y,t)$. The volume flow sensor provided an estimate of the spatially averaged velocity of the jet $\langle U \rangle(t)$. This section describes the procedures of: i) checking the operation of the LDA system, and ii) calibrating the volume flow sensor.

3.7.1 Checking Operation of the LDA System

Figure 26 shows the configuration of the single channel LDA system. It includes a 35 mW Spectra Physics He-Ne laser, TSI sending and receiving optics with focal length $f = 250$ mm, TSI photomultiplier and TSI 1980 Counter. The output of the counter was read by the Apple IIe computer when the counter was run in the Auto mode.

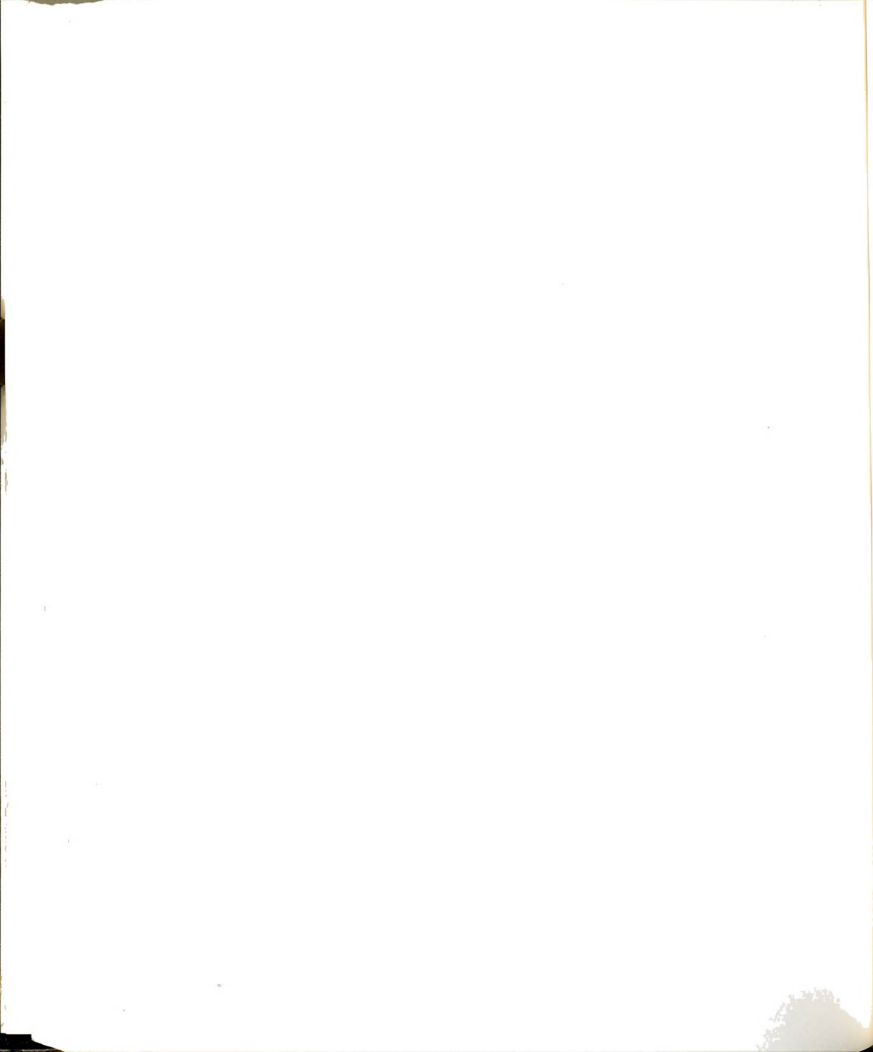
Figure 27 provides a schematic representation of the arrangement for checking the operation of the LDA system against a known input velocity. A circular, clear plastic disk was mounted on a variable speed Ul2FGT dc gear motor with a gear ratio of 16:1. The front surface of the disk was made to intersect the measurement volume (the intersection point of the two laser beams; see Figure 27). The vertical component of the disk velocity at the point of intersection is given by



$$v = 2\pi fr \sin\theta \quad \text{m/s} \quad (123)$$

where, f is the rate of rotation of the disk in hertz, r is the radius of the disk in m at the point of intersection and θ is the angle as shown in Figure 27. A tachometer was used to determine the angular frequency of the rotating disk. The velocity v was computed by using equation (123).

When the measurement volume of the LDA system intersects the front surface of the disk a Doppler signal is generated. The receiving optics of the LDA system sends the signal to the Counter which determines the Doppler-shifted frequency due to the vertical velocity component of the rotating disk. The Apple IIe computer samples 4096 data points at a user specified rate and determines the velocity for each data point. The computer generates a histogram from the 4096 data points and also computes the mean and the rms velocities. Tests were conducted both in the forward and backward scattering modes. Figure 28 is a plot of the average of the disk velocity found by the LDA versus the disk velocity found by using equation (123). Figure 29 presents a plot of the ratio of the rms of the LDA velocity to its mean velocity versus the velocity of the disk found by using equation (123).

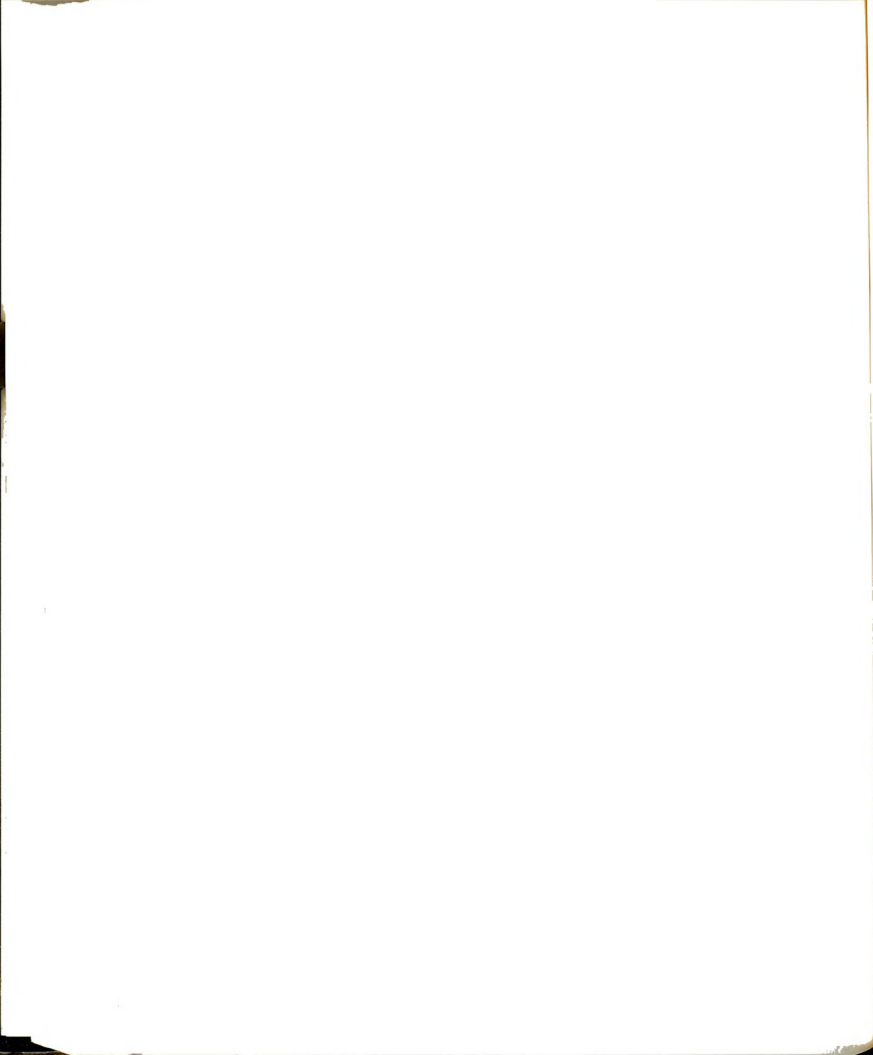


3.7.2 Calibration of Volume Flow Sensor

The principle of operation of the Volume Flow Sensor (VFS) is described in Section 3.2.1. Figure 30 presents the experimental arrangement for its calibration. In order to simulate the rise of liquid in the receiver (see Figure 17) the VFS is driven into the stationary liquid at a desired velocity. The velocity of the VFS and the corresponding rate of rise of pressure $\frac{dp_I}{dt}$ are determined to provide the independent and the dependent variables, respectively. The Linear Variable Differential Transformer (hereinafter referred to as LVDT), shown in Figure 31, was used to monitor the position of the traverse. The pressure p_I of the air trapped in the cup was sensed by the Validyne DP15-22 pressure transducer. Before the VFS was calibrated, the pressure transducer and the LVDT were tested and calibrated; the following is a description of their calibration.

3.7.2.1 Calibration of Pressure Transducer

The pressure transducer was calibrated by connecting it in parallel with a water manometer. Pressure was applied to both, to displace the water in the manometer by 12.7 cm while the span of the pressure transducer was set so that the output was equal to the maximum input voltage of 5 V, for the IFA200 A/D converter. A number of readings were then taken at intermediate pressure values in order to check the linearity of the transducer. Figure 32 is a plot of the output voltage of the transducer as a function of the input pressure.



3.7.2.2 Calibration of LVDT

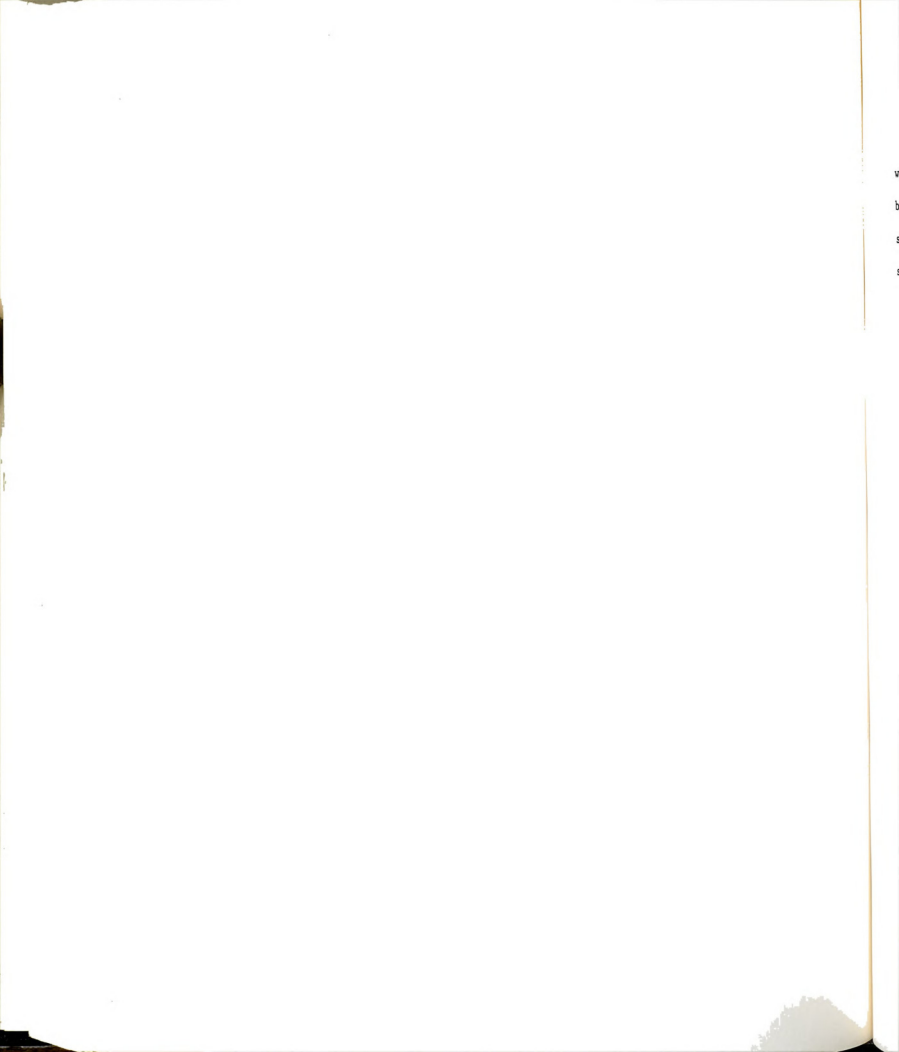
Figure 31 shows the Linear Variable Differential Transformer manufactured by Schaevitz Engineering. Its component parts are an inductive coil and a core. The coil is excited by an ac signal and the ac output of the LVDT depends upon the displacement of the core with respect to the primary coil. To calibrate the LVDT, a sinusoidal signal at 2.5 kHz was applied to the primary coil and, with a known displacement of the core, the input and the output signals were recorded by the computer. Using the position of the coil as independent variable and the ratio of rms of output to rms of input voltage as dependent variable a linear regression was performed resulting in

$$\text{Ratio } \left(\frac{\sigma_o}{\sigma_i} \right) = 0.284375 - 0.0412275 Z \quad (124)$$

and the standard deviation (residual) was 5.60993×10^{-4} . Here Z is the position of the core from the origin. Figure 33 is a plot of the Ratio as a function of position Z.

3.7.2.3 Data Acquisition and Processing

Having checked and calibrated the component parts of the VFS its calibration was carried out. Figure 34 is a flow chart of the program used for calibrating the VFS. Figure 35 is a plot of $\frac{dp_I}{dt}$ as a function of the velocity of the cup. Linear regression was performed on the data resulting in



$$\frac{dp_I}{dt} = -0.000879 + 0.4477062 V_{cup} \quad (125)$$

with standard deviation of the residual = 0.3643×10^{-3} . The calibration of the VFS was performed in a water-glycerol mixture of density $\sigma = 1120 \frac{kg}{m^3}$. When another liquid of density ρ was used, the second coefficient in equation (125) is adjusted as

$$\beta_2 = 3.9974 \times 10^{-4} \rho \quad (126)$$

Equation (125) then becomes

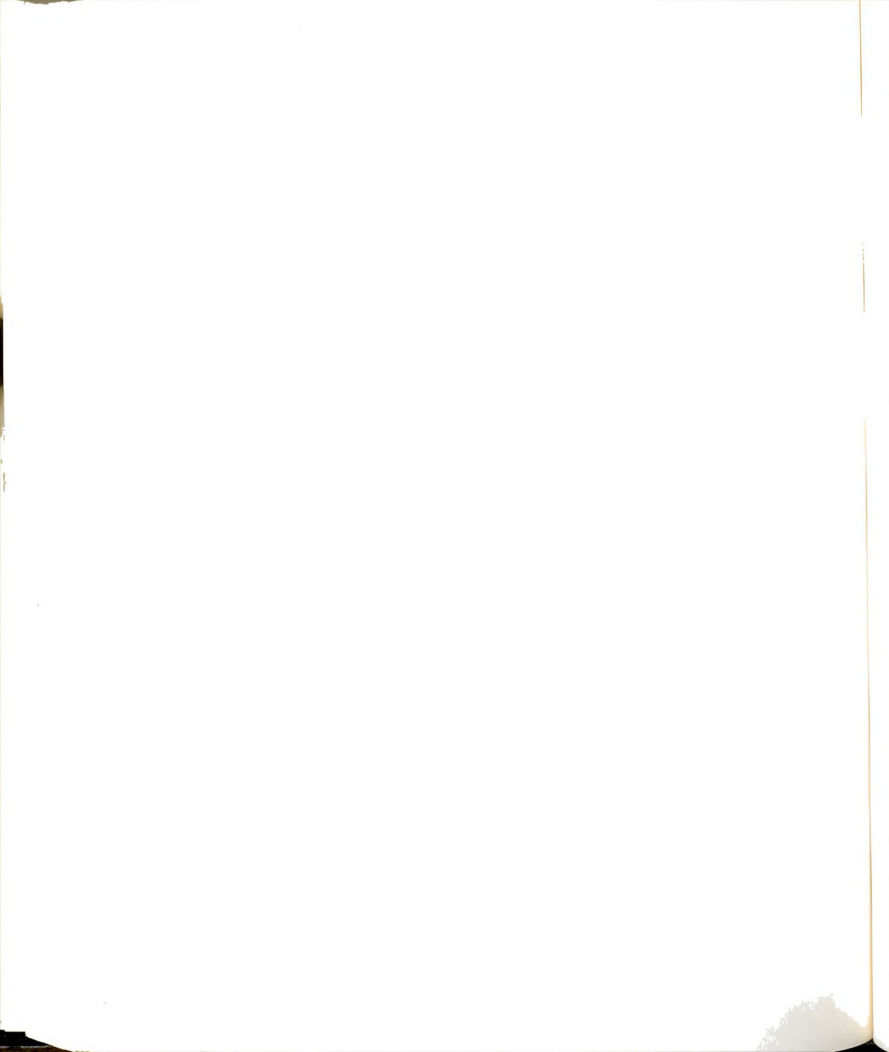
$$\frac{dp_I}{dt} = -0.000879 + 3.9974 \times 10^{-4} \rho V_{cup} \quad (127)$$

The performance of the VFS has been tested from time to time by comparing the velocity estimated by it against the estimate obtained by photographically recording the fall of liquid in the plenum.

3.8 Methods of Flow Visualization

Three different techniques have been attempted in this study; these include:

- i) Schlieren
- ii) Hydrogen bubble



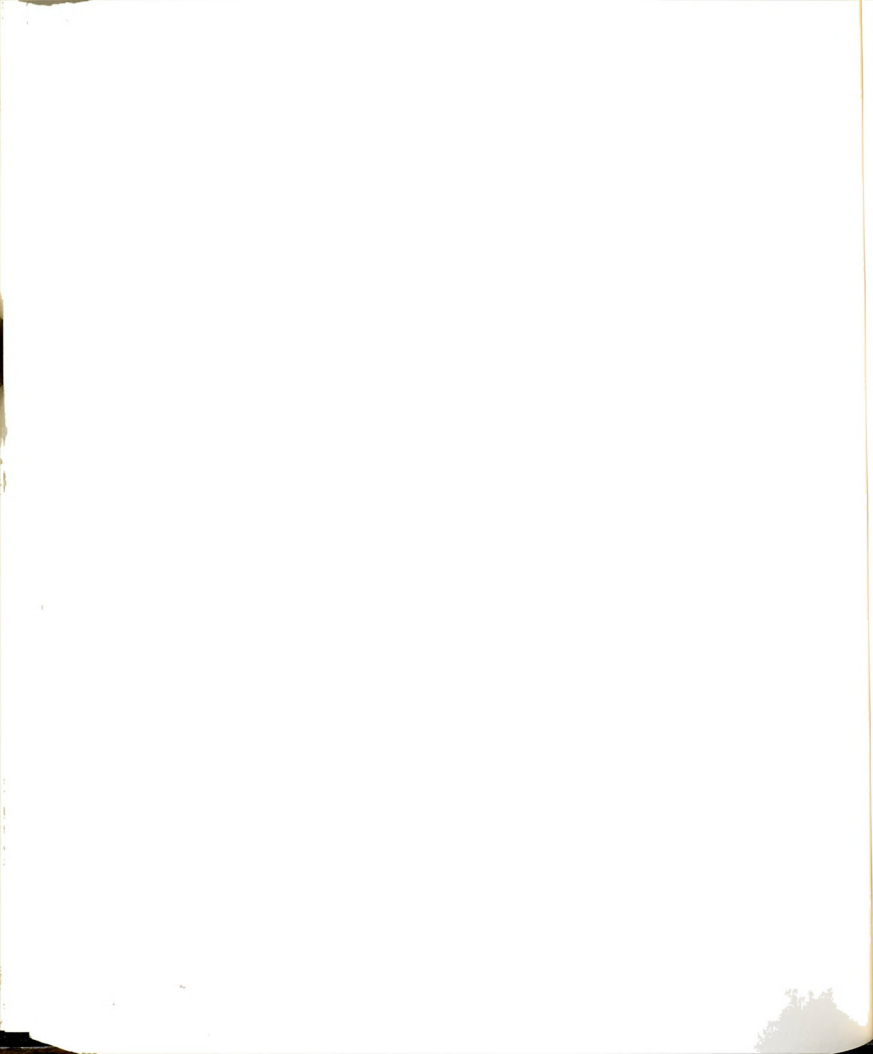
iii) Dye

This section describes briefly the three methods and the reason why the dye method has been found most suitable in this study.

3.8.1 Schlieren

Figure 36 is a schematic representation of the configuration used for the schlieren flow visualization. The glass tank was filled with a water-glycerol mixture; the mixture was 37% glycerol in concentration by weight with a value of kinematic viscosity $\nu = 2.92 \times 10^{-6} \text{ m}^2/\text{s}$ and a refractive index of $n = 1.404$. A water-sugar mixture of the same density but with a different refractive index: $n = 1.367$ was injected in the midplane of the plenum to mark the boundaries of the jet. When the experiment was run, the injected mixture formed part of the jet fluid and the difference in the refractive indices of the two mixtures created schlieren pattern given the parallel rays of the incident light; see Figure 36. Figure 37 is a photographic record of this flow visualization technique. This experimental method worked as desired; however,

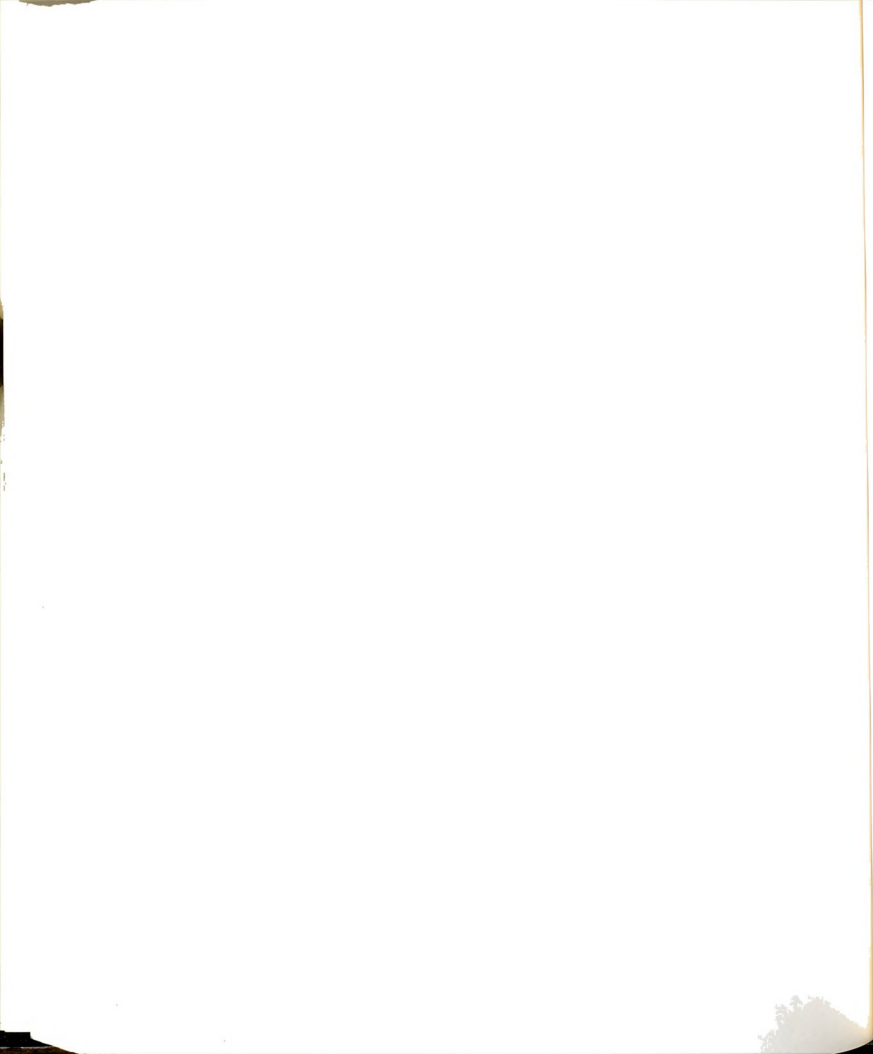
- i) Given the available spherical mirrors of diameter 18.5 cm, the longitudinal extent of the flow field that could be visualized was limited to about 10 cm or 4 slit widths.



- ii) The dye method of flow visualization was much more efficient in terms of experiment time and it was equally or more effective.
- iii) As more and more water-sugar mixture was added to the test liquid (water-glycerol) the jet boundary became difficult to discern.
- iv) There was an unknown effect of the substantial mismatch in the kinematic viscosity between the test liquid and the contaminant (water-sugar mixture) which marked the boundaries of the jet.

3.8.2 Hydrogen Bubble Technique

A 0.127 mm diameter Ni-Cr wire, supported horizontally across the jet and charged to a potential of about 30 volts above the ground potential in the tank produced hydrogen bubbles that were used to visualize the flow. The bubbles in the middle of the jet moved downstream while others moved upstream and it was not clear whether those moving upstream were following the reversed flow associated with the vortex motions or they were influenced by their buoyancy. In view of this it was concluded that this technique is most suitable in horizontal and planar flows where the buoyant effects are orthogonal to the velocity field.

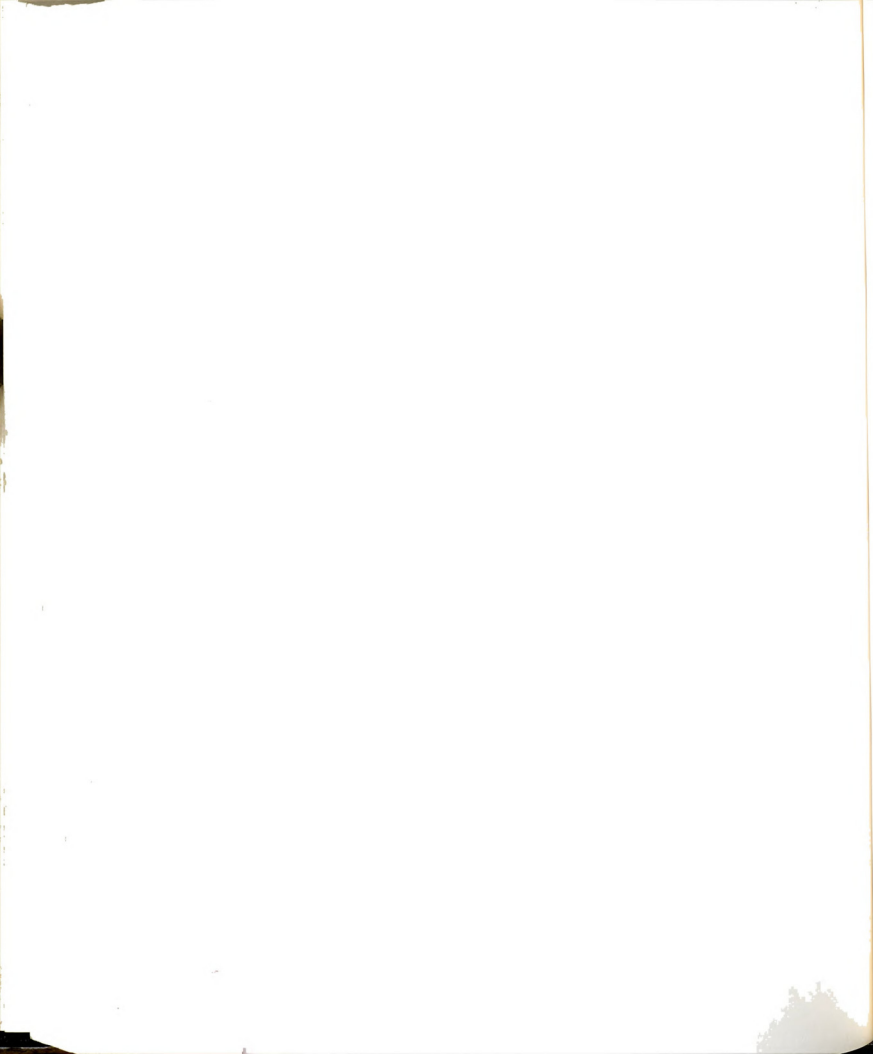


3.8.3 Dye Injection

Food color dye was used to prepare the colored liquid for flow visualization. This liquid had nominally the same density as that of the test liquid. Figure 38 shows the apparatus for the injection of the dyed liquid. The following protocol was used for this visualization technique. After the liquid head was raised in the NH and sufficient time had been allowed for the disturbance level to decrease, the stopcocks in the dye lines were opened and the level of the bottle containing the dye was slowly raised. The dye first flowed to a header and through tygon tubes into the plenum. The dye was caused to flow at such a small rate that no dye jets were formed. Under the pressure of the liquid head in the NH, the dye simply flowed out in the form of a hemisphere and got spread on the nozzle plates. See Figure 38. When the circular dye stain got big enough the flow was stopped and after waiting for about 60-90 seconds, the experiment was run as described in Section 3.6.

In the mid plane of the jet, the boundary layer which forms on the nozzle plates is comprised of dyed liquid. The jet boundary, thus, gets marked as the colored boundary layer separates at the knife edge. Depending upon the jet Reynolds number the jet boundary shows various features. (See Chapter 4.)

Continual addition of dye in each experiment to about 0.2 cubic meter of liquid in the glass tank resulted in a discoloration of the



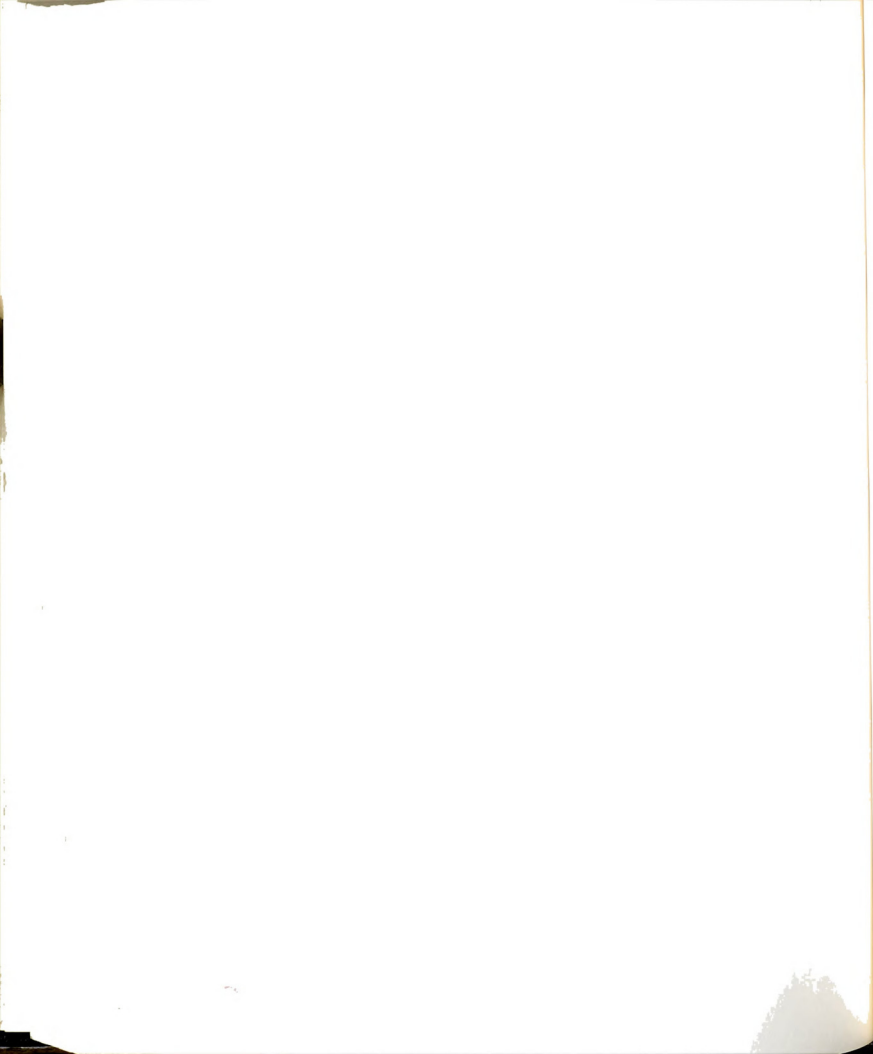
test liquid. In order to return this liquid to a colorless state, a small amount (300 - 400 ml) of chlorine was added to the tank. (The chlorine served to bleach the dye). No adverse effect of the addition of chlorine was detected. Using this technique, nominally 6 - 8 experiments could be performed before it was necessary to add the chlorine again.

The dye method was found to be most suitable and it was used for further experiments. A wide range of Reynolds number and slit widths have been used in these experiments. Experiments have been carried out both with water and water-sugar mixture of various concentration as working liquid. A large data base has been created from over 1000 photographic records of the position of vortex pairs in these experiments.

3.9 Data Acquisition

Figure 39 provides a side view of the experimental facility and a block diagram showing the input and outputs. The PDP 11/73 computer provided the input in the form of timed pulses to the stepper motor. The outputs from the experiment were digitized by the same computer using the IFA200 A/D converter. (See Section 3.4 for details of the computer system). This section describes the details of data acquisition in this study.

The number of signals that were recorded during the experimental run depended upon whether flow visualization pictures were being taken

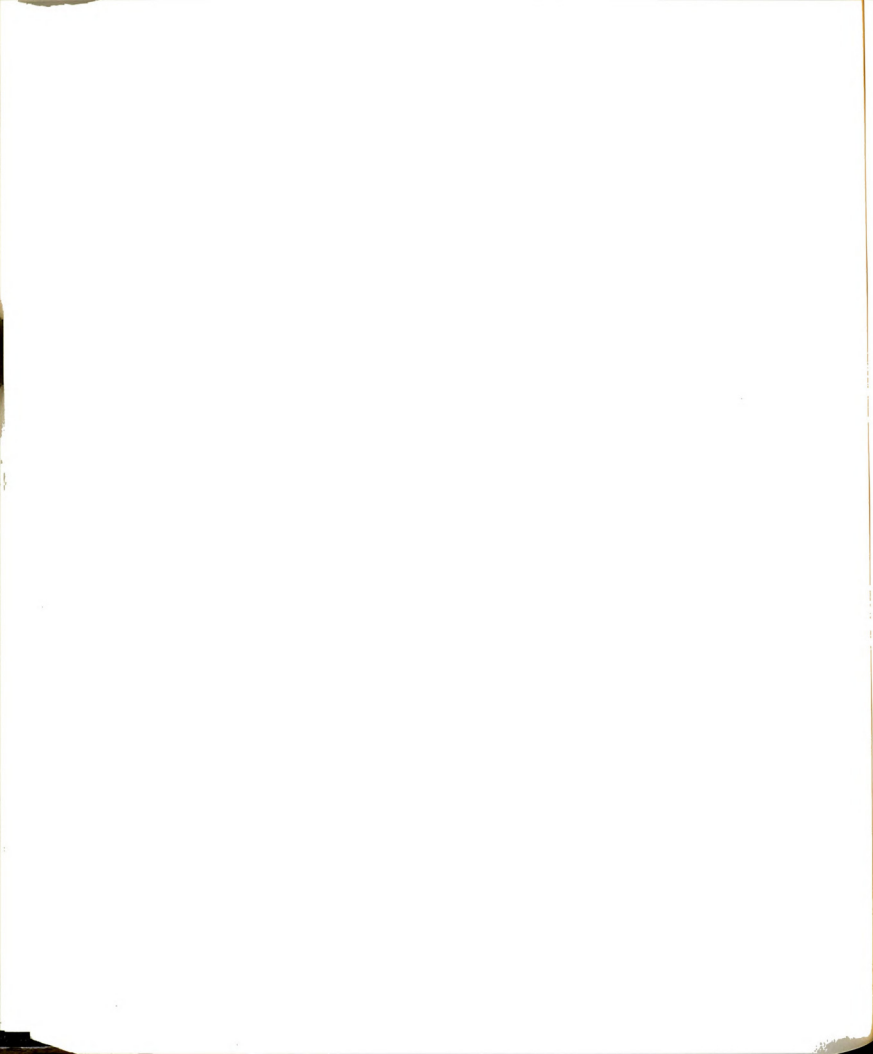


or velocity data using the LDA were to be recorded. Two pressure signals were, however, always recorded: the cavity pressure $p_{NH}(t)$ and the cup pressure $p_I(t)$. Whereas, $p_I(t)$ gave an estimate of the spatial average velocity $\langle U \rangle$ of the jet, the cavity pressure was used to monitor the overall performance of the experiment. It can also be used to get an independent estimate of $\langle U \rangle$. This was done and the difference between the two estimates never exceeded 3%.

3.9.1 Flow Visualization

Black and white flow visualization pictures were taken by a Nikon F3 motorized camera at a rate of 4 or 6 frames per second. In addition to the two signals $p_{NH}(t)$ and $p_I(t)$, another signal, related to the camera shutter release time, was also digitized. As shown in Figure 39, this signal was derived as the output of a comparator circuit.

Figure 40 is a diagram of the comparator circuit. The hot shoe of the camera served as an electrical switch for the comparator circuit. Whenever, the camera's shutter was released the comparator generated a TTL level voltage. This voltage dropped back to ground level as soon as the shutter got closed. The output of the comparator, thus, provided a signal $C(t)$ with sharp spikes which were located at times when the pictures were taken. The rate at which IFA200 digitized the data depended upon the desired shutter release time which in turn depended upon the Reynolds number of the experiment. At $Re=800$, the data were recorded at 200 Hz, whereas at $Re=2400$, a data rate of

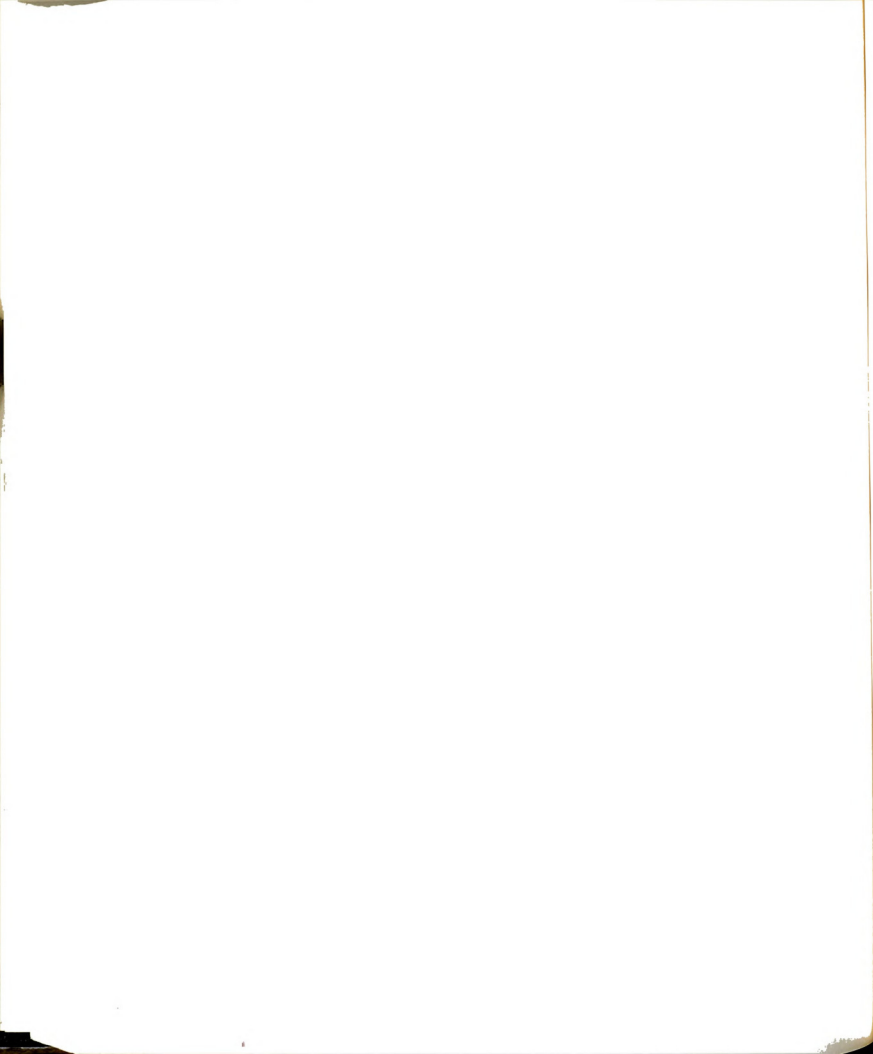


500 Hz was used so as not to miss any pulse. This arrangement thus provided not only the timings between the pictures but also the time of the first picture with respect to the start of the experiment.

3.9.2 Velocity Measurement using LDA

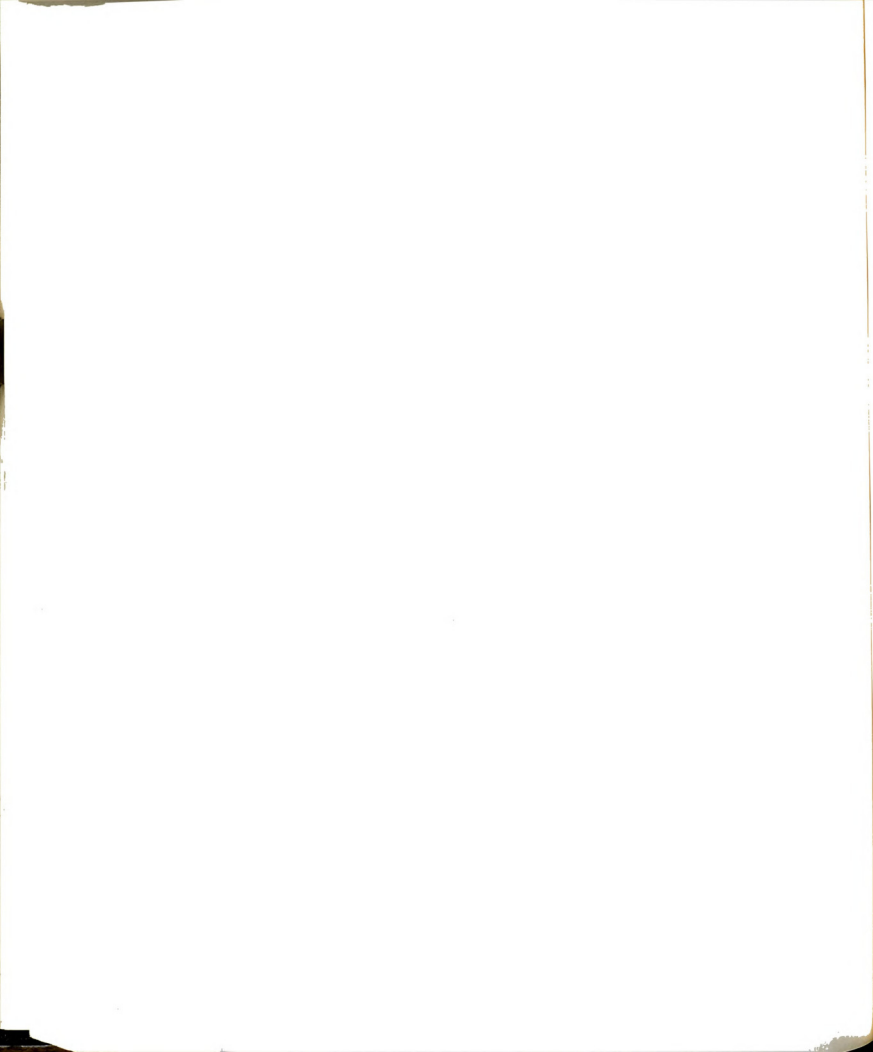
Figure 26 is a schematic representation of the configuration used to acquire the LDA data using the TSI single channel LDA system. The TSI 1980 Counter outputs the voltage corresponding to the Doppler shift frequency using a 40 pin connector. Because of this the data could not be recorded directly on the PDP 11/73 system. An Apple IIe computer with an interface card and software developed by TSI (in Applesoft Basic) was used for acquiring the data. The user specifies the characteristics of the LDA system when the TSI's program is called. A maximum of 4096 data points can be recorded at the user specified rate. In the present study, 4096 data points were recorded at a 308 Hz rate. All data were stored in Applesoft binary format.

In order to know the beginning and the end time of the data acquisition by the Apple IIe with respect to the valve opening time, the comparator circuit (see Section 3.9.1) was used along with another switching circuit (see Figure 41) and a simple electrical switch. Also, modifications were made in the TSI program so that data acquisition began when triggered by the switching circuit. Section 3.6 describes the initiation of the experimental run using the PDP 11/73 computer system. After a few minutes from the start of the experiment, when the transients had died down, the electrical switch



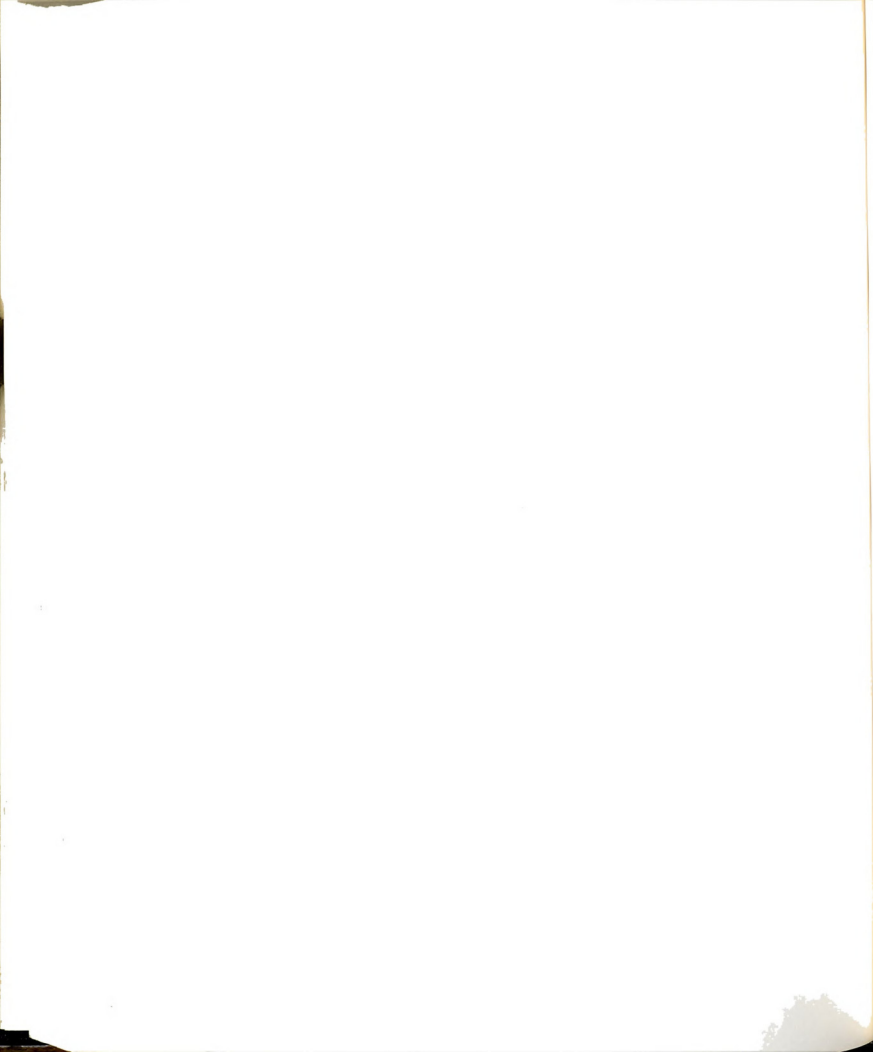
(see Figure 26) was manually turned off. This caused a step change in the output of the comparator which was digitized by the IFA200; it also caused the switching circuit to send a 5 volt signal to the game port of the Apple IIe system. The program running on the Apple IIe continuously monitored the voltage level of this port and the data acquisition began as soon as the voltage level became high. When the Apple IIe indicated the end of the data acquisition, the switch was turned on. This caused the output of comparator to become low. In this way, the beginning and the end timings of the LDA data were determined.

The uncertainty in the measurements conducted by a typical LDA system is quoted to be $\pm 0.5\%$ [see, for example, Durst, Schierholz and Wunderlich (1987)]. Since the TSI system used in this investigation is a standard system, the same limits of uncertainty are expected to be applicable. The uncertainty related to the statistical considerations was checked by computing the running averages of the measured velocity $u(t)$. More specifically, the average based upon the total data acquisition time, T_d , was compared with the average based upon a running time defined as $T_d \cdot \frac{(i-1)T}{20}$, $i=1,2,\dots,21$. Here, T is the time period of the dominant fluctuation in the measured velocity time history. The maximum deviation between the running average and the average based upon T_d did not exceed $\pm 1\%$. Hence, given the oscillating nature of the flow field, the average based upon T_d yields a good estimate of the average velocity.



3.9.3 Combined Flow Visualization and LDA Velocity-Sensing

The techniques described in Sections 3.9.1 and 3.9.2 were combined to acquire both qualitative and quantitative data to better understand the instability phenomena. A front surface mirror with a narrow slit = 53 mm x 3.5 mm and a white cardboard with a small circular hole were used, as shown in Figure 42, to combine the two methods. After the the experiment was started by the PDP 11/73 system, the camera was fired at an appropriate time. This caused the comparator circuit to generate a TTL level pulse. As shown in Figure 42, this pulse was fed to: i) the Apple IIe computer to cause it to begin taking LDA data, and ii) the PDP 11/73 computer for digitization to mark the beginning of data acquisition. In this way, the LDA velocity data and the camera timings could be referred to a common time base.



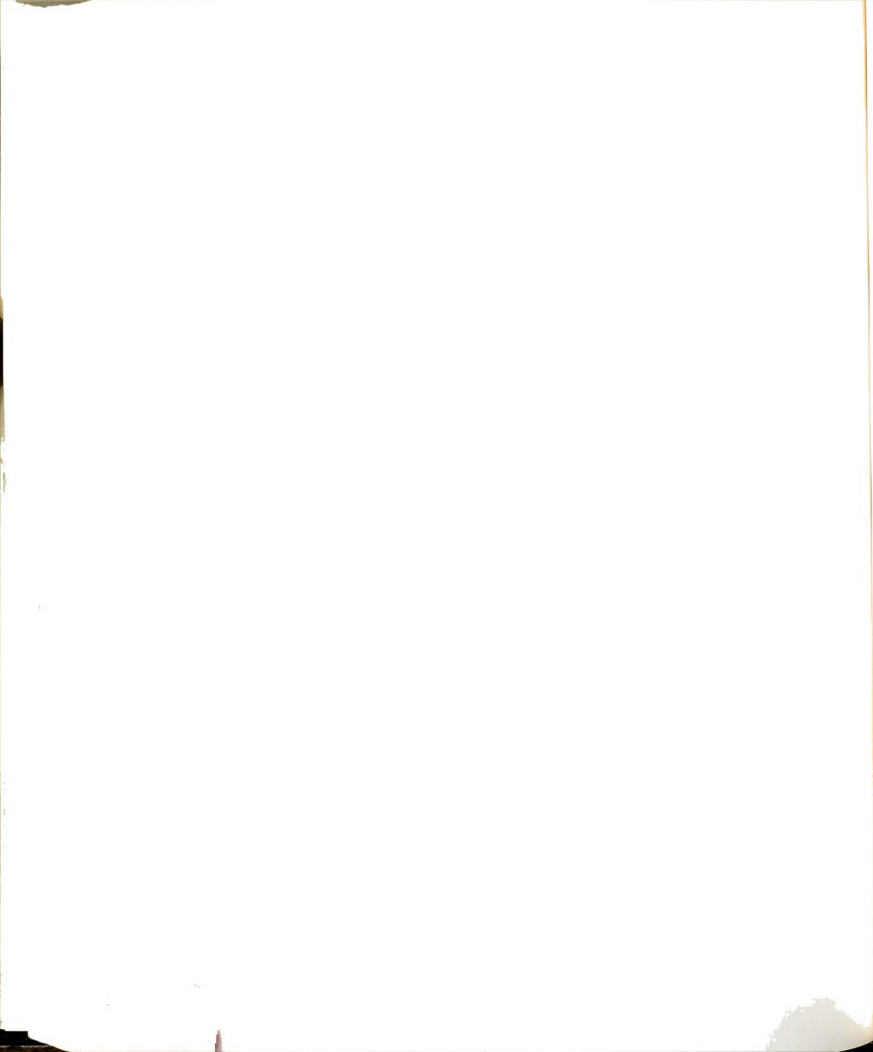
FLOW VISUALIZATION: QUALITATIVE RESULTS & DISCUSSION

4.1 Introduction

The near-field of the slit jet flow field was visualized using food color dye; the details of the technique and the experimental procedures have been described in Chapter 3. The purpose of the flow visualization was:

- i) to make qualitative observations of the near-field of the jet over a large range of Reynolds number (i.e., up to 4000) and covering a region up to 4-8 slit widths downstream;
- ii) to obtain quantitative results related to the passage of the two-dimensional vortical motions, like passage frequency, convection speed of vortices, and spacing between vortices.

About 50 sets of photographic records, with 32-40 photographs per set, were acquired over the range $75 \leq Re \leq 3500$, and for five

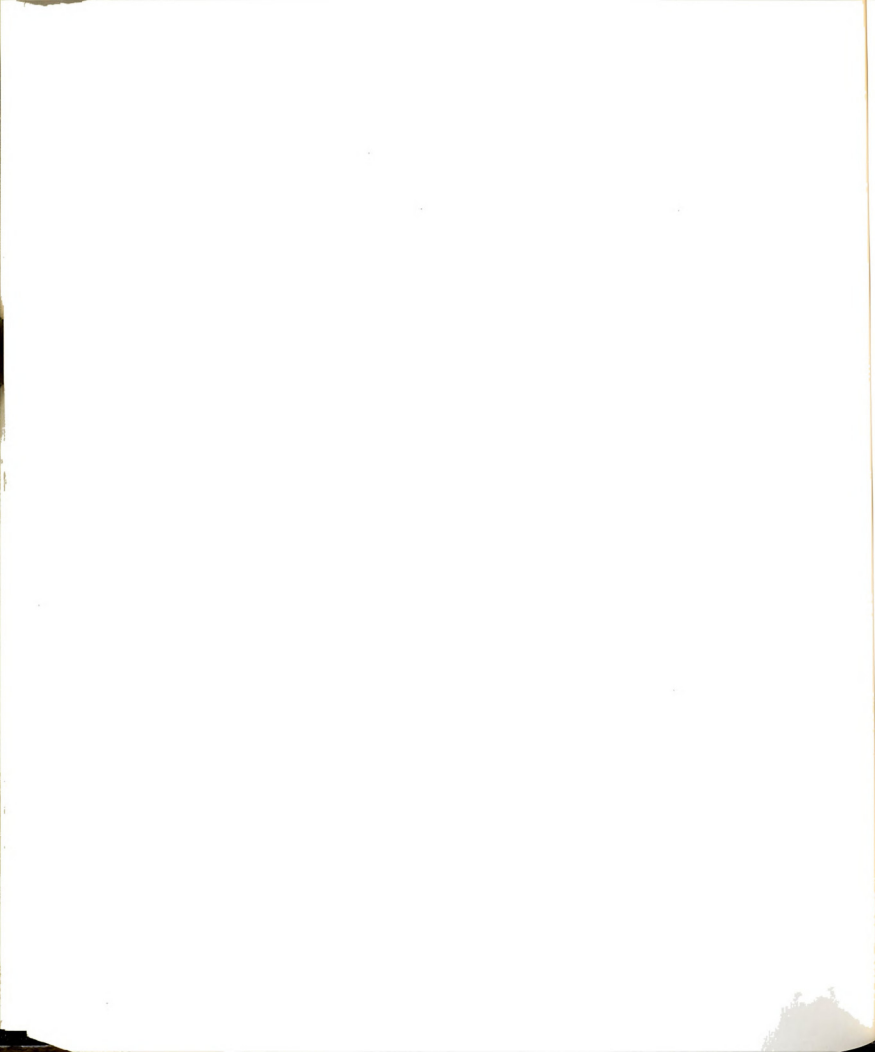


different slit widths $w = 1.40, 1.51, 1.99, 2.57, \text{ and } 2.63 \text{ cm}$. For experiments at low values of Re a water-sugar mixture was used as the working liquid. For higher values of the Re , water was used as the working fluid. Experiments at some values of Re were repeated with different size widths, w , to explore the presence of geometry dependent effects.

Yih (1959) and Meroney (1985) have shown that under steady conditions eddies are formed in the two corners of a channel-like plenum as shown schematically in Figure 43. The influence of these eddies in the present quasi-steady flow facility was checked by conducting experiments under two conditions: i) side bleed ports closed, and ii) bleed ports open. No systematic influence of different bleed settings on the results was observed; hence, most of the data reported herein were obtained for the bleed closed condition.

Section 3.6 describes the procedure for executing the experiments in this investigation. Two different protocols were used for filling the plenum:

- i) filling by inducing the recharge flow from the reciever to the upper plenum through the slit jet opening;
- ii) by using the filling device shown in Figure 18.

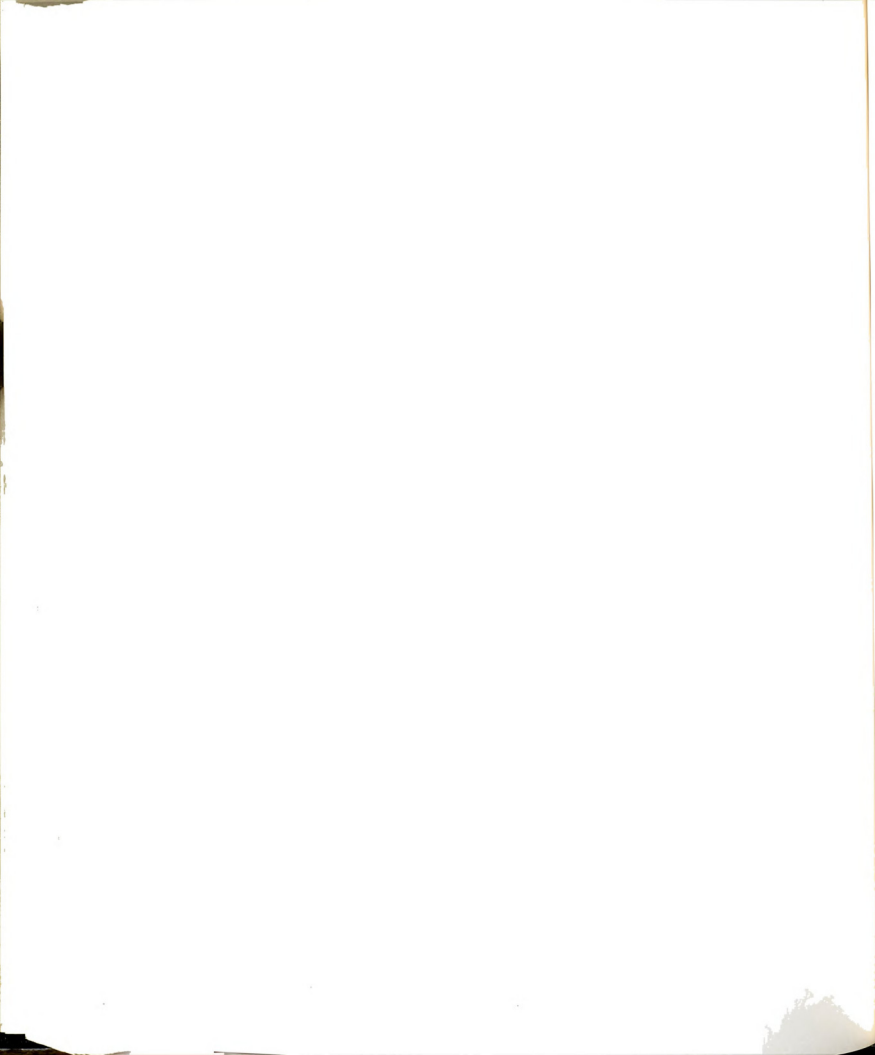


The range of Re covered for the experiments was 75-1280 for the first protocol and 1000-3500 for the second. Based upon a comprehensive examination of the flow visualization records, it is inferred that, qualitatively, the process of formation of a symmetric vortex street in the common range of Re exhibits similar features. Hence, the method of recharging the plenum does not materially influence the flow field, and a common description of the process of formation of the symmetric vortex street will be presented.

The objectives of this chapter are:

- i) to identify the patterns which commonly occur in the flow field;
- ii) to determine the Reynolds number dependence of these patterns;
- iii) to describe the pairing of, and other interactions between, the symmetric motions;
- iv) to identify the loss of symmetry in the streamwise location of the vortex motions.

Section 4.2 presents an evaluation of the width of the dye streak with respect to the estimate of the displacement thickness δ_d at the separation lip. Section 4.3 describes the common patterns and Section



4.4 presents the various regimes of the slit-jet flow field based upon Re . In section 4.5, the interaction between the symmetric motions are described, and Section 4.6 deals with the loss of symmetry in the streamwise locations of the two vortices of a pair.

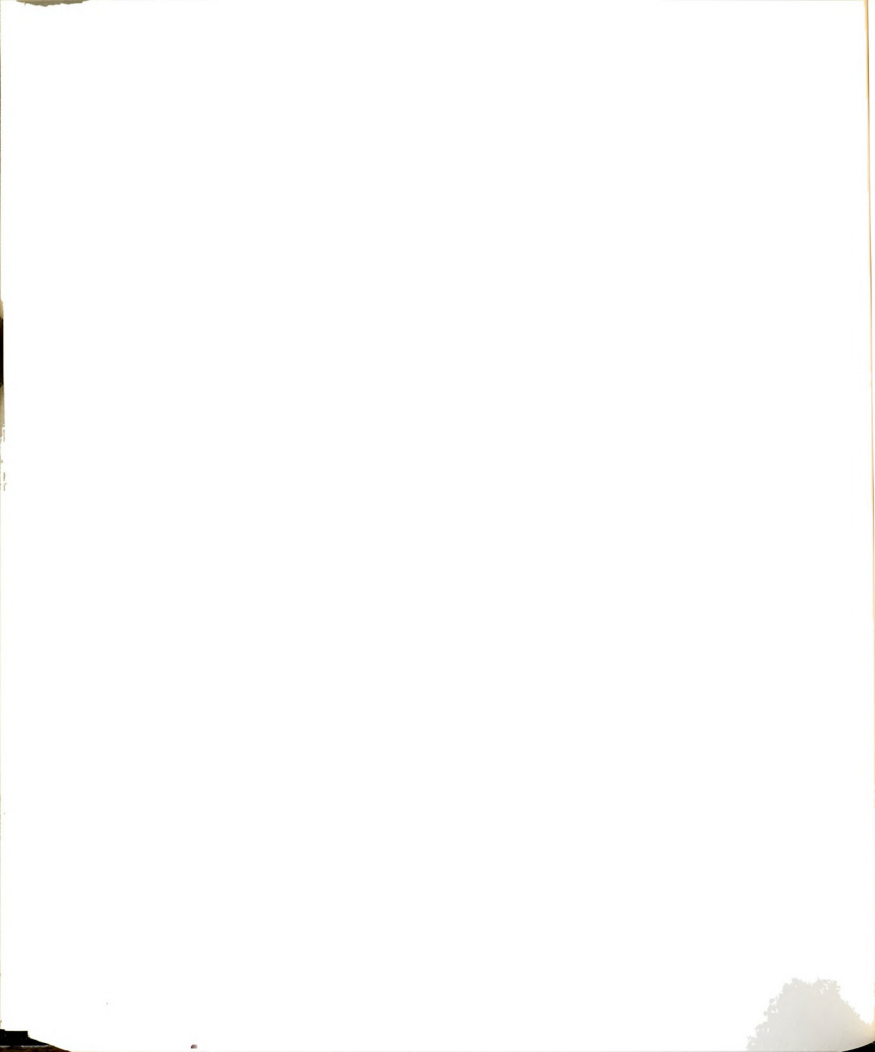
4.2 Width Evaluation of the Dye Streak

The purpose of evaluating the width of the dye streak was to relate this width to the width of the vortical fluid separating at the lip of the nozzle plates. Using an image processor, the widths of the dye streaks were estimated from the photographs of various experimental runs. The average width, w_{ave} , was found to be $0.025w \leq w_{ave} \leq 0.046w$ with w decreasing from 2.63 to 1.40 cm.

Figure 44 shows the distribution of the nondimensional displacement thickness, δ_d/w , as a function of Re . From the plot it is apparent that the vortical fluid is completely marked by the dye.

4.3 Common Patterns of the Flow Field

Several common patterns or distinctive features have been identified in the slit-jet flow field. Some of these features are always observed whenever a jet starts from rest; the others are observed in a specific range of Reynolds number that is particular to that feature.

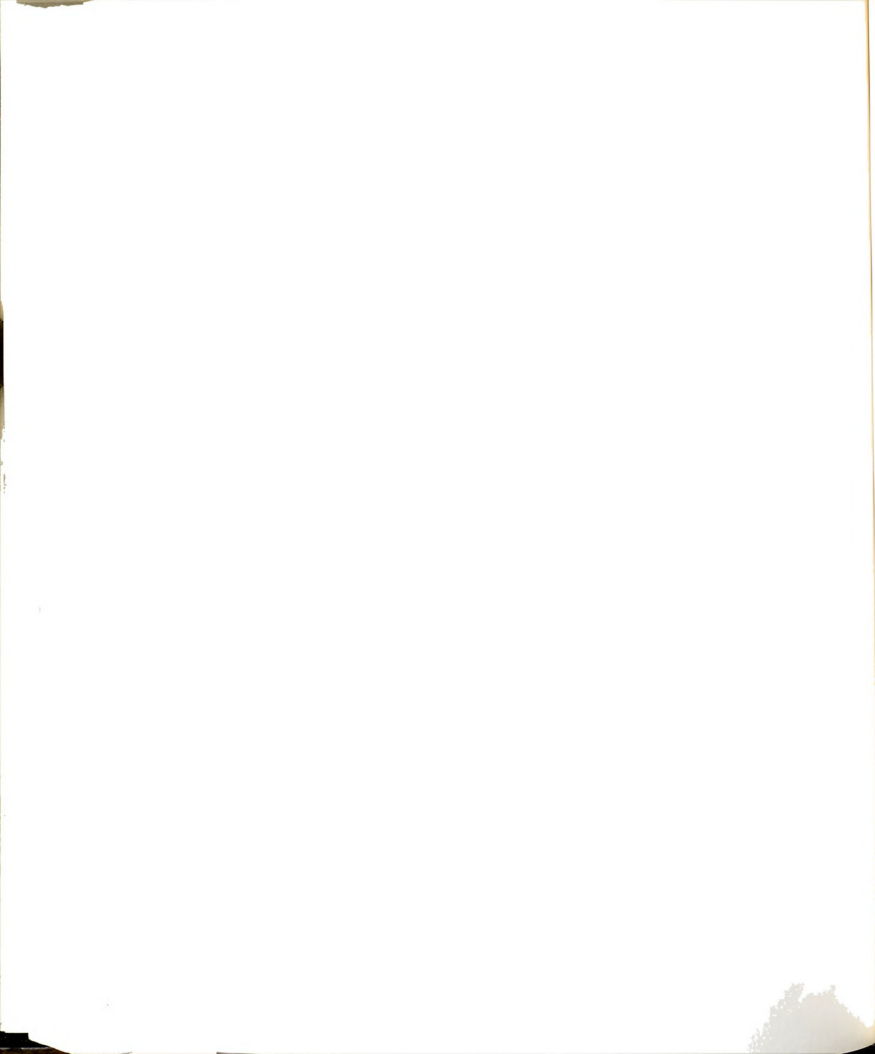


4.3.1 Starting Vortex Pair

As the flow starts from rest, two large, counterrotating vortices are formed as the jet makes its way into the quiescent ambient. This pair of vortices forms at all values of Re and it will be termed the "Starting Vortex Pair (SVP)" in this discussion. See Figures 45, 46, and 47 at three different values of Re .

Behind the SVP, the jet column exhibits an outward displacement of the dye streak. This "swollen" region of the jet stream is called a "bulge" as shown in Figures 45, 46, and 47. With the passage of time, the kinematics of the jet associated with the bulge causes it to deform, resulting in the appearance of another identifiable feature at the upstream edge of the convecting bulge. This feature will be identified herein as a "kink". Examples are shown in Figure 46(c) and Figure 47(b). The same mechanism predominantly leads to an overlapping of the dye streaks at the kink, as shown in Figure 47(c), which is called a "foldover". From the sequence of photographic records at equispaced times, the velocities of the SVP and the bulge (or kink or foldover) have been determined. The ratio of the velocity of the bulge to the SVP, V_b/V_s , has been found to be strongly dependent upon Re as shown in Figure 48. This figure also shows the variation of $V_b/\langle U \rangle$ and $V_s/\langle U \rangle$ as functions of Re .

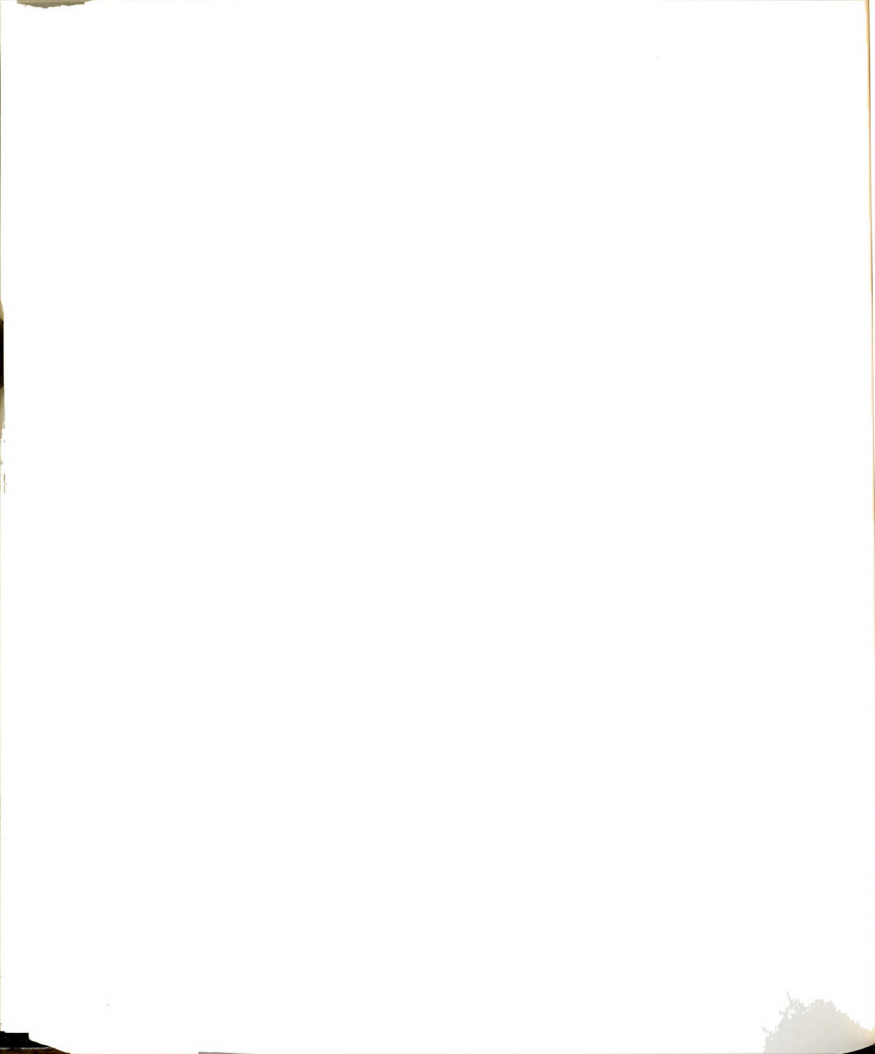
The fate of the foldover has been found to be dependent upon the Reynolds number. At values of Re for which $V_b/V_s < 1$, the feature



(bulge, kink or foldover) behind the SVP cannot "move into" the SVP and the foldover appears to keep growing with sharp pointed edges; see Figure 47(c). However, for $1 < V_b/V_s < 1.2$ the foldover has been found to "move into" the SVP, which is replaced by another bulge. Figure 49 shows the passage of a foldover in the SVP and the appearance of a second bulge. In the case of a relatively high Reynolds number (≈ 980), the foldovers have been found to roll into two dimensional vortex motions and this event has been termed as "rollover". Figure 50 shows the formation and subsequent evolution of the SVP (marked by 1) and the following distinctive motions are marked by 2, 3, 4,.... Whereas the features 2 and 3 coalesce with the SVP in the form of a foldover, the features 4 and 5 evolve into rollovers before coalescing. Table 2 presents the ratio of speeds, V_b/V_s , of bulges 2-5 with respect to the SVP.

Table 2 - V_b/V_s at $Re = 980$

Bulge No.	t^*	V_b/V_s	Remarks
2	11.46	2.81	Short life span Figure 50 (a,b)
3	12.53	1.35	From bulge to foldover (b,c)
	13.59	2.14	Moving into the SVP (c,d)
4	13.59	1.23	From bulge to rollover (c,d)
	14.66	2.64	Moving into the SVP (d,e)
	15.73	1.54	Inside the SVP (e,f)
5	14.66	0.99	From bulge to foldover (d,e)
	15.73	1.72	From foldover to rollover (e,f)
	16.80	0.96	Pairing with bulge No. 6 (f,g)
	17.87	2.16	Moving into the SVP (g,h)
	18.90	10.8	Inside the SVP (h,i)



4.3.2 Bulges with Overriding Unit Vortices at Low Re

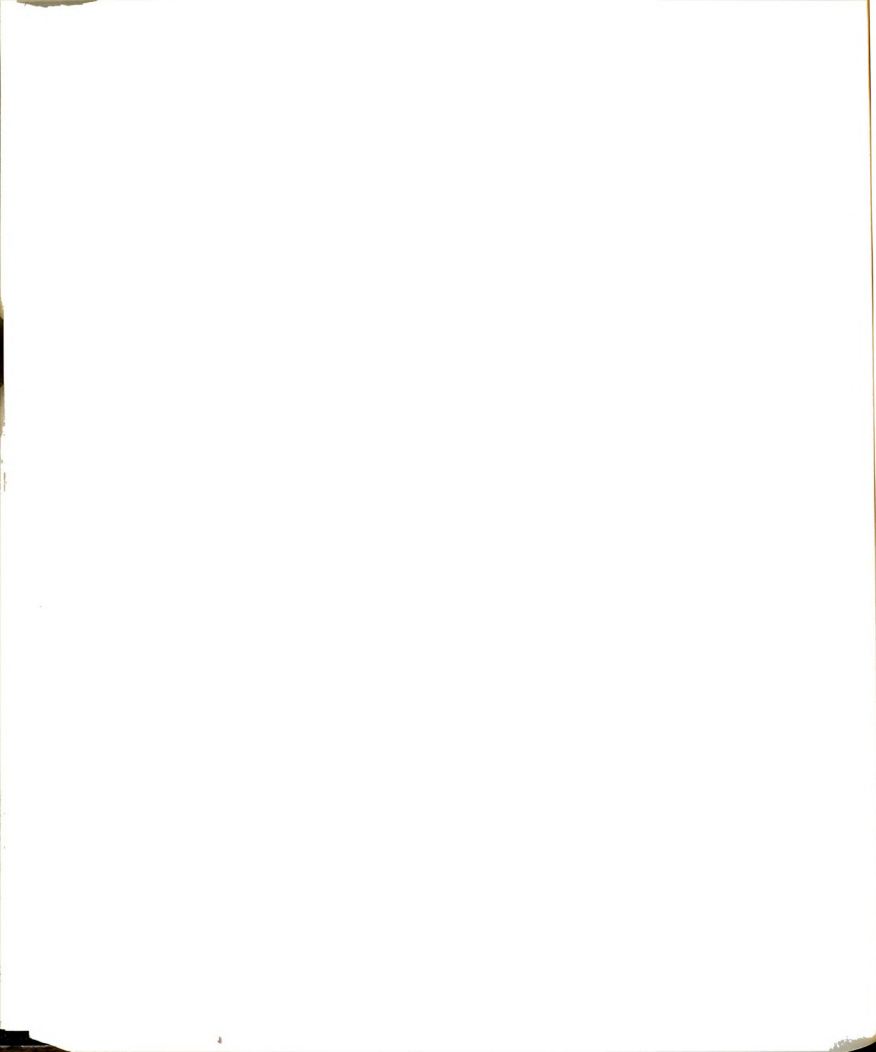
For values of $1 < V_b/V_s < 1.2$ ($157 < Re < 210$), the bulges which form on the jet column are marked by symmetric small scale vortices as shown in Figure 51. These vortices are called unit vortices. Since $V_b/V_s > 1$, the foldovers coalesce with the SVP and new bulges appear on the jet column; three such features can be identified in Figure 51(d). No rotation of the foldovers or agglomeration of unit vortices into large scale motions has been observed at these values of Re.

4.3.3 Bulges on Jet Boundary with Large Scale Vortex Formations

For values of $Re \geq 268$, the jet column has been observed to be marked by the formation of bulges and their gradual evolution into large scale symmetric vortex motions. Figure 52 presents the behavior of the slit-jet flow fields at $Re \approx 510$ and 1200. The vortex street is nominally symmetric and two dimensional in nature. The observations of BW were based on the motions of the large scale symmetric vortex pairs as shown in Figure 52.

4.3.4 Formation of Unit Vortices at High Re Values

For values of $Re \geq 2300$ the near-field of the jet column is marked by small spots of accumulated dye which are called unit vortices. In some experimental runs, the unit vortices have been consistently observed at low values of Re, for example, $Re \approx 900$, as shown in Figure 53. In other cases, at low Re values, their appearance has been found to be intermittent. Figure 53 exhibits the

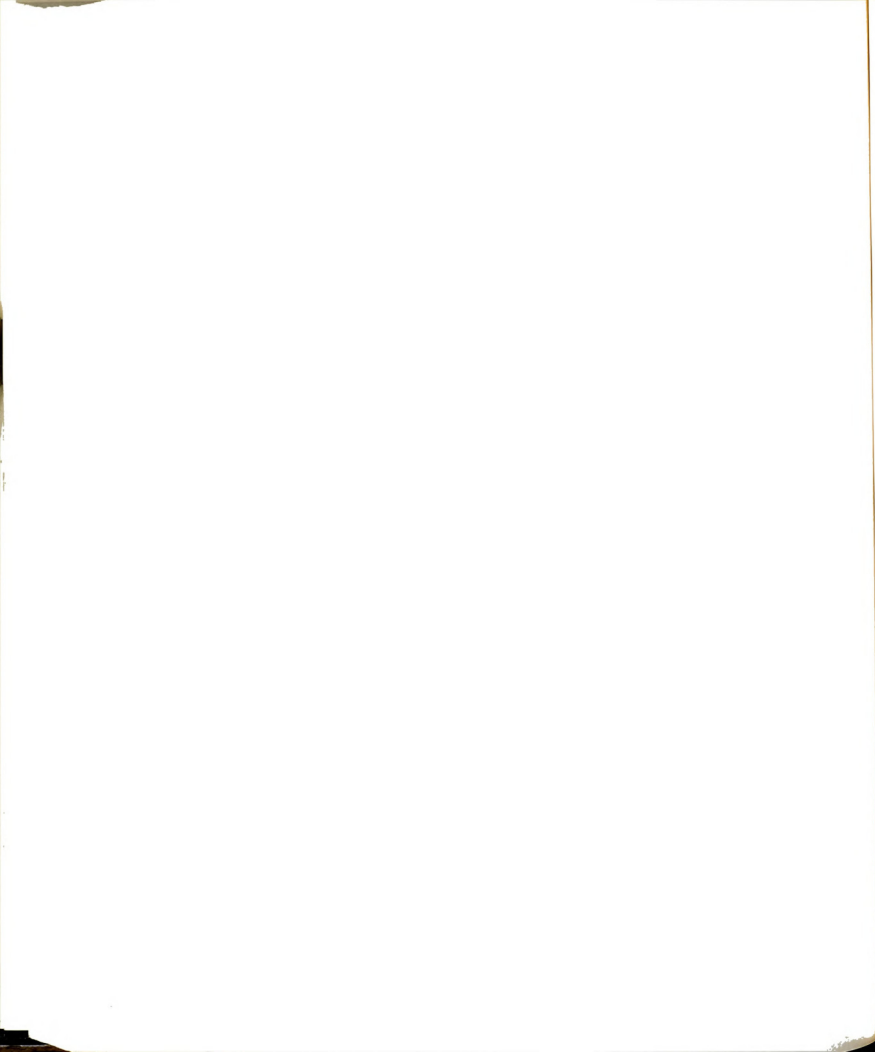


presence of unit vortices on the jet column preceding the large scale vortex motions.

The presence of unit vortices was inferred by FK in connection with their hypothesis that "large scale vortices result from the agglomeration of unit vortex motions". From the photographic data in this study, it is concluded that the unit vortex motions do not play an active role in the formations of large scale vortices in the "low" Re range of 930-1700. As shown in Figure 53(b) ($Re = 1044$), the unit vortices are carried by the large scale instability as a bulge rolls over into a vortex pair. For the "high" Re range (> 2300) the role of unit vortices in the formation of large scale motions could not be ascertained because of the relatively slow framing rate of the camera.

4.4 Various Regimes Based on Reynolds Number

Based on a comprehensive examination of the flow visualization records of the slit-jet flow field, the range of Reynolds numbers over which the experiments were conducted can be divided into four regimes. The boundaries of these regimes are not precisely known because of rather large intervals in Re at which the experiments were carried out.



4.4.1 $Re < 157$

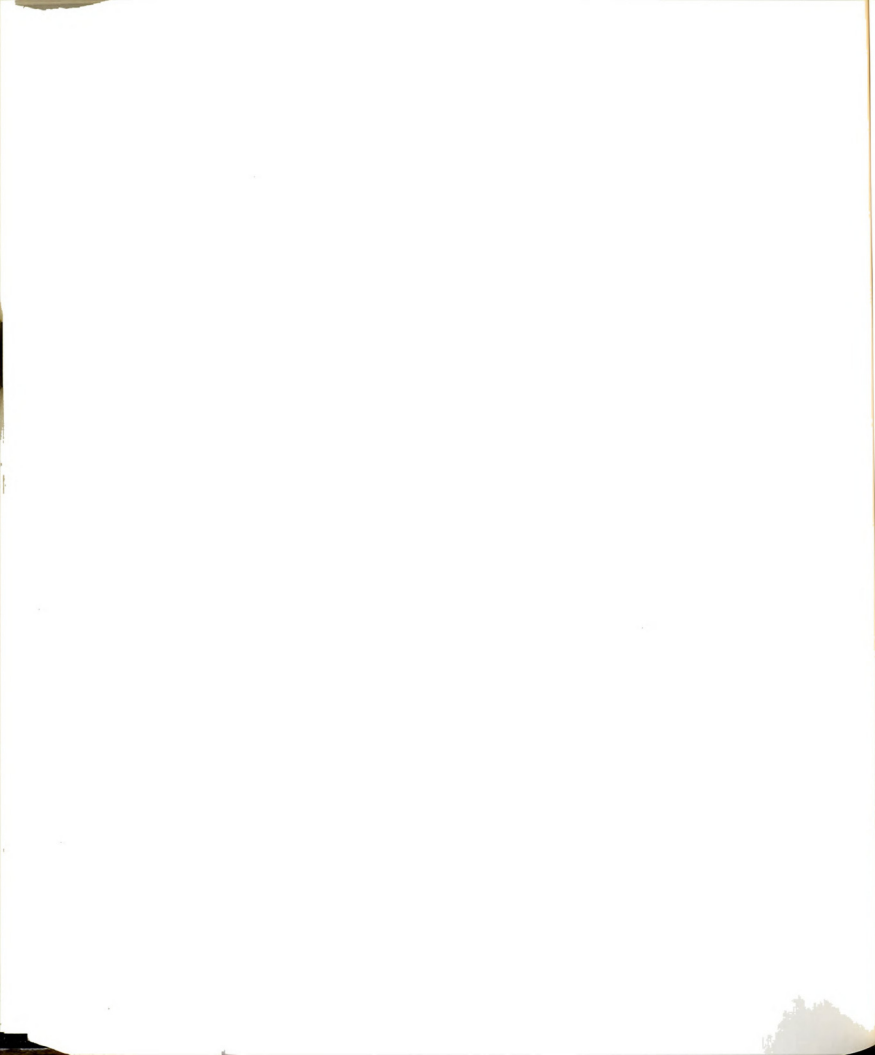
No large scale vortex motions are observed over this range of Re except for the starting vortex pair. In addition, the jet column exhibits the formation of a bulge which later evolves into a kink and then into a foldover. This has been shown in Figures 45, 46, and 47. As shown in Figure 48, over this range of Re , $V_b/V_s < 1$. Figure 54 presents the development of the jet at three different values of Re and at a common time $t^* = 18$. Note that for these conditions, $V_b/V_s < 1$.

4.4.2 $157 \leq Re \leq 210$

The instability of the slit-jet flow field begins to appear in this range of Reynolds number. Two phenomena are observed:

- i) formation of unit vortices on the jet boundary;
- ii) coalescence of bulges (or foldovers) with the SVP and an appearance of more bulges on the jet column.

Whereas, the second phenomenon is related to $V_b/V_s > 1$ in this range of Re , the appearance of unit vortices might be a result of the Kelvin-Helmholtz instability of the shear layers of the two-dimensional jet. Note that Figure 55, which presents the continued evolution of the jet flow presented in Figure 49, exhibits the features identified as i) and ii) above.



4.4.3 $268 \leq Re \leq 1700$

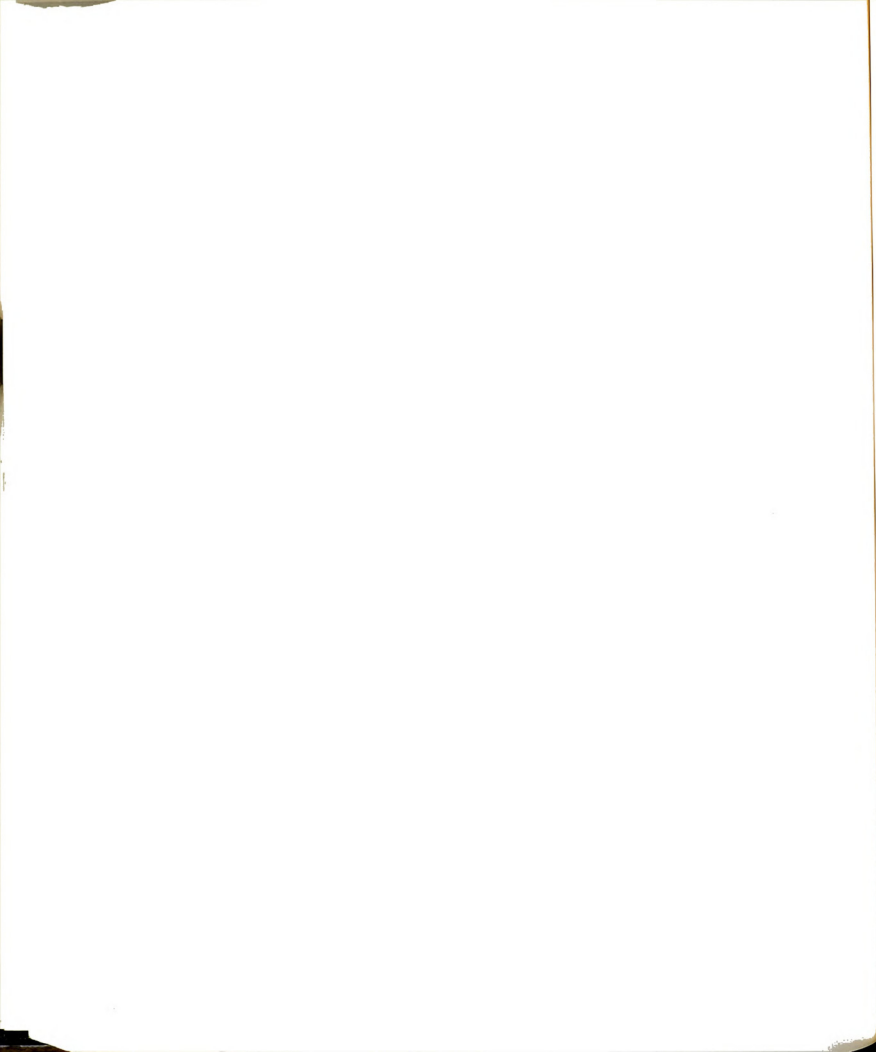
This wide range of Reynolds number is marked by the repeated formation of symmetric, large scale, two-dimensional vortex motions similar to those observed by BW; see Figure 52. The observations related to this flow regime are presented in Sections 4.4.3.1 and 4.4.3.2.

In Section 4.4.3.1, the process of formation of symmetric motions is described. This description is based upon a comprehensive observation of a large number of photographic records. Section 4.4.3.2 presents some examples of the exceptions to the general observations described in Section 4.4.3.1.

4.4.3.1 Formation of Symmetric Motions

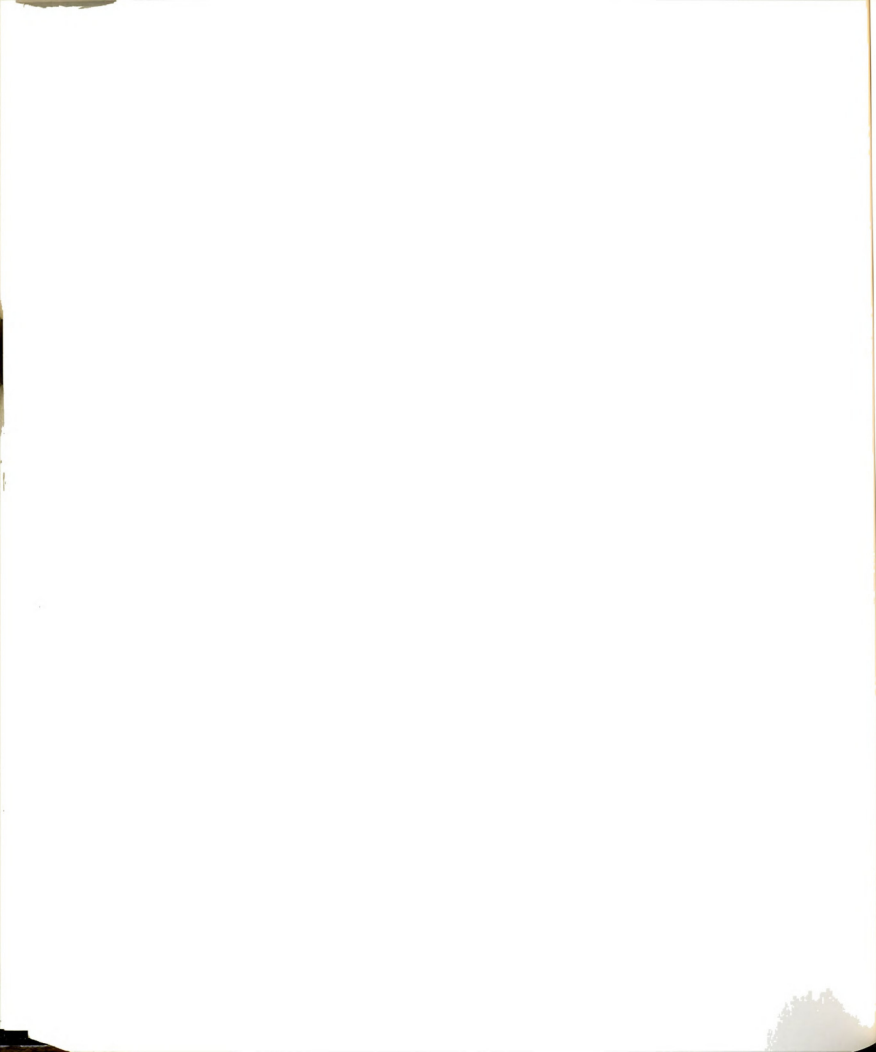
Figures 56, 57 and 58 are representative sequences of the photographic records in this range of Reynolds numbers. Figure 59 is a schematic representation of the process of vortex formation. Because of a similarity in the features which lead to the formation of a large scale vortex pair, for e.g., G in Figure 59, and those which appear upstream of a SVP, the same terms have been used to describe the process of formation of the two-dimensional vortex motions.

The various stages of evolution of a fully formed vortex pair, like No. 8 in Figure 56(h), can be traced back to the bulge in Figure 56(b); this has been identified as C in Figure 59. The formation of



a bulge is associated with an outward deflection of the jet boundary which implies the presence of a v -component of velocity in addition to the u -component. The v -component acts asymmetrically with respect to the centerline of the jet and, therefore, represents a varicose type of instability. It is conjectured that the symmetric deformation of the jet boundary which results in the formation of a bulge is caused by a localized pressure rise. In other words, the bulges are formed as a result of a cyclic rise and fall of the pressure in the jet.

As shown in Figure 59, an inflection point (B) of the dye streak is observed upstream of the bulge (C). The inflection point evolves into a kink in the dye streak; see Figure 56(c) and feature D in Figure 59. In the next stage, as in the case of the flow behind the SVP, the kink evolves into a foldover. This is shown in Figure 56(d) and by the feature E in Figure 59. The evolution and growth of a foldover implies the presence of a sharp gradient in $u(y)$. The straight edges of the foldover (see Figure 56(d)) marked by (i) and (ii) in Figure 59, at some stages of their evolution, stop protruding further and begin to roll as shown in Figure 56(f) and feature F in Figure 59. As before (Section 4.3.1), the evolution of a foldover has been termed as rollover. It is to be noted that the process of evolution of foldover into rollover is more pronounced at higher values of Re than at lower values of Re . See the process of vortex formation at these values of Re in Figures 56, 57, and 58. The rotation of (i) and (ii) (in Figure 59) in the counterclockwise direction requires the v -component of velocity to play a dominant role, which is different from the role of v during the evolution and growth of a foldover. Continued rotation



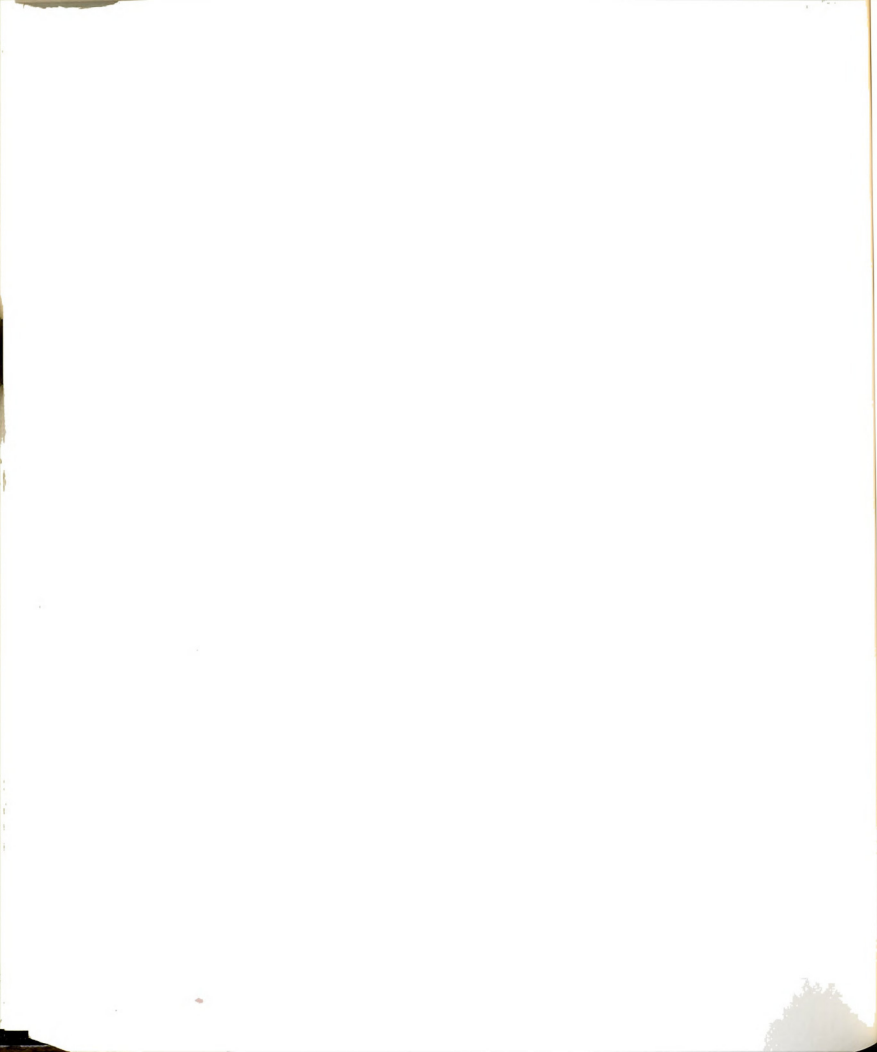
and convection of the fluid particles in a rollover results in a fully formed vortex pair like the feature G in Figure 59.

4.4.3.2 Some Exceptions to the Common Observations

The process of vortex formation and growth in an unexcited jet is not truly periodic in nature. For example, there are variations in the locations of bulge formations and in their growth pattern. One of the more commonly observed phenomena is that not all the bulges evolve into large scale motions. See, for example, bulge number 7 in Figure 56(a). This has been found to be especially true at lower values of Reynolds number in this range (268-1700). It has been observed that the growth process stops at some stage of development, leaving behind a mark of dye. See Figure 60 at $Re = 362$ and $w = 2.63$ cm. In general, it can be noted that as the Re increases, more and more bulges evolve into large scale motions.

Sometimes, an accumulation of dye is observed on the jet boundary along with a kink, but, without an apparent formation of a bulge. See Figure 61. Most of these features do not develop into full vortex pairs and get reduced to a mark of dye. See Figure 62.

At the lower end of this range of Re (i.e., $Re = 300$), the process of vortex formation has been found to exhibit some size dependent effects. Figure 63 shows the flow field at $Re \approx 280$, $\tau^* \geq 30$, and in jets with 3 different widths. In the narrower jets, ($w = 1.51$ cm and 1.99 cm) at least one foldover has formed within $x = 4w$, whereas, in

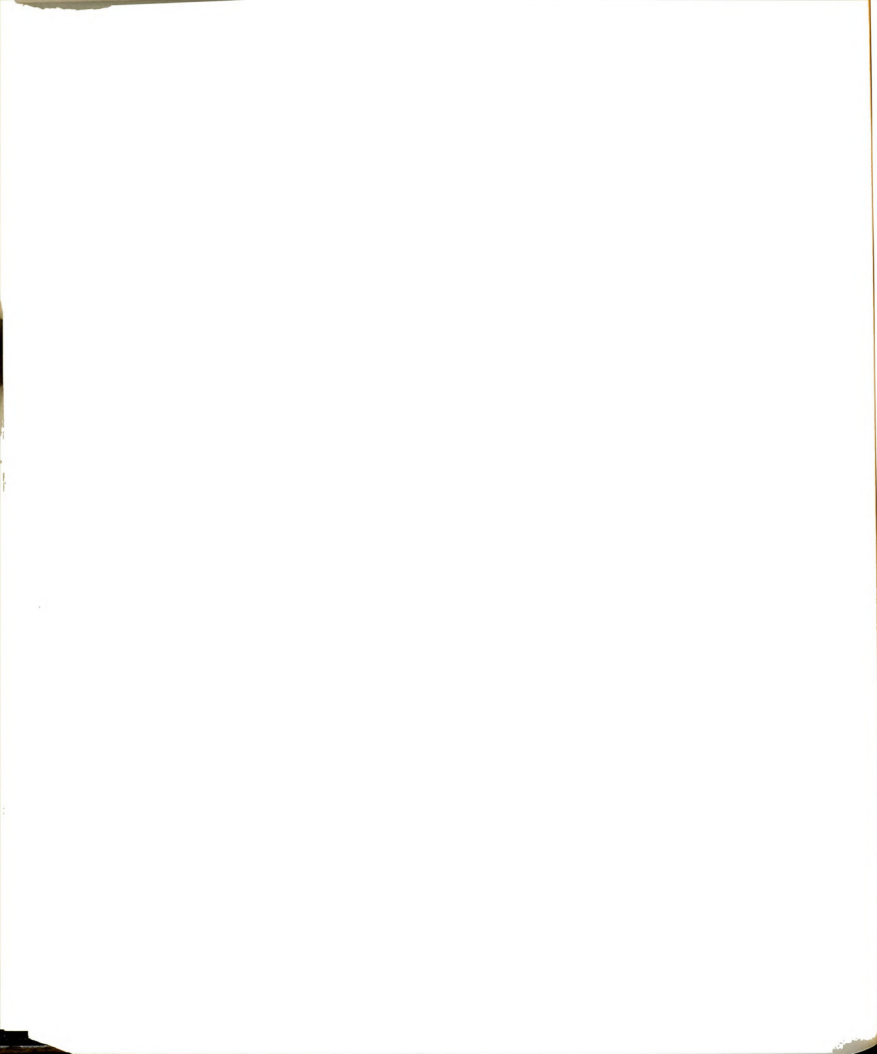


the case of the widest jet ($w = 2.63$ cm) only a kink has formed within $x = 4w$. In addition, in (a), a number of spots of dye can be identified on the jet column; these spots of dye had initially appeared as bulges. This geometry dependent effect seems to decrease as Re increases as shown in Figure 64 at $Re \approx 420$, $t^* \geq 30$ and in the same jets.

4.4.4 $Re > 2300$

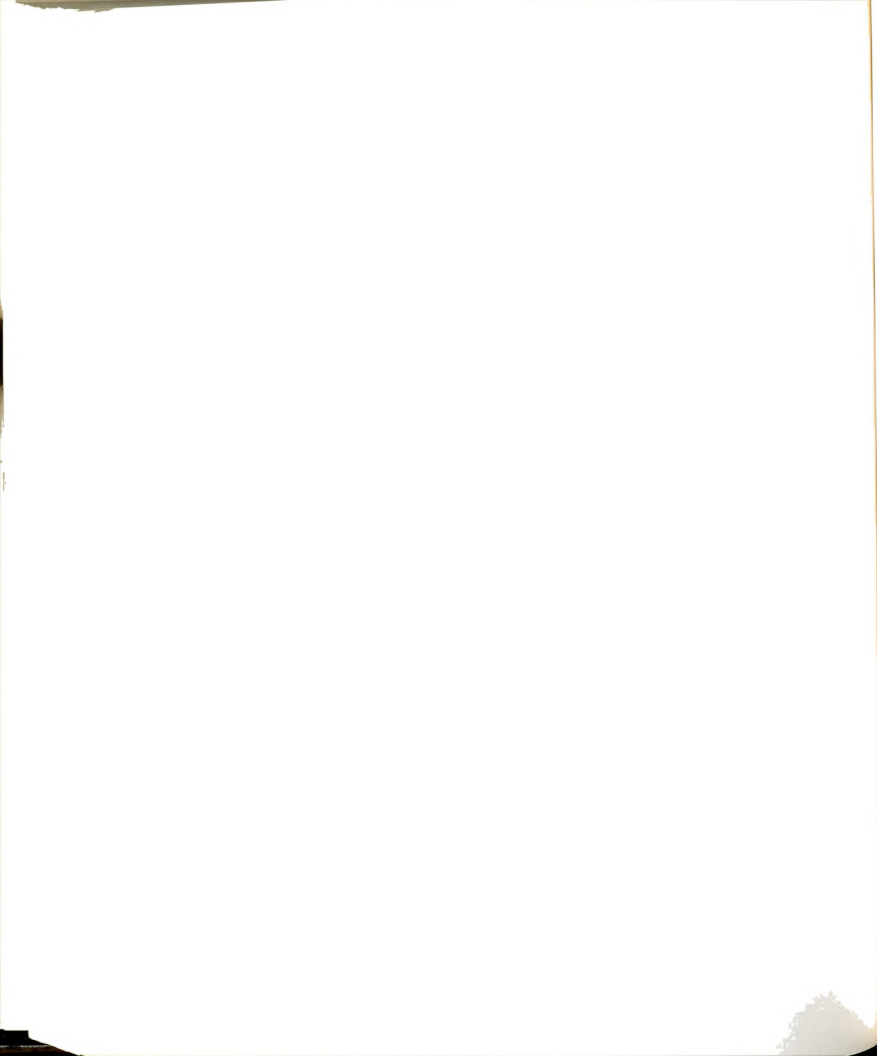
The results that are reported for this range of Re are based upon the exploratory experiments which were conducted to check whether or not vortex motions are observed at $Re > 1600$. No experiments were conducted between $Re = 1700$ and $Re = 2300$, and therefore, the boundary between this regime and the previous regime ($268 \leq Re \leq 1700$) is not precisely known. The largest value of Re upto which the experiments were conducted was 3469. In all experiments in this regime, contrary to the observations of BW and FK, vortex motions were consistently observed.

This flow regime differs from the previous regime with respect to the formation of unit vortices in the near-field of the slit-jet flow field. As shown in Figure 53(c), the dye streak breaks up into unit vortices as it separates from the nozzle plates. Farther downstream, as in the case of the previous regime, large scale motions are formed. However, both the unit vortices and the large scale vortices appear diffuse.



Figures 65 through 68 show the development of the jet for four different values of Re . The same recording equipment (Nikon F3 motorized camera) was used for data acquisition in this high Re range as was used in the low Re range (< 1700). As it is apparent from these figures, the 6 Hz framing rate ($\Delta t \langle U \rangle / w \geq 0.5$) of the camera was not fast enough to catch the details of the instability process at these values of Re . Hence the process of formation of large scale motions and the role of unit vortices in the process cannot be precisely described. From the limited information available, the process of vortex formation appears to be different from the process described in Section 4.4.3. It has been observed from the photographs of this regime that only in some cases do the large scale motions evolve from a bulge as shown in Figures 67 and 68.

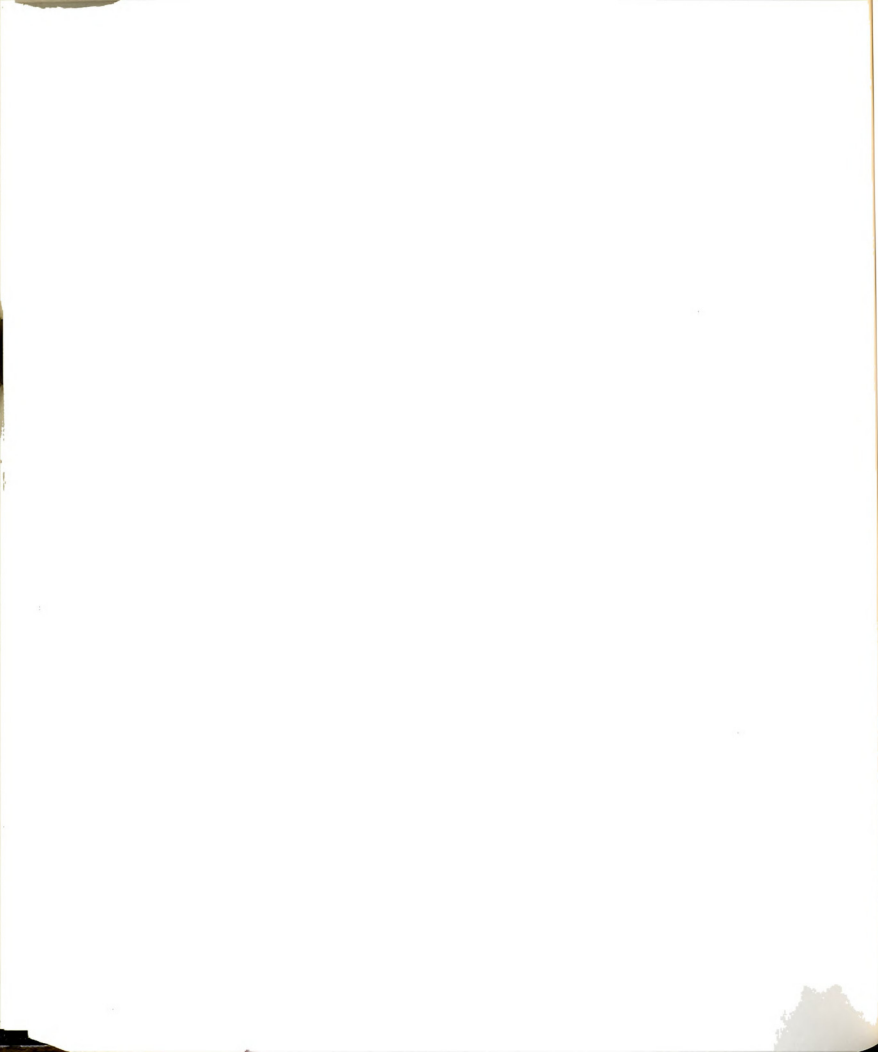
Based on the observations of the slit-jet flow field in this range of Re , it is concluded that the formation of these motions is not limited to a Re value ≈ 1500 as reported by BW. FK used hot-wire measurements in an air jet and reported that "well defined results" could be obtained only up to $Re \approx 1170$. They further reported that "a regular vortex street was not observed for $Re > 1750$ ".



4.5 Interactions Between Symmetric Motions

It was sometimes observed that two pairs of vortex motions (at various stages of their development) undergo an interaction which resulted in a symmetrically placed merged pair. The word "pairing" was used to describe this process by Winant and Browand (1974) and will also be used here. As shown in Figures 58, 61, 62, 67 and 69, for various values of Re , the interactions between symmetric motions normally occur at distances beyond one to two slit widths from the exit plane of the jet. The process of pairing occurs in one of the two following ways:

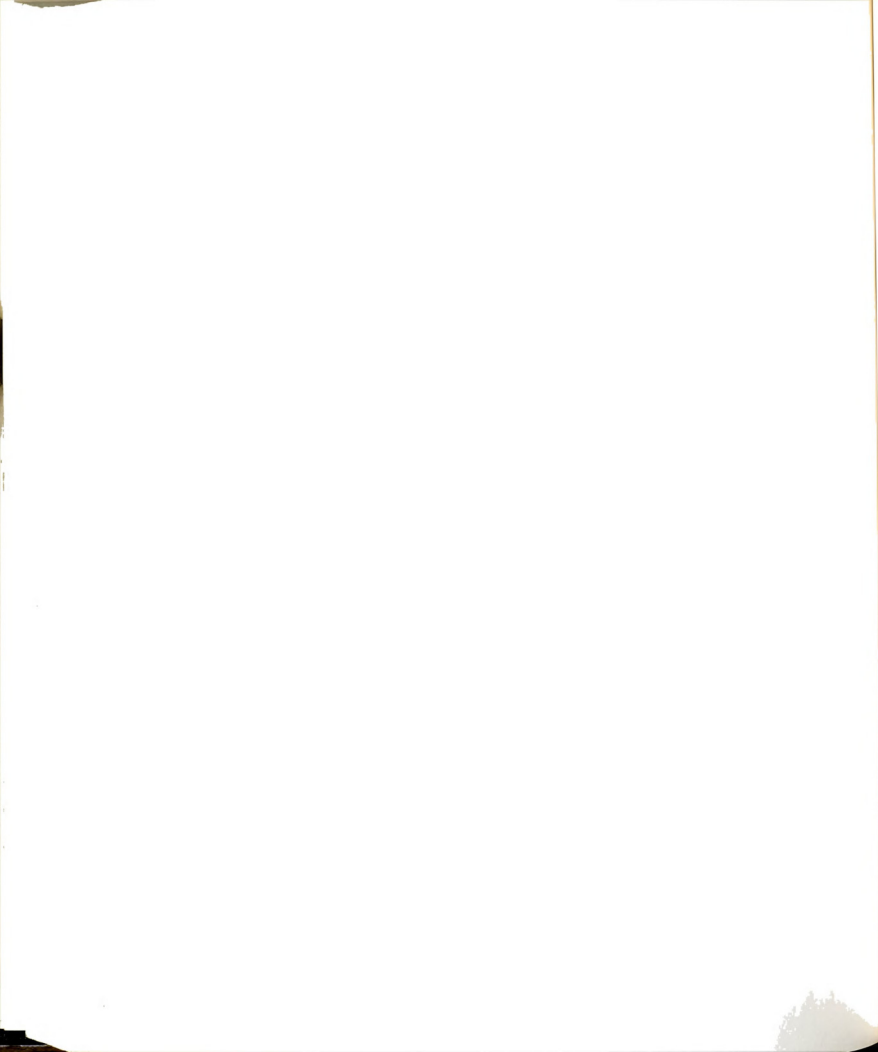
- i) Two pairs fuse together as the distance between the approaching upstream pair and the downstream pair becomes small enough, as shown in Figure 61(c).
- ii) The upstream vortex pair approaches the other pair and passes through it; the two pairs then revolve around each other before fusing together. See for example vortex number 8 and 9 of Figure 62(a). Also see vortex number (10,11) and 12 in Figure 67(c). Freymuth (1966) observed the phenomena of the passage of one vortex motion through the other and their rotation about a common axis in an excited axisymmetric jet. He referred to this as "slipping" of vortices.



Most of the interactions of the large scale motions are symmetric in nature. However, at times, some asymmetry has been observed in the locations of the components of the interacting pairs; see Figure 58. Typically, however, symmetry returns after the interactions are complete as shown in Figure 70. Another asymmetric interaction, which has only been infrequently observed, is the pairing on only one side of the centerline of the jet. An example is shown in Figure 71.

As stated earlier, most of the interactions involve two vortex pairs. However, at Re values of 1500 and greater, a rare event of simultaneous coalescence of upto three vortex pairs has been observed. See Figure 72. Note that (14,15), (16,17), and 18 form a divergent straight line arrangement in Figure 72(a) and a merged cluster in Figure 72(c). Similar behavior was observed in at least three other experiments.

Regarding the sequential mergers between previously paired vortex motions, Winant and Browand (1974) have reported up to four sequential pairings in their two stream shear layer. They have also commented that more than one pairing has not been observed in the jet flows (axisymmetric or planar). Here in the case of the slit-jet, up to two pairings are common and at times 3, 4 and even 5 pairings can be observed. Figure 73 shows the pairings of vortex pairs 24, 25, 26, 27, and 28, 29 and Figure 74 shows the pairing of conglomerates 24-27 and (28,29) resulting in five pairings.



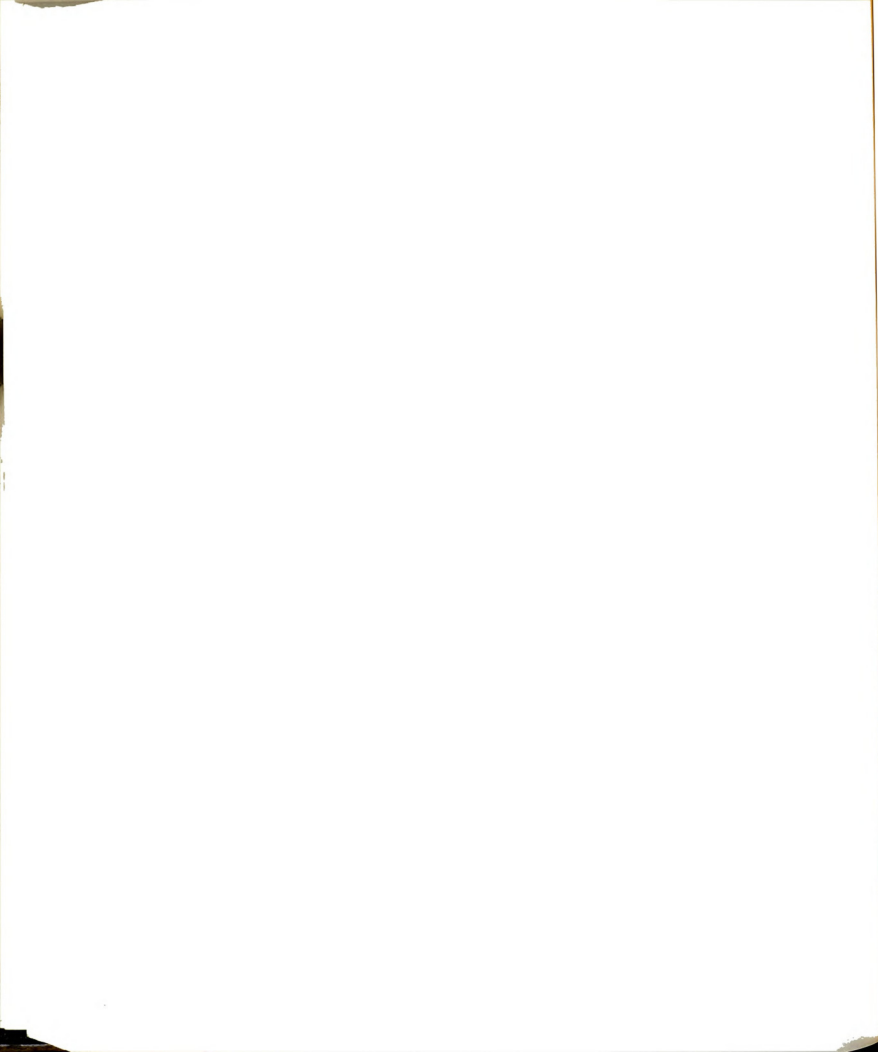
4.6 Loss of Symmetry in Vortex Street

The findings of this study regarding the behavior of the symmetric vortex motions are quite different from the observations reported by BW. The findings of the two studies are summarized below:

Beavers and Wilson	Present
1. In most cases, the "breakup of the pattern" occurs as a result of "one vortex pair passing inside another", i.e., due to pairing.	The pairing of large scale motions has not been found responsible for the "breakup" of the pattern.
2. As Reynolds number increases, the number of vortex pairs in the regular pattern decreases. At very high values, no more than one pair could be observed.	This pattern of loss of coherence has not been observed. Even at high values of Re , several vortex pairs can be identified.
3. No vortex motions are observed for Re greater than 1500.	The upper limit of formation of the vortex street in the slit-jet flow field lies beyond $Re \approx 1500$. The symmetric motions have been observed at Re values as high as 3469, and their presence have been inferred from the periodic fluctuations in the velocity $u(x=2, y=0, t)$ at Re values ≈ 6200 .

Regarding the breakup of the vortex pattern, it has been observed in this investigation that before this happens, one of the following three events occur:

- a) Asymmetric pairing. See Figure 75 at $Re = 1004$. It is to be noted that even though the symmetric coherent pattern has



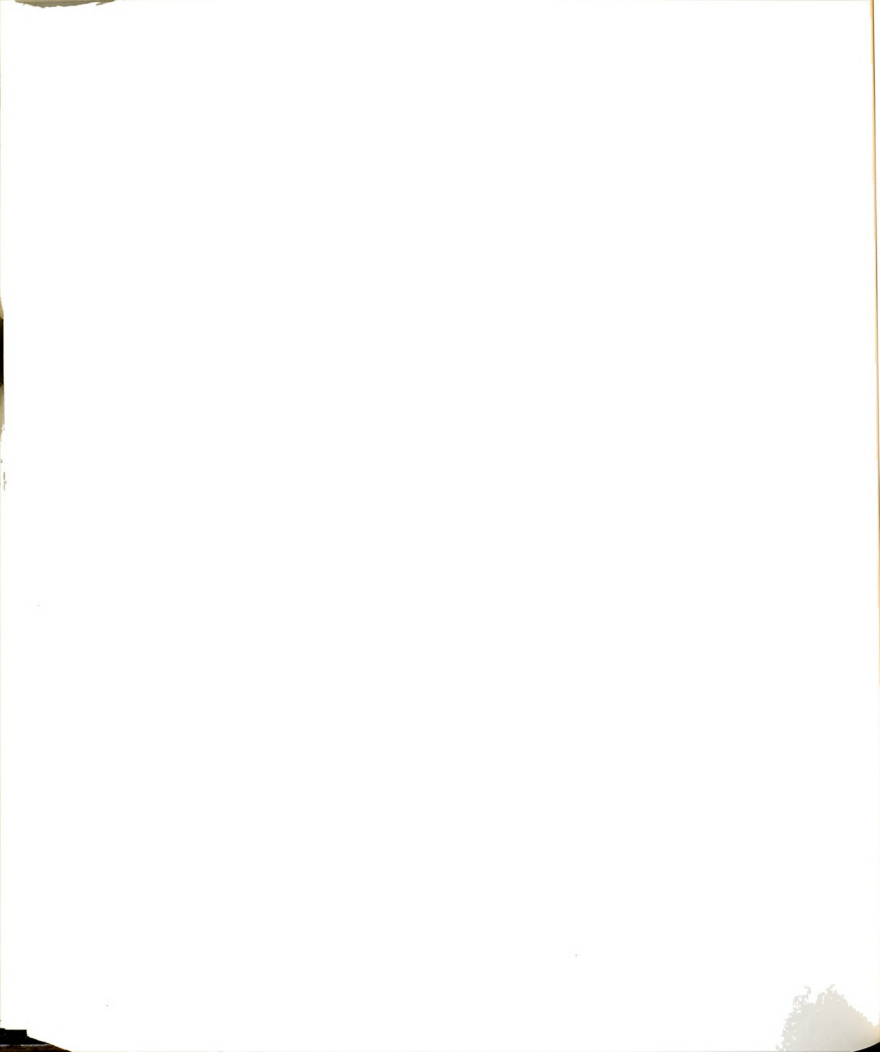
been lost due to asymmetric interactions, the newly forming vortices exhibit a symmetric coherent pattern.

- b) Three-dimensional instability of the two-dimensional vortex cores. See Figure 76 which shows the loss of symmetric pattern due to the tilting of vortices in the streamwise direction. However, the loss of symmetric coherence at any given time does not propagate upstream or in time. At later times, the symmetric pattern of vortex motions reestablishes itself. Parenthetically, this suggests that the instability which causes the loss of the symmetric pattern is convective in nature, whereas the slit-jet instability which causes symmetric vortex motions is absolute in nature.

- c) Formation of too many vortices, i.e., reduced spacing between symmetrically placed vortex pairs. See Figure 57.

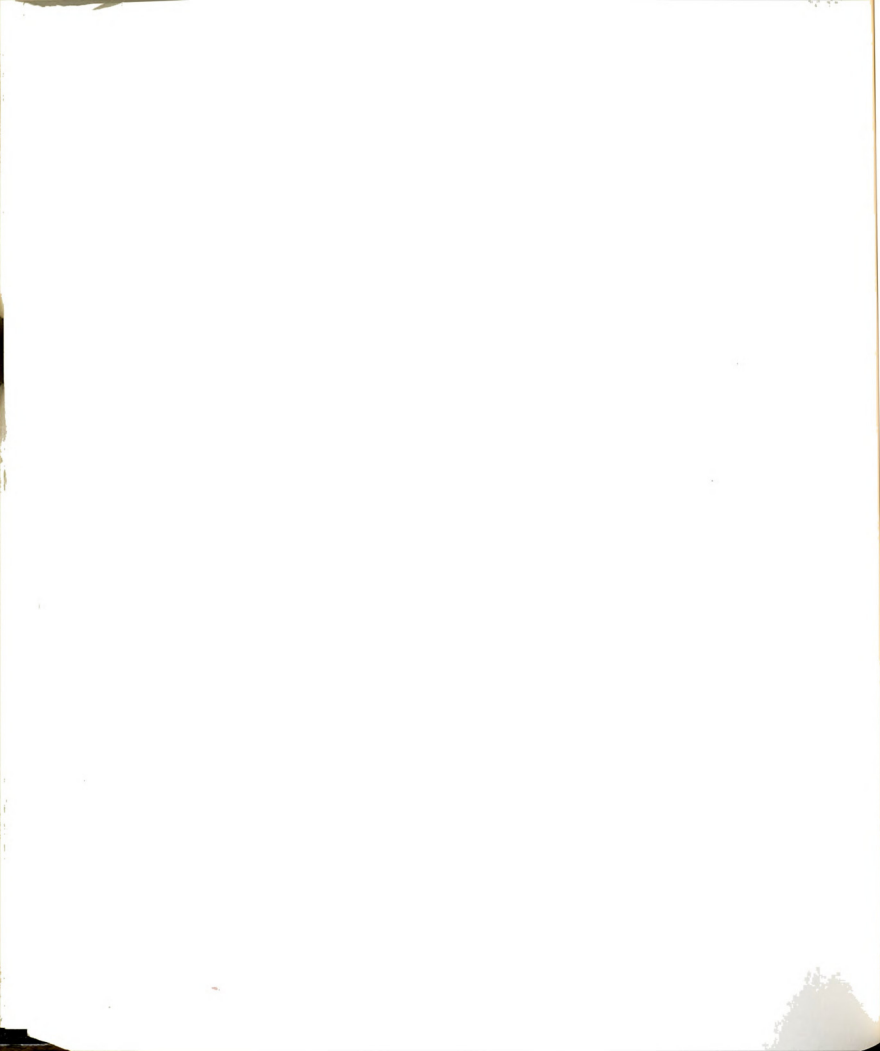
The above mentioned events cause only a temporal disruption of the symmetric vortex pattern. That is, as the disturbance convects downstream, the symmetric pattern again emerges. Sometimes, a pairing or tripling event has been found to reorganize the vortices--which had tilted in the streamwise direction--into two-dimensional symmetric vortex pairs. See Figure 77.

The symmetric vortex pattern of the slit-jet flow field has been found to evolve into a sinuous mode at low values of Re (e.g., $Re =$



300) and at distances exceeding 6-8 slit widths from the exit plane.

See Figures 56 and 63.

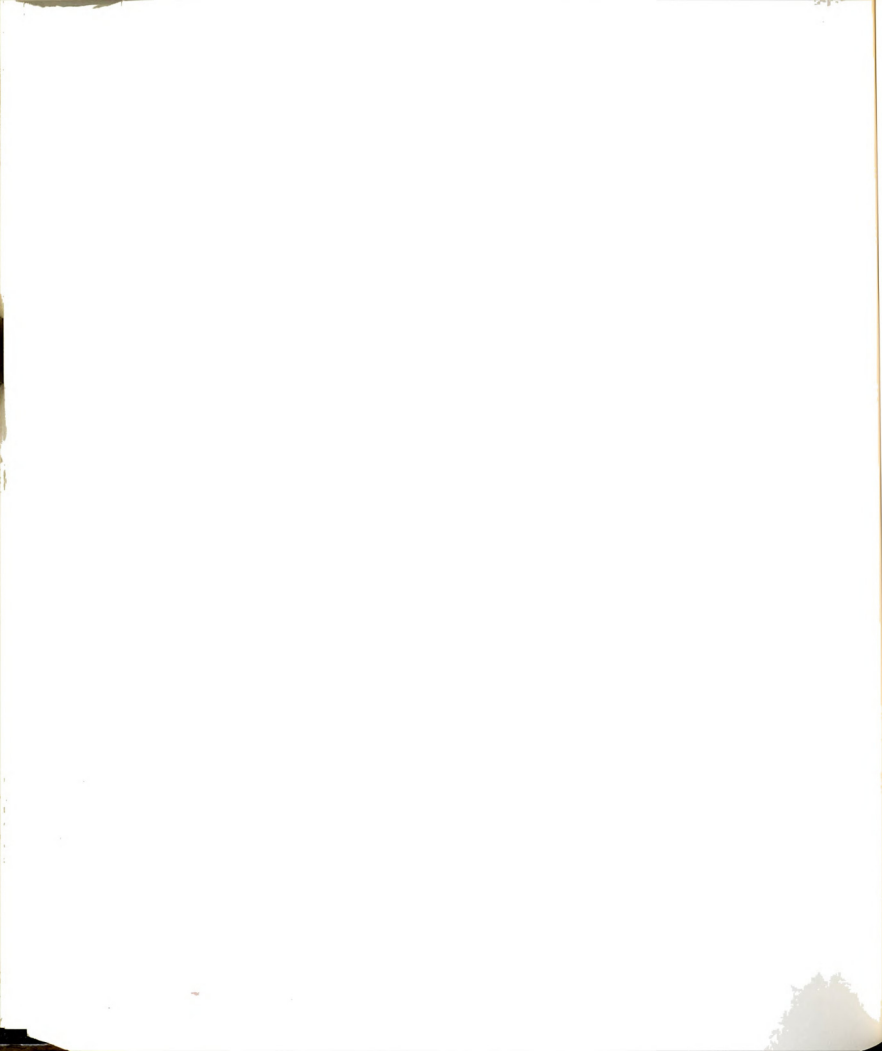


ALGORITHMS FOR PROCESSING THE PHOTOGRAPHIC DATA

5.1 Introduction

This chapter describes in detail:

- i) the algorithms that have been used for data reduction and creation of data base for flow visualization experiments;
- ii) the algorithms for computing the geometric/kinematic properties and the stability characteristics of the slit-jet flow field from the data base;
- iii) an example showing how the technique has been applied.



5.2 Creation of Data Base for Flow Visualization Experiments

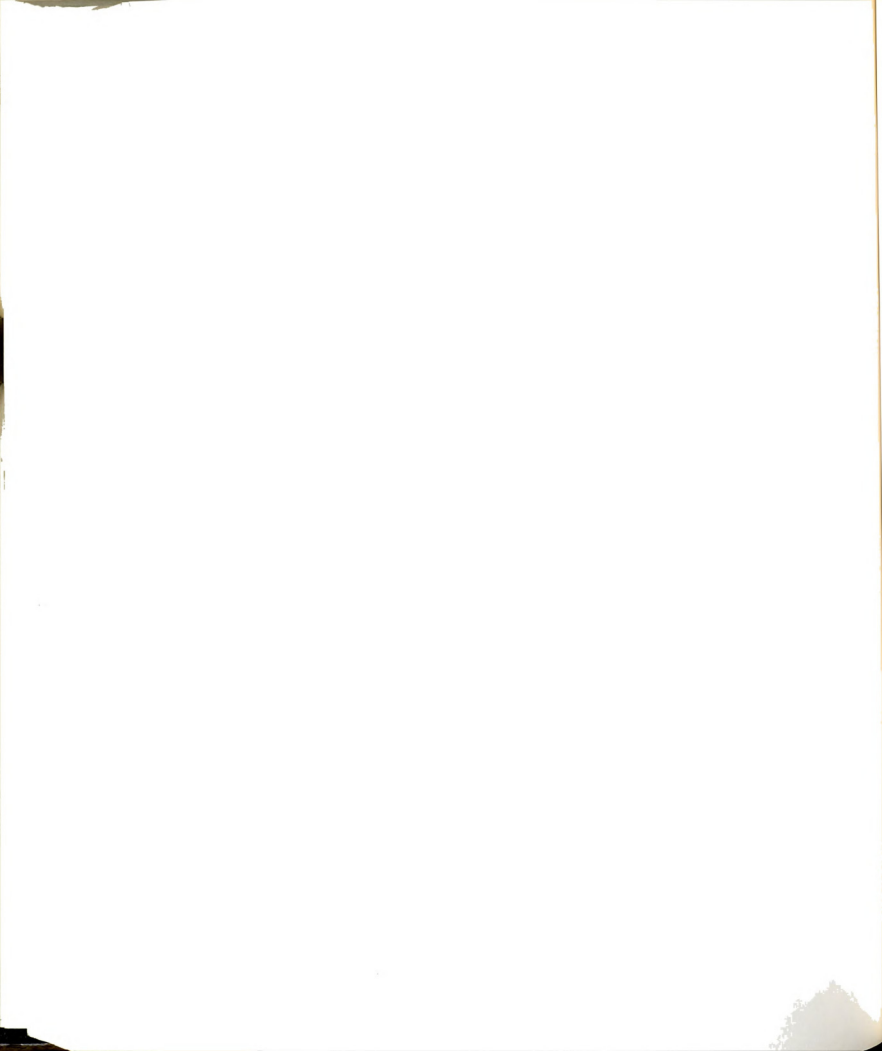
The data reduction process in these experiments involved:

- i) converting the pressure time series, $p_I(t)$, to the spatial average velocity of the jet, $\langle U \rangle$;
- ii) for flow visualization experiments digitizing the location of the vortices in each picture, determining the timing for each picture, and combining these information items in a single file together with other conditions of the experimental run;
- iii) for LDA measurements converting the Apple Soft binary data to ASCII format, transferring them to the PDP 11/73 system and then converting them to velocity time history.

This section describes the data reduction procedures in detail.

5.2.1 Computation of Spatially/Temporally Averaged Velocity of Jet

To determine the spatial/temporal average velocity $\langle U \rangle$ of the jet, the rate of rise of liquid in the receiver (V_{cup}) was first determined by using equation (127); see Section 3.7.2.3. For a liquid of known density, V_{cup} is directly proportional to the $\frac{dp_I}{dt}$. This rate of change of pressure was found by fitting the measured $p_I(t)$ data using a linear model

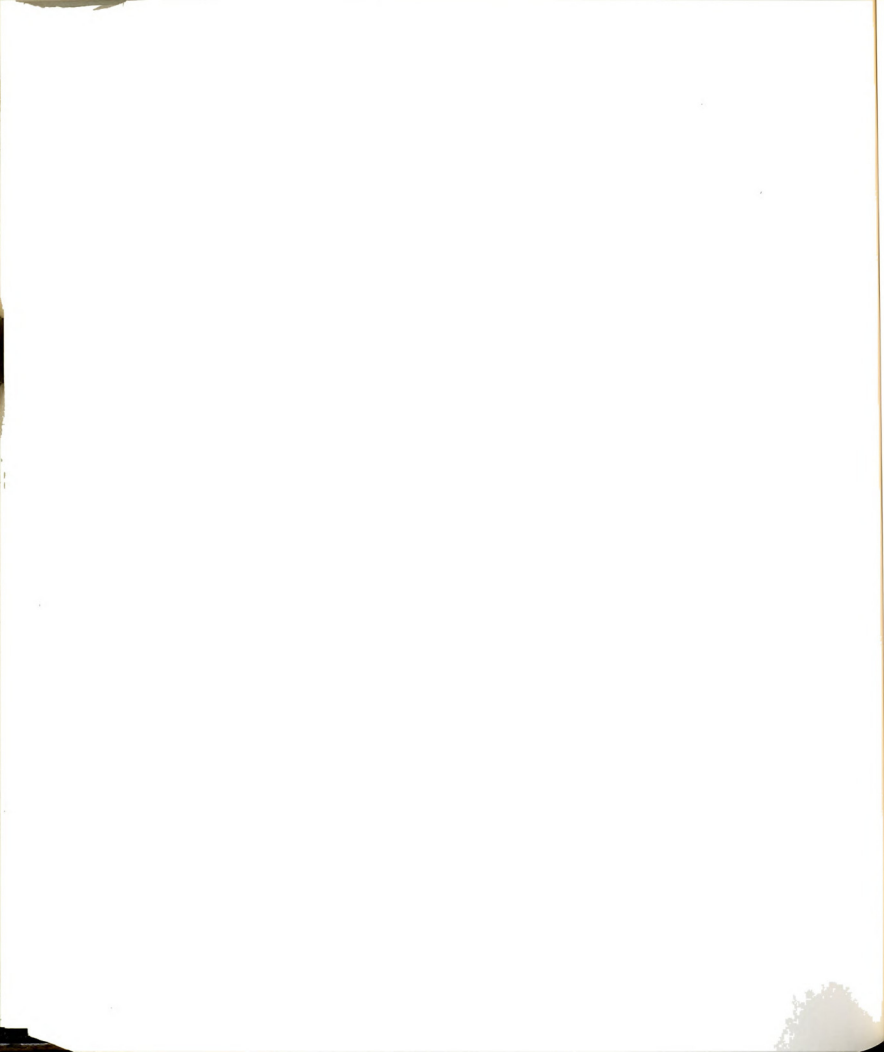


$$\eta = \beta_0 + \beta_1 t \quad (128)$$

and using the coefficient β_1 . (See Appendix B for details of selecting a linear model.) Note that $\beta_1 = \frac{dp_I}{dt}$ was used in equation (127). Using the principle of conservation of mass, the spatial average velocity of the jet was found from

$$\langle U \rangle = \frac{V_{cup} A_r}{A_j} \quad (129)$$

If the data from the entire experimental run (except for the transients in the beginning and the end) are used in determining β_1 in equation (128), the resulting velocity $\langle U \rangle$ will be an estimate of the spatial/temporal average velocity of the jet. On the other hand, an estimate of the spatial average velocity at a given time t can be found by using a limited amount of data, spanning over $(t-\Delta t)$ to $(t+\Delta t)$, to fit the model. This strategy was employed to determine the velocity at the times pictures were taken in the flow visualization experiment. A value of Δt equal to 2.5 times the integral time scale ($= \frac{w}{\langle U \rangle}$) was used to estimate the coefficients β_0 and β_1 at any given time t . This value was chosen because it was found that for most of the experimental runs the residual does not vary much for values of $\Delta t > 2 \frac{w}{\langle U \rangle}$.



5.2.2 Picture Timings or Beginning and End Time for LDA Data

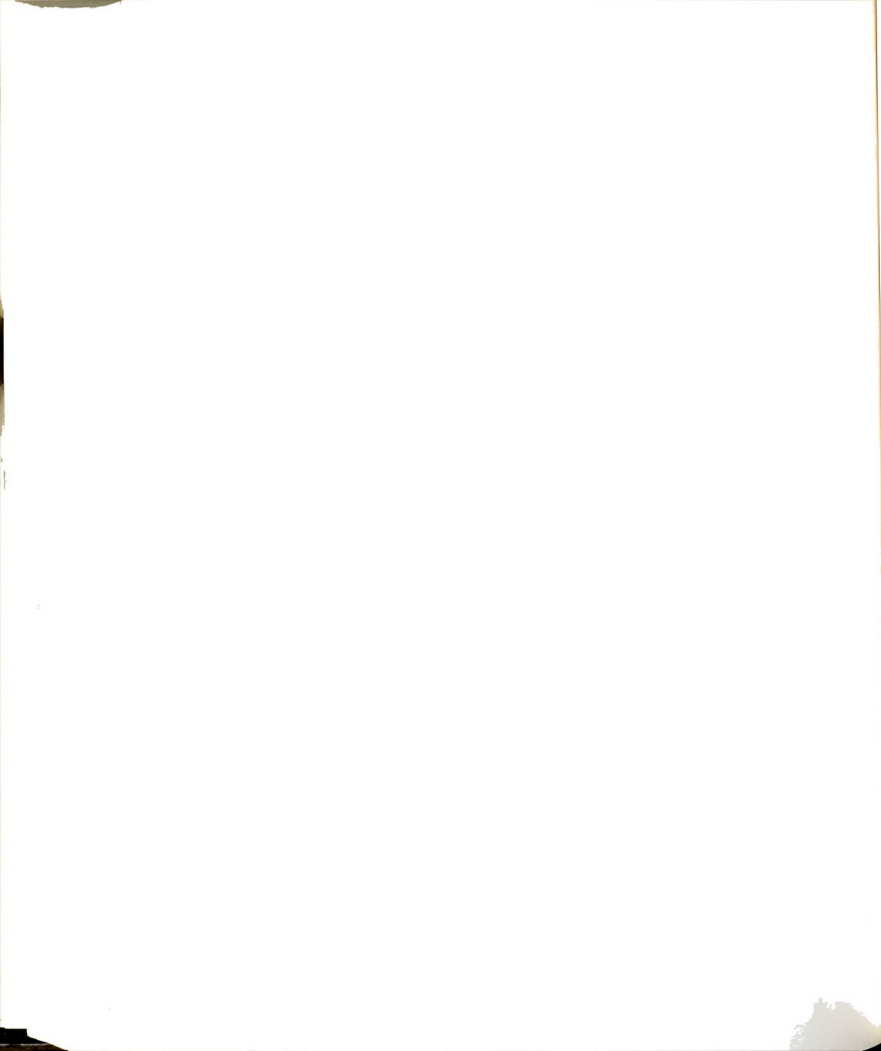
Figure 78 is a plot of the comparator output, $C(t)$, along with $p_I(t)$ and $p_{NH}(t)$ signals. As shown in this figure, the output signal of the comparator is marked by a spike in the voltage whenever the camera was fired. The processing program determined these spikes by differentiating the time signal and comparing it with the TTL voltage level. If the TTL level was exceeded, the program recorded the time t as the time a picture was taken.

For experiments in which the laser Doppler velocity data were measured using the Apple IIe computer, the beginning and the end time of the LDA data acquisition were similarly determined from the recorded output of the comparator.

5.2.3 Digitization on PRIME 750 Computer System.

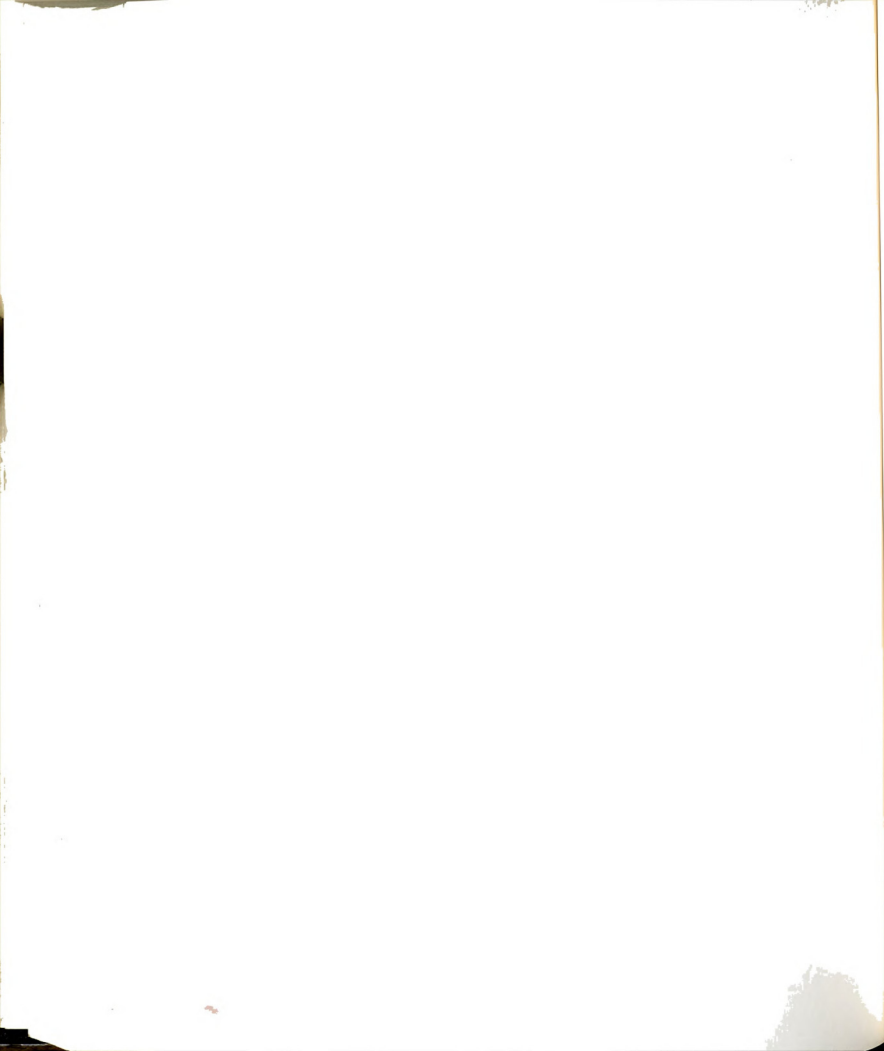
The pictures that were taken in a flow visualization experiment were digitized on the PRIME 750 Computer system of the CASE Center for Computer-Aided Engineering and Manufacturing. The PRIME computer is equipped with a large digitizing tablet and a locator mouse. A picture was taped to the tablet and, after defining the axes and the origin of a picture, the location of vortices were digitized.

Figure 79 is a typical representation of the photographs that have been digitized. Since the mid plane of the NH was in focus to take the pictures, the knife edges of the nozzle plates are blurred.



Thus, they could not be used for measuring the slit width w or for reference purposes. However, the metal taps which are located in the mid plane were used as fiducial points. The intersection of one of taps with the nozzle plates on the right hand side of centerline of the jet served as origin, the underside of the nozzle plates was used as one of the axes and the tip of one of the taps on the left hand side of centerline of the jet was used as a reference point.

In a given set of photographs (about 36 in number), all the vortex pairs are numbered 1 to n beginning with the pair furthest from the exit plane in the first picture. In the second picture, the pairs of the first picture were traced along with any new ones which get added at the top. The vortex pairs which undergo coalescence and form one vortex pair have been designated by the indices of the contributing vortex pairs separated by a coma. For example in Figure 79, vortex pairs 9 and 10 which had merged earlier have been designated by (9,10). In the process of digitizing, the merged pair of vortices were digitized as many times as the number of vortex pairs that had coalesced together. This was necessary to keep proper accounting of the the vortices as each photographic record was digitized. This strategy also allowed proper digitization of the vortex pairs which undergo "leapfrogging" before fusing together. If a vortex pair went out of the field of view or if the dye got diffused so much that the pair could not be identified, it was considered to be lost and its entry was dropped. In this way, the same number of location files have been generated as the number of pictures in a given set.

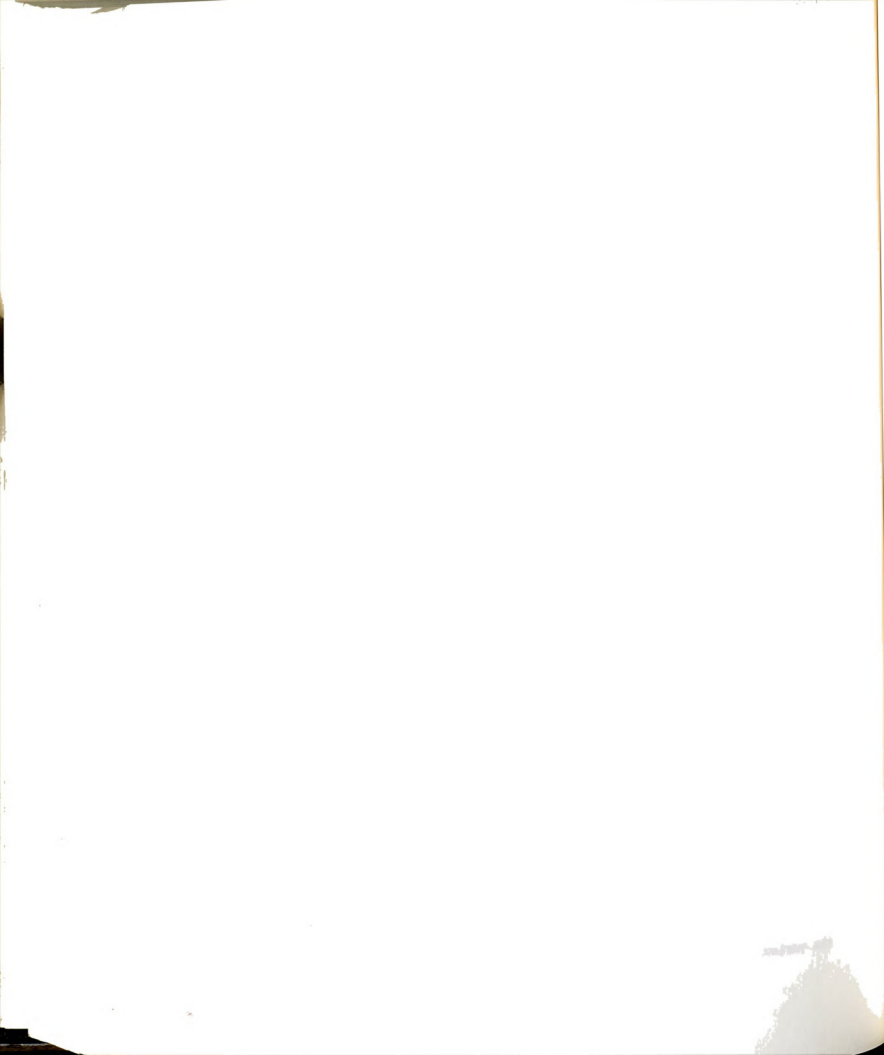


5.2.4 Combining Information: Time, $\langle U \rangle$ and Position of Vortex Pairs

The data files containing the location of vortex pairs were transferred to the PDP 11/73 system to be combined with the timing and velocity data for each picture. Using a program (PSTPR5) the timings of the pictures were found along with the spatial average velocity $\langle U \rangle(t)$ at these times (see Sections 5.2.1 and 5.2.2). The output of PSTPR5 were stored in a file. Another program CSJD1 then combines the timing and velocity data with the corresponding position data for each photograph. The output of CSJD1 contained all the pertinent information about the experiment. In addition, for each photograph, the output contained the number of vortex pairs digitized, the time of the photograph and the corresponding spatial average velocity of the jet $\langle U \rangle$. This was followed by the spatial locations for each vortex pair.

5.3 Algorithms for Processing Photographic Database

Section 5.2 described the procedures for extracting information from the photographic records and combining it with the time and velocity information to generate a comprehensive database for each experimental run; such a database will be referred to as a photographic database. In this section, algorithms will be presented to further process the photographic database. Algorithms to evaluate the geometric/kinematic properties of the slit-jet flow fields are presented in Section 5.3.1 and the algorithms to compute the Strouhal number, the convection speed of the vortices, and the wavelength of the vortex street are presented in Section 5.3.2.



5.3.1 Algorithms for Geometric/Kinematic Properties of the Jet Flow Fields

5.3.1.1 Space-Time ($x^* - t^*$) Plots of Vortices

The average of the nondimensional distances x_k/w from the exit plane of the jet of the two vortices of a given pair can be expressed as a function of the nondimensional time $t < U/w$; see Figure 80. This functional relationship can be expressed as a space-time plot. Namely, for the k th vortex in the j th photograph (at time t^*)

$$x_k^*(t^*) = \frac{x_k^j(\text{left}) + x_k^j(\text{right})}{2w} \quad (130)$$

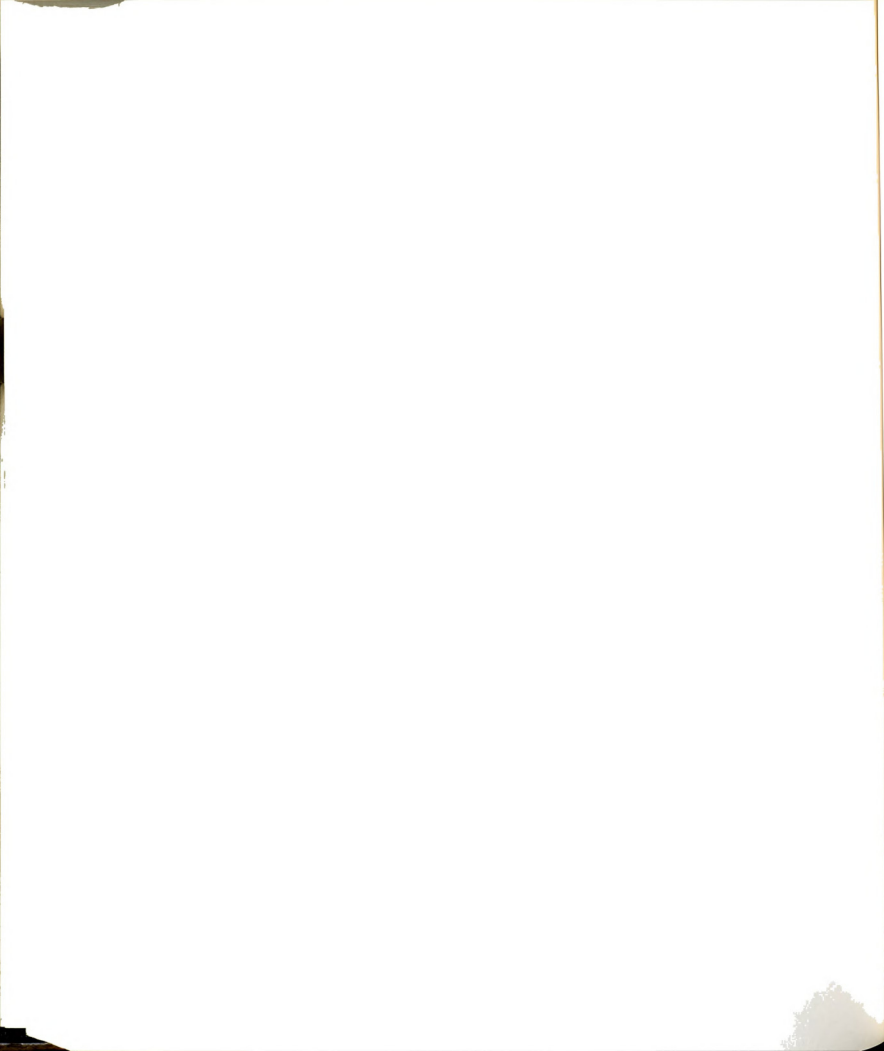
The symbols used here have been defined in Figure 80. This expression will also be used to determine the location of a given vortex pair in the computation of quantities like Strouhal number, convection velocity and the spacing between vortex pairs.

5.3.1.2 Lateral Spacing Between Vortices of Individual Pairs

The lateral spacing d_k/w between the vortices of the k th pair as a function of distance from the exit plane can be computed, as shown in Figure 80, from

$$d_k^*(x_k^*, t^*) = \frac{y_k^j(\text{left}) - y_k^j(\text{right})}{2w} \quad (131)$$

where x_k^* is given by equation (130).



5.3.1.3 Difference in Axial Location of the Two Vortices of a Pair

In Section 5.3.1.1, the average of the axial distances from the exit plane of the jet was used to prepare the space-time plot of vortices. In this section an algorithm is presented to prepare plots showing the difference in the axial location between the vortices of a pair; this difference will serve as an estimate of asymmetry in the locations of vortex pairs. As shown in Figure 80, for the k th vortex pair, the asymmetry, a_k/w , is computed as a function of the distance from the exit plane as

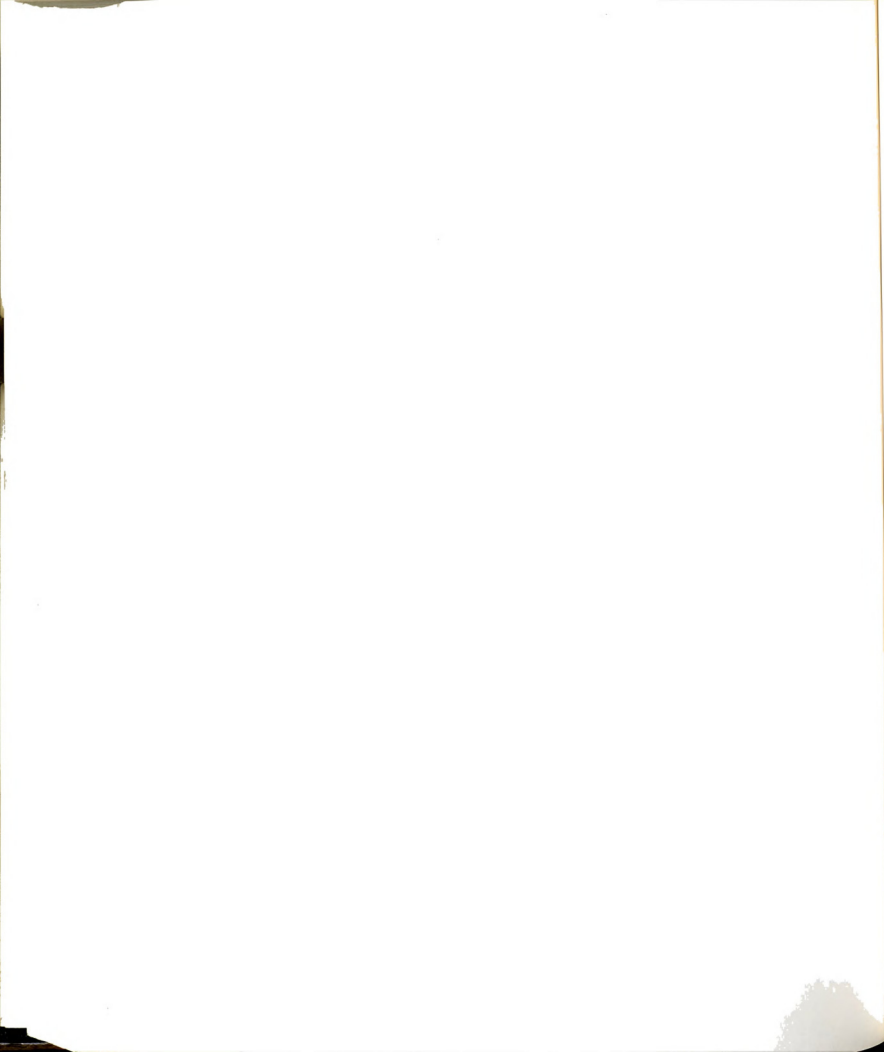
$$a_k^*(x_k^*, t^*) = \frac{x_k^j(\text{left}) - x_k^j(\text{right})}{w} \quad (132)$$

where x_k^* is given by equation (130).

5.3.2 Algorithms to Compute Vortex Street Parameters

Three parameters, Strouhal number (St_F), convection velocity (u_c), and wavelength (λ), are computed from the photographic observations of the slit-jet flow field. Because the photographic records present the whole flow fields at equispaced times, each of these parameters can be determined independently at a given distance downstream of the exit plane. Sections 5.3.2.1 through 5.3.2.4 describe the procedure for computing these parameters.

For a periodic process, the parameters St_F , u_c , and λ are interrelated as



$$St_F = \frac{u_c^*}{\lambda^*} \quad (133)$$

where $u_c^* = u_c / \langle U \rangle$ and $\lambda^* = \lambda / w$. The observations of the photographic records of the vortices in the slit-jet flow field, however, indicate that the process of formation, translation, and interaction of vortex pairs is quasi-periodic in nature. This means that, in general, the independent estimates of these three parameters will not satisfy the above relationship. Considering the randomness of an unexcited jet, a statistical method has been formulated to compute the overall estimates of u_c^* and λ^* from their respective independent estimates and the estimate of St_F such that equation (133) is satisfied. Section 5.3.2.5 describes the details of this method.

5.3.2.1 Strouhal Number $St_F(x/w)$

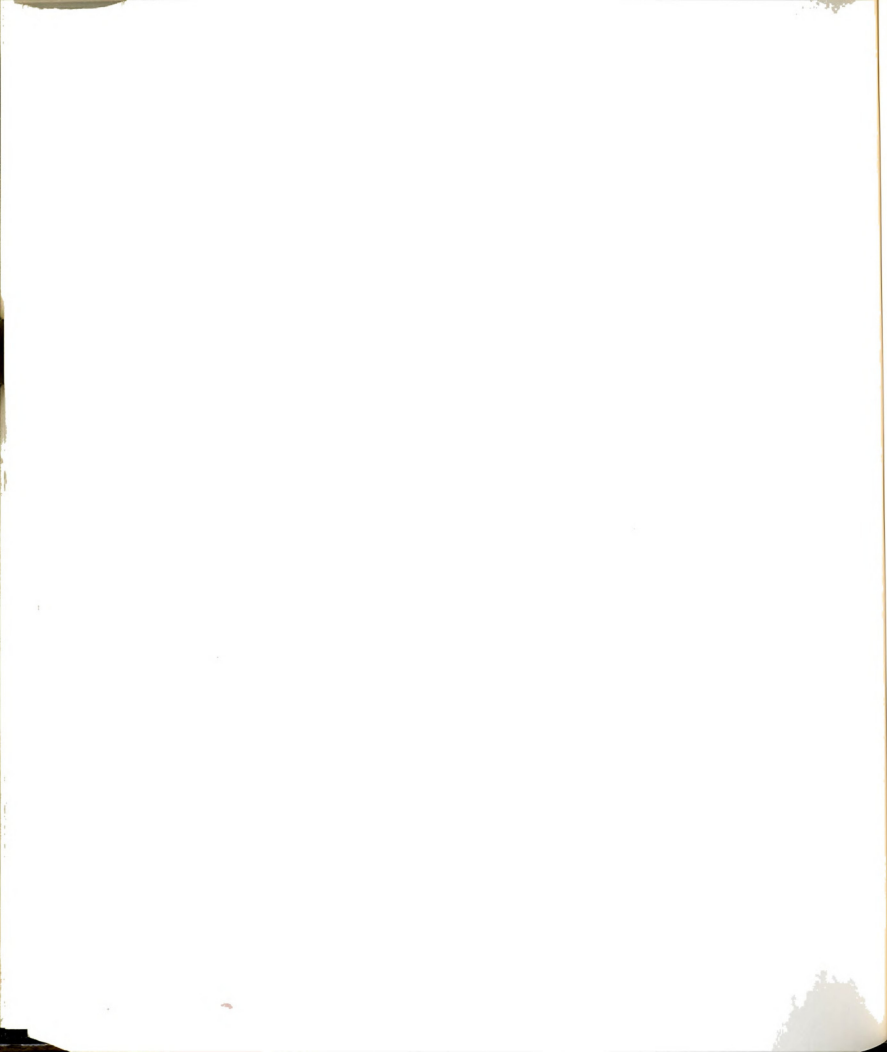
The Strouhal number of the slit-jet flow field based upon the observed vortex motions at a given distance x/w from the exit plane is defined as

$$St_F(x^*) = \frac{f_F(x^*)w}{\langle U \rangle} \quad (134)$$

where $f_F(x^*)$ is the passage frequency of vortex pairs at x^* . The passage frequency $f_F(x^*)$ is determined from

$$f_F(x^*) = \frac{\text{No. of vortex pairs crossing plane at } x^*}{\text{Total time}} \quad (135)$$

This definition of St_F provides an unbiased estimate of Strouhal



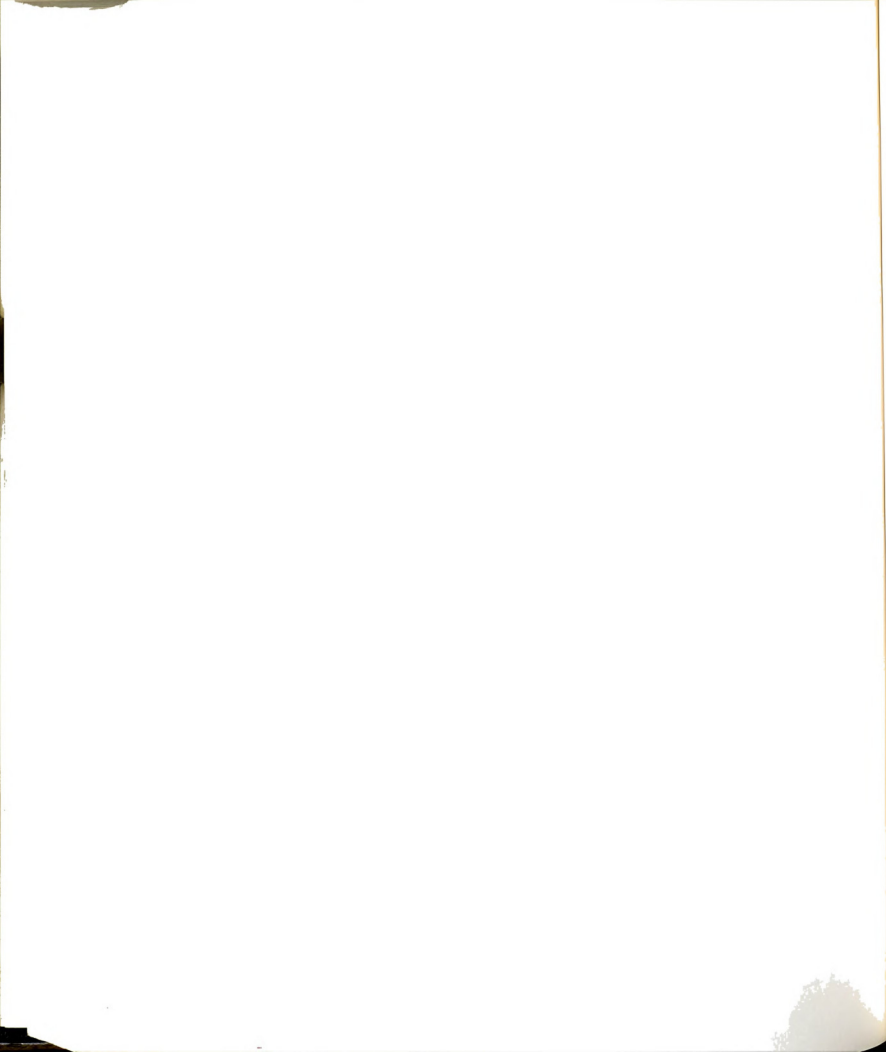
number; BW used this definition for their reported values of St for a given Reynolds number.

5.3.2.2 Translation Speed $c_k(x/w)$ of Vortex Pairs

The translation speed of the k th vortex pair is computed from its positions x_k^j and x_k^{j+1} before and after the plane of observation and the time taken to cover the distance $(x_k^{j+1} - x_k^j)$. As shown in Figure 81, there are four possibilities of the location of the k th vortex pair with respect to the plane of observation located at a distance x_o from the exit plane. The four cases are:

- i) x_k^j and x_k^{j+1} "far" removed from x_o ;
- ii) x_k^j "far" removed but x_k^{j+1} in "close" proximity to x_o ;
- iii) x_k^j and x_k^{j+1} in "close" proximity to x_o ;
- iv) x_k^j in "close" proximity to x_o and x_k^{j+1} "far" removed.

The closeness of a vortex pair to the plane of observation is determined with respect to the longitudinal spacing, L , between the vortex pairs at the plane of observation. However, since the spacing L is not known a priori, the computations are carried out in two stages. In the first stage, a rough estimate of L is obtained, and in the second stage, based upon the four possibilities of the location of



a vortex pair, another estimate is computed. The two stages of calculations are described below.

Stage I:

a) Determine the speed with which the k th vortex pair crosses the plane of observation (at x_o from the exit plane) from

$$c_k = \frac{x_k^{j+1} - x_k^j}{t_{j+1} - t_j} \quad (136)$$

b) Compute the average value of convection velocity from the individual estimates of c_k :

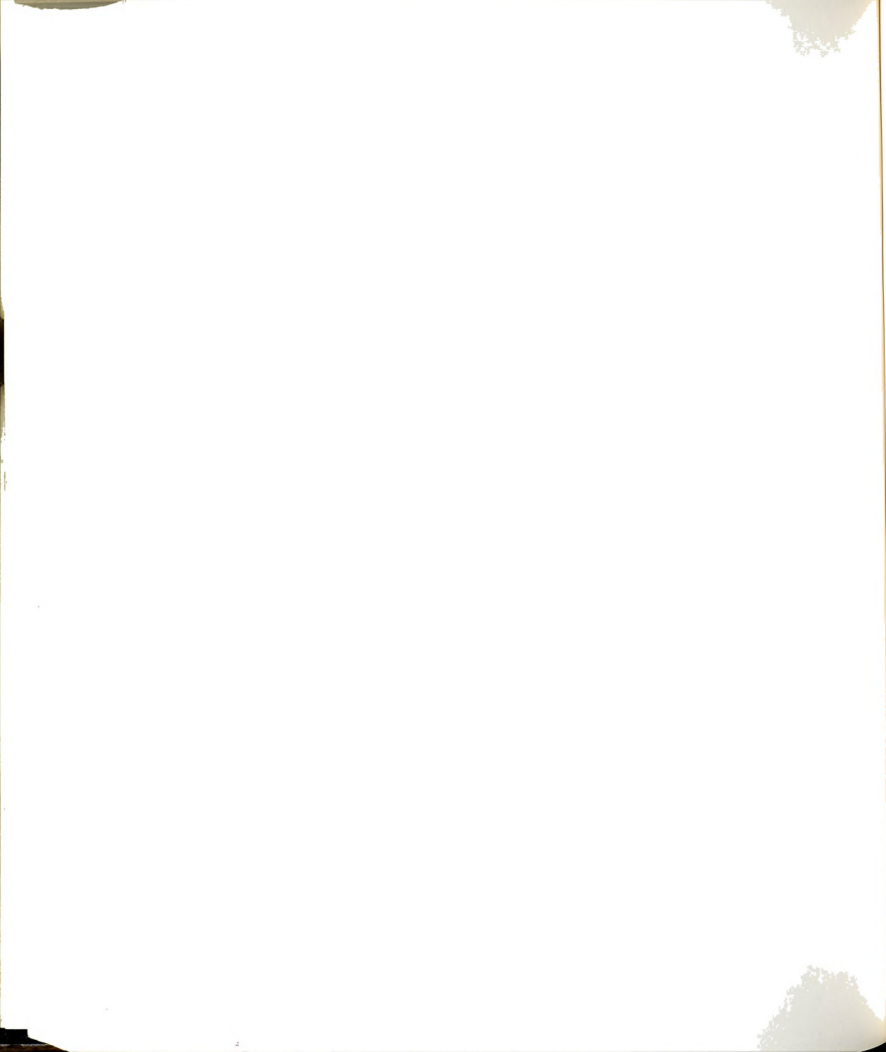
$$\bar{c} = \frac{1}{N} \sum_{k=1}^N c_k \quad (137)$$

c) Determine the overall passage frequency of the vortices using equation (135).

d) Using the relationship for a periodic process, compute the first estimate of the spacing from

$$L = \frac{\bar{c}}{f_F} \quad (138)$$

e) Define a window around the plane of observation with a user specified width, $2T_w$, equal to, for example, 20% of L . Hence, if a vortex pair comes within 10% of L , on either side of the plane of



observation, it would be considered to be in close proximity to the plane.

Stage II:

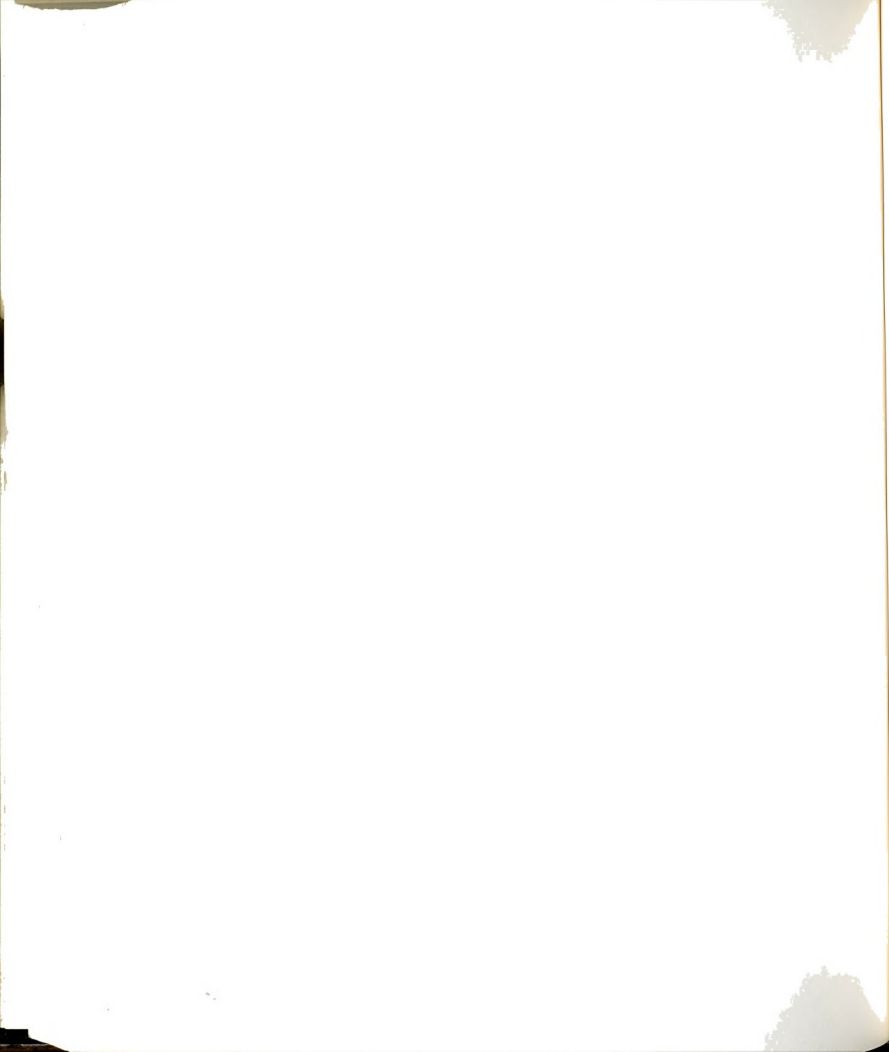
a) Recompute the velocity of each vortex pair depending upon its "closeness" to the plane of observation as

$$c_k = \frac{x_k^m - x_k^n}{t_m - t_n} \quad (139)$$

where $m = j+1$ for cases (i), (iii), and (iv) or $j+2$ for case (ii), respectively, and $n = j$ for cases (i), (ii), and (iii) or $j-1$ for case (iv), respectively.

b) Using equation (137) an average estimate of the translation speed of the vortices can be determined.

In computing an estimate for the average speed, care is taken to not include the translation speed of those vortices which undergo pairing in the vicinity of the plane of observation. Similarly, average values for the distance L between the vortices exclude those conditions where the vortices have paired near the plane of observation. The decision: "have two vortex motions paired at a given distance from the exit plane?" is based upon the average longitudinal spacing L between the two vortex pairs. A user specified parameter, T_p , which is based upon the average spacing, L , is used. If the distance



between the centers of the two vortex pairs is found to be less than T_p , then the vortex pairs are considered paired and the translation speed is not included in the average estimate. Since in the first stage of calculations L is not known, the initial value for T_p is based upon the width of the jet. Typically, T_p is set equal to 5 to 10% of w or L .

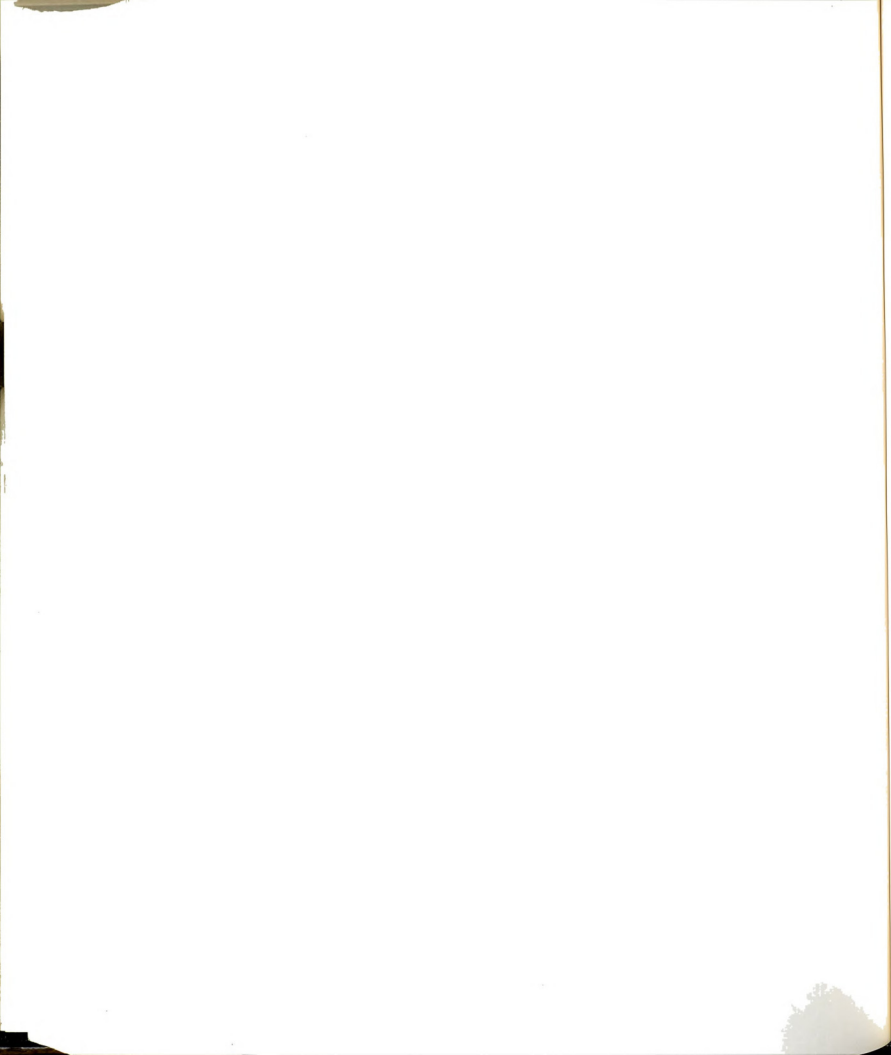
5.3.2.3 Passage Time t_k^p

The passage time of the k th vortex pair past the plane of observation (located at x_o from the exit plane) is computed from c_k as

$$t_k^p = \frac{x_o - x_k^m}{c_k} + t_m \quad (140)$$

where $m = j$ for cases (i), (ii), and (iii) or $j-1$ for case (iv).

The passage time t_k^p has been used to determine the population of vortex spacings (Section 5.3.2.4) and the difference in the passage time $\delta t_k = t_k^p - t_{k-1}^p$ between two vortex pairs has been used to compute the population of a local Strouhal number $\frac{w}{\delta t_k \langle U(\tau) \rangle}$. Note that the mean values provided by these populations can be compared with λ and St_F , respectively.



5.3.2.4 Longitudinal Spacing Between Vortex Pairs

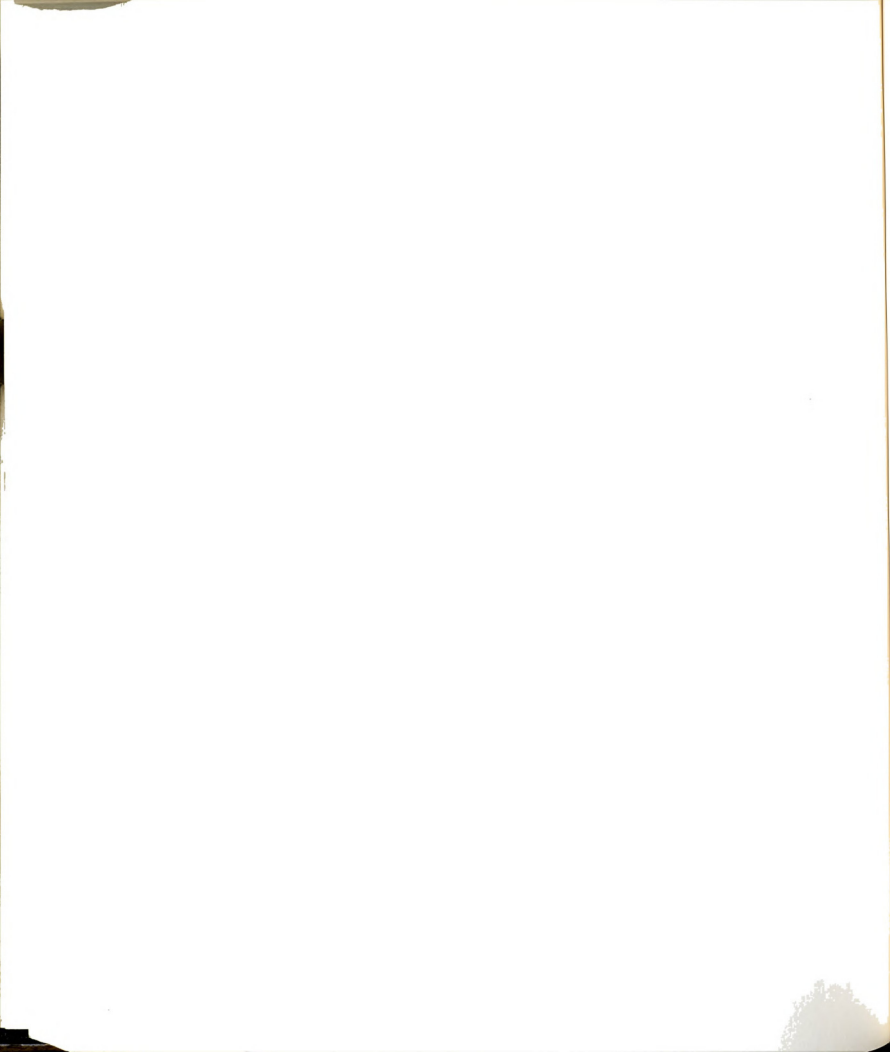
An average estimate of the longitudinal spacing, L , between vortex pairs can be computed in two different ways: i) indirectly by using the relationship (138), and ii) directly from the photographic records. The two methods are described below.

i) Assuming the process of vortex formation and translation to be periodic, equation (138) can be used to determine the average spacing between vortex pairs. The average speed of translation of vortices c_k is found from the population given by the equation (137) and the passage frequency is given by the equation (135).

ii) The longitudinal spacing L_k of the k th vortex pair with respect to the neighboring vortex pairs ($k-1$ and $k+1$) can be determined from the photographic database. The calculation is based upon the location of the vortex pair with respect to the plane of observation as described in Section 5.3.2.2. Figure 82 is a schematic representation of the locations of the vortex pairs in consecutive photographic records j . The spacing L_k is obtained as

$$L_k = (1 - \zeta_k)(x_{k-1}^m - x_k^m) + \zeta_k(x_k^n - x_{k+1}^{n+1}) \quad (141)$$

where $m = j$ and $n = j+1$ for cases (i), (iii) and (iv) or $m = j+1$ and $n = j+2$ for case (ii), respectively. Here ζ_k is the weighting function based upon the arrival time of the k th vortex at the plane of



observation. It is found from

$$\zeta_k = \frac{t_k^p - t_j}{t_{j+1} - t_j} \quad (142)$$

An average value of the spacing \bar{L} from the population L_k is computed from:

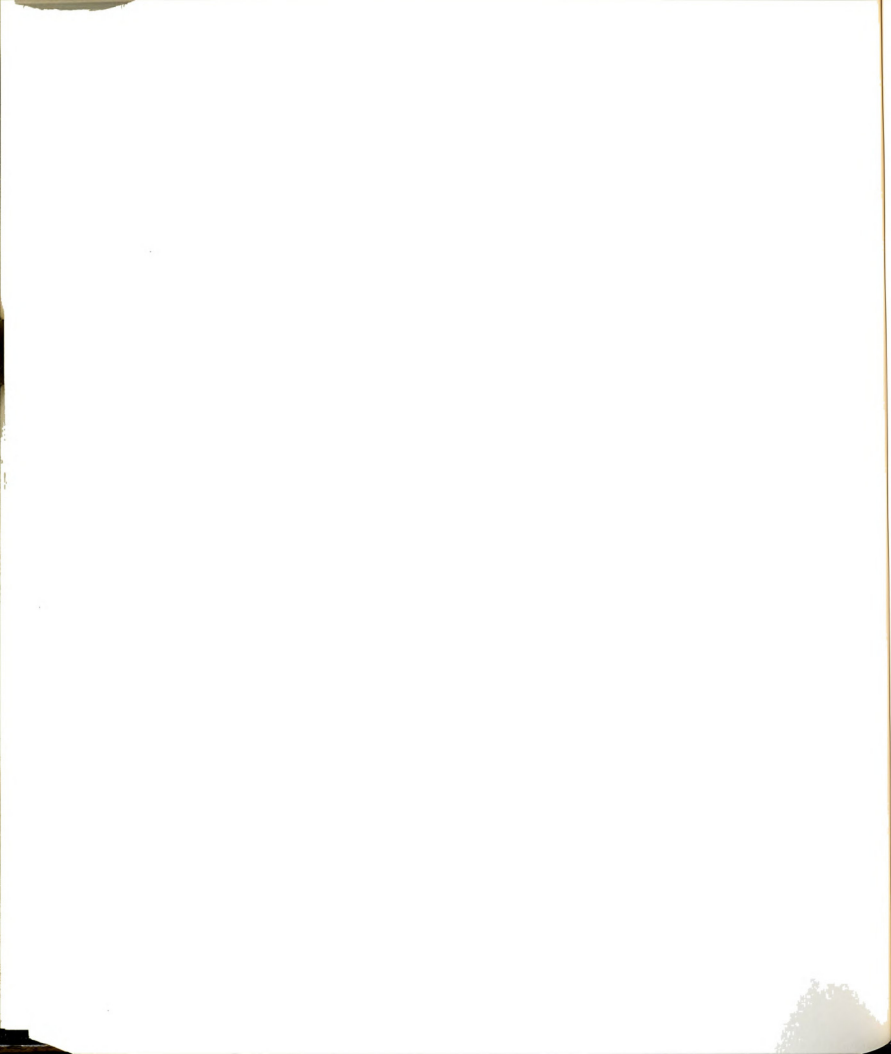
$$\bar{L} = \frac{1}{N} \sum_{k=1}^N L_k \quad (143)$$

5.3.2.5 A Statistical Method to Compute Estimates of u_c and λ :

A statistical approach has been developed to compute an overall estimate of the convection velocity u_c and the wavelength λ , using i) St_F (see Section 5.3.2.1), ii) $c_k/\langle U \rangle$ (see Section 5.3.2.2), and iii) L_k/w (see Section 5.3.2.4). Figure 83 shows a schematic plot of $c_k/\langle U \rangle$ versus L_k/w at a given plane of observation. The straight line passing through the origin of the plot represents St_F at this plane. The cluster of points represents the behavior of individual vortex pairs in the given experiment. The desired statistical estimates: u_c and λ , are assumed to satisfy

$$\frac{u_c}{\langle U \rangle} = St_F \frac{\lambda}{w} \quad (144)$$

or



$$u_c^* = C \lambda^* \quad (145)$$

where C is a constant. Let the mark $*$ on the straight line OC in Figure 83 denote one of the possible combinations of (u_c^*, λ^*) . The distance, δ_k , of $*$ from one of the entries (L_k^*, c_k^*) is expressed as

$$\delta_k^2 = (u_c^* - c_k^*)^2 + (\lambda^* - L_k^*)^2 \quad (146)$$

The distance δ_k represents the deviation in the nondimensional passage frequency of the k th vortex from the overall nondimensional passage frequency St_F . The sum of the squares, S , of the δ_k values, provides a measure of the deviation between the selected point, $*$, and the population of $[c_k^*, L_k^*]$ values.

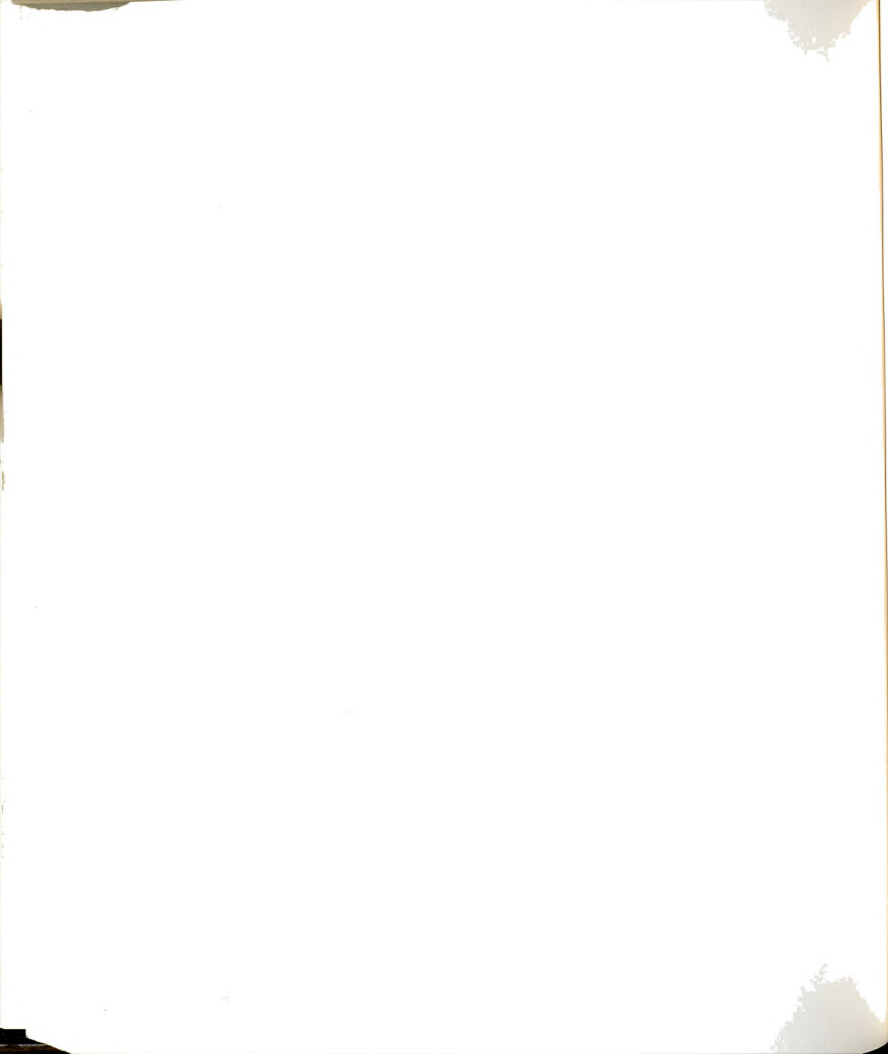
$$S = \sum_{k=1}^N [(u_c^* - c_k^*)^2 + (\lambda^* - L_k^*)^2] \quad (147)$$

Using equation (145)

$$S = \sum_{k=1}^N [(C\lambda^* - c_k^*)^2 + (\lambda^* - L_k^*)^2] \quad (148)$$

Equation (148) shows that S is a function of a single parameter λ^* . S can be minimized with respect to λ^* by finding $\partial S / \partial \lambda^*$ and setting it equal to zero, i.e.,

$$\frac{\partial S}{\partial \lambda^*} = \sum_{k=1}^N 2[C(c_k^* - \lambda^*) + (\lambda^* - L_k^*)] = 0 \quad (149)$$



or

$$\sum_{k=1}^N [(C^2+1)\lambda^* - (L_k^* + Cc_k^*)] = 0 \quad (150)$$

which yields,

$$\lambda^* = \frac{1}{N} \frac{1}{(C^2+1)} \sum_{k=1}^N [L_k^* + Cc_k^*] \quad (151)$$

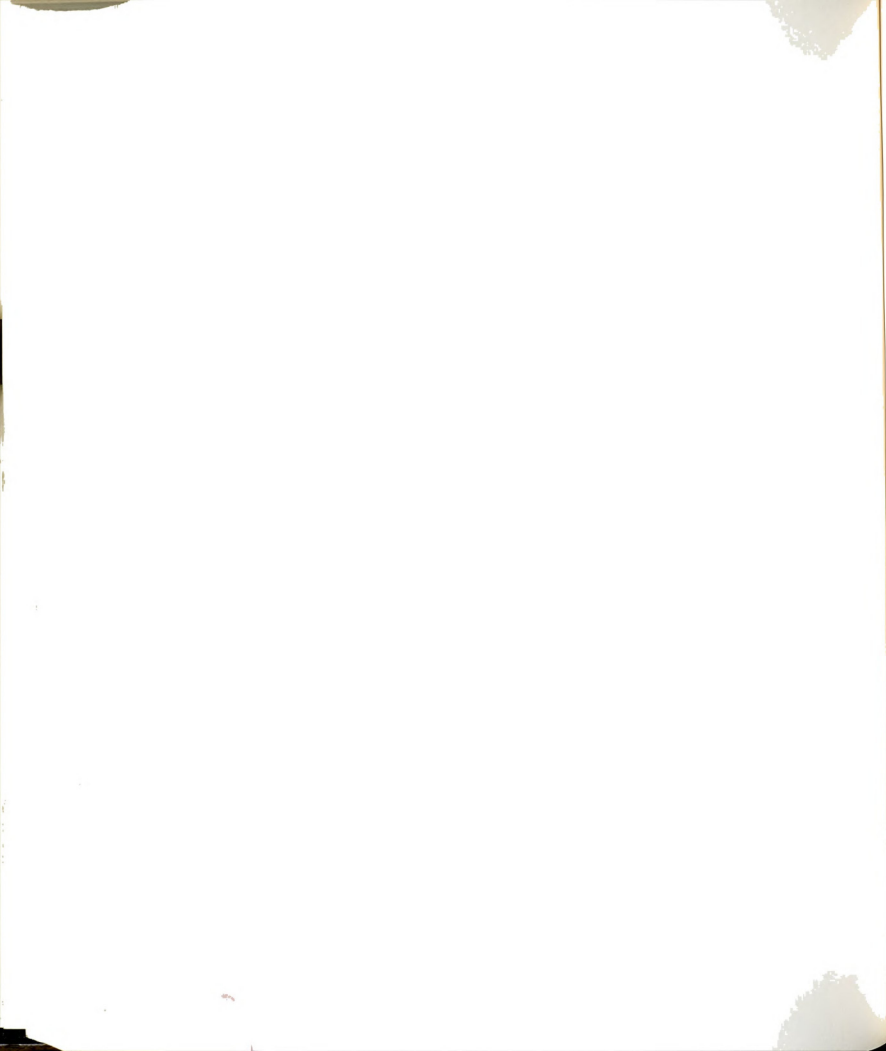
or,

$$\lambda^* = \frac{1}{(C^2+1)} [\bar{L}^* + C\bar{c}^*] \quad (152)$$

where \bar{L}^* and \bar{c}^* are the average values of L_k^* and c_k^* . Having found λ^* from equation (152), u_c^* can be found from equation (145). The residual of the fit is obtained from

$$\sigma = \sqrt{\frac{S}{(N-2)}} \quad (153)$$

where S is given by equation (148) and N is the total number of entries of c_k and L_k .

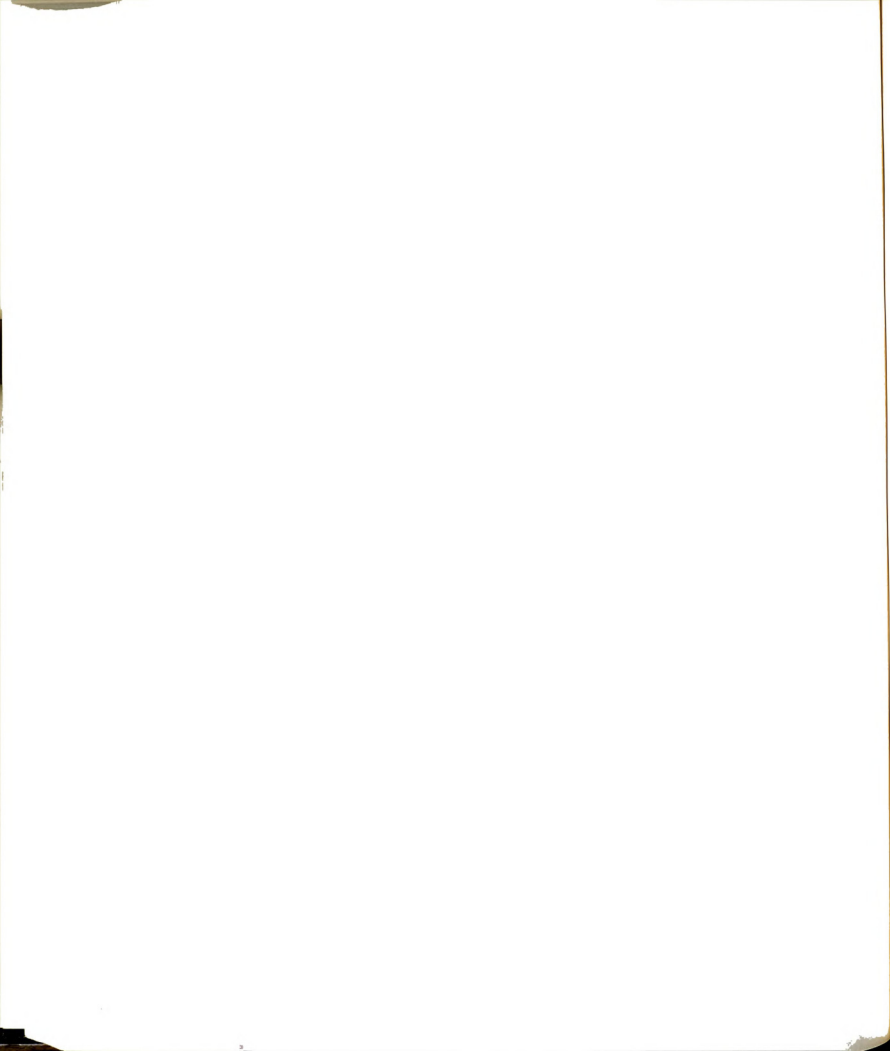


5.4 Example Calculations

In this section the processed results of one of the experimental runs are presented to demonstrate the functioning of the algorithms presented in Sections 5.3.1 and 5.3.2. The data set used here was acquired without the use of the filling device. The width of the jet was 2.63 cm and a water-sugar mixture was used as the working liquid. The Reynolds number was 980. Figure 50 presents a part of the sequence of photographic records from the start of this experiment. Section 5.4.1 presents the geometric/kinematic properties of this flow field and Section 5.4.2 presents the results of the calculations of the stability characteristics of the vortex street.

5.4.1 Geometric/Kinematic Properties

The geometric/kinematic properties of the vortices in the flow field are presented in the space-time plot shown in Figure 84. In the plot, the average location of the two vortices of a pair have been connected by straight line segments (see Section 5.3.1.1). The plot shows the distances from the exit plane at which vortices begin to form; a considerable variation is observed in these distances. For this data set, the formation of two-dimensional symmetric motions occurs over a range $0.75 \leq x/w \leq 2.0$. The plot also shows the location of vortex pairings which mostly occur beyond $x/w=3$. As shown in Figure 50, a number of vortices coalesce with the starting vortex pair. Figure 84 shows this interaction during the times $10 \leq t^* < 18$.



The plots showing the lateral spread, d_k/w , between the vortex centers and the difference in the axial location, a_k/w , have been included in with other data sets and are presented in Chapter 6.

5.4.2 Parameters of the Vortex Street

A computer program (PWIP7E) has been developed to compute the three parameters St_F , u_c , and λ at a desired plane from the exit plane of the jet. As mentioned in Section 5.3.2, two user-specified parameters, T_p and T_w , are used in the processing of the digitized photographic data. The influence of these parameters on the calculations of St_F , u_c , and λ is first presented in Section 5.4.2.1 and the discussion of the results is presented in Section 5.4.2.2. The data set which was used in Section 5.4.1 is again used in this section.

5.4.2.1 Choice of Control Parameters T_p and T_w

Five different combinations of the control parameters (T_p, T_w) have been used: (0.05,0.05), (0.05,0.1), (0.1,0.05), (0.1,0.1), and (0.1,0.2). These numbers indicate the fractions of first estimates of L/w . Table 3 and Figures 85 through 91 present the results of these computations.

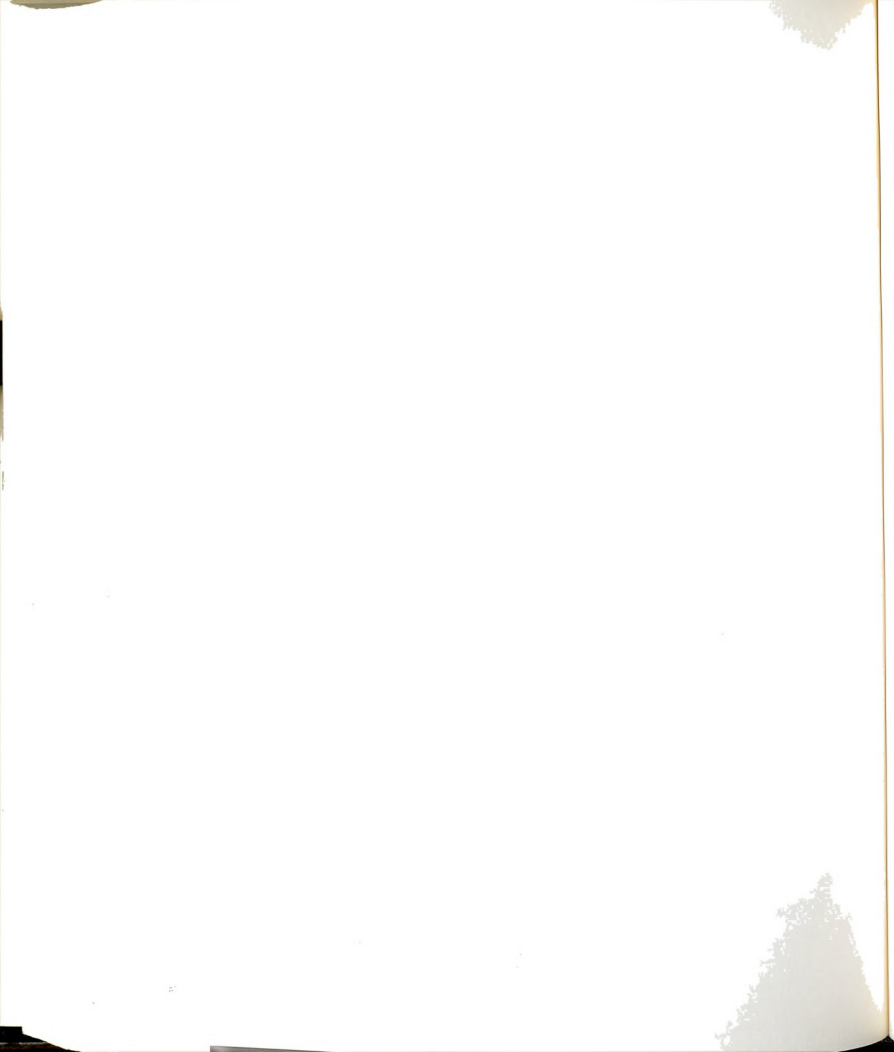


Table 3 - Influence of T_p, T_w on St_F, u_c and λ

$T_p, T_w = .05, .05$										
x/w	St_F	c^* (Av R)	L^*	L^* (Av R)	λ^*	u_c^*	σ	Pred.		
2.00	0.782	0.751 0.257	0.960	0.856 0.209	0.903	0.706	0.351	1		
2.25	0.789	0.761 0.261	0.965	0.895 0.232	0.922	0.728	0.359	1		
2.50	0.794	0.787 0.243	0.990	1.009 0.283	1.002	0.796	0.382	1		
2.75	0.797	0.817 0.270	1.025	0.984 0.269	1.000	0.797	0.390	1		
3.00	0.782	0.833 0.298	1.066	1.042 0.584	1.051	0.822	0.671	2		
3.25	0.749	0.873 0.283	1.166	1.161 0.460	1.163	0.870	0.553	3		
3.50	0.718	0.892 0.257	1.242	1.186 0.262	1.205	0.865	0.378	4		
3.75	0.724	0.880 0.273	1.216	1.183 0.385	1.202	0.870	0.484	4		
4.00	0.699	0.891 0.302	1.276	1.342 0.599	1.341	0.937	0.685	5		
4.25	0.633	0.942 0.339	1.488	1.341 0.557	1.408	0.891	0.677	7		
4.50	0.599	0.962 0.353	1.604	1.310 0.428	1.426	0.855	0.611	8		
4.75	0.581	0.972 0.408	1.673	1.283 0.417	1.451	0.843	0.709	8		
5.00	0.584	0.991 0.397	1.696	1.360 0.606	1.537	0.898	0.845	8		

$T_p, T_w = .05, .1$										
x/w	St_F	c^* (Av R)	L^*	L^* (Av R)	λ^*	u_c^*	σ	Pred.		
2.00	0.786	0.755 0.257	0.960	0.872 0.229	0.912	0.717	0.357	0		
2.25	0.789	0.754 0.258	0.956	0.926 0.231	0.937	0.740	0.354	1		
2.50	0.794	0.786 0.244	0.989	1.012 0.286	1.003	0.797	0.385	1		
2.75	0.797	0.819 0.262	1.028	1.005 0.270	1.014	0.808	0.385	1		
3.00	0.782	0.854 0.288	1.093	1.079 0.566	1.084	0.848	0.650	2		
3.25	0.749	0.870 0.285	1.163	1.153 0.455	1.157	0.866	0.550	3		
3.50	0.724	0.883 0.250	1.219	1.187 0.266	1.198	0.868	0.375	4		
3.75	0.729	0.877 0.266	1.202	1.221 0.377	1.222	0.891	0.472	4		
4.00	0.726	0.901 0.287	1.240	1.180 0.535	1.221	0.887	0.620	4		
4.25	0.661	0.947 0.341	1.433	1.265 0.466	1.340	0.886	0.602	6		
4.50	0.585	0.924 0.338	1.578	1.347 0.422	1.453	0.851	0.601	8		
4.75	0.581	0.976 0.404	1.679	1.279 0.440	1.465	0.852	0.749	8		
5.00	0.548	0.986 0.411	1.800	1.302 0.612	1.513	0.829	0.919	8		

$T_p, T_w = .10, .05$										
x/w	St_F	c^* (Av R)	L^*	L^* (Av R)	λ^*	u_c^*	σ	Pred.		
2.00	0.782	0.751 0.257	0.960	0.856 0.209	0.903	0.706	0.351	1		
2.25	0.789	0.761 0.261	0.965	0.895 0.232	0.922	0.728	0.359	1		
2.50	0.794	0.787 0.243	0.990	1.009 0.283	1.002	0.796	0.382	1		
2.75	0.765	0.812 0.274	1.061	1.020 0.248	1.035	0.792	0.379	2		
3.00	0.782	0.833 0.298	1.066	1.042 0.584	1.051	0.822	0.671	2		
3.25	0.749	0.873 0.283	1.166	1.161 0.460	1.163	0.870	0.553	3		
3.50	0.718	0.892 0.257	1.242	1.186 0.262	1.205	0.865	0.378	4		
3.75	0.661	0.884 0.276	1.337	1.254 0.356	1.288	0.851	0.466	6		
4.00	0.666	0.906 0.303	1.362	1.330 0.615	1.362	0.906	0.702	6		
4.25	0.598	0.899 0.295	1.503	1.417 0.525	1.463	0.875	0.620	8		

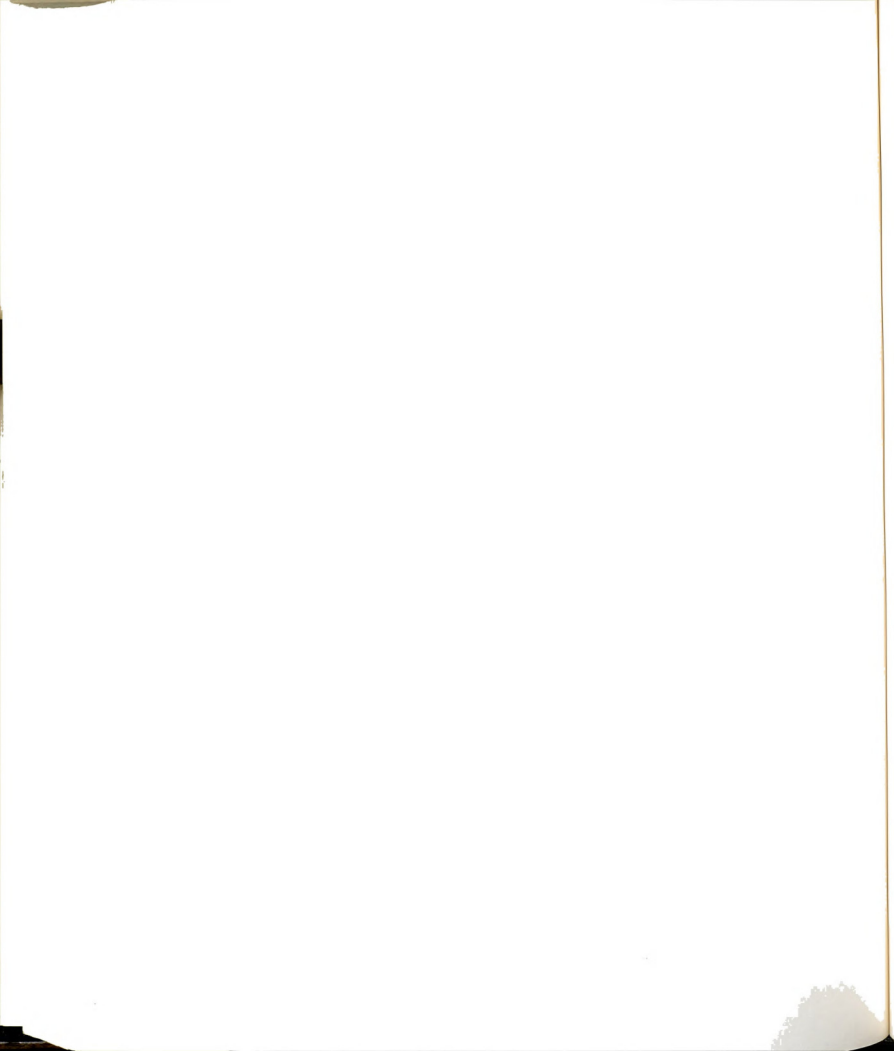


Table 3 (cont'd.).

4.50	0.599	0.962	0.353	1.604	1.310	0.428	1.426	0.855	0.611	8
4.75	0.581	0.972	0.408	1.673	1.283	0.417	1.451	0.843	0.709	8
5.00	0.548	1.003	0.408	1.832	1.479	0.504	1.662	0.910	0.788	9

$$T_p, T_w = .10, .10$$

x/w	St _F	c* (Av R)	L*	L* (Av R)	λ^*	u _c *	σ	Pred.
2.00	0.786	0.755 0.257	0.960	0.872 0.229	0.912	0.717	0.357	0
2.25	0.789	0.754 0.258	0.956	0.926 0.231	0.937	0.740	0.354	1
2.50	0.794	0.786 0.244	0.989	1.012 0.286	1.003	0.797	0.385	1
2.75	0.765	0.814 0.266	1.064	1.042 0.245	1.050	0.804	0.371	2
3.00	0.782	0.854 0.288	1.093	1.079 0.566	1.084	0.848	0.650	2
3.25	0.749	0.870 0.285	1.163	1.153 0.455	1.157	0.866	0.550	3
3.50	0.724	0.883 0.250	1.219	1.187 0.266	1.198	0.868	0.375	4
3.75	0.696	0.890 0.265	1.280	1.236 0.380	1.258	0.876	0.476	5
4.00	0.697	0.911 0.291	1.307	1.255 0.550	1.293	0.901	0.635	5
4.25	0.595	0.917 0.306	1.543	1.359 0.437	1.431	0.851	0.560	8
4.50	0.585	0.924 0.338	1.578	1.347 0.422	1.453	0.851	0.601	8
4.75	0.581	0.976 0.404	1.679	1.279 0.440	1.465	0.852	0.749	8
5.00	0.548	0.986 0.411	1.800	1.302 0.612	1.513	0.829	0.919	8

$$T_p, T_w = .10, .20$$

x/w	St _F	c* (Av R)	L*	L* (Av R)	λ^*	u _c *	σ	Pred.
2.00	0.783	0.740 0.200	0.944	0.898 0.239	0.916	0.717	0.320	0
2.25	0.785	0.764 0.245	0.972	0.953 0.264	0.960	0.754	0.368	1
2.50	0.790	0.780 0.253	0.987	1.001 0.238	0.996	0.787	0.355	1
2.75	0.816	0.804 0.241	0.986	1.016 0.433	1.004	0.819	0.507	1
3.00	0.816	0.841 0.279	1.031	1.022 0.374	1.026	0.837	0.477	1
3.25	0.757	0.847 0.246	1.120	1.158 0.381	1.144	0.866	0.466	3
3.50	0.730	0.887 0.263	1.216	1.249 0.410	1.246	0.909	0.498	4
3.75	0.696	0.901 0.271	1.294	1.203 0.447	1.253	0.872	0.536	5
4.00	0.697	0.895 0.271	1.284	1.207 0.438	1.252	0.873	0.527	5
4.25	0.595	0.928 0.319	1.561	1.389 0.412	1.471	0.875	0.550	8
4.50	0.585	0.932 0.335	1.591	1.371 0.488	1.488	0.871	0.659	8
4.75	0.586	0.952 0.362	1.624	1.314 0.634	1.477	0.866	0.835	8
5.00	0.569	1.029 0.409	1.809	1.193 0.584	1.419	0.807	0.919	8

For this data set, the first plane of observation is located at $x = 2w$. This location was decided by the program PWTP7E based upon the largest distance x^* of vortex formation; i.e., the largest distance at which a bulge, which led to a vortex motion was observed. See

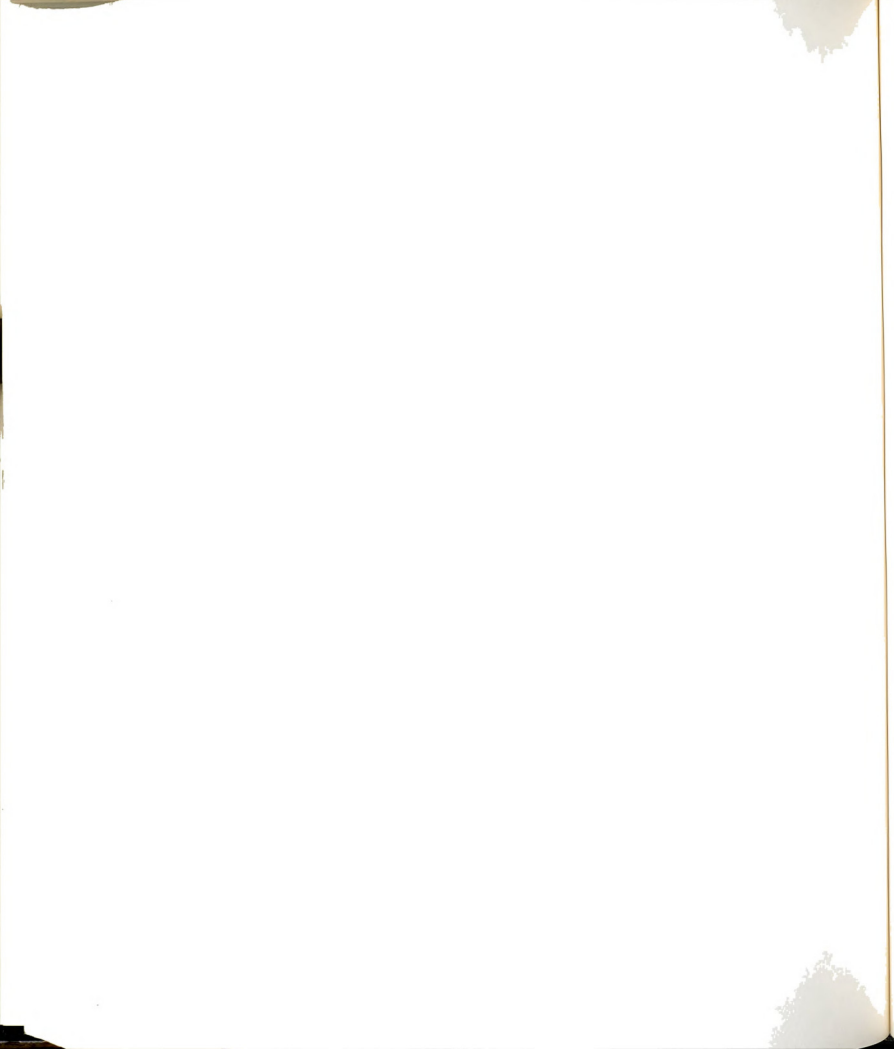


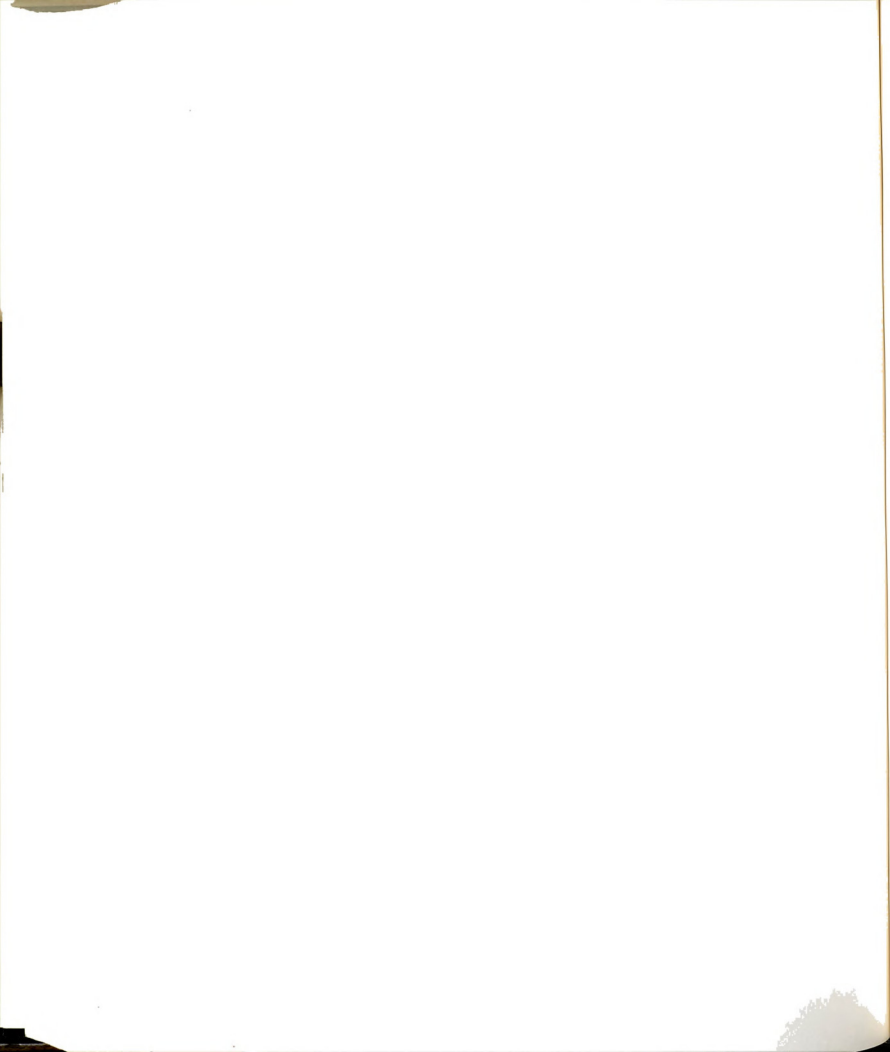
Figure 84. In this case, this distance was $x=1.92w$ and the computations began at $x=2w$. In addition to specifying (T_p, T_w) the user also specifies the size of the increments in x for computation and for reporting the results. For this case, the computations were carried out at distances $0.05w$ apart, whereas the results have been reported at increments of $0.25w$.

The results of the calculations show that, whereas some of the quantities exhibit negligible dependence on the combination of control parameters, (T_p, T_w) , others show considerable dependence. For example, the quantities which show negligible dependence are:

- i) the distribution of St_F as shown in Figure 85 and presented in column 2 of Table 3;
- ii) the distribution of mean and rms of c_k^* shown in Figure 86 and tabulated in columns 3 and 4 of the Table 3;
- iii) the distribution of $u_c^*(x)$ shown in Figure 87 and presented in column 9 of the Table 3.

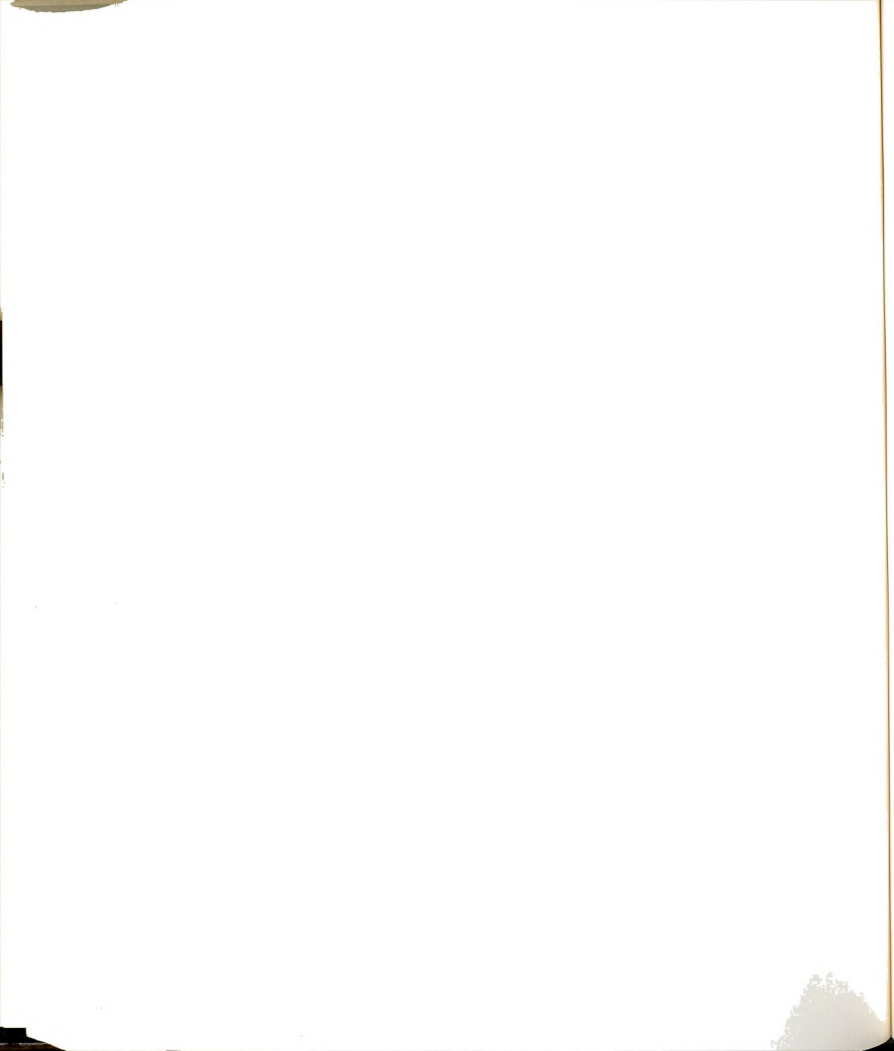
The quantities that show significant dependence on the control parameters (T_p, T_w) are:

- i) the distribution of L^* (computed from St_F and \bar{c}^*) shown in Figure 88 and presented in column 5 of the Table 3;



- ii) the distribution of mean and rms of L_k^* as shown in Figure 89 and presented in columns 6 and 7 of the Table 3;
- iii) the distribution of λ^* as shown in Figure 90 and presented in column 8 of the Table 3;
- iv) the distribution of the residual of the fit (of St_F through c_k^* and L_k^*) as shown in Figure 91 and presented in column 10 of the Table 3;
- v) the number of paired vortices at a given plane of observation as presented in the last column of Table 3.

It is to be noted that most of the scatter in the plots (Figures 89, 90, and 91) occur in the vicinity of locations where pairings take place. Based upon the observations presented above, specifically Figures 88, 90, and 91, the appropriate choice of the control parameters T_p and T_w appear to be 0.1 and 0.05 of the longitudinal vortex spacing at each x station. This choice of T_p will allow two vortices to be considered paired if their centers are located within 10% of the wavelength at the given plane of observation. The choice of $T_w = 0.05L^*$ will create a "window" around the plane of observation with a width which is 10% of the wavelength at that location. The following calculations of St_F , u_c , and λ have been executed with $T_p = 0.1L/w$ and $T_w = 0.05L/w$. The results of calculations presented in Chapter 6 are also based upon the same values of T_p and T_w .

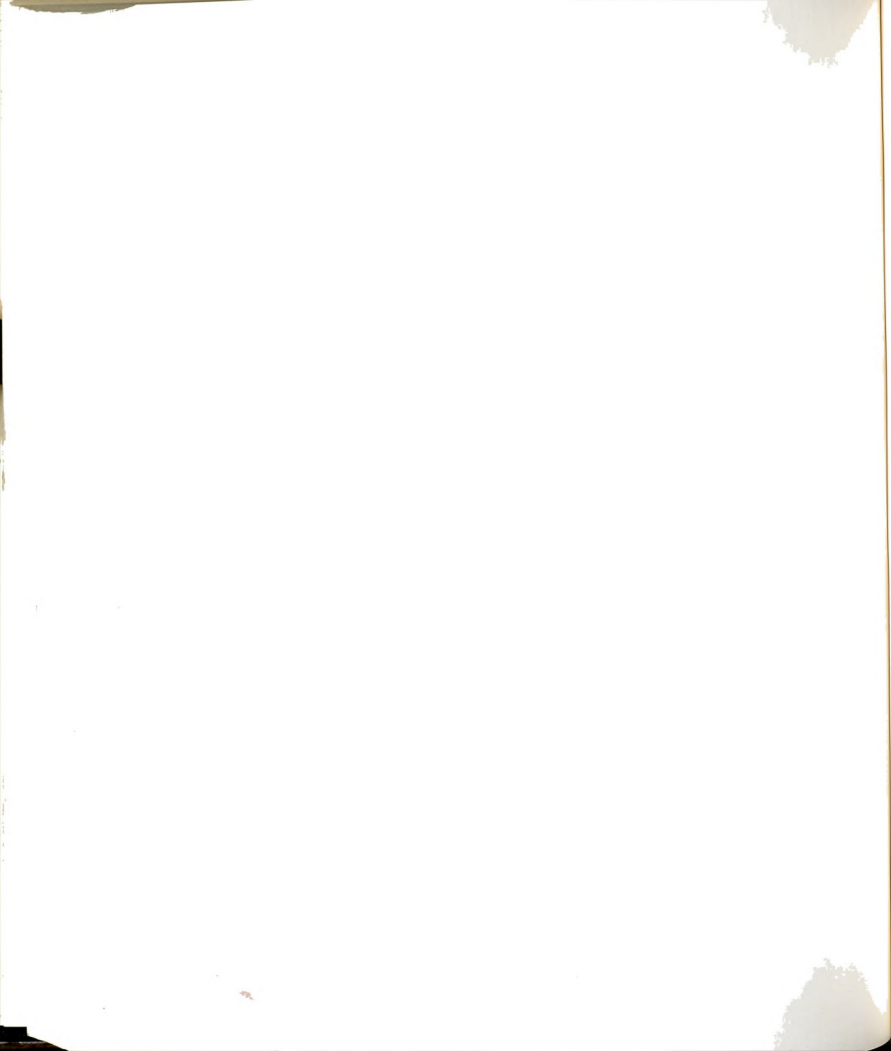


5.4.2.2 Discussion of Results

Figure 85 presents the streamwise distribution of St_F . The value of St_F remained nominally constant over $2 \leq x/w \leq 3$. Beyond $x=3w$, the value of St_F begins to decrease. The drop in St_F with increasing x^* should be in steps indicating the process of pairing at specific locations. However, because of the large step size in x and the randomness of an unexcited jet, the steps are not apparent, and Figure 85 presents a linearly decreasing $St_F(x^*)$ distribution. The value of St_F drops from approximately 0.8 at $x^*=2$ to 0.6 at $x^*=4.5$, indicating that 25% of the indicated number of vortices have paired.

Figure 92 shows the distribution of the population: $\frac{w}{\delta t_k \langle U(t) \rangle}$, around St_F at each x^* location for $T_p, T_w = 0.1, 0.05$. When two vortices are about to pair, the difference in their arrival times, δt_k , at the plane of observation becomes small, resulting in large values of $\frac{w}{\delta t_k \langle U(t) \rangle}$.

Comparison of Figures 86 and 87 (see columns 3 and 9 of the Table 3) indicates that the two estimates of convection speed, \bar{c}^* and u_c^* , exhibit a similar trend up to $x^*=4$, i.e., a linear increase in the convection speed with increasing distance from the exit plane. Beyond this location, whereas \bar{c}^* continues to increase, u_c^* begins to decrease. The latter trend is consistent with the fact that the jet speed begins to drop at the end of the potential core.

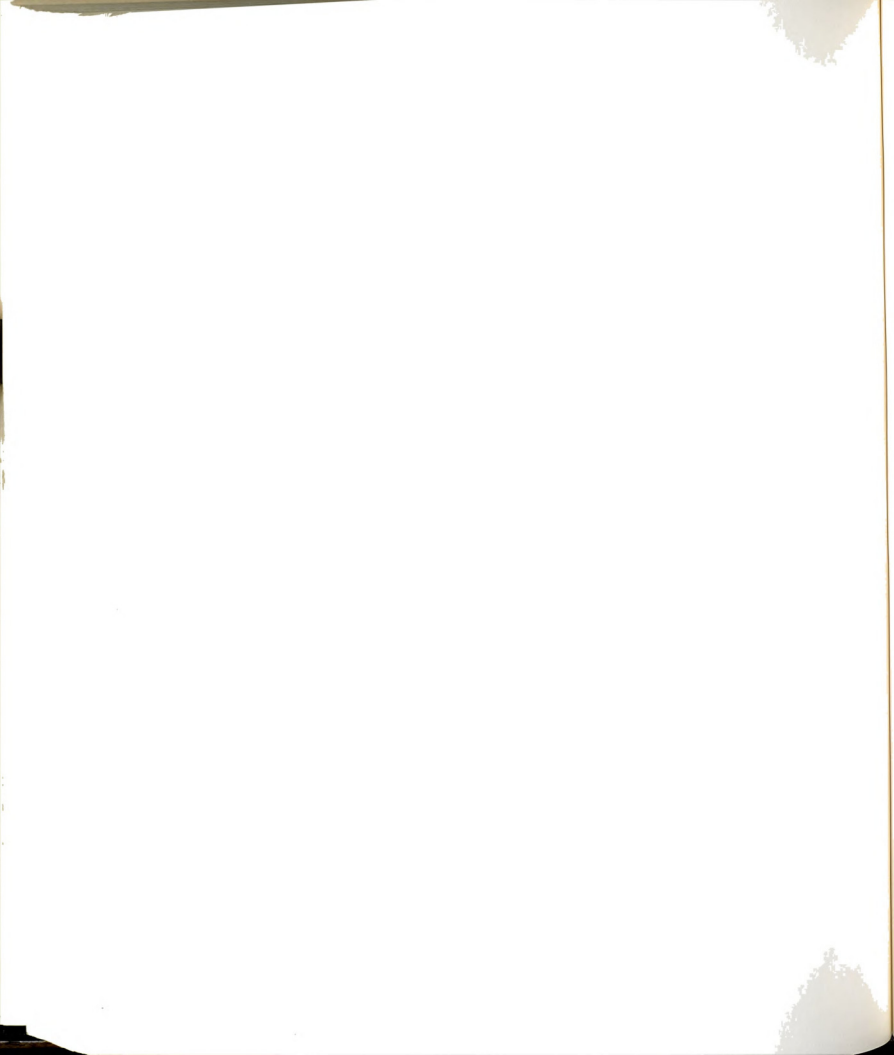


The distribution of longitudinal spacing between vortices are presented in Figures 88, 89, and 90. As shown in Figure 88, the spacing L^* , based upon St_F and \bar{c}^* , shows a nonlinear rise with x^* . However, the average of L_k^* (see Figure 89) and λ^* (see Figure 90) show a nominally linear increase in the longitudinal spacing with x^* . The last of these estimates, λ^* , is based upon the statistical model, (see Section 5.3.2.5) and it is considered to present the true behavior of the longitudinal spacing between the vortices. According to this distribution, the wavelength increases from $0.9w$ at $x^*=2$ to $1.6w$ at $x^*=5$. A linear fit through the data yields

$$\lambda^* = 0.385 + 0.240 x^* \quad (154)$$

with residual equal to 0.044 and the coefficient of determination $r=0.98$.

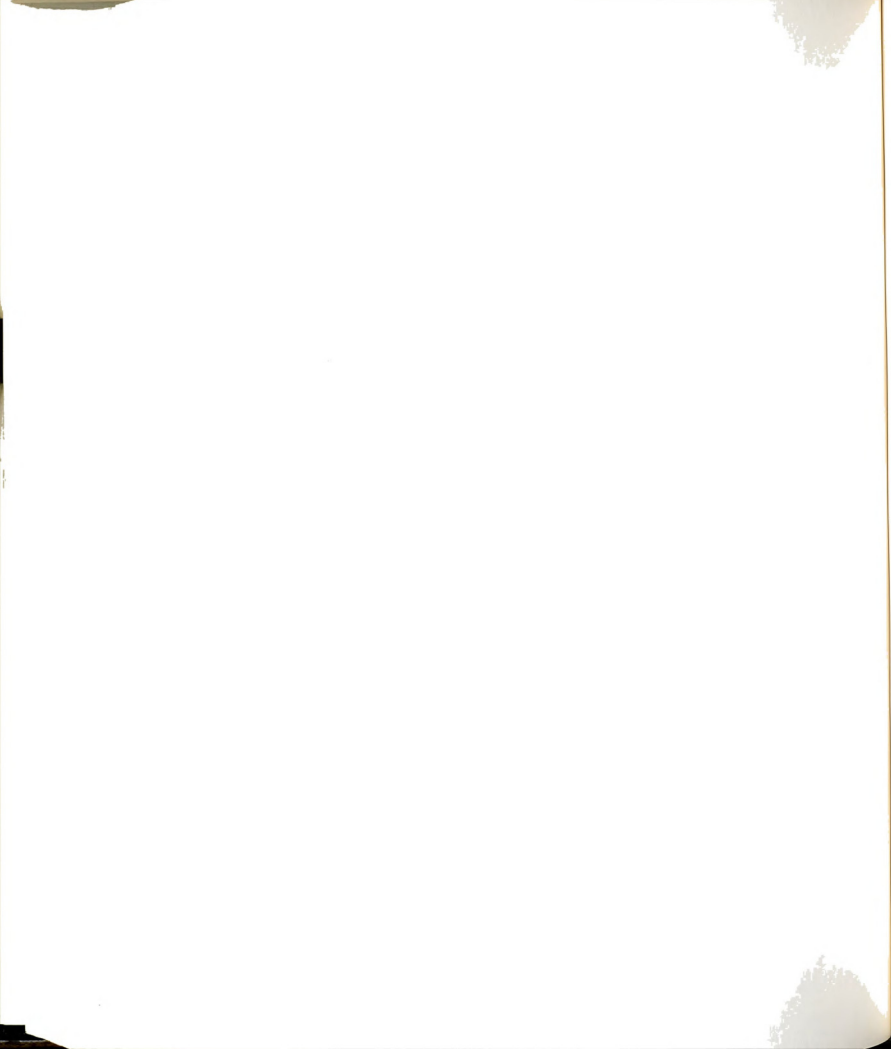
Figure 91 presents the distribution of the residual of the fit of St_F through c_k^* and L_k^* . Beyond $x^*=2.75$, there is a sharp increase in the values of the residual. This is related to two factors: (i) the occurrence of pairing at large distances from the exit plane, and (ii) decreased number of data points.



QUANTITATIVE RESULTS USING PROCESSED DIGITIZED DATA

6.1 Synopsis

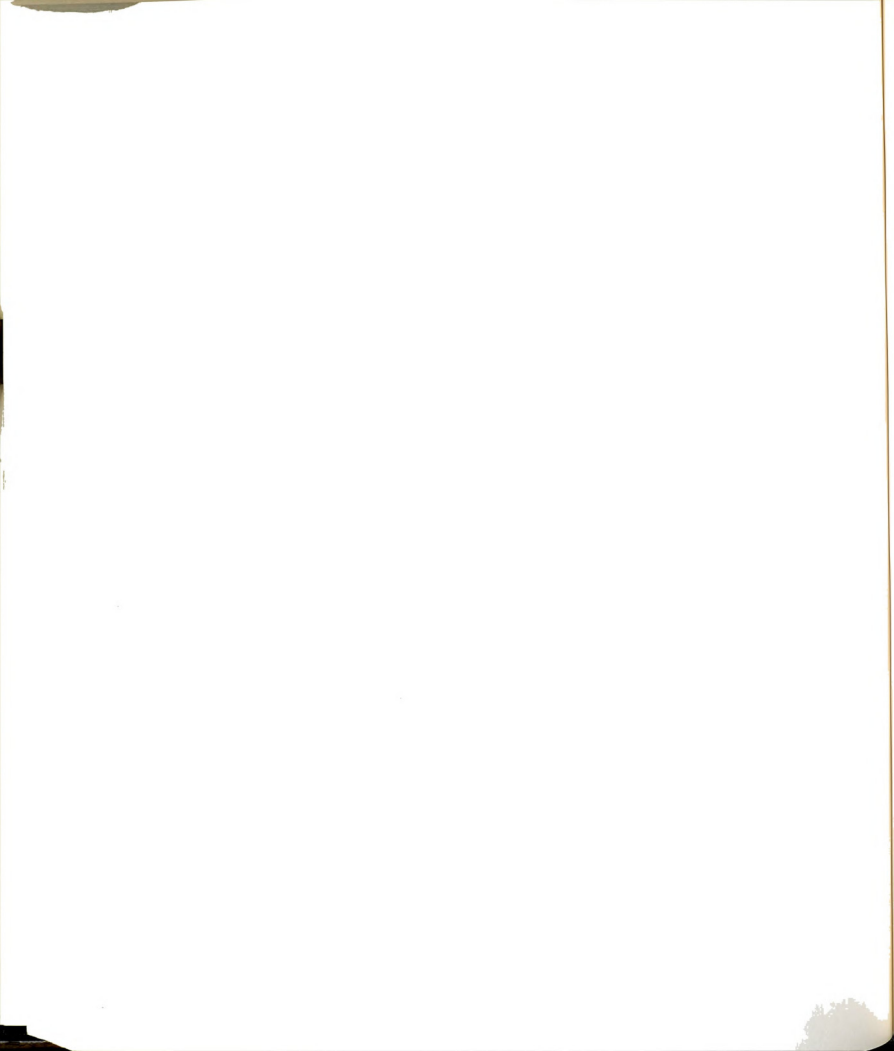
The photographic records (32 - 40 in number) from each experimental run are quite rich in information related to the stability of the slit-jet flow field. The qualitative aspects of the stability phenomena have been summarized in Chapter 4. The details of creating a database from these experiments have been described in Chapter 5 which also outlines the algorithms for further processing these data. As described in Chapter 5, two aspects of the flow field are to be investigated: i) the geometric/kinematic properties, and ii) the stability characteristics. The purpose of this chapter is to present the quantitative results extracted from the photographic database, which describe these two aspects of the flow field. These results have been grouped over small ranges of Re . Seven such groups cover the Re range $260 \leq Re \leq 3500$. For values of $Re \leq 1000$, the experiments in each group were conducted with slits of various sizes and two different



working liquids. Appendix C provides the details of experimental conditions.

The geometric/kinematic properties of the vortices in the flow field have been investigated over each range of Re by using two measures of the relative positions of the vortices of a pair. The first of these properties, the lateral spacing between the two vortices of a pair, shows that the average value of this quantity nominally remains constant with increasing x for $Re < 700$, however, for higher values of Re , the average spacing increases with x . The rms value of the lateral spacing shows a similar trend. The second of the geometric/kinematic properties, the difference in the axial positions of the two vortices of a pair, shows that the average value of the difference, for $Re < 700$, nominally remains zero over the range $x/w = 6$. At the higher values of Re some x dependence has been observed for $x/w > 3$.

The three interrelated instability characteristics St_F , u_c^* and λ^* of the slit-jet flow field have also been computed over small ranges of Re . Whereas, the streamwise distribution of u_c^* shows a good collapse of the data over each range of Re , the distributions of St_F and λ^* exhibit considerable scatter. Either there is some unknown parameter which is responsible for this scatter or as described by FK, "the physical process that controls the spacing of the vortex motions is not rigidly determined by the kinematic scales U_0 and w , although this

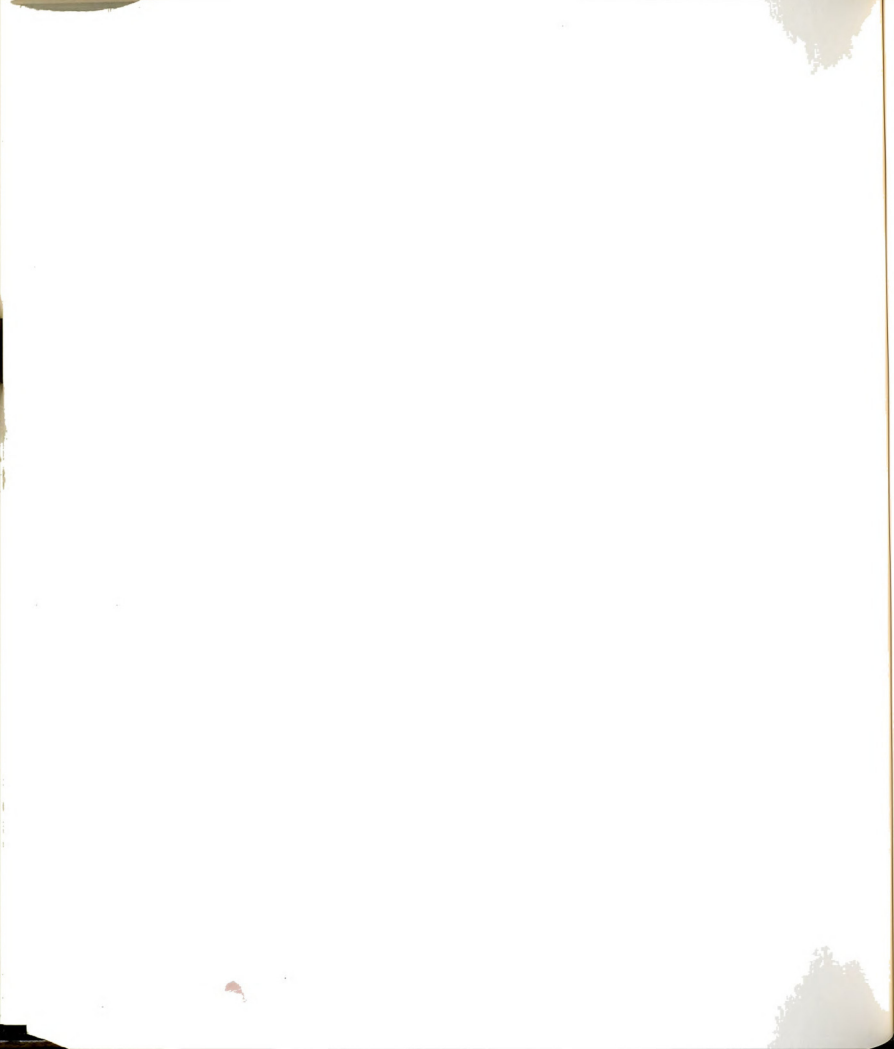


spacing is well-defined for a given experiment, as shown by figure 4" (of their paper).

This chapter has been divided into three additional sections: Section 6.2 presents the details of the geometric/kinematic properties of the flow field, Section 6.3 deals with the instability characteristics, and Section 6.4 presents the conclusions.

6.2 Geometric/Kinematic Properties of the Jet Flow Fields

Three quantities have been evaluated from the photographic database to describe the geometric/kinematic characteristics of the jet flow fields. These quantities are based upon the identification of a distinctive pair of features in the dye streaks that mark the two sides of the jet. The following items (i - iii) identify the specific data processing that was based upon the digitized records of these features: i) space (x) - time plots where x is the average streamwise position of the center of the symmetric features, ii) the lateral spacing between the centers of the vortices of a given pair, and iii) the difference in the axial locations between the centers of the vortices of a given pair.

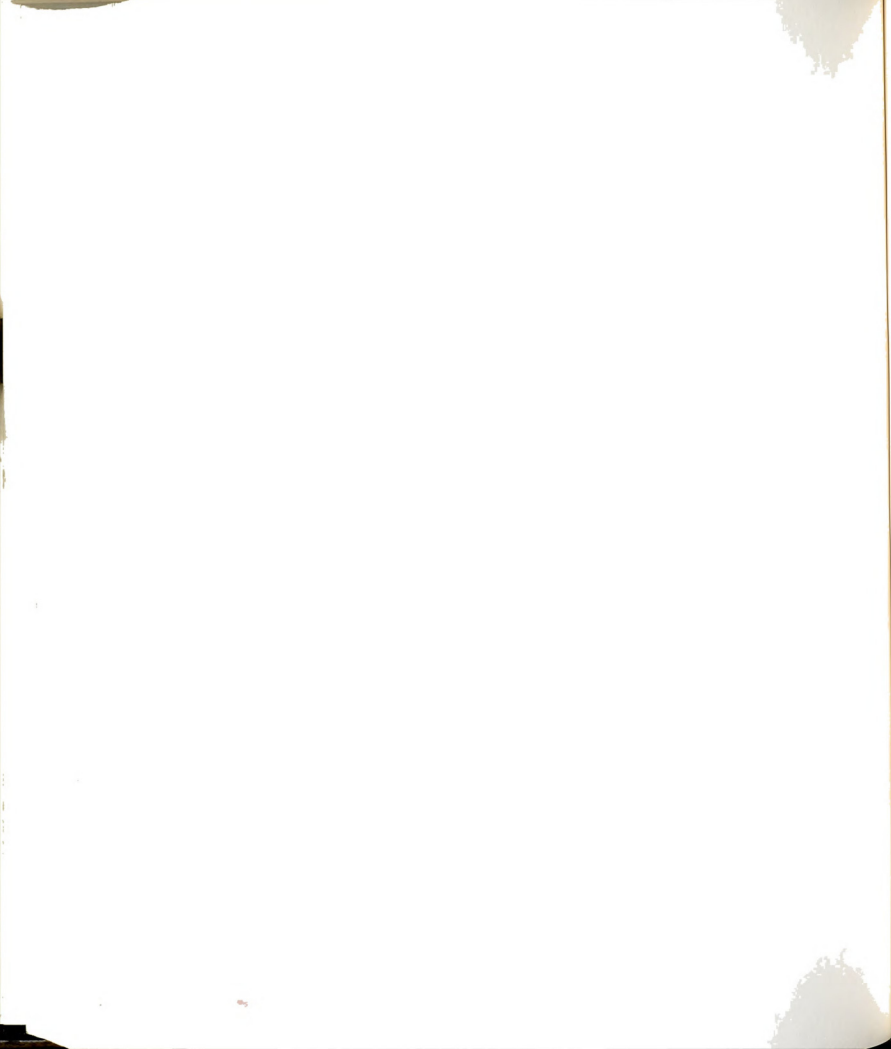


6.2.1 Space-Time (x^* , t^*) Plots of Vortices

Figures 93 through 97 are representative space-time plots of vortices at five different values of Re over the range 260-3500. The balance of the space-time data plots are presented in Appendix C including a tabular description of the conditions under which the experiments were conducted.

The space-time plots present the general behavior of the vortex pairs. Observations made from the plots are:

- i) The nondimensional distance downstream of the exit plane and the times at which symmetric motions first appear on the jet boundary can be observed. In some cases there appears to be considerable variation in the distance from the exit plane at which the distinctive features (i.e., the bulges) first appear; see Figure 95 and Figure 97. In other cases, there is little variation and most bulges form within $x/w = 1$. See Figures Figure 93, Figure 94 and Figure 96.
- ii) Interactions among the symmetrically placed motions can be observed. In the case of pairings between two vortex pairs, the upstream pair accelerates and overtakes the downstream pair. In some cases, however, the upstream pair passes by the downstream without pairing on the first interaction. In these cases, the pairing event is subsequently observed. This is shown by the crossing of trajectories of the inter-



acting vortices in the space-time plot as shown in Figure 94 and Figure 95.

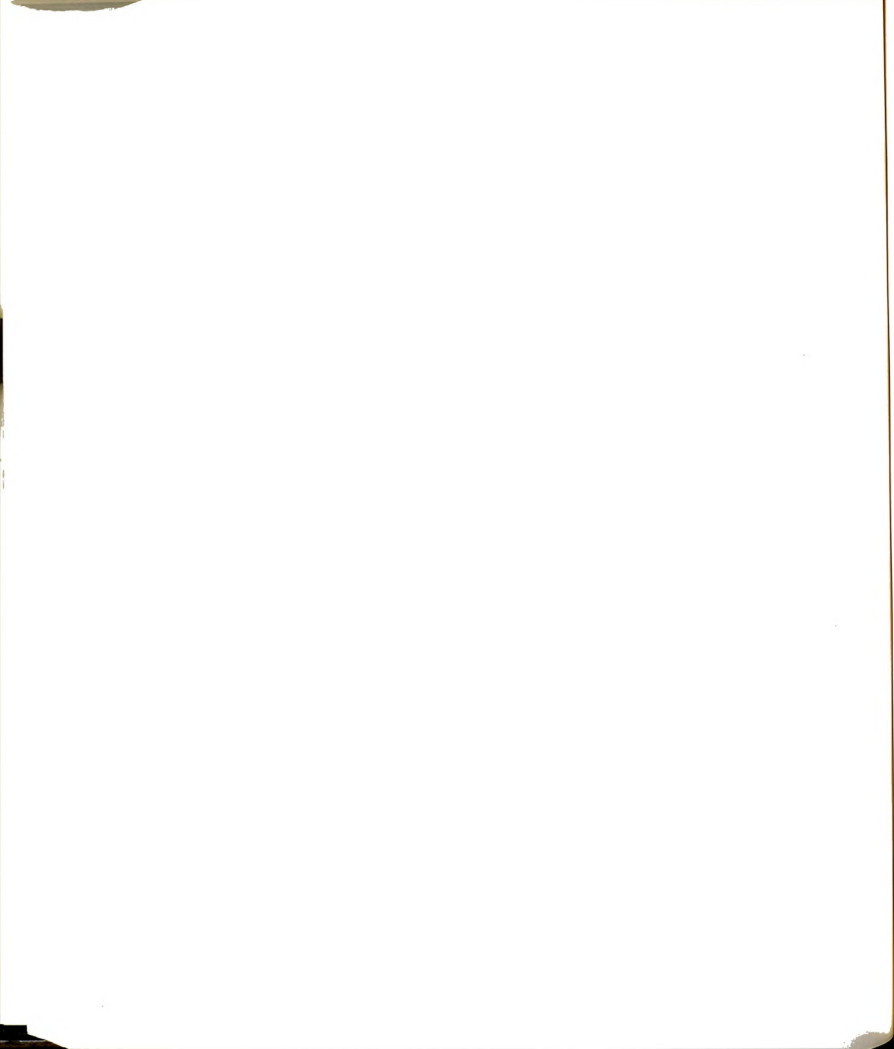
iii) Figure 97 at $Re = 3401$, exhibits five sequential pairings between vortex pairs at $t^* = 15$. Figure 73 and Figure 74 present the flow visualization pictures of the event.

iv) The space-time plots show that the convection speed of most of the vortices increase with the downstream distance.

6.2.2 Lateral Spacing Between Vortices of Individual Pairs

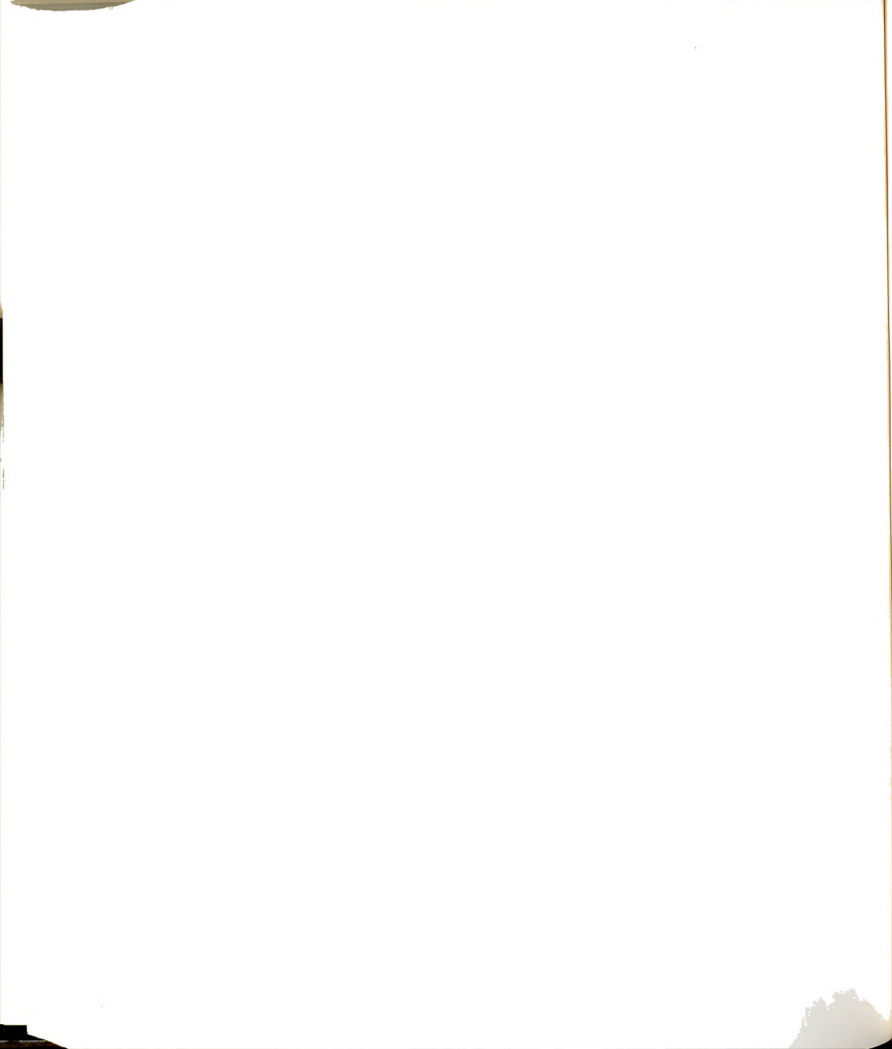
Plots of lateral spacing, d_k/w , of the k th vortex pair as a function of its streamwise location, x_k/w , have been prepared by using the algorithm described in Section 5.3.1.2. Figures 98 through 104 present the plots of lateral spacing for various ranges of Re . The average and the rms values of the lateral spacings at selective x^* have also been plotted in these figures. These statistics were collected in "windows" which were defined around each of these locations with a width which was 10 % of the respective x^* location.

The scatter in the plots of lateral spacing, for $Re > 300$ and $x^* > 3$, is caused by the motion of the vortices of a pair towards each other or away from one another. This happens especially when the two vortices are about to undergo pairing as shown in Figure 70. In this figure, as the vortex pair number 14 approaches the pair number 13, the two vortices of the former pair move closer to one another and



that of the latter move away. However, in general, the average spacing between the vortices increases with increasing distance from the exit plane. The rms of the spacing also increases with the downstream distance.

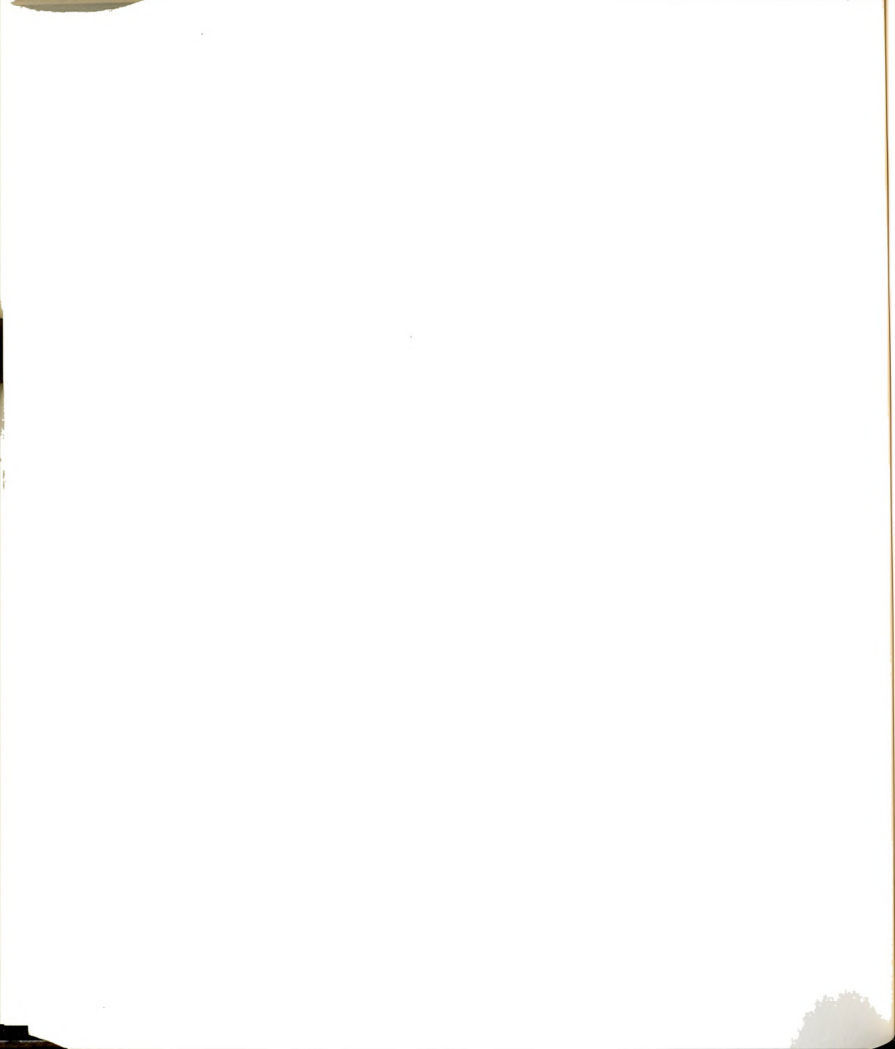
From the plots presented in Figures 98 through 104 it is not clear whether the lateral spacing, $d^*(x^*, Re)$, of a given vortex pair over $0.5 \leq x/w < 6$ exhibits small or large variations about its mean value of spacing. In order to assess this variation, the measured $d_k^*(x/w)$ values of the k th vortex pair were fit by a second order polynomial using the ordinary least squares technique. These values are designated by \hat{d}_k^* . The sum of the squares of the residuals between the measured (d_k^*) and the fitted (\hat{d}_k^*) values was determined at each of the x^* locations where the mean and the rms of lateral spacing were computed (Figures 98 through 104). Figures 105 through 111 present at each of the x^* locations the ratio of the residual of the fitted data and the rms of the population. These plots also include the values of rms of the lateral spacing at these locations. From the plots, for $Re > 300$, it is observed that in the near-field of the jets ($x/w \leq 2$) the residual of the fits is of the same order of magnitude as the rms of the population in the vicinity of the respective x/w locations. However, for $x/w > 2$, the residual of the fits is about 60% of the rms of the population and in some cases the ratio keeps decreasing with increasing x/w . This indicates that beyond $x/w > 2$, $d_k^*(x/w)$ exhibits small variations about their respective mean values. In other words,



the vortex pairs nominally maintain their lateral spacing as they convect downstream.

6.2.3 Difference in Axial Locations of the Vortices of a Pair

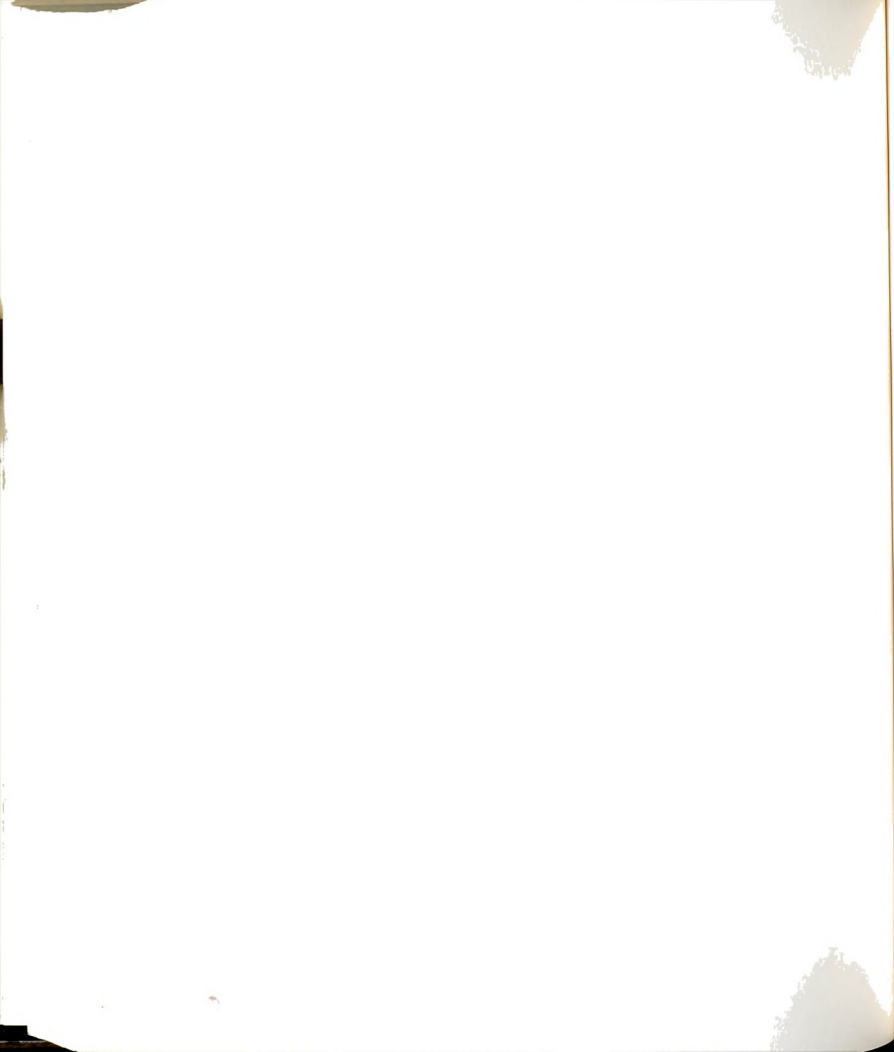
The vortex street of the slit-jet flow field has been observed to be symmetric i.e., the two vortices of a pair, at a given time, are nominally at the same distance from the exit plane of the jet. The photographic records of the flow visualization experiments presented in Chapter 4 show that the growth, translation and interaction of the two-dimensional vortex motions are not always symmetric in nature. The estimate of the presence of asymmetry, a_k/w , in the k th vortex pair has been computed by using the algorithm presented in Section 5.3.1.3 and the photographic database. The results are presented in Figures 112 through 118 for each of seven Re ranges. The means and the standard deviations of the population shown in Figures 112 through 118, at selective x^* locations have been computed as described in Section 6.2.2. The plots show that for $Re \leq 700$, the average value of a_k^* nominally remains zero. At higher values of Re some asymmetry is observed for $x/w > 3$; see Figures 115 and 117. Figure 116 shows an unusually large value of a_k^* of 0.05 over the entire range $0.5 \leq x/w < 6$. However, at the largest Re values (≈ 3000) as shown in Figure 118, the average value of a_k^* remains zero over the observed x domain. The rms value of a_k^* remains small in the near-field and then increases as x/w increases. In general, the rms value of a_k^* remains within 0.25.



The difference in the axial locations of a given vortex pair, as a function of x^* , were also fit by a second order polynomial to compare the residual of the fit with the rms of the population at each of the selective x^* locations. The results are presented in Figures 119 through 125 for various ranges of Re . Except for the case over the Re range 1257-1272 (Figure 123), it is observed that for $x/w > 3$, the residual of the fit decreases to approximately 50% of the rms of the population. This indicates that for $x/w > 3$, the differences in the axial spacings exhibit relatively small variations about their mean values.

From the geometric/kinematic properties of the slit-jet flow fields it is concluded that:

- i) The average lateral spacing between the vortices of a pair, over a given small range of Re , increases with increasing downstream distance. Also, at a given x/w location, the average spacing increases with increasing Re value.
- ii) The jet with higher values of Re exhibits some asymmetry in the location of the two vortices of a pair for $x/w > 2.5$.
- iii) The large scatter in the plots of lateral spacing (Figures 99 through 104) and the asymmetry (Figures 112 through 118) is not caused by a large scatter in the distribution of these quantities about their mean values; but, rather by a



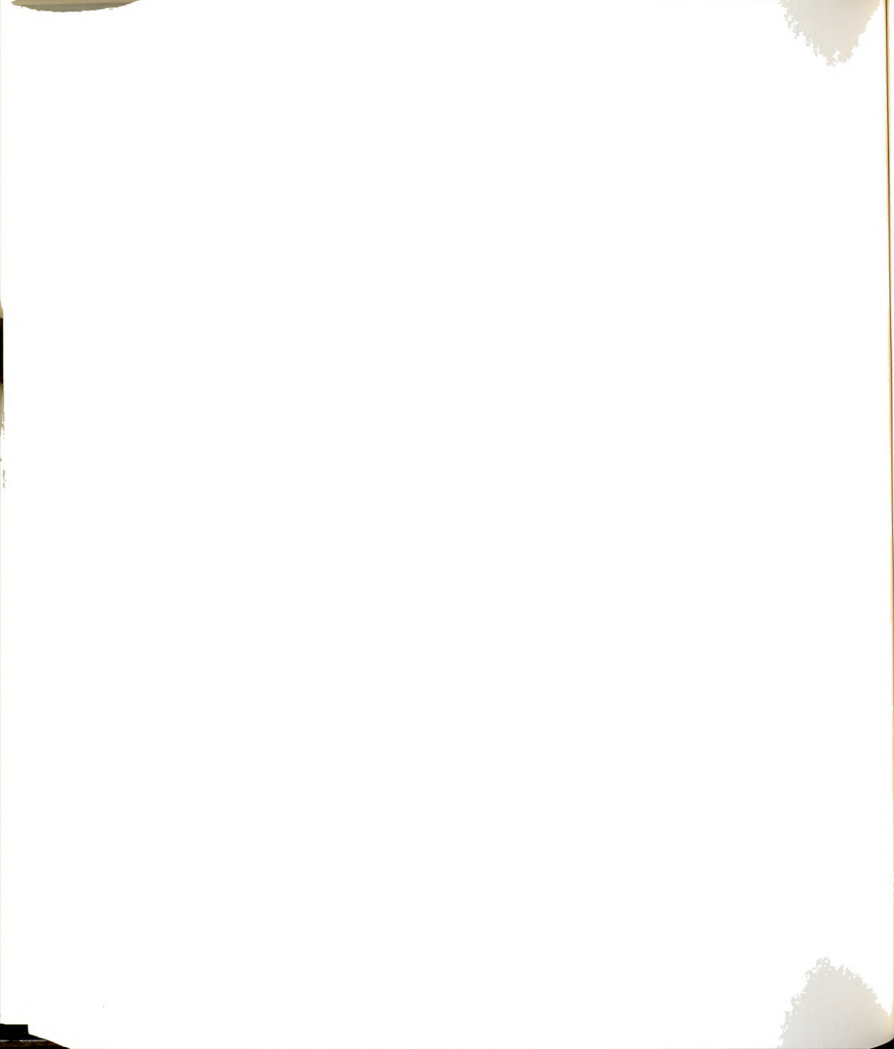
large scatter in the distribution of mean values of each vortex pair.

6.3 Stability Characteristics of the Slit-Jet Flow field

The three interrelated stability characteristics: Strouhal number (St_F), the convection velocity (u_c^*) and the wavelength (λ^*), have been computed from the photographic database by using the algorithms presented in Section 5.3.2. Results have been compiled over small ranges of Re for jets of all sizes. A comparison of the estimates of Strouhal number based upon the flow visualization data (St_F) and the measured LDA velocity data (St_V) will be presented in Chapter 7.

6.3.1 Distribution of Strouhal No. $St_F(x^*)$

Figures 126 through 133 present the distribution of Strouhal number in eight different ranges of Re . Figures 126, 127, 129 and 130 show results from jets of various widths. An observation of these plots shows that there is considerable variation in St_F values for jets of various sizes. For example in Figure 126 the smallest value of $St_F \approx 0.39$ for $w = 1.51$ cm, and, the largest value of $St_F \approx 1$ for $w = 2.63$ cm. A similar trend is observed in other plots as well. Figures 128, 131, 132 and 133 present $St_F(x^*)$ results from one size jet only. The plots show considerably less variation in St_F and indicate the reproducibility of the experimental results.



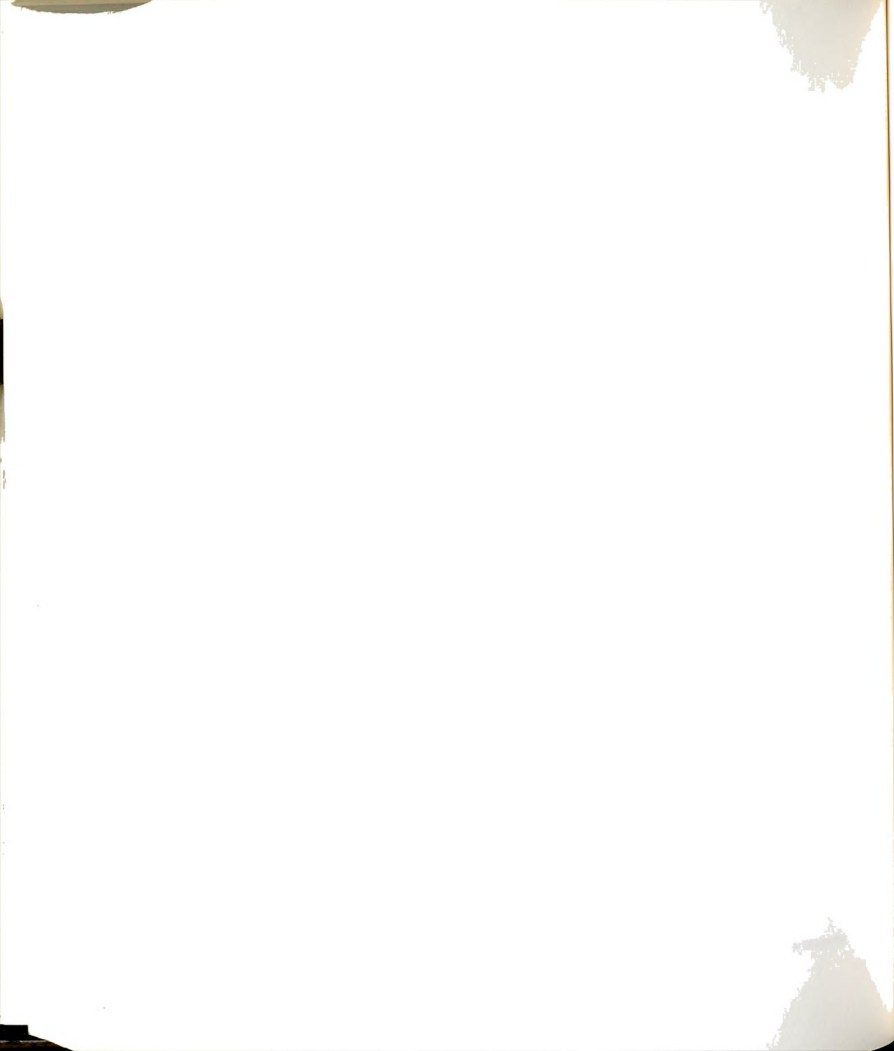
Several reasons are possible for the observed variation of $St_F(x^*)$. The possibilities include:

- i) presence of geometry dependent effects, like the influence of finite aspect ratio B/w , finite nondimensional width H/w of the channel-like plenum, finite nondimensional height h/w of the nozzle plate above the floor, and the nondimensional thickness t_N/w of the nozzle plates;
- ii) presence of a source of disturbance, like the frequency of the stepper motor which was used to drive the bleed valve;
- iii) presence of disturbances associated with the filling process;
- iv) vibration of the nozzle housing (NH) at its natural frequency.

6.3.1.1 Examination of the Possible Sources of variation in $St_F(x^*)$

In this section the possibility of the existence of each of the above mentioned sources of disturbance will be examined.

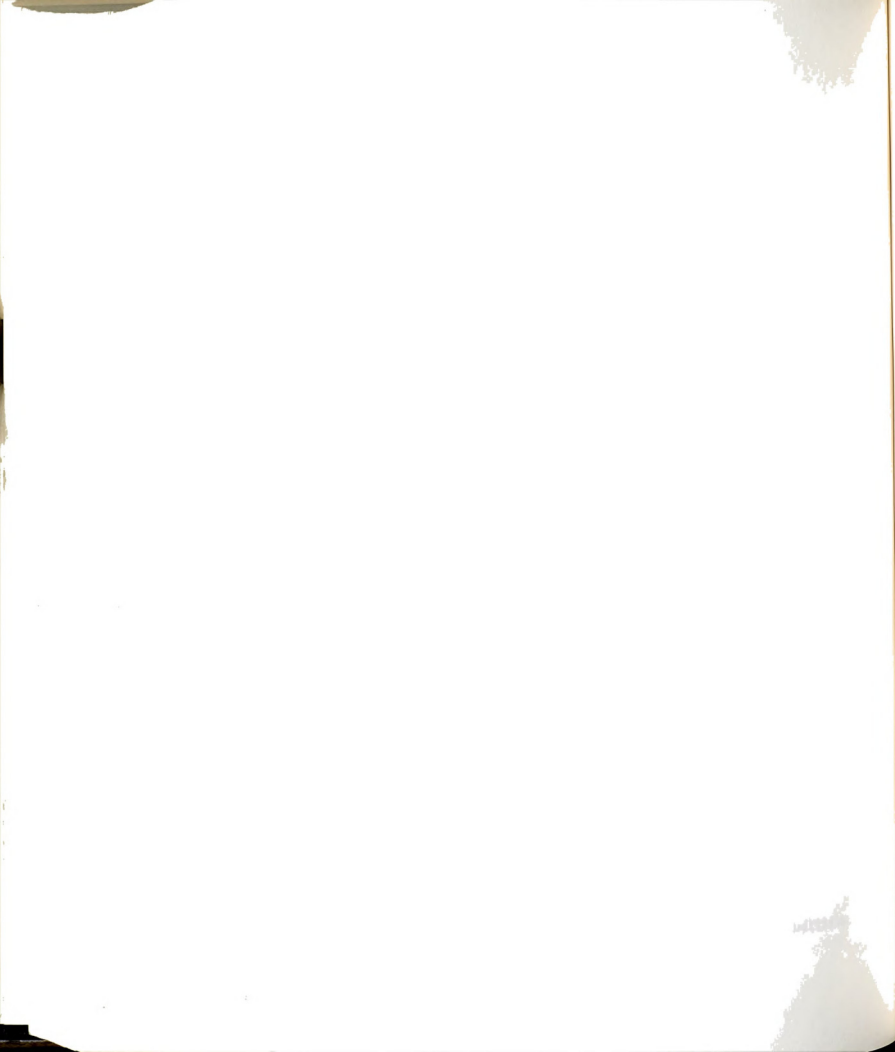
i) Variations in the four geometrical parameters, B/w , H/w , h/w , and t_N/w were produced as a result of variations in w . No attempts were made to change the parameters independently. Given this condition, only the influence of B/w on St_F will be analyzed. Figure 134 presents the variation of St_F as a function of Re with B/w as a



parameter. The values of St_F presented here relate to the rate of formation of bulges. This information is considered to be of primary interest given the focus of this study, i.e., to investigate the instability phenomena in the slit-jet flow field. Again, as noted before, for similar values of Re large scatter is observed not only for different values of B/w , but, also for the same values of B/w ; no systematic variation with B/w is, however, discerned. In addition, the plots of lateral spacing between the two vortices of a given pair (Figures 98 through 104) do not indicate the presence of geometry dependent effects. Note that the ranges of B/w and H/w in the present investigation are considerably larger than the corresponding ranges of the parameters in the BW experiments.

Sato (1960) showed that the Strouhal number based upon the exit momentum thickness and the maximum jet exit velocity was nominally independent of Re_θ . However, the use of θ_0 and U_0 to nondimensionalize the frequency of formation of bulges in the present investigation did not reduce the amount of scatter. Figure 135 shows the distribution of $St_\theta = f_F \theta_0 / U_0$ as a function of Re . (Note that θ_0 was estimated by using the Thwaites method as described in Chapter 2.) Again, no systematic influence of B/w is apparent.

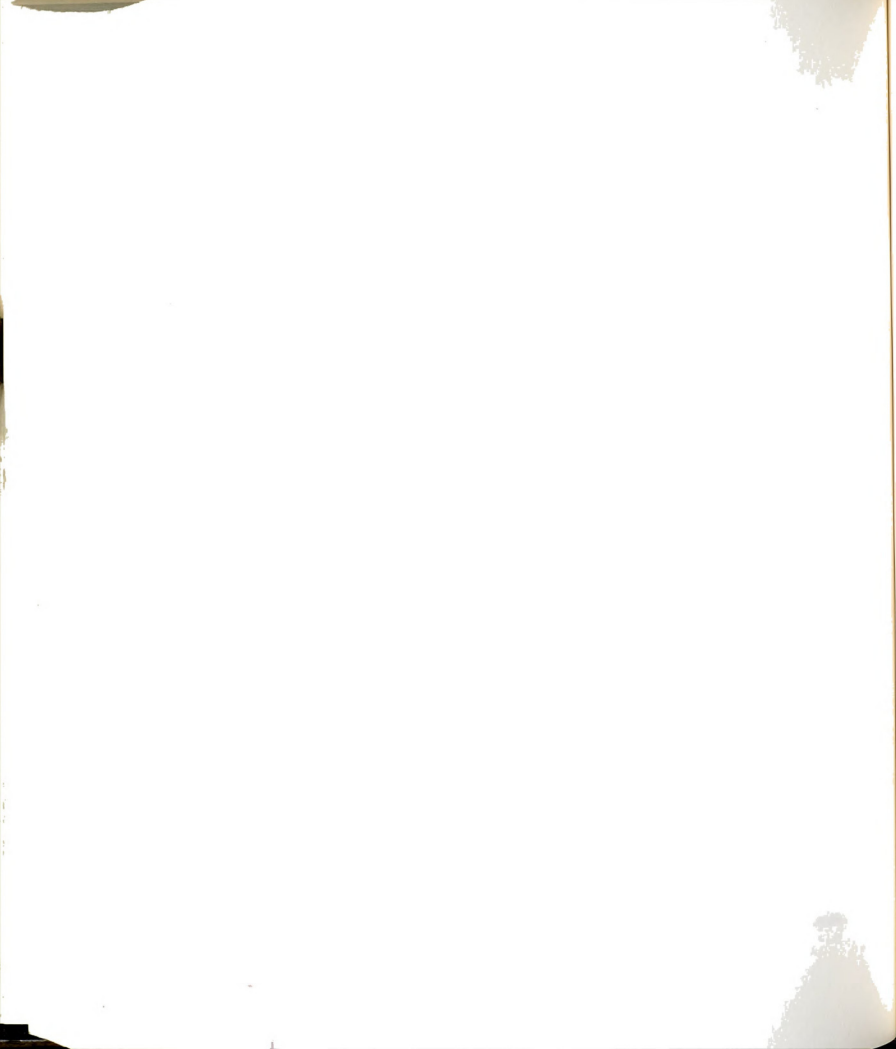
Figures 136 and 137 present the plots of St_F at two x/w locations as a function of Re with B/w as a parameter. These plots show a considerable decrease in the variation in St_F values as compared to the distribution shown in Figure 134. Figure 138 presents the



distribution of St_F as a function of Re with B/w as a parameter as reported by BW. Even though the scatter in Figure 138 is quite small, it is not clear whether or not this plot can be compared with Figures 136 and 137 of the present investigation. Their method of acquiring the data (passage frequency of vortices and velocity of jet) was quite different from the method used in this investigation. BW reported that the passage frequency of vortex motions was determined by counting the vortices at some location downstream of the exit of the jet. It is not clear whether one single x/w location was used for counting or different x/w locations were used for different size jets. It is inferred from the text that the latter was true. Further, it is also inferred that only those motions were counted which had, in the present nomenclature "rolled up". The present investigation reveals that not all the bulges develop into fully formed vortex pairs. In other words, the counting based upon bulges will result in a higher frequency than the counting based upon the "rolled up" motions.

ii) The stepper motor is not considered as a possible source of disturbance because the speed of the motor varied considerably from the start of the experiment to the end. For example, at $Re=1000$, for $w=2.57$ cm and water as the working fluid, the speed of the motor at the start of the experiment was ≈ 0.02 rev/sec and at the time the data were acquired the stepper motor ran at 0.05 rev/sec. By the end of run (long after the data were acquired) the speed increased to over 2 rev/sec.

iii) Regarding the disturbances associated with the filling process it will be shown in Chapter 7, based upon a series of experiments



using laser Doppler anemometry, that no influence of the filling process exists in three different measures of the flow field.

iv) No tests were conducted to check the resonance of the NH at its natural frequency.

6.3.1.2 Conclusion

Based upon the discussion of the previous section, the following possibilities could exist:

- i) The NH may have vibrated at its natural frequency with the liquid in the system responding to the vibration. This may have resulted in a modification of the growth process of the most unstable disturbance.
- ii) The process of formation and growth process of vortex motions is not a well regulated process (see the comments by FK regarding the variations in the results from one run to the other), specifically at low values of Re (≤ 1000).
- iii) There exists an unknown parameter which influences the instability process.

Regarding the influence of Re , it is observed that for values of $Re > 1000$, the values of St_F related to the formation of bulges (Figure 134) in the jet with $B/w = 10.7$, show considerable scatter but little dependence on Re . The mean and the rms values of St_F are found to be

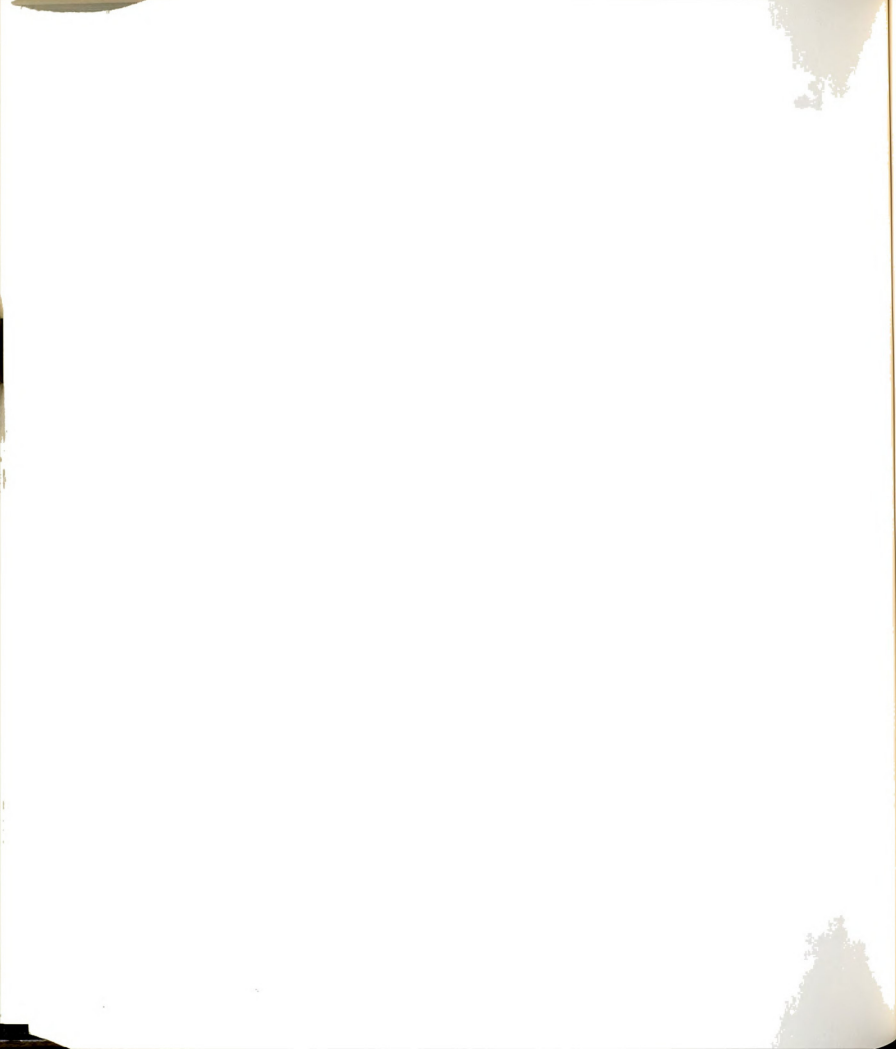


1.64 and 0.22, respectively. At $x/w=2.2$ (Figure 136) the mean value of St_F reduces to 0.98 with rms equal to 0.18. These values will be compared in Chapter 7 with the values of Strouhal number St_v determined from the measured velocity data in the jets with $B/w=10.7$ and 21.7.

6.3.2 Convection Velocities u_c^* of the Vortex Motions

The nondimensional convection velocity, $u_c(x/w)/\langle U \rangle$, of the vortices in the slit-jet flow field have been computed from the photographic database using the algorithms presented in Sections 5.3.2.2 and 5.3.2.5. Figures 139 through 146 present the streamwise variation of u_c^* . These data are organised in the same Reynolds number groupings as were used to present the streamwise variation of St_F . Compared with the strong dependence of $St_F(x^*)$ on the width of the jet, the $u_c^*(x^*)$ data exhibit negligible dependence on w . Although the scatter in the data is sufficiently large that a definitive interpretation cannot be inferred, it appears that $u_c^*(x^*)$ exhibits a weak dependence on Reynolds number.

The plots of distribution of $u_c^*(x^*)$ show that the vortex motions in the form of bulges begin to convect with speeds of the order of $0.6\langle U \rangle$ and accelerate before achieving a constant speed. The magnitude of the acceleration appears to depend upon the Re value and the distance of the vortices from the exit plane. The convection speed tends to level off around $x/w = 3$. The scatter in the data at larger



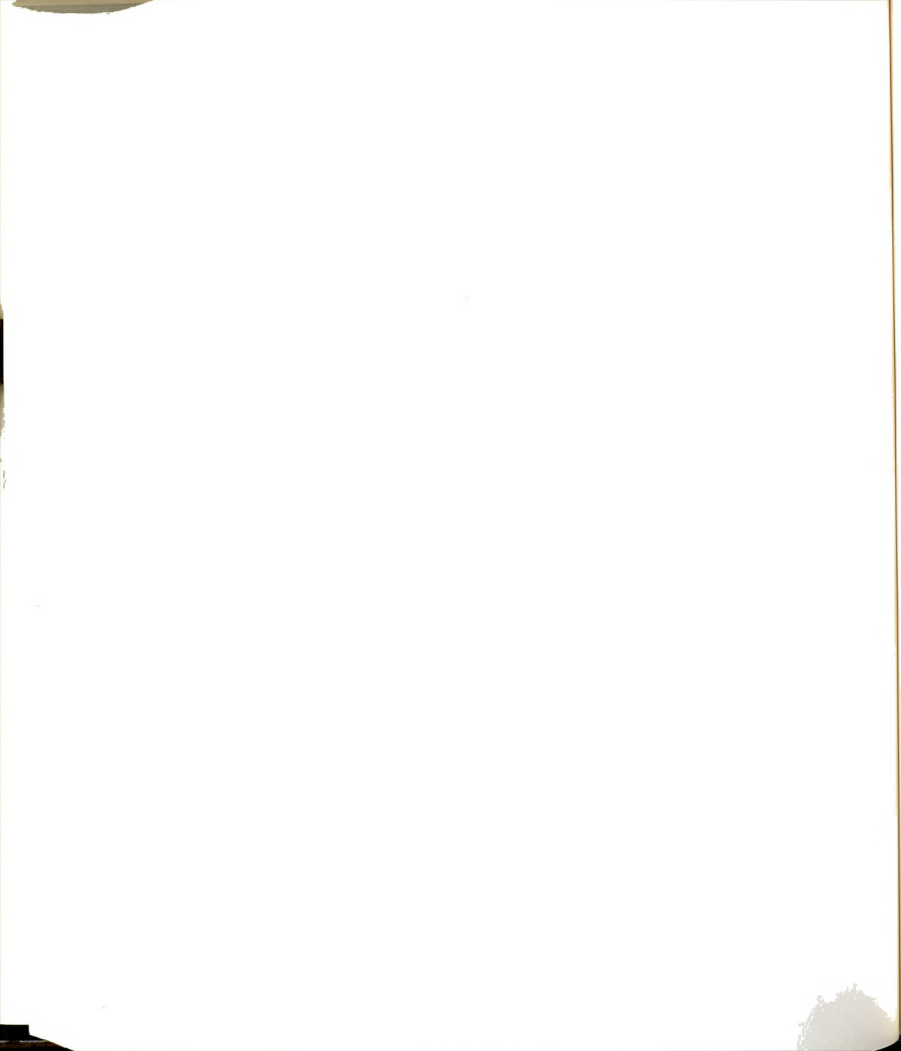
x locations ($> 3w$) prevents a definitive conclusion to be drawn; however, in some cases the vortices exhibit a decelerating trend.

FK reported $u_c/U_0 \approx 0.51$ in the Re range 847-1168 and $w = 1.6$ cm. This result was computed from the measurements over $1 \leq x/w \leq 2$. Using $C_D = 0.705$ (this estimate is based upon the results of the present investigation), their result becomes $u_c/\langle U \rangle = 0.72$ which is slightly larger than the value of u_c^* in the present case at $x/w = 1.5$, and in the same range of Re ; see Figure 143.

6.3.3 Distribution of Wavelength $\lambda^*(x^*)$

The algorithms of Sections 5.3.2.4 and 5.3.2.5 have been used to process the photographic database to compute the nondimensional wavelength $\lambda(x^*)/w$. The results of these calculations are presented in Figures 147 through 154. Each plot covers the same Re range as was used for the $St_F(x^*)$ plots presented in Figures 126 through 133. These plots, like the $St_F(x^*)$ plots, exhibit considerable variations, especially for Re values up to 700. At values of $Re > 900$, this variation is decreased. Similar trend is also evident in the photographic records of BW.

A common feature of the distribution of $\lambda^*(x^*)$ over the entire range is the observation that λ^* increases with increasing distance from the exit plane. However, for Reynolds number ≤ 700 a consistent trend cannot be established; see Figures 147 through 154. But, at values of $Re > 900$, the $\lambda^*(x^*)$ distribution exhibits a linear increase

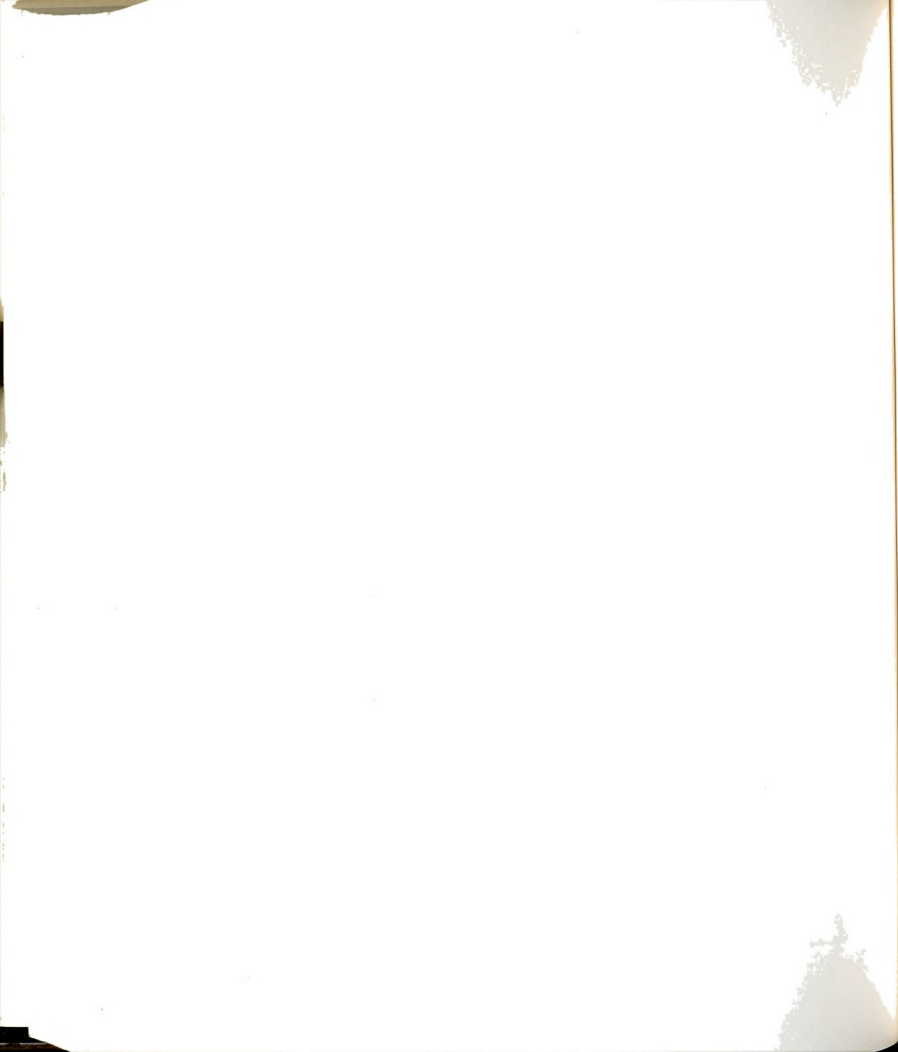


with x/w ; see Figures 151 through 154. Even though, the $\lambda^*(x^*)$ data at low Re values do not exhibit a linear rise, a linear model:

$$\hat{\lambda} = Ax^* + B \quad (155)$$

was used to determine the slope, A, and the intercept, B, of $\lambda^*(x^*)$ distribution for each of the experimental run. The ordinary least square technique was used to perform the regression. Figure 155 presents the slope, A, of the linear fit for each case as a function of Re. The same symbols have been used over small ranges of Re. Similarly, Figure 156 presents the intercept, B, of the linear regression for each data set. The figures show a systematic variation in the slopes and the intercepts of $\hat{\lambda}$ with increasing values of Re. The slope first increases with Re and approaches a plateau around $Re \approx 1500$. The intercept exhibits a gradual decrease in value with increasing Re. Note the decreasing scatter in the value of intercepts in a given range as Re increases. These plots show that even though the streamwise distribution of λ^* exhibits large variations and little consistent trend, especially at Re values < 700 , the slope and intercept plots exhibit a consistent trend as a function of Re.

FK inferred $\lambda^*(x^* = 1.5) = 1.2$ from the same data which were used to determine St and u_c^* . This value is almost twice the value of λ^* found in the present investigation in the similar range of Re; see Figure 151.



6.4 Conclusions

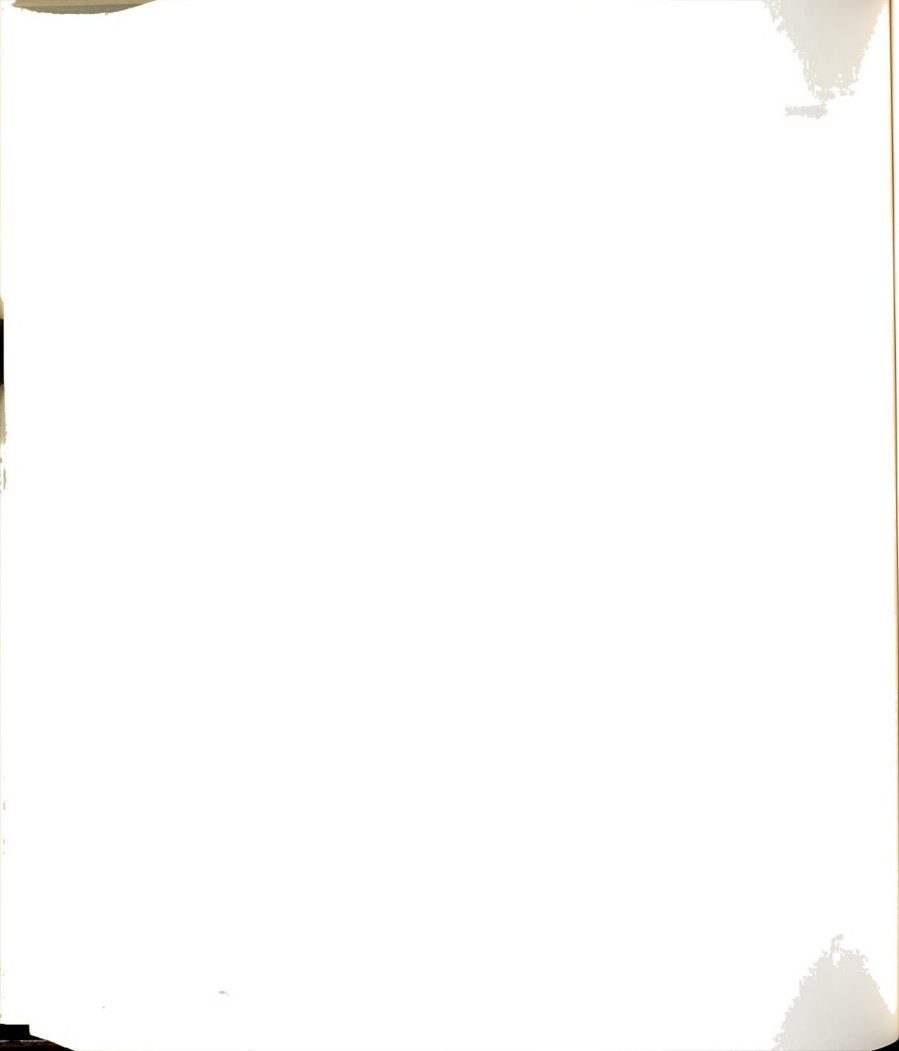
From the results of this chapter and the discussions related to the qualitative aspects of the slit-jet flow field in Chapter 4, it is concluded that the stability and the resulting processes in the slit-jet flow field that result in the symmetric vortex formations are more complex than those identified by BW and FK. The first two of the three instabilities of the slit-jet flow field that were identified by FK (see Section 1.3.1) have been confirmed by the results of this study with the exception that a large scale vortex motion has not been observed to result from an agglomeration of a number of unit vortices as conjectured by FK. Also, the proposed (FK) third instability which prevents the formation of symmetric vortex street for $Re > 1600$ has not been observed. Large scale vortex motions have been observed even up to $Re \approx 3500$.

The question of whether or not what has been described here - as the large scale instability - is actually a manifestation of the shear layer instability was investigated. The momentum thickness, θ , of the free boundary layer governs the shear layer instability [Michalke (1965) and Freymuth (1966)]. For a steady discharge from the nozzle, θ_0 at the separation lip should not vary with time. In the slit-jet flow field, the appearance of a bulge in the dye streak has been shown (Chapter 4) as the first manifestation of the instability. This leads to the formation of a large scale vortex motion. If the instability is governed by a steady parameter like θ_0 , the bulge should nominally



appear at the same nondimensional distance from the exit plane for a given value of Re . Using the present photographic data, the mean, X_b , and the standard deviation, σ_b , of the location of the appearance of bulges were determined for each experimental run. In general, X_b would be greater than the true value, because of relatively low sampling rate of the camera. Because the scatter in the data is caused in part by the inability of the recording mechanism to register the event at its inception the average estimate of the location of bulge formation, X_b , was adjusted by subtracting 1.5 times the estimate of σ_b . Figure 157 presents the adjusted location of bulge formation, $(X_b - 1.5\sigma_b)$, as a function Re . There is considerable scatter in the the data specially for $Re < 1500$. From this figure it is concluded that the formation of a bulge is not controlled by a steady parameter like θ_0 . Hence, the instability which results in the formation of large scale motions in the slit-jet flow field is not considered to be related to the shear layer instability.

The results of this study show considerable scatter in the values of Strouhal number, $St_F(x^*)$, for similar values of Re . (See Figures 134, 136, and 137). A similar scatter was observed by FK in their air jet with $B/w=26.25$. In the present investigation, none of the factors which were examined to determine the cause of the scatter in the $St_F(x^*)$ distributions could be linked to the observed behavior. Either there is an unknown parameter which is responsible for the observed large variations in St_F or the instability process of a naturally excited slit-jet is not a well regulated process; FK

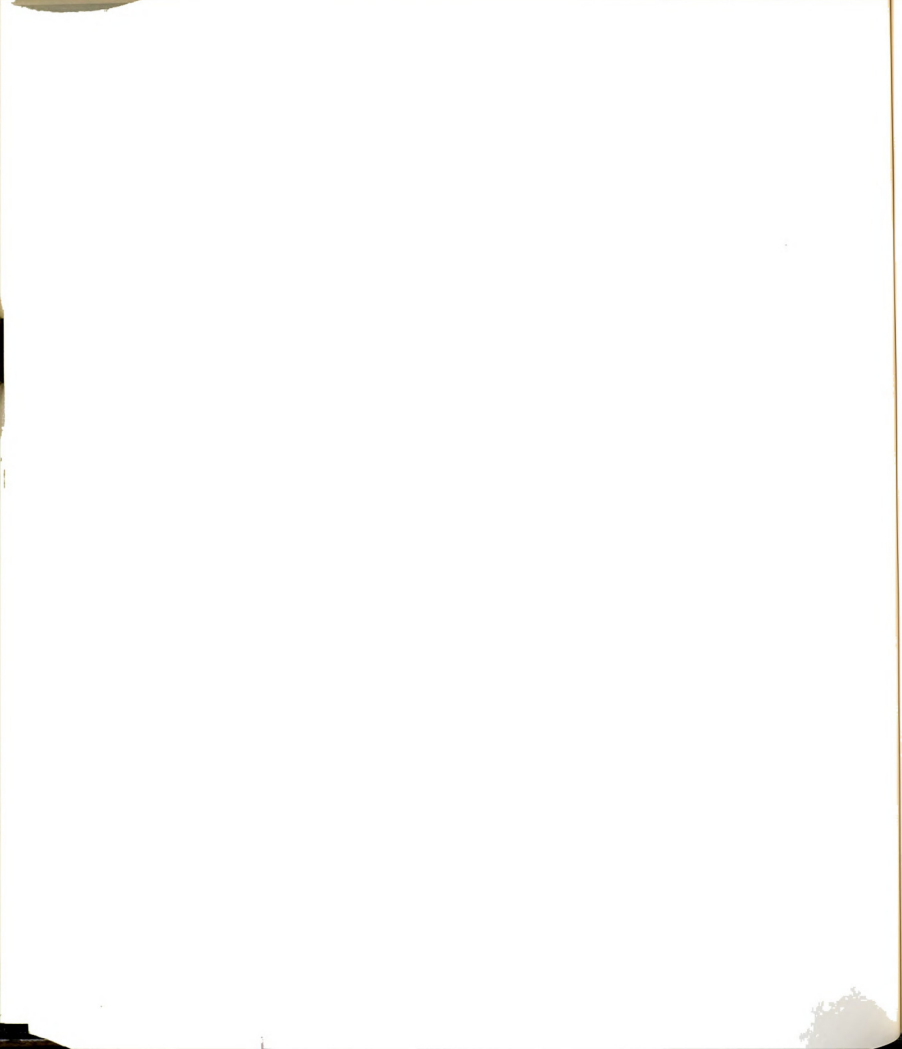


reported a similar behavior in their experiments conducted over a small range of Re , 847-1148.

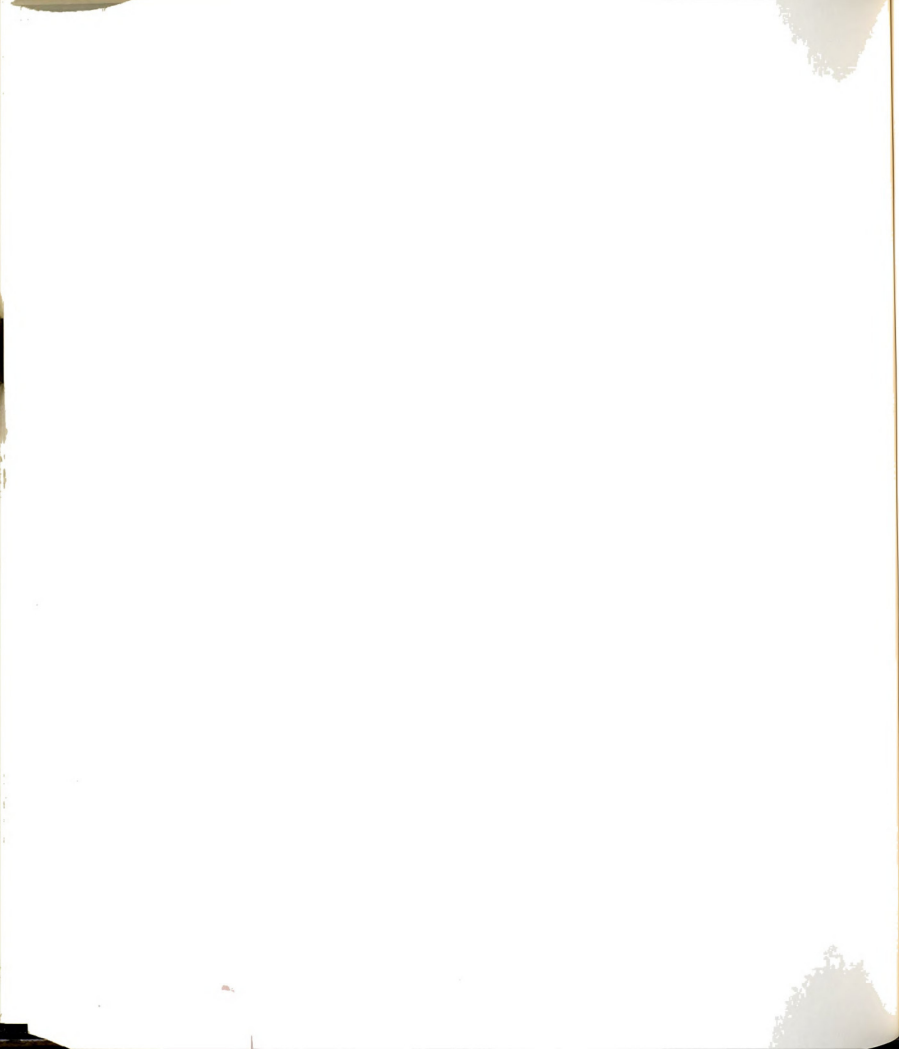
The results of BW (see Figure 138) show considerably less scatter in the distribution of St_F as a function of Re . Significant differences in the experimental techniques may account for the differences in the observations. Specifically, the BW values for the passage frequency were obtained by visually observing the flow and counting the passage of the observed vortex motions. Since they did not specify the x/w value used for the passage location and since these might have been paired motions, the relationships of their Strouhal numbers to those of the present study are uncertain.

The streamwise distribution of the convection velocity of the vortex pairs in the slit-jet flow field exhibit the most coherent representation of the three instability characteristics. The vortex motions undergo acceleration for $x/w \leq 3$, and then the velocity levels off. In some cases, the vortices appear to undergo deceleration for $x/w > 3$. The acceleration of vortex pairs results in the increase in the spacing, λ , between vortex motions while St remains nominally constant. However, the greatest increase in λ is caused by the pairing of two or more vortex pairs which also results in a decrease in St .

Even though the plots of streamwise distribution of λ^* do not present a coherent picture at low values of Re (up to $Re \approx 700$), the slopes ($d\lambda^*/dx^*$) and the intercepts ($\lambda^*(0)$) of the linear fit through



the data do exhibit a consistent behavior over the entire range. See Figures 155 and 156.

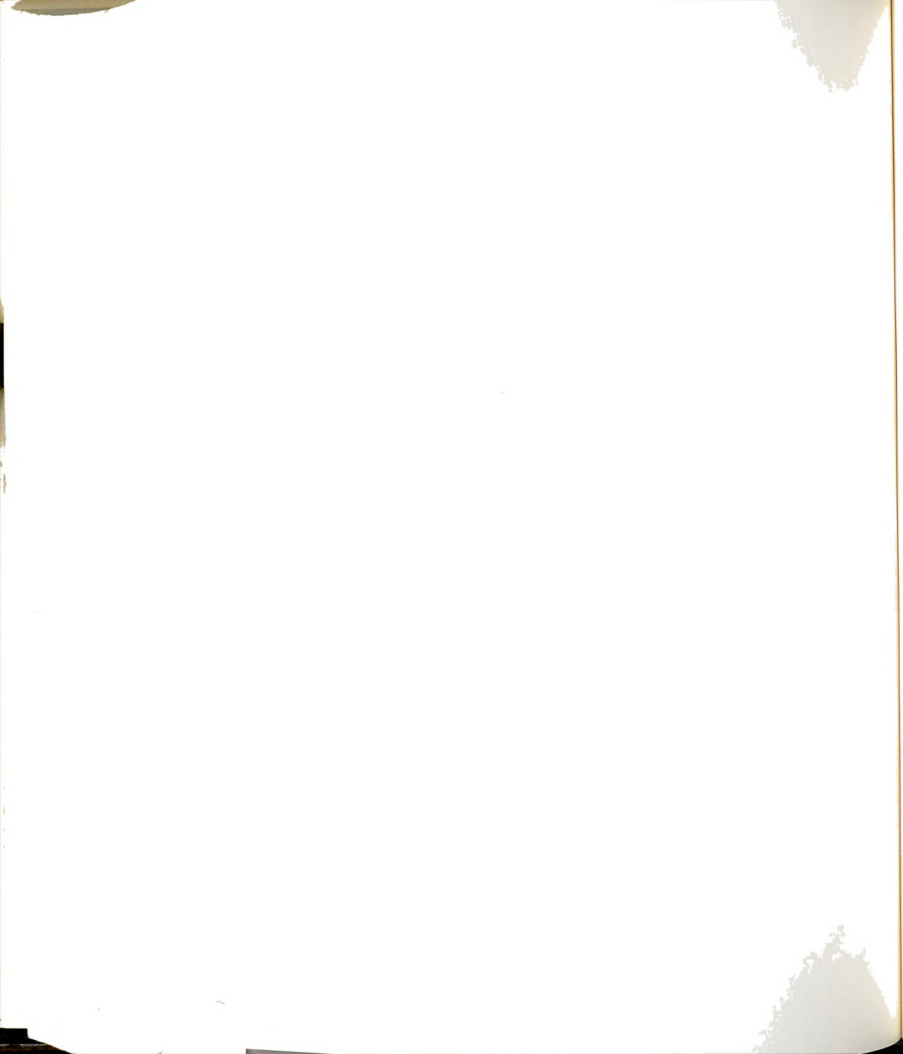


VELOCITY MEASUREMENTS USING LASER DOPPLER ANEMOMETRY

7.1 Introduction

This chapter presents the results of measurements of the longitudinal component of velocity, $u(x,y,t)$, in the slit-jet flow field. The data were acquired using a single channel laser Doppler anemometer. The details of the experimental configuration and data acquisition have been presented in Chapter 3.

Section 7.2 presents discharge coefficient values of the slit-jet as a function of Re . Velocity field information, specifically, the time series from the lateral and longitudinal surveys of $u(x,y,t)$ and the mean and rms velocity profiles computed from $u(x,y,t)$, is presented in Section 7.3. In addition, the computed distribution of $\bar{u}^*(x^*,y^*=0)$ and the analytical models of $\bar{u}^*(x^*=c,y^*)$ are also presented in this section. Section 7.4 presents the technique of computing the power spectral density function for the measured $u(x,y,t)$ data. Section 7.5 deals with the identification of background



disturbances in the plenum using the power spectrum of $u(x, y=0, t)$. Section 7.6 presents the results of computations of Strouhal number from the power spectrum of $u(x, y, t)$.

7.2 Discharge Coefficient C_D of the Slit-Jet

The discharge coefficient of a nozzle or other constriction is a characteristic of practical significance. For a slit-jet it is defined as

$$C_D = \frac{\int_A \vec{V}(0, y, z) \cdot \hat{n} \, dA}{U_0 A_j} \quad (156)$$

where $\vec{V}(0, y, z)$ is the velocity vector at the exit plane of the jet, \hat{n} is a unit vector in the outward normal direction (along x axis here). U_0 is the maximum velocity which the jet achieves at approximately $x/w=1$, and, A_j is the area of the jet given by $w \times B$. In terms of the spatial average velocity, $\langle U \rangle$, defined as

$$\langle U \rangle = \frac{1}{A_j} \int_A \vec{V} \cdot \hat{n} \, dA \quad (157)$$

the discharge coefficient becomes

$$C_D = \frac{\langle U \rangle}{U_0} \quad (158)$$

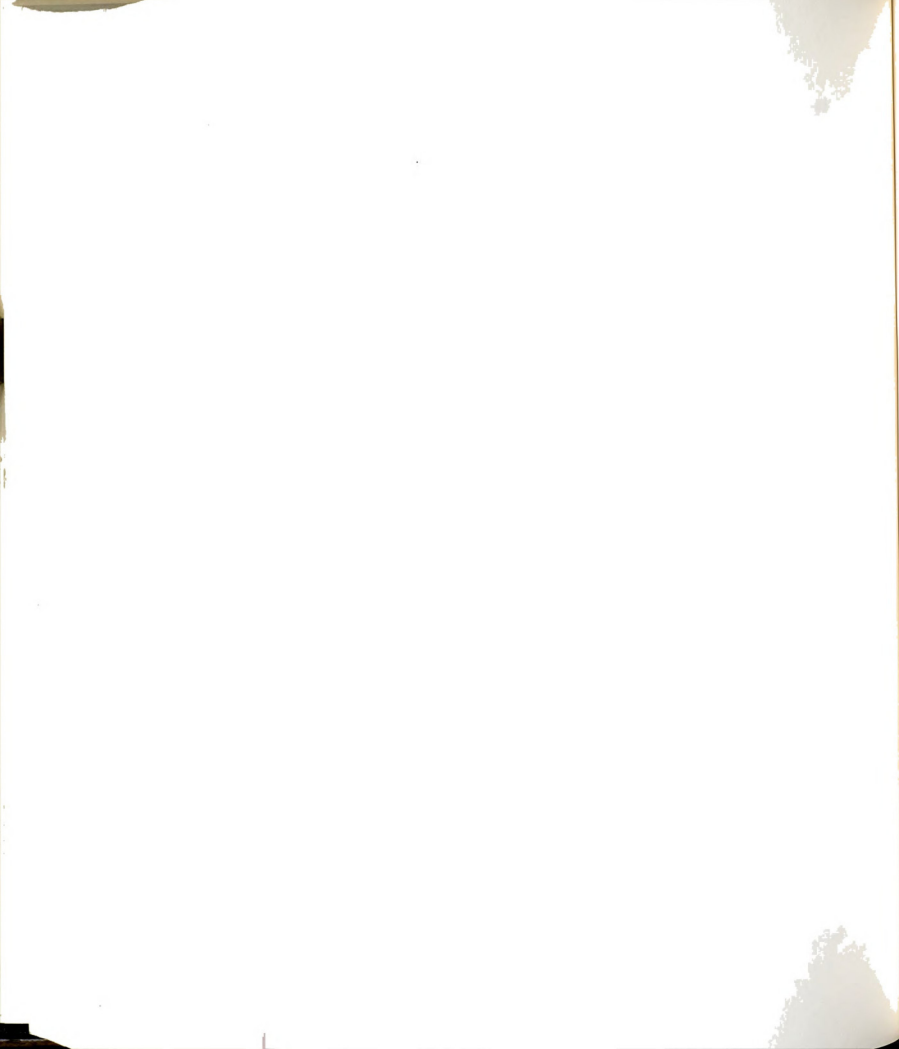
The two velocities, $\langle U \rangle$ and U_0 , were simultaneously measured over a wide range of Re (100-6500). The spatial average velocity, $\langle U \rangle$, was inferred from the output of the Volume Flow Sensor (VFS) as described



in Section 3.2.1. The calibration, data acquisition and processing details have been presented in Sections 3.7.2, 3.9, and 5.2.1, respectively. The maximum velocity U_0 of the jet along the centerline was measured nominally at $x/w \approx 2.2$ using the single channel LDA system. (Section 3.9.2. describes the details of the data acquisition). At low values of Re , the measurements were conducted in a water-sugar mixture. (See Section 3.2.3.)

Figure 158 presents the values of discharge coefficient, C_D , as a function of Re . At low values of Re (< 800), C_D shows a strong Re dependence which becomes weaker as Re increases. For sufficiently large values of Re (≥ 3000) C_D achieves an asymptotic value equal to 0.68. This value is about 11% larger than the value (0.611) predicted by the inviscid flow analysis. (See Section 2.2.3)

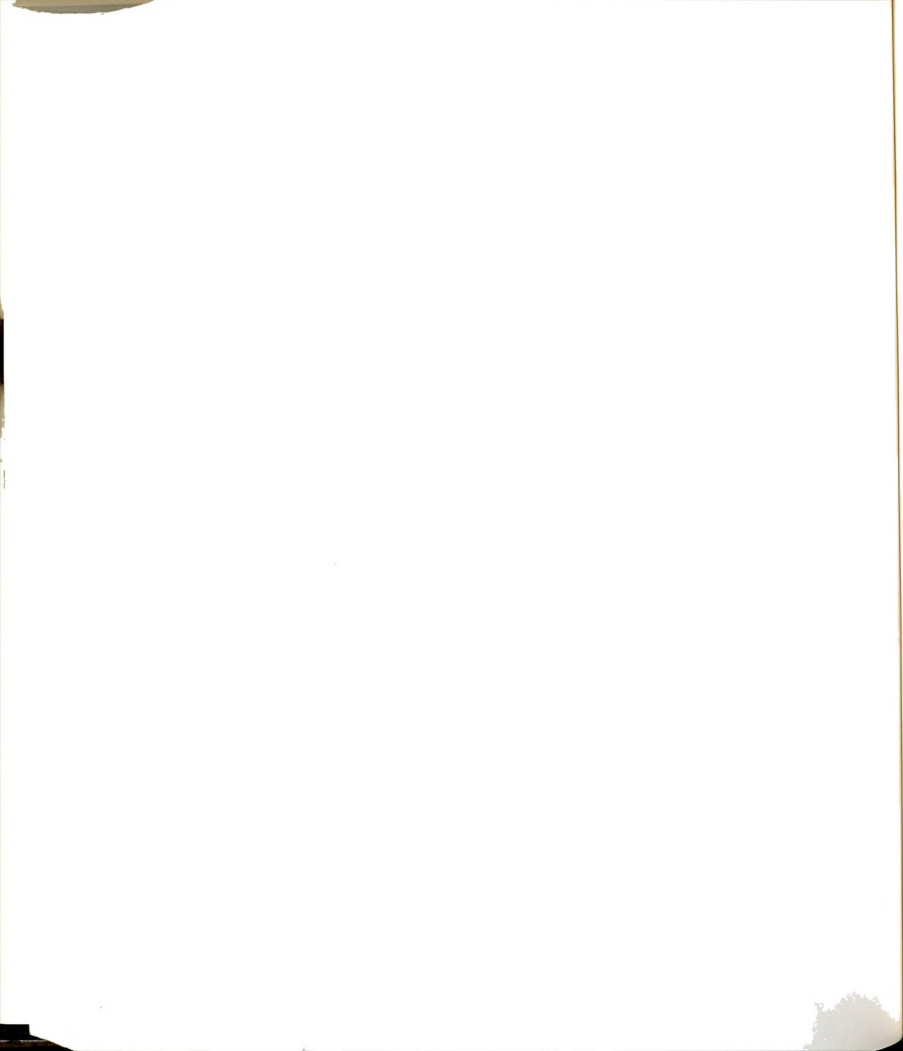
The decrease in the value of C_D with increasing Re indicates the decreasing influence of viscous effects on the flow over the nozzle plates. The loss of momentum in the boundary layer fluid permits the fluid near $x \approx 0$ and $y \approx \pm w/2$ to follow a trajectory which has a radius of curvature that is smaller than that of an inviscid fluid. As the Reynolds number increases, the boundary layer becomes thinner and the trajectory of the separating streamline exhibits a larger radius of curvature; the discharge coefficient shows a corresponding decrease. In the limit as Re becomes large, the value of C_D would be expected to approach 0.611, the value of C_D for an inviscid jet.



The apparent asymptotic approach to 0.68 in Figure 158 suggests the presence of a geometry dependent effect on the C_D values. Specifically, it is inferred that the $\vec{V}(0, y \approx \pm w/2, z)$ values are influenced by the thickness t_N of the nozzle plate and possibly by the wedge angle. Support for this inference is provided by the C_D data in which two different slit-widths were used. Specifically, in the jet with $w=1.27$ cm, the C_D values asymptote to 0.71 whereas those for the jet with $w=2.57$ cm continue to decrease and assume an asymptotic value of 0.68. This suggests that the contraction of the jet is greater for $t_N/w=0.5$ than in case of $t_N/w=1$.

The influence of the geometry of the nozzle plate on $\vec{V}(0, y \approx \pm w/2, z)$ is suspected to be caused by an alteration of the entrainment path in the near-field of the jet. In the case of the smaller jet ($t_N/w=1$), there will be more obstruction to the entrainment flow than in the case of the wider jet ($t_N/w=0.5$). Variations in the entrainment flow can alter the pressure field in the vicinity of the jet exit, thus, allowing the smaller width jet to contract less at the "vena contracta" as compared to the contraction of the wider jet. The overlapping of the C_D values, for the two jets, below $Re \approx 1500$ suggests that for these values of Re the near-field is less sensitive to the geometry of the nozzle.

It is known from the previous studies and the results of Chapter 4 that the jet becomes unstable and develops vortex motions for Re values greater than 250. Figure 158, however, shows a continuous



decrease in the C_D values with increasing Re without any marked variation around $Re \approx 250$. It is inferred that the formation of the vena contracta is influenced only by the development of the boundary layers on the nozzle plates and not by the formation of vortices downstream of the exit plane.

7.3 Velocity Field Information

This section describes in detail the results of longitudinal and lateral surveys of the streamwise component of velocity $u(x,y,t)$. The results include the mean and the fluctuating fields of $u(x,y,t)$ in the streamwise and lateral direction. The results related to the spectral contents of $u(t)$ (frequency domain information) are presented in Section 7.5.

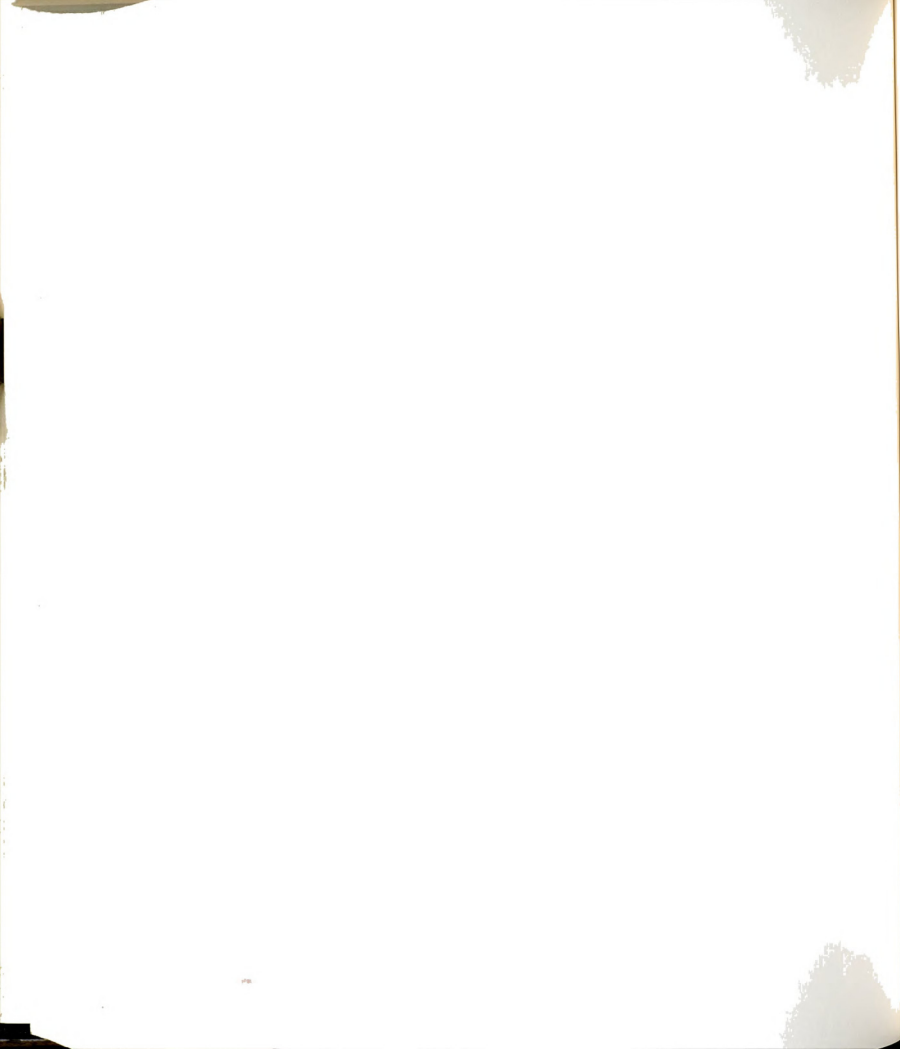
7.3.1 Longitudinal Surveys

7.3.1.1 Introduction

Velocity surveys along the centerline of the jet extended over $-1 \leq x/w \leq 2.4$, except for one case in which the measurements were made up to $x=4.6w$. These measurements covered Reynolds number values from 500 to 2900. In all cases water was used as the working fluid.

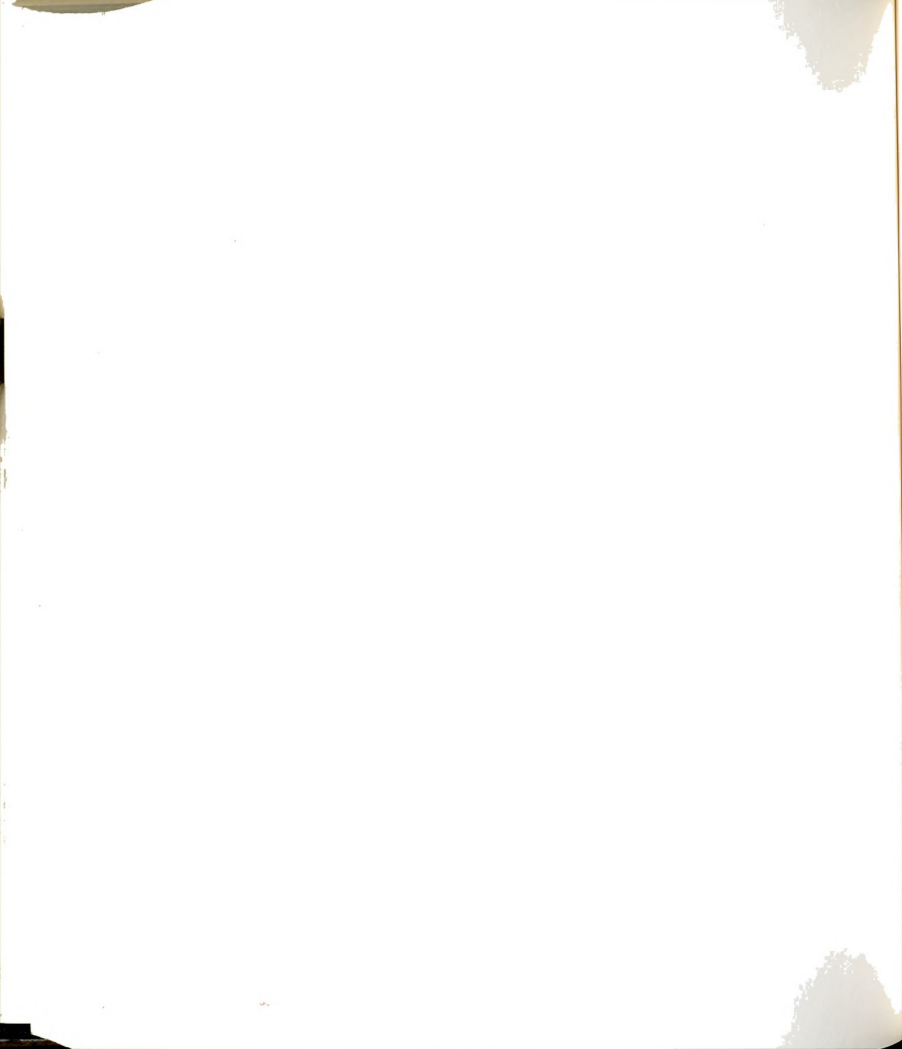
The objectives of the longitudinal survey were:

- i) Compare the measured longitudinal mean velocity distribution with the inviscid distribution determined in Chapter 2.



- ii) Determine the growth of velocity fluctuations along the centerline of the jet and to compare this growth with the value predicted by the inviscid, linearized, spatial stability theory.
- iii) Determine the passage frequency of the vortex motions as a function of the downstream distance, x/w , using spectral methods.
- iv) Determine the region of the flow where the growth of disturbances begin.

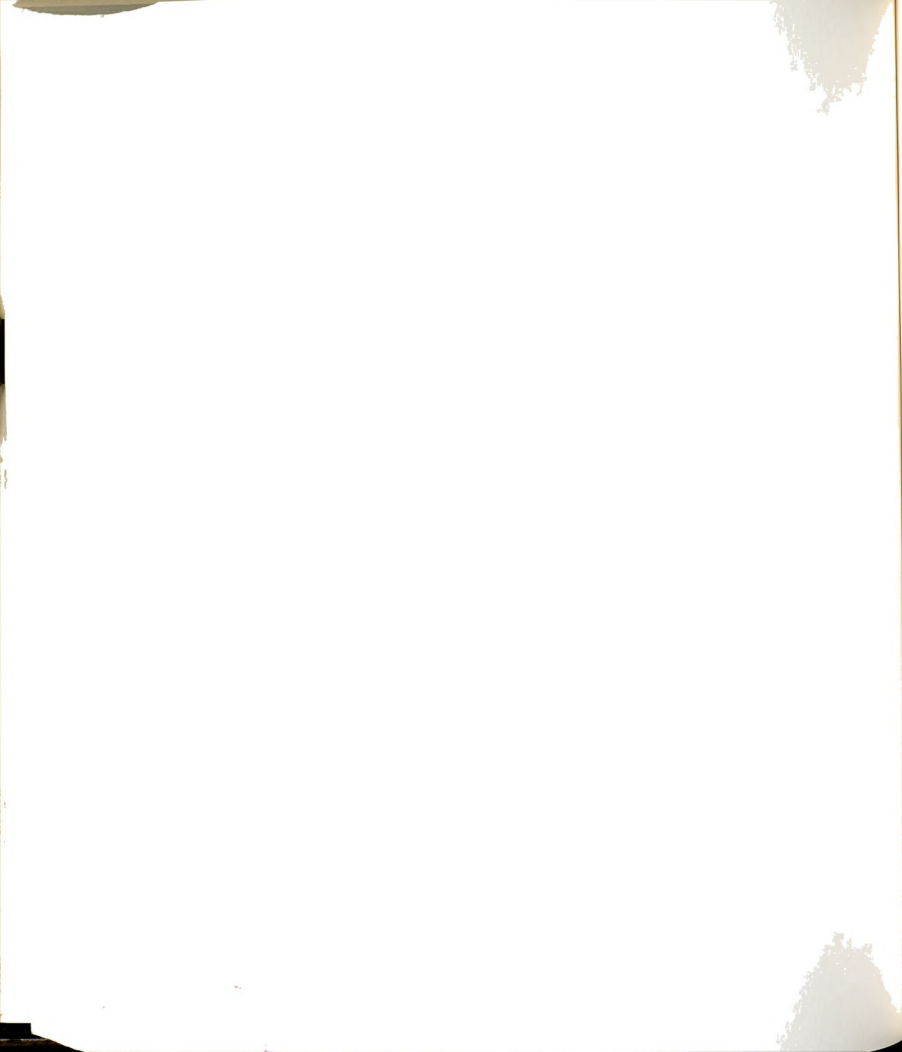
Figure 159 is a schematic representation of the configuration used for velocity traversals. For the longitudinal survey, the LDA measuring volume (mv) was traversed along the centerline of the jet by raising or lowering the supporting base of the LDA system. Before the experiments were run the location of the mv was determined accurately with respect to the exit plane of the jet and another reference mark outside the glass tank. After the base was raised or lowered the new height of the mv was determined with respect to the known reference mark. Hence, the location of the mv could be determined with respect to the exit plane of the jet. The position of the measurements was accurate within ± 0.25 mm.



7.3.1.2 Velocity Time Histories at Selected Locations

Figures 160 through 167 present the measured time histories of $u(x^*, y^*=0, t^*)/\langle U \rangle$ at various values of Re . A total of 4096 data points were recorded at a sampling rate of 308 Hz. The plots presented in Figures 160 through 167 have been prepared by plotting every third point (effective sampling rate = 77 Hz; this plotting protocol was required to prevent the composite plotting files from becoming excessively large).

An examination of the traces presented in Figures 160 through 167 shows that in some cases, especially in the neighborhood of $x/w=1$, the beginning portion of the velocity signal shows large velocity fluctuations. See Figure 161. The fluctuations are observed to diminish as time proceeds. It is conjectured that these fluctuations are signatures of the strating vortex pair. These portions of the time series showing the spurious fluctuations have not been included in determining the various quantities of interest. Apart from this ambiguity, the time traces of Figures 160 through 167 reveal the development of the jet and the growth of disturbances. Note that the time traces, over a six-fold range of Re , exhibit the same trend for the growth of disturbances.



7.3.1.3 Mean and Rms Velocity Distributions

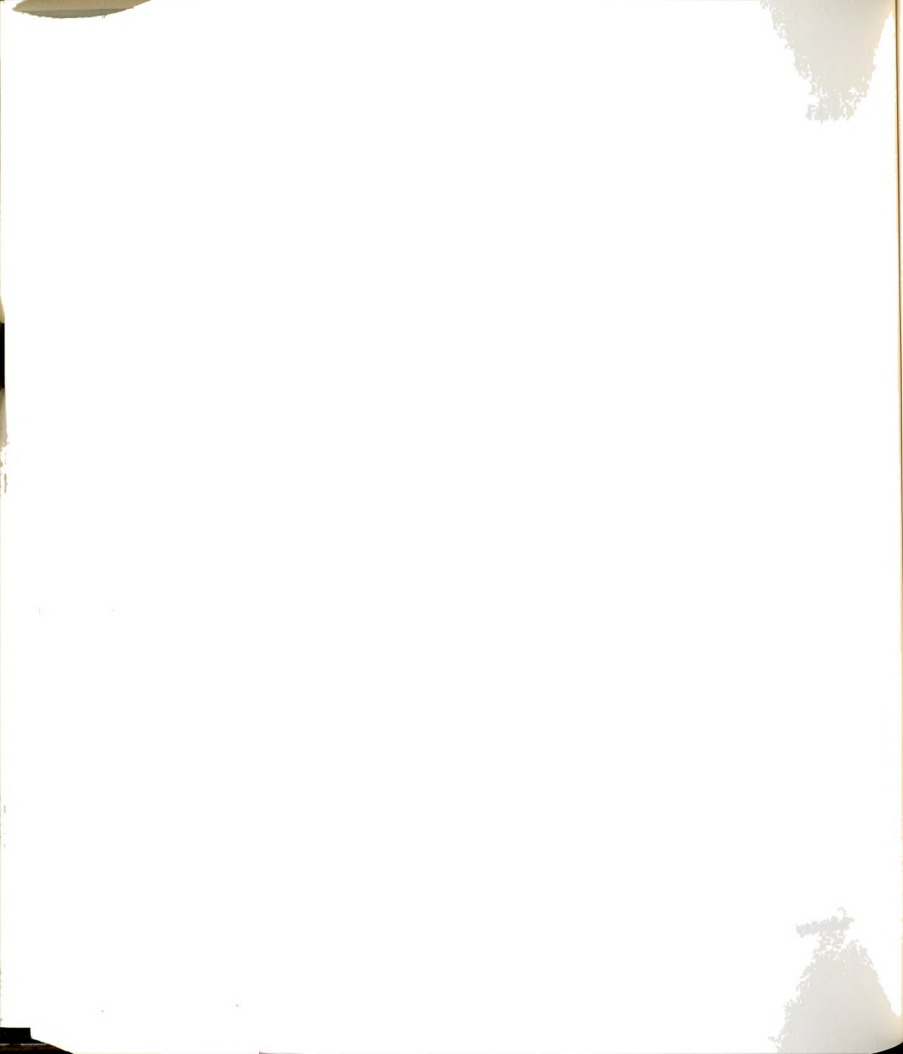
The mean and root mean square values of the centerline velocity data were determined from the time traces shown in Figures 160 through 167. Since each time trace was the output of an independent experimental run, the $u(t)$ values of a given run were normalized by the spatially and temporally averaged velocity, $\langle U \rangle$, of the same run. In general, the value of $\langle U \rangle$ varied from run to run. The total variation was small; the values were nominally contained within $\pm 2\%$ of the mean with a maximum deviation of 5% . The time mean values of the normalized velocities $\bar{u}(x,0)/\langle U \rangle$, for a given Re , were interrogated to determine the maximum normalized velocity $\bar{u}(x_m,0)/\langle U \rangle$. The maximum value occurred over the range $1 \leq x/w \leq 2.4$. The ratio, $\bar{u}(x_m,0)/\langle U \rangle$, was used to normalize all the previously normalized velocities as

$$\bar{u}^*(x^*, y^* = 0) = \frac{[\bar{u}(x^*, y^* = 0)/\langle U \rangle]}{[\bar{u}(x_m^*, y^* = 0)/\langle U \rangle]} \quad (159)$$

The rms values were normalized as

$$\bar{u}^*(x^*, y^* = 0) = \frac{[\bar{u}(x^*, y^* = 0)/\langle U \rangle]}{[\bar{u}(x_m^*, y^* = 0)/\langle U \rangle]} \quad (160)$$

Figure 168 is a plot of the mean velocity distribution $\bar{u}^*(x^*, y^* = 0)$. The solid line represents the distribution based upon the potential flow calculations (see Section 2.2). The figure shows that the jet issues from the slot with a velocity which is about 0.65 of U_0 . The velocity approaches a maximum value (U_0) at nominally $x/w=1$. Beyond



$x=3w$ the centerline velocity begins to decrease, apparently because the propagation of shear effects has reached the centerline.

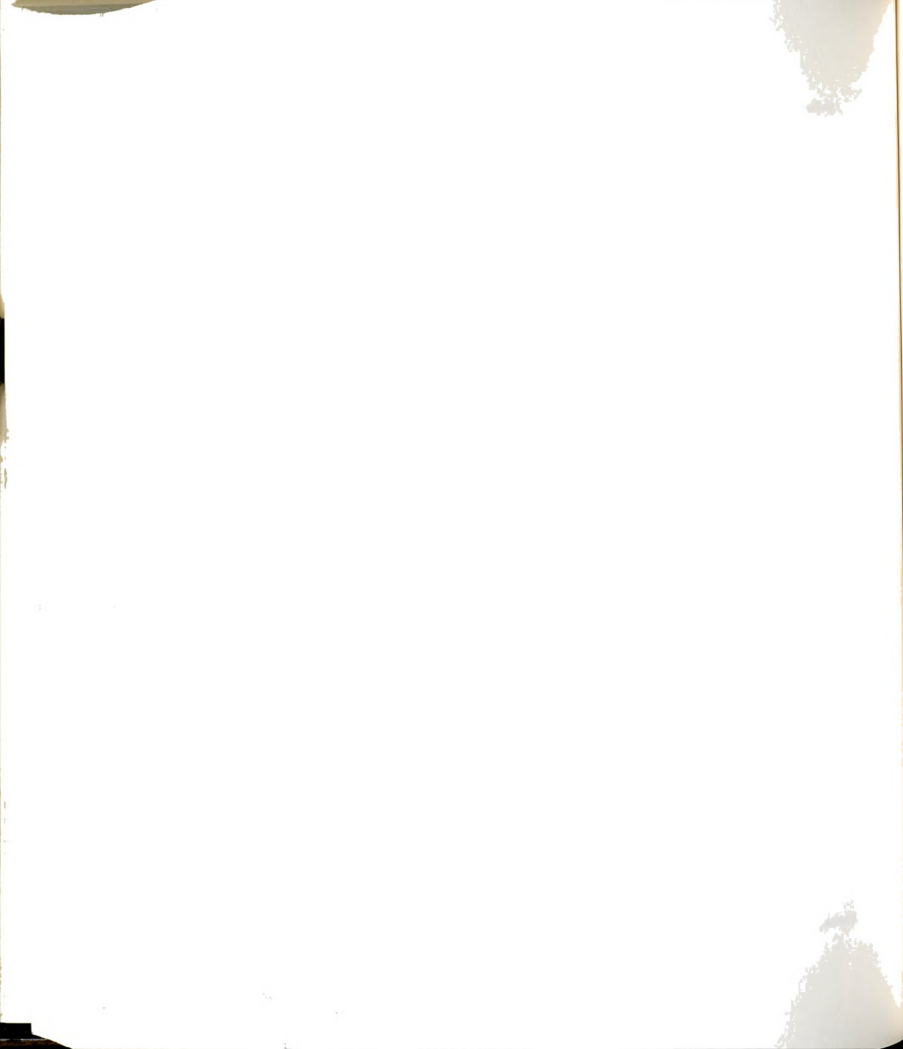
Figure 168 shows excellent agreement between the calculated and the measured (over a six-fold range of Re) values of $\bar{u}(x^*)/U_0$. This agreement supports the earlier conjecture regarding the absence of shear effects in the core region of the jet up to $x=3w$. The mean centerline velocity, $\bar{u}(x^*, y^* = 0)$, is thus governed by the mean Euler-s equation (see Section 2.5.2). Neglecting the contribution of the fluctuating component of velocity, $\overline{u'^2}$, the equation is expressed as

$$\frac{\bar{p}_k}{\rho} + \frac{1}{2}\bar{U}^2(x,0) = C \quad (161)$$

Considering the good agreement between the calculated and the measured $\bar{u}^*(x^*, y^* = 0)$ over the Re range 500-2900, the strong dependence of C_D on Re (see Section 7.2) over the same Re range shows that the influence of shear effects (development of boundary layers) on the nozzle plates is offset by some other physical effect. The Euler-n equation relates the centerline pressure, $\bar{p}_k(x,y=0)$, to the radius of curvature, R , and the velocity, V , along a curved streamline (see Figure 169), i.e.,

$$\bar{p}_k(x,y=0) = p_{amb} + \int_1^2 \frac{\rho V^2}{R} dn \quad (162)$$

where, p_{amb} is the ambient pressure in the receiver and n is the

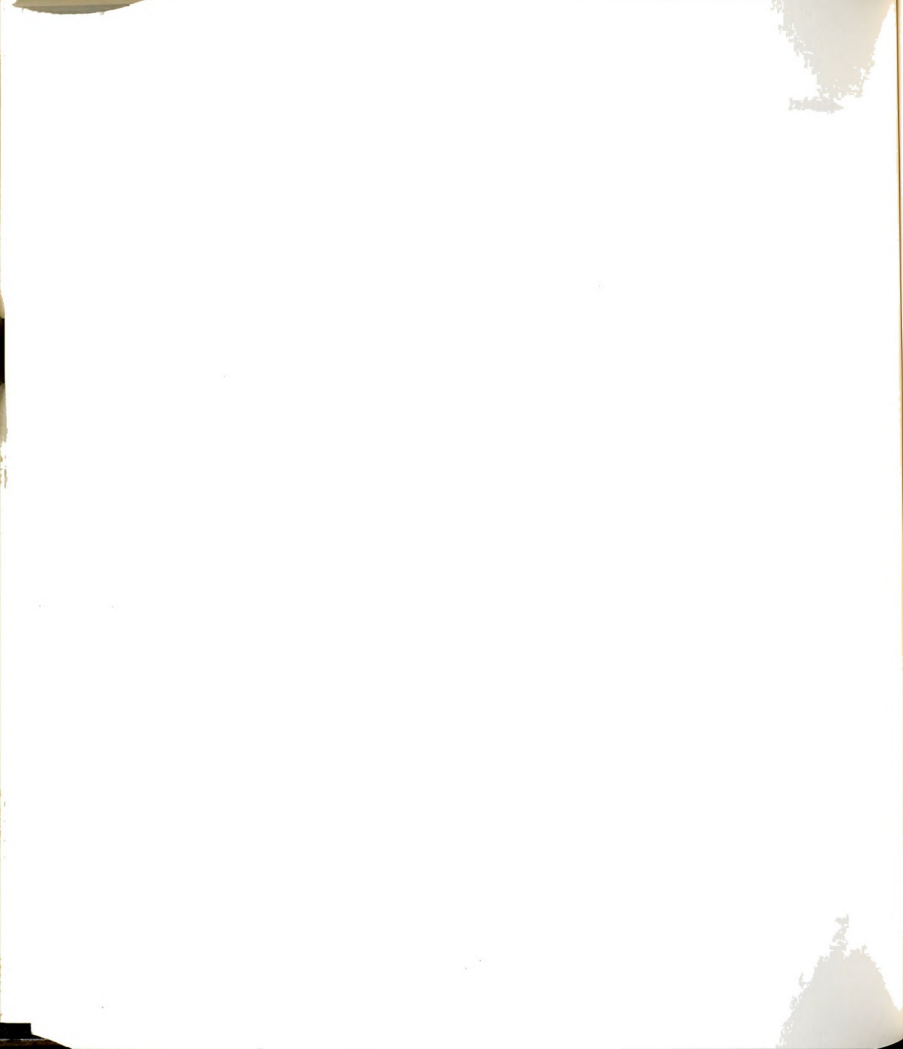


direction normal to the streamline. It has been argued in Section 7.2, based upon the distribution of C_D with Re (up to $Re \approx 3500$), that the radius of curvature of the separating streamline increases with increasing value of Re . Hence, the integration path 1-2 shown in Figure 169 will also change with Re so that the nondimensional pressure distribution remains the same along the centerline. In other words, an adjustment in the curvature of the streamlines in the vicinity of the exit plane of the jet is believed to be responsible for $\bar{p}_k(x, y=0)$ to follow the inviscid behavior.

The distribution of the log of the normalized rms of the centerline velocity, $\bar{u}^*(x^*)$, is presented in Figure 170. The plot shows that the total disturbance grows exponentially over the region $-1 \leq x/w \leq 2.4$. In order to determine whether the growth rate depends upon the flow Reynolds number, the slope of the normalized distribution at each Re value was calculated. The result, plotted in Figure 171, does not indicate any systematic dependence of the growth rate on Reynolds number. The straight line presents the best fit through the data. The line is expressed as

$$\text{Growth rate} = 0.538 + 5.18 \times 10^{-6} Re \quad (163)$$

The standard error in the two coefficients are 2.94×10^{-2} and 1.79×10^{-5} , respectively. The slope of the straight line based upon natural log is equal to 1.24.

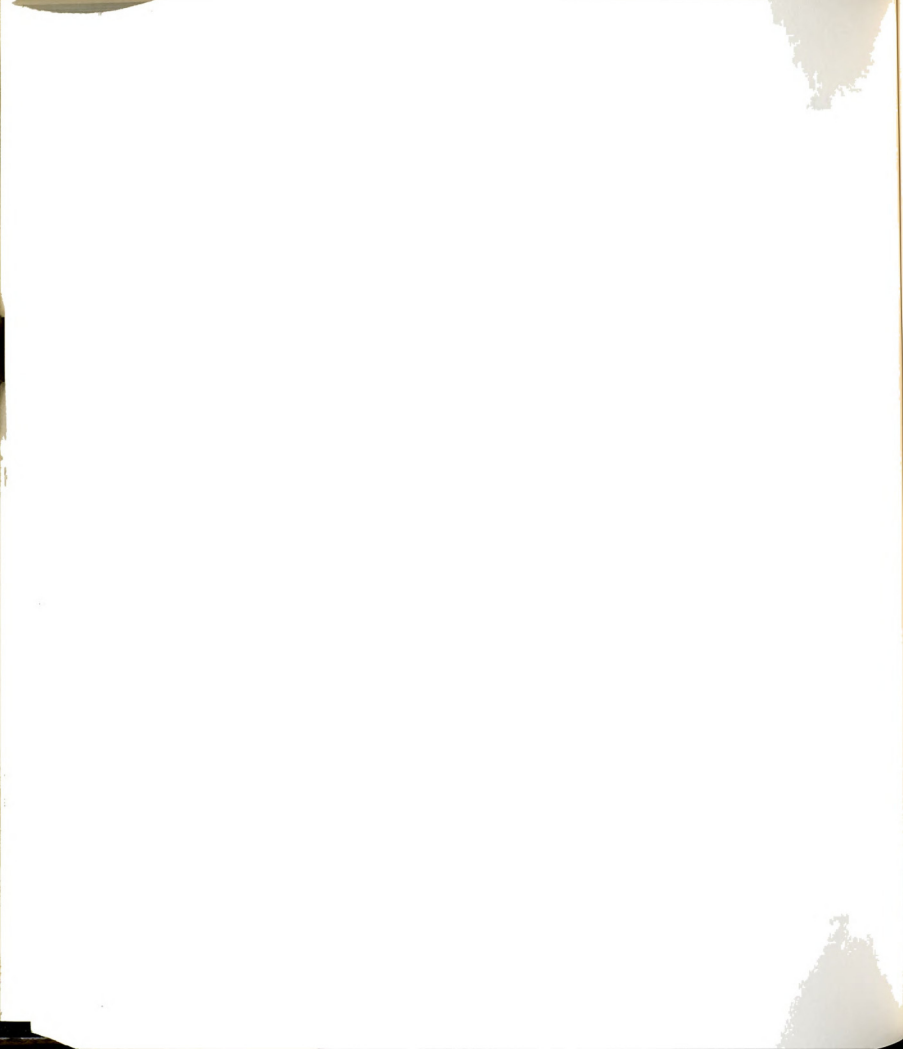


7.3.2 Lateral Surveys

7.3.2.1 Introduction

A 2.57 cm wide jet was used to conduct the lateral survey of $u(x=c, y, t)$ at two x/w locations and two values of Re , 1600 and 3000. The two locations, $x/w=1$ and $x/w=2.4$, at which these surveys were conducted, were chosen from the $\bar{u}^*(x^*, y^*=0)$ distribution (see Figure 168). Since the mean velocity $\bar{u}^*(x^*, y^*=0)$ nominally became equal to the maximum velocity U_0 at $x/w=1$, it was expected that the distribution $\bar{u}^*(x^*=1, y^*)$ would represent the basic flow state to be used in the inviscid stability analysis. The location $x/w=2.4$ was chosen because beyond this location the velocity fluctuations ceased to grow exponentially. The objectives of the lateral survey were:

- i) Determine the mean velocity profiles $\bar{u}^*(y^*)$ at the two locations.
- ii) Use the measured $\bar{u}^*(y^*)$ data to estimate the parameters in the analytical models of the mean velocity profiles. The fitted profiles have been used in the inviscid instability equations.
- iii) Observe the propagation of shear effects towards the center of the jet.



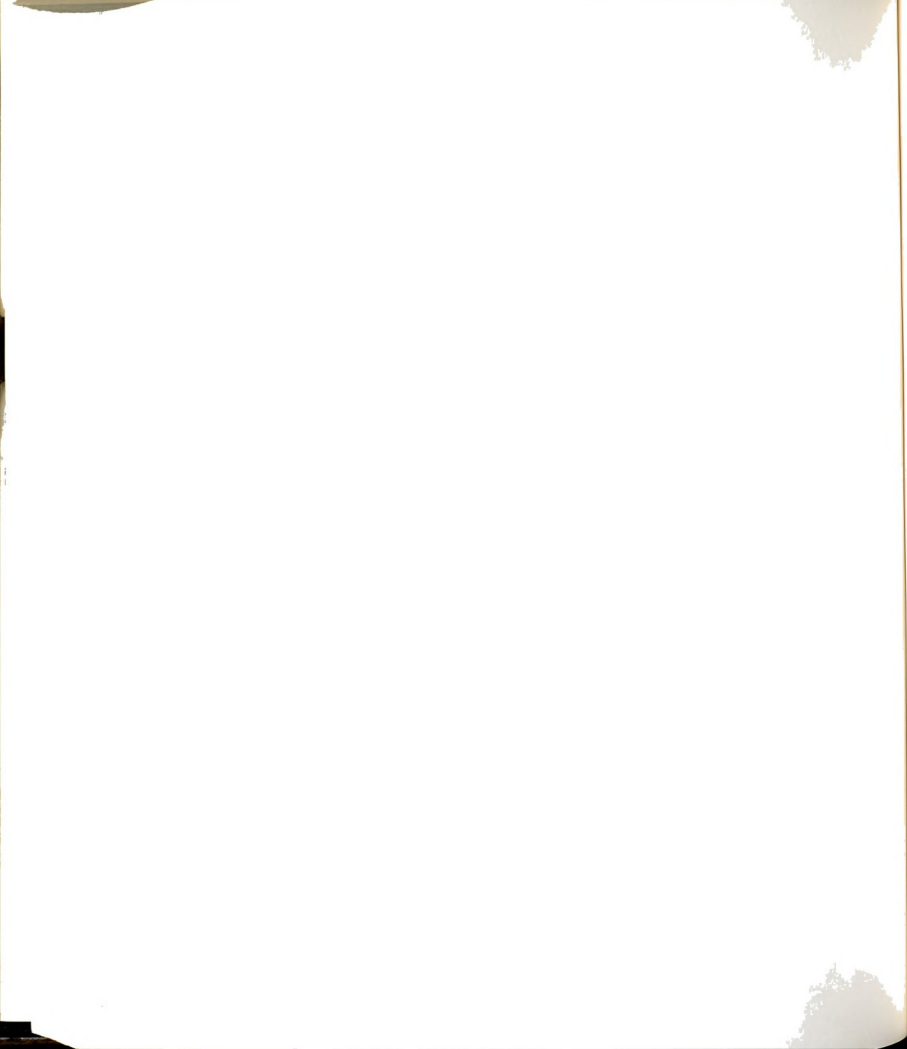
- iv) Estimate the half width of the jet.

Figure 159 shows the traversing mechanism which was used to move the jet facility with respect to the stationary LDA system. The traverse could be positioned with an accuracy of ± 0.25 mm. Since no frequency shifting was incorporated in the LDA system the velocity data near the edges of the jet were in error because of velocity reversals.

7.3.2.2 Velocity Time Histories at Selected Locations

Figures 172 and 173 present the normalized time traces of the velocity at $x/w=1$ and 2.4 at $Re=1600$. Figures 174 and 175 are the time traces at $Re=3000$ and the same x/w locations. As in the case of longitudinal surveys, 4096 data points were sampled at 308 Hz. However, as before, in preparing these plots (Figures 172 through 175) only a fourth of the total number of data points have been used. In these plots (Figures 172 through 175) the time series from those regions have not been included which showed velocity reversals. As an example, Figure 176 presents time series from two y locations at $Re=1600$, at which flow reversals are inferred to have taken place.

The plots of $u^*(y^*, t^*)$ at $x/w=1$, and both values of Re (Figures 172 and 174) show qualitative differences in the velocity time histories at the corresponding y locations across the jet. These differences can be described as an apparent increase in the magnitude of the velocity fluctuations as $|y/w|$ increases; also, for the same y/w

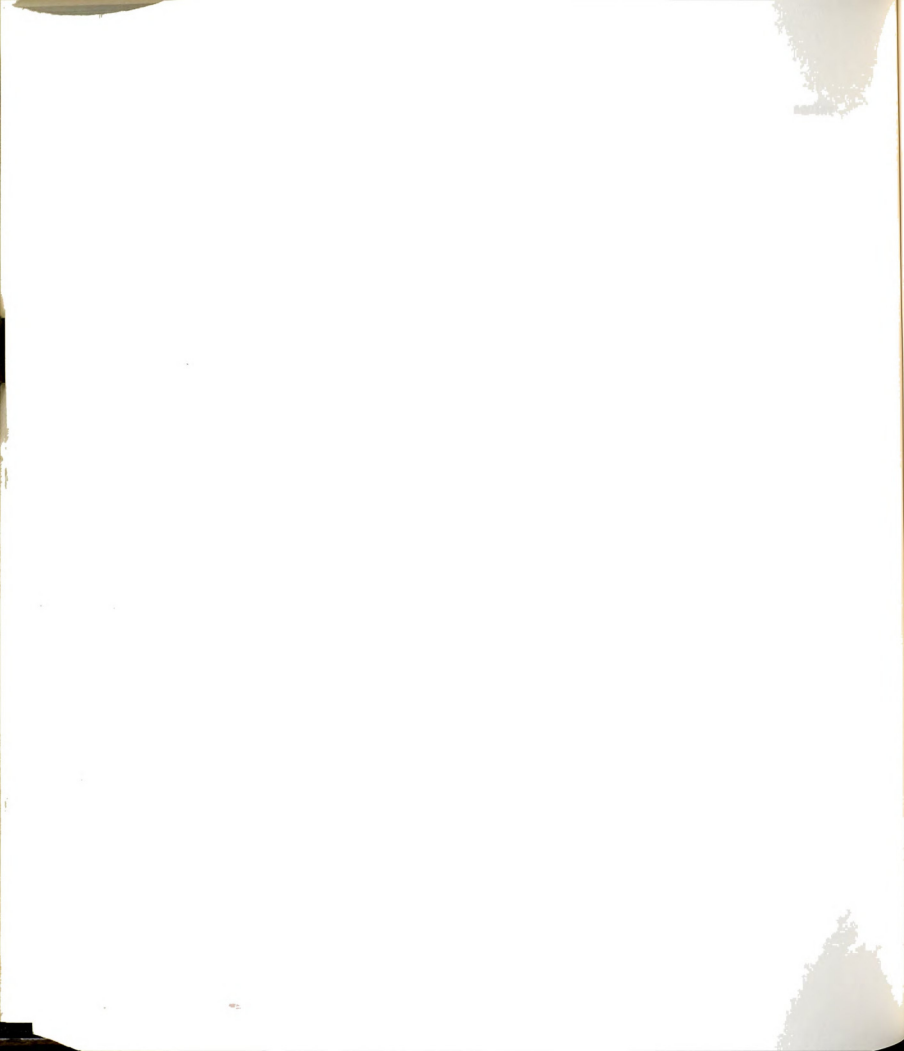


values, the magnitude of the velocity fluctuations for $Re=1600$ are somewhat larger than those for the higher Re case. Note the velocity time traces at $y/w=\pm 0.35$ at $Re=1600$ and $y/w=\pm 0.31$ at $Re=3000$; these y/w locations are quite close to the locations where the value of the mean velocity $\bar{u}(y)$ is half the value of the maximum velocity U_0 on the centerline.

The plots of $u(y^*, t^*)/\langle U \rangle$ at $x/w=2.4$ and both values of Re (Figure 173 and Figure 175), qualitatively show similar trends in the velocity time histories. It is suspected that at $Re=1600$ and $y=-0.51w$ (see Figure 173) some velocity reversals took place.

7.3.2.3 Mean and Rms Velocity Distributions Across the Jet

The mean and root mean square values of the longitudinal velocity data were determined from the time traces shown in Figures 172 through 175. The same procedure was used in normalizing the $\bar{u}(x=c, y)$ and $\bar{u}(x=c, y)$ data as was used in the case of longitudinal distributions of the mean, $\bar{u}(x, y=0)$, and the rms, $\bar{u}(x, y=0)$, velocities. See equations (159) and (160).

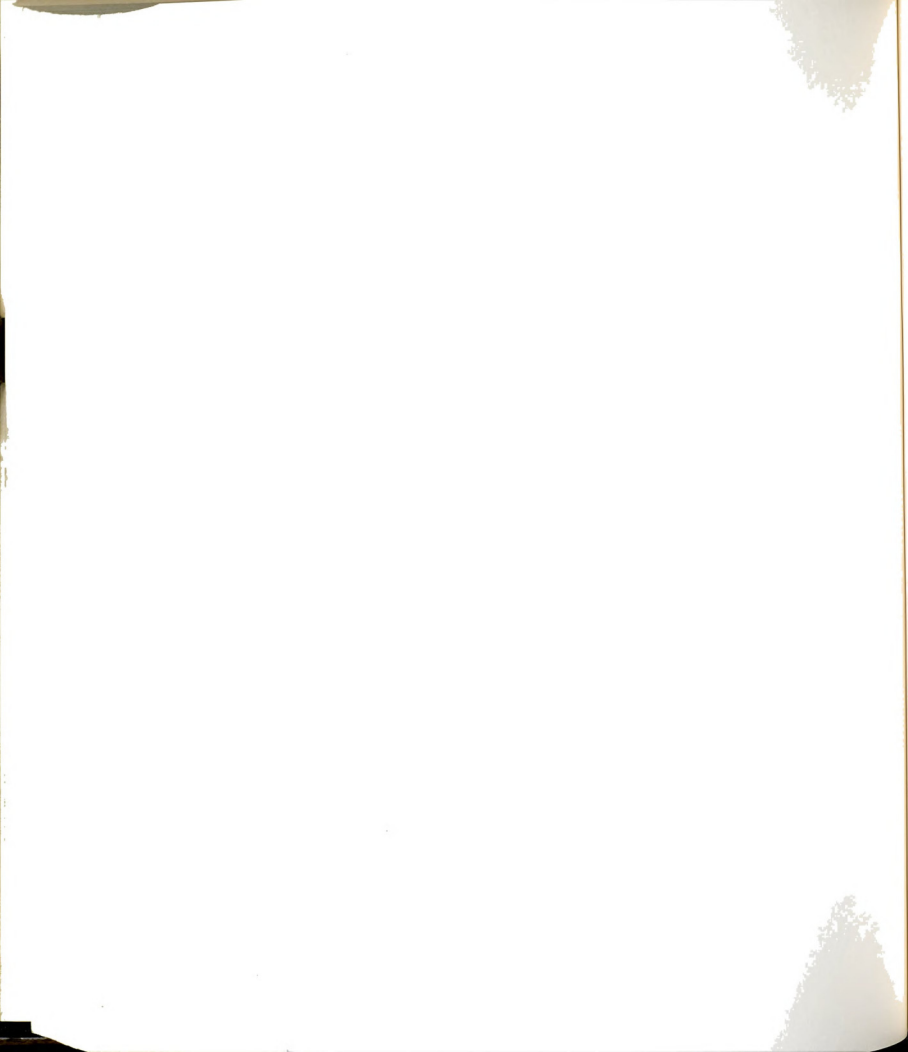


7.3.2.3.1 Velocity Distributions at $x/w=1$

Figure 177 and Figure 178 are the distributions of $\bar{u}^*(y^*)$ and $\bar{u}^*(y^*)$, respectively, at two values of Re . No data have been included from the regions where velocity reversals took place. The mean velocity profiles (Figure 177) at both values of Re have a top-hat distribution. The corresponding rms velocity profiles (Figure 178) show small values of \bar{u}^* ($\approx 5\%$) in the core region of the jet and considerably larger values ($\approx 17\%$) near the half width of the jet. Whereas the mean velocity profiles do not show a systematic dependence on Re , the rms velocity profiles do show considerable differences.

7.3.2.3.2 Velocity Distributions at $x/w=2.4$

The mean and rms velocity distributions at both values of Re are presented in Figure 179 and Figure 180, respectively. Again, only the data from those locations have been included at which no velocity reversals took place. The mean velocity profiles (Figure 179) do not exhibit a flat region and the velocity field is considerably wider than at $x = 1w$. Again, no systematic dependence of the mean velocity profiles on Re is observed. The rms velocity profiles as shown in Figure 180, at both values of Re , have a nominally uniform distribution across the jet.



7.3.2.4 Analytical Models of the Mean Velocity Profile

Equations (3) and (4) (Bickley and Montgomery profiles, respectively; see Section 1.2.3.1) are two of the analytical models of the mean velocity profiles which have been used by prior investigators to study the stability of two-dimensional jets. In this investigation, the mean velocity distribution at $x/w = 1$ was modelled by the Montgomery profile

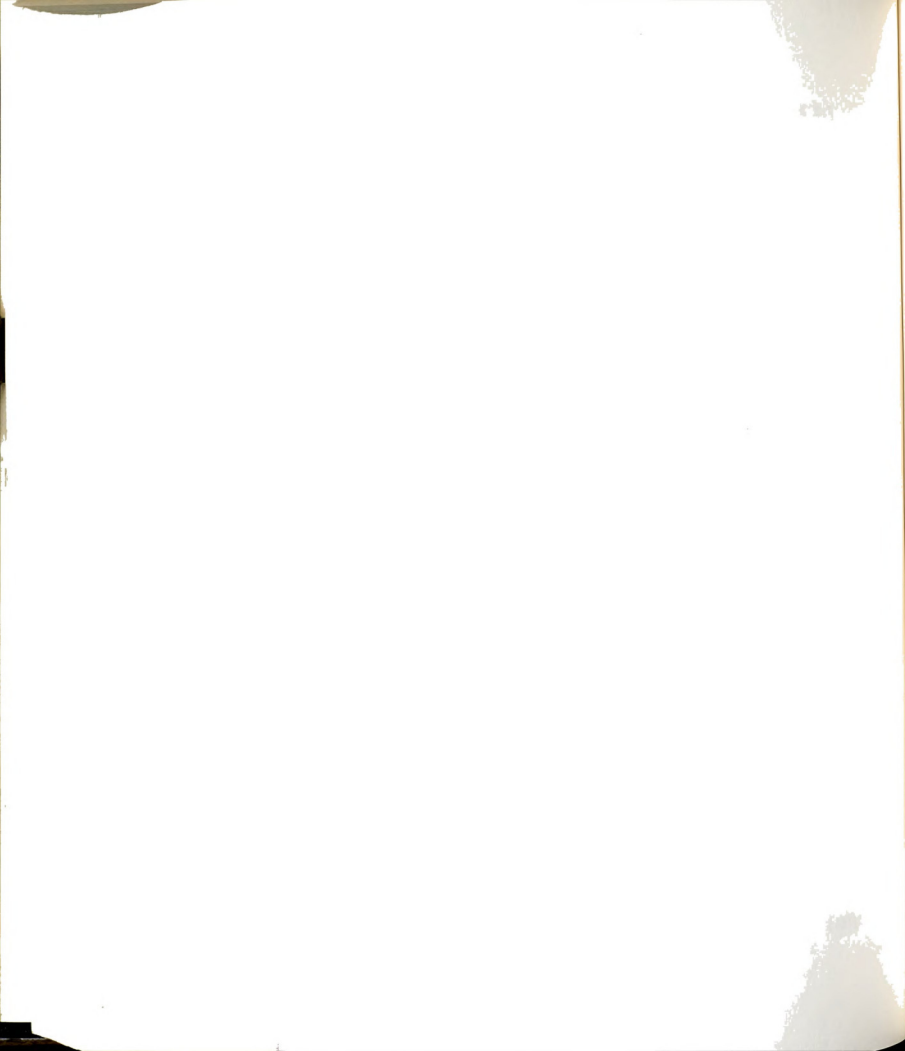
$$u(y) = \begin{cases} 1 & |y| \leq y_0 \\ \cosh\left[\frac{|y| - y_0}{\beta}\right] \exp\left[-0.5\left\{\frac{|y| - y_0}{\beta}\right\}^2\right] & |y| \geq y_0 \end{cases} \quad (164)$$

where y_0 and β are the two parameters. The former controls the extent of the flat region of the jet and the latter the slope. At $x/w = 2.4$, both the Montgomery profile and the Bickley profile were used to model the velocity distribution. The Bickley profile is expressed as

$$u(y) = \text{sech}^2(y/a) \quad (165)$$

where a is the parameter to be determined from the data.

A nonlinear parameter estimation program (developed by Beck (1989)) was used to determine the parameters y_0 and β in equation (164) and the parameter a in equation (165). The two parameters were



determined sequentially using the Modified Box Kanemesu method [Beck and Arnold (1977)].

7.3.2.4.1 Velocity Profile at $x/w = 1$

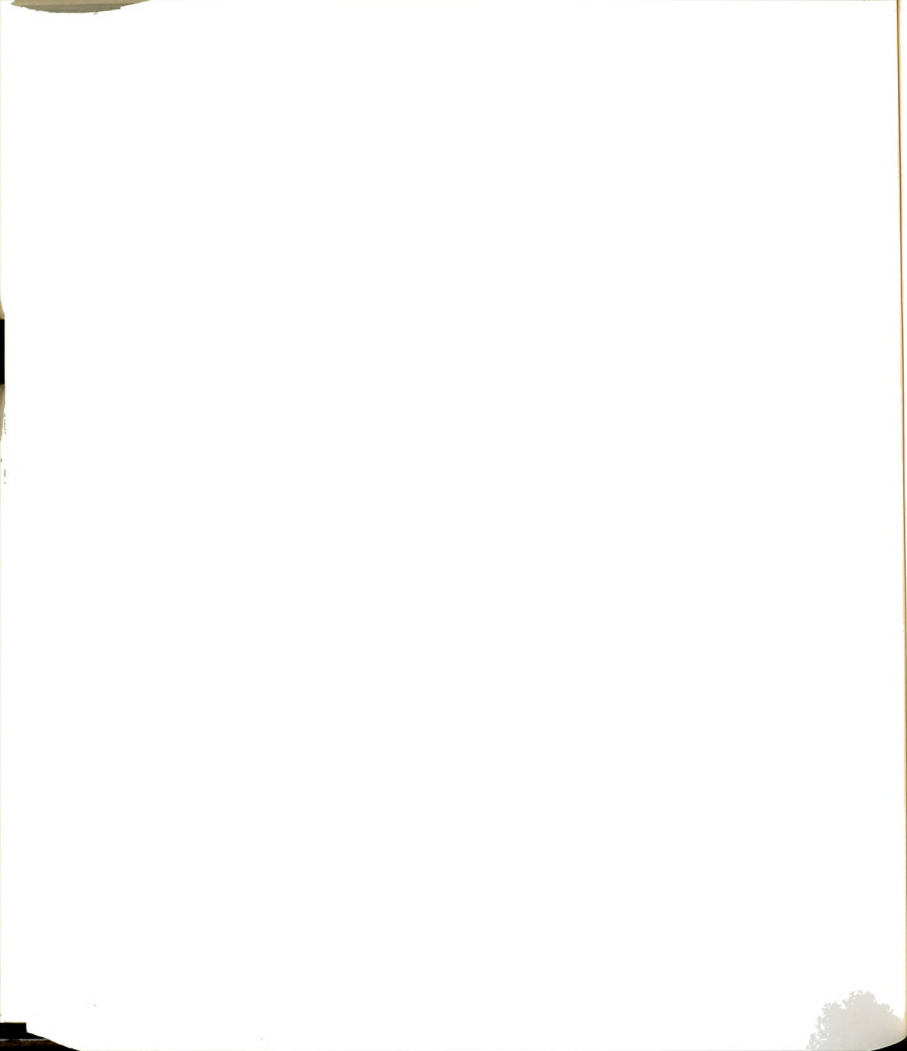
Using the data shown in Figure 177 (combined data for $Re = 1600$ and 3000), the two parameters were determined by using the ordinary least squares method to minimize the sum of squares of the residuals. The values of the parameters are

$$y_0 = 0.2019 \pm 0.0794 \text{ for } 95\% \text{ confidence interval}$$

$$\beta = 0.0685 \pm 0.0379 \text{ for } 95\% \text{ confidence interval}$$

Figure 181 shows the experimental data and the fitted curve. The data in closed symbols indicate the locations where some flow reversals may have taken place; these points were not included in the least squares fit.

As shown in Figure 181, the Montgomery profile models the measured mean velocity profile very well. The flat region of the jet extends over $-0.2 \leq y/w \leq 0.2$. The half width b of the jet, defined as the value of y at which $\bar{u}(x,y) = 0.5U_0$, was determined from the fitted profile. At $x/w=1$, $b=0.338w$. The analytical model expressed by the equation (164) has been used to investigate the stability of the flow. See Section 8.3.



7.3.2.4.2 Velocity Profile at $x/w=2.4$

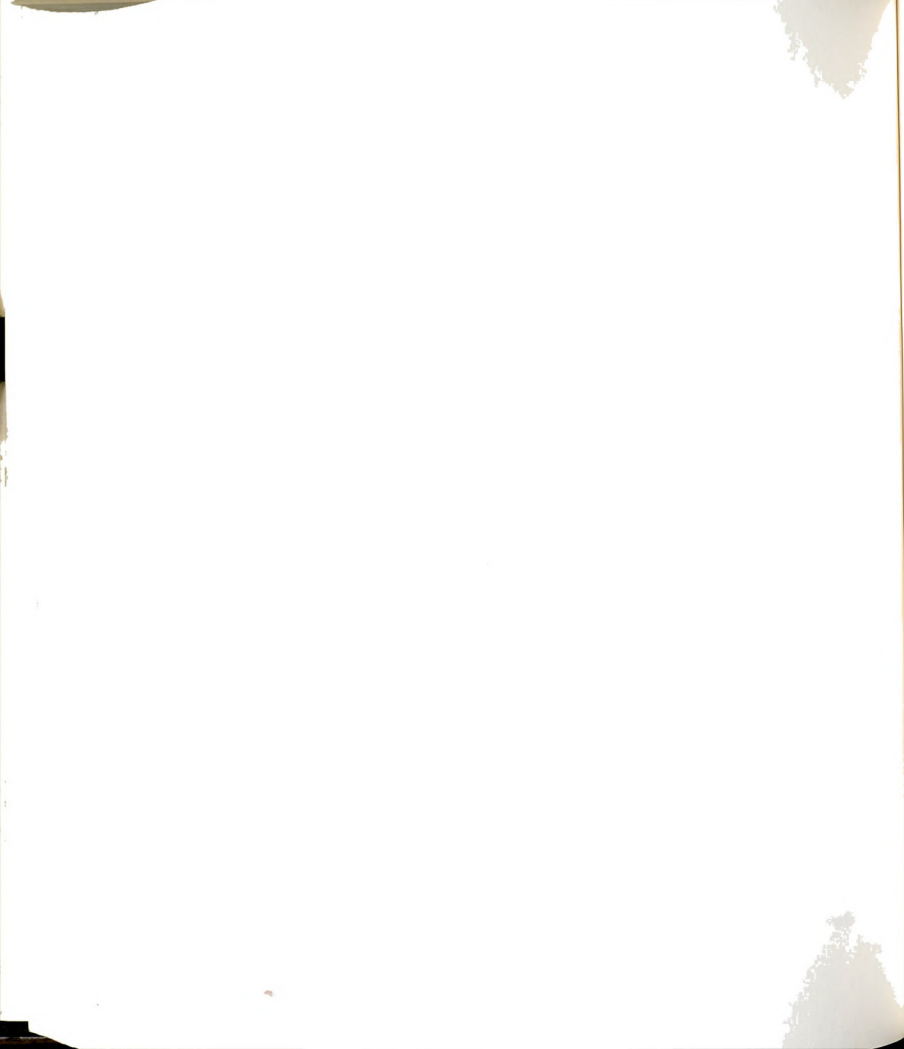
Figure 179 shows the measured $\bar{u}^*(y^*)$ distribution at $x/w=2.4$. A similar attempt to fit equation (164) with two parameters y_0 and β did not succeed. However, with y_0 set equal to zero (i.e. no flat region), the program was used to determine β which was found to be

$$\beta = 0.216 \pm 0.043 \text{ for } 95\% \text{ confidence interval.}$$

The measured data and the fitted curve are presented in Figure 182. The data in closed symbols were not included in the determination of β . The fit in this case is not so good as in the case of the data at $x/w=1$. The trend, however, is clear: in the near-field of the jet, the top-hat mean velocity profile of the jet (Figure 181) evolves into a rounded velocity distribution (Figure 182) as the distance from the exit plane increases. Equation (165) expresses the normalized velocity profile for the Bickley Jet which has a rounded velocity distribution. Using the same data which were used for the Montgomery profile, the nonlinear parameter estimation program yielded

$$a = 0.529 \pm 0.122 \text{ for } 95\% \text{ confidence interval.}$$

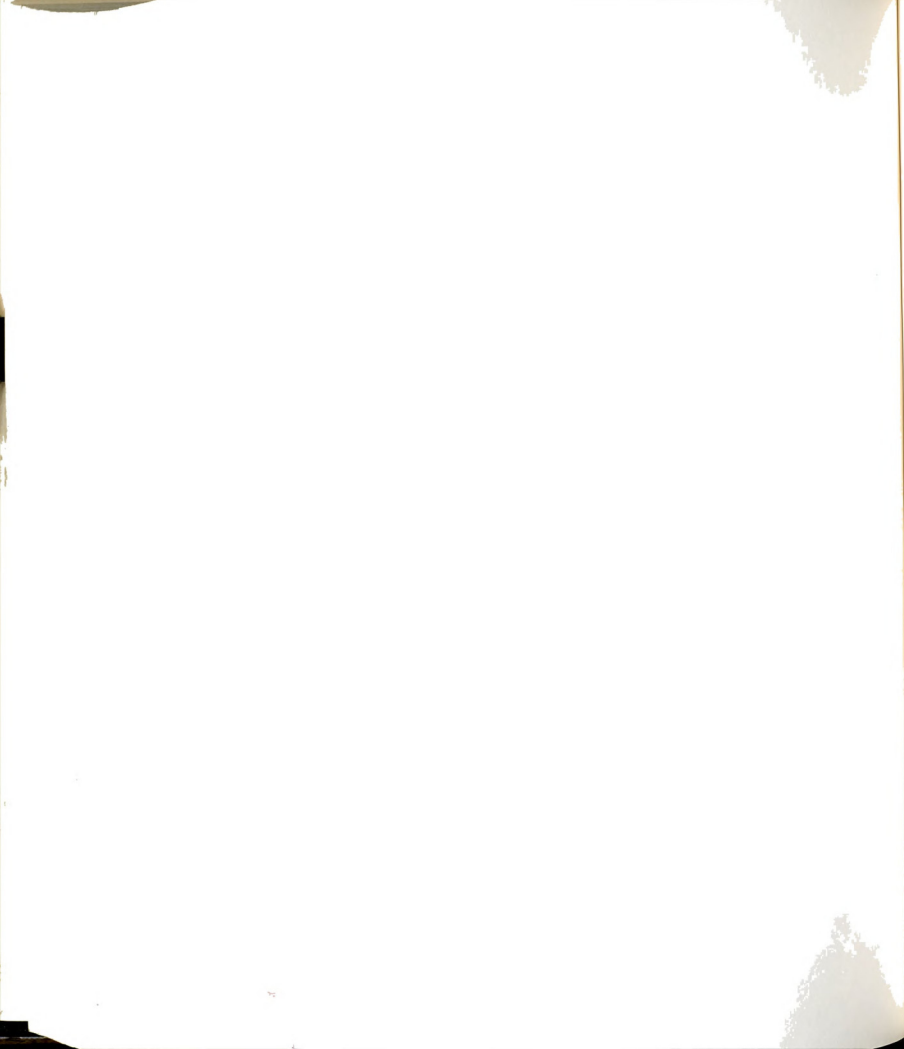
Figure 183 shows that the fitted curve and the experimental data agree quite well in the high speed region of the jet. In the low speed region, however, this profile predicts higher values of velocities. As far as the overall fit is concerned, the Montgomery profile seems to



better represent the measured data; this is inferred from the data which were not included in determining the parameters of the velocity profile function. These data, from the locations where some flow reversal took place, give a higher estimate of the mean velocity, i.e., their true locations should be somewhat lower than shown in Figure 182 and Figure 183. The Montgomery profile appears to predict this behavior better than the Bickley profile.

The half width, b , of the jet at $x/w=2.4$ was determined both for the Montgomery and Bickley profiles. For the former, $b=0.437$ and for the latter, $b=0.467$.

A comparison of the mean velocity profiles at $x/w=1$ and $x/w=2.4$, shows the erosion of the flat region of the jet within a streamwise distance of $1.4w$. The nature of the velocity profile rapidly changes over this distance. Between these two locations, the rate of decay of the flat region of the jet is about twice the rate of growth of the half width of the jet.



7.4 Autospectrum - Definition, Examples and Uses

Section 7.4.1 presents the definition of power spectral density function, or autospectrum, of a discrete time series like the measured velocity data, $u(t)$, in this investigation. Section 7.4.2 presents examples of the autospectra of $u(t)$ and the uses of this function in this study.

7.4.1 Power Spectral Density Function

The power spectral density function or autospectrum $\tilde{G}(f_k)$ of a discrete variable x_n is defined as [Bendat and Piersol (1971)]

$$\tilde{G}(f_k) = \frac{2h}{N} |X_k|^2 \quad (166)$$

where

$$X_k = \sum_{n=0}^{N-1} x_n \exp[-j \frac{2\pi kn}{N}] \quad (167)$$

is the discrete Fourier transform of the discrete time series x_n . N is the number of points in the measured data array and h is the sampling time interval. The discrete frequency f_k is expressed as

$$f_k = \frac{k}{Nh} \quad k=0,1,\dots,N-1. \quad (168)$$

If the variable x_n is replaced by the measured, discretized velocity samples of $u'(t) [= u(t) - \bar{u}]$, the $\tilde{G}(f_k)$ represents the autospectrum of

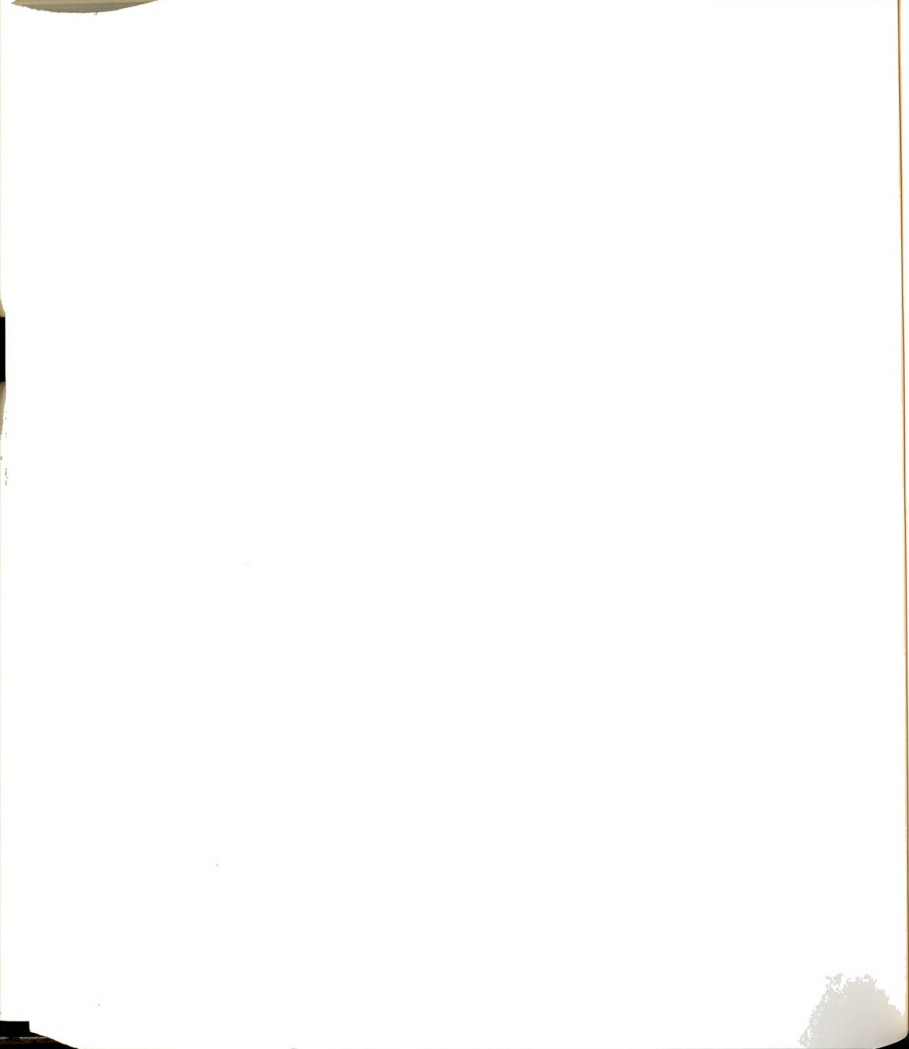


the velocity field. Methods of Fast Fourier Transform (FFT) were used to estimate X_k . A total of 4096 data points were used in the FFT computations, and, a partial Hanning window was used to decrease the power leakage to the side lobes. Variance of $u(t)$ was used to normalize the estimates of the power spectral density function.

7.4.2 Examples and Uses.

Figure 184 and Figure 185 present the normalized autospectra at two different values of Re in a jet at $x/w=1$. Whereas, the autospectrum in Figure 184 shows the presence of a dominant disturbance at a frequency $f_k=1.32$ Hz, the autospectrum of Figure 184 has two equally dominant disturbances at $f_k=1.36$ and 2.67 Hz, respectively. In the case of the former, the frequency of the dominant disturbance in the velocity field can be taken to represent the passage frequency of the vortex motions. In the case of the latter, such a passage frequency cannot be defined.

The autospectra of the velocity field has been used in Section 7.5 to identify the background disturbances, and in Section 7.6 to determine the nondimensional passage frequency of the vortex motions or Strouhal number St_v .



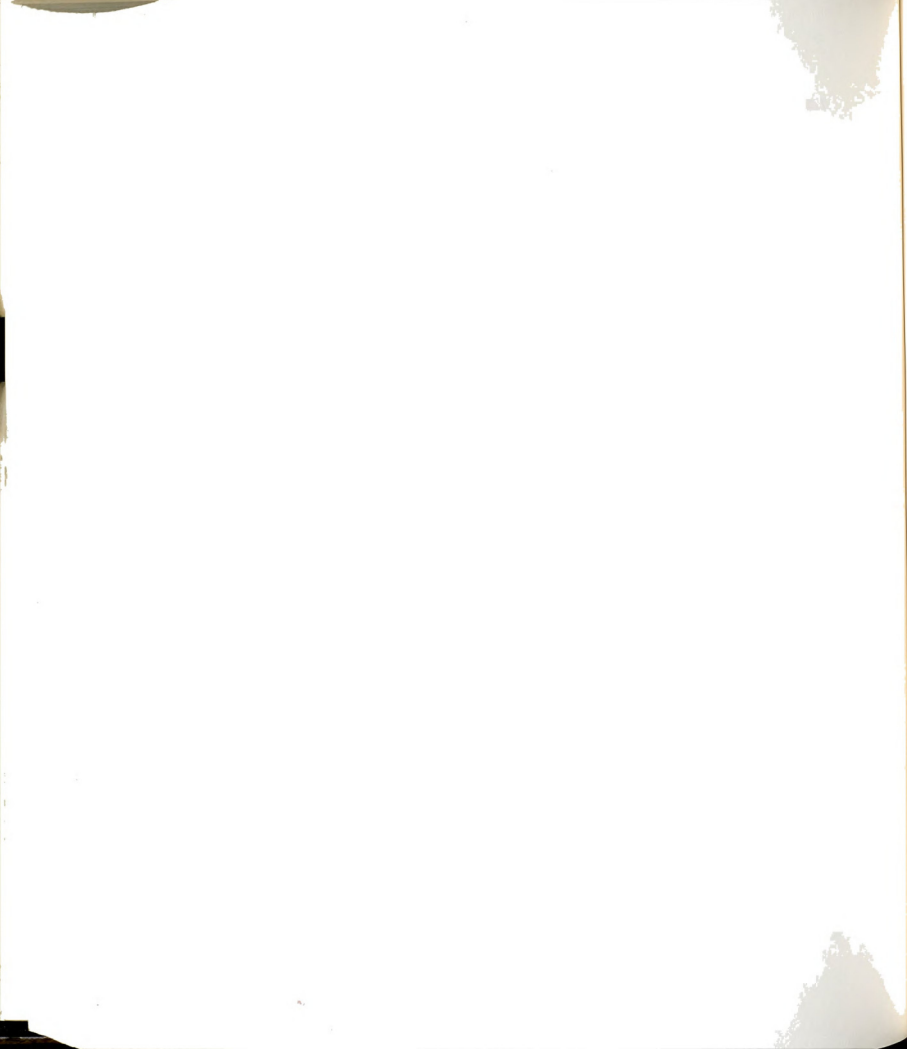
7.5 Identification of Background Disturbances Using the Autospectra

The normalized power spectral density function, $\bar{G}(f_k)$, provides a useful tool to identify frequencies at which substantial disturbances may be present. Ideally, in an investigation designed to study the instability of a jet, the magnitude of the background disturbances in the plenum should be quite small when compared with the intensity of fluctuations in the active regions of the jet. In addition, the background disturbances should be like "white noise", i.e., their spectrum should be flat. In practice, however, the spectrum of the background disturbances is not flat, and, perturbations at some frequencies can be identified. The disturbances at these frequencies may or may not influence the natural growth of disturbances caused by the instability of the jet. For the flow facility used in the present investigation, two possible sources of generation of background disturbances are:

- i) the process of filling the plenum;
- ii) during the execution of the experiment.

The purpose of this section is to examine the autospectra of the velocity data to identify the influence of the background disturbances over a wide range of Re :

- i) at $x/w \approx 2.0$ for two different protocols of filling the plenum, viz, with and without the use of the filling device;



- ii) at $x/w \approx -1$, in jets with two different widths and with the use of the filling device.

7.5.1 Influence of Disturbances Induced by Two Different Filling Processes

Experiments were conducted over a wide range of Re (300-6500) in a jet with $w=2.55$ cm in order to study the influence of the nature of background disturbances on the development of the jet. Two different types of disturbances were naturally generated in the plenum during the filling process depending upon whether or not the filling device was used. (See Section 3.2.2.)

Figure 186 illustrates the autospectra of $u(t)$ at $Re=950$ for two different protocols of filling the plenum. The curve marked with NF indicates that the filling device was not used, whereas the curve marked with F indicates that the filling device was used. Similarly, Figure 187 presents the autospectra for the two cases at $Re=2000$. Whereas, at $Re=950$, the frequency of the dominant mode is equal to 0.527 ± 0.0375 Hz for both cases, at $Re=2000$, the frequency of the dominant perturbation for the NF case is 1.280 ± 0.0375 Hz and for the F case it is 1.656 ± 0.0375 Hz. This difference at $Re=2000$ is attributed to the reproducibility of the experiment rather than to the influence of the background disturbances. In some cases, as shown in Figure 185 two or more peaks of comparable strength occur in the autospectra. Figure 188 is a composite plot of the frequency, f_k , of the dominant fluctuation as a function of Re for the two cases; the open symbols



represent the NF case whereas the closed symbol the F case. This plot includes information from the autospectra in which multiple peaks were observed; such cases occurred both for F and NF conditions. The plot clearly shows that no significant differences exist between the F and NF cases. The linear rise of frequency with Re confirms the observation of BW. (See Figure 8 of their paper.)

The velocity data that were used to compute the autospectra and generate Figure 188 were also used to determine two additional measures of the flow field: the discharge coefficient C_D , and the normalized rms of the velocity fluctuations \tilde{u}/U_0 , as a function of Re. Figure 189 presents the distribution of C_D with respect to Re. Again the open symbols represent the NF condition and the closed symbols the F condition. Similarly, Figure 190 presents the distribution of \tilde{u}/U_0 as a function of Re. For $Re > 3500$, the values of rms, \tilde{u}/U_0 , for F cases are observed to be smaller than the corresponding values for NF cases (with the exception of the $Re \approx 4200$ condition). The reason for this is not clear; however, it can be argued that since no consistent trend is observed in the f and C_D distributions (Figure 188 and Figure 189), the observed trend in \tilde{u}/U_0 distribution is not related to the nature of disturbances.

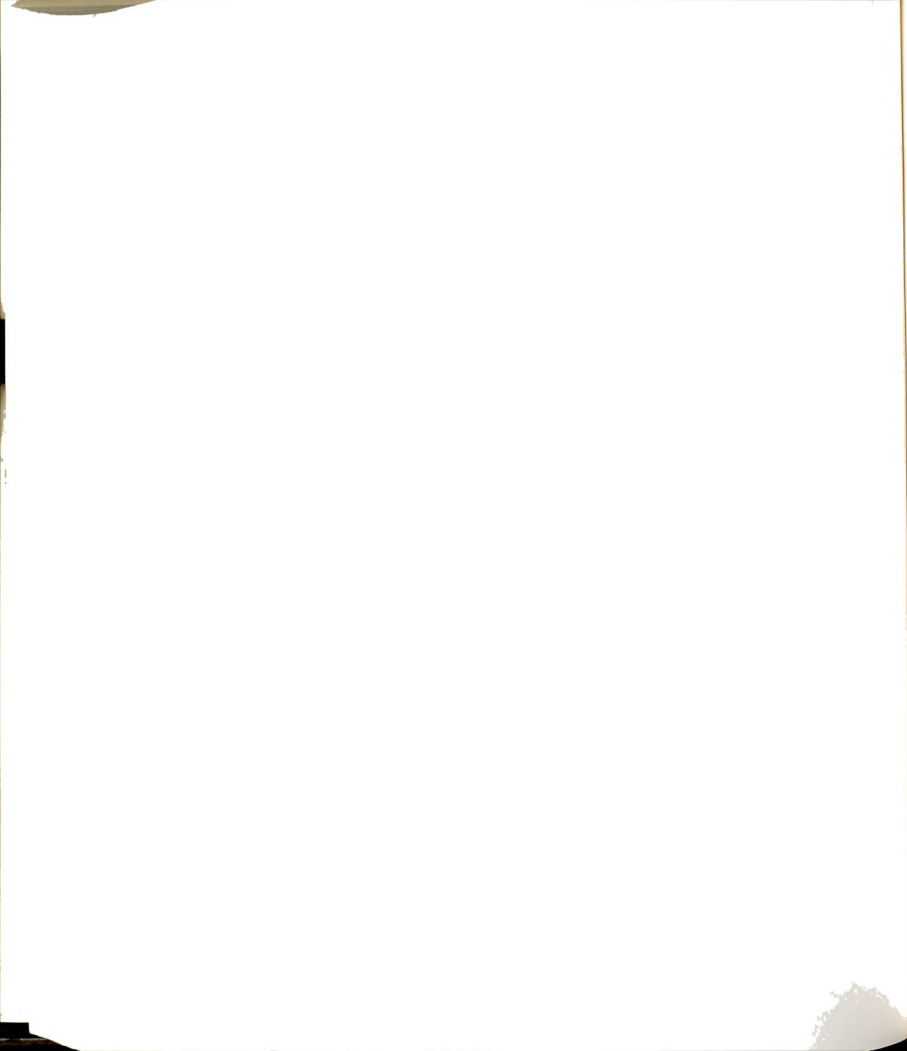
It is therefore concluded, based upon two different measures of the flow field at $x/w=2$, that the two different residual disturbances in the plenum do not influence the development of the jet. As noted in Section 3.6, according to the protocol of executing the



experiments, a time period of five minutes or more was allowed to elapse between the filling of the plenum and the execution of the experiment. It is believed, based upon some exploratory experiments (results not included here), that the waiting period helped minimize the residual disturbances to a level that the background disturbances did not influence the development of the jet. This shows that in a gravity driven flow facility like the present one, if the generation of disturbances can be controlled during the execution of the experiment, the resulting flow field would be free from extraneous disturbances since the disturbances induced during the charging of the plenum can be effectively minimized by allowing a longer waiting time.

7.5.2 Background Disturbances in the Plenum

The autospectra of $u(t)$ data from the plenum, about one slit width upstream of the nozzle plates, were examined over a wide range of Re (500-2900) in order to determine whether or not the background disturbances could be treated as white noise. Water was used as the working fluid and the filling device was used for charging the plenum. Figure 191 is a plot of the distribution of the intensity of velocity fluctuations as a fraction of the total rms of the velocity fluctuation, $\bar{u}(f)/\bar{u}$, at $x/w=-1$. These plots show that the residual disturbances are not like white noise; note the presence of some disturbances in the autospectra in the frequency range of 2-3 Hz. For some reason in the Re range ≈ 1000 , ($Re=988$ and 1011), the peak contribution of this disturbance to the total rms is of the order of 15%; in all other cases it is less than 10%. It is believed that the



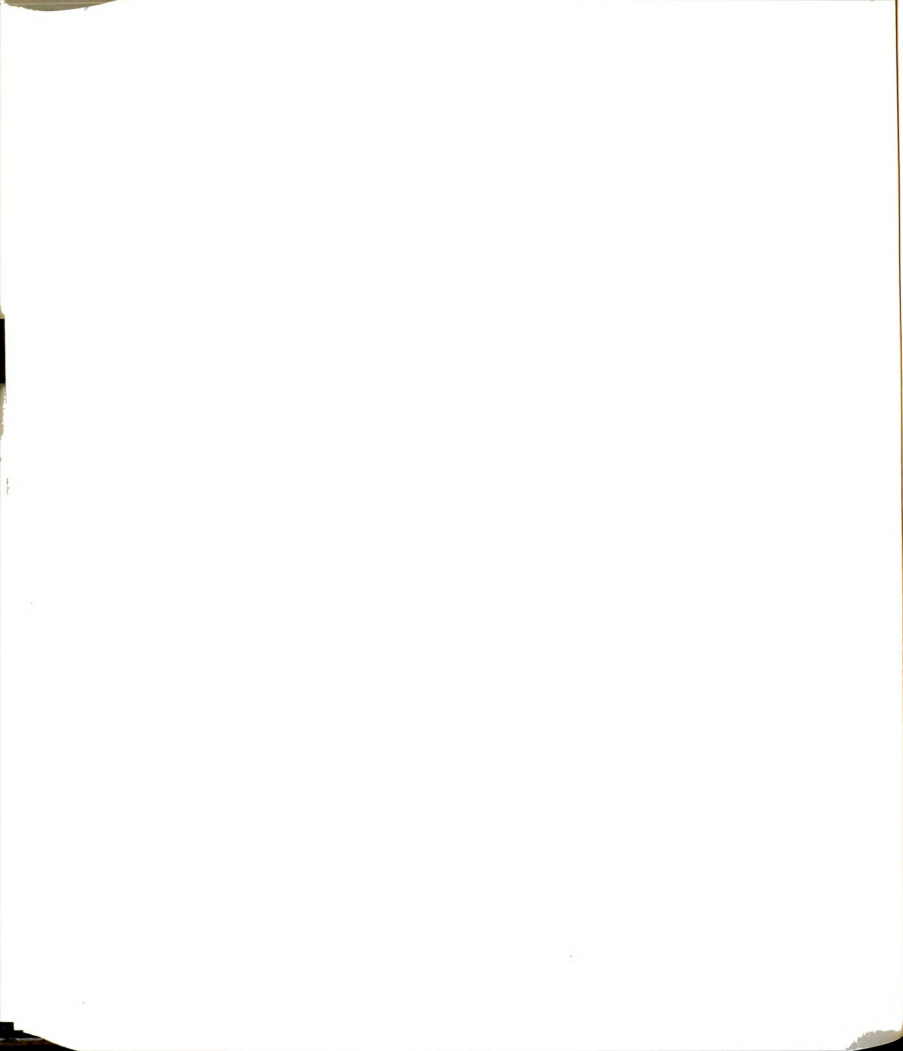
presence of this disturbance in the frequency range of 2-3 Hz is not a width dependent phenomena: two of the cases presented in Figure 191 ($Re=509$ and 1231) are for a jet with $w=1.27$ cm, whereas the rest are for a jet with $w=2.57$ cm. The origin of the disturbance shown in Figure 191 is not known. It could be the residual effect of the use of the filling device in the plenum which needs a longer time to decay, or, it could be introduced during the execution of the experiment.

It will be shown in a later section, by comparing the results of experiments from jets of two different slit widths, that the presence of this disturbance does not alter the process of the natural growth of disturbances. In other words, even though the disturbance field is not like white noise the slit-jet flow field is robust enough to select the disturbance at a specific frequency which represents the stability frequency of the flow field

7.6 Determination of Strouhal Number St_V from the Autospectra

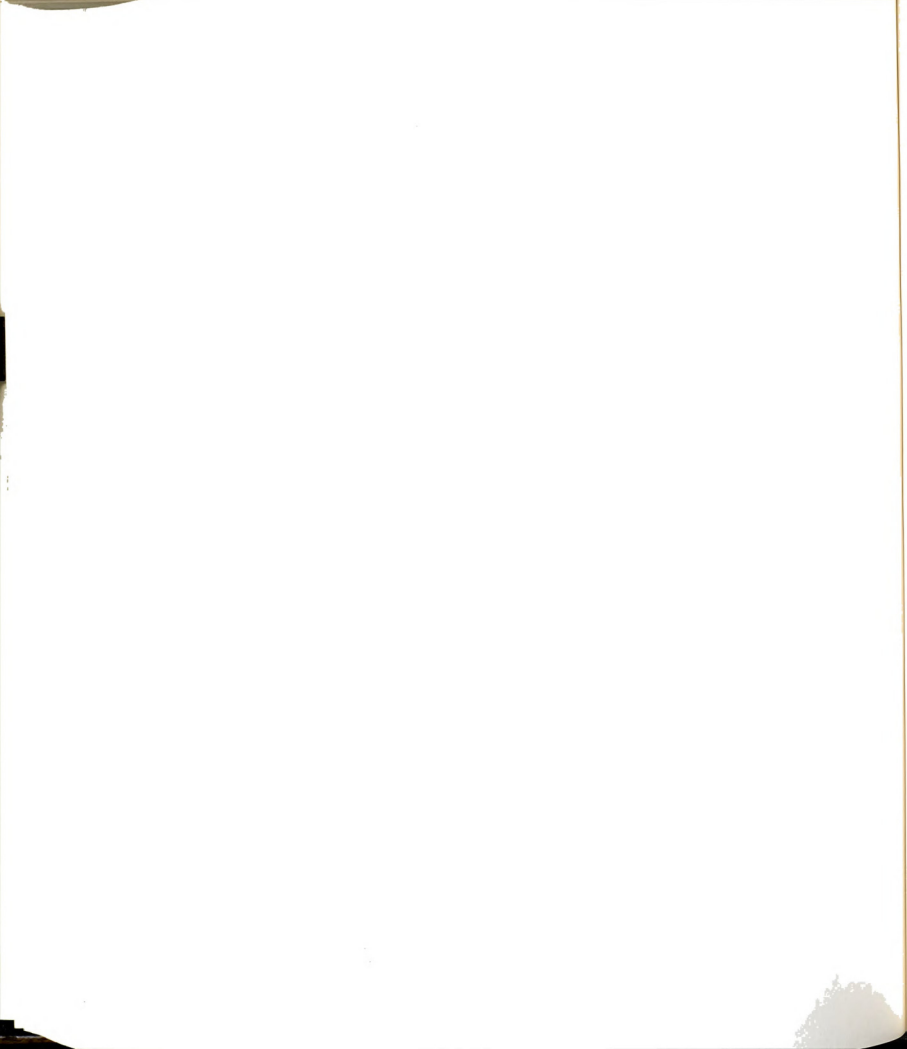
The nondimensional passage frequency of the vortex motions (or Strouhal number) was determined from the flow visualization data (St_F). These results were presented in Section 6.3.1. In principle, the same information can be derived from the time traces of the measured velocity (Figures 160 through 167). The Strouhal number, St_V , from the velocity data has been determined from

$$St_V = \frac{f_V w}{\langle U \rangle} \quad (169)$$



where f_v is the frequency of the dominant fluctuation in the power spectral density function, $\tilde{G}(f_k)$, of the measured velocity, $u(t)$. See Section 7.4. f_v is taken to represent the passage frequency of the vortex motions. It was argued in Section 7.4 that, whereas, a power spectrum with a single dominant peak (see Figure 184) can be used to estimate the passage frequency of vortex motion, no such unambiguous information can be derived from a power spectrum which exhibits multiple peaks of nominally equal strength. See Figure 185. Hence, for consistency, only those autospectra have been used to estimate the Strouhal number, St_v , in which the ratio of the magnitude of the second dominant peak to the magnitude of the dominant peak does not exceed 0.35. For example, the autospectrum of Figure 184 satisfies this criterion, but, the autospectrum of Figure 185 does not.

Section 7.6.1 presents the estimates of St_v as a function of Re at two x/w locations. In Section 7.6.2 the spatial behavior of the growth/decay of the disturbances at specific values of St_v is illustrated using the plots of $\tilde{u}(St_v, Re, x^*)/\tilde{u}(Re, x^*)$. Section 7.6.3 presents the results from the combined LDA-flow visualization experiments.



7.6.1 Distribution of $St_V(x^*, Re)$

Figure 192 presents the distribution of St_V as a function of Re at $x/w=1$. Each data point in this plot represents the nondimensional frequency of a dominant fluctuation which satisfies the criterion established in the introductory remarks of Section 7.6. Given the scatter in the data no systematic dependence on Re can be discerned. The average and the rms values of St_V are 0.70 and 0.07, respectively. Figure 193 presents the distribution of $St_V(Re)$ at $x/w=2.2$; data from two different jets are included. At this location, using the data from both jets, the average and the rms values of St_V are 0.52 and 0.07, respectively.

In Section 7.5.2 it was shown that the autospectra of $u(t)$ in the plenum over a wide range of Re was not like white noise because of the presence of a disturbance around $f_k \approx 2.5$ Hz. (See Figure 191.) The robustness of the slit-jet flow field in the presence of this disturbance will be shown here. Figure 193 shows good agreement between the estimates of St_V for two different size jets. The ratio of their widths is 2.02:1. Note that when the slit width w is reduced by a factor r , the frequency f_v must increase by r^2 to yield the same Strouhal number for the same value of Re . This is shown below.

The characteristic velocity $\langle U \rangle$ can be expressed as

$$\langle U \rangle = \frac{\nu Re}{w} \quad (170)$$



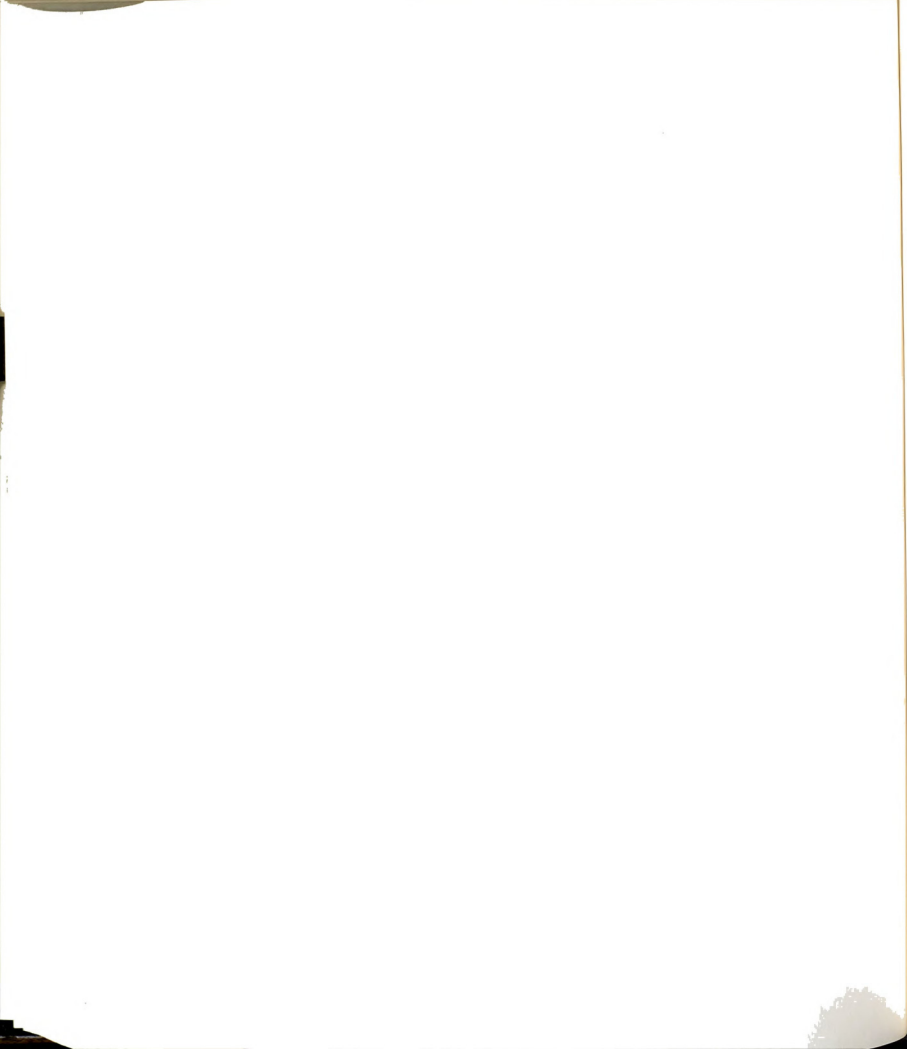
Substituting this in equation (169) St_V becomes

$$St_V = \frac{f_V w}{\langle U \rangle} = \frac{f_V w^2}{\nu Re} \quad (171)$$

In the present case $r=2.02$. Hence, for the smaller size jet ($w=1.27$ cm) the frequency of the dominant mode should be 4.1 times the frequency in the wider jet ($w=2.57$ cm). Figure 194 presents the frequency of the dominant mode in the two jets as a function of Re . (Same data were used to prepare the plot shown in Figure 193.) The solid lines in Figure 194 are the best straight line fits through the data. Both lines were forced to pass through the origin. The ratio of their slopes is 4.72 which is about 15% larger than the expected value of 4.1. The good agreement between the expected and the measured values of the frequency ratio, at a given value of Re , shows that the instability process in the slit-jet flow field is insensitive to the presence of low level extraneous disturbances in the plenum, i.e., the disturbance at the instability frequency can grow even in the presence of very low level background disturbances.

7.6.2 Distribution of $\tilde{u}(St_V, Re, x^*)/\tilde{u}(Re, x^*)$

The plots of $St_V(Re)$ presented in the previous section show an overall behavior of the dominant disturbance in the flow field at specific x/w locations. However, the disturbances at specific St_V grow in the downstream direction, reach a maximum value and then decay. This aspect of the growth and decay of disturbances is examined from the plots of $\tilde{u}(St_V, Re, x^*)/\tilde{u}(Re, x^*)$. This quantity is



calculated from the normalized power spectral density function, $\bar{G}(St_V)$; the square root of the product of $\bar{G}(St_V)$ and ΔSt_V yields the desired ratio. It also expresses the contribution of the velocity fluctuations at a certain x/w location for a given St_V to the total velocity fluctuations.

An examination of the autospectra of $u(t)$ for a given value of Re and at various x/w locations shows that the intensity of disturbances at certain frequencies attain significantly higher values than the disturbances at other frequencies. These frequencies were identified and the contribution of the corresponding disturbances to the total disturbance, $\tilde{u}(St_V, Re, x^*)/\tilde{u}(Re, x^*)$, was determined. For example, Figure 195 is a plot of the ratio $\tilde{u}(St_V, Re, x^*)/\tilde{u}(Re, x^*)$ as a function of x/w at $Re \approx 1000$. It illustrates the growth and decay of disturbances at three values of St_V , namely, 1.7, 1.2, and 0.55. Note that the fluctuation at $St_V=1.7$ in Figure 195 corresponds to the ubiquitous disturbance around 2.5 Hz. It is observed that at this value of Re the disturbance at $St_V=1.7$ grows very little ($< 10\%$) and then is attenuated. The perturbation at $St_V=1.2$ and 0.55 both grow up to $x/w=1$. Beyond this location the perturbations at $St_V=1.2$ decay whereas those at $St_V=0.55$ continue to grow.

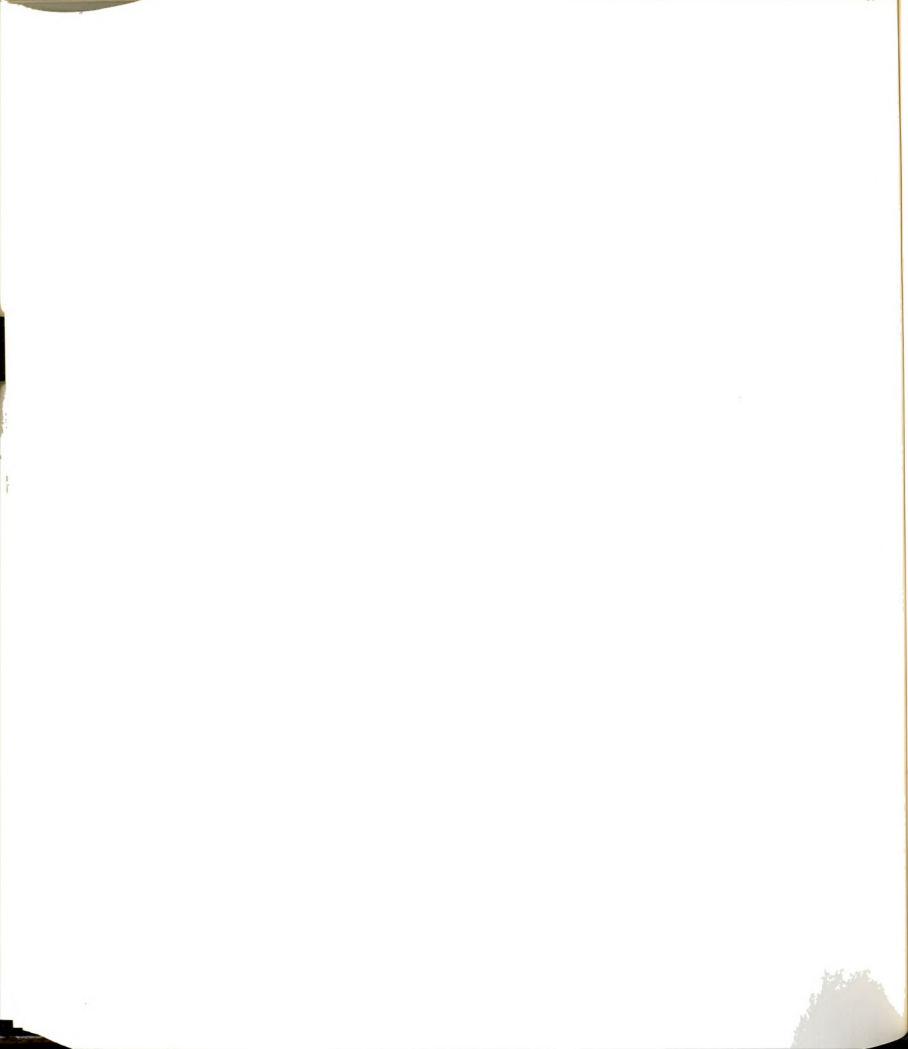
Figure 196 is another example of growth/decay pattern at $Re \approx 1300$. Here, the disturbance at $St_V=1.3$ represents the background disturbance at 2.5 Hz. As before, this disturbance exhibits some growth in the range $0 \leq x/w \leq 1$ before it decays. The perturbation at $St_V=0.7$ shows



considerable growth between x/w equal to 0 and 1 followed by a decay for $x/w > 1$. Similarly, the perturbations at $St_V = 0.3$ grows considerably between $x/w = 0.5$ and 2.2. The spatial lag in the growth of these perturbations and a reduction in the values of their frequency nominally by a factor of 2 suggest the occurrence of pairing between vortices which results in frequency halving. However, it is not clear whether or not the perturbation at $St_V = 0.7$ represents the first subharmonic of the background disturbance at $St_V = 1.3$. On the other hand, the perturbation at $St_V = 0.3$ is considered to represent the first subharmonic of the disturbance at $St_V = 0.7$. This conjecture is based upon the magnitude of the ratio $\tilde{u}(St_V, Re, x^*) / \tilde{u}(Re, x^*)$. Note that, whereas the perturbations at $St_V = 0.7$ and 0.3 become as large as 30% of \tilde{u} , the disturbance at $St_V = 1.3$ remains less than 15% of \tilde{u} .

Figure 197 presents the fluctuation intensities at selected Strouhal numbers for $Re = 2300$. Here the disturbance at $St_V = 0.80$ corresponds to the disturbance at 2.5 Hz. In this case, unlike the first two examples (Figure 195 and Figure 196) the frequency of disturbance in the plenum appears to correspond to an instability frequency of the slit-jet flow field. Again, as in the previous example, the growth of disturbances at $St_V = 0.4$ and $St_V = 0.2$ suggest the occurrence of pairing between vortex motions.

The following observations are based on the data of Figures 195, 196 and 197:

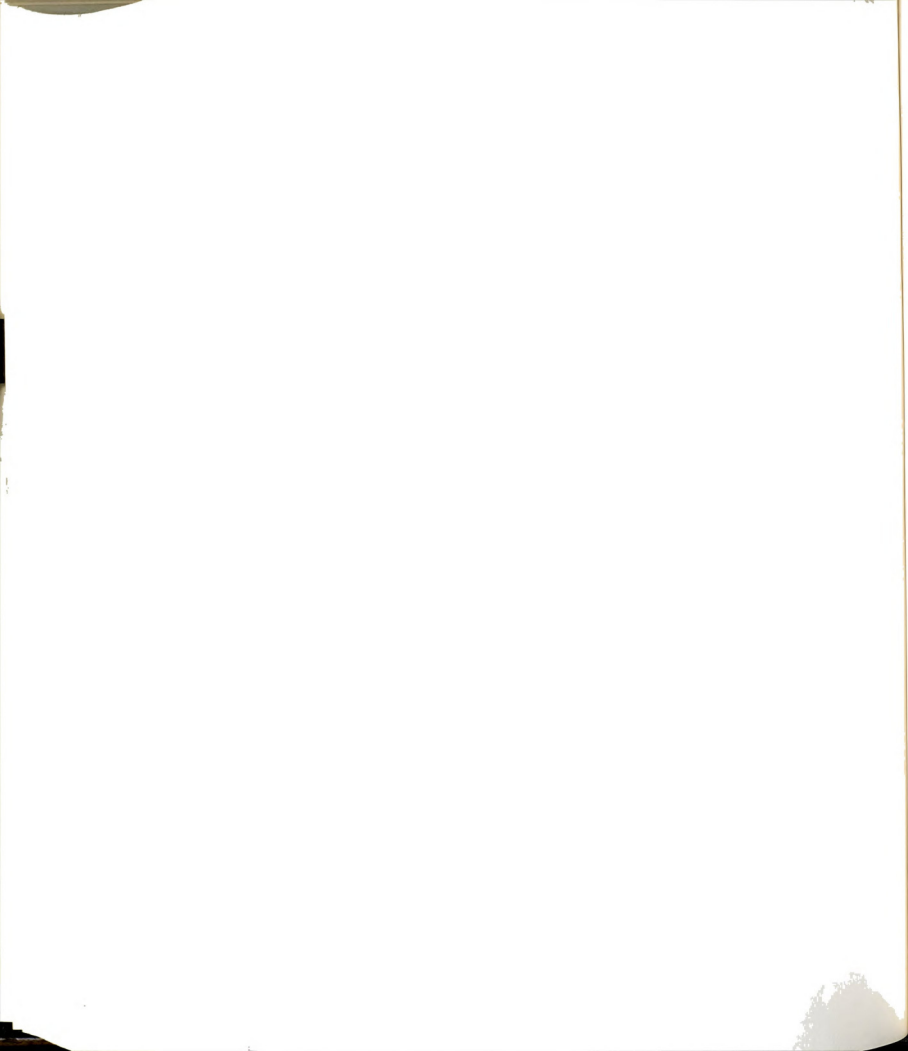


- i) The disturbances at specific frequencies begin to grow at a critical streamwise location x_c/w . From the limited available data x_c/w is estimated to be 0.25. Note that, as shown in Figure 170, the total rms grows exponentially over the range $-1 \leq x/w \leq 2.4$. This shows that, the disturbances at all frequencies grow equally up to x_c/w and then the disturbances at specific frequencies are amplified at a higher rate.
- ii) The disturbances at specific frequencies grow to a maximum value of 30% of the rms before beginning to decay.
- iii) There appears to be an attenuation of fluctuations in the neighborhood of $x/w \approx 0$.

7.6.3 Strouhal No. from the Combined LDA-Flow Visualization Experiments

A number of experiments were conducted with simultaneous flow visualization and measurement of jet velocity on the centerline of the jet. The details of the technique have been presented in Section 3.9.3. The experiments were run in a jet with $w=2.57$ cm and with water as working fluid. The Re range was 1000-3500. LDA velocity measurements were made at one of three locations $x/w=0.78$, 0.86, and 1.91.

The values of Strouhal number, St_F , were computed from the photographic records of the flow visualization experiments as described in

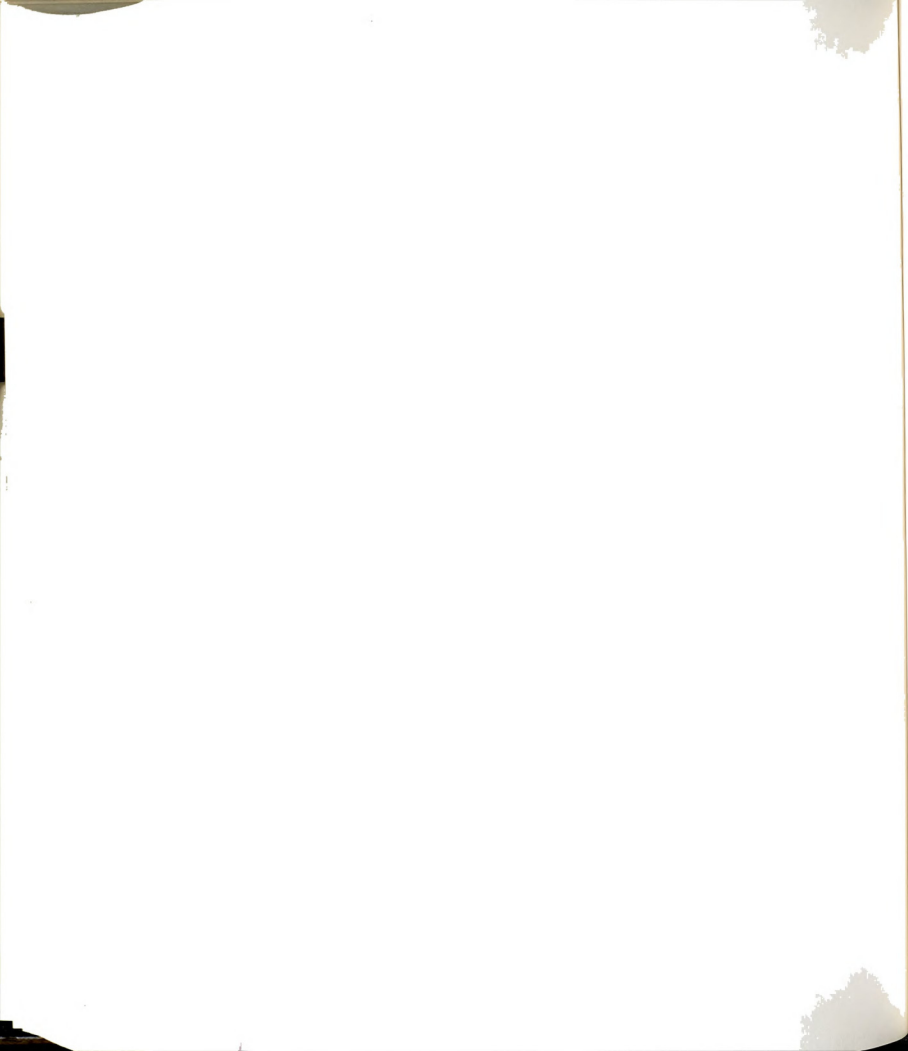


Chapters 5 and 6. The techniques described in this chapter (Sections 7.4 and 7.6) were used to compute St_V . Table 4 presents the values of St_V and St_F and the ratio of the two. A hyphen in the St_V column in Table 4 indicates that the autospectrum for that particular case did not exhibit a dominating peak. (See Section 7.6 for the criterion of accepting the frequency of a peak in the autospectrum as the passage frequency of vortex motions.)

Table 4 - St_F and St_V from the Combined LDA-Flow Visualization Experiments

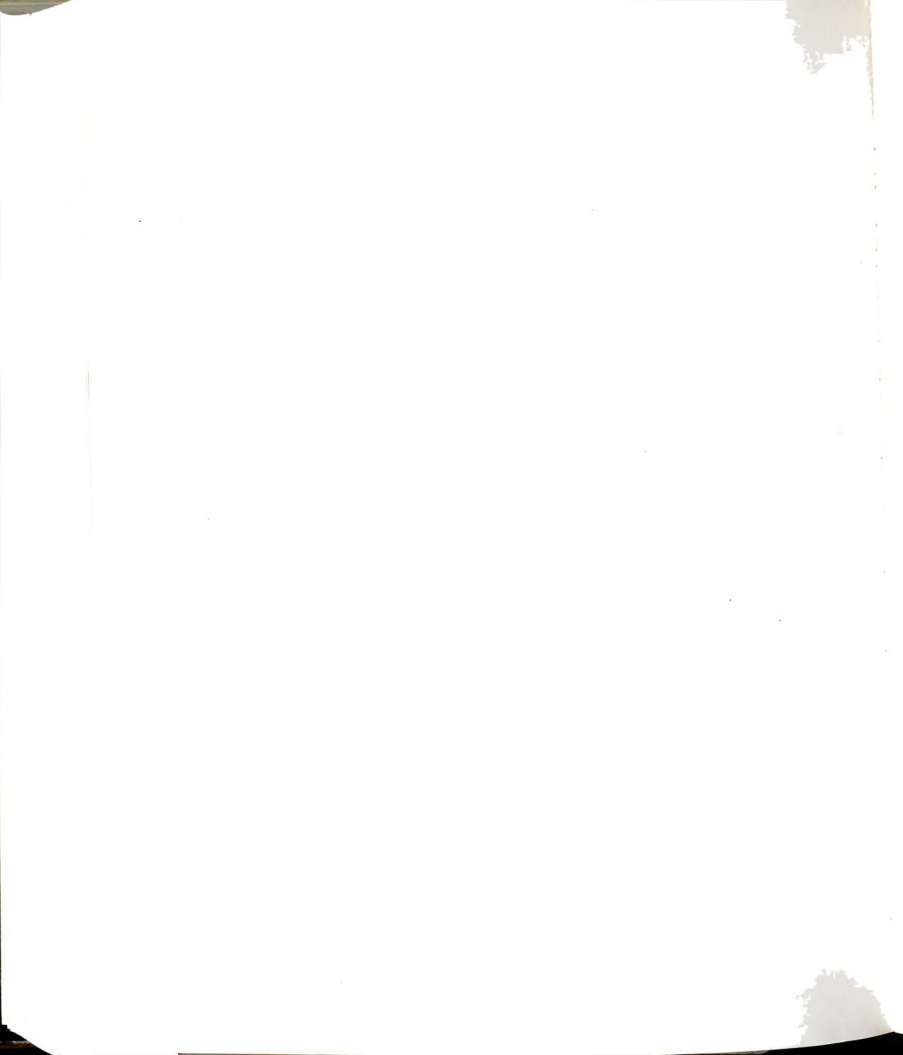
No.	x^*	Re	St_V	St_F	$\frac{St_F}{St_V}$
1	0.78	2299	0.79	2.11	2.68
2		2949	0.65	1.97	3.04
3		2964	0.64	1.89	2.94
4	0.86	1027	0.81	1.50	1.84
5		1063	-	1.43	-
6		1074	0.73	1.48	2.02
7		1685	-	1.39	-
8		1697	-	1.38	-
9	1.91	1001	0.47	0.98	2.07
10		1004	-	1.38	-
11		1571	0.54	0.93	1.73
12		1580	0.55	1.05	1.91
13		3389	-	1.24	-
14		3401	-	1.45	-
15		3469	0.50	1.34	2.67

Table 4 shows that the values of St_F and St_V do not agree for all values of Re and at each x/w location. The average value of the ratio St_F/St_V for $x/w < 1$, is 2.50 with an rms value equal to 0.54. At $x/w = 1.91$, the average and rms values of the ratio St_F/St_V are 2.10 and 0.41, respectively.



The nominal factor of 2 in the values of St_F and St_V suggest that the identifiable motions form at approximately twice the rate of the velocity fluctuations on the centerline of the jet. It was shown in Chapter 4 that the formation of a bulge marks the beginning of the process of the formation of a large scale vortex motion. Regarding the formation of the bulges it was conjectured that a localized rise of pressure in the jet caused a bulge to form. Based upon the results of this section, i.e., $St_F \approx 2St_V$, and the conjecture related to the formation of bulges, it might be argued that the pressure fluctuations occur at twice the frequency of the velocity fluctuations. The validity of this hypothesis will be tested in Section 8.4 using the model for the pressure fluctuations on the jet centerline which was developed in Section 2.5; the measured data will be used to evaluate the parameters in the model.





31293008955829





S. K. ALI * VOL 2

PH.D.

100
392
THS

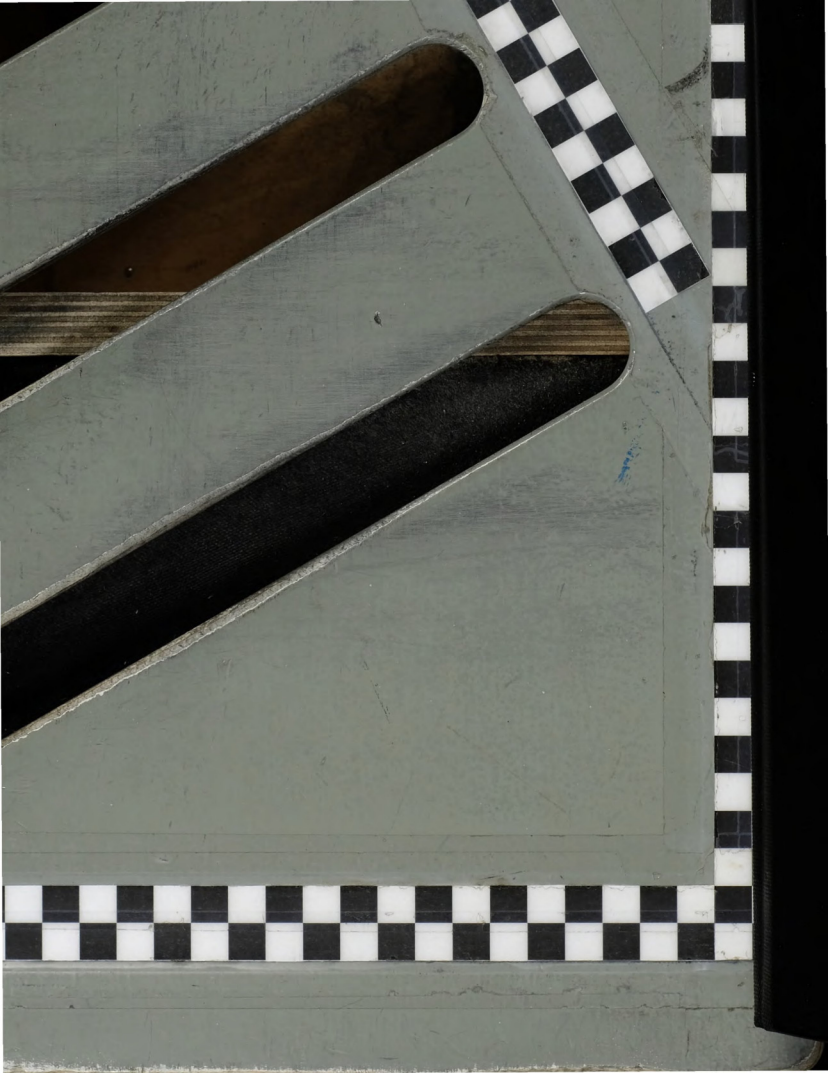
1991

PHD

100
392
THS

1991

PH.D.





LIBRARY
Michigan State
University

PLACE IN RETURN BOX to remove this checkout from your record.
TO AVOID FINES return on or before date due.

DATE DUE	DATE DUE	DATE DUE

MSU Is An Affirmative Action/Equal Opportunity Institution

c:\circ\date\due.pm3-p.1



INSTABILITY PHENOMENA IN A
TWO-DIMENSIONAL SLIT-JET FLOW FIELD

Volume II

By

Syed Khurshed Ali

A DISSERTATION

Submitted to
Michigan State University
in partial fulfillment of the requirements
for the degree of

DOCTOR OF PHILOSOPHY

Department of Mechanical Engineering

1991



STABILITY OF THE SLIT-JETS - INFERENCES, RESULTS AND DISCUSSION

8.1 Introduction

This chapter presents considerations of the the stability of the slit-jet flow field using the measured velocity data. The details of the velocity data have been presented in Chapter 7. This chapter is divided into four sections. Section 8.2 presents inferences on the stability characteristics of the slit-jet flow field based upon the power spectrum of $u(t)$ data which have been presented in Section 7.6. The results of the linearized stability calculations using the mean velocity profile $\bar{u}^*(y^*)$ are presented in Section 8.3. Section 8.4 determines the growth of pressure and velocity fluctuations along the centerline of the jet to test the hypothesis that the formation of bulges is caused as a result of a cyclic rise and fall of the pressure in the jet.



8.2 Inferences from the Autospectra of $u(x, y=0, t)$

This section presents inferences related to the growth of disturbances and formation of large scale vortex motions in the slit-jet flow field. The autospectra of the velocity data have been used in drawing these inferences.

8.2.1 Region of "Non-Selective" Growth of Disturbances

The region extending over $-1 \leq x/w \leq x_c^*$ (where x_c^* is a critical location) is considered to be a region of nonselective growth of disturbances. This consideration is based upon the observation that, whereas, \bar{u}/U_0 grows exponentially over $-1 \leq x/w \leq 2.4$ (see Figure 170), the autospectra of $u(t)$ over the range $-1 \leq x/w \leq 0.5$ suggest that the disturbances at all frequencies grow equally, i.e., no selective growth of a particular frequency occurs in this range. See Figures 195, 196, and 197. From the limited information available at discrete x/w locations, it is conjectured that the critical location x_c^* at which disturbances at specific frequencies begin to grow exponentially occurs between $x/w=0.25$ and 0.5 .



8.2.2 Region of "Selective" Growth of Disturbances

Beyond x_c/w (the critical location; see Section 8.2.1) the autospectra of $u(t)$ suggest that the slit-jet flow field begins to act as a "fine-tuned" amplifier; i.e., the instability mechanism of the slit-jet flow field allows only the disturbance at a particular frequency to grow. Hence, the region beyond x_c/w is considered as the region of selective growth of disturbances.

8.2.3 Influence of Pairing of Vortices on $St_V(x^*)$

It is known from the results of flow visualization experiments that vortex motions undergo mutual interactions leading to pairing which results in frequency halving. This process occurs over some finite spatial domain of the flow field which may be described as a "region of mutual interaction". The autospectra of $u(t)$ in this region would exhibit at least two dominant peaks. Figure 198 illustrates the transition of flow field (through pairing), at $Re=510$, from $St_V=0.71$ at $x/w=0.9$ to $St_V=0.37$ at $x/w=2.12$. It is believed that the autospectra of $u(t)$ at $x/w=1.34$ lies in the region of mutual interaction. Note that the autospectrum at $x/w=1.34$ shows fluctuations at $St_V=0.37$, 0.76 and also at 0.56 which is the average value of 0.37 and 0.76 .

8.2.4 Quasiperiodicity in an Unexcited jet

A comprehensive examination of the flow visualization results (Chapters 4 and 6) and the results of measured velocity (Chapter 7) indicate the presence of quasiperiodicity in the naturally excited jets. This results in variations in the estimates of quantities like Strouhal number and wavelength. Better estimates of the instability characteristics would seem to require longer duration data records.

8.3 Stability Calculations Using the Lateral Mean Velocity Profiles

In Section 2.4 formulations were developed and a procedure was outlined to solve the linearized Euler equation of motion for a given mean velocity profile, $\bar{u}^*(y^*)$, as the basic flow state. The analytical models of the measured mean velocity profile determined in Section 7.3.2.4 were used to perform the stability calculations at two x/w locations. This section presents the results of these calculations.

It was shown in Section 7.3.1.3 that the mean centerline velocity, $\bar{u}(x, y=0)$, reaches its maximum value U_0 nominally at $x/w=1$, remains constant until $x/w=2.4$ where it begins to decay. In other words, over the domain $1 \leq x/w \leq 2.4$, $\frac{\partial \bar{u}}{\partial x}(x, y=0) = 0$. However, the measured mean velocity profiles, $\bar{u}(x=c, y)$, at $x/w=1$ and 2.4 show that strong changes occur in the flow field over this streamwise distance of $1.4w$. Stability calculations have been carried out at both x/w locations assuming that the local velocity profile represents a parallel (and non developing) velocity field.



8.3.1 Computations at $x/w = 1$.

Figure 199 presents the plot of eigenvalues for Montgomery velocity profile expressed by the equation (164) with $y_0=0.202$ and $\beta=0.068$. There are two solutions [Mattingly and Criminale (1971)] for a symmetric velocity profile. One of these results in symmetric (varicose) vortex motions and the other in asymmetric (sinuous) vortex motions. In this investigation, the former (symmetric) solution is designated by the letter 'A' and the latter (asymmetric) by the letter 'B'. Figure 199 shows both the solutions. For the solution A the maximum growth rate, $-\alpha_I=3.535$, occurs at $\omega=2.880$ ($St_I=0.664$) with $\alpha_r=5.081$ ($\lambda/w=1.237$) and phase speed $c_I=0.822$. For the solution B, the quantities are $-\alpha_I=3.24$, $\omega=3.240$ ($St_I=0.747$), $\alpha_r=6.253$ ($\lambda/w=1.005$) and $c_I=0.751$. Note that $C_D=0.69$ has been used to compute St_I and c_I ; see Section 2.4.

A comparison of the growth rates of the two solutions A and B, shows that the symmetric solution has a higher growth rate than the asymmetric solution. In other words, the results of the calculations predict a symmetric vortex street which is observed experimentally over the range $270 < Re < 3500$.

Comparing the calculated eigenvalues with the experimentally determined values, it is conjectured that the calculated growth rate $\alpha_I=3.54$ cannot be compared with the experimentally determined growth rate $d[\ln(\tilde{u}/U_0)]/dx^* = 1.24$, because the latter is based upon the growth



of perturbations at all frequencies. The predicted St_I from both solutions (A and B) fall within the scatter of $St_V(x \approx 1)$. Comparing with the results of flow visualization experiments, the measured and the predicted values of Strouhal number and wavelength do not agree; however, the predicted value of the phase speed is of the same order of magnitude as the measured convection velocity.

Returning to the plot of the eigenvalues in Figure 199, it is noted that the two solutions A and B begin to converge at large frequencies, and, beyond $\omega = 5$ ($St_I = 1.2$) they become identical. This behavior is attributed to a rather large separation between the two shear layers ($2y_0 = 0.4w$) [Koochesfahani (1989)]; at large values of the disturbance frequency, ω , the two shear layers behave independently and the two solutions, A and B, converge to the solution of a single shear layer.

8.3.2 Computations at $x/w = 2.4$

Figures 200 and 201 exhibit the plots of eigenvalues for Montgomery and Bickley velocity profiles, respectively. The same data were used to determine the parameters of the two profiles (see Section 3.2.4.2). Table 5 presents the values of St_I and λ_I/w , computed from ω and α_I , respectively, for the maximum growth rate $-\alpha_I$.



Table 5 - Eigenvalues at maximum growth rate

Type of Profile	Solution A				Solution B			
	St_I	λ_I/w	$-\alpha_i$	c_I	St_I	λ_I/w	$-\alpha_i$	c_I
Montgomery	0.27	3.19	0.88	0.87	0.22	3.01	1.03	0.65
Bickley	0.17	6.23	0.15	1.03	0.11	5.22	0.52	0.57

Both solutions (A and B) of each profile predict very small values of St_I and large values of λ_I/w as compared with the experimentally determined values. The predicted phase speed for solution A for both profiles falls within the scatter of the experimentally determined convection speeds at $x/w=2.4$. Comparing the predicted growth rates, $-\alpha_i$, for solutions A and B of each profile, the solution B (asymmetric mode) has a higher growth rate for both profiles. This suggests that as the flat part of the jet is eroded, the asymmetric mode tends to become stronger. Even though the observed vortex motions at $x/w=2.4$ remain symmetric in nature, the prediction indicates that this type of velocity profile (one without flat region in the center) would induce an asymmetric vortex street. The flow visualization experiments show that at low values of Re (≤ 400), the jet develops a sinuous mode beyond $x=6w$. See Figures 56 and 63. Even though this observation is compatible with the linear theory prediction, the basic aspects of the theoretical formulation are violated by the measured velocity field data.



The velocity profile at $x/w=2.4$ should not be expected to represent the basic flow state for the slit-jet flow field, because, the experimental results show that the exponential growth of disturbances continue only up to $x/w=2.4$ and the mean velocity on the centerline begins to decrease downstream of this x location. However, the important conclusion that is drawn from the calculations at $x/w=1$ and 2.4 is related to the nature of the vortex street: for a top-hat velocity profile (a developing jet flow) the vortex motions are symmetrically placed about the centerline, whereas, for a profile with no flat part (like a fully developed Bickley profile) the vortex motions are arranged asymmetrically about the centerline. The results of this investigation thus confirm the observations made by Husain, et. al. (1983) and Chambers, et. al. (1985) that for a top-hat velocity profile the symmetric mode has a higher growth rate than the asymmetric mode.

8.4 Growth of Pressure Fluctuations Along the Jet Centerline

A model was developed in Section 2.5 for the spatial growth of pressure fluctuations along the centerline of the jet using the unsteady Euler's equation. This section presents the predictions of the model using the results of measured velocity data (Chapter 7) and some of the quantitative results from the flow visualization data (Chapter 6).

The justification for the use of an inviscid model is based upon:



- i) The mean velocity profile along the centerline of the jet (Figure 168) suggests that the shear effects become important only beyond $x/w \approx 2.4$. Hence the unsteady inviscid equation of motion can be applied near the centerline in the near-field of the jet exit (i.e., $x/w \leq 2.4$).
- ii) The autospectra of $u(x, y=0, t)$ show that the growth of disturbances begins in the neighborhood of $x/w \approx x_c^*$. In other words, this location can be modelled as the terminal node of the pressure and velocity fluctuation waves.
- iii) In Chapter 4 it was shown that the formation of large scale motions begins with the development of bulges over the range $0.5 \leq x/w \leq 1.5$. It has been conjectured that the formation of bulges is caused by a localized rise in pressure. Hence, the continual formation of bulges at a near constant rate over some spatial domain suggests that the pressure rises and falls in a quasi periodic way over space and time. This justifies the need to develop a model for pressure fluctuations.



8.4.1 Choice of Parameters and Results

Equation (106), which describes the spatial and temporal variations in pressure fluctuations p'_k is reproduced as

$$p'_k(s, t) = \left[-\frac{u_a \omega}{\alpha_r^2 + \alpha_i^2} \right] \exp(-\alpha_i s) [\alpha_r \cos(\alpha_r s - \omega t) + \alpha_i \sin(\alpha_r s - \omega t)] \\ - \bar{U}(s) u_a \exp(-\alpha_i s) \cos(\alpha_r s - \omega t) - \frac{u_a^2}{4} \exp(-2\alpha_i s) \cos 2(\alpha_r s - \omega t) \quad (172)$$

There are four parameters, α_r , α_i , ω and u_a in this equation. Two of the parameters, α_r and ω , can be readily specified from the measured data. From the values of St_V at $x/w \approx 1$ and $500 < Re < 3000$ (Figure 192), $\omega = 4.4$. The spacings λ/w between the vortices were evaluated from the flow visualization observations. As shown in Figures 147 through 154, λ/w varies with Re . Using λ/w at $x/w = 1$ and for two values of Re , 1000 and 3000, the α_r values are equal to 10.4 and 18.3, respectively. The magnitude of the fluctuating velocity u_a at origin ($s=0$; i.e., the location of the terminal node of velocity and pressure fluctuation) was estimated from the average of $\bar{u}(St_V=0.7)/U_0$ at $x/w=0.5$ and over a wide range of Re , 500-2900. This value was found to be 6.24×10^{-4} . The results of the linear stability analysis (see Section 8.3), based upon the velocity profile $\bar{u}(y)/U_0$ at $x/w=1$, predict the most unstable mode to have a growth rate $-\alpha_i=3.54$ at a Strouhal number $St_I=0.66$. Since the predicted and the measured values of Strouhal number agree quite well ($St_V=0.7$; see Figure 192), $-\alpha_i=3.5$ has been used in the calculation of pressure fluctuations. Note that based upon the

distribution of the root mean square values of the measured velocity fluctuations the average value of the growth rate was found to be 1.24. (See Figure 170.)

Calculations for pressure fluctuations have been performed at locations which cover the x/w range over which the bulge formations have been observed. (See the space-time plots of vortices in Figures 93 through 97 and in Appendix C.) Three locations that have been used are $s=0.5$, 1.0 and 1.5. (Note that s is referenced from the critical location, $(x_c, 0)$, which is based upon the plots of power spectra of $u(x, y=0, t)$ in the near-field. Specifically, x_c for most data appears to be $0.25w$ downstream of the exit plane.) Figure 202 presents $p'_k(t)$ and $v'(t)$ for $-\alpha_i=3.5$, $\alpha_r=10.4$, $\omega=4.4$ and $u_a=6.24 \times 10^{-4}$ at the three streamwise locations. At all these locations the pressure and the velocity fluctuations are nominally π radians out of phase and no frequency doubling is observed in $p'_k(t)$. This shows that the first and the second terms of equation (172) nominally balance one another. Note that a doubling in the frequency of pressure fluctuations will occur at larger values of s for the same value of $-\alpha_i$. However, at values of $s > 2$ ($x/w > 2.25$), this result will not support the hypothesis that the bulge formations are caused by a localized rise of pressure in the jet, because, the formation of the bulges occur over $0.5 < x/w \leq 2$. In addition, for these distances from the exit plane, the inviscid Euler's equation will not be applicable because of the penetration of the shear effects towards the centerline of the jet. On the other hand, it is also to be noted that a doubling in the frequency in the



pressure fluctuations can occur at smaller values of s (≤ 1.5) for a larger value of the growth rate. However, in this case, the results predict the intensity of velocity fluctuations to become excessively large. For example, a value of $-\alpha_i = 7$ leads to a p'_k frequency of nominally twice that of the velocity fluctuation but the corresponding velocity magnitude is more than seventy times the measured intensity at $x/w \approx 2.4$. Hence, it is apparent that this analytical description of pressure fluctuations does not provide an explanation for the observed result presented in Section 7.6.3, namely, $St_F \approx 2St_V$.

8.4.2 Discussion

The simple inviscid model for pressure fluctuations based upon the unsteady Euler-s equation was evaluated in the previous section using the measured data. The results show that in the near-field, where the formation of bulges are observed, the pressure and velocity fluctuations occur at the same frequency. Since, the observed values of St_F and St_V presented in Section 7.6.3 show that St_F is nominally equal to $2St_V$, these inviscid flow results do not support the hypothesis that the bulges form as a result of a localized rise of the pressure in the vicinity of the exit plane of the jet.

9.1 In

Th
for fu
the co

9.2 C

F
ponent
phenom
port th
two su
alit-j
bility

CONCLUSIONS AND RECOMMENDATIONS

9.1 Introduction

The conclusions from this investigation and the recommendations for future work are presented in this chapter. Section 9.2 presents the conclusions and Section 9.3 outlines the recommendations.

9.2 Conclusions

Flow visualization and the measurement of the longitudinal component of velocity $u(x,y,t)$ were used to investigate the instability phenomena of the slit-jet flow field. The results of this study support the following conclusions. The conclusions have been arranged in two subsections. Section 9.2.1 presents the general properties of the slit-jet flow field and Section 9.2.2 presents the details of its stability characteristics.

$\bar{u}($

exe

po

th

ve

fe

(S

 $\bar{u}($

sh

an

me

b/

do

th

ap

be

up

Bj

9.2.1 General Properties of the Slit-Jet

1) The distribution of the mean of the longitudinal velocity, $\bar{u}(x^*, 0)/U_0$, over $-1 \leq x/w \leq 4.65$ and over the Re range, $510 \leq Re \leq 2854$, shows excellent agreement with the velocity distribution based upon the potential flow solution. (See Figure 168.) The measurement shows that the jet achieves its maximum velocity at approximately $x/w=1$. The jet velocity begins to decrease for $x/w \geq 3$ which indicates that shear effects have penetrated to the centerline by this nominal x location. (See Figure 168.)

2) Measurements show that the mean velocity profile, $\bar{u}(x^*=c, y^*)/\langle U \rangle$, changes considerably between $x/w=1$ and 2.4.

2a) At $x/w=1.0$, the lateral distribution of the mean velocity shows a "top-hat" profile with a flat region over $-0.2 \leq y/w \leq 0.2$. An analytical expression suggested by Montgomery was used to fit the measured profile. From the fitted curve, the half width of the jet, b/w , was found to be 0.338. (See Figure 181.)

2b) At $x/w=2.4$, the lateral distribution of the mean velocity does not exhibit a flat region. The measured profile was fitted with the Montgomery profile and also with the Bickley profile. The former appears to fit the data better near the edges, whereas the latter is a better representation of the data in the center of the jet. Based upon the fitted Montgomery profile, $b/w=0.437$, whereas based upon Bickley profile, $b/w=0.467$. (See Figure 182 and Figure 183.)

dis
pro
of
gro

dec
dec
par
lla
(Se
the
enc

ca.
li
rec
the
vic
va
va
de
di
op

3) The erosion of the flat region of the jet within a streamwise distance of $1.4w$ shows the rapidly changing nature of the velocity profile in the slit-jet flow field. Between $x=lw$ and $2.4w$, the rate of decay of the flat region of the jet is about twice the rate of growth of the half-width of the jet.

4) The discharge coefficient, C_D , of the slit-jet sharply decreases with increasing Re , up to $Re=800$. (See Figure 158.) The decrease in C_D becomes gradual beyond this value; for $Re \geq 3000$ C_D apparently achieves an asymptotic value of 0.68. This value is about 11% larger than the value (0.611) predicted by the inviscid analysis. (See Section 2.2.2.3.) From these observations, it is inferred that the formation of large scale vortex motions at $Re=250$ does not influence the distribution of $C_D(Re)$.

The development of the boundary layers on the nozzle plates causes the speed of the fluid particles along the separating streamlines to be smaller than the inviscid speed U_0 . These particles with reduced speed can follow a path with a smaller radius of curvature than that which is computed for an inviscid fluid. This results in a wider jet with $C_D > 0.611$. This effect is more pronounced at lower values of Reynolds numbers. The apparent asymptotic approach of C_D to values larger than 0.611 (see Figure 158) is attributed to geometry dependent effects. Specifically, the data from jets with two different slit sizes exhibits this influence for $Re > 1500$. It is conjectured that the finite thickness t_N of the nozzle plates alters

the

Th

con

ter

obt

set

or

wo

u

mi

of

(S

bu

Re

9,

75

in

en

ra

the path of the entrainment flow in the vicinity of the jet exit. This would modify the pressure field which in turn, would change the contraction of the jet. The relevant parameter is t_N/w for the characterization of this physical effect. For $Re \leq 1500$, based upon the two observed cases with $t_N/w = 0.5$ and 1, the near-field appears to be less sensitive to this geometry dependent effect. It is not clear whether or not the observed behavior is universal, i.e., whether the behavior would be the same for $t_N/w \rightarrow 0$.

5) Like the mean velocity profile, the rms velocity profile, $\bar{u}(x^*, y^*) / \langle U \rangle$, also changes considerably between $x/w = 1$ and 2.4.

5a) At $x/w = 1.0$, the rms velocity profile $\bar{u}(y^*)/U_0$ goes through a minimum in the central part of the jet and maxima near the half-widths of the jet. Also, the $\bar{u}(y^*)/U_0$ profile shows some dependence on Re . (See Figure 178.)

5b) At $x/w = 2.4$, the rms velocity $\bar{u}(y^*)/U_0$ is uniformly distributed across the jet and the profile shows no systematic dependence on Re . (See Figure 180.)

2.2 Stability Characteristics

1) Based upon the flow visualization experiments, the range of Re 5-3500 is subdivided into four regimes:

1a) $Re \leq 157$. No vortex motions are observed except for the starting vortex pair (SVP) which is followed by a bulge or one of its evolved forms, a kink or a foldover. (See Figures 45, 46 and 47.) The ratio of the speeds of the bulge to the SVP, V_b/V_s , remains less than

1.

and

49.

jet

vit

hou

vor

the

rar

nat

The

and

jet

The

tic

of

gic

laz

68.

rol

car

gra

tha

1. (See Figure 48.)

1b) $157 \leq Re \leq 210$. V_b/V_s exceeds 1 in this range (see Figure 48) and this allows the foldovers to pass "into" the SVP. (See Figure 49.) As one foldover merges with the SVP, another bulge forms on the jet column, i.e., a cyclic process of bulge formation and its merger with the SVP is established. Small accumulations of dye along the jet boundary are observed for these conditions. These are termed: "unit vortices". (See Figure 49.) There is no apparent interaction between the unit vortices. No large scale vortices were observed in this range of Reynolds number.

1c) $268 \leq Re \leq 1700$. This large range is marked by the repeated formation of large scale vortex motions. (See Figures 56, 57, and 58.) These observances generally confirm the observations reported by BW and FK. For $Re > 930$, in some cases unit vortices were observed on the jet column preceding the formation of large scale vortex motions. These unit vortices have not been found to play any role in the formation of the large scale vortices. This is contrary to the hypothesis of FK that the large scale vortices are formed as a result of an agglomeration of the unit vortices.

1d) $2300 < Re < 3500$. Over this range both the unit vortices and the large scale vortices are consistently formed. (See Figures 65 through 68.) Because of the limitations of the recording equipment, both the formation of the unit vortices and the formation of large scale vortices cannot be fully described. However, it is apparent from the photographic records (see Figures 65 through 68 and Figures 72 through 74), that the large scale vortex motions are quite diffused almost from

the

ti

fi

15

im

Re

ov

oc

re

ra

co

un

Co

ha

pr

Re

of

st

re

ve

Ex

bo

their inception; probably, the unit vortices become turbulent by the time they become part of a large scale vortex motion.

Three modes of instability are recognized in the slit jet flow field [FK]. The appearance of unit vortices over the low Re range, 157-210, and over the range 2300-3500 is caused by the hydrodynamic instability of the free shear layers. The appearance of bulges at low Re values of 87-210 and the formation of large scale vortex motions over the range 270-1700 and 2300-3500 are the result of processes that occur at a large scale due to the second mode of instability. The reason for the absence of unit vortices in most of the cases in the range 270-1700 is not clear. It is noteworthy but it has not been incorporated into a comprehensive theory, that the first observation of unit vortices coincides with the ratio V_b/V_s becoming 1 at $Re=150$. Contrary to the results of BW and FK, the large scale vortex motions have been consistently observed in this study up to $Re=3500$ and their presence has been inferred from the measured velocity data up to $Re=6500$. (See Figure 188.) In other words, the suggested third mode of instability (FK) has not been confirmed by the results of this study at least up to a value of Re which is four times the value reported by BW and FK.

2) The sequence of events leading to the formation of large scale vortex motions for the range $270 \leq Re \leq 1700$ have been identified. The formation of a bulge, which causes an inflection point in the jet boundary has been identified as the first visual manifestation of the

vari

local

bulg

the

a m

Rule

and

time

caus

even

of v

scal

i.e.

veloc

with

been

varicose type jet instability.

It was conjectured that the formation of a bulge resulted from a localized rise in pressure in the jet. Hence, the cyclic formation of bulges at a certain rate would imply that the pressure in the jet in the vicinity of the exit plane fluctuated at the same rate. However, a model for pressure fluctuations in the jet which is based upon the Euler's equation did not support this conjecture. (See Sections 2.5 and 8.4.)

3) The regular symmetric pattern of the vortex street is sometimes disrupted. Three different events have been identified as the cause of disruption. However, the perturbations associated with these events have been found to convect downstream and the symmetric pattern of vortex motions reestablishes itself.

These observations (2-3) parenthetically suggest that the large scale instability of the slit-jet flow field is absolute in nature, i.e., once started it sustains itself and is not convected away.

4) The distribution of the rms of the longitudinal component of velocity $\bar{u}(x^*, y^*=0)/U_0$ exhibits an exponential growth over $-1 \leq x^* \leq 2.4$ at a growth rate equal to 1.24. No systematic influence of Re has been found on the growth rate over the range 500-2900.

5) The analytical models of the mean velocity profile at $x/w=1$

and
sili
the
lax
sub
jet

vel
(var
not
peri

(196
prod
terl

Mont
pred
the
woul
and
al.
jet.

hanc
weve

and 2.4 were used to investigate the stability characteristics of the slit-jet flow field. The theoretical results have been compared with the experimental results as described below. Note that over the range $1 \leq x/w \leq 2.4$, even though $\frac{d\bar{u}}{dx}(x,0)=0$ the velocity profile $\bar{u}(y)$ undergoes a substantial change: the flat part of the jet core is rounded and the jet becomes wider. (See Figures 181, 182, and 183.)

5a) The results of calculations at $x/w=1$, show that for a top-hat velocity profile the growth rate for the symmetric vortex motions (varicose type instability) is higher than for the asymmetric vortex motions (sinuous type instability). This result supports the experimental observations [Husain, et. al. (1983), Chambers, et. al. (1985) and present] that for a top-hat (developing) type of velocity profile the vortex motions are symmetrically placed about the jet centerline.

5b) At $x/w=2.4$, the stability calculations were executed both for Montgomery profile and Bickley profile. The results for both profiles predict that for a velocity profile without a significant flat region the asymmetric disturbances grow faster than the symmetric ones. This would result in an asymmetric vortex street [Savic(1941) and Mattingly and Criminale(1971)] as has been shown experimentally by Husain, et. al. (1983) for a fully developed, laminar velocity profile in a plane jet.

5c) For the top-hat velocity profile, the most unstable disturbance has a growth rate $-\alpha_1=3.54$, the Strouhal number $St_1=0.66$, the wavelength $\lambda_1/w=1.24$ and the corresponding phase speed $c_1=0.82$.

data

the

to a

tors

by t

exam

ence

vibr

the

tor

the

is n

unce

that

deter

well

paper

shows

and

are e

value

$\mathcal{H}_P(\mathcal{R})$

6) The Strouhal number has been estimated from the photographic data base (St_F) and also from the measured velocity data (St_v).

6a) Large variations in the $St_F(x^*)$ values have been observed in the near field ($0.5w < x < 2w$). Beyond $x=4w$, the $St_F(x^*)$ curves converge to an average value ≈ 0.5 . (See Figures 126 through 133.) Several factors, including the influence of aspect ratio, B/w , vibration caused by the stepper motor and the influence of background disturbances were examined. These factors do not appear to be responsible for the presence of the observed scatter. However, it is possible that either the vibration of the nozzle housing at its natural frequency triggered by the running of the stepper motor or the presence of some unknown factor was responsible for large variations in the values of St_F . Also, the possibility that the development and growth of large scale motions is not a well regulated process cannot be ruled out. Regarding this uncertainty FK made this comment: "Apparently, the physical process that controls the spacing of the vortex motions is not 'rigidly' determined by the kinematic scales U_0 and w , although this spacing is well-defined for a given experiment, as shown by figure 4." of their paper.

For the unpaired large scale motions the variation of St_F with Re shows some scatter but no systematic dependence on Re . The average the rms values of St_F over $1000 < Re < 3500$, in a jet with $B/w=10.7$, equal to 1.64 and 0.22. (See Figure 134.) At $x/w=2.2$, the two values are 0.98 and 0.18. (See Figure 136.)

6b) The variation of Strouhal number St_v with Re , like the Re) data, shows considerable scatter with little systematic

depe

equa

the

data

The

to e

fail.

from

coul

the

cid

x/w

as c

on

dece

The

ble

most

u(x,y

dependence on Re . The average and the rms values of St_V at $x/w \approx 1$ are equal to 0.70 and 0.07, respectively. (See Figure 192.) At $x/w \approx 2.2$ the respective values are 0.52 and 0.07. (See Figure 193.)

6c) Values of Strouhal numbers based upon the flow visualization data St_F , and the measured velocity data St_V , are obviously not equal. Their ratio, St_F/St_V , has been found to be nominally 2. The attempt to explain this result using the model for pressure fluctuations failed. (See Section 8.4.) The parameters of the model were evaluated from the measured velocity results. Based upon these parameters, it could not be shown that the pressure fluctuations occurred at twice the frequency of the velocity fluctuations.

6d) The Strouhal number St_I computed from the linearized, inviscid equation of motion compares quite well with the St_V values at $x/w \approx 1$.

7) The convection velocity u_c^* distributions show a small scatter compared with the $St_F(x^*)$ distributions and very little dependence on Re . The vortices appear to accelerate initially and then decelerate. (See Figures 139 through 146.)

The reasons for the acceleration of the vortices are not clear. The formation of a vena contracta could not be argued to be responsible for this effect, because, as shown in Figures 139 through 146, in all cases the vortices accelerate up to $x/w \approx 3$. (Note that the velocity U_0 approaches U_0 around $x/w \approx 1$.)

The
compares
executed

8)
large sca
up to Re
becomes n

The
factors:
more vort

In
the Re rat
stability

9.3 Recor

The
study has
are to &
satisfy so

1) T
the dischar
as well) st

The measured value of u_c^* at $x/w=1$ and over the range $1500 < Re < 3000$ compares well with the estimate based upon the stability calculations executed for the velocity profile at $x/w=1$.

8) Like $St_F(x^*)$, the $\lambda^*(x^*)$ distributions exhibit a relatively large scatter. This is especially evident at low values of Re (e.g., up to $Re=700$). At higher values of Re the distribution of λ^* with x^* becomes nominally linear.

The increase in $\lambda^*(x^*)$ with increasing x^* is caused by two factors: the acceleration of the vortices and the pairing of two or more vortices.

In contrast to the u_c^* values, the values of λ^* at $x/w=1$ and over the Re range 1500-3000 do not agree with the estimates based upon the stability calculations.

3 Recommendations

The list of conclusions presented in Section 9.2 shows that this study has raised a number of questions. The following recommendations are to gain a better understanding of the instability phenomena and satisfy some concerns related to the experimental techniques.

1) The influence of the finite thickness of the nozzle plates on discharge coefficient (and possibly on the stability of the jets) should be investigated.

2) The bounds
checked using a high
the nonappearance
should be investigated

3) The correl
 V_s/V_s becoming 1 for
marks the instabili
believed to indicate

4) Combined p
the jet will reveal:

i) the relati
peak in the

ii) the phase r
fluctuation

iii) the rate of
those of th

5) Lateral surv
perimental techniques
in the LDA system

2) The boundaries of the suggested regimes of Re need to be checked using a high speed recording equipment. Also, the reasons for the nonappearance of unit vortex motions in the Re range 268-1700 should be investigated.

3) The correlation in the first appearance of unit vortices and V_b/V_s becoming 1 for $Re \approx 150$ need to be investigated. The former event marks the instability of the free shear layer, whereas, the latter is believed to indicate the activation of the large scale instability.

4) Combined pressure-velocity measurements in the near-field of the jet will reveal:

- i) the relationship between the formation of bulges and the peak in the pressure cycle;
- ii) the phase relationship between the pressure and the velocity fluctuations;
- iii) the rate of growth of pressure fluctuations as compared with those of the velocity fluctuations.

5) Lateral surveys of $u(t)$ should be conducted with improved experimental techniques, for example, using a frequency shifting module in the LDA system to accommodate small flow velocities and flow

reversals near the
should be conducted
4 to investigate the
velocity profile to

6) Theoretical
with proper mean vel

7) Velocity s
the near field to de
tion) between the
growth of disturbance
boundary depends upon

8) Determine
mutual interaction b
dependence.

9) Flow visual
tended to values of
whether an upper l
patterns are observe
vortices in the form

10) Investigate
weak and strong forc

reversals near the edges of the jet. In addition, the lateral surveys should be conducted at a number of x stations over the range $0 \leq x/w \leq 4$ to investigate the transformation of the jet from a top-hat mean velocity profile to a rounded one.

6) Theoretical investigations of the instability of the slit-jet with proper mean velocity profile need to be executed.

7) Velocity surveys along the centerline should be conducted in the near field to determine the critical boundary (i.e., x_c/w location) between the proposed regions of non-selective and selective growth of disturbances. (See Section 8.2.) Also, check whether this boundary depends upon Re .

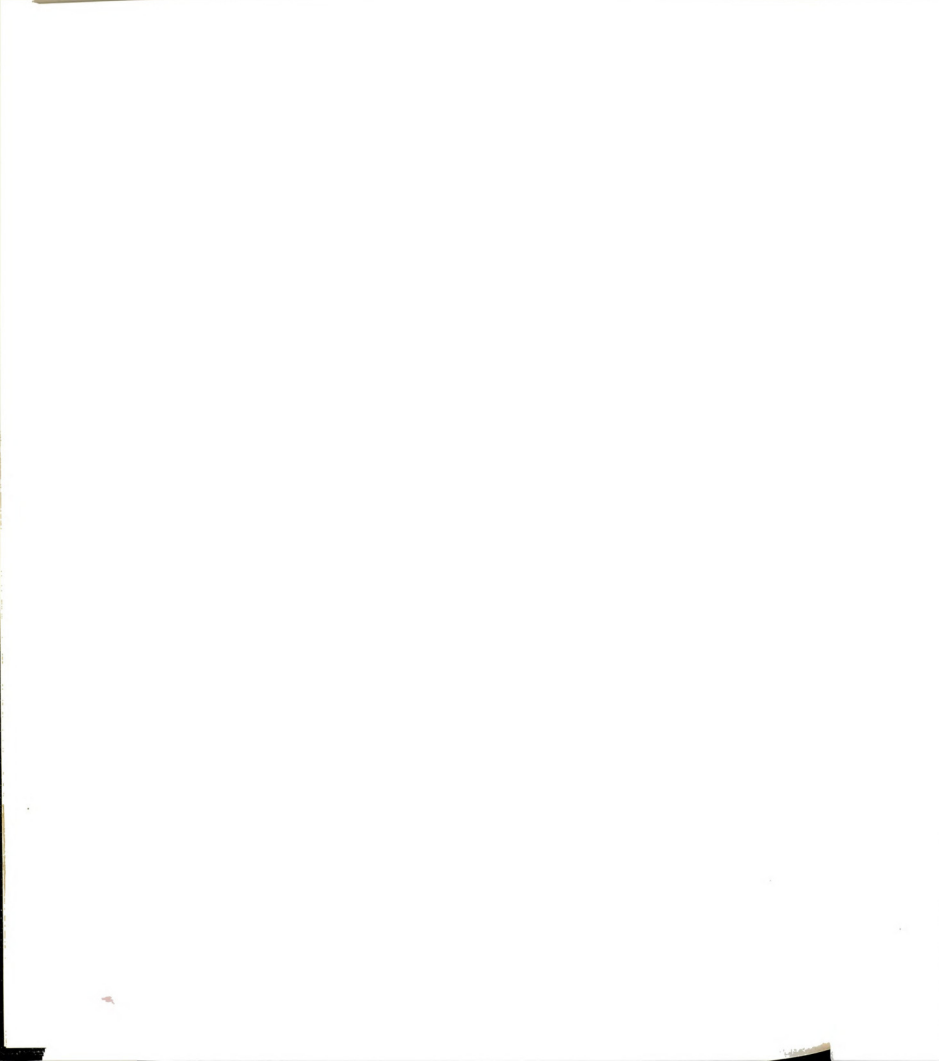
8) Determine the extent of, and, the location of the region of mutual interaction between vortices and check whether there is a Re dependence.

9) Flow visualization of the slit-jet flow field should be extended to values of $Re > 3500$ using a high speed camera to determine whether an upper limit in Re exists beyond which no symmetric vortex patterns are observed. This would also reveal the role of unit vortices in the formation of large scale vortex motions.

10) Investigate the instability of the jet under the condition of weak and strong forcing to determine the sensitivity of the slit-jet

flow field to extrac

flow field to extraneous disturbances.



FIGURES



Figure 1. Schematic:

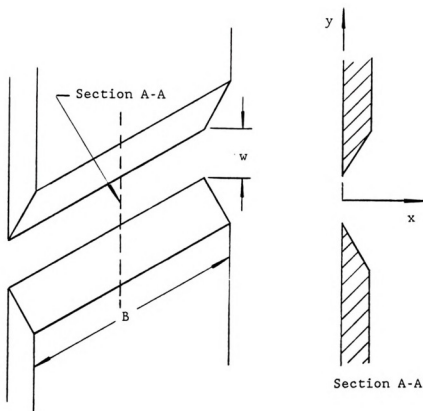


Figure 1. Schematic representation of the two-dimensional slit-jet.

High pressure
primary liquid



Mixing throat

Discharge



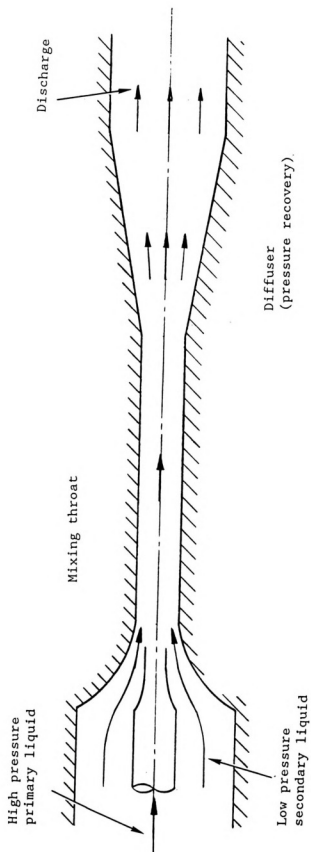


Figure 2. A Jet Pump.



A

Figure 3. Schematic
finite, channel-1
trajectories of t
 $z = (x_1 + ix_2)$.



Figure 4. Schematic
infinite plenum.

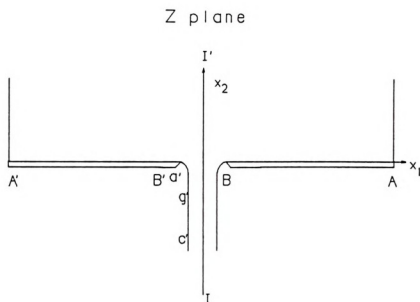


Figure 3. Schematic representation of a slit-jet issuing from a finite, channel-like plenum. The boundaries of the plenum and the trajectories of the separating streamline define the complex plane: $z = (x_1 + ix_2)$.

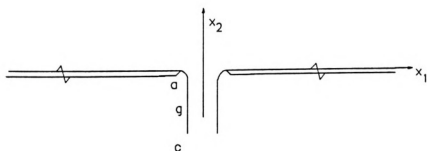


Figure 4. Schematic representation of a slit-jet issuing from an infinite plenum.

+

A

Fi

ζ' plan



Fi

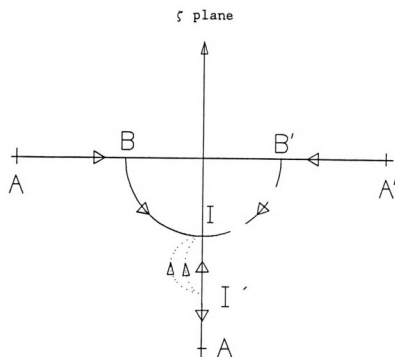


Figure 5. Schematic representation of ζ plane.

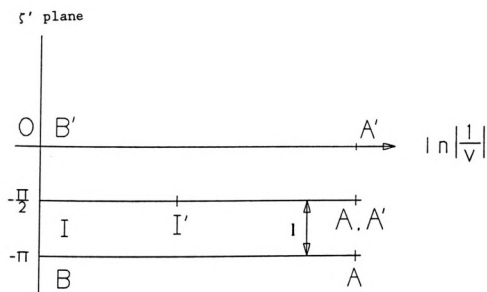


Figure 6. Schematic representation of ζ' plane.

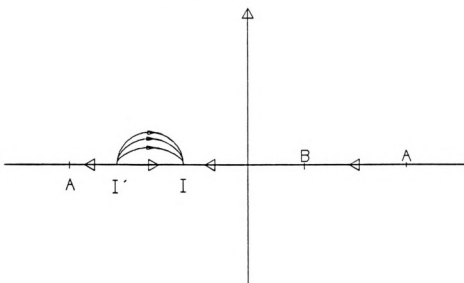


Figure 7

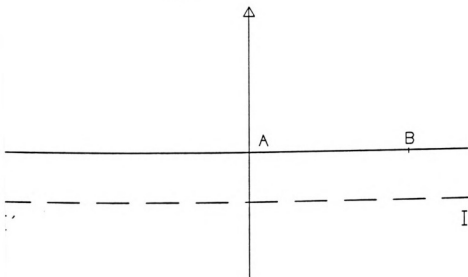


Figure

t-plane

Figure 7. Schematic representation of t plane.

w-plane

Figure 8. Schematic representation of w plane.



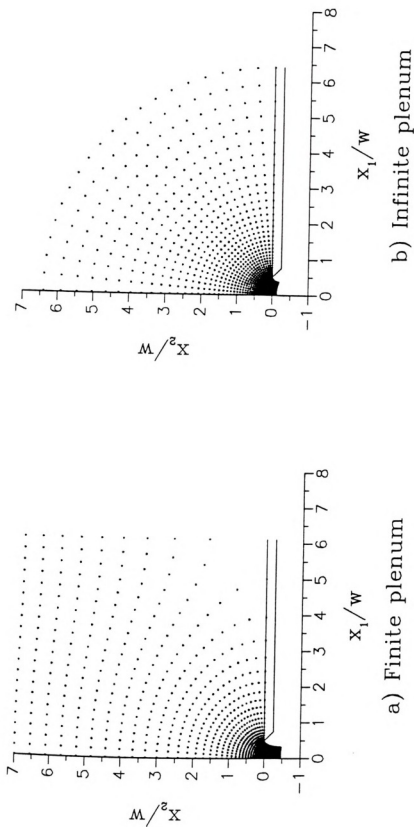


Figure 9. Streamline pattern upstream of a slit-jet issuing from
 a) a finite, channel-like plenum with $m = 20$, and b) an infinite plenum.



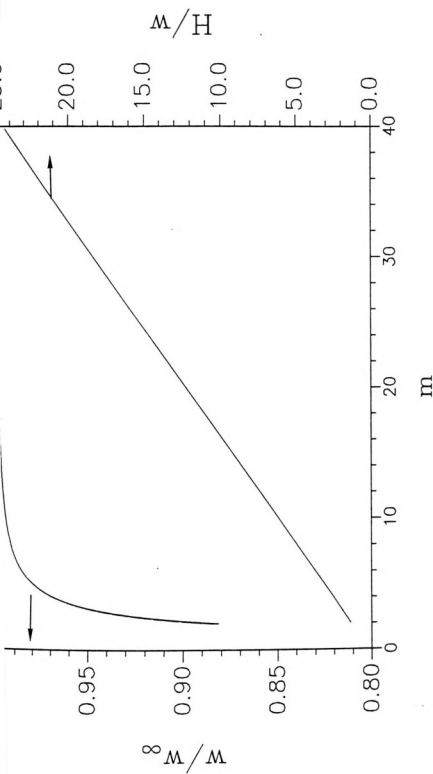


Figure 10. Influence of m on the ratio of slit widths w/w_∞ and the proximity ratio H/w .



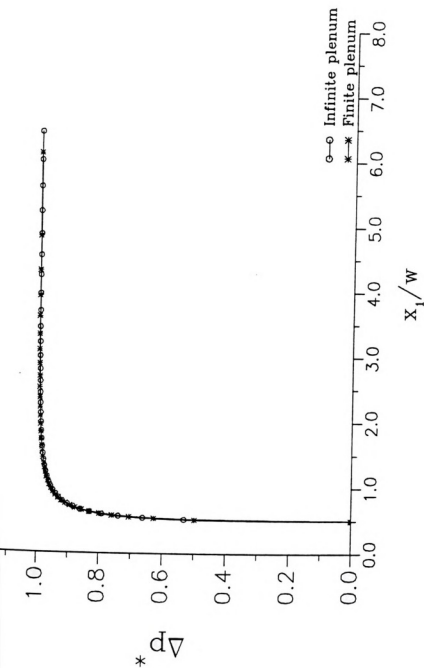


Figure 11. Normalized pressure distribution on the nozzle plate for a finite ($m=20$) and an infinite plenum.



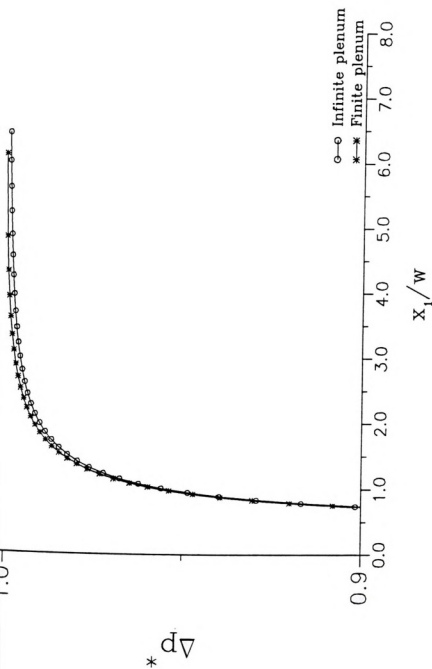


Figure 12. Normalized pressure distribution on an expanded pressure axis.

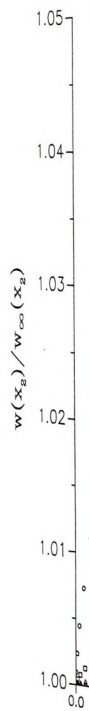


Fig.
Proc.

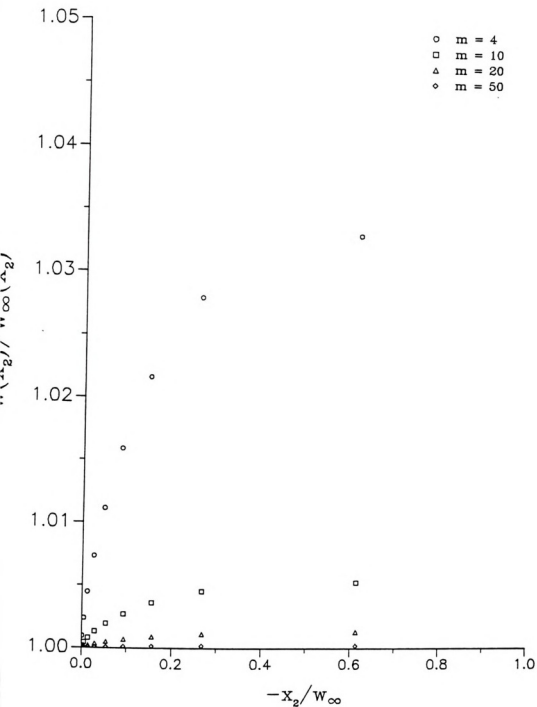


Figure 13. Comparison of the widths of the jets issuing from a finite ($m = 20$) and an infinite plenum.

x_1

Figure 14. Sc
with velocity
nozzle plate.

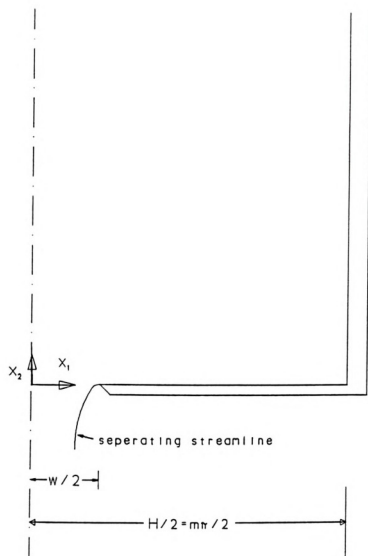


Figure 14. Schematic representation of the separating streamline with velocity U_0 and the limits of integration for flow on the nozzle plate.

Figure 15. De
flow along th
modelled as s

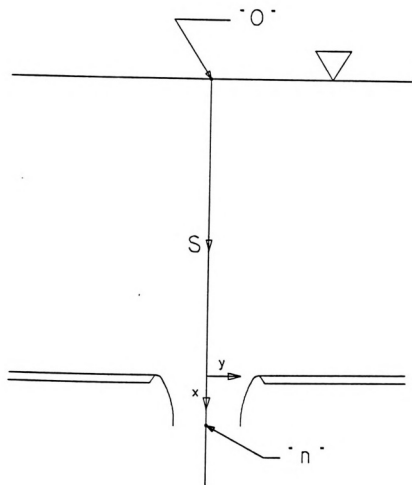


Figure 15. Definition sketch for the stability analysis. The flow along the the center streamline between "o" and "n" is modelled as steady flow.



Figure 16. Schematic of variable width slit jet and variable width bleed port configurations.

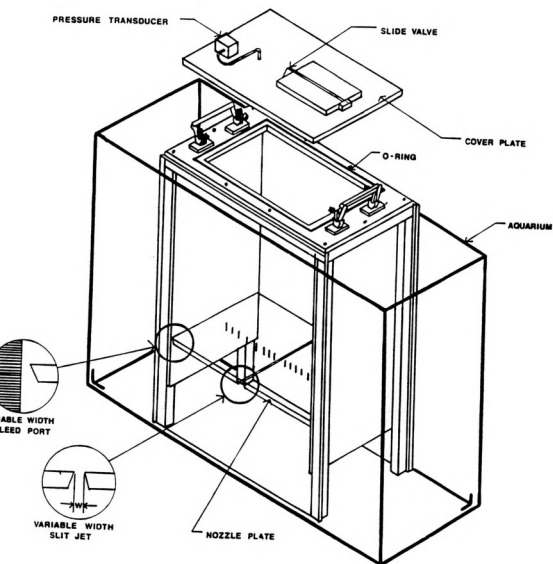
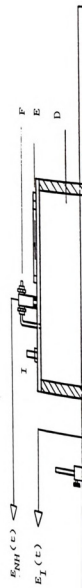


Figure 16. Schematic representation of the gravity driven, steady state, finite duration liquid flow facility.



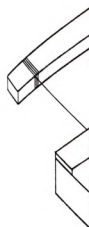


Figure 18. Schem
A: Plastic tube,
E: Handle to man

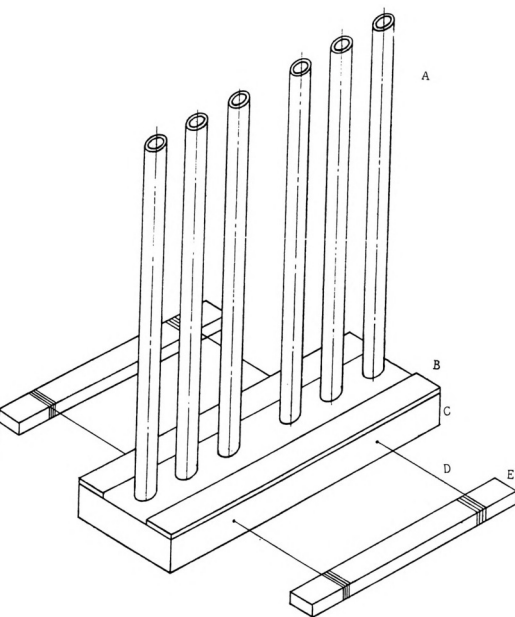


Figure 18. Schematic representation of the Filling Device (FD).
A: Plastic tube, B: Rubber gasket, C: Styrofoam base, D: String,
E: Handle to maneuver the device.

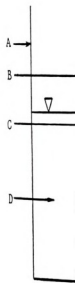


Figure 19.
dimensional.
C: Two-dimen

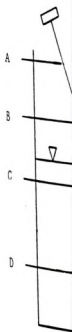


Figure 20.
the format:
housing, c:

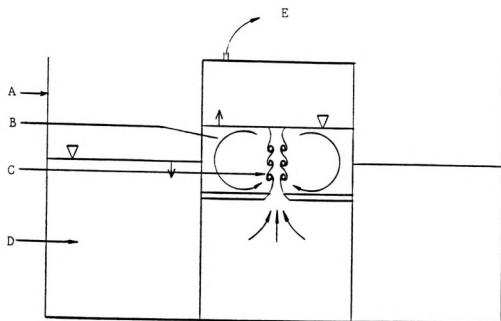


Figure 19. Schematic representation of the formation of two-dimensional vortices in the plenum. A: Glass tank, B: Plenum, C: Two-dimensional vortices, D: Receiver, E: To vacuum tank.

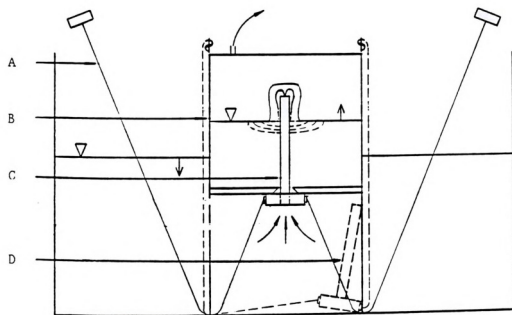


Figure 20. Schematic representation of the use of FD to prevent the formation of vortices in the plenum. A: String, B: Nozzle housing, c: Filling device (FD), D: FD parked during experiment.



Figure 21. So
the filling p

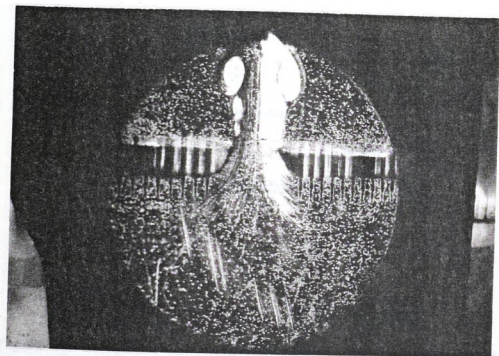


Figure 21. Schlieren visualization of vortex formation during the filling process.

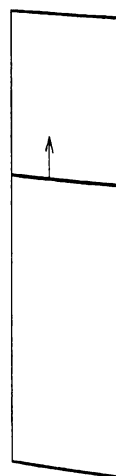


Figure 22. Schematic of CV_1 used in flow

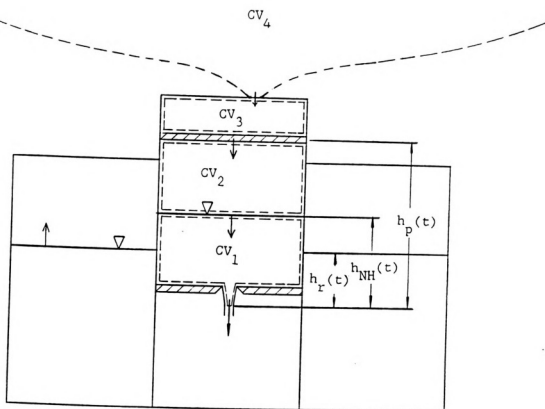


Figure 22. Schematic representation of the four control volumes CV_i used in flow modelling.

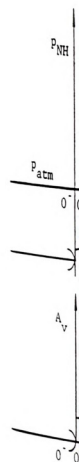
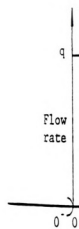


Figure 23.

$q (-C_D U^2 A)$
at $t=0$ is

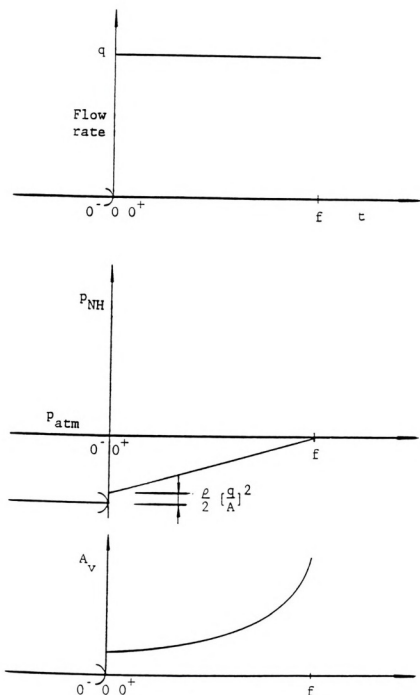


Figure 23. Schematic representation of the time histories of q ($-C_D U_0 A_j$), p_{NH} and A_v . A step change in the jet velocity at $t=0$ is assumed in the analysis.

BUI
ARR

REA
CLC

JOG
MOT

I = I

Figure 24. Flow
motor.

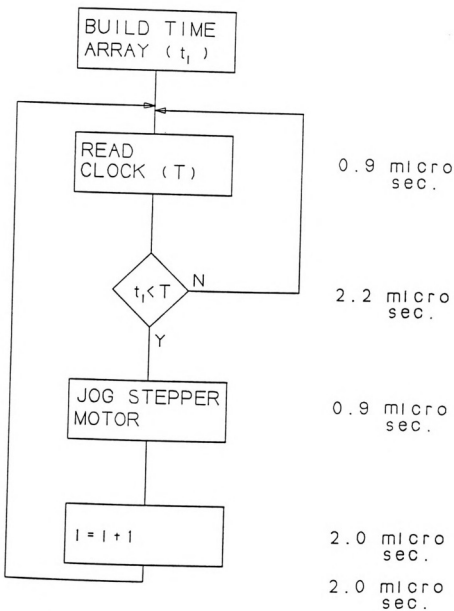


Figure 24. Flow chart of the "tight wait loop" to jog the stepper motor.

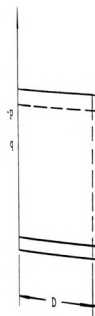


Figure 25. Schematic diagram of the cavity pressure response through the bleeder valve.

- D: Settling time
- A: Adjustment period
- T: Transient period
- E: Period of the response with t as the control and
- U: Uncontrolled

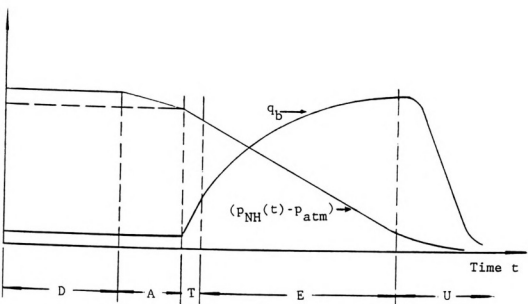


Figure 25. Schematic representation of the time histories of the cavity pressure, p_{NH} , and the rate of flow of air through the bleed valve, q_b .

- D: Settling time for the decay of filling disturbances.
- A: Adjustment period $p \rightarrow p_{NH}(0^+)$. The DEC a/d converter begins monitoring the cavity pressure.
- T: Transient period: $\frac{\partial U}{\partial t} \neq 0$.
- E: Period of the experiment: p_{NH} varies linearly with t as the bleed valve is opened under software control and the TSI a/d converter acquires data.
- U: Uncontrolled ending period.



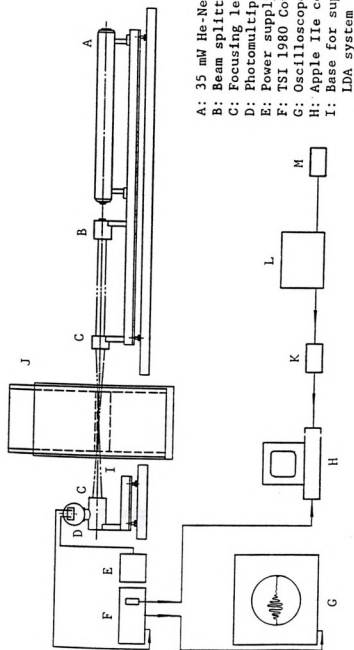
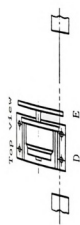
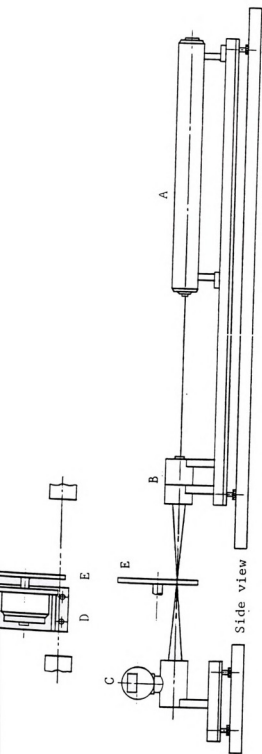


Figure 26. Configuration of the single channel LDA system.





- A: 35 mW He-Ne laser
 B: Beam splitter and focusing lens
 C: Photomultiplier
 D: Variable speed dc gear motor
 E: Plastic wheel
 θ : 25.4 degrees.

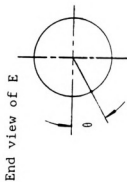


Figure 27. Schematic representation of the arrangement to check the performance of the LDA system.

1.0

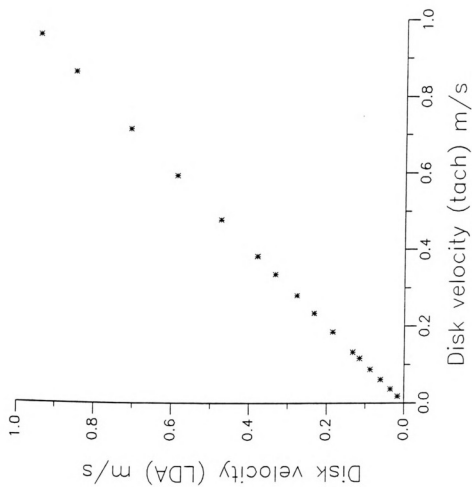


Figure 28. Comparison of disk velocity measured by the LDA and the tachometer.

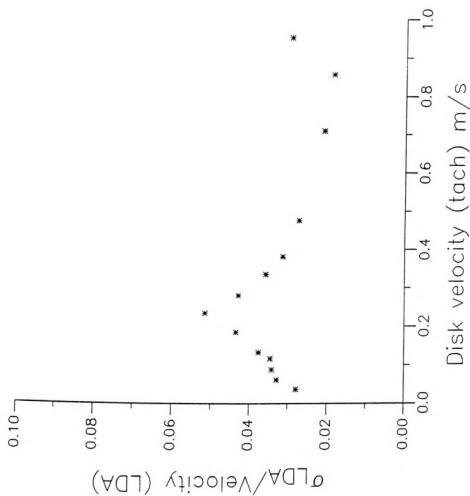


Figure 29. Normalized rms of the disk velocity.

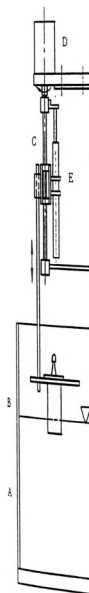


Figure 30. Scheme
calibrating the
liquid, B: VFS,
controlled step
transformer (LVD)

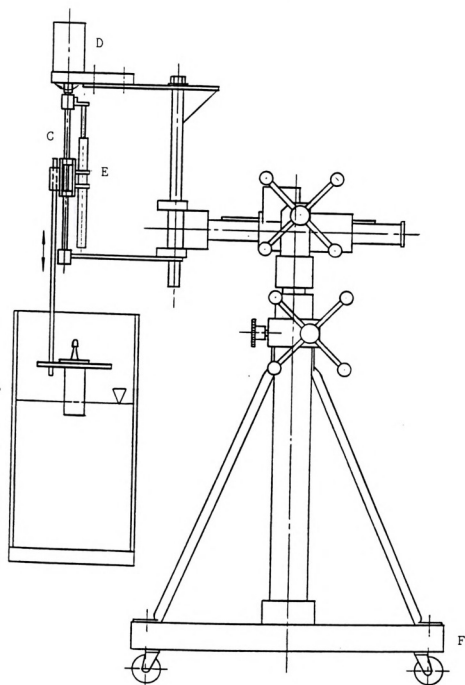


Figure 30. Schematic representation of the arrangement for calibrating the Volume Flow Sensor (VFS). A: Glass tank with liquid, B: VFS, C: Vertical traversing mechanism, D: Computer controlled stepper motor, E: Linear variable differential transformer (LVDT), F: Tripod with support arm.



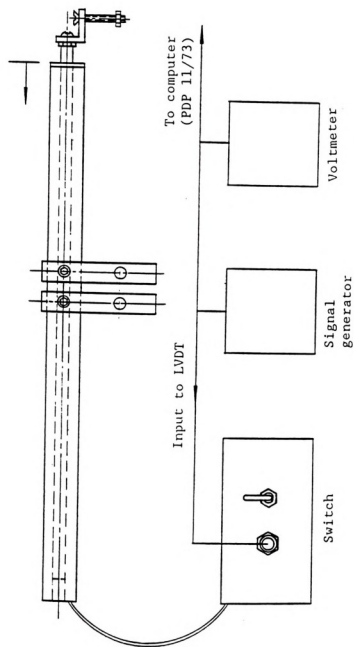


Figure 31. Schematic representation of the Linear Variable Differential Transformer (LVDT).

1
6

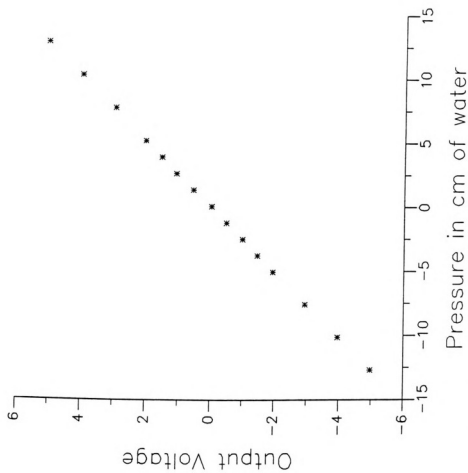


Figure 32. Calibration data for the pressure transducer used in the VFS.

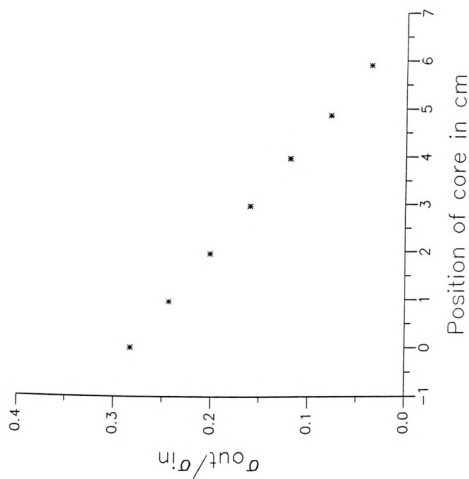


Figure 33. Calibration data for the LVDT used in the calibration of VFS. See Figure 30 for the experimental configuration.

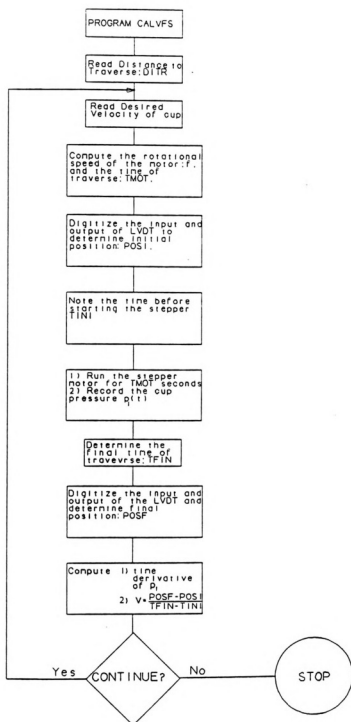


Figure 34. Flow chart for calibrating the VFS.

0.25
0.20

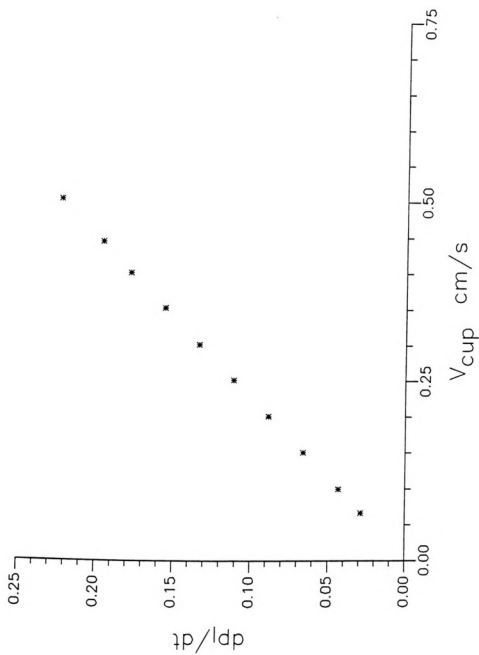
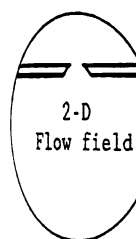


Figure 35. Rate of pressure rise in the cup as a function of its velocity.

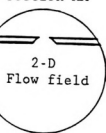
Section AA



A

Figure 36. S
schlieren f

Section AA



- A: From Ar ion laser
- B: Front surface planar mirror
- C: 10X microscope objective
- D: Spherical mirror f=1.5 meter
- E: Test field
- F: 35 mm motorized camera
- G: Ground glass screen
- H: Knife edge with fine position adjustments.

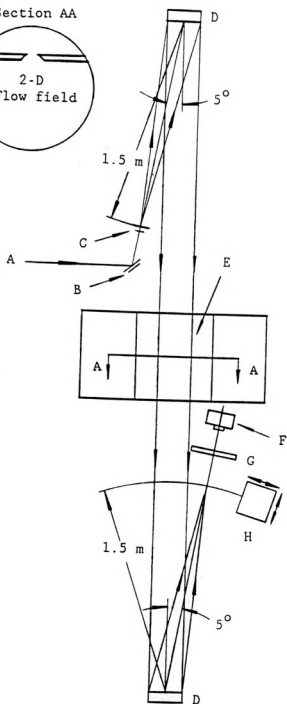


Figure 36. Schematic representation of the ray diagram for the schlieren flow visualization.



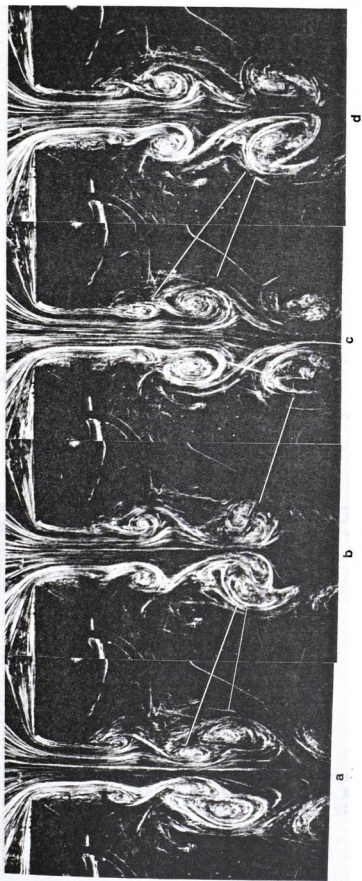


Figure 37. Flow visualization photographs of the slit-jet flow field using the schlieren technique: $Re = 1400$ and $w = 2.63$ cm.

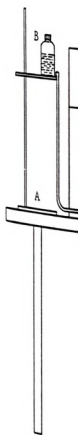


Figure 38. S
injecting dy
dye, C: Plas
of dye spre

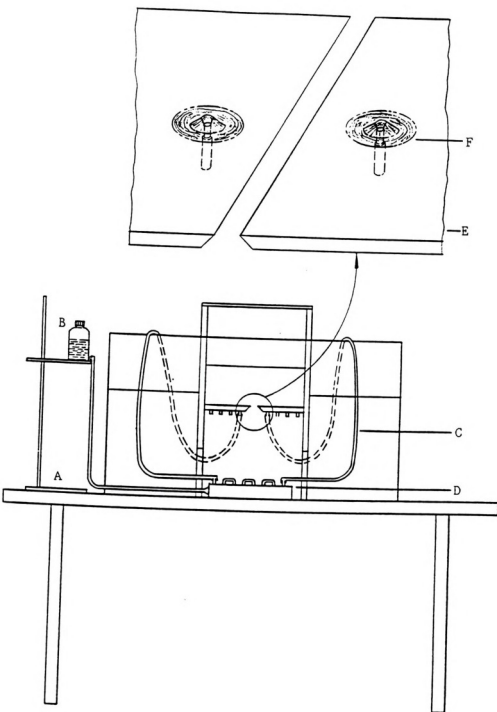


Figure 38. Schematic representation of the arrangement for injecting dye on the nozzle plates. A: Stand, B: Bottle with dye, C: Plastic tubing, D: Header, E: Nozzle plate, F: Jet of dye spreading on the nozzle plates.

A: Glass tank with liquid
 B: Glass fluid surface
 C: Pressure transducer
 range: 12.5 cm water
 D: Pressure transducer
 range: 12.5 cm water

PDP 11/73
 Apple IIe

$E_{NH}(t) \rightarrow$
 $E_T(t) \rightarrow$
 $G(t) \rightarrow$
 $E_{LDA}(t) \rightarrow$

Flow Facility

Timed
 Pulses

PDP 11/73

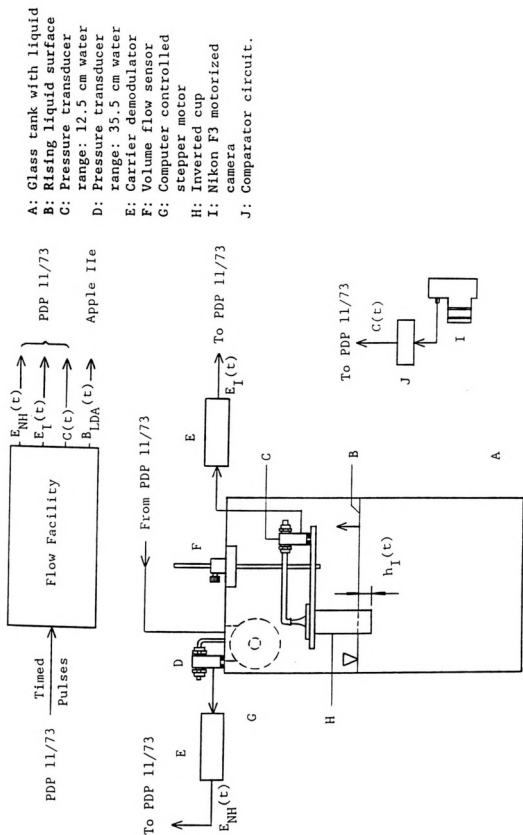


Figure 39. Side view of the flow facility with incoming and outgoing signals.

1/6 CD4049



Signal

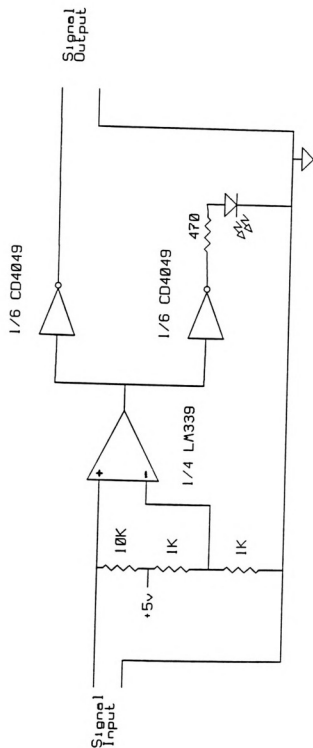
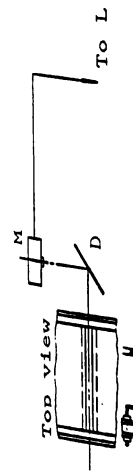


Figure 40. Schematic representation of the comparator circuit.





A: 35 mW laser
 B: Beam splitter
 C: Focusing lens
 D: Front surface mirror at 45°
 E: Receiving optics

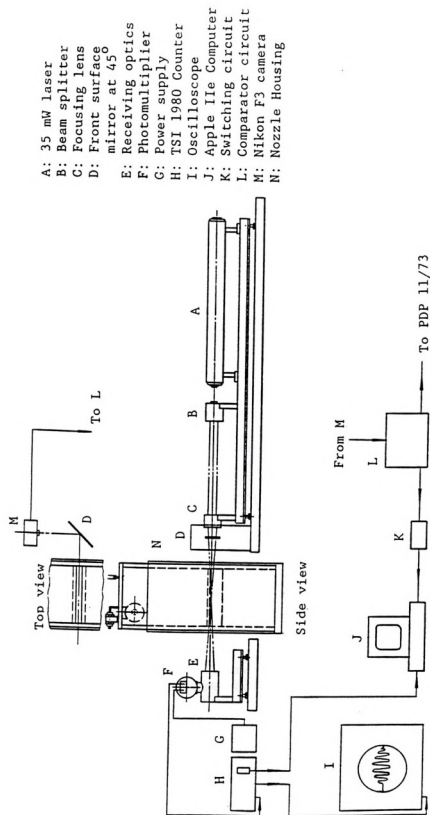


Figure 42. Schematic representation of the configuration for combined LDA-flow visualization experiments.



Corner

Figure 4
channel.

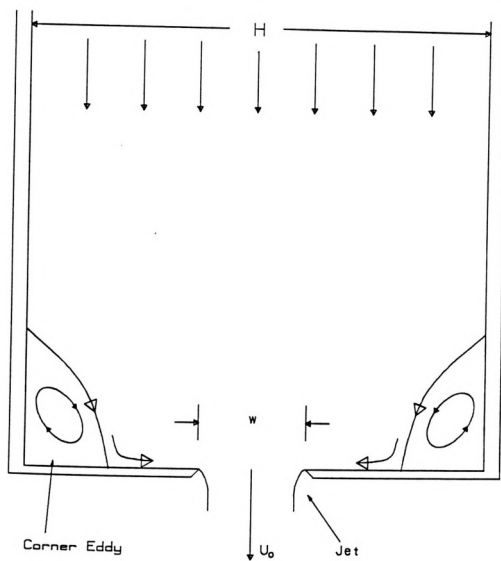


Figure 43. Schematic representation of the corner eddies in a channel-like plenum under steady flow conditions.

0.05
0.04

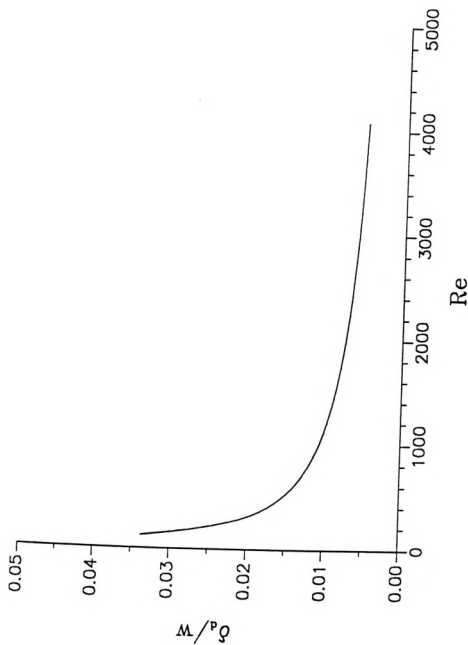
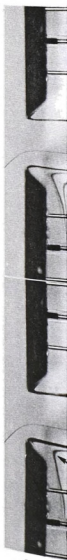


Figure 44. Variation of δ_d/w as a function of Re .



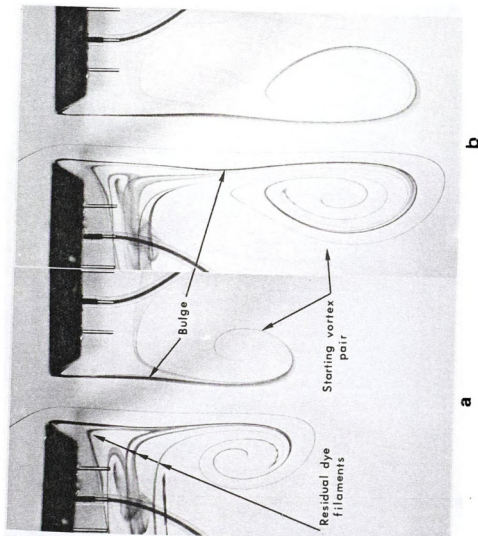


Figure 45. Jet development at $Re=87$, $V_p/V_\infty=0.68$ and $w=1.99$ cm. The nondimensional times are a) 11.8 and b) 18.1. Up to this time the bulge behind the SVP remains undeformed.



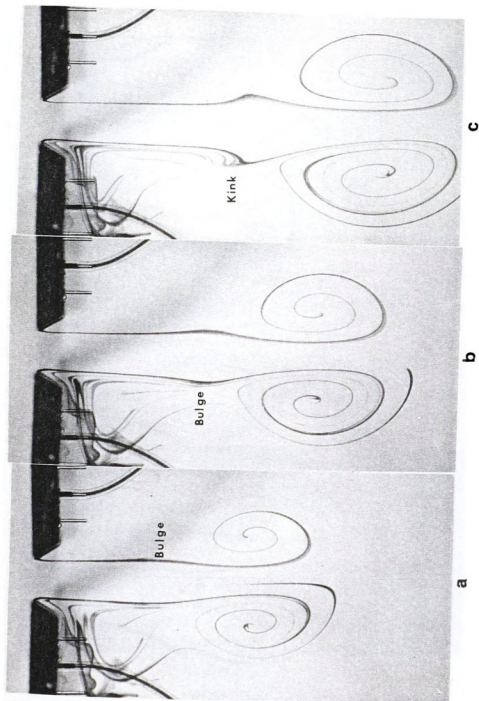


Figure 46. Jet development at $Re=105$, $V_b/V_s=0.70$ and $w=1.99$ cm. The nondimensional times are a) 14.2, b) 18.1 and c) 22.4. By $t^*=22.4$, the bulge has evolved into a kink. Note the increased inward displacement of the separating streamline position as compared to that in Figure 45.



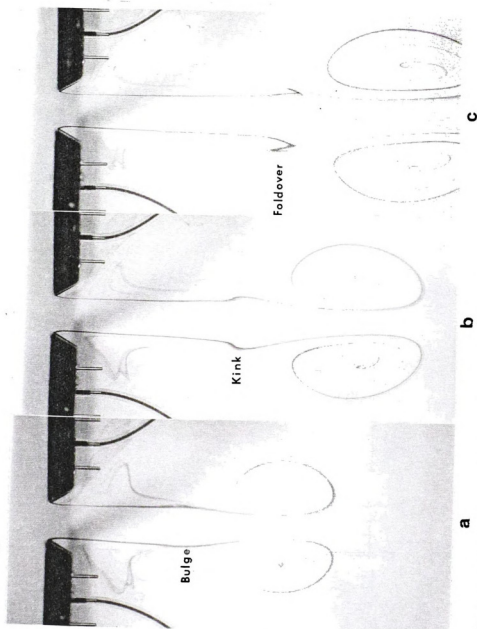
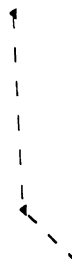


Figure 47. Jet development at $Re=129$, $V_p/V_s=0.72$ and $w=1.99$ cm. The nondimensional times are a) 16.9, b) 22.5 and c) 27.0. By $t^*=22.5$, the bulge has evolved into a kink and by $t^*=27$ the kink has evolved into a foldover. Note the development of the vena-contracta.

1.25
1.00



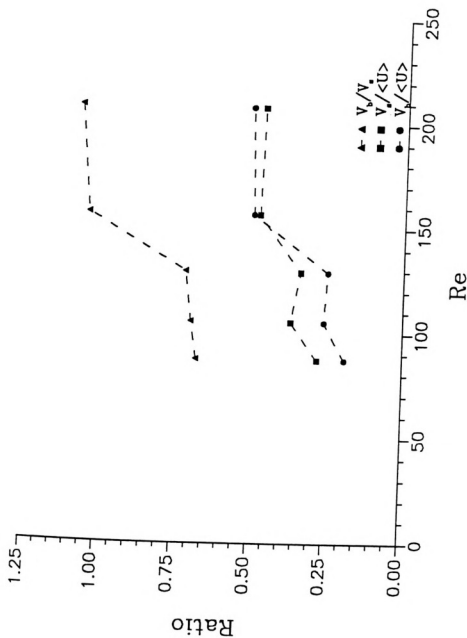


Figure 48. Ratio of bulge velocity to the velocity of the starting vortex pair as a function of Re . The figure also shows the distribution of $V_b/\langle U \rangle$ and $V_s/\langle U \rangle$ as functions of Re .



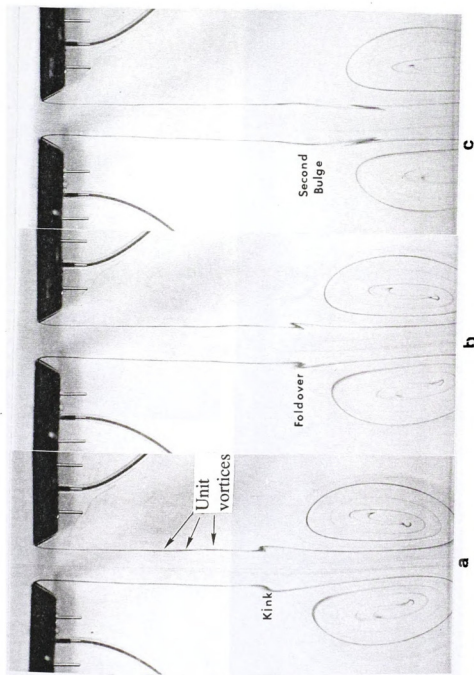


Figure 49. Jet development at $Re=156$, $V_b/V = 1.04$ and $w=1.99$ cm. The nondimensional times are a) 22.7, b) 24.1 and c) 26.8. In a) a bulge has evolved into a kink; in b) the kink has evolved into a foldover. Since $V_b/V_s > 1$, the foldover in c) is passing into the SVP. Note the formation of another bulge behind the SVP. This was the smallest Reynolds number at which unit vortices were first observed on the jet column.



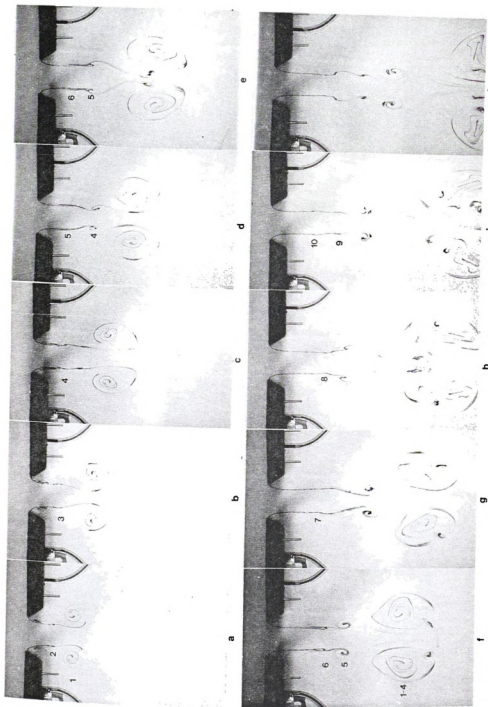
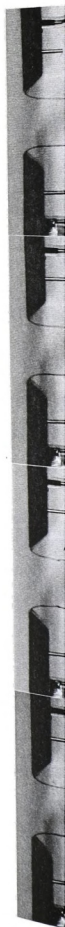


Figure 50. Jet development at $Re=980$ and $W=2.63$ cm. The nondimensional times are a) 10.9, b) 12.0, c) 13.1, d) 14.1, e) 15.2, f) 16.3, g) 17.3, h) 18.4, i) 19.5 and j) 20.5. The SVP is designated by 1. The indices 2, 3, ... designate the newly forming distinctive motions. Bulges 2 and 3 merge with the SVP without evolving into rollovers. However the bulge No. 4 evolves into a vortex pair before coalescing with the SVP.



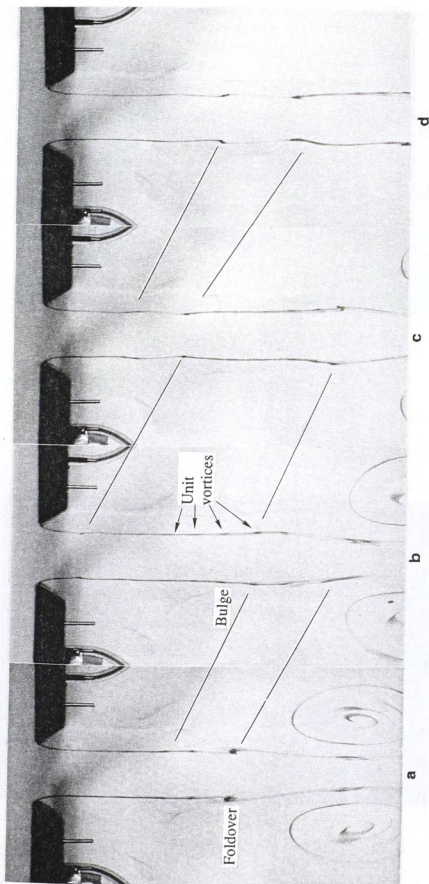


Figure 51. Jet development at $Re=207$, $w=2.63$ cm and $V_b/V_s=1.07$. The nondimensional times are a) 12.5, b) 15.1, c) 17.7 and d) 20.2. A number of dark spots in the svp in a) indicate the mergers of kinks/foldovers with the svp. The foldover in a) is approaching the svp in b) and another bulge has formed with overriding unit vortices. In d) three bulges can be identified.



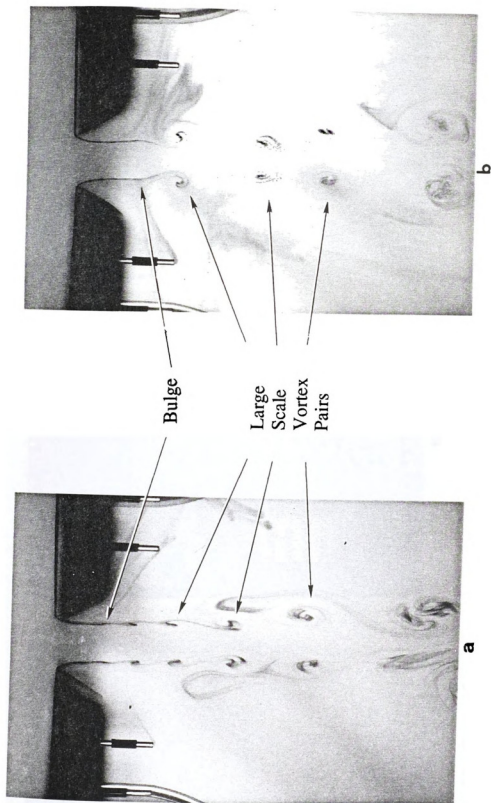
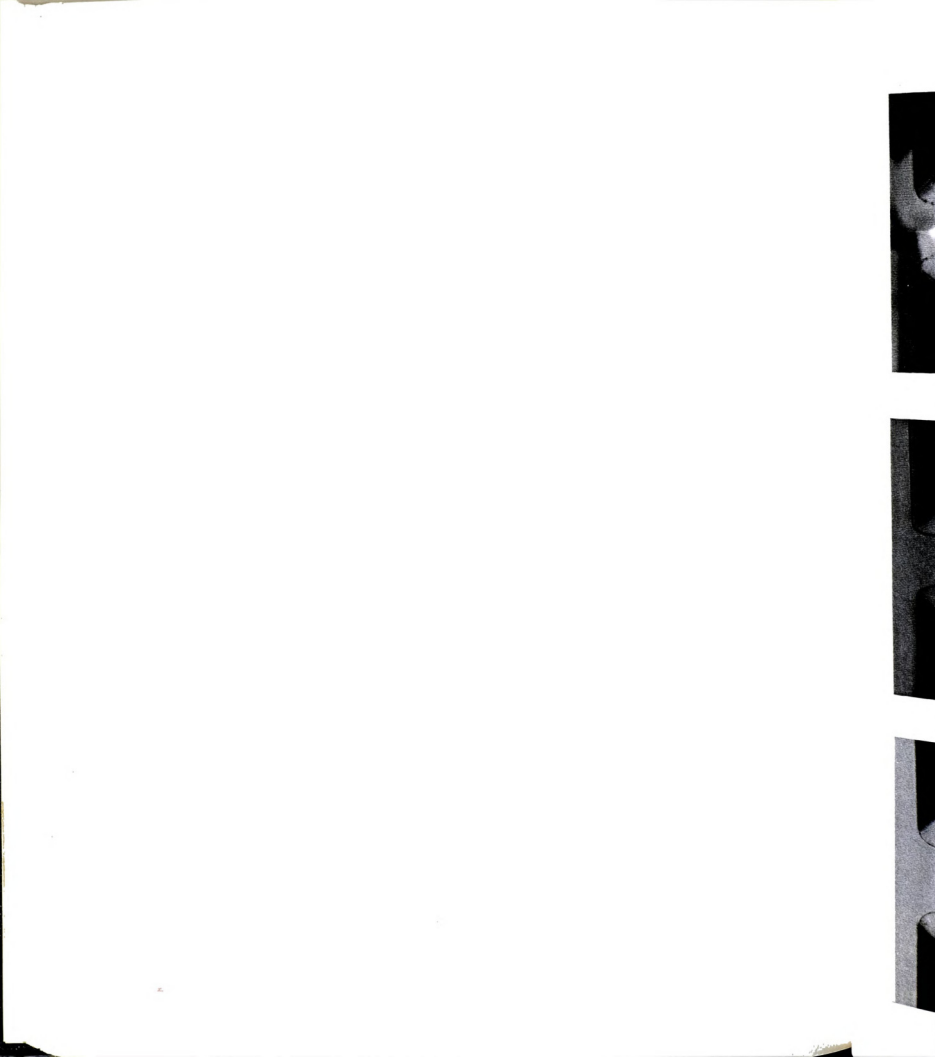


Figure 52. Formation of bulges and large scale vortex motions at two values of Re :
 a) 510 and b) 1200. Nominally similar features are observed over the Reynolds number range 276-1700.



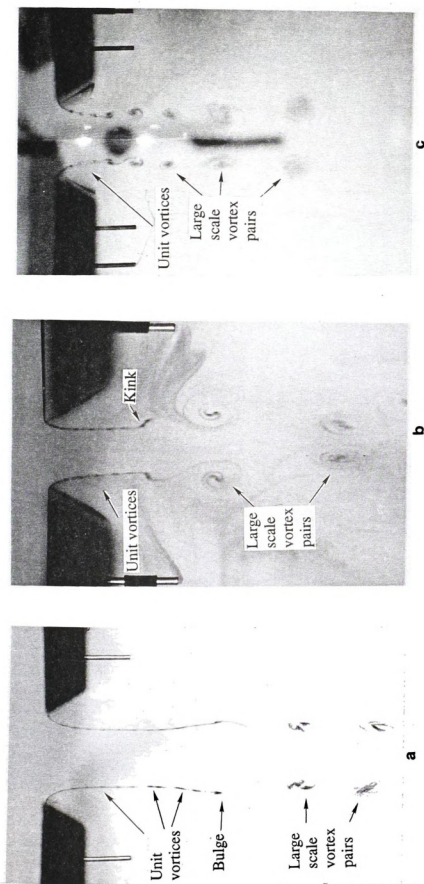


Figure 53. Formation of unit vortices in the slit-jet flow field along with the large scale vortex motions; Re_w and t^* are: a) 980, 2.63 cm and 24.8; b) 1044, 1.40 cm and 36.8 and c) 2949, 2.57 cm and 14.2.



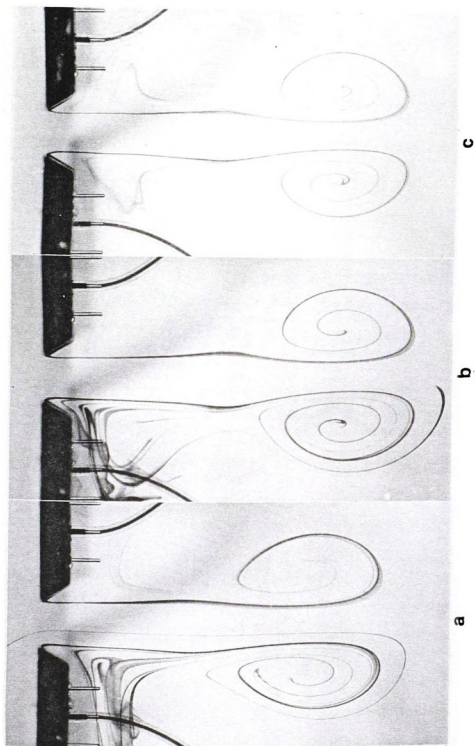


Figure 54. Jet development at three values of Re ; $V_b/V_s < 1.0$, $w = 1.99$ cm and $t^* = 18.1$. Re and V_b/V_s are a) 86 and 0.68, b) 105 and 0.70 and c) 129 and 0.72.



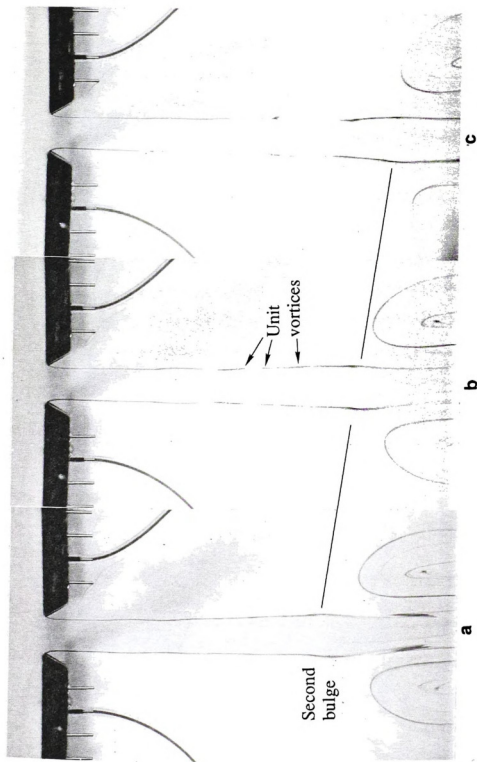


Figure 55. The slit-jet flow field of Figure 49 at later times. The nondimensional times are: a) 28.2, b) 30.2 and c) 32.3. In a) the first bulge is passing into the SVP, whereas in c) as the second bulge is approaching the SVP more bulges have formed on the jet column.



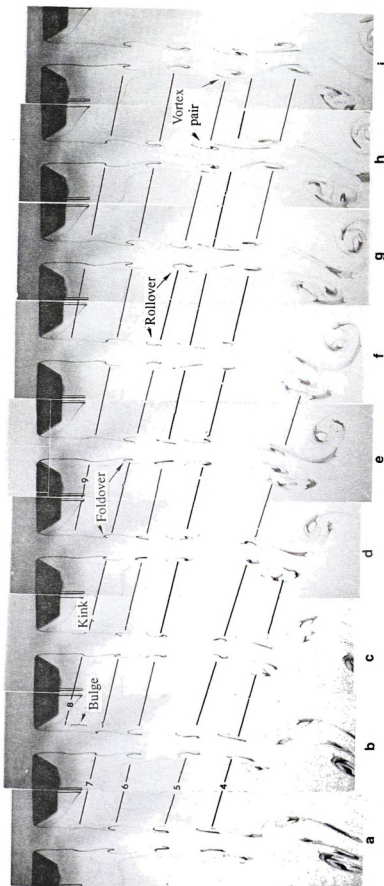


Figure 56. Sequence of photographs at $Re=281$ and $w=1.51$ cm exhibiting the formation of two dimensional vortex pairs. The nondimensional times are: a) 42.3, b) 43.4, c) 44.5, d) 45.7, e) 46.8, f) 47.9, g) 49.1, h) 50.2 and i) 51.3. Note: i) the formation of vortex No. 8 in h) can be traced back to the bulge in b). ii) the growth of bulge No. 7 stopped around $t^*=46$; in the remaining photographs it simply appears as a mark of dye. iii) the jet exhibits development of sinusoid mode beyond $x^*=8$.

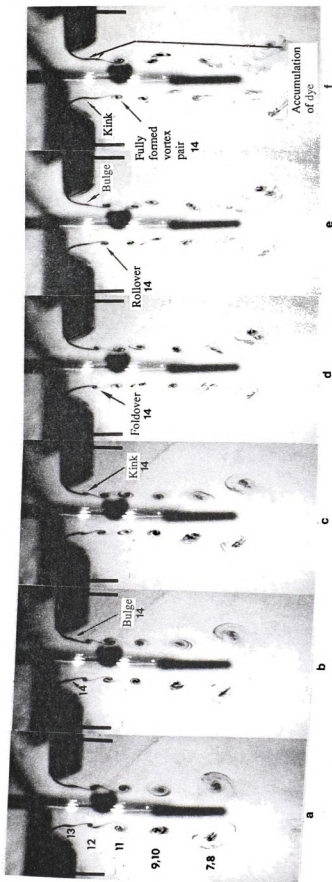
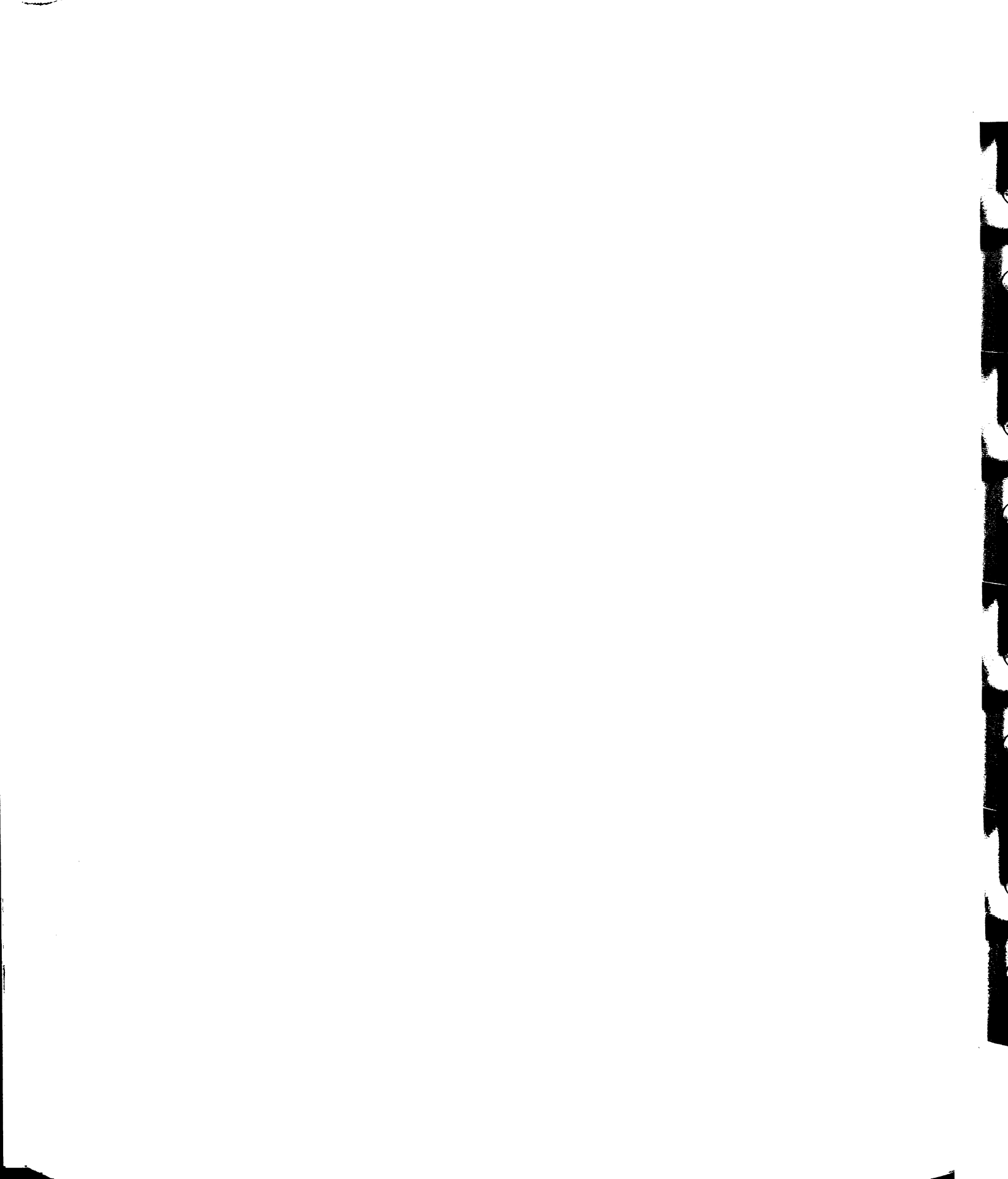


Figure 57. Process of vortex formation at $Re=1063$ and $w=2.57$ cm. The nondimensional times are: a) 17.0, b) 17.3, c) 17.5, d) 17.8, e) 18.1 and f) 18.4. The formation of vortex No. 14 in f) can be traced back to the bulge in b). In e) bulge No. 15 is beginning to form. Note in f) the symmetric accumulation of spots of dye as the bulge No. 15 is evolving into a kink.



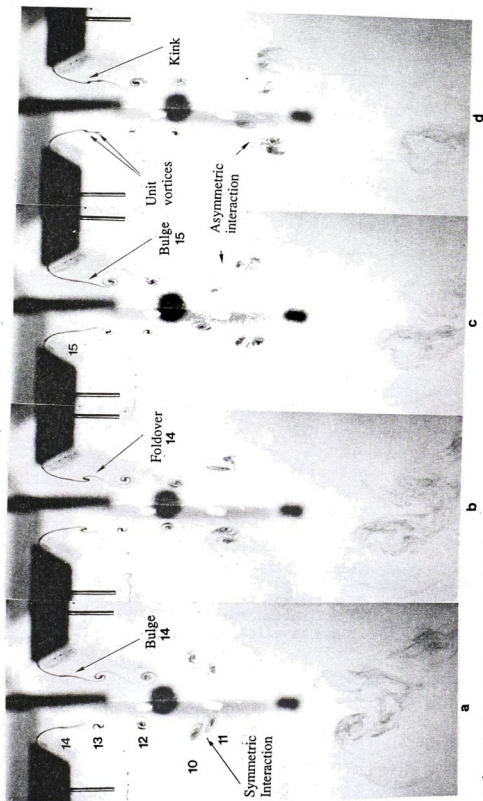


Figure 58. Process of formation of symmetric vortex street at $Re=1580$ and $w=2.57$ cm. The nondimensional times are: a) 13.8, b) 14.2, c) 14.6, and d) 15.0. Note the two spots of dye which appear to be unit vortices downstream of the kink No. 15. Also note the symmetric interaction between vortex pairs 10 and 11 in a) and somewhat asymmetric interaction between (10,11) and 12 in c) and d). Figure 70 presents a continuation of this sequence up to $t^*=16.2$.

Figure
formati
feature.
B: Infl
dye str
pair.

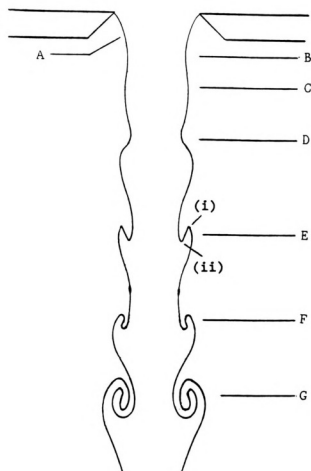
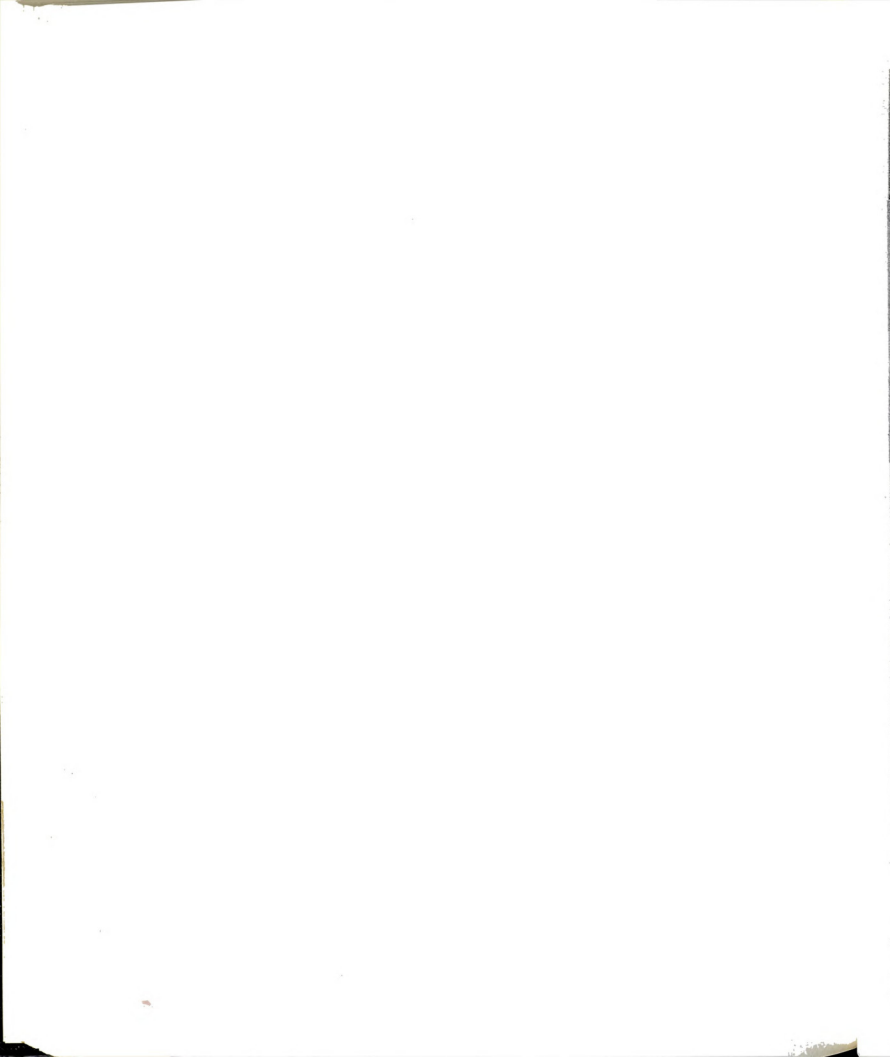


Figure 59. Schematic representation of the process of vortex formation in the near-field of the slit-jet flow. Various features are identified as: A: Formation of vena contracta, B: Inflexion point in the dye streak, C: Bulge, D: Kink in the dye streak, E: Foldover, F: Rollover and G: Fully formed vortex pair.



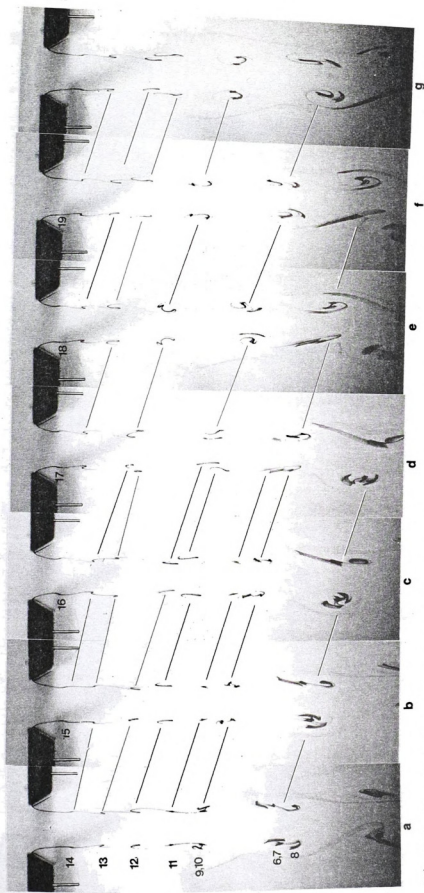


Figure 60. Jet development at $Re=362$ and $w=2.63$ cm. The nondimensional times are: a) 25.5, b) 26.3, c) 27.1, d) 27.9, e) 28.7, f) 29.5 and g) 30.3. Note that the growth of the features marked by the indices 11, 13, 14 and 16 stopped at some point of time. The features then simply became a mark of dye or became part of another vortex pair.

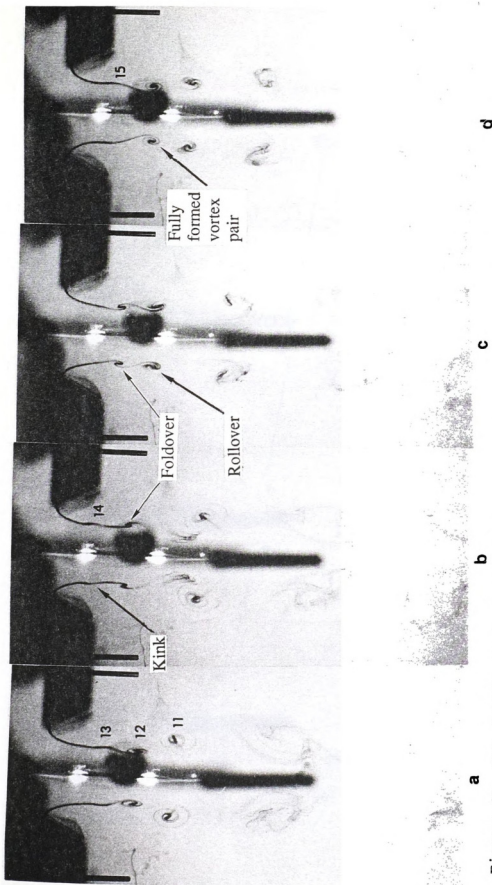


Figure 61. Jet development at $Re=1685$ and $w=2.57$ cm. The nondimensional times are: a) 15.5, b) 15.9, c) 16.3 and d) 16.8. Vortex No. 14 in contrast to No. 13 has formed without an apparent formation of a bulge; in d) bulge No. 15 has formed. Note the interaction between the vortices 11 and 12 starting in b) and completing in d).

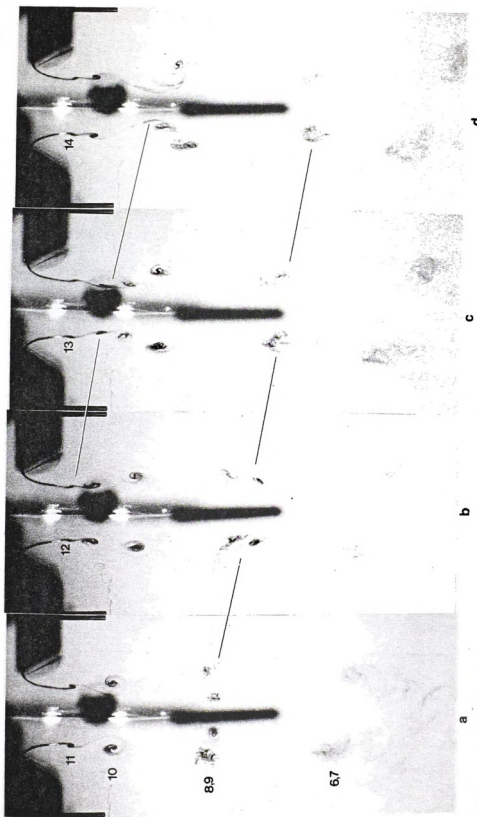


Figure 62. Jet development at $Re=1697$ and $w=2.57$ cm. The nondimensional times are: a) 14.9, b) 15.3, c) 15.7 and d) 16.1. Entities 12 and 14 appear as accumulation of dye and produce a kink in the jet boundary. Kink No. 12 grows into a foldover before disintegrating and becoming a part of vortex No. 11 which is itself in the process of coalescing with vortex No. 10. Also note the interaction between vortices 8 and 9.



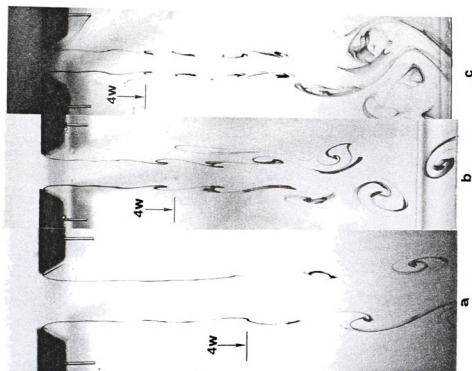
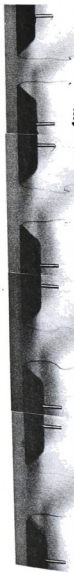


Figure 63. Jet development at $Re=280$ in three different jets. Re , w and t^* are:
 a) 281, 2.63 cm and 29.7, b) 276, 1.99 cm and 39.3 and c) 280, 1.51 cm and 39.3. Note the pattern of vortex motions in the 3 jets.



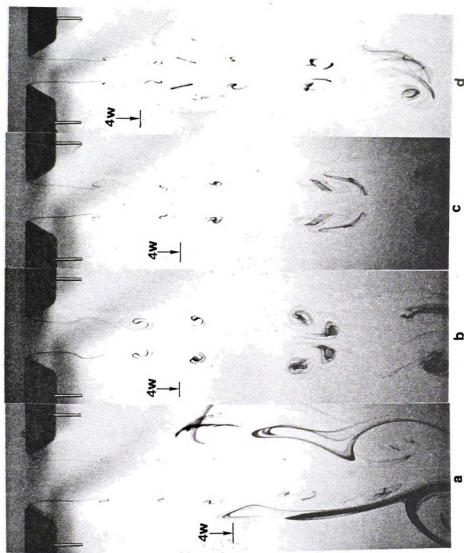


Figure 64. Jet development at $Re=420$ in three different jets. Re , w and t^* are: a) 408, 2.63 cm and 38.9, b) 426, 1.99 cm and 38.7, c) 426, 1.99 cm and 57.0 and d) 421, 1.51 cm and 57.



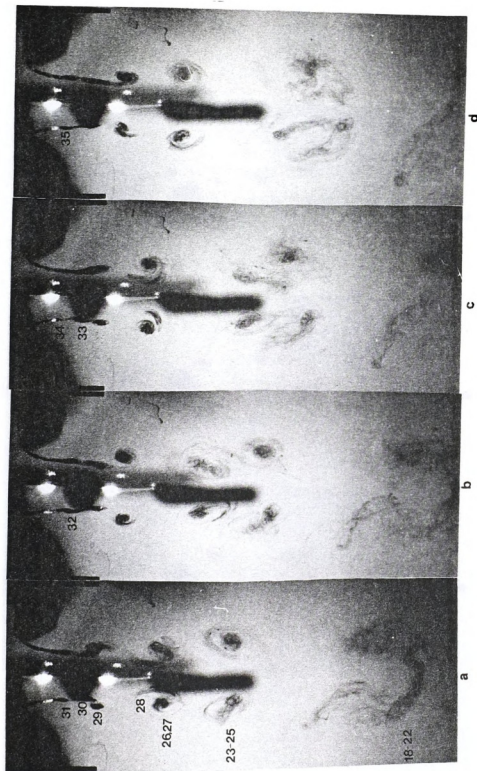


Figure 65. Jet development at $Re=2299$ and $w=2.57$ cm. The nondimensional times are a) 18.1, b) 18.6, c) 19.1 and d) 19.7. Note the formation of unit vortex motions as the dye streak separates from the nozzle plates.



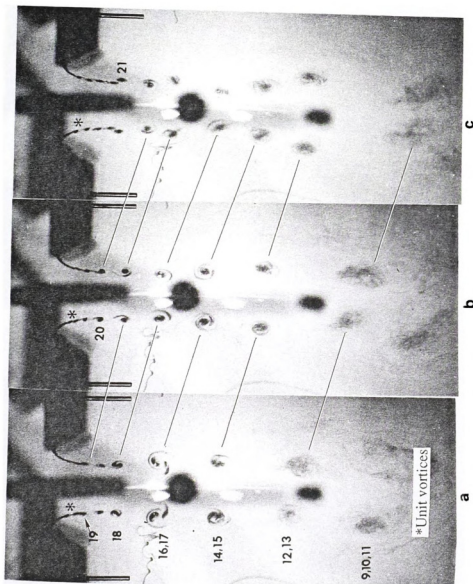


Figure 66. Unit vortices in the near field of a slit-jet at $Re=3401$ and $w=2.57$ cm. The nondimensional times are a) 20.5, b) 21.3 and c) 22.1. Note the absence of a bulge as large scale vortices numbers 19 and 20 form.



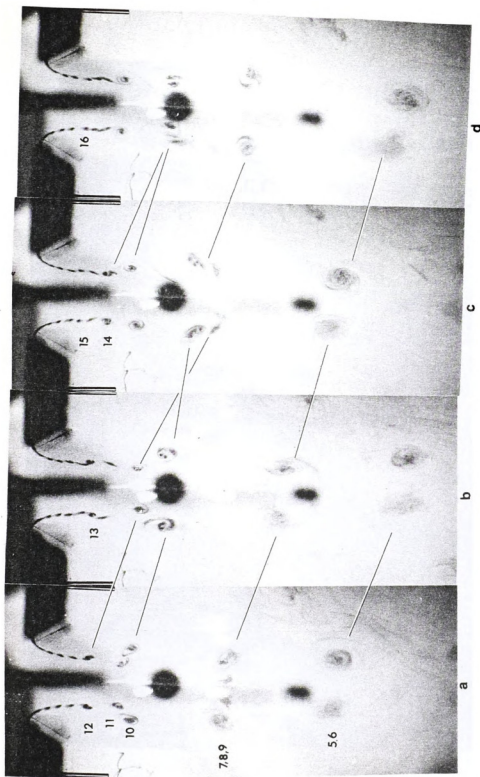


Figure 67. Process of vortex formation at $Re=3389$ and $w=2.57$ cm. The nondimensional times are a) 14.4, b) 15.2, c) 16.0 and d) 16.7. Note: i) asymmetry in the process of formation of vortex No. 13. ii) the formation of vortex No. 15 resembles the process described for Re range < 1700 . iii) the interaction between (7,8) and 9 in a), between 10 and 11 in a), between (10,11) and 12 in b) and between 13 and 14 in d). Also note that in c) vortex No. 12 has passed through (10,11).



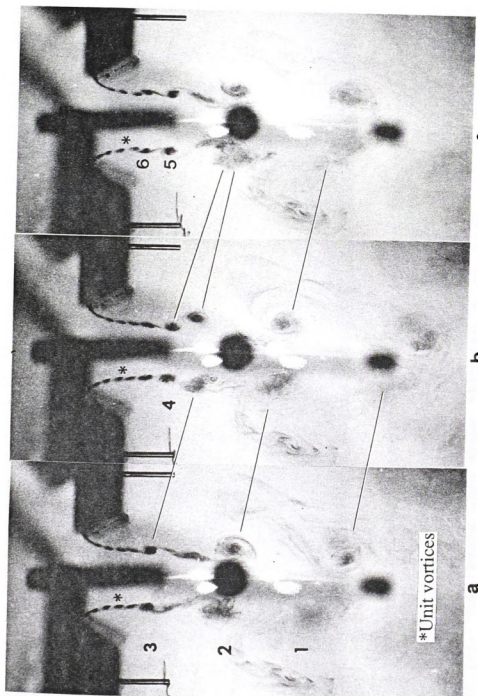
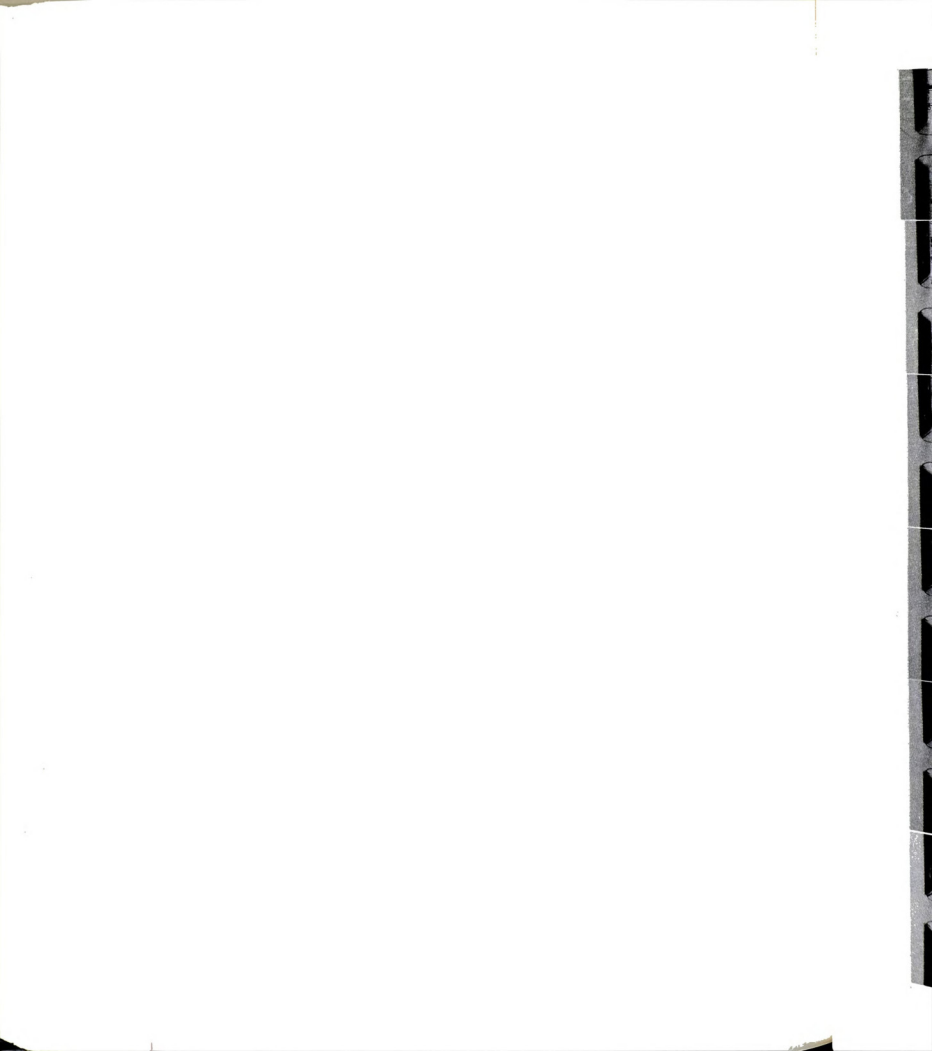


Figure 68. Jet development at $Re=3469$ and $w=2.57$ cm. The nondimensional times are a) 10.4, b) 11.2, and c) 12.0. Note: i) the unit vortices in the nearfield. ii) the absence of bulge as vortex No. 4 forms in b). iii) bulge formation precedes the growth of vortices 3, 5 and 6.



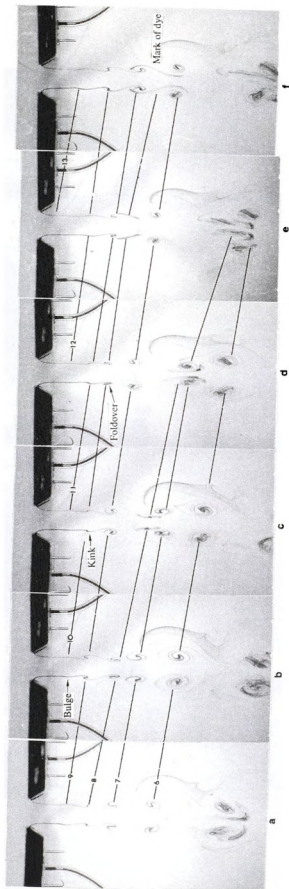


Figure 69. Interaction between symmetric vortex motions at $Re = 678$ and $w = 1.99$ cm. The nondimensional times are a) 50.2, b) 51.3, c) 52.5, d) 53.6, e) 54.8 and f) 55.9. Starting in (b) vortices 7 and 8 began to interact and before the pairing was over, (7,8) started to interact with vortex number 6 in (d). Note the large longitudinal spacing in (f) between the conglomerate (6,7,8) and the vortex number 9; similar spacing can also be observed in (a). The figure also shows that the bulge number 10 which formed in (b) did not become a vortex pair; rather, it disintegrated into a mark of dye by $t^* = 54.8$ in (f).



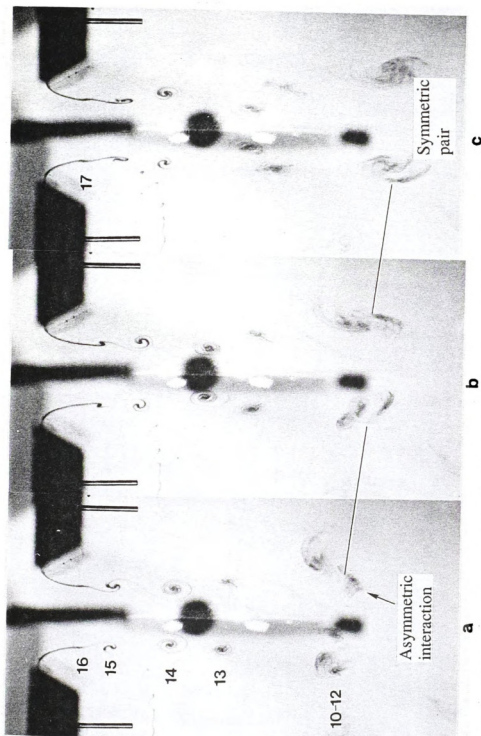
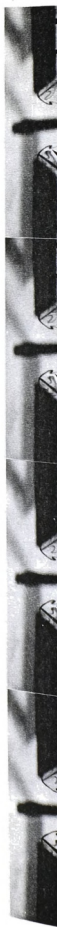


Figure 70. Continuation of the sequence of photographs presented in Figure 58. The nondimensional times are a) 15.4, b) 15.8, and c) 16.2. Note the asymmetry during the interaction between (10,11) and 12 in a) and the return of symmetry in c) as the interaction is completed.



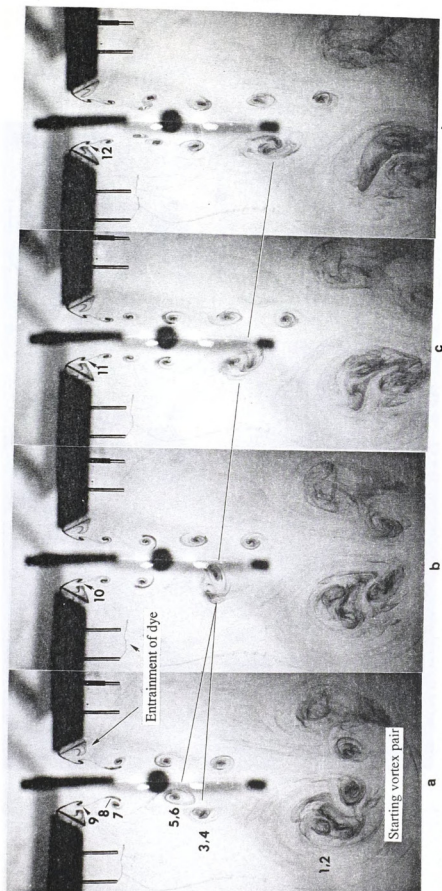


Figure 71. One sided pairing event between pairs (3,4) and (5,6) at $Re=1001$ and $w=2.57$ cm. The nondimensional times are a) 10.0, b) 10.6, c) 11.1 and d) 11.6.



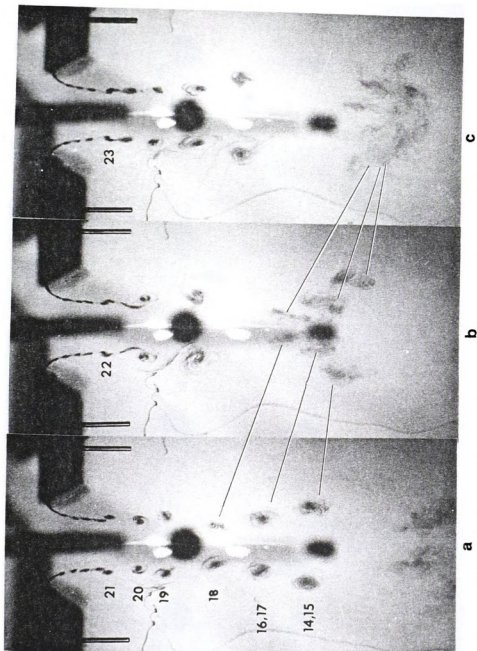
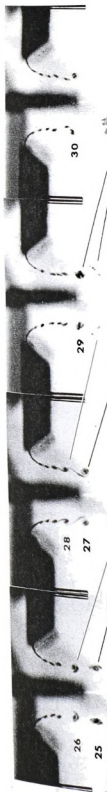


Figure 72. Simultaneous coalescence of three vortex pairs at $Re=3401$ and $w=2.57$ cm. The nondimensional times are a) 22.1, b) 22.9 and c) 23.6.



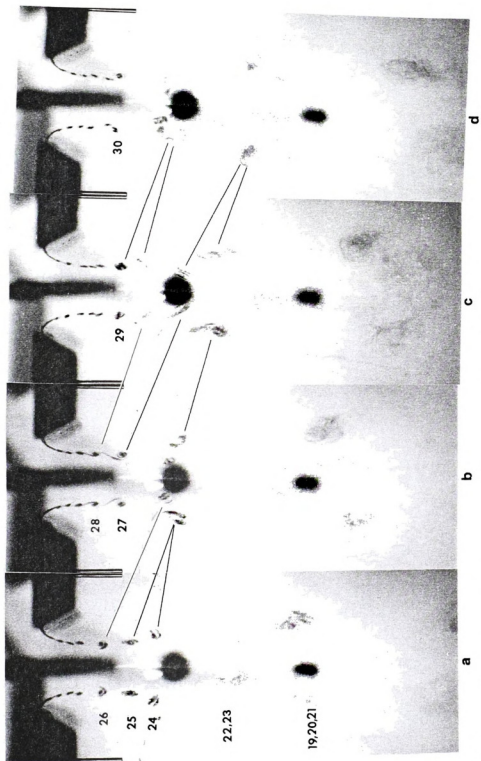


Figure 73. First stage of formation of five pairings at $Re=3401$ and $w=2.57$ cm. The nondimensional times are a) 25.2, b) 26.0, c) 26.7 and d) 27.5. Note that vortex pairs 24 and 25 pair and they are joined by 26 in b) and by 27 at some time between c) and d). Also 28 and 29 are undergoing pairing in d).



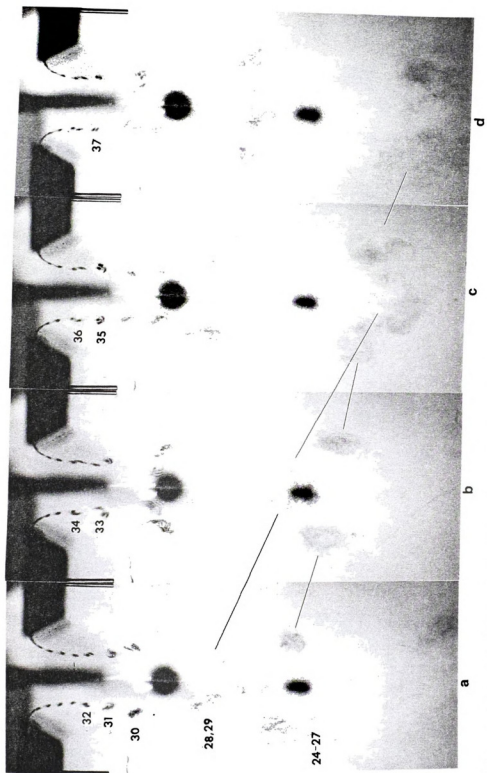
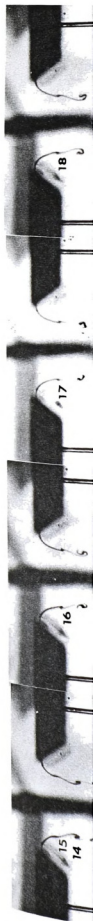


Figure 74. Second stage of formation of five pairings at $Re=3401$ and $w=2.57$ cm. The nondimensional times are a) 28.3, b) 29.1, c) 29.8 and d) 30.6. The pair (28, 29) begins to approach the conglomerate (24-27) in a) and by d) a new pair has been formed which comprises of five pairings.



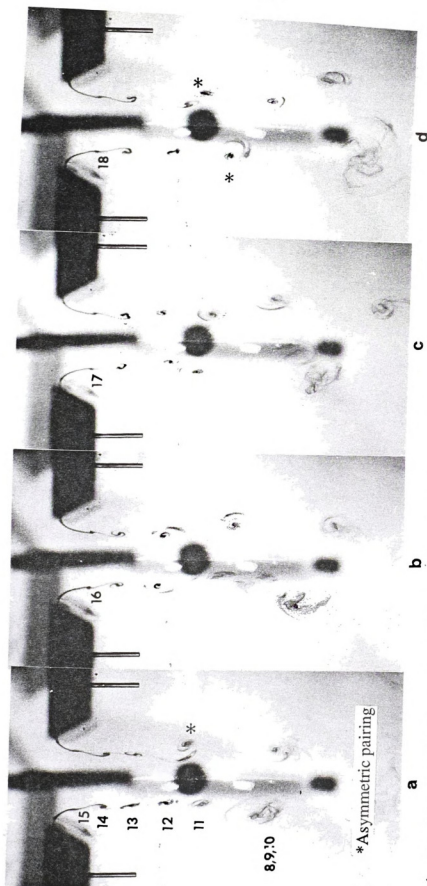
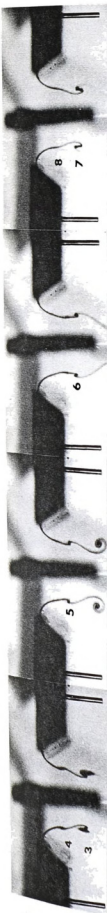


Figure 75. Loss of symmetry due to asymmetric pairing at $Re=1004$ and $w=2.57$ cm. The nondimensional times are a) 13.7, b) 14.5, c) 15.2 and d) 16.0. In a) the vortices of the pair (8-10) are beginning to displace with respect to one another, while, vortices 11 and 12 are about to pair on the right hand side of the centerline. Similarly, asymmetric pairing can be observed in d). Note, however, that the newly forming vortices in c) and d) are symmetrically located with respect to the centerline.



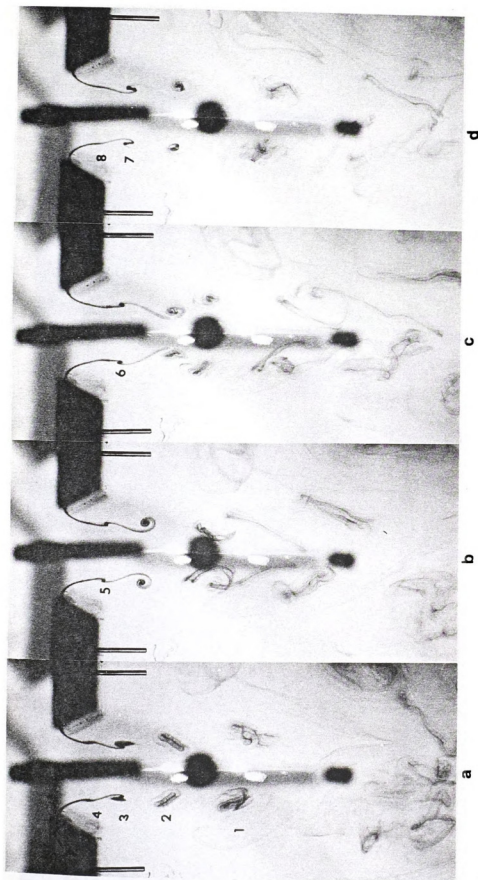
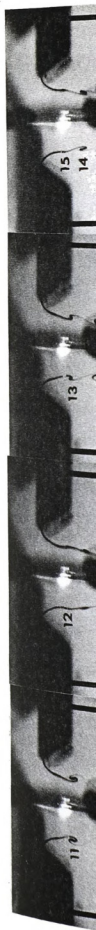


Figure 76. Loss of symmetric vortex street due to three dimensional instability of the two-dimensional vortex cores. Flow $Re=1571$ and $w=2.57$ cm. The nondimensional times are a) 8.5, b) 9.6, c) 10.7 and d) 11.8. Note the reestablishment of the symmetric, two-dimensional vortex pattern in d).



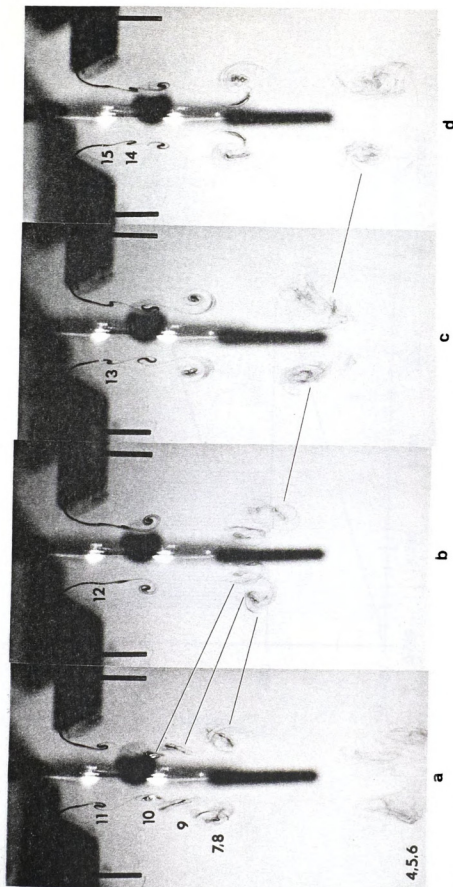


Figure 77. Reorganization of vortex motions at $Re=1027$ and $w=2.57$ cm. The nondimensional times are a) 11.0, b) 12.7 and c) 13.6. Vortex pair numbers (7,8) and 9 have been tilted in a). Between a) and b) the pairs (7,8), 9 and 10 begin to undergo coalescence and by d) they appear to have regained the two-dimensional character.

0.00

500

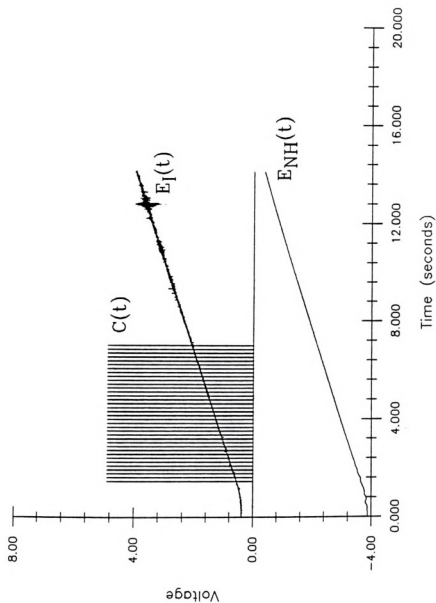


Figure 78. A representative sample of the data recorded by the A/D converter during a flow visualization experiment. $E_I(t)$ and $E_{NH}(t)$ are the voltages corresponding to $P_I(t)$ and $P_{NH}(t)$. The output, $C(t)$, of the comparator circuit indicates the times at which photographs were taken.



Figure 79. A ty
have been digit
The coalesced p
by a coma as 9,

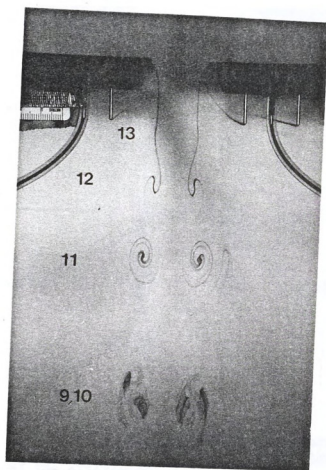


Figure 79. A typical representation of the photographs that have been digitized. Each vortex pair is marked by a number. The coalesced pairs are designated by two numbers separated by a coma as 9,10 in this photograph.



Figure 80. Sol
vortex pair in
the start of

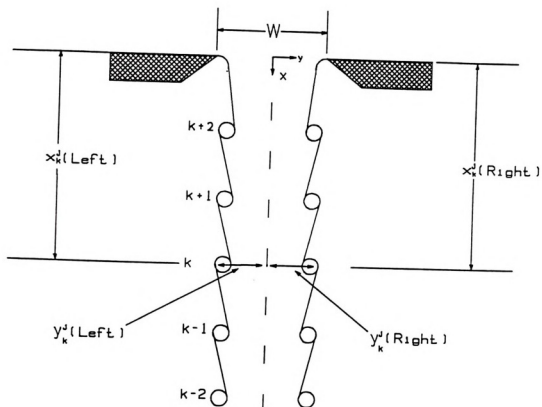


Figure 80. Schematic representation of the location of the k th vortex pair in the j th photograph which is at time t_j after the start of the experiment.

○ ○ $1.7x$

(1)

(111)

○ ○ $1x$

(11)

○ ○ $1x$

(1)

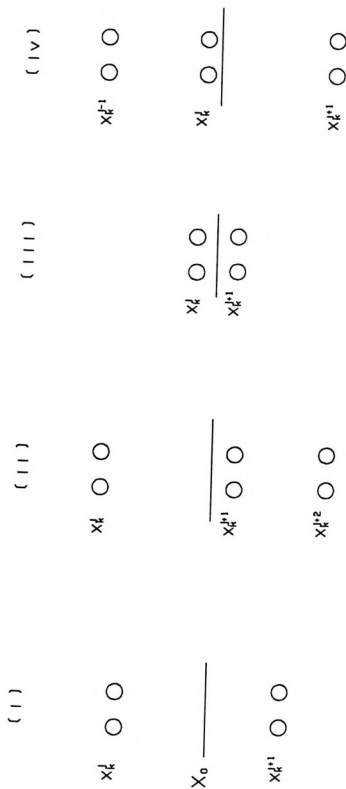


Figure 81. Four possible cases of positions of the k th vortex pair with respect to the plane of observation at x_k^I from the exit plane. The index j denotes the picture number at time t_j .

Cases 1

$$X_k^j$$

$$X_o \begin{matrix} X_k^j \\ X_{k-}^j \end{matrix}$$

Case 2

$$X_{k-}^j$$

$$X_o \begin{matrix} X_k^j \\ X_{k-}^j \end{matrix}$$

Case 4

$$X_{k-}^{j-1}$$

$$X_o \begin{matrix} X_k^{j-1} \\ X_{k-}^{j-1} \end{matrix}$$

Figure 82. s
vortex pair
and $(k+1)$. The
The curly br
determining
indicates th

Cases 1 & 3

$$\begin{array}{ccc}
 & t_j & t_{j+1} \\
 & \begin{array}{ccc} x_{k+1}^{j-1} & \circ & \circ \end{array} & \\
 x_0 \begin{array}{ccc} x_k^j & \circ & \circ \\ x_{k-1}^j & \circ & \circ \end{array} & \frac{\circ}{\circ} & \left\{ \begin{array}{ccc} x_{k+1}^{j+1} & \circ & \circ \\ x_k^{j+1} & \circ & \circ \\ x_{k-1}^{j+1} & \circ & \circ \end{array} \right\}
 \end{array}$$

Case 2

$$\begin{array}{ccc}
 & t_j & t_{j+1} & t_{j+2} \\
 & \begin{array}{ccc} x_{k+1}^j & \circ & \circ \end{array} & & \\
 x_0 \begin{array}{ccc} x_k^j & \circ & \circ \\ x_{k-1}^j & \circ & \circ \end{array} & \frac{\circ}{\circ} & \left\{ \begin{array}{ccc} x_{k+1}^{j+1} & \circ & \circ \\ x_k^{j+1} & \circ & \circ \\ x_{k-1}^{j+1} & \circ & \circ \end{array} \right\} & \left\{ \begin{array}{ccc} x_{k+1}^{j+2} & \circ & \circ \\ x_k^{j+2} & \circ & \circ \\ x_{k-1}^{j+2} & \circ & \circ \end{array} \right\}
 \end{array}$$

Case 4

$$\begin{array}{ccc}
 & t_{j-1} & t_j & t_{j+1} \\
 & \begin{array}{ccc} x_{k+1}^{j-1} & \circ & \circ \end{array} & \begin{array}{ccc} x_{k+1}^j & \circ & \circ \end{array} & \\
 x_0 \begin{array}{ccc} x_k^{j-1} & \circ & \circ \\ x_{k-1}^{j-1} & \circ & \circ \end{array} & \frac{\circ}{\circ} & \left\{ \begin{array}{ccc} x_{k+1}^{j-1} & \circ & \circ \\ x_k^{j-1} & \circ & \circ \\ x_{k-1}^{j-1} & \circ & \circ \end{array} \right\} & \left\{ \begin{array}{ccc} x_{k+1}^{j+1} & \circ & \circ \\ x_k^{j+1} & \circ & \circ \\ x_{k-1}^{j+1} & \circ & \circ \end{array} \right\}
 \end{array}$$

Figure 82. Scheme for determining the spacing L_k of the k th vortex pair with respect to the neighboring vortex pairs: $(k-1)$ and $(k+1)$. The index j denotes the photograph number at time t_j . The curly bracket indicates the vortex pairs which are used in determining L_k . The solid line at x_0 from the exit plane indicates the plane of observation.

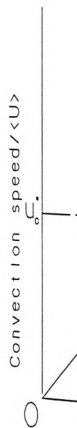


Figure 83. Schematic of the overall effect of St_F and the frequency on the convection speed of each vortex pair.

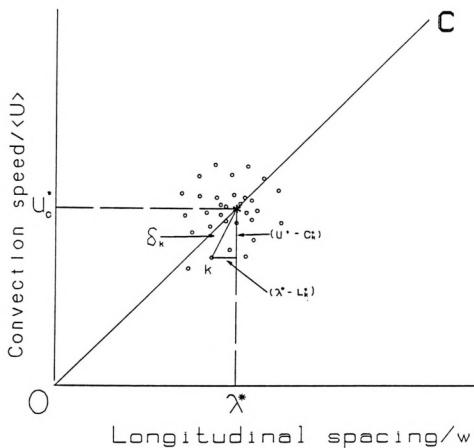


Figure 83. Schematic representation of the technique used to find the overall estimates of λ^* and u_c^* from the measured St_F and the independent estimates of L_k^* and c_k^* of each vortex pair. The slope of the line OC is equal to St_F .

10.00
8.00

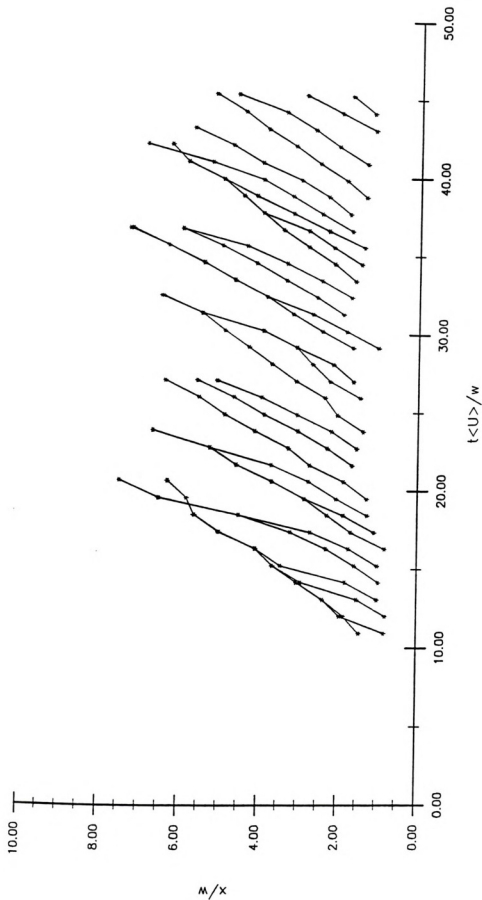


Figure 84. Space-time plot of vortices from the start of the experimental run. Up to 5 vortices merge with the starting vortex pair over $10 < t < 18$. Around $t = 35$, a large cluster of vortices is formed due to 3 sequential pairings.

2.00

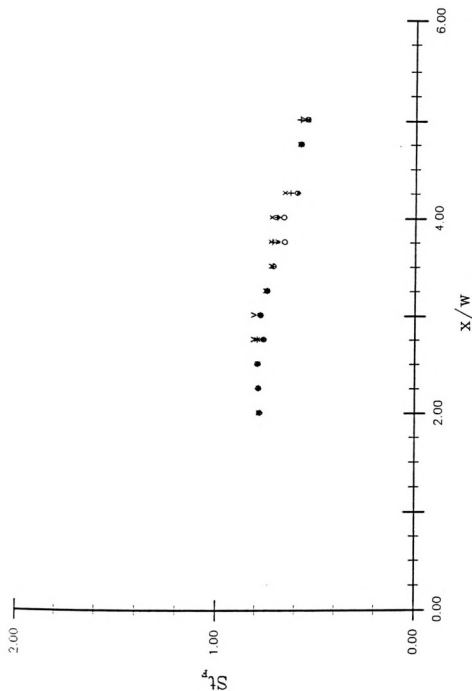


Figure 85. Streamwise distribution of St_F for five combinations of the control parameters T_p , T_w ; 0.05, 0.05 +; 0.1, 0.1 *; 0.05, 0.1 x; 0.1, 0.05 o and 0.1, 0.2 v.

2.00

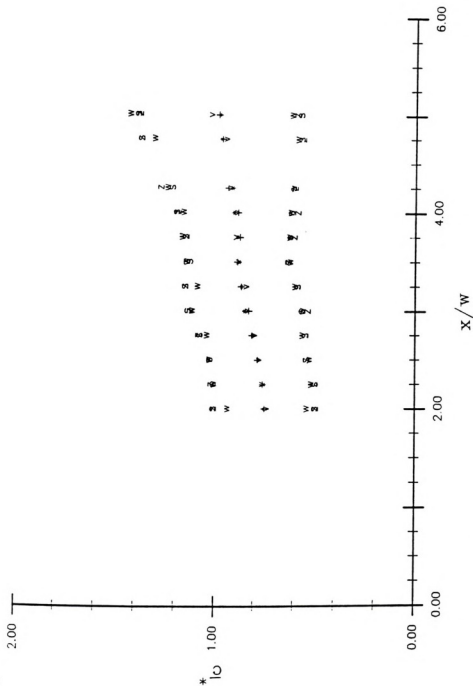


Figure 86. Distribution of mean and rms values of convection velocity, c_k^* , of vortices for three combinations of T and T_v : 0.05, 0.05, +, z; 0.1, 0.1 *, s and 0.1, 0.2 v, w. The mean values are represented by the first symbol, whereas the second symbol indicates the standard deviation from the mean value.

2.00



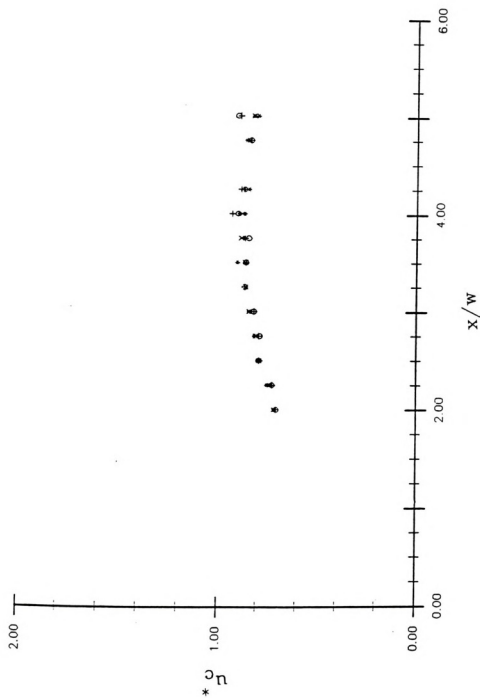


Figure 87. Streamwise distribution of u^* for five combinations of T_p and T_w . See Figure 85 for legend.

$\otimes +$
 $\otimes >$
 \otimes
 $\otimes \otimes$

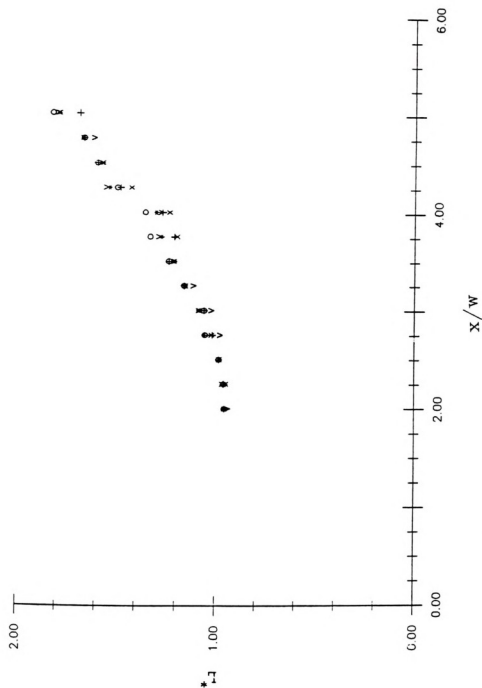


Figure 88. Distribution of the estimate of longitudinal spacing L^* based upon St_F and c^* . See Figure 85 for legend.

NO 2
3

N 3
3

300 N

3

N 3

N

2.00

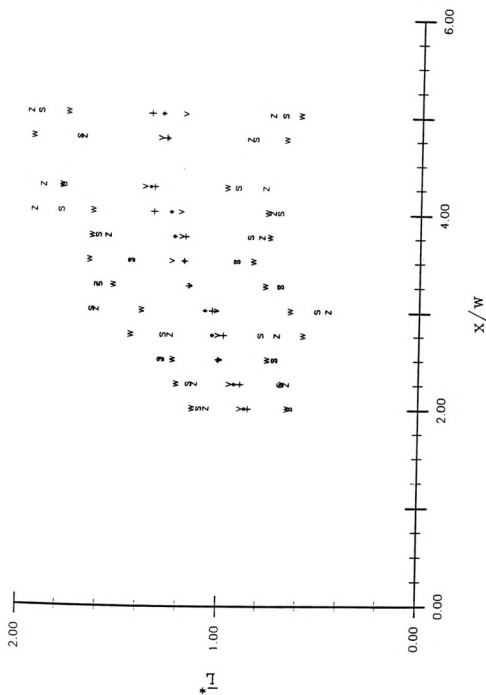


Figure 89. Distribution of mean and rms values of longitudinal spacing, l^* , between vortices for three combinations of T and T_p . For legend see Figure 86.

2.00

0

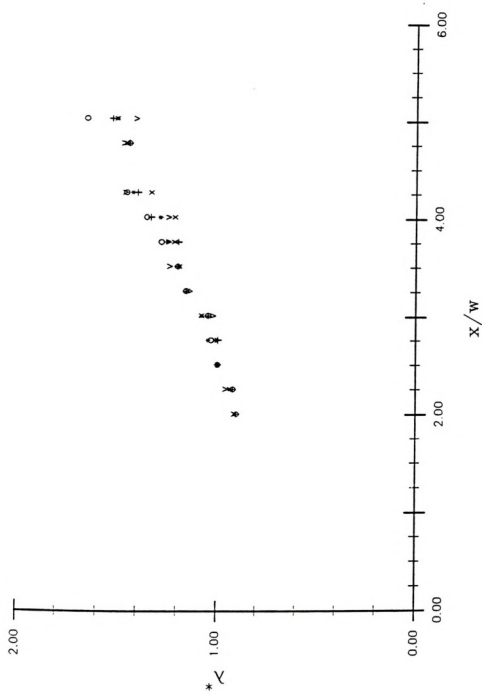


Figure 90. Streamwise distribution of λ^* for five combinations of T_p and T_w . For legend see Figure 85.

• + 0
>

080
100

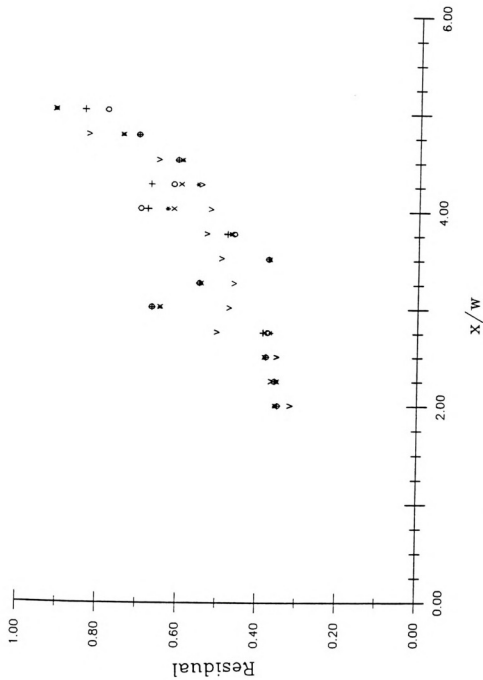


Figure 91. Residual of the regression of St_F through c_k^* and L_k^* for five combinations of T_p and T_w . For legend see Figure 85.

per
5.00
4.00

c
c
c
c

c

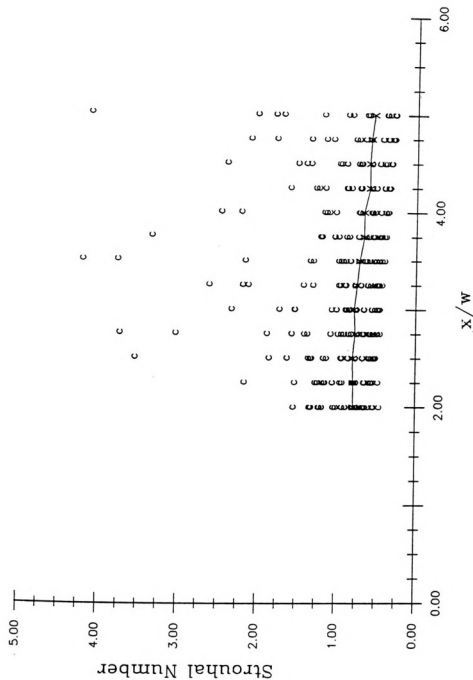


Figure 92. Comparison of St_F with Strouhal number based upon the difference in the passage time, δt_k , between two vortex pairs. c: Strouhal number based upon δt_k ; x: St_F . The solid line connects the values of St_F .

10.00
8.00



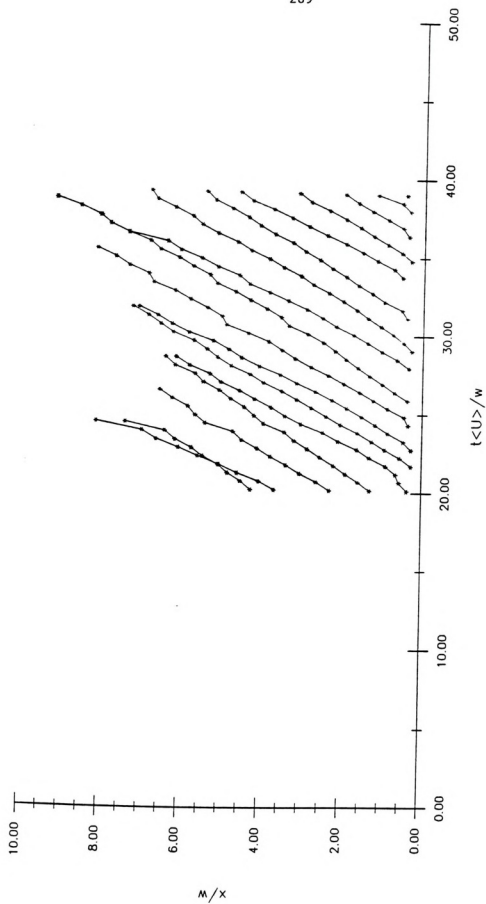


Figure 93. Space-time plot of vortices at $Re = 269$ and $w = 1.99$ cm.

10.00
5.00

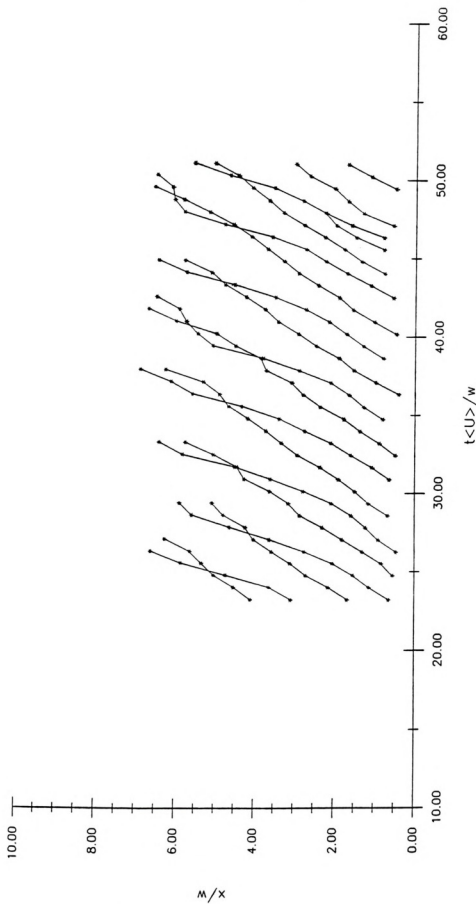


Figure 94. Space-time plot of vortices at $Re = 696$ and $w = 2.63$ cm.

10.00
8.00



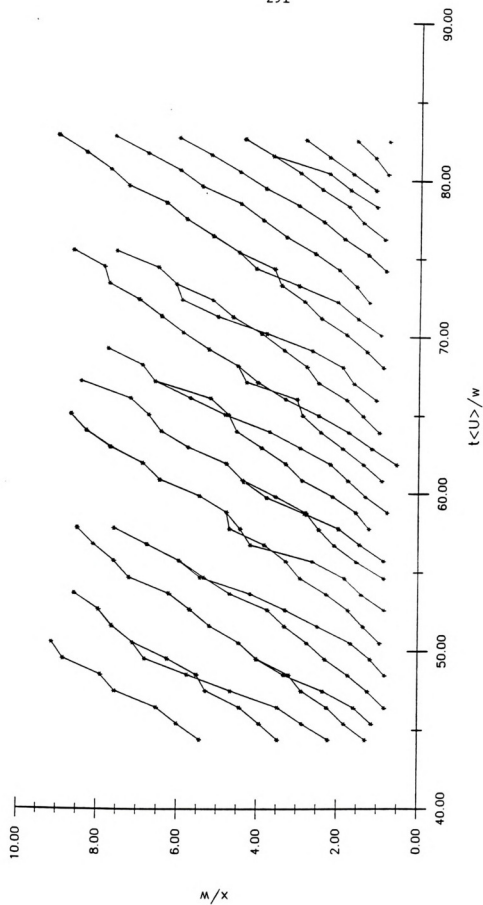


Figure 95. Space-time plot of vortices at $Re = 1269$ and $w = 1.40$ cm.

10.00
8.00

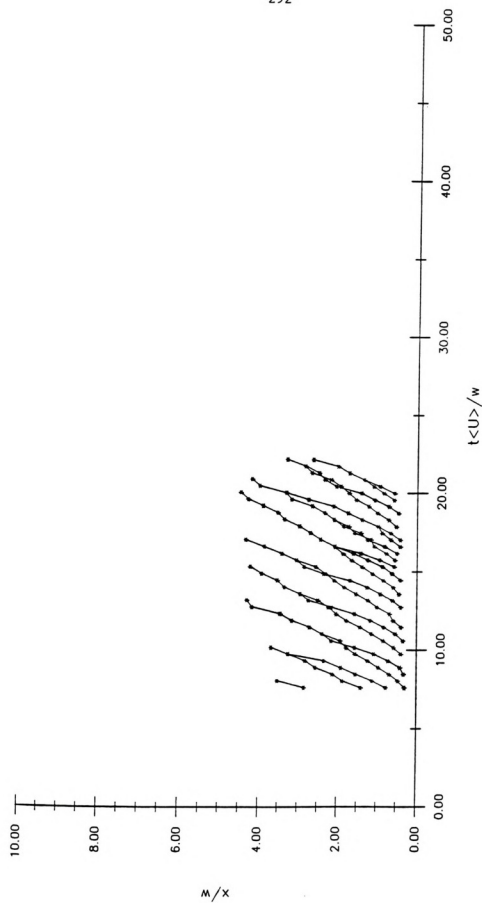


Figure 96. Space-time plot of vortices at $Re = 1697$ and $w = 2.57$ cm.

10.00
8.00

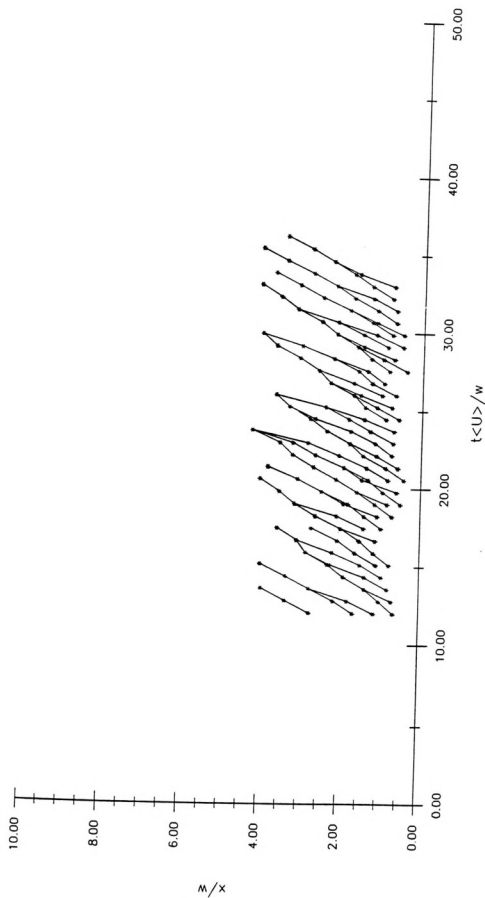


Figure 97. Space-time plot of vortices at $Re = 3401$ and $w = 2.57$ cm.

2.00



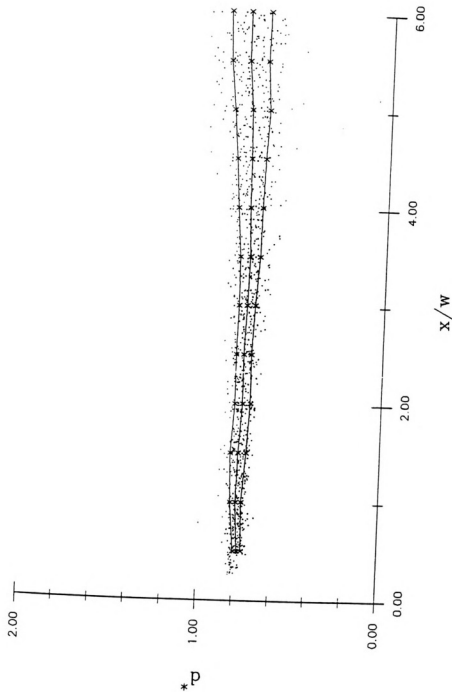


Figure 98. Normalized lateral spreading between vortices of given pairs over the Re range of 269-285. At selective streamwise locations, the middle x represents \bar{d} and the outer x's have been plotted at 1 standard deviation from the mean value.

2.00



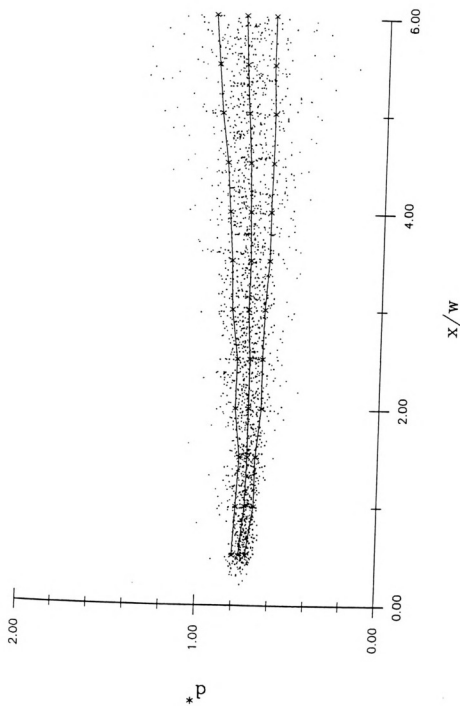


Figure 99. Normalized lateral spreading between vortices of given pairs over the Re range of 362-525. See Figure 98 for details.

200

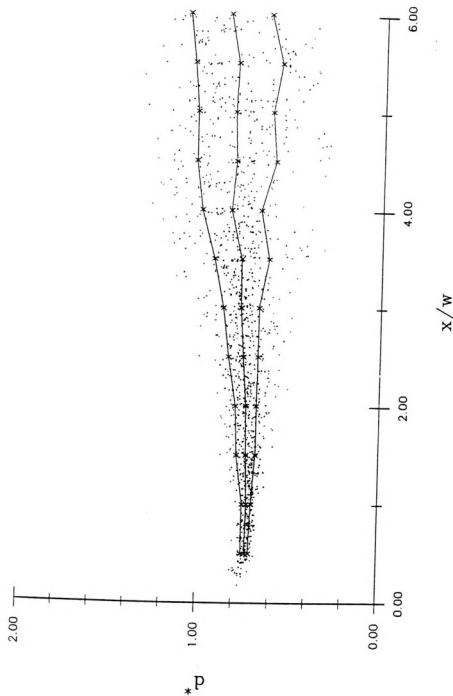


Figure 100. Normalized lateral spreading between vortices of given pairs over the Re range of 640-698. See Figure 98 for details.

2.00

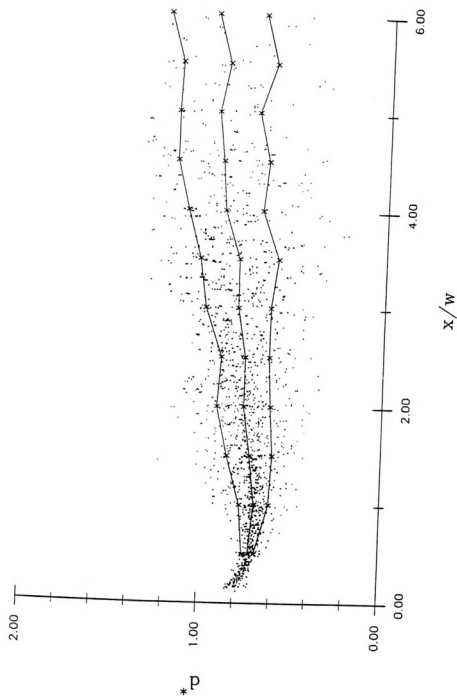


Figure 101. Normalized lateral spreading between vortices of given pairs over the Re range of 930-1074. See Figure 98 for details.

2.00

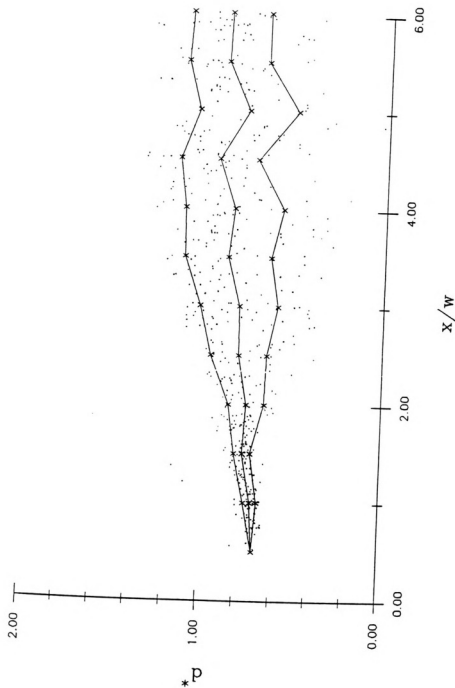


Figure 102. Normalized lateral spreading between vortices of given pairs over the Re range of 1257-1272. See Figure 98 for details.

2.00

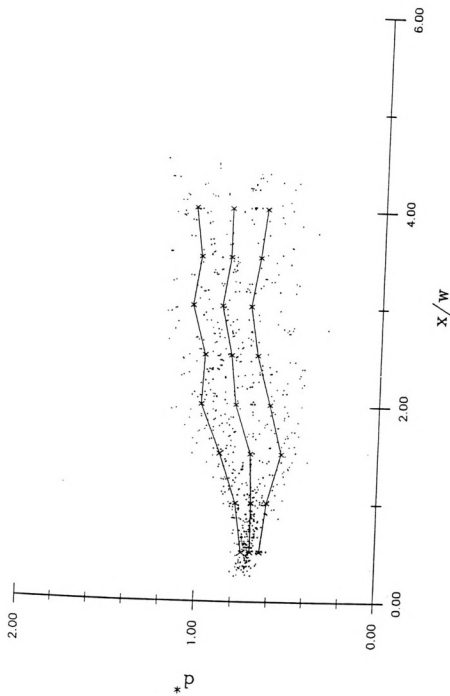


Figure 103. Normalized lateral spreading between vortices of given pairs over the Re range of 1571-1697. See Figure 98 for details.

2 00

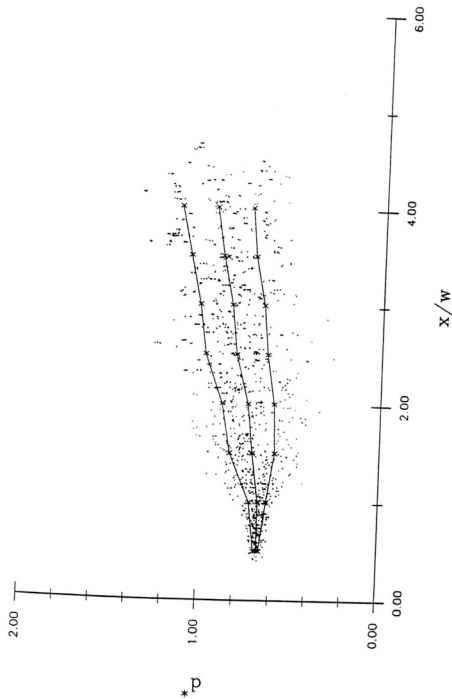


Figure 104. Normalized lateral spreading between vortices of given pairs over the Re range of 2949-3469. See Figure 98 for details.

2.00



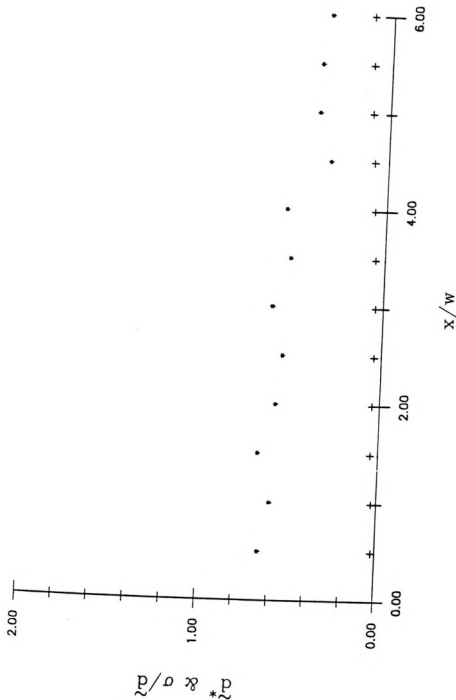


Figure 105. Statistical details of the lateral spreading of vortices in the Re range of 269-285. +: The rms of the population at selective X/W value; *: the ratio of the residual of the least square fit to the rms of the population denoted by +.

2.00



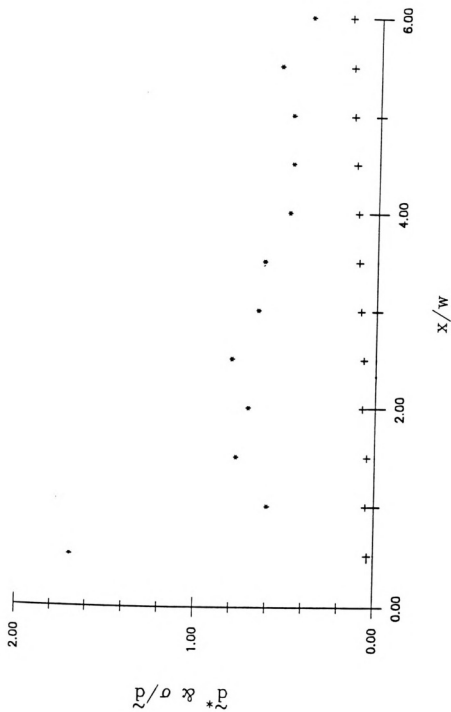


Figure 106 . Statistical details of the lateral spreading of vortices in the Re range of 362-525 . For legend see Figure 105.

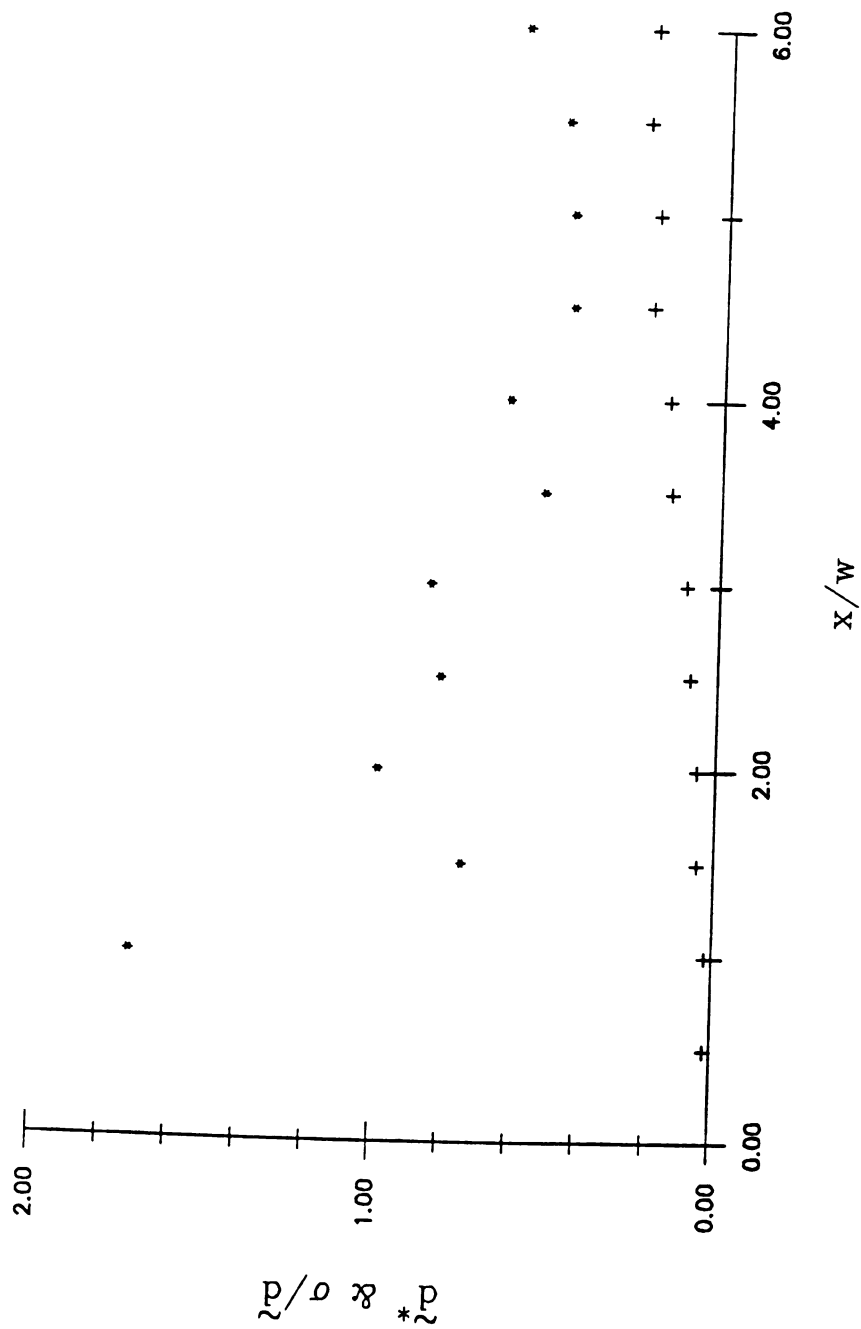


Figure 107. Statistical details of the lateral spreading of vortices in the Re range of 640-698. For legend see Figure 105.

2.00

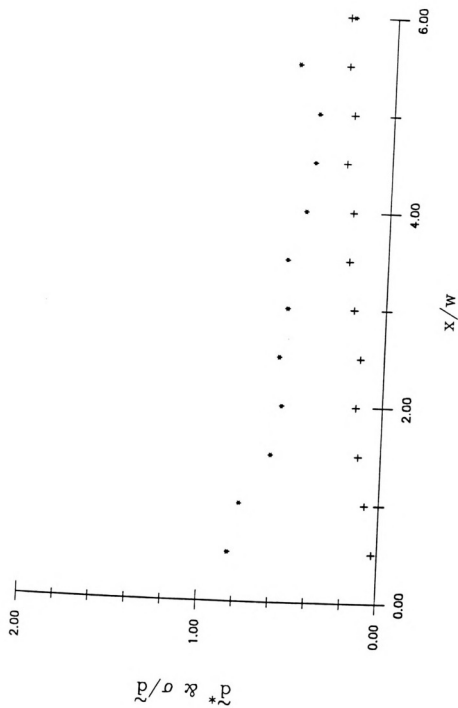


Figure 108. Statistical details of the lateral spreading of vortices in the Re range of 930-1074. For legend see Figure 105.

2.00

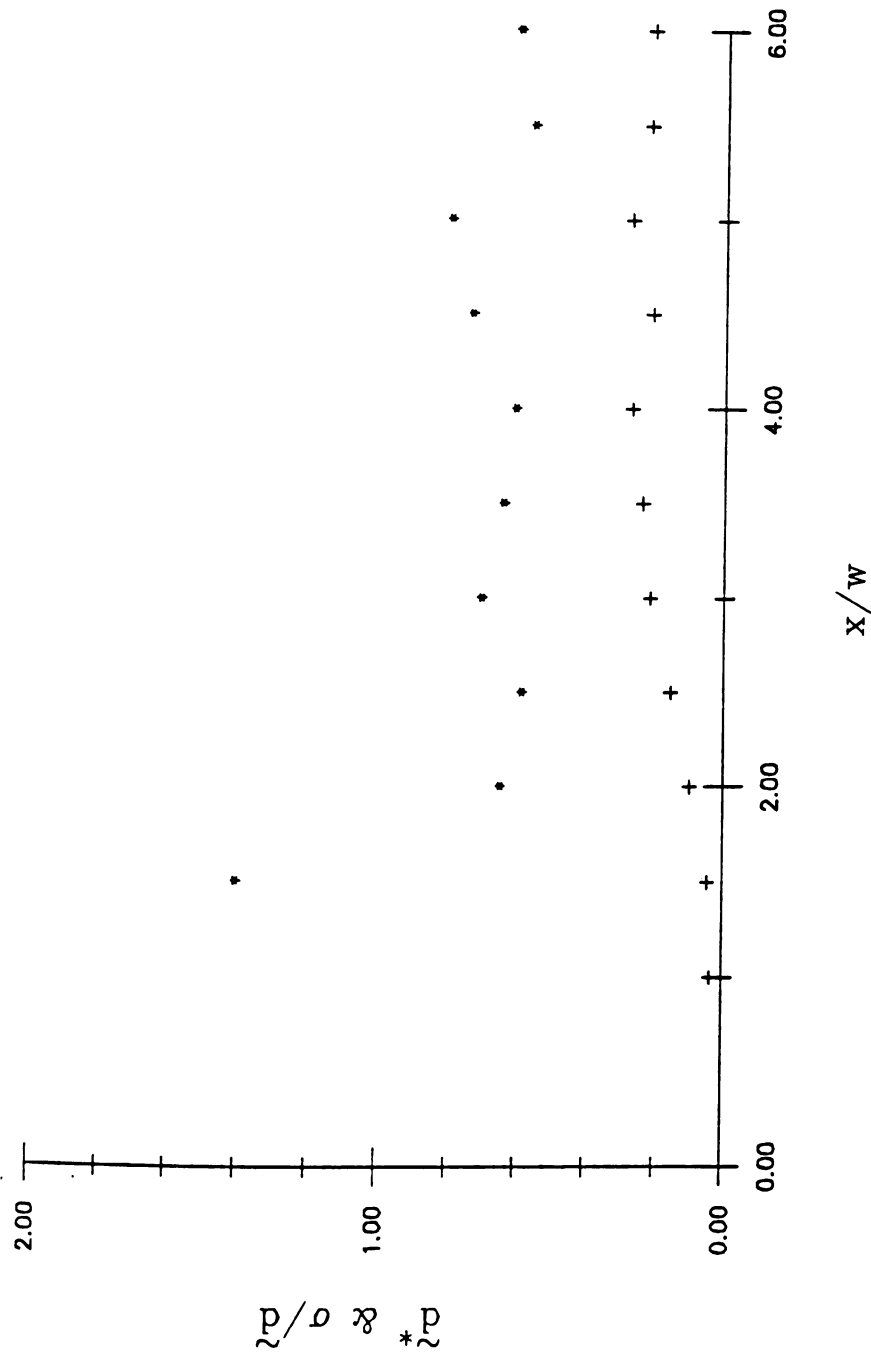


Figure 109. Statistical details of the lateral spreading of vortices in the Re range of 1257-1272. For legend see Figure 105.

2.00

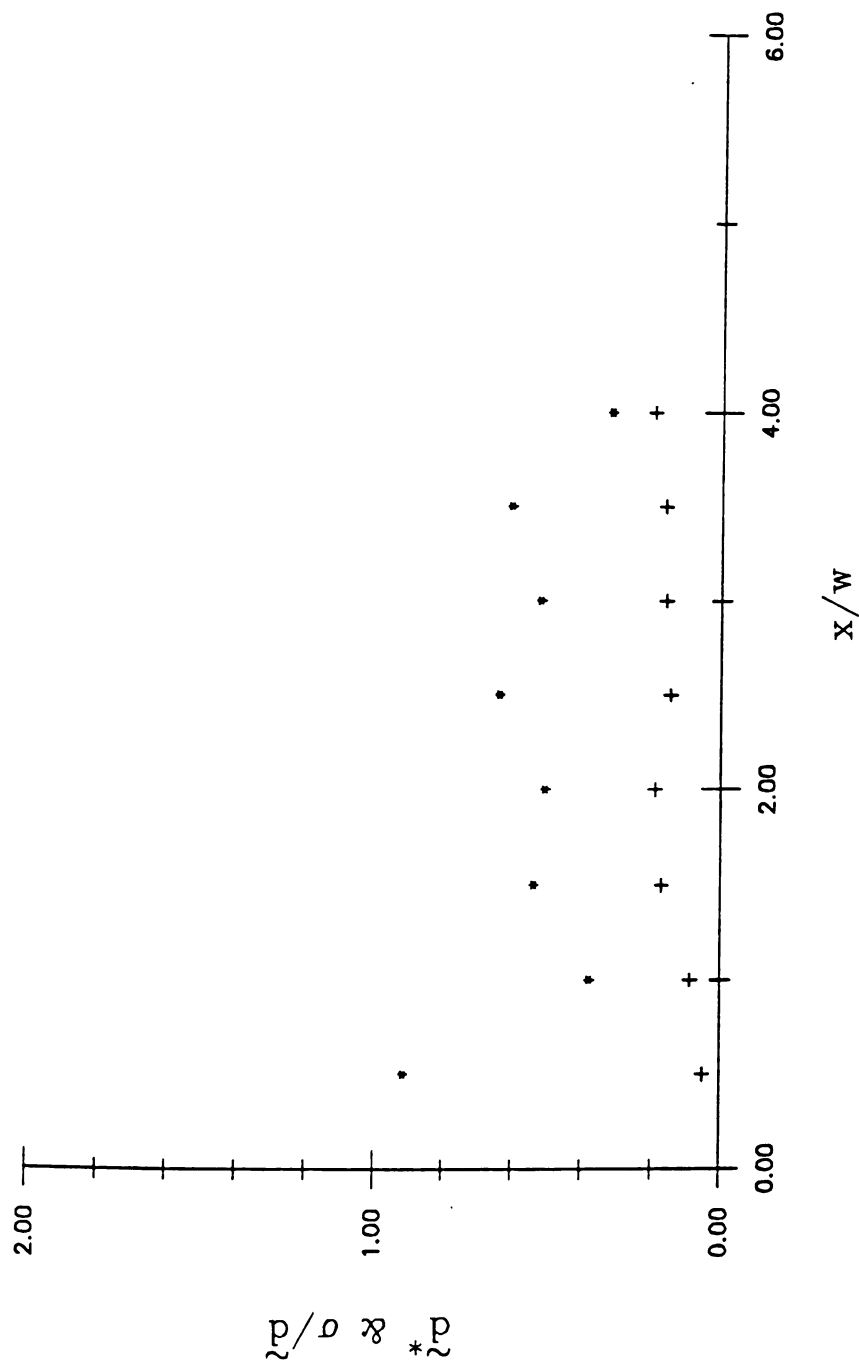


Figure 110. Statistical details of the lateral spreading of vortices in the Re range of 1571-1697. For legend see Figure 105.

2.00



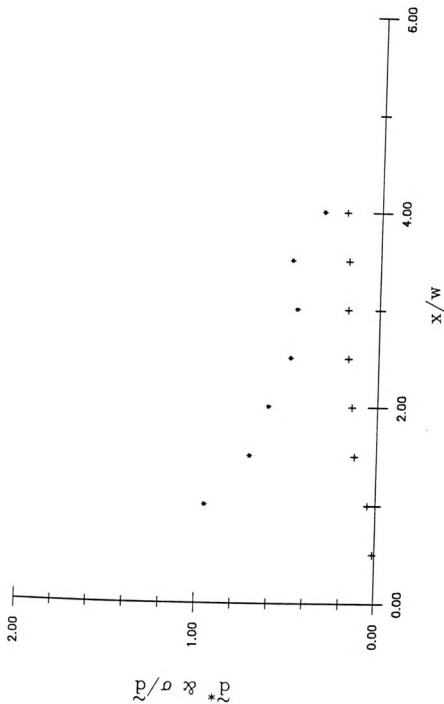


Figure 111. Statistical details of the lateral spreading of vortices in the Re range of 2949-3469. For legend see Figure 105.

1.00



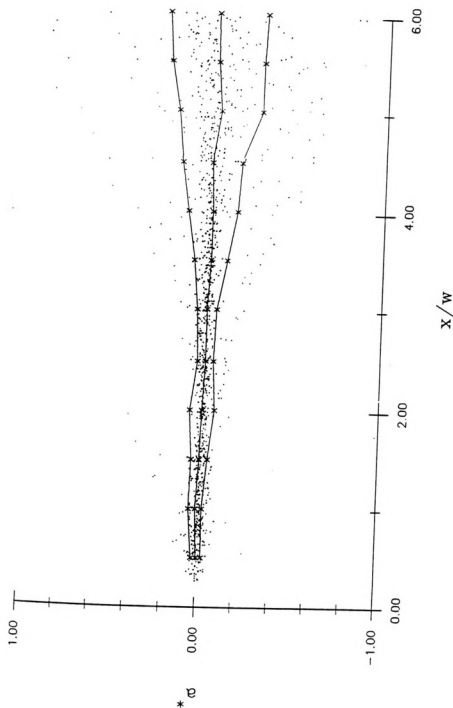


Figure 112. Normalized asymmetry estimate of the "symmetric" vortex street in the Re range of 269-285. See Figure 98 for details.

1.00

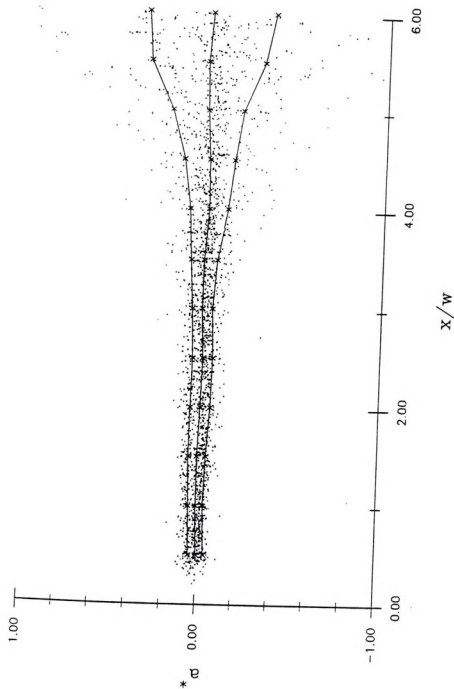


Figure 113. Normalized asymmetry estimate of the "symmetric" vortex street in the Re range of 362-525. See Figure 98 for details.

1.00

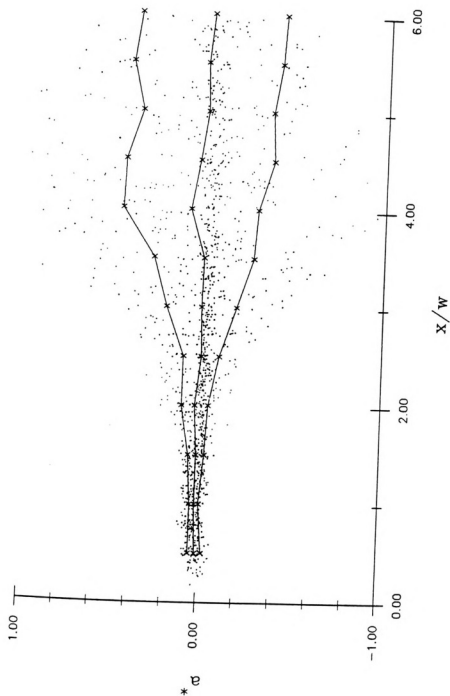


Figure 114. Normalized asymmetry estimate of the "symmetric" vortex street in the Re range of 640-698. See Figure 98 for details.

1.00

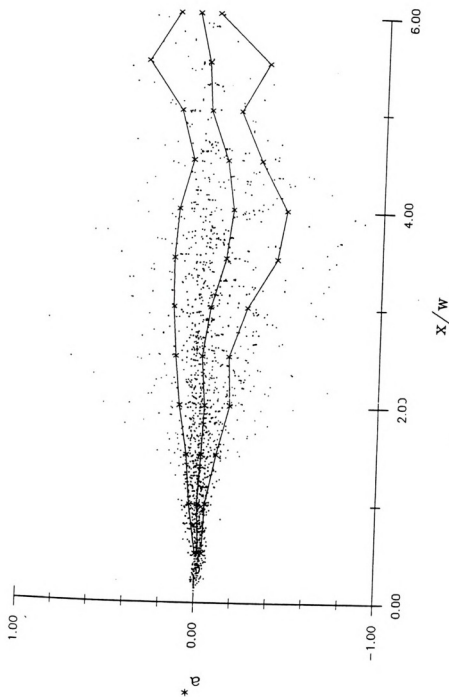


Figure 115. Normalized asymmetry estimate of the "symmetric" vortex street in the Re range of 930-1074. See Figure 98 for details.

1.00

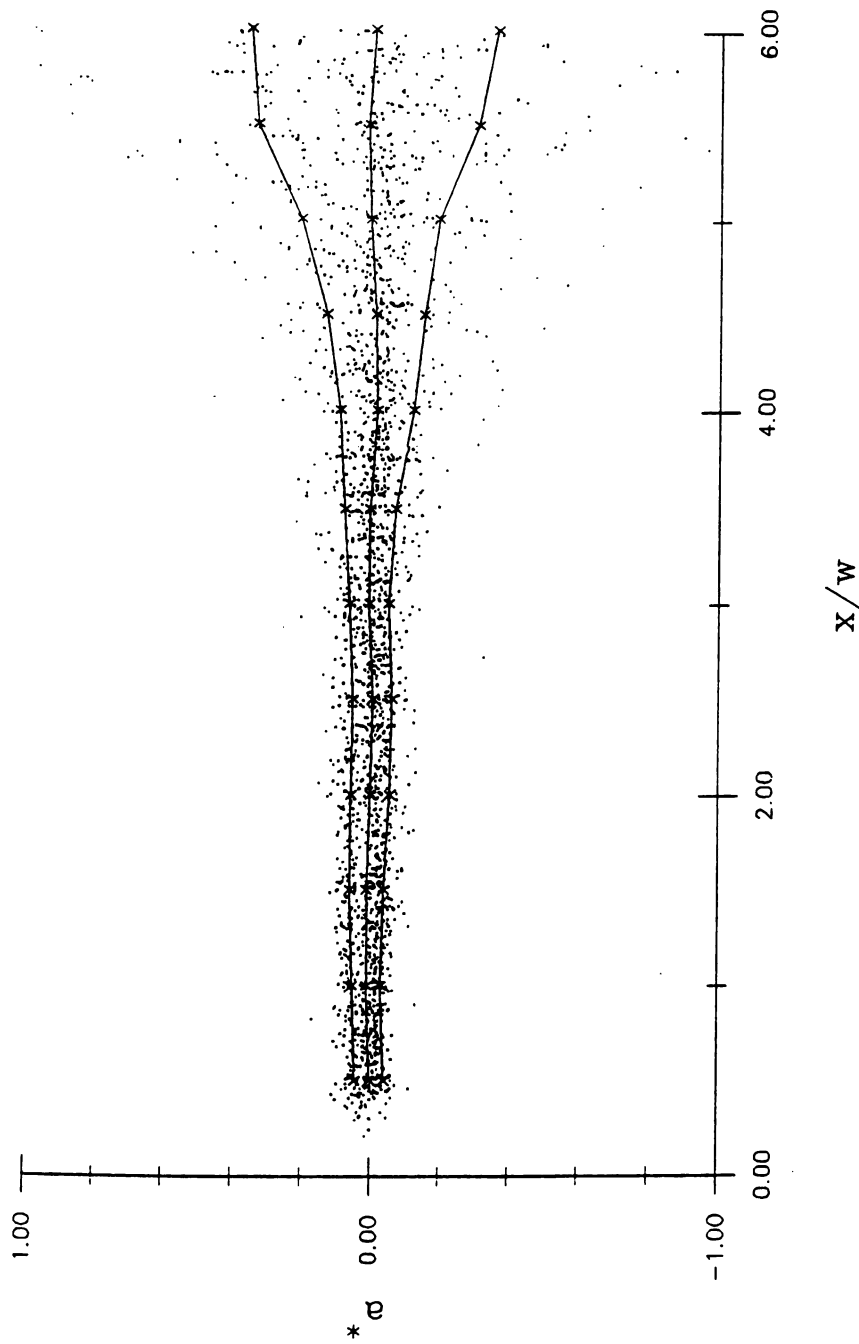


Figure 113. Normalized asymmetry estimate of the "symmetric" vortex street in the Re range of 362-525. See Figure 98 for details.

1.00

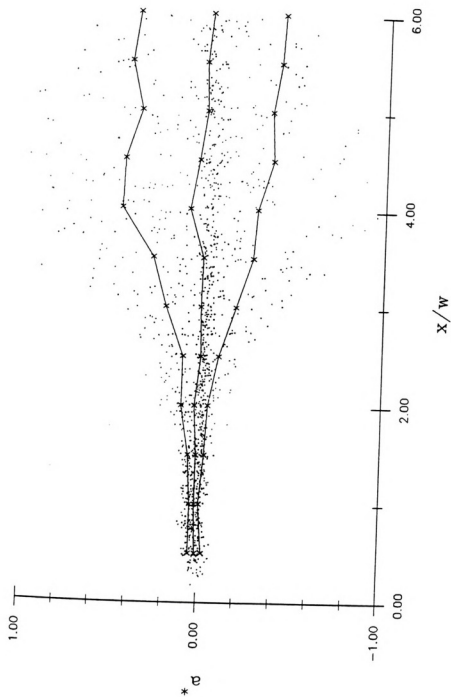


Figure 114. Normalized asymmetry estimate of the "symmetric" vortex street in the Re range of 640-698. See Figure 98 for details.

1.00

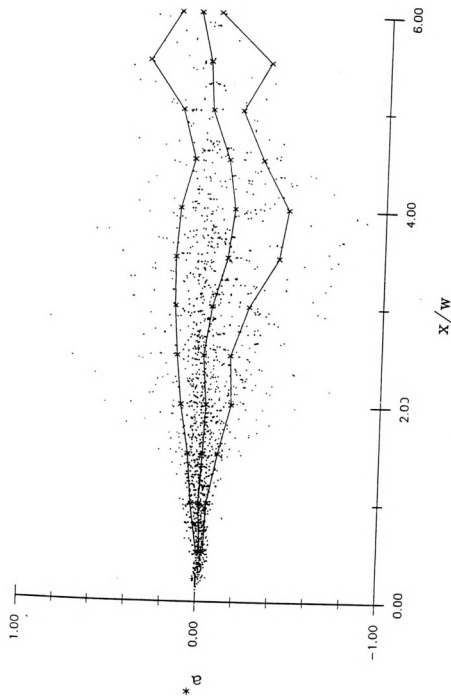
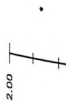


Figure 115. Normalized asymmetry estimate of the "symmetric" vortex street in the Re range of 930-1074. See Figure 98 for details.

2.00



A vertical scale bar with tick marks and a small dot above it.

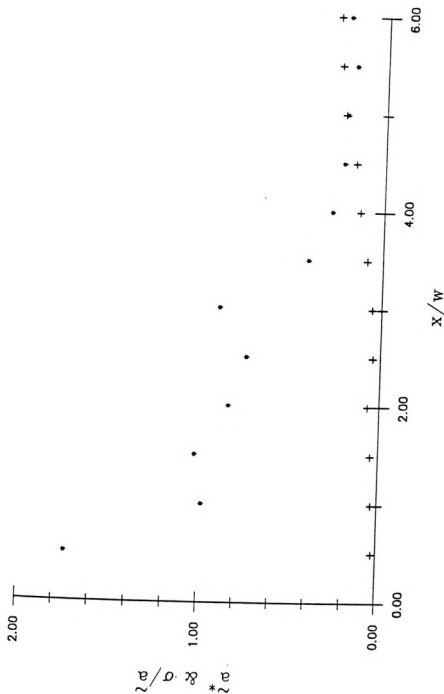


Figure 119. Statistical details of the symmetry of the "symmetric" vortex street over the Re range of 269-285. See Figure 105 for details.

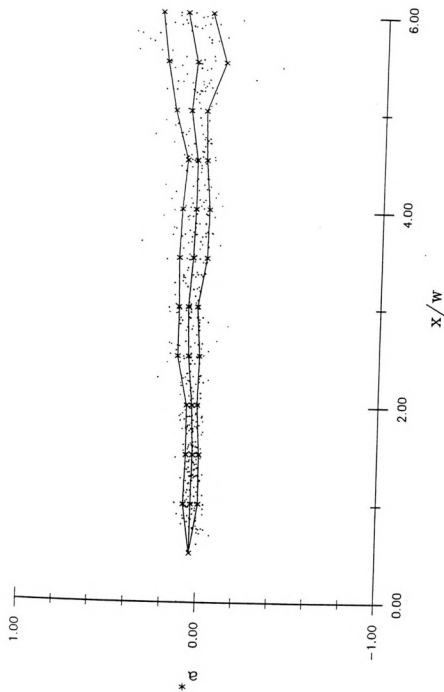


Figure 116. Normalized asymmetry estimate of the "symmetric" vortex street in the Re range of 1257-1272. See Figure 98 for details.

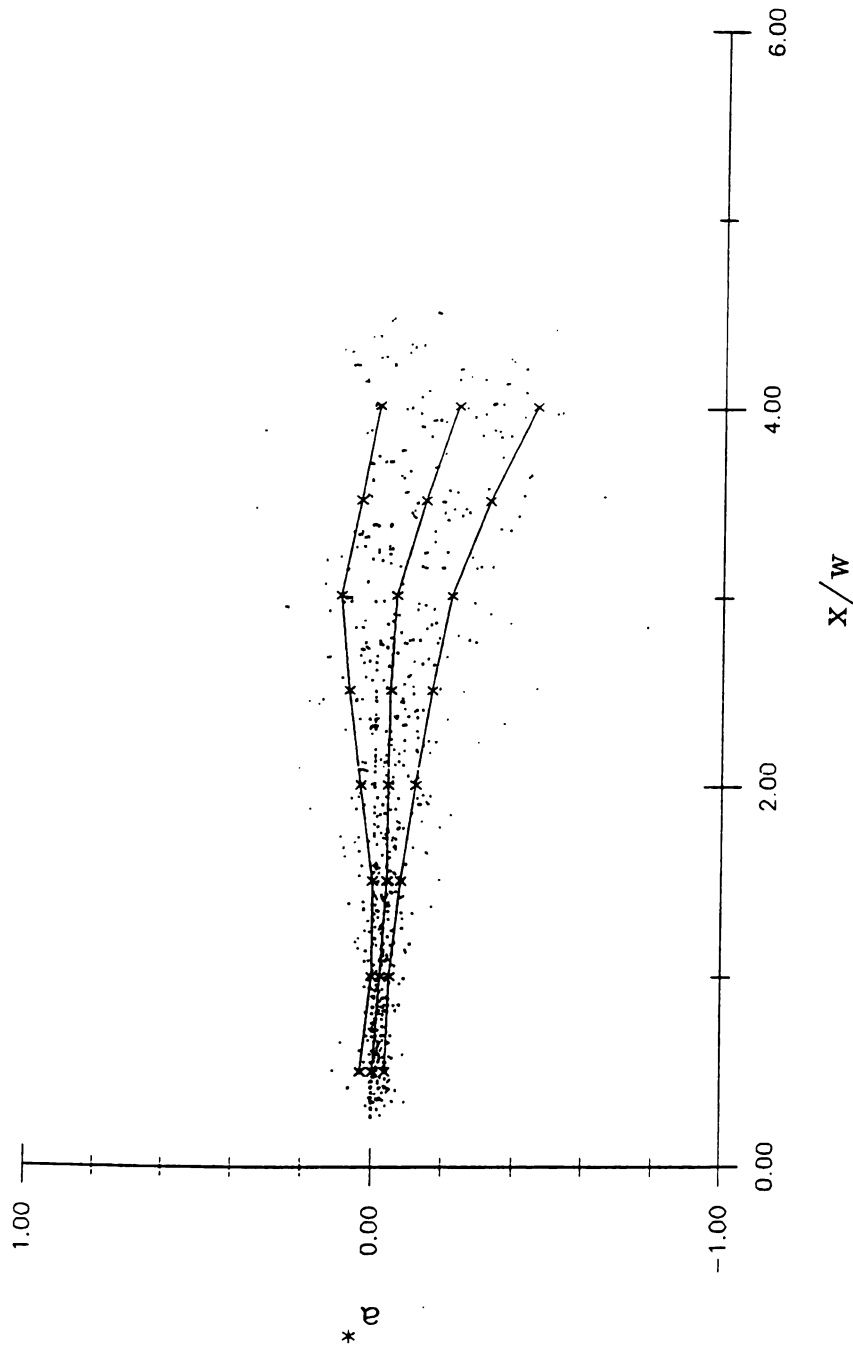


Figure 117. Normalized asymmetry estimate of the "symmetric" vortex street in the Re range of 1571-1697. See Figure 98 for details.

1.00

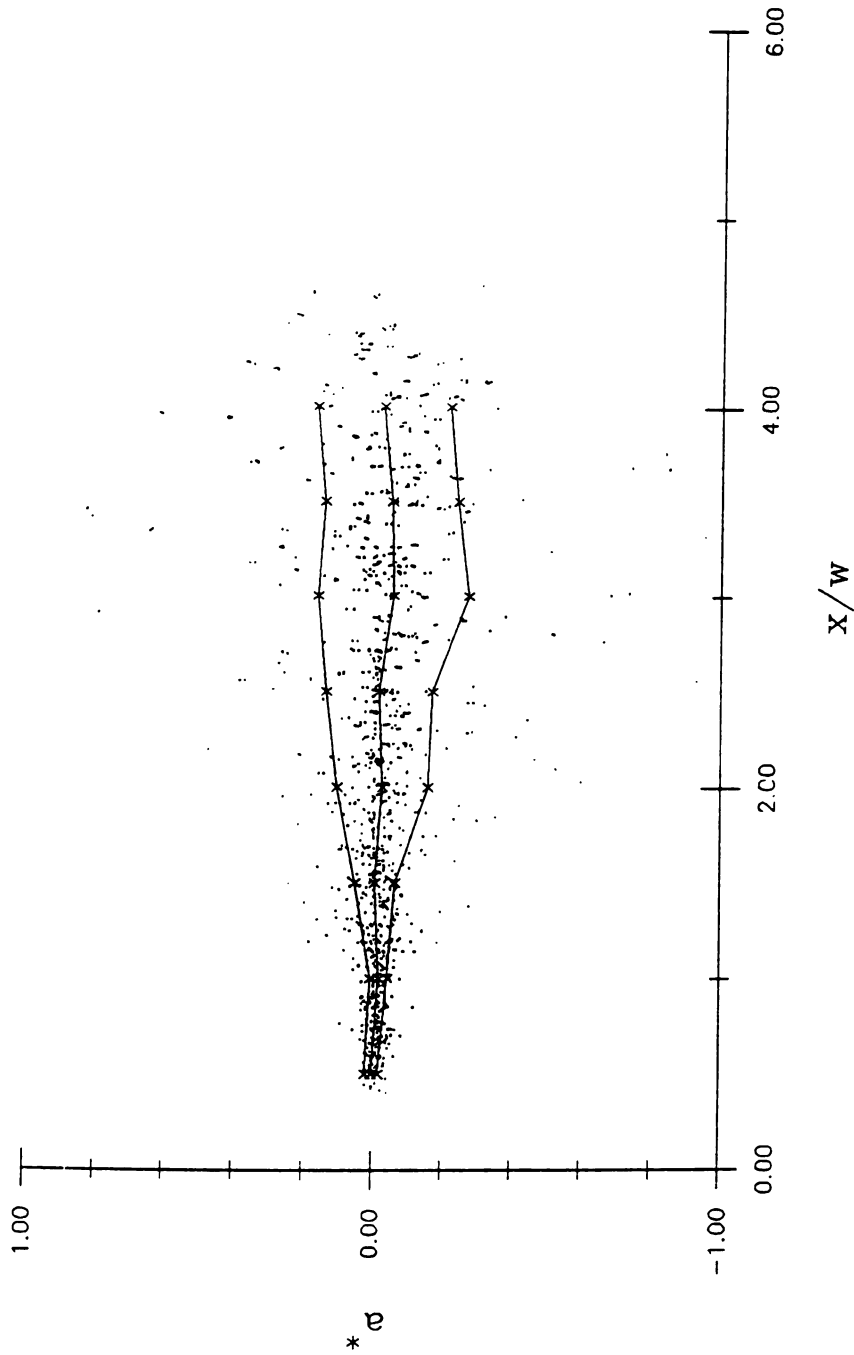


Figure 118. Normalized asymmetry estimate of the "symmetric" vortex street in the Re range of 2949-3469. See Figure 98 for details.

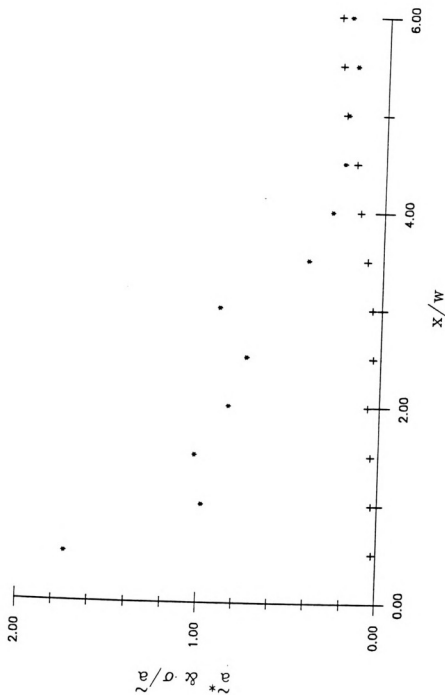


Figure 119. Statistical details of the symmetry of the "symmetric" vortex street over the Re range of 269-285. See Figure 105 for details.

2.00

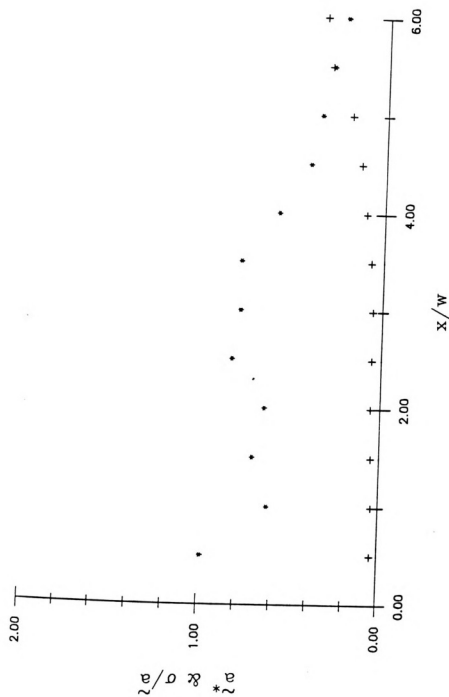


Figure 120. Statistical details of the symmetry of the "symmetric" vortex street over the Re range of 362-525. See Figure 105 for details.

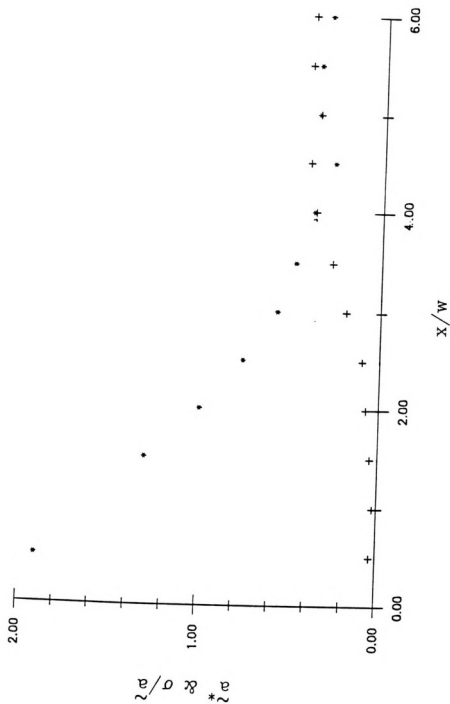


Figure 121. Statistical details of the symmetry of the "symmetric" vortex street over the Re range of 640-698. See Figure 105 for details.

2.00

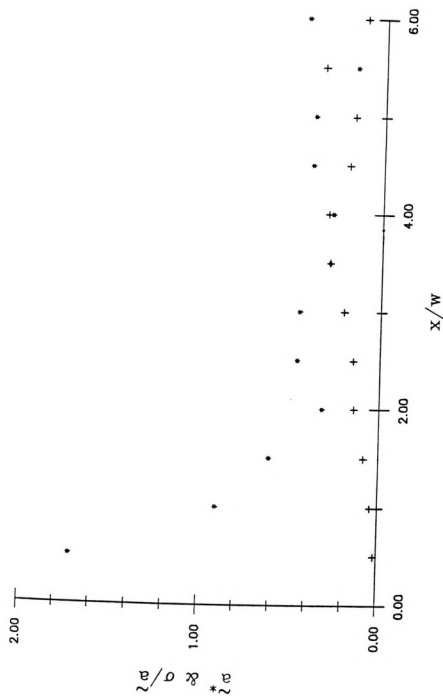


Figure 122. Statistical details of the symmetry of the "symmetric" vortex street over the Re range of 930-1074. See Figure 105 for details.

2.00

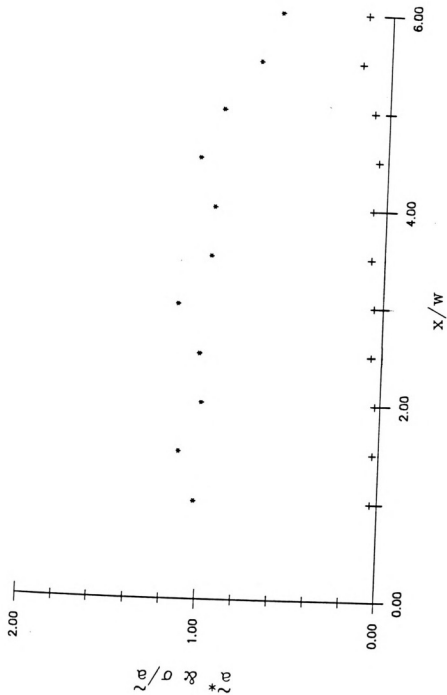


Figure 123. Statistical details of the symmetry of the "symmetric" vortex street over the Re range of 1257-1272. See Figure 105 for details.

2.00

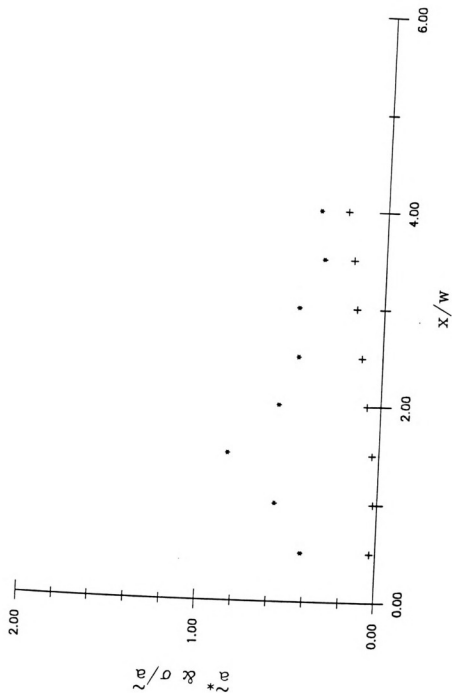


Figure 124. Statistical details of the symmetry of the "symmetric" vortex street over the Re range of 1571-1697. See Figure 105 for details.

2.00

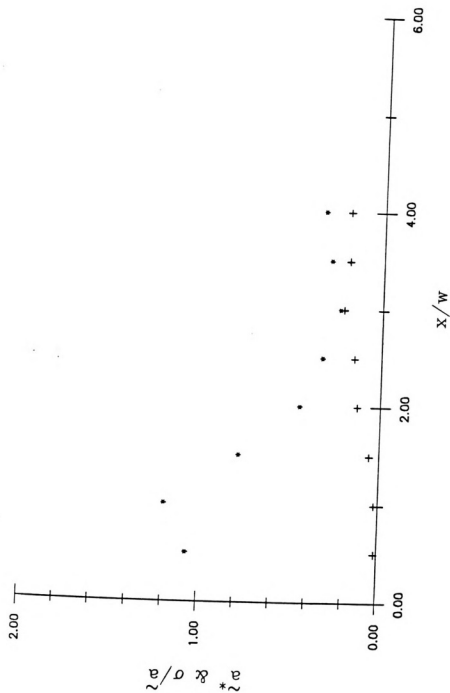


Figure 125. Statistical details of the symmetry of the "symmetric" vortex street over the Re range of 2949-3469. See Figure 105 for details.

2.00

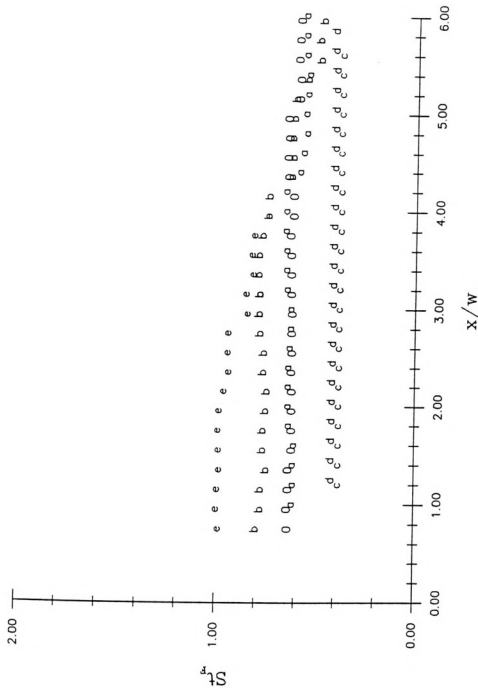


Figure 126. Distribution of St_p in the Re range of 269-285. A water-sugar mixture was used in all these cases. The Re values and the jet widths in cm are 0: 269, 1.99; a: 269, 1.99; b: 276, 1.99; c: 277, 1.51; d: 280, 1.51; e: 285, 2.63.

2.00

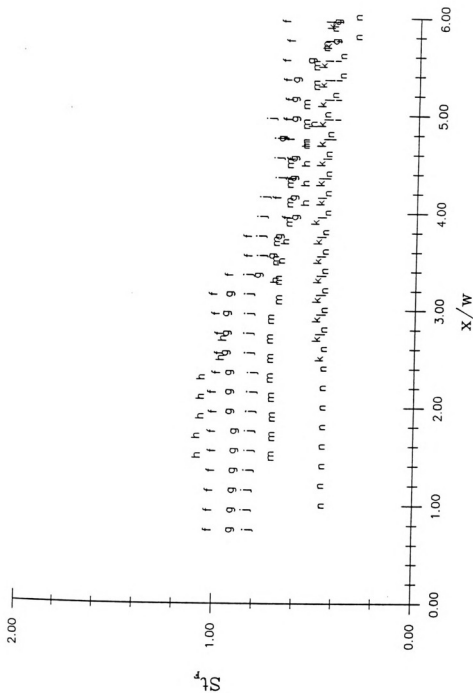


Figure 127. Distribution of St_p in the Re range of 362-426. A water-sugar mixture was used in all cases except for the case designated by h. The Re values and the jet widths in cm are: f: 362, 2.63; g: 373, 2.63; h: 396, 1.4; i: 407, 1.51; j: 408, 2.63; k: 412, 1.51; l: 421, 1.51; m: 423, 1.99; n: 426, 1.99.

2.00

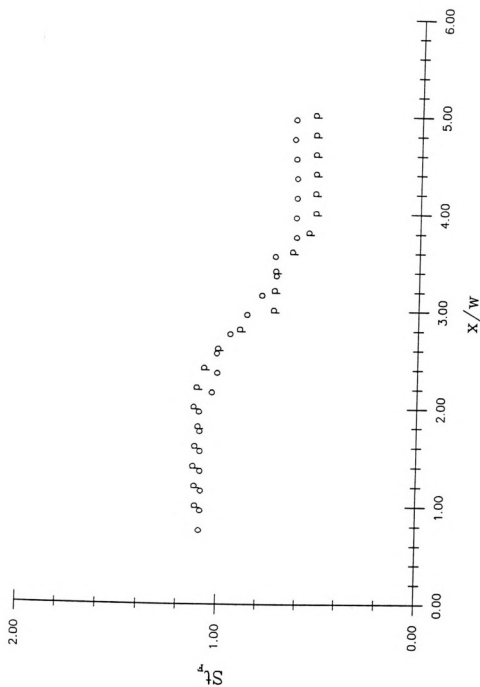


Figure 128. Distribution of St_F in the Re range of 510-525. Water was used as the working fluid. The Re values and the jet width in cm are: o: 525, 1.4; p: 510, 1.4.

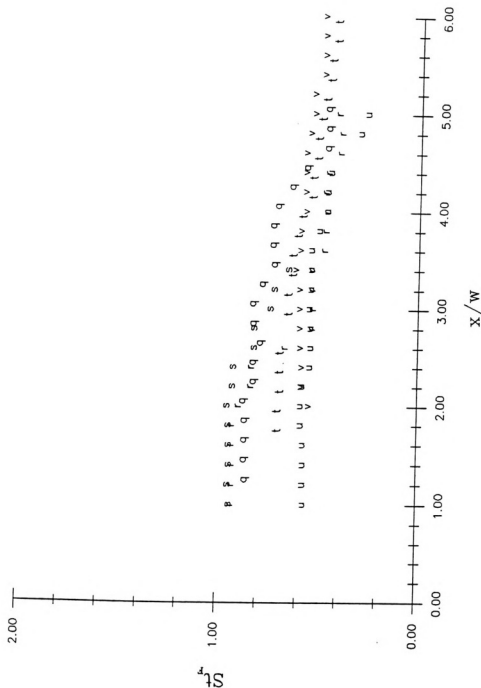


Figure 129. Distribution of St_F in the Re range of 640-700. Water was used as the working fluid for the cases designated by the symbols q, r and s. For the cases designated by t, u and v a water-sugar mixture was used. The Re values and the jet width in cm are: q: 640, 1.4; r: 640, 1.4; s: 640, 1.4; t: 679, 1.99; u: 696, 2.63 and v: 698, 1.99.

2.00 T
A A
B B B B

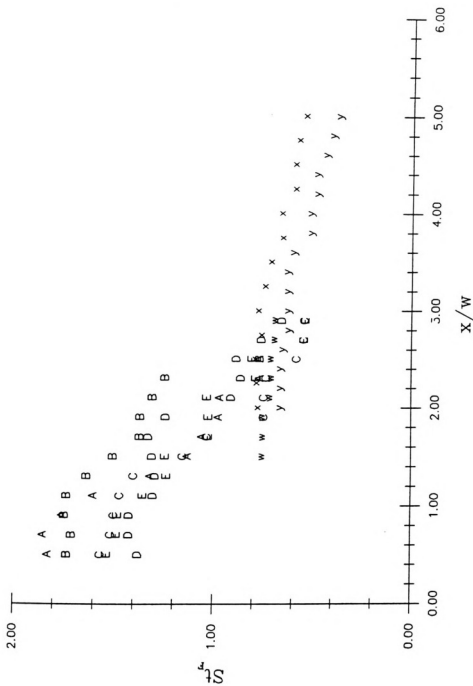


Figure 130. Distribution of St_r in the Re range of 930-1074. Water was used as the working fluid in all the cases except in the case designated by x. The Re values and the jet width in cm are: w: 930, 1.4; x: 980, 2.63; y: 1046, 1.4; A: 1001, 2.57; B: 1004, 2.57; C: 1027, 2.57; D: 1063, 2.57 and E: 1074, 2.57.

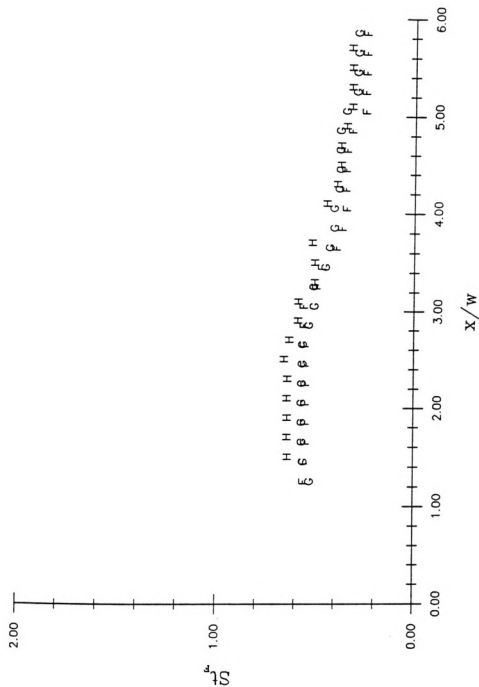


Figure 131. Distribution of St_F in the Re range of 1257-1272. Water was used as the working fluid. The Re values and the jet widths in cm are: F: 1257, 1.4; G: 1269, 1.4 and H: 1272, 1.4.

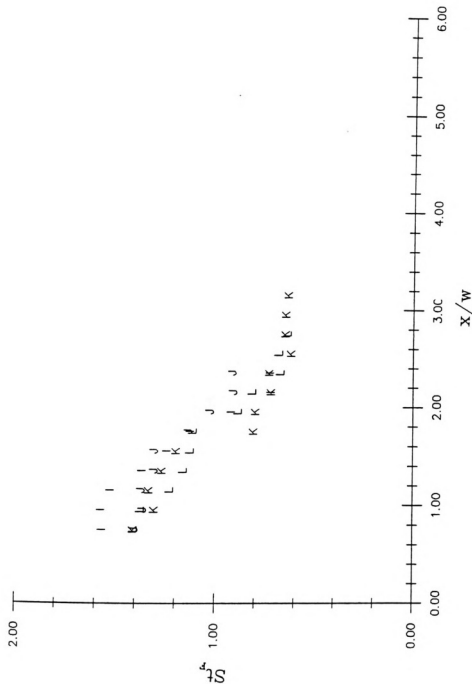
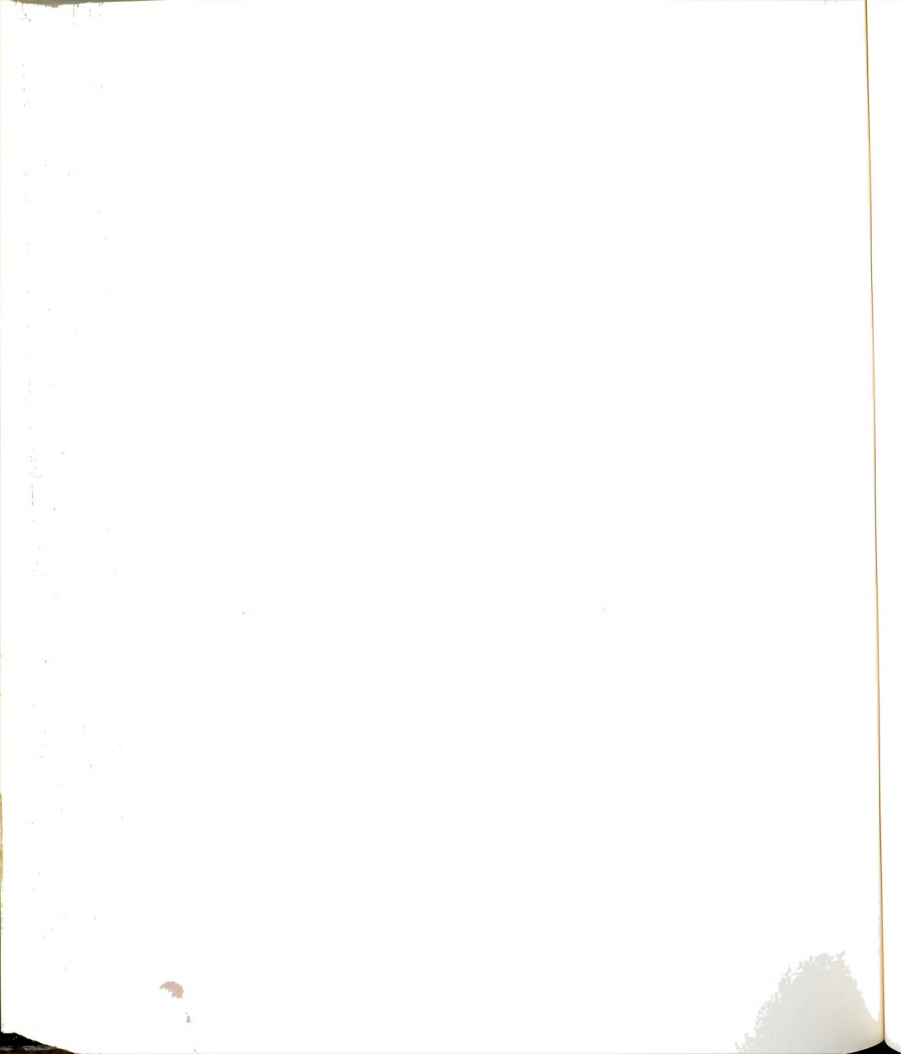


Figure 132. Distribution of St_F in the Re range of 1570-1700. Water was used as the working fluid. The Re values and the jet widths in cm are: I: 1571, 2.57; J: 1580, 2.57; K: 1685, 2.57 and L: 1697, 2.57.



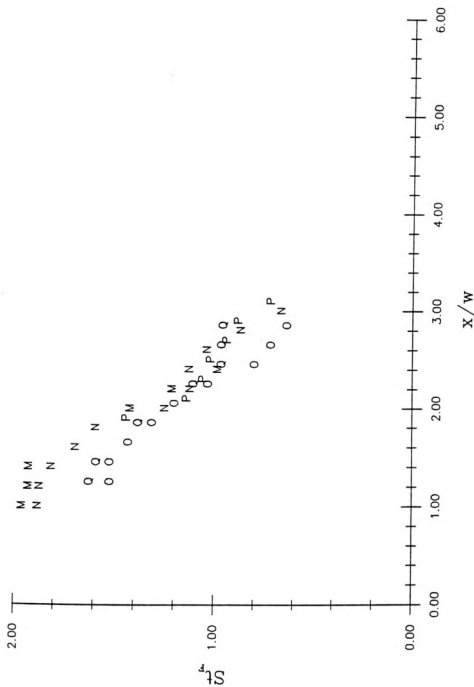


Figure 133. Distribution of St_p in the Re range of 2949-3400. Water was used as the working fluid. The Re values and the jet widths in cm are: M: 2949, 2.57; N: 2964, 2.57; O: 3389, 2.57; P: 3401, 2.57 and Q: 3469, 2.57.



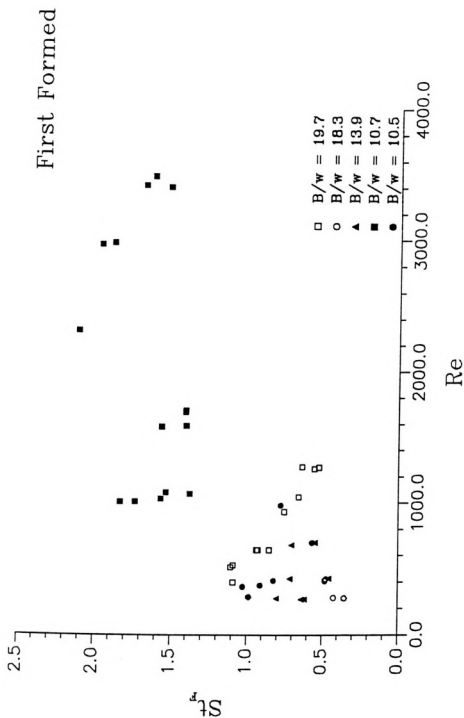
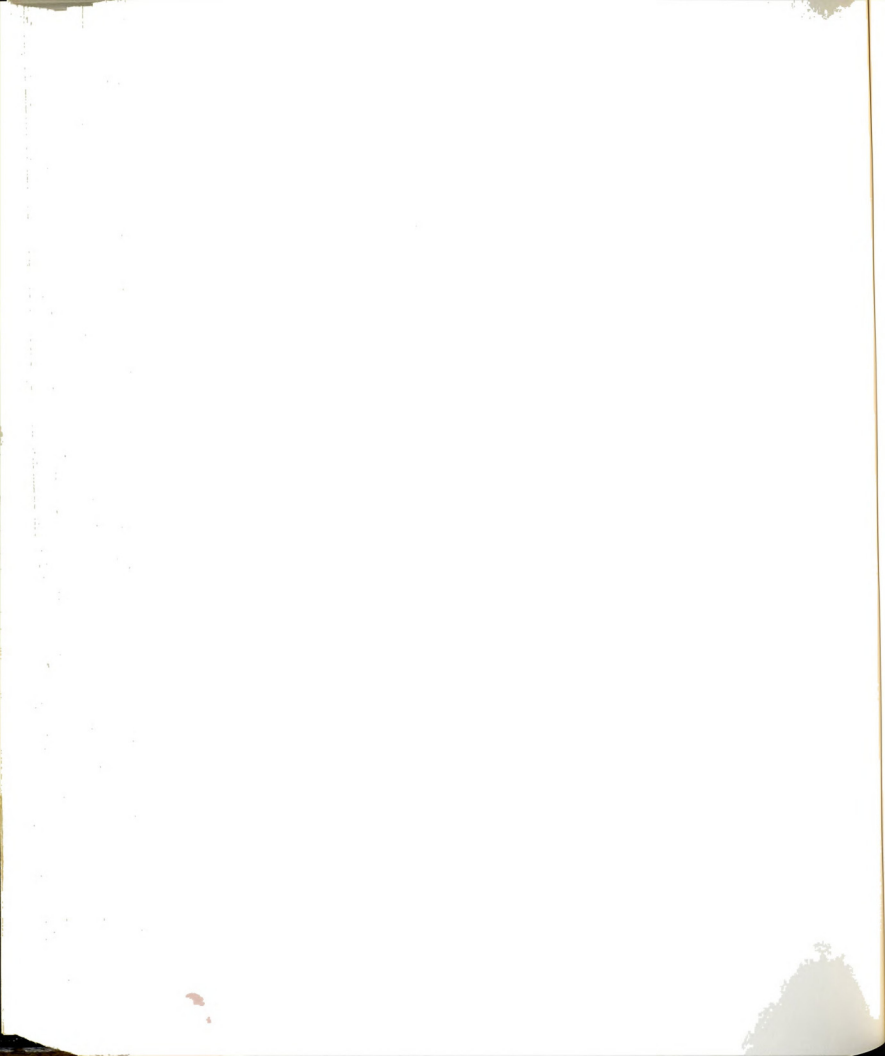


Figure 134. Distribution of St_F as a function of Re with the aspect ratio, B/w , as a parameter. Note that these St_F values were derived from the rate of formation of bulges.



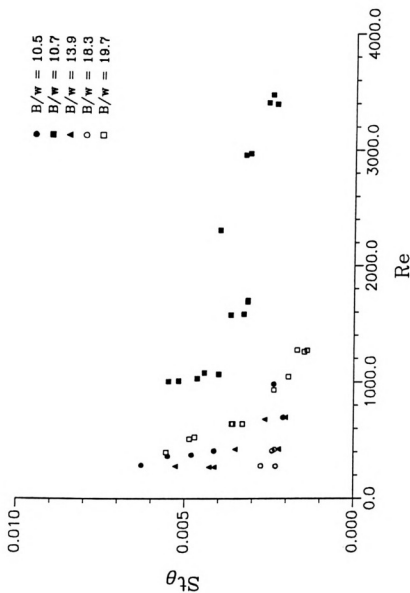
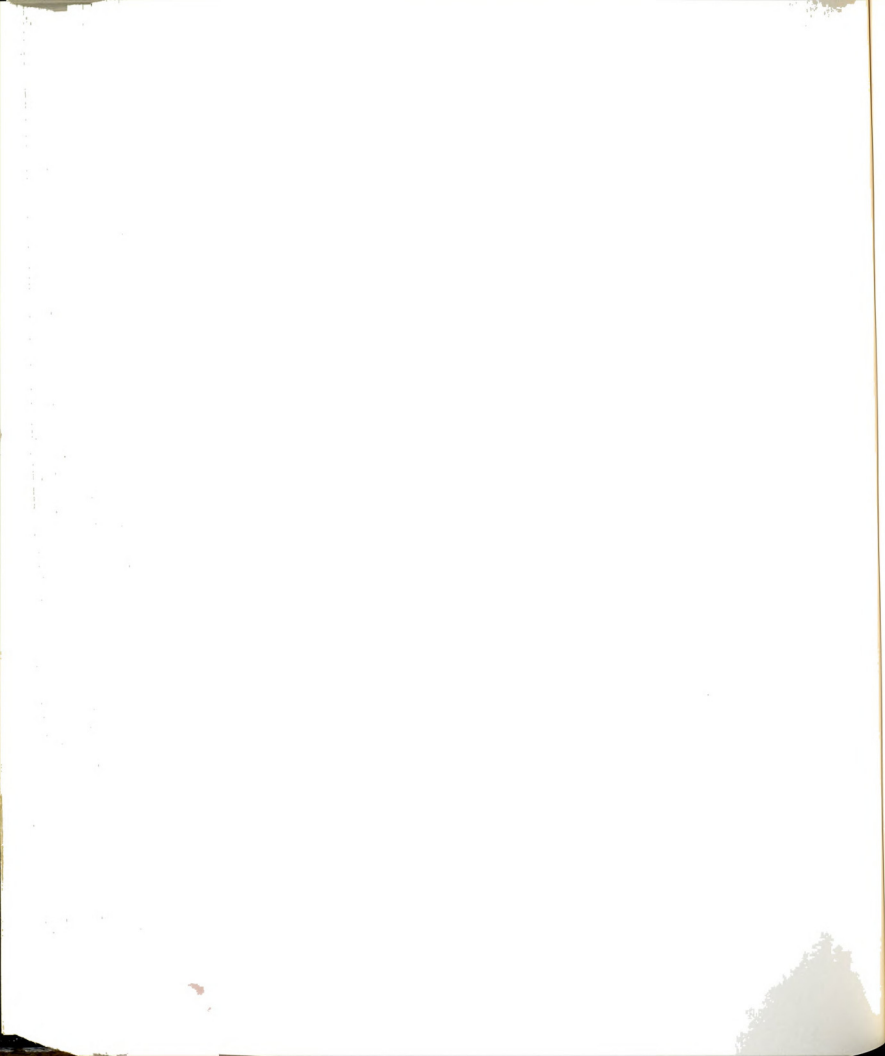


Figure 135. Distribution of St_θ as a function of Re with B/w as a parameter. θ_0 and U_0 have been used to nondimensionalize the rate of formation of bulges.



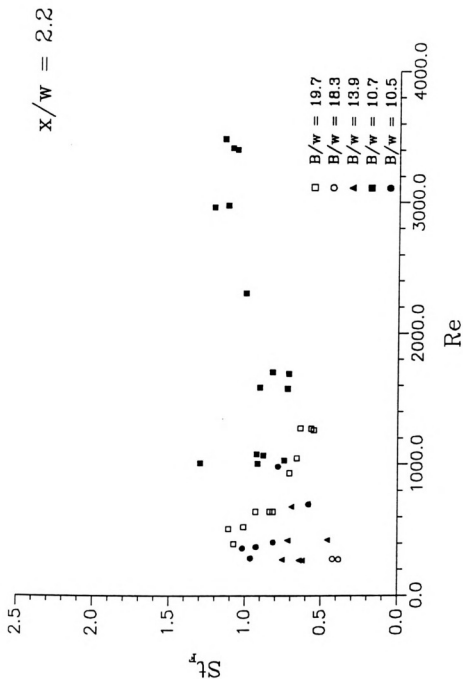
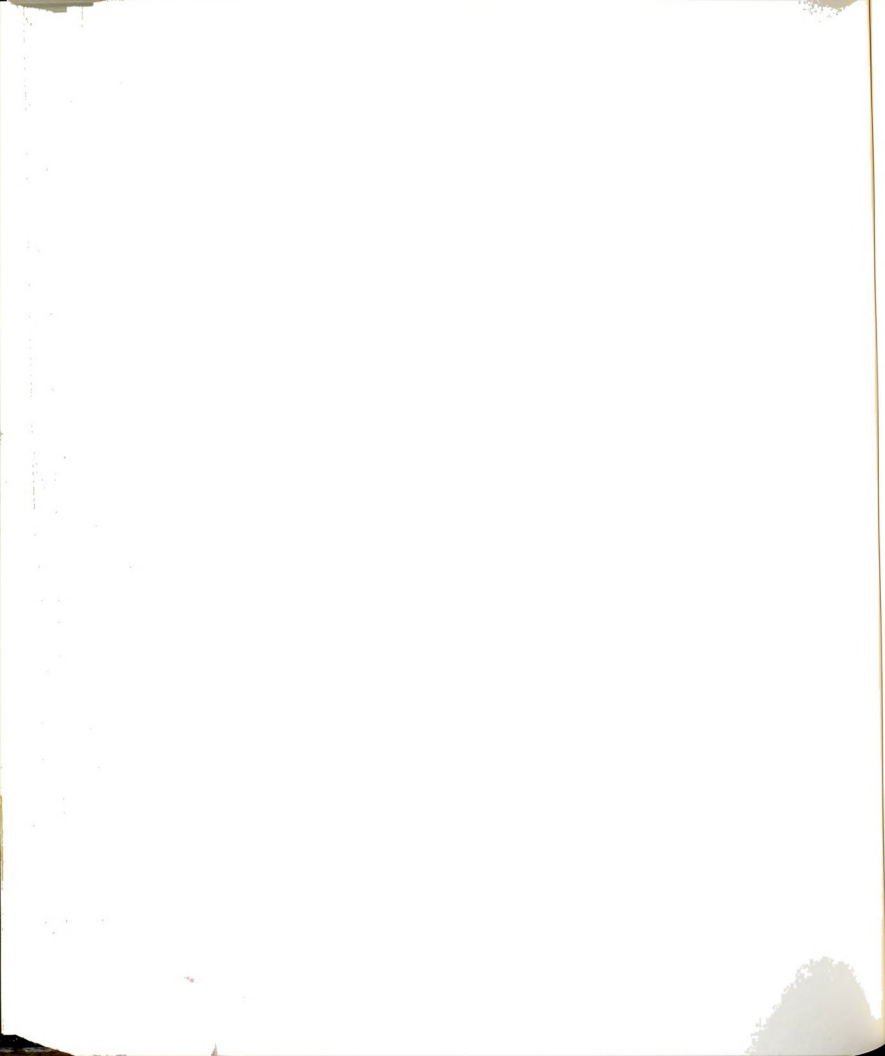


Figure 136. Distribution of St_F as a function of Re with B/w a parameter. These values of St_F were recorded at $x/w = 2.2$.



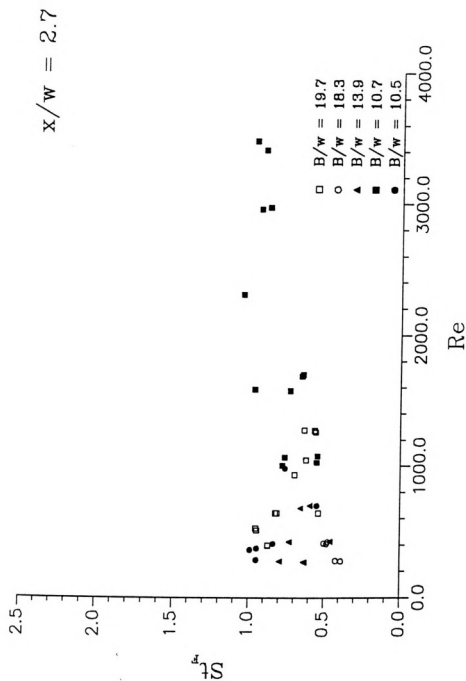
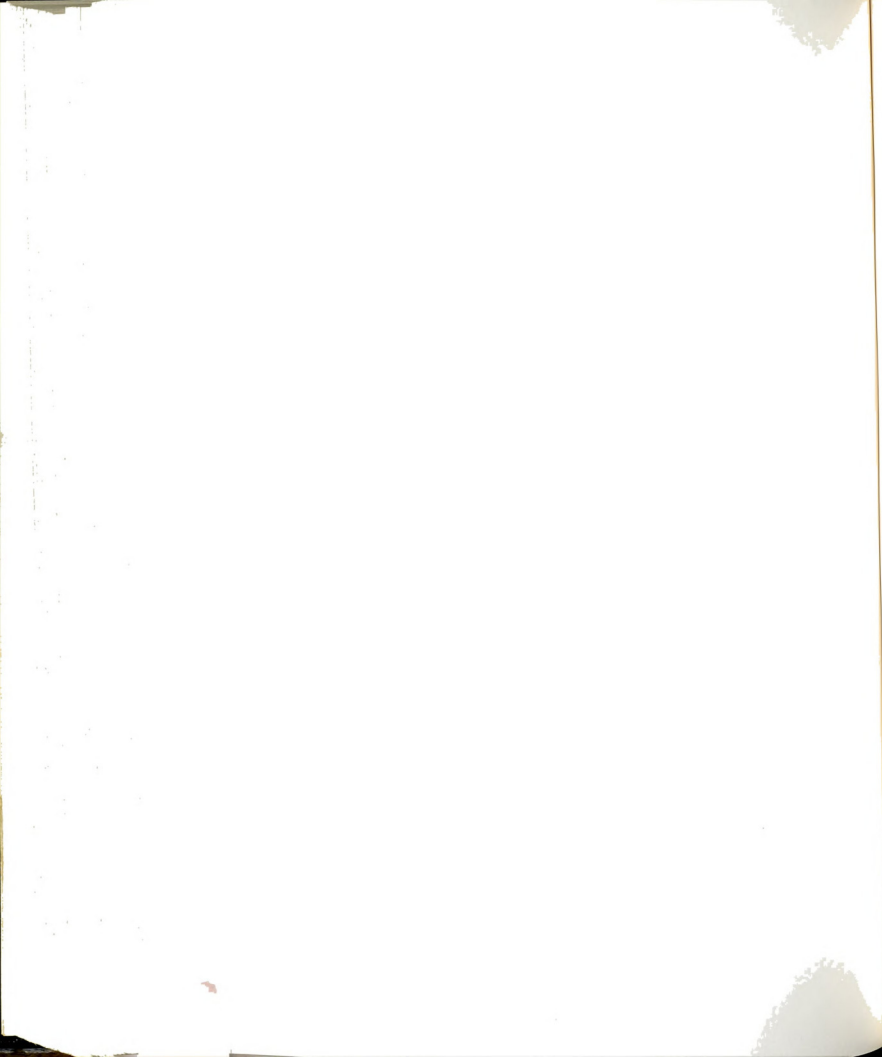


Figure 137. Distribution of St_F as a function of Re with B/w as a parameter. These values of St_F were recorded at $x/w = 2.7$.



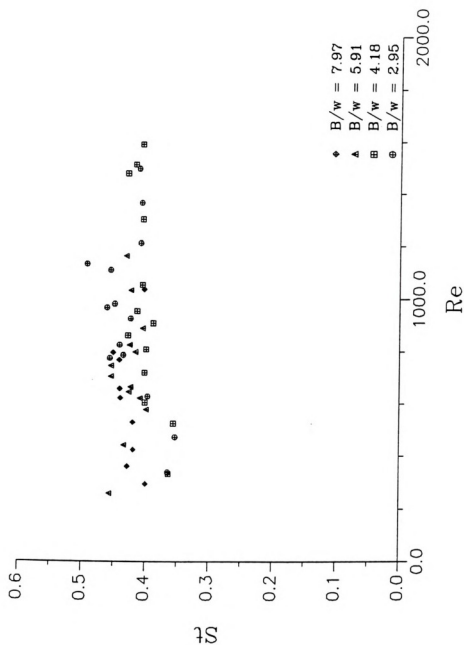
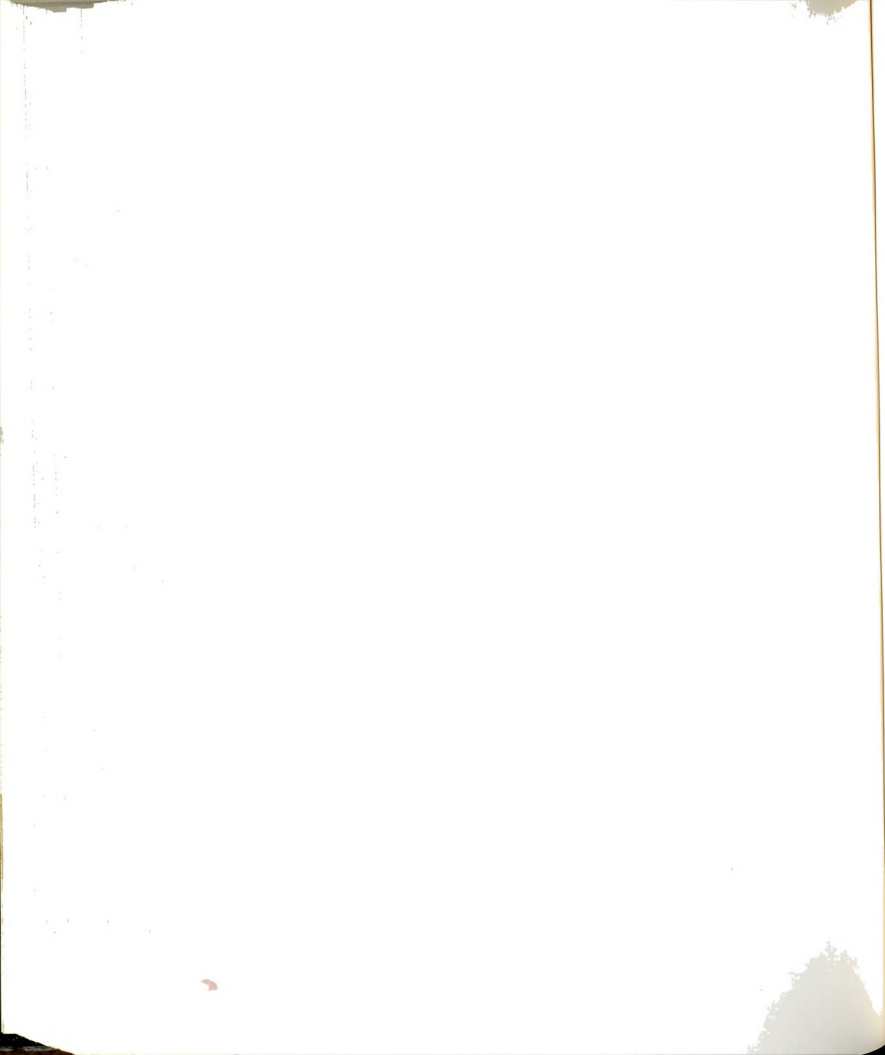


Figure 138. Distribution of Strouhal number as a function of Re with B/w as a parameter. This figure is a reproduction of Beavers and Wilson (1970) data.



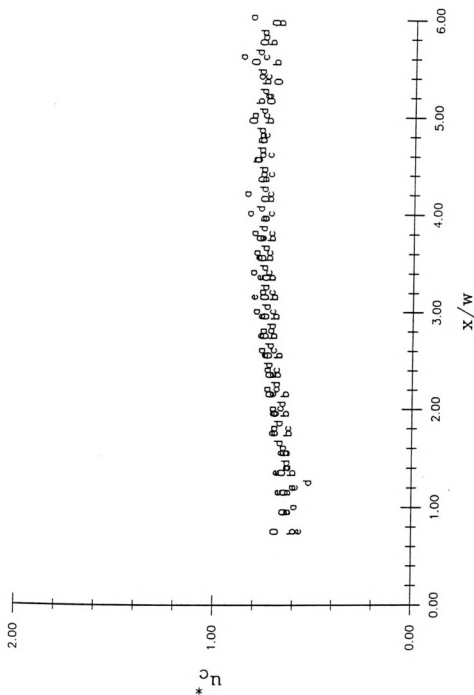
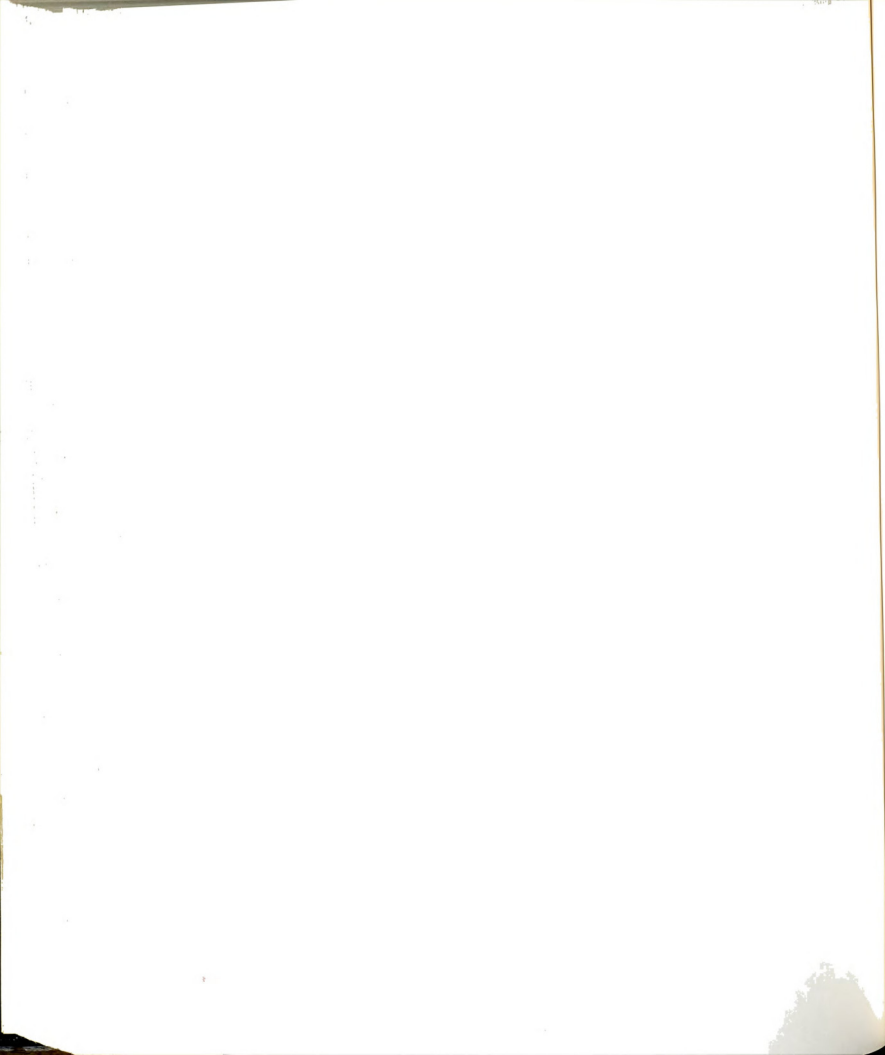


Figure 139. Distribution of $u^*(x)$ in the Re range of 269-285. For legend see Figure 126. Note the good collapse of data for jets of all sizes.



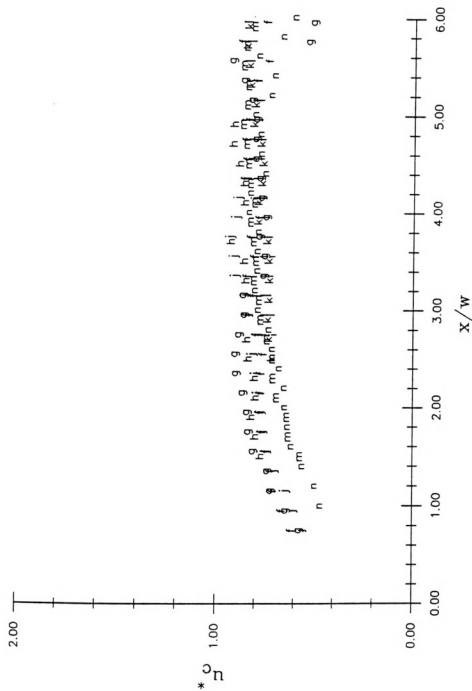
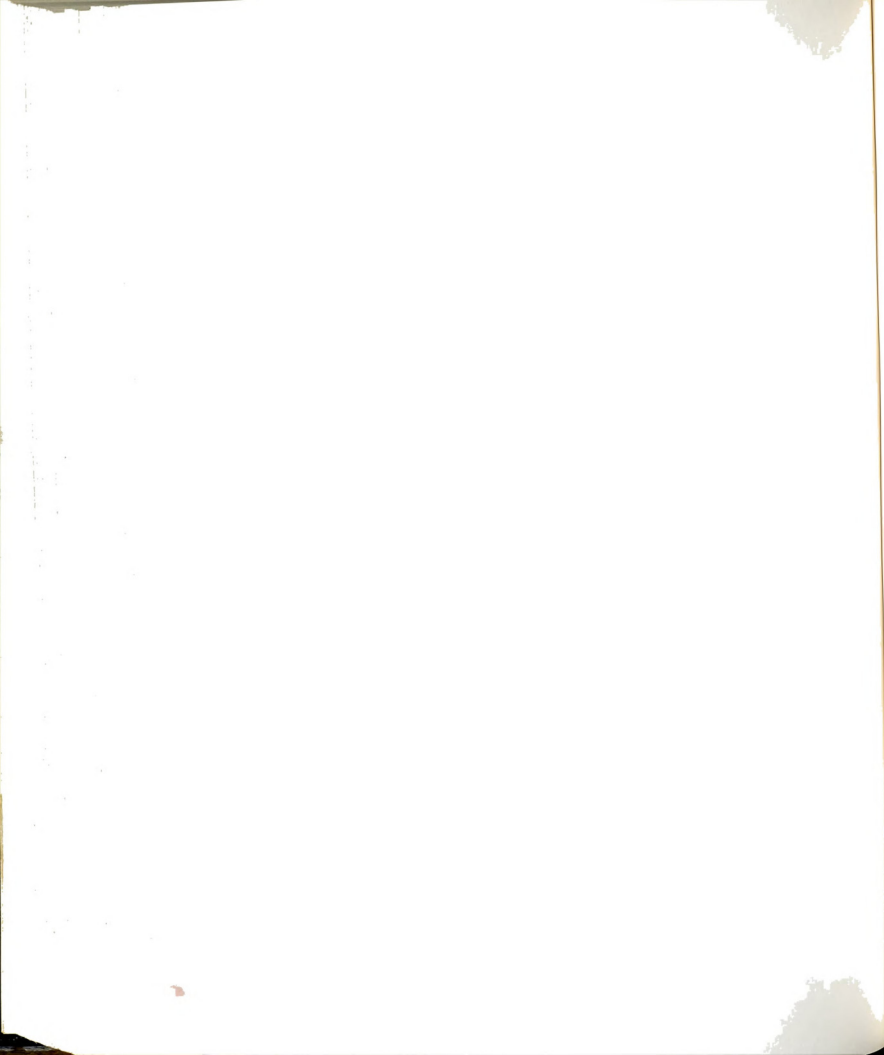


Figure 140. Distribution of $u_c^*(x)$ in the Re range of 362-426.
For legend see Figure 127.



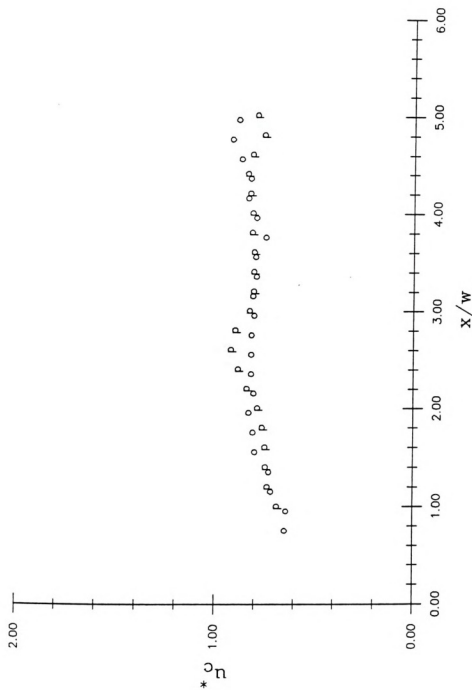
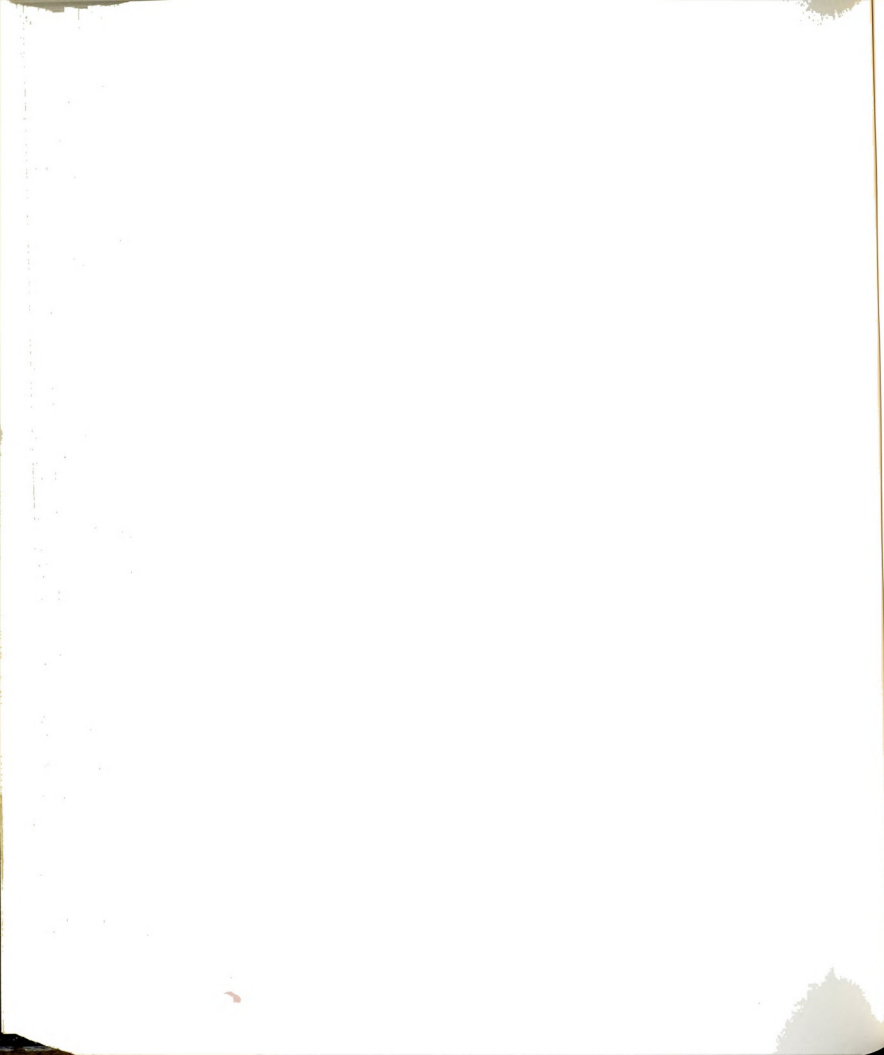


Figure 141. Distribution of u_c^* in the Re range of 510-525.
For legend see Figure 128.



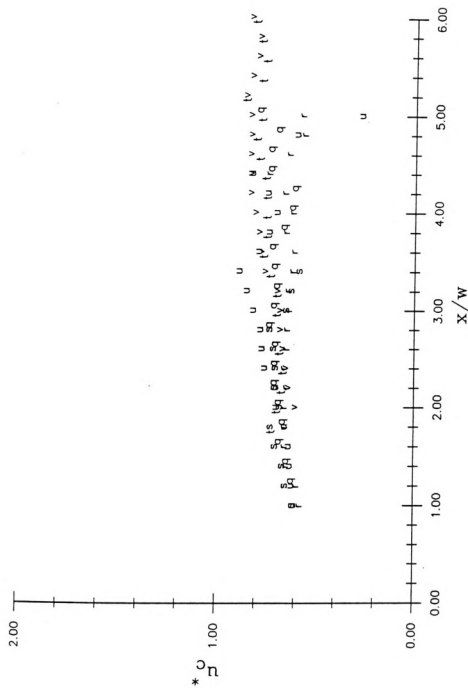
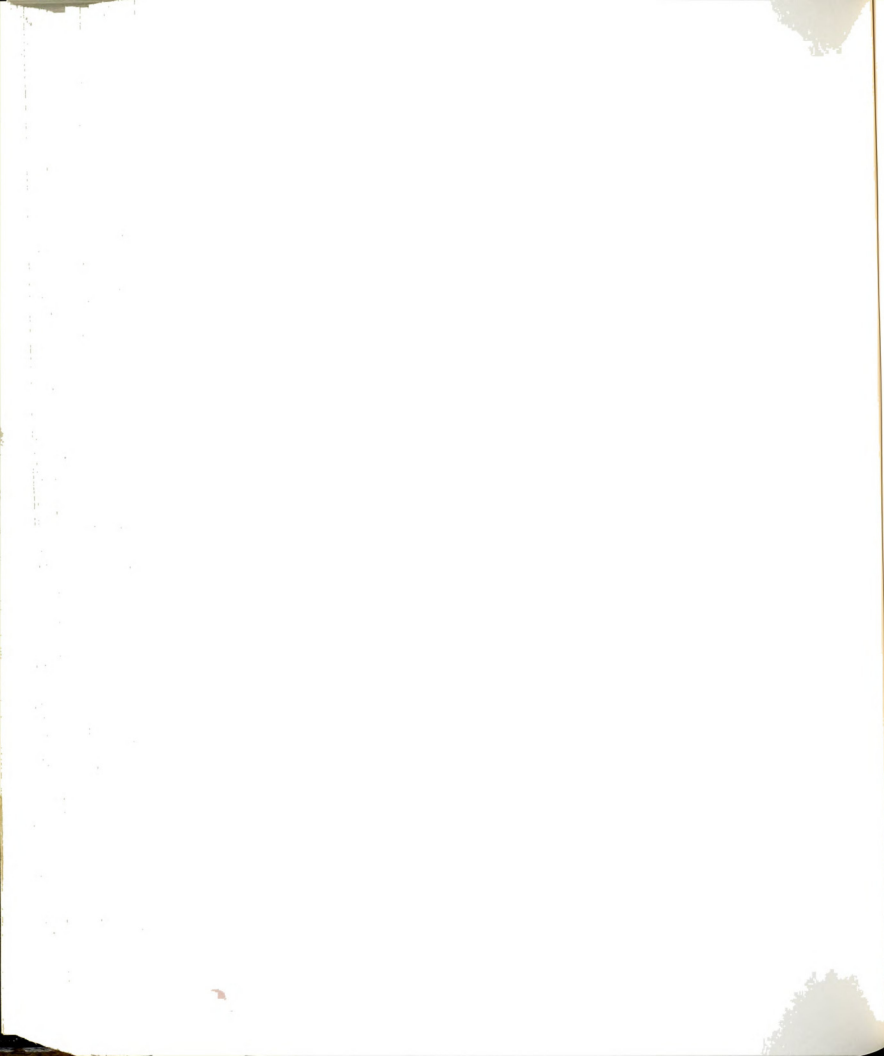


Figure 142. Distribution of u_c^* in the Re range of 640-700.
For legend see Figure 129.



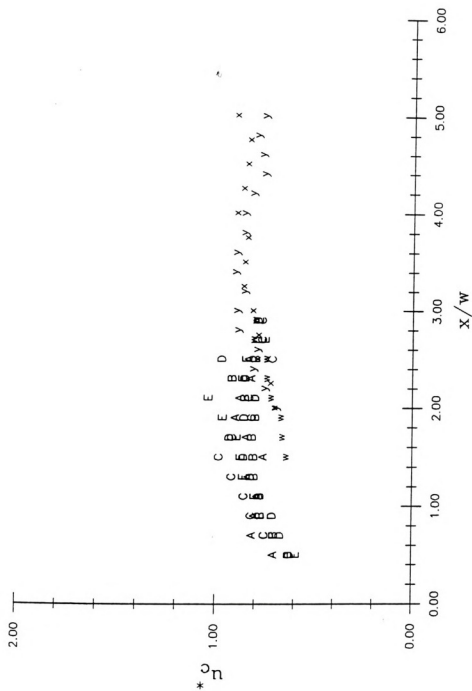
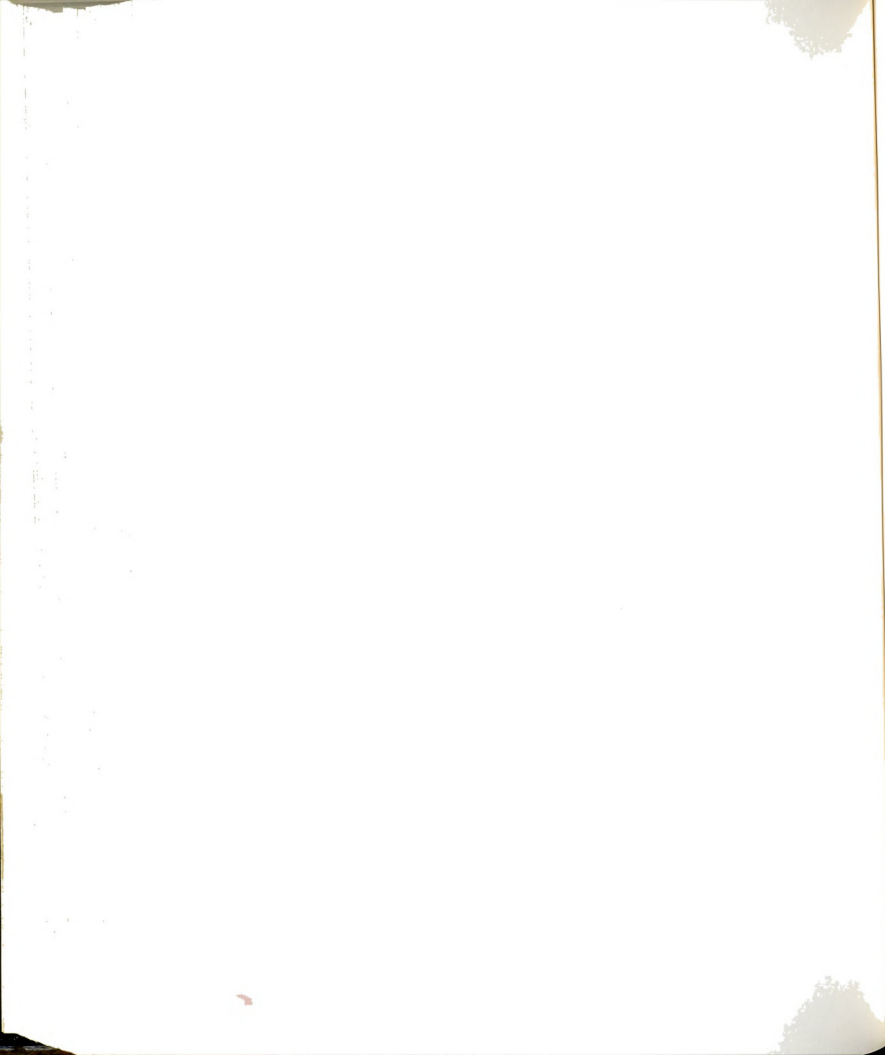


Figure 143. Distribution of $u_c^*(x)$ in the Re range of 930-1074.
For legend see Figure 130.



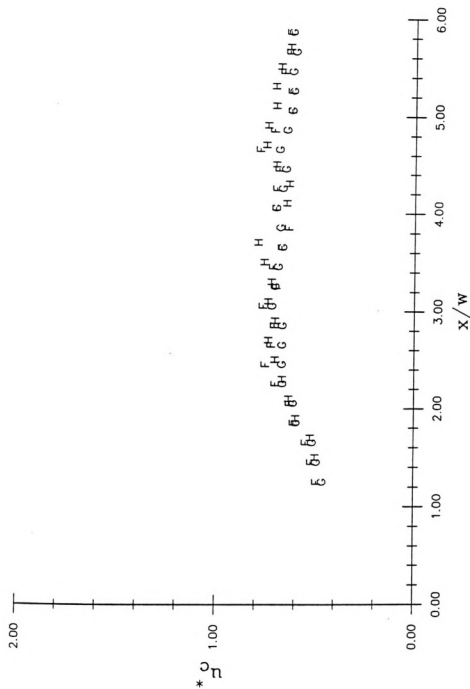
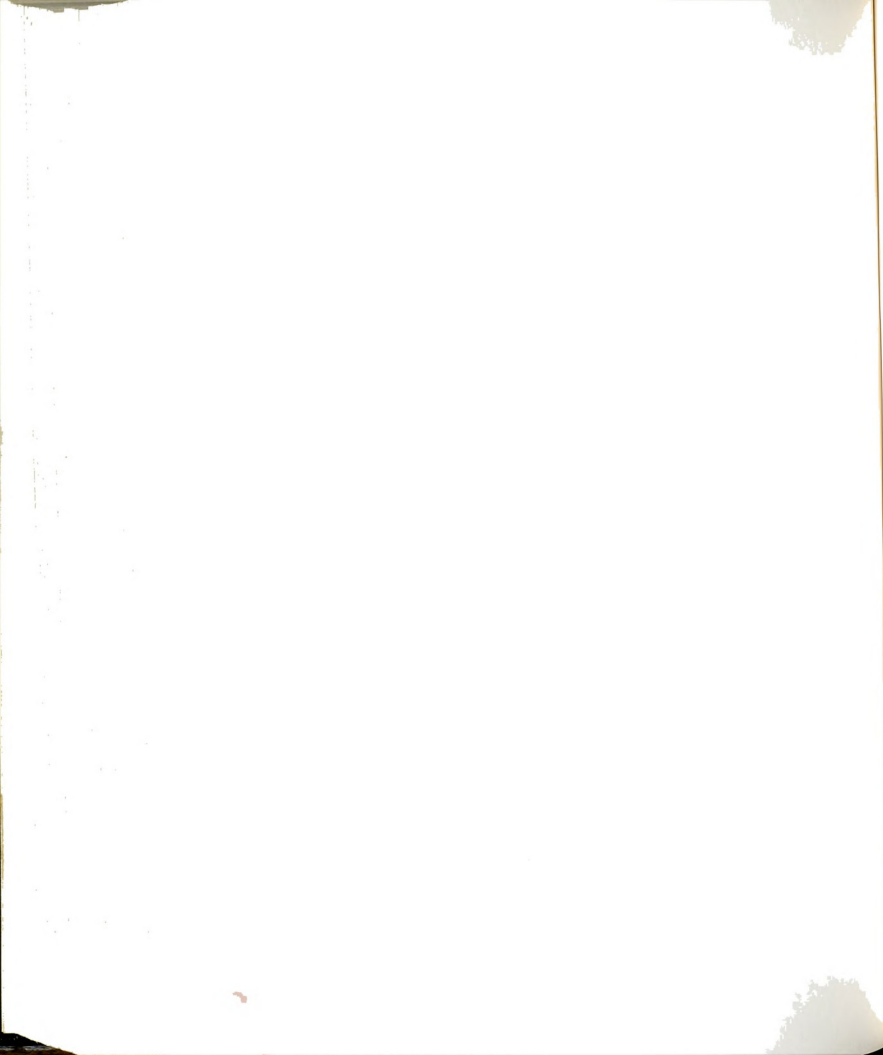


Figure 144. Distribution of $u_c^*(x)$ in the Re range of 1257-1272.
For legend see Figure 131.



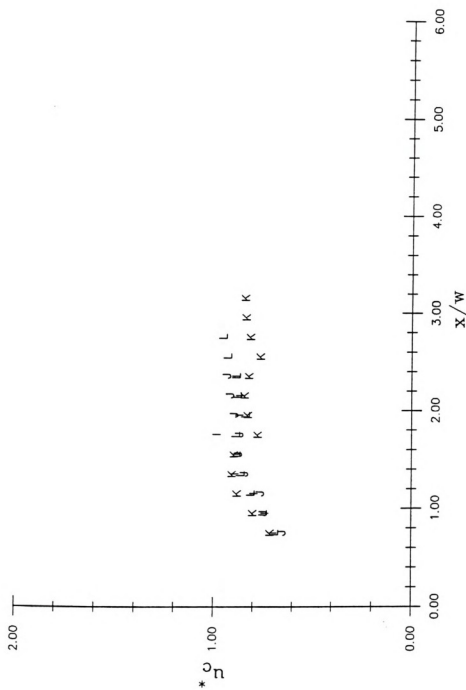
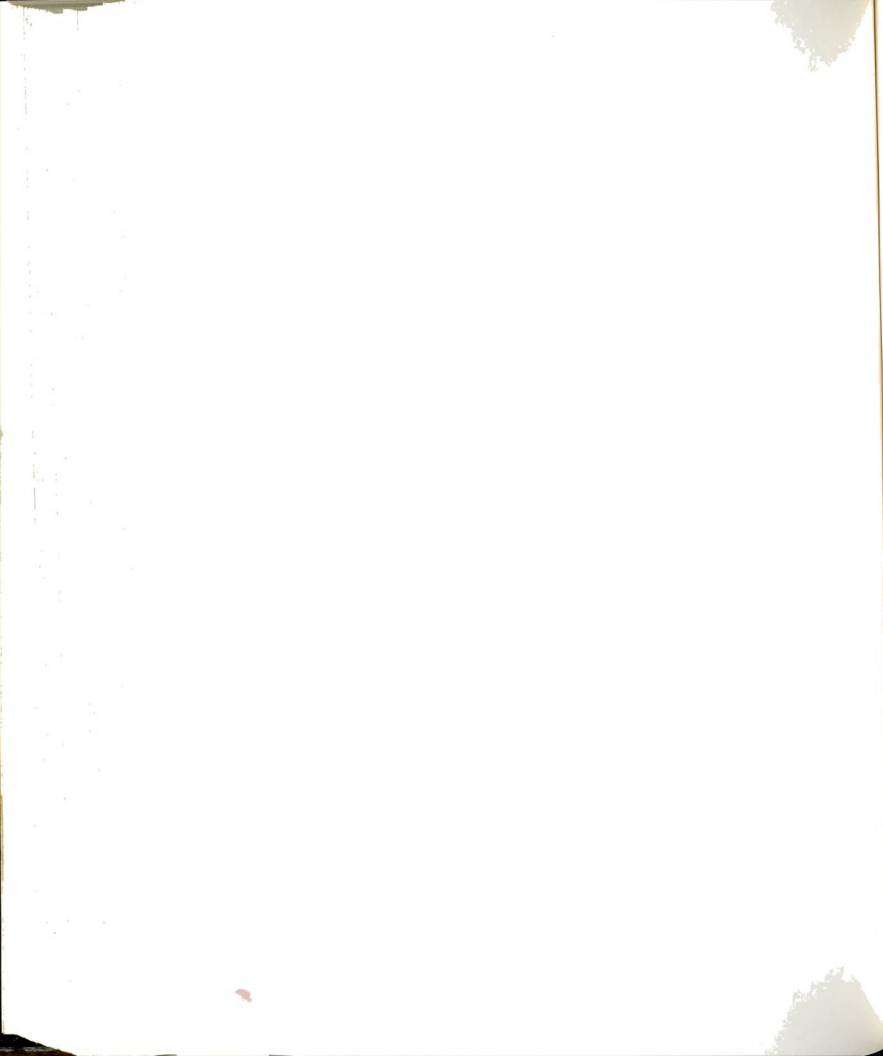
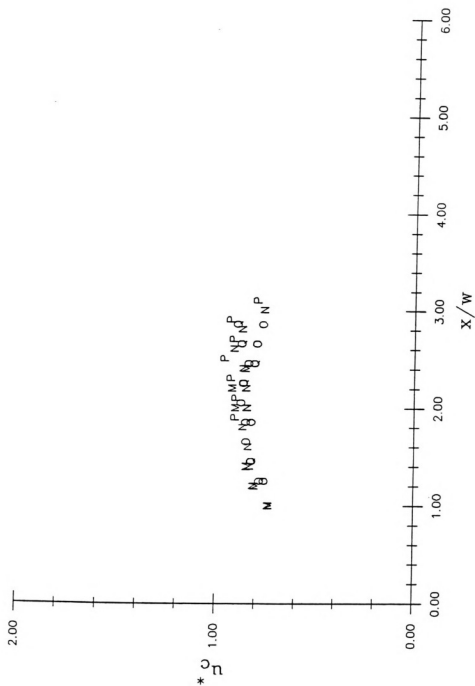
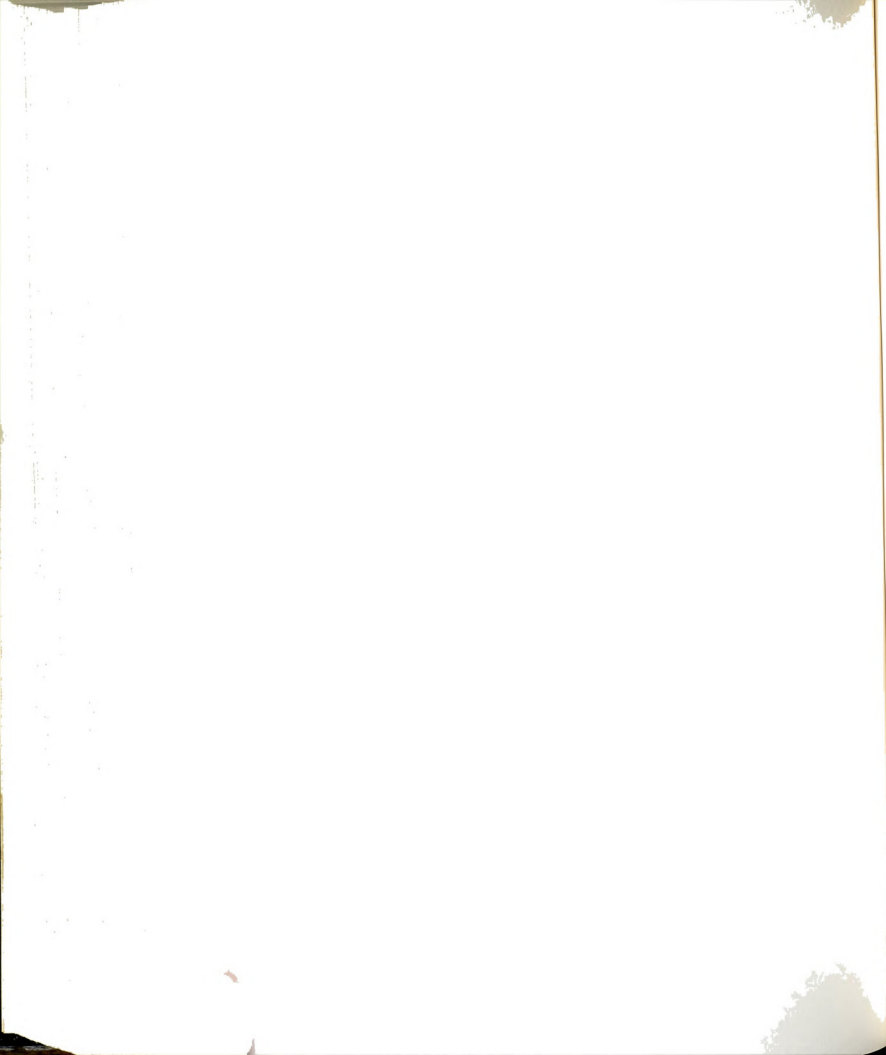


Figure 145. Distribution of u_c^* in the Re range of 1570-1700. For legend see Figure 132.







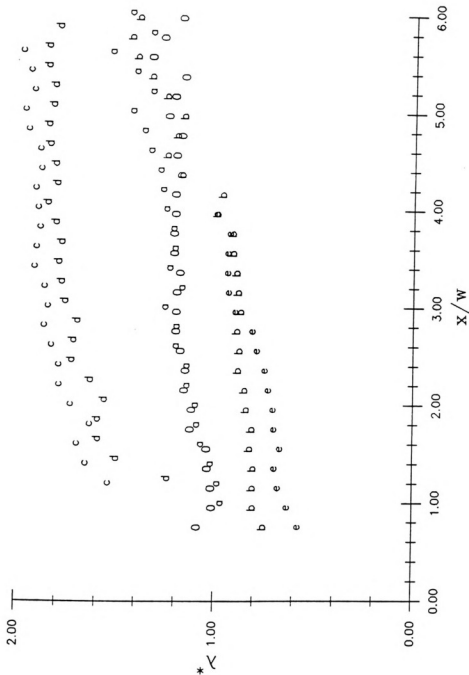
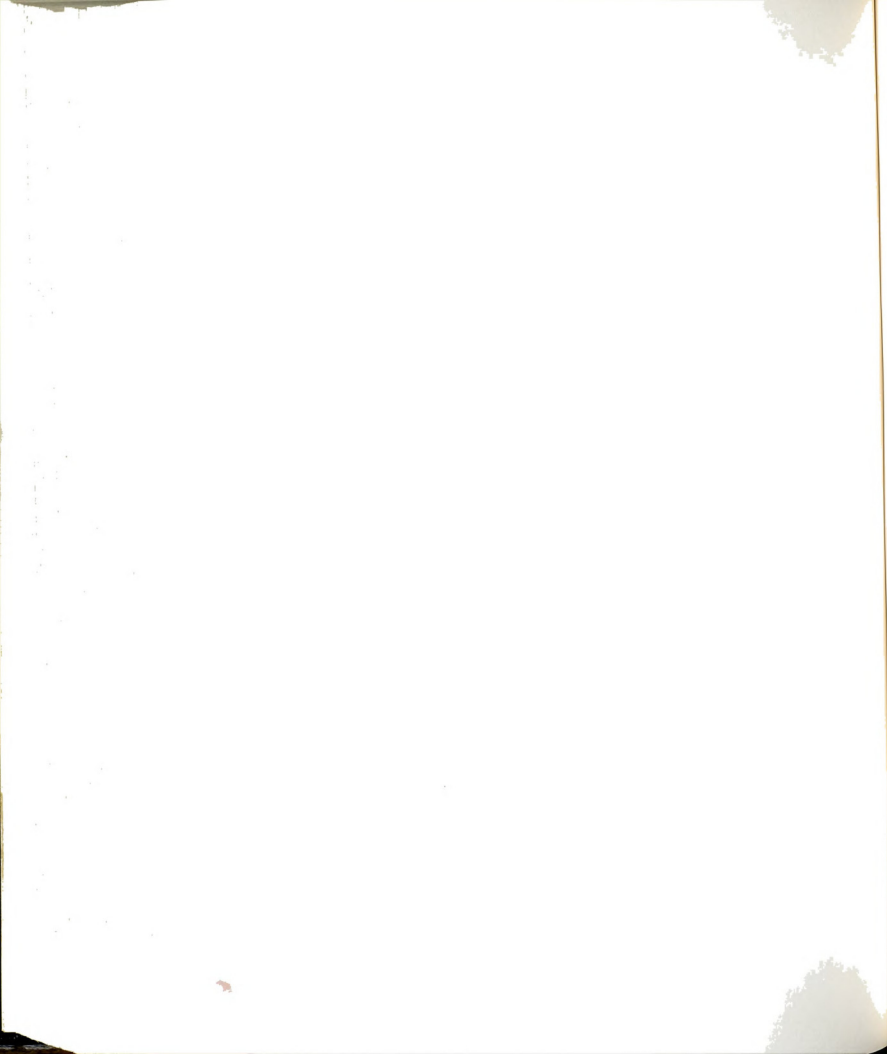


Figure 147. Distribution of $\lambda^*(x^*)$ in the Re range of 269-285. For legend see Figure 126. Note that the variations in λ^* for jets of various sizes are consistent with the variations in St_F (see Figure 126) and u^* (see Figure 139).



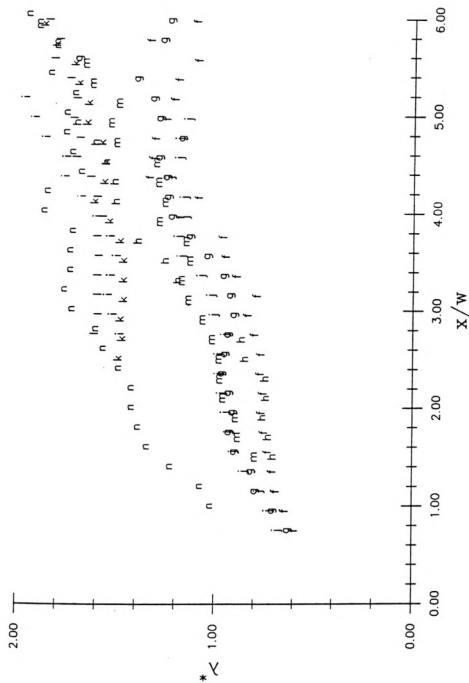
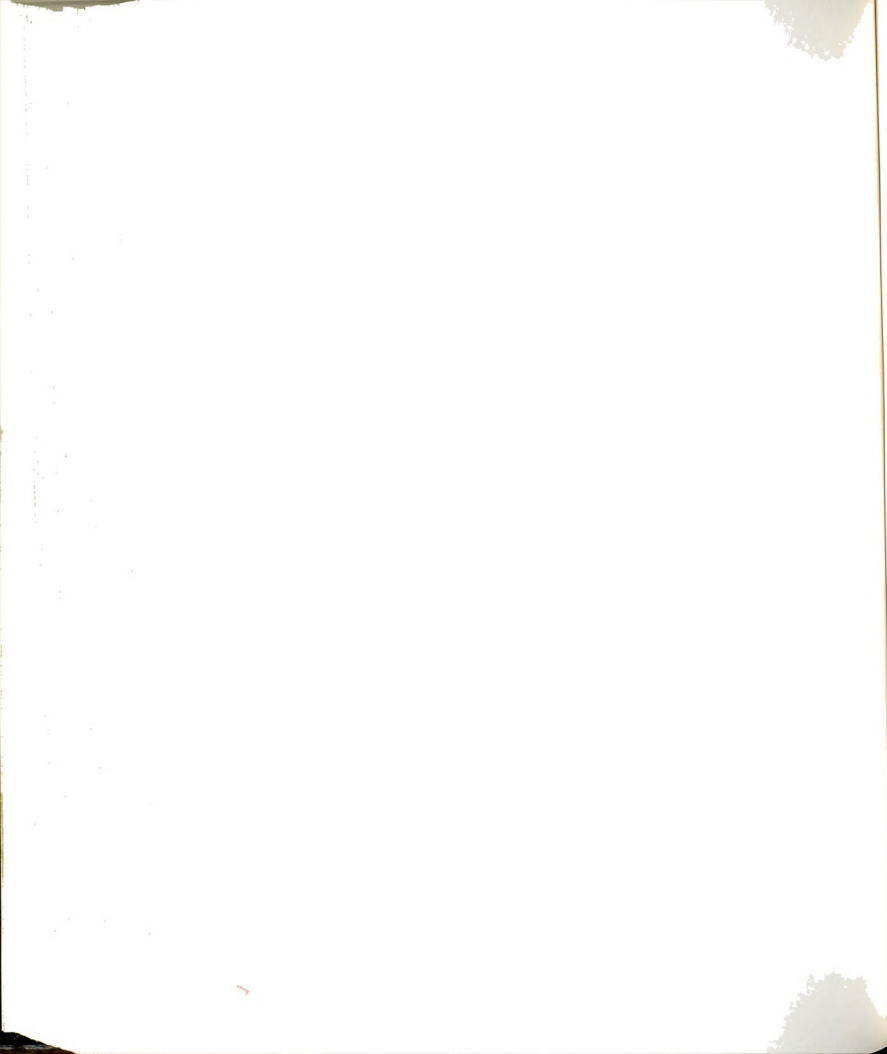


Figure 148. Distribution of $\lambda^*(x^*)$ in the Re range of 362-426.
For legend see Figure 127.



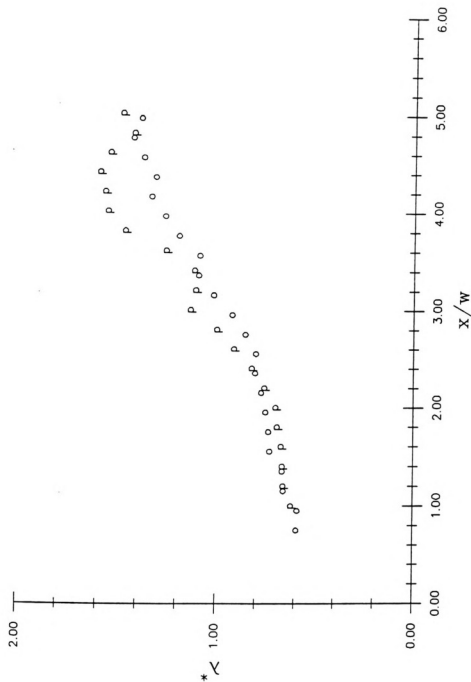
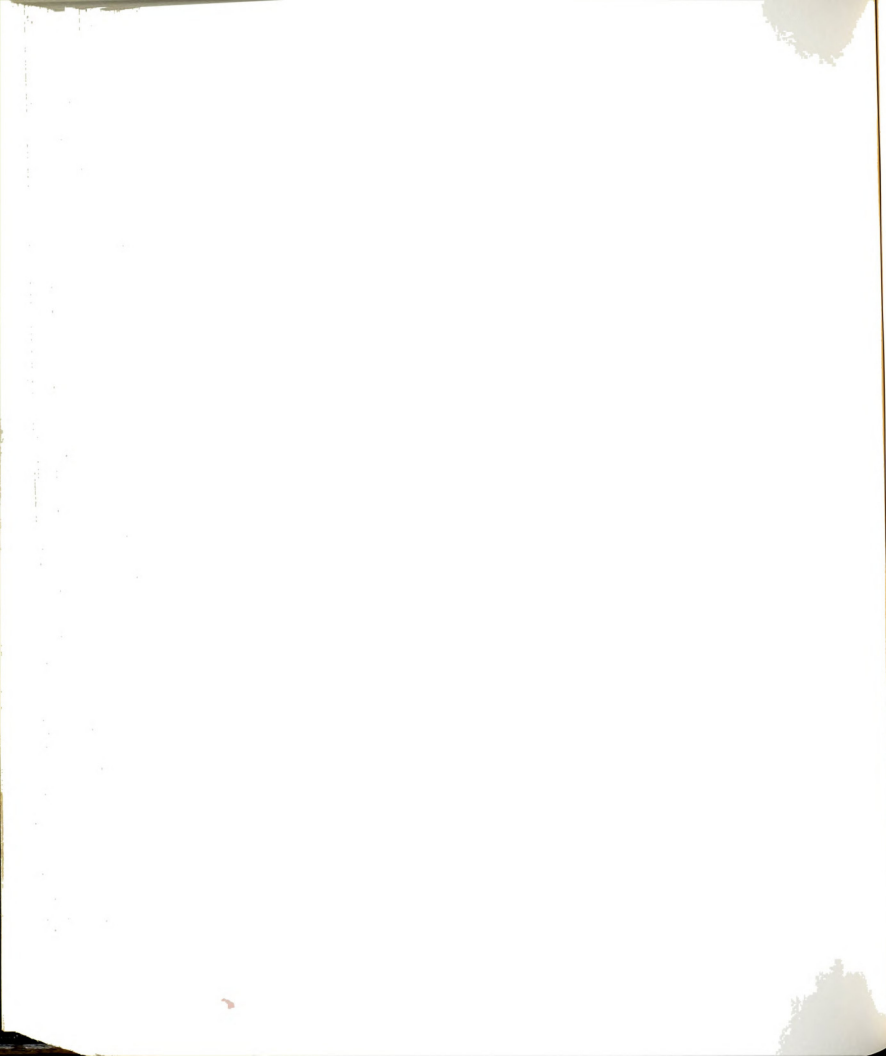
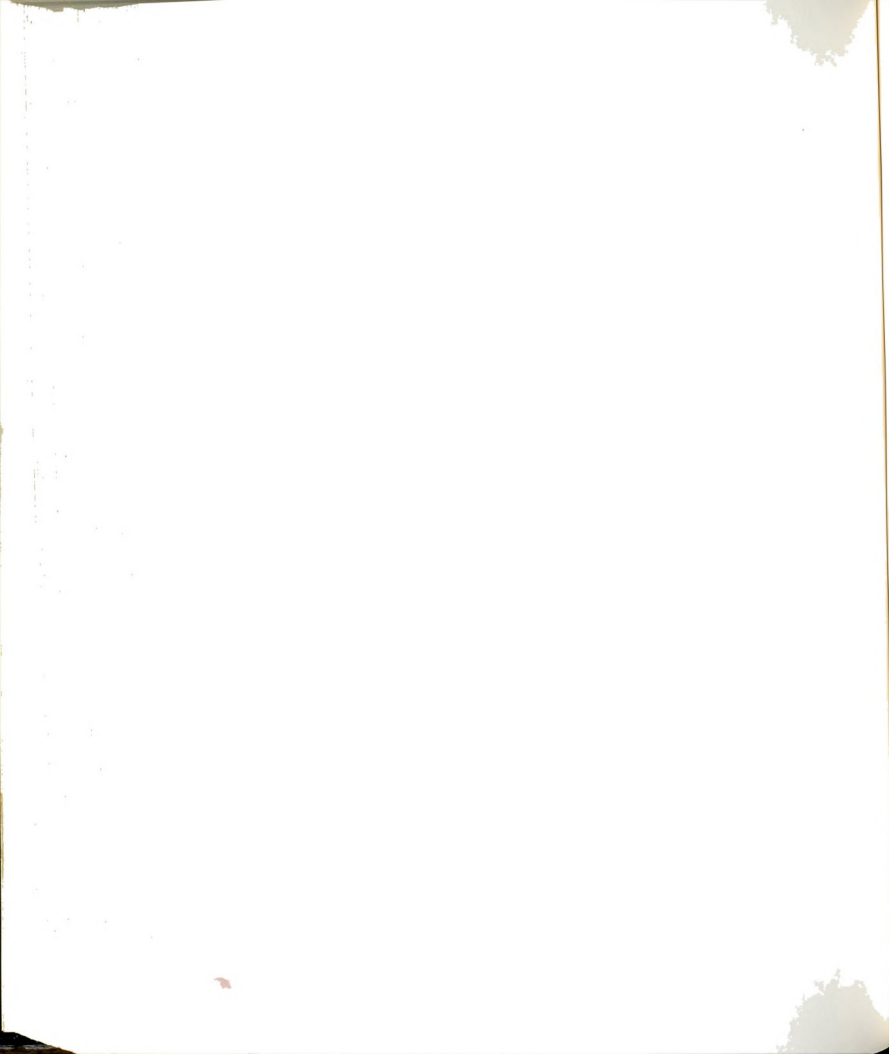


Figure 149. Distribution of $\lambda^*(x^*)$ in the Re range of 510-525.
For legend see Figure 128.





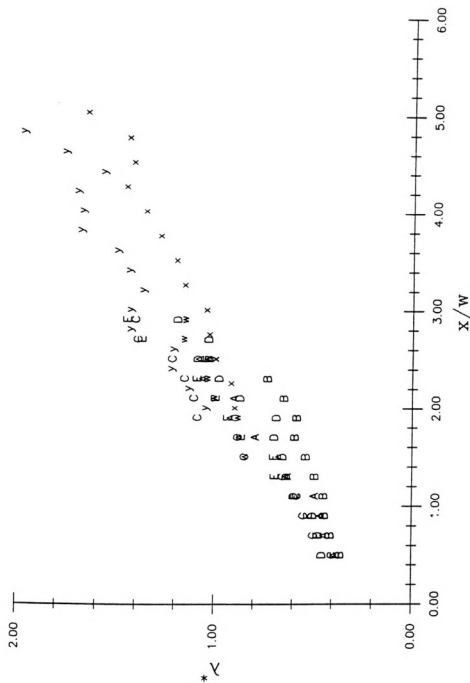
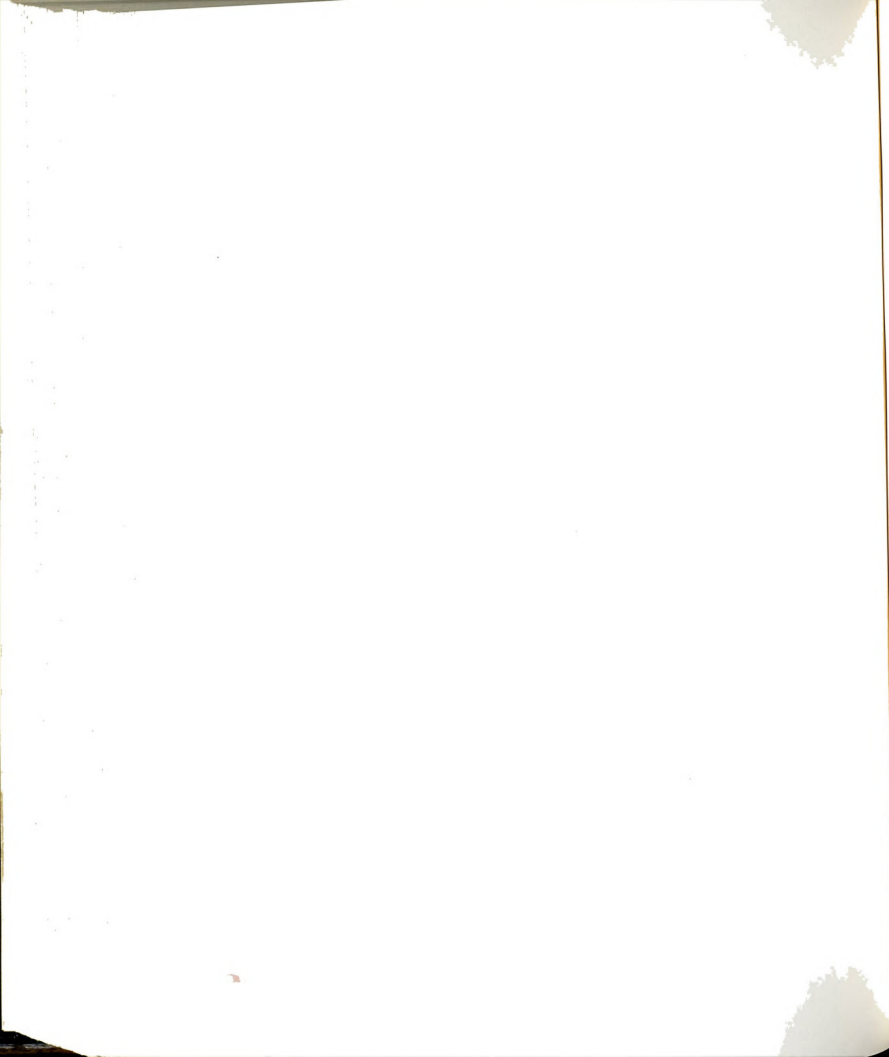


Figure 151. Distribution of $\lambda^*(x)$ in the Re range of 930-1074.
For legend see Figure 130.



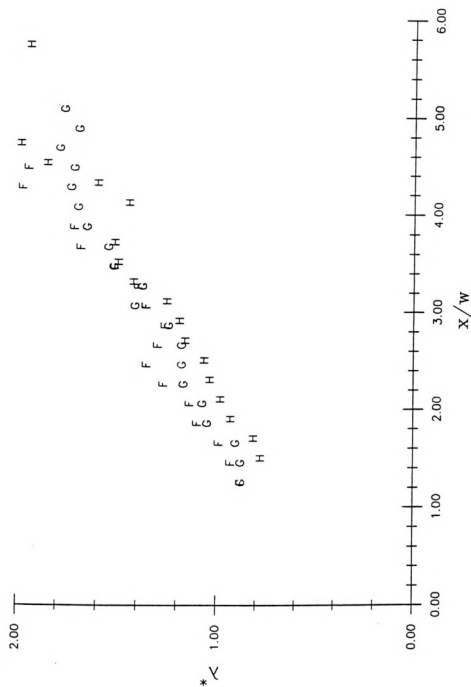
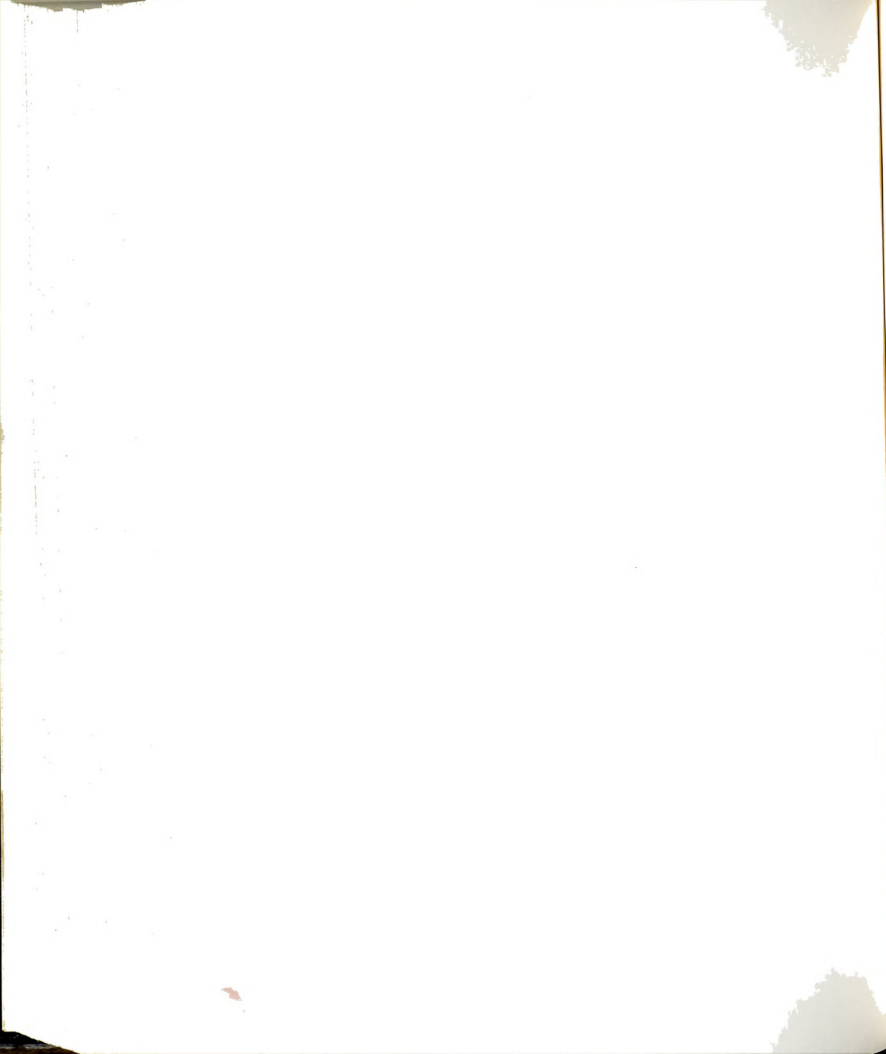


Figure 152. Distribution of $\lambda^*(x)$ in the Re range of 1257-1272.
For legend see Figure 131.



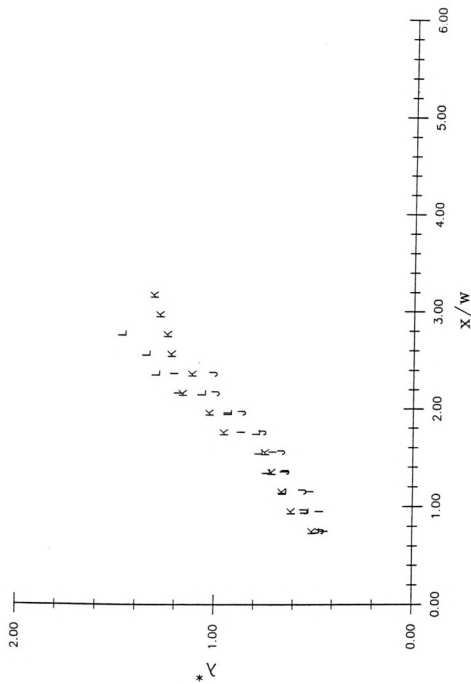
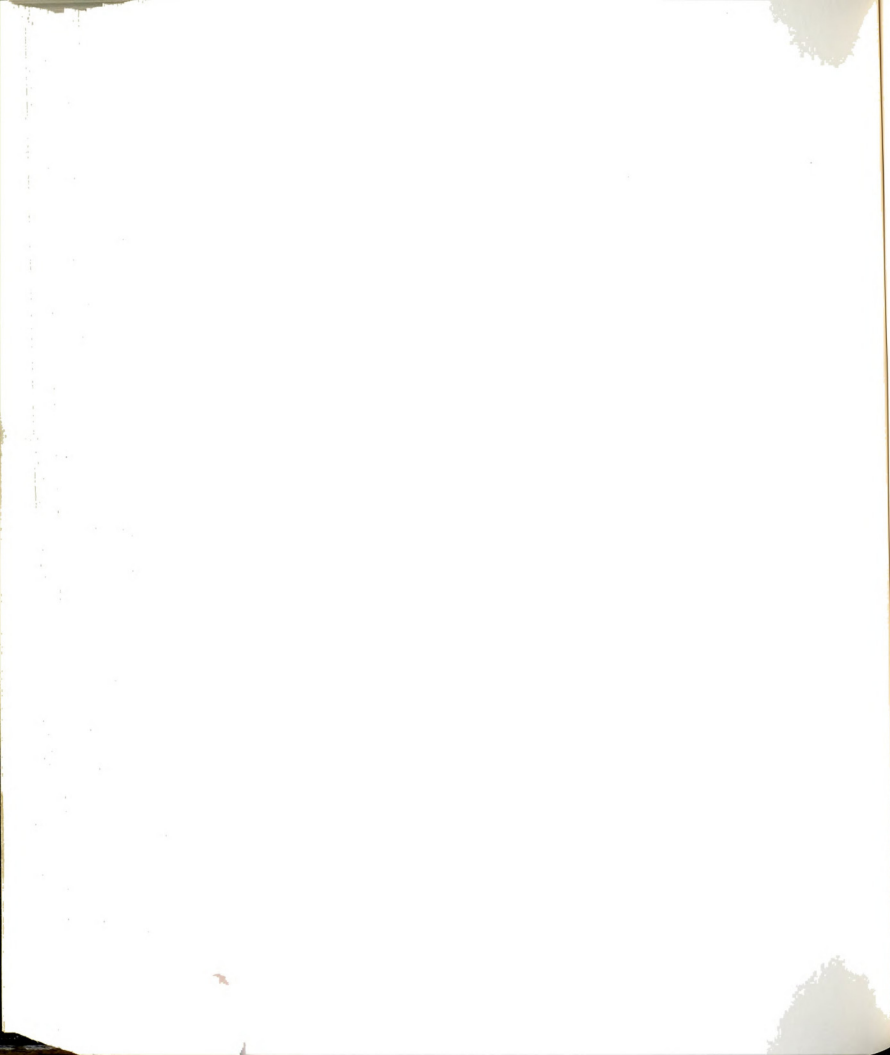


Figure 153. Distribution of $\lambda^*(x^*)$ in the Re range of 1570-1700.
For legend see Figure 132.



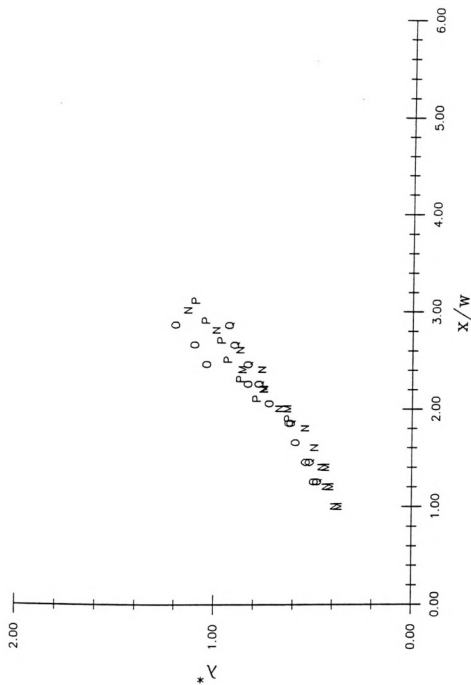
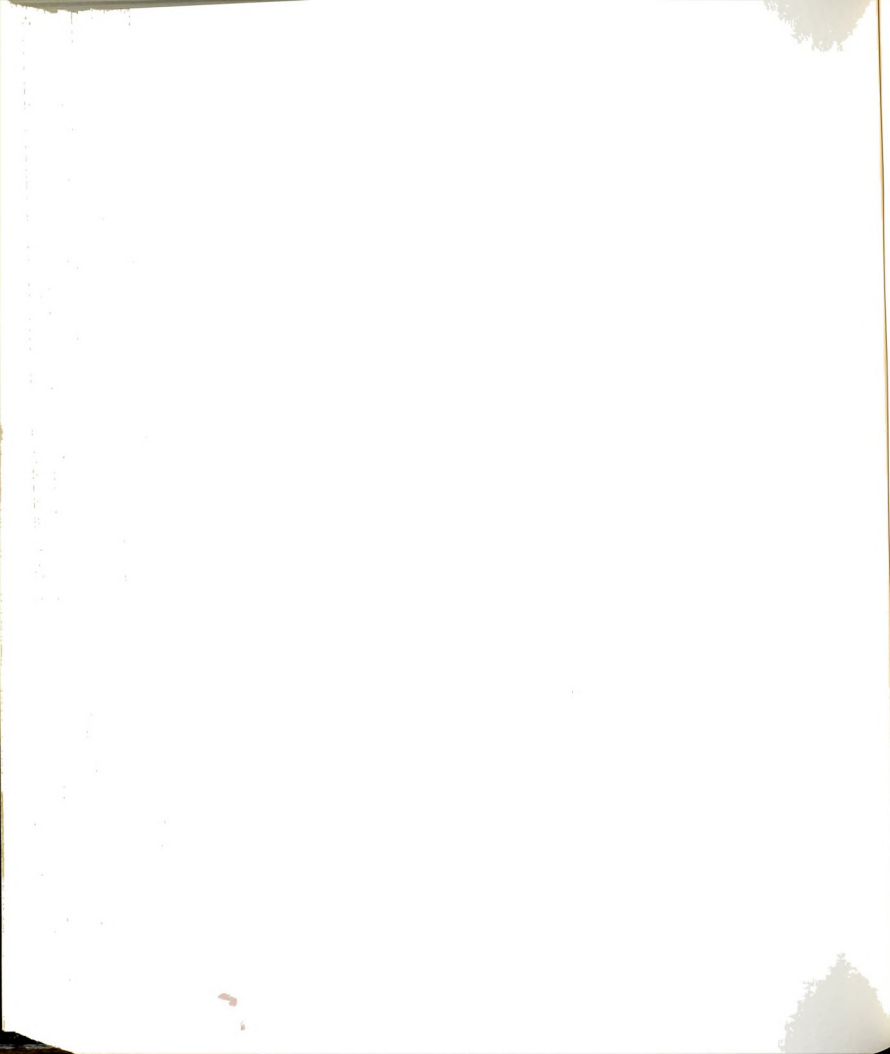


Figure 154. Distribution of $\lambda^*(x)$ in the Re range of 2949-3469.
For legend see Figure 133.



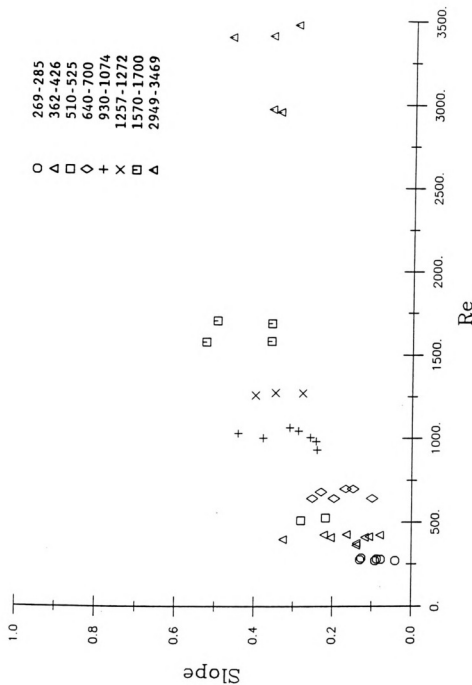
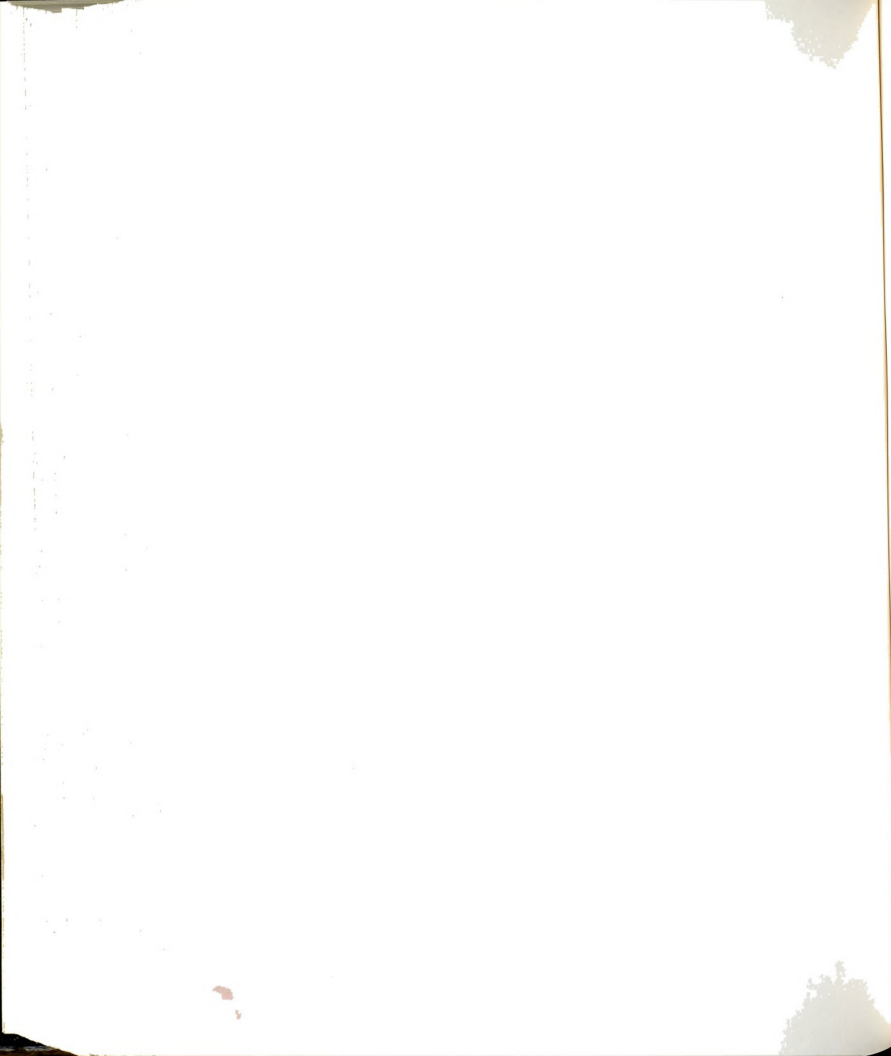


Figure 155. Slopes of the streamwise distribution of $\lambda^*(x^*)$ as a function of Re. The data have been grouped in the same ranges as were used in the plots St_F , uc^* and λ^* .



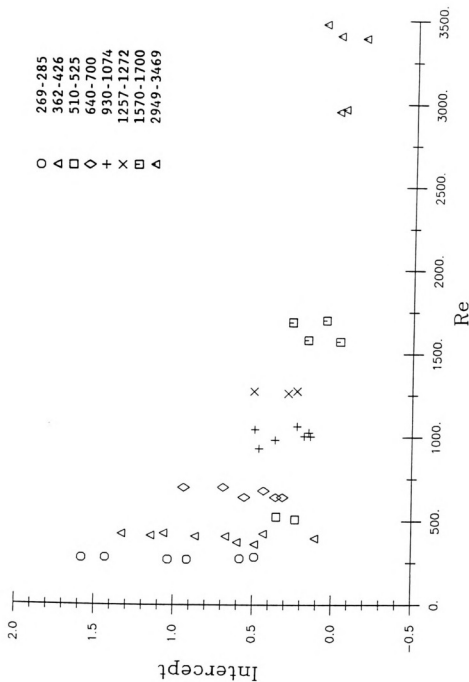
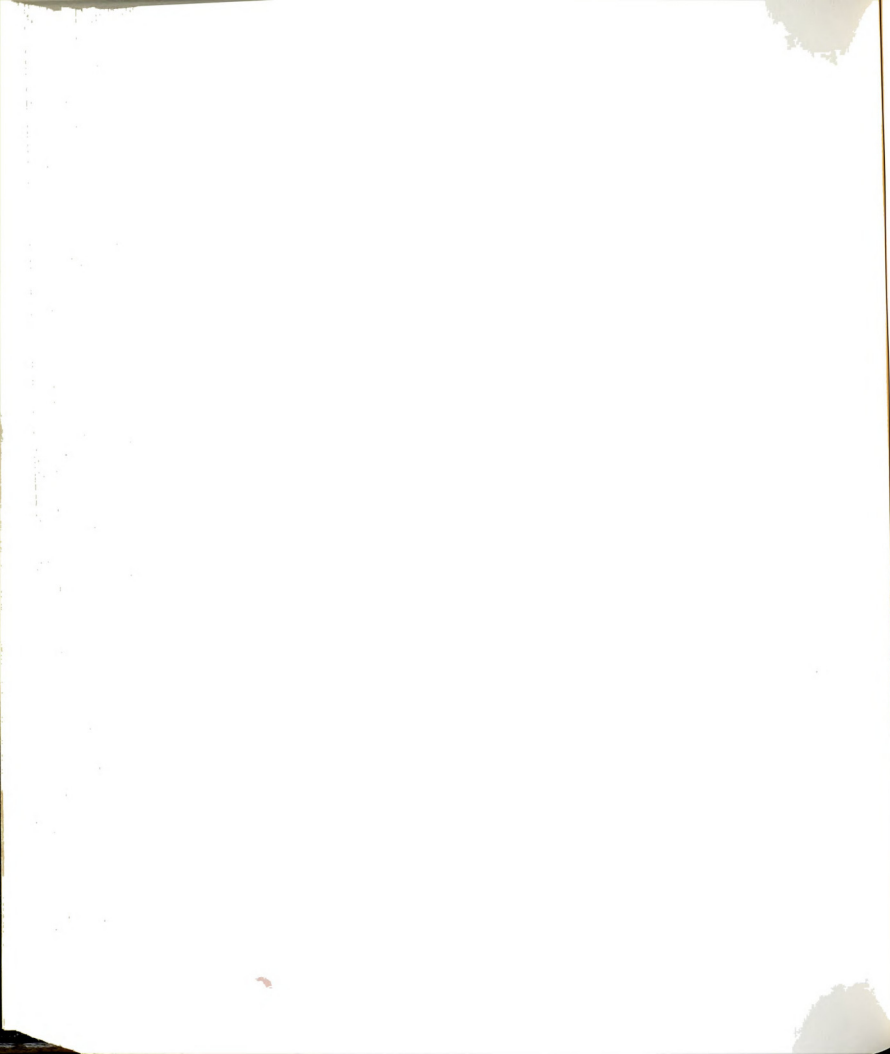


Figure 156. Intercepts of streamwise distribution of λ^* as a function of Re .



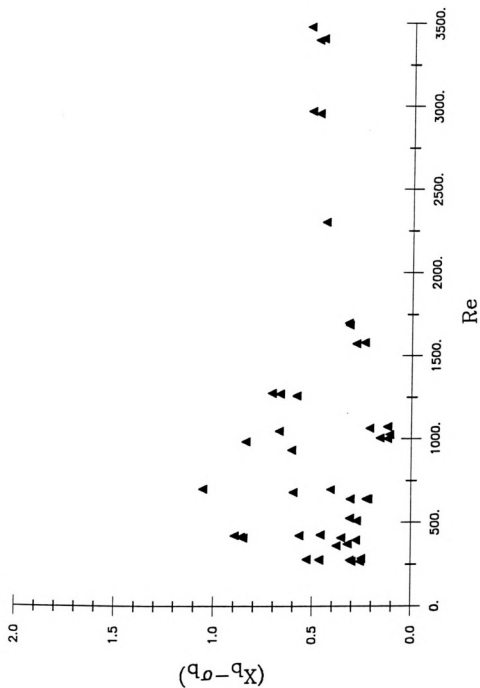
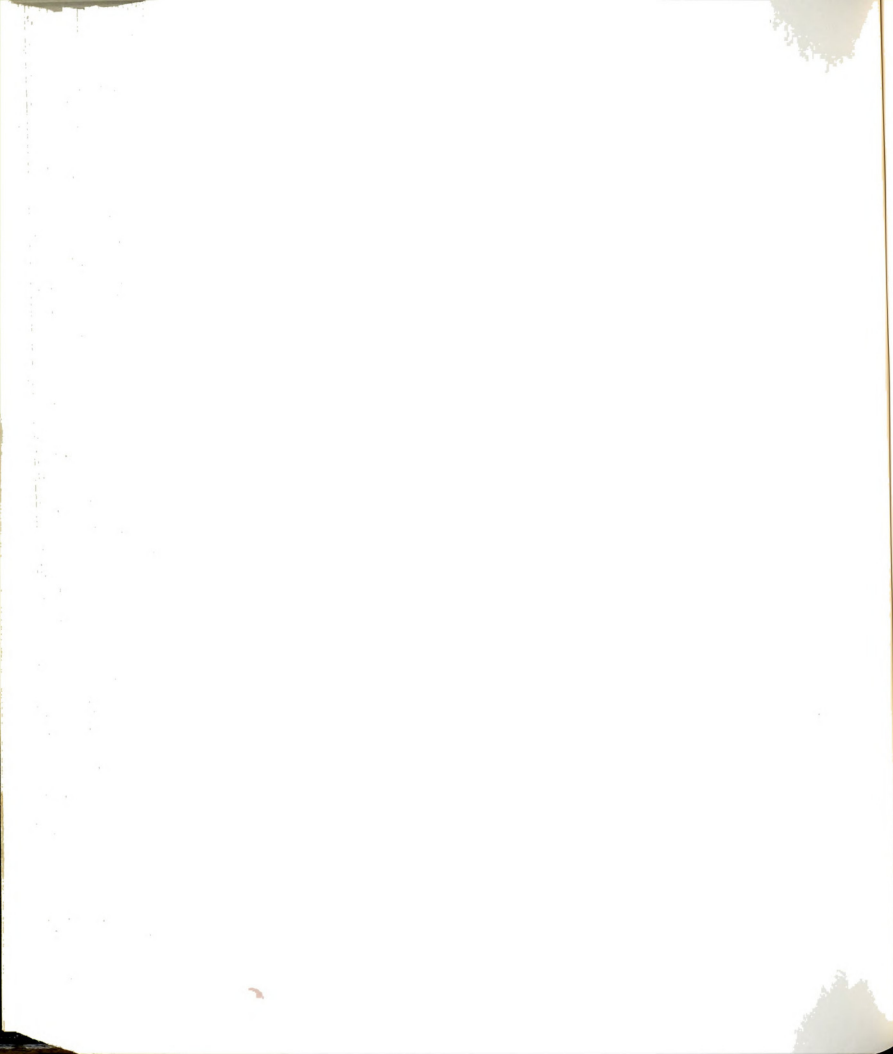


Figure 157. Distribution of the estimate of nondimensional location of the formation of bulges as a function of Re .



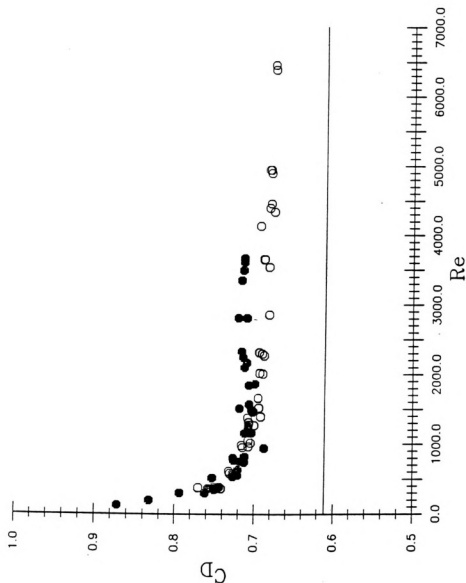
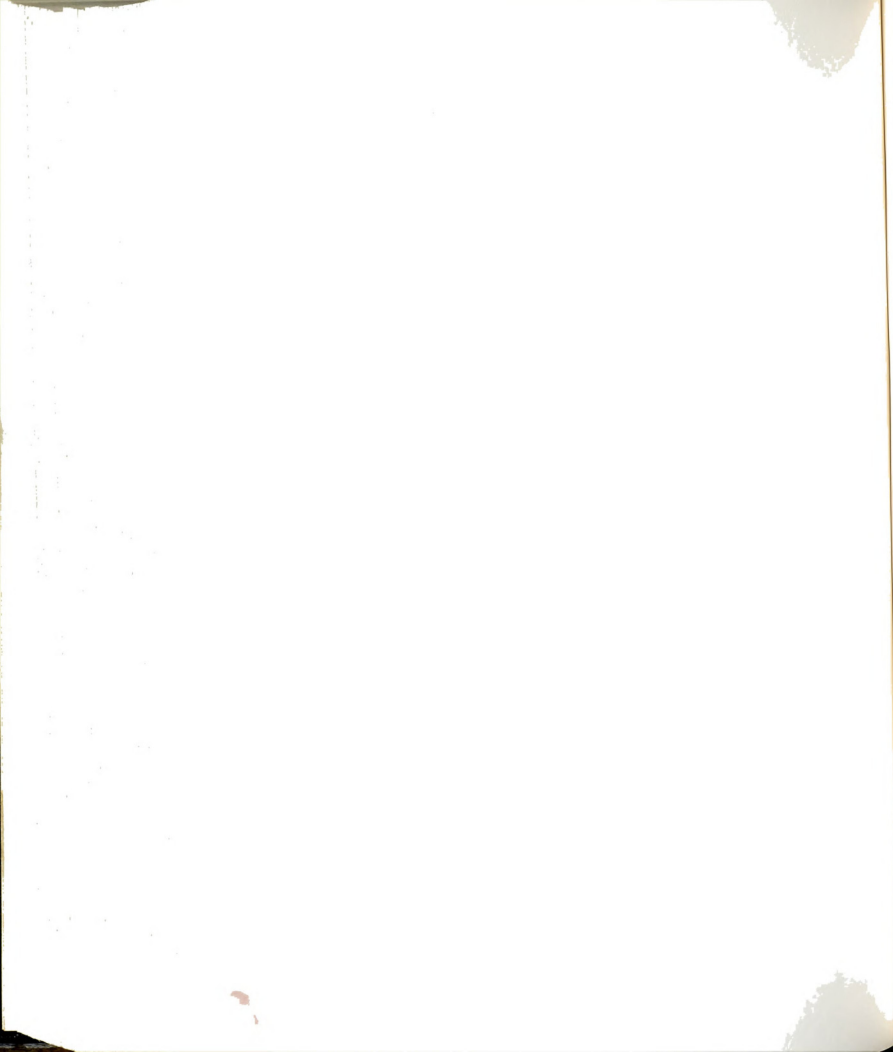


Figure 158. Distribution of discharge coefficient, C_D , as a function of Re in jets with two different slit widths. The closed symbols represent the measurements made in a jet with $B/w=21.7$ ($\tau_N/w=1$) and the open symbols represent the case with $B/w=10.8$ ($\tau_N/w=0.5$). The solid line represents C_D for an inviscid jet.



- A: Single channel
LDA system
B: Flow facility
C: Table to support LDA
D: Table to traverse B
E: Base of LDA system

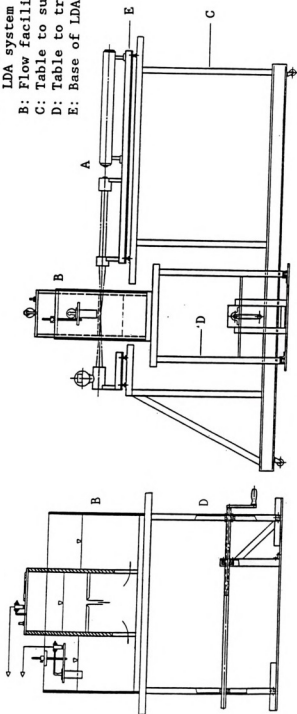
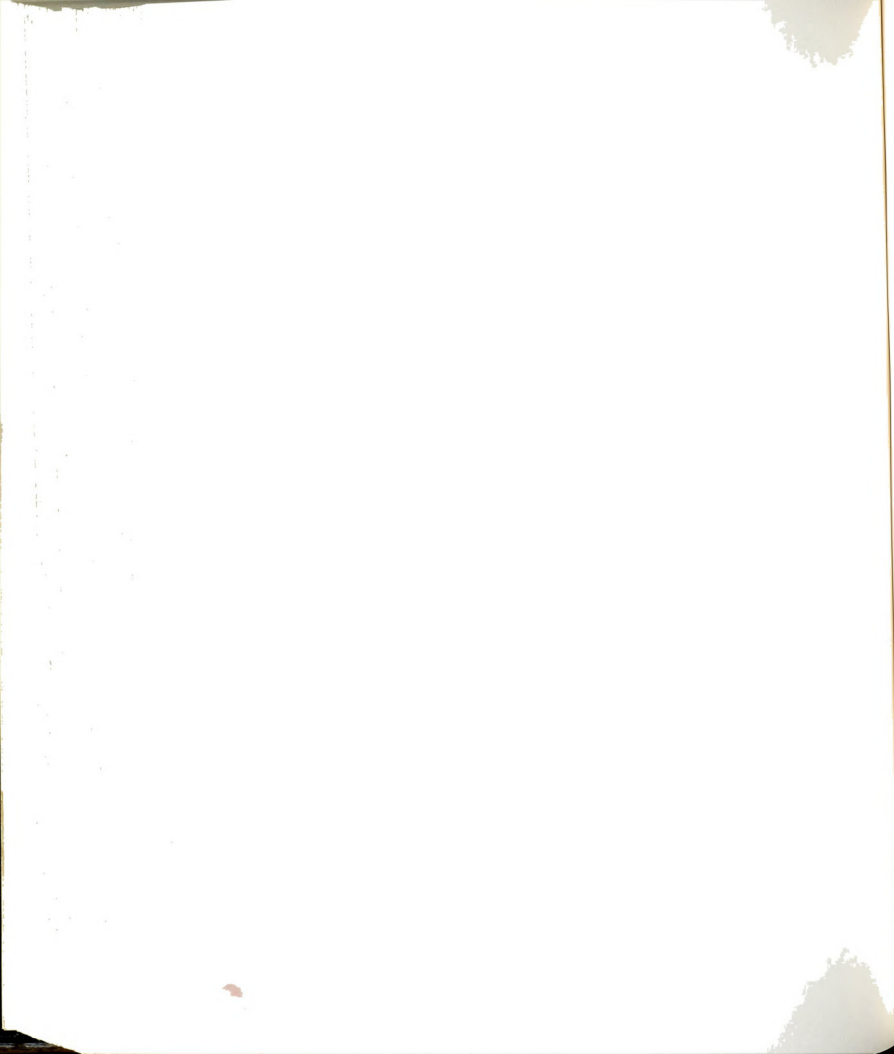


Figure 159. Schematic representation of the mechanism for velocity traversals. For longitudinal surveys the base of the LDA was raised or lowered using plastic blocks. For lateral surveys the flow facility was traversed across the LDA.



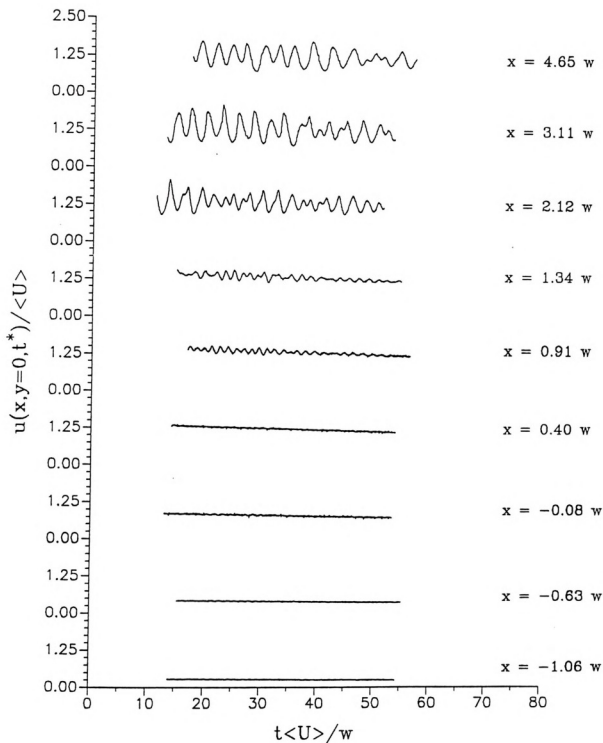
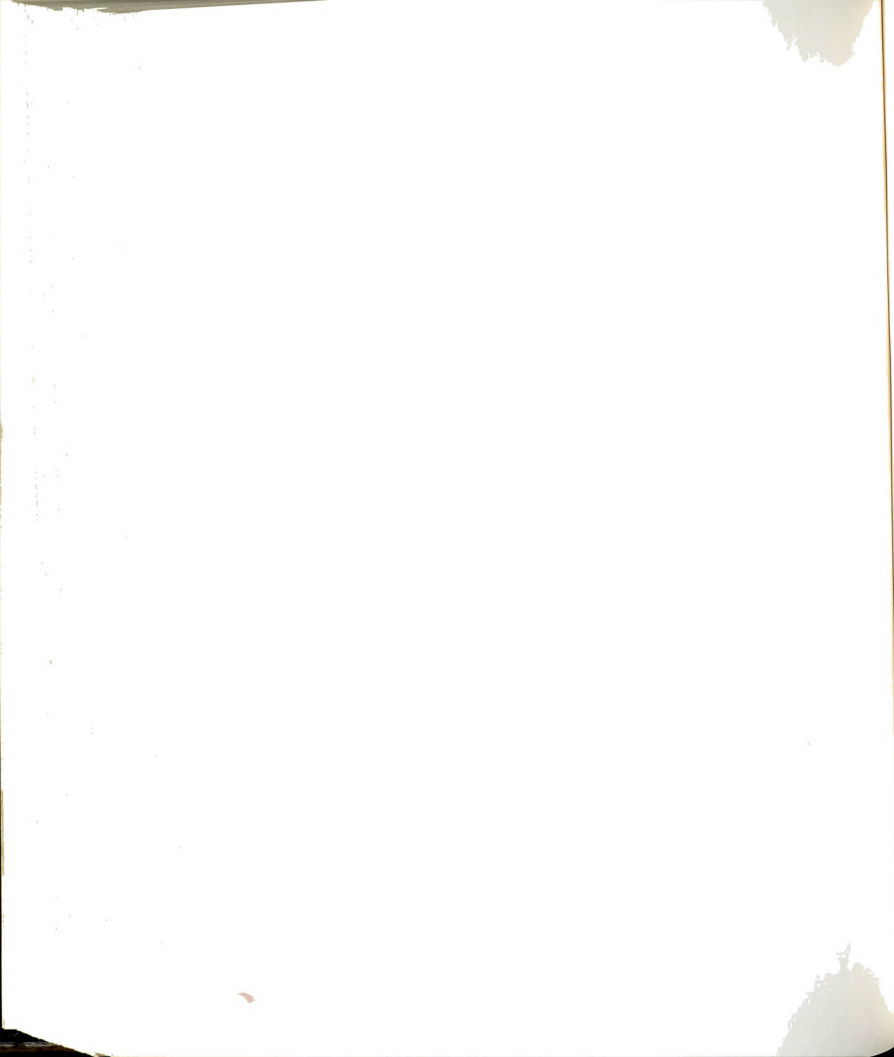


Figure 160. Nondimensional velocity time histories along the centerline of the jet at $Re=509$ and $w=1.27$ cm.



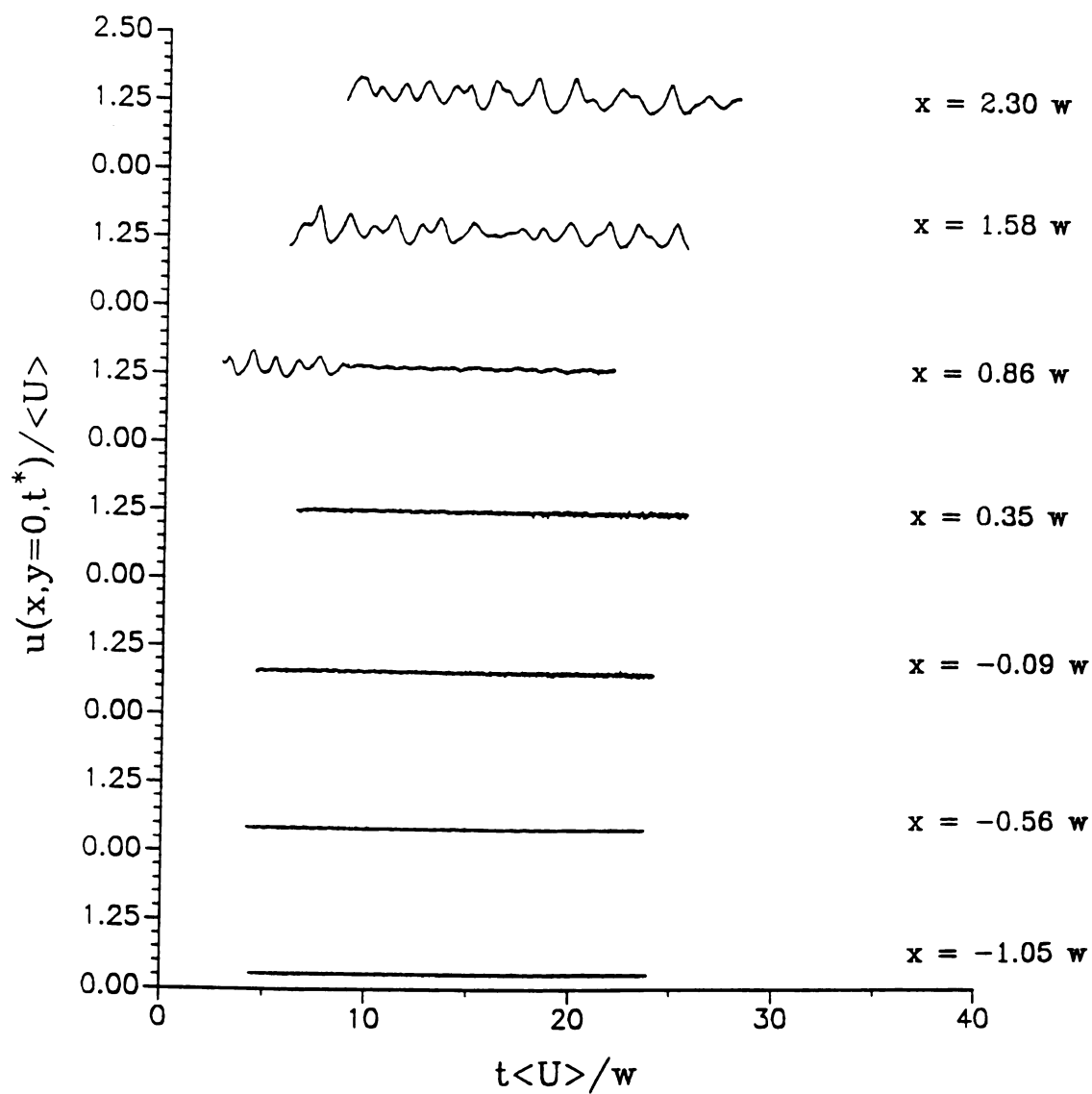
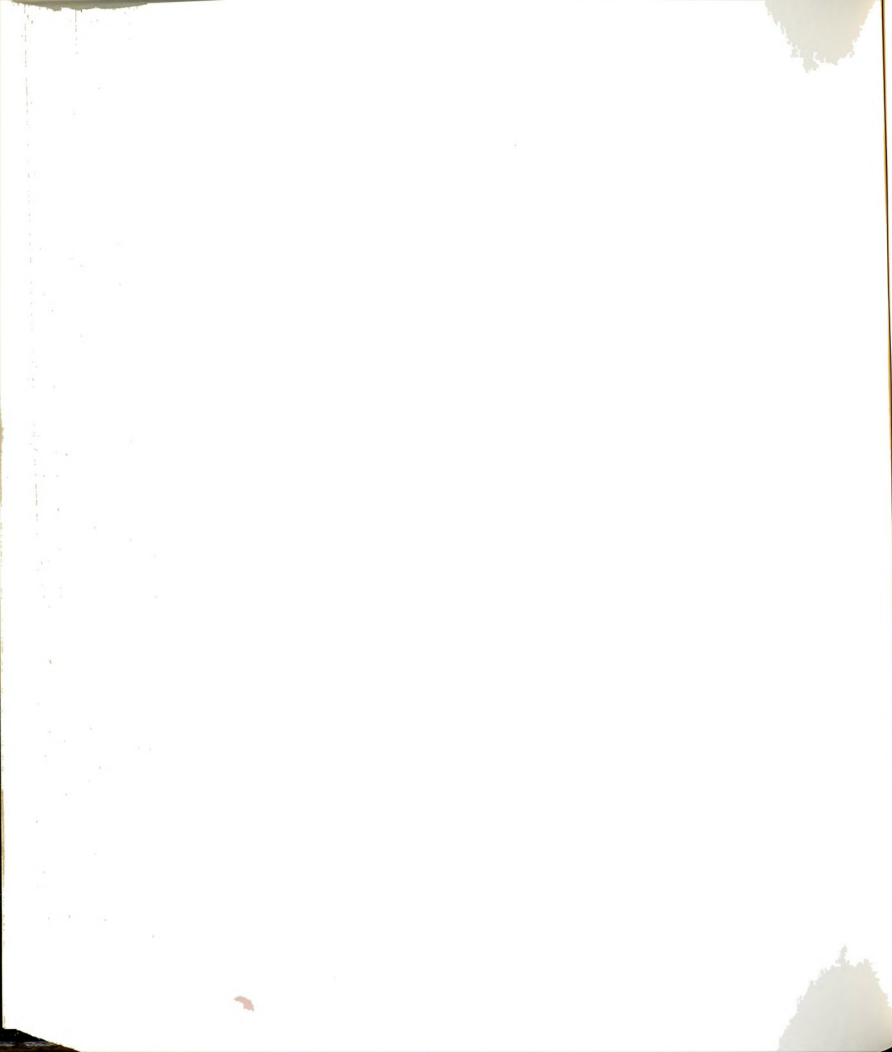


Figure 161. Nondimensional velocity time histories along the centerline of the jet at $Re=1011$ and $w=2.57$ cm.



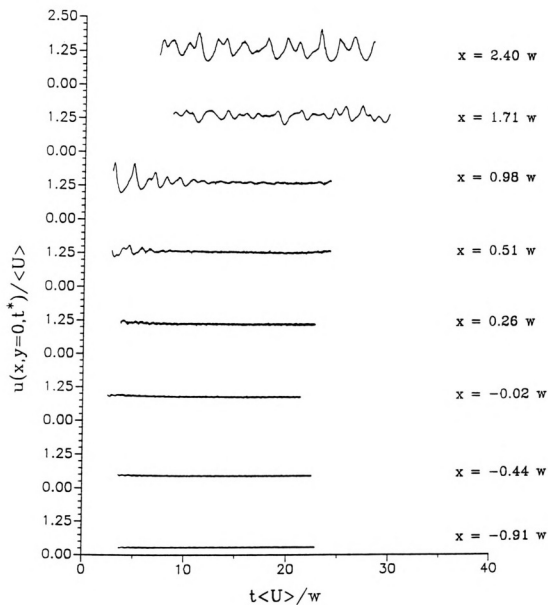
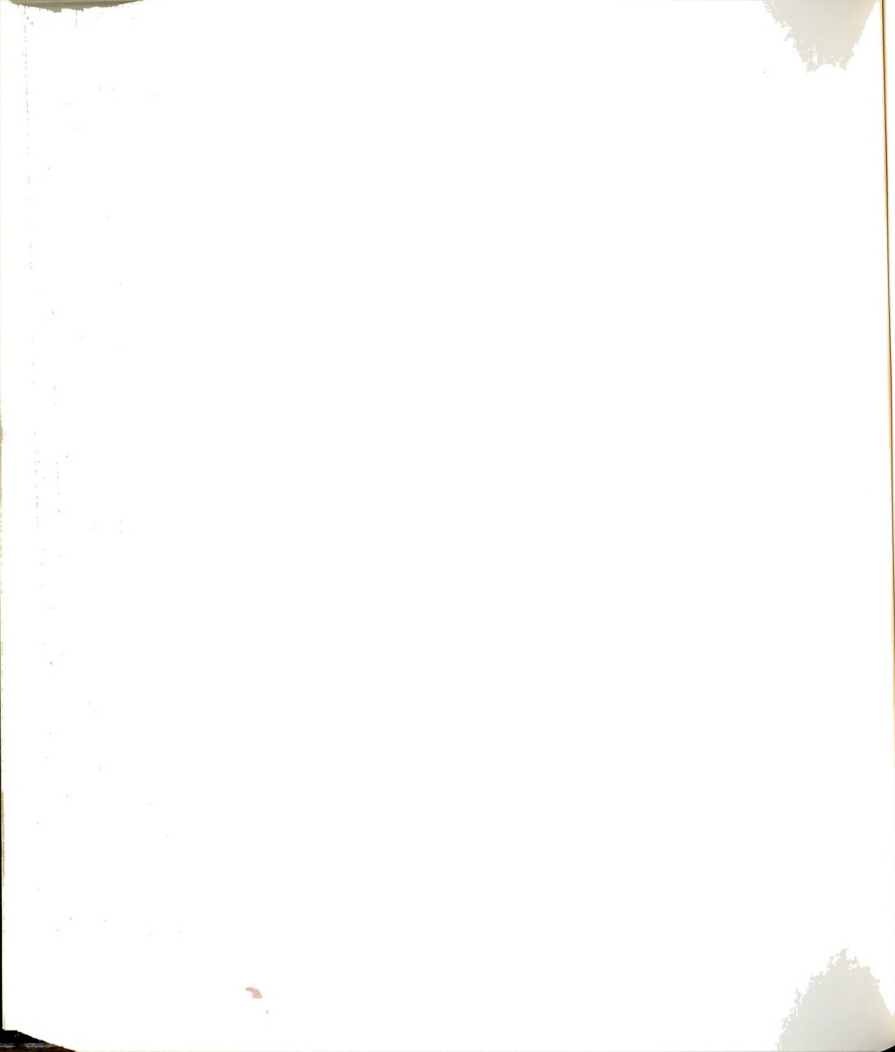


Figure 162. Nondimensional velocity time histories along the centerline of the jet at $Re=1021$ and $w=2.57$ cm.



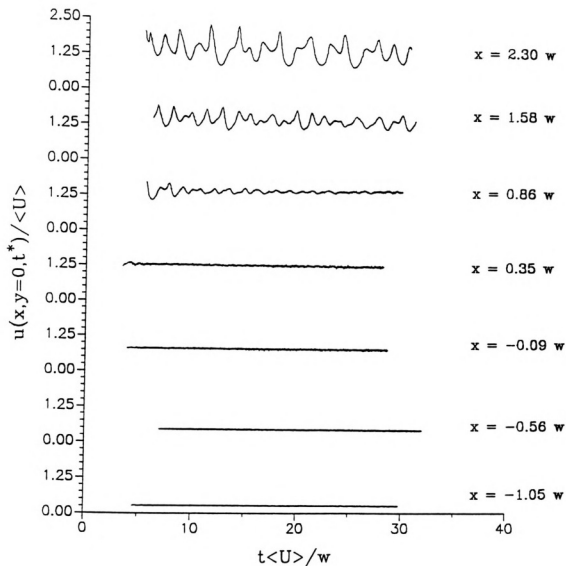
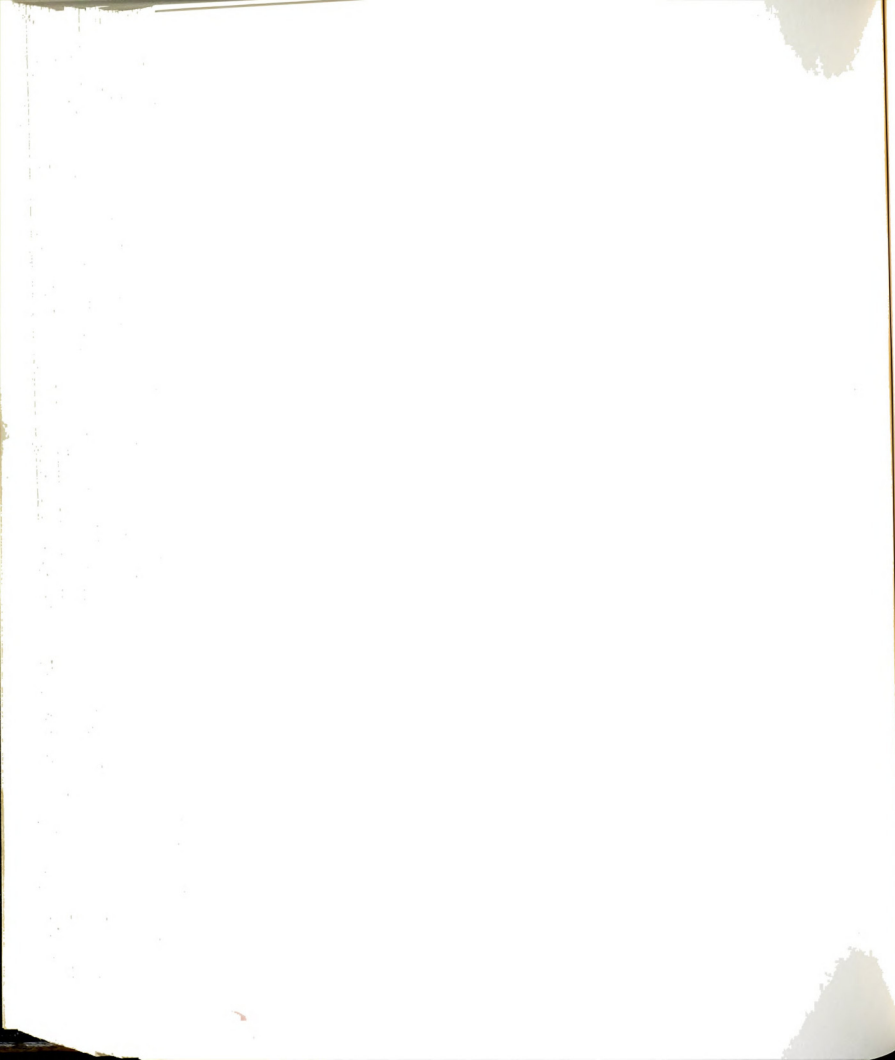


Figure 163. Nondimensional velocity time histories along the centerline of the jet at $Re=1293$ and $w=2.57$ cm.



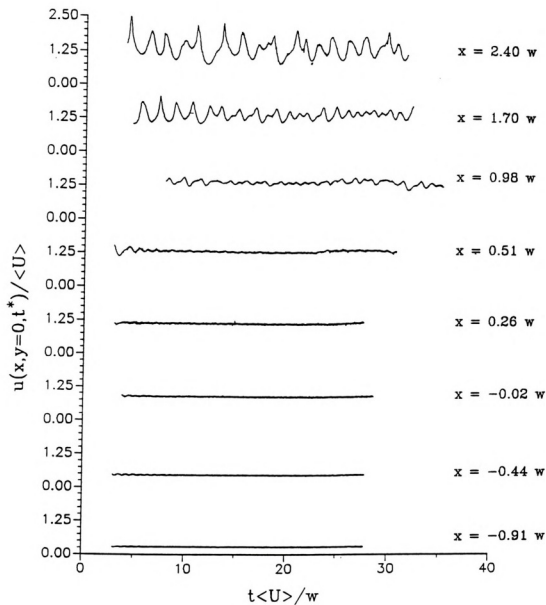
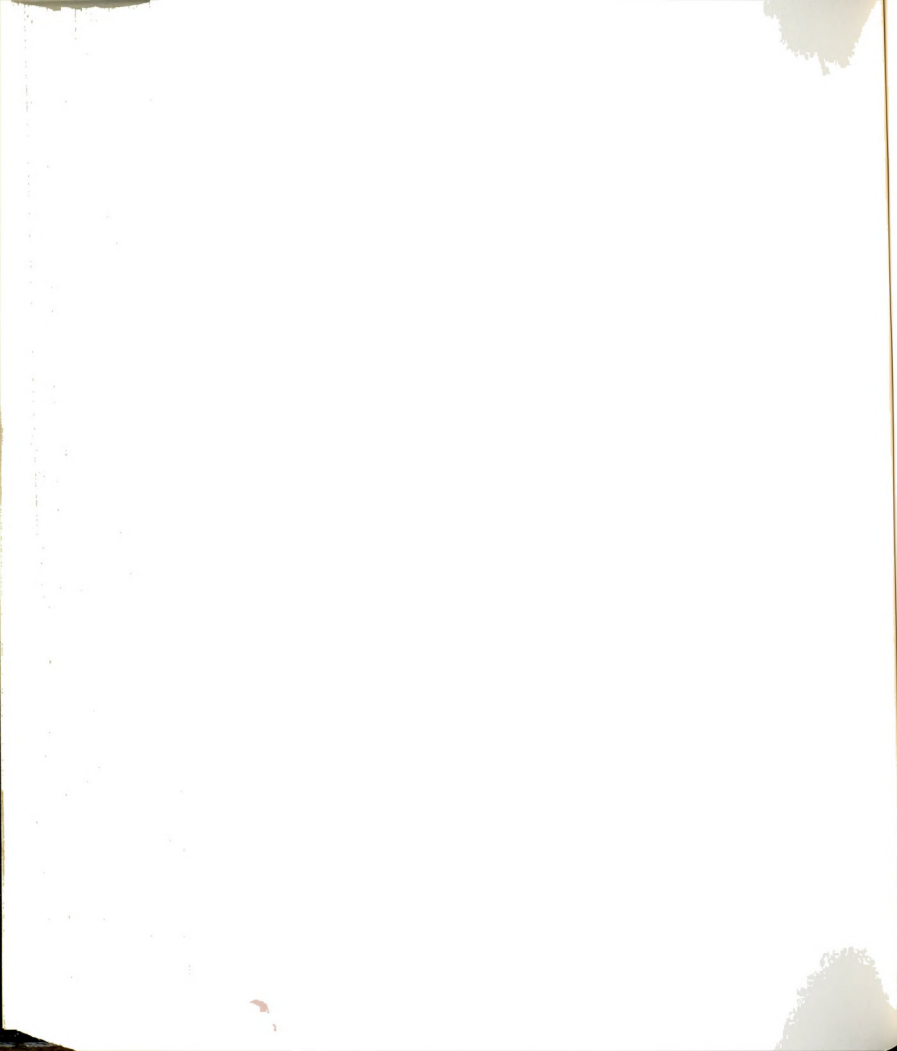


Figure 164. Nondimensional velocity time histories along the centerline of the jet at $Re=1328$ and $w=2.57$ cm.



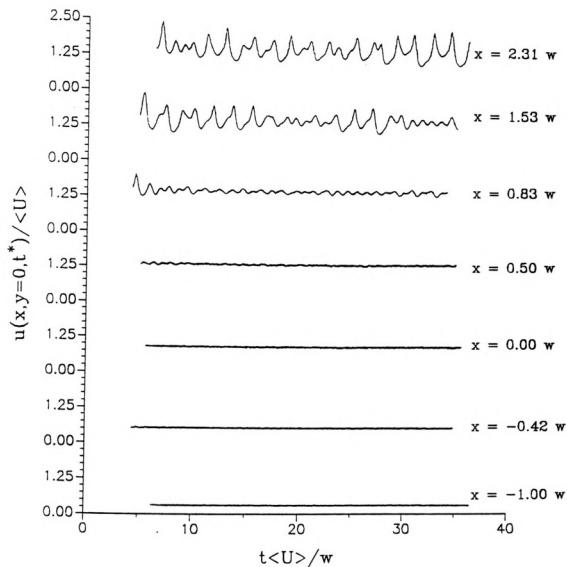
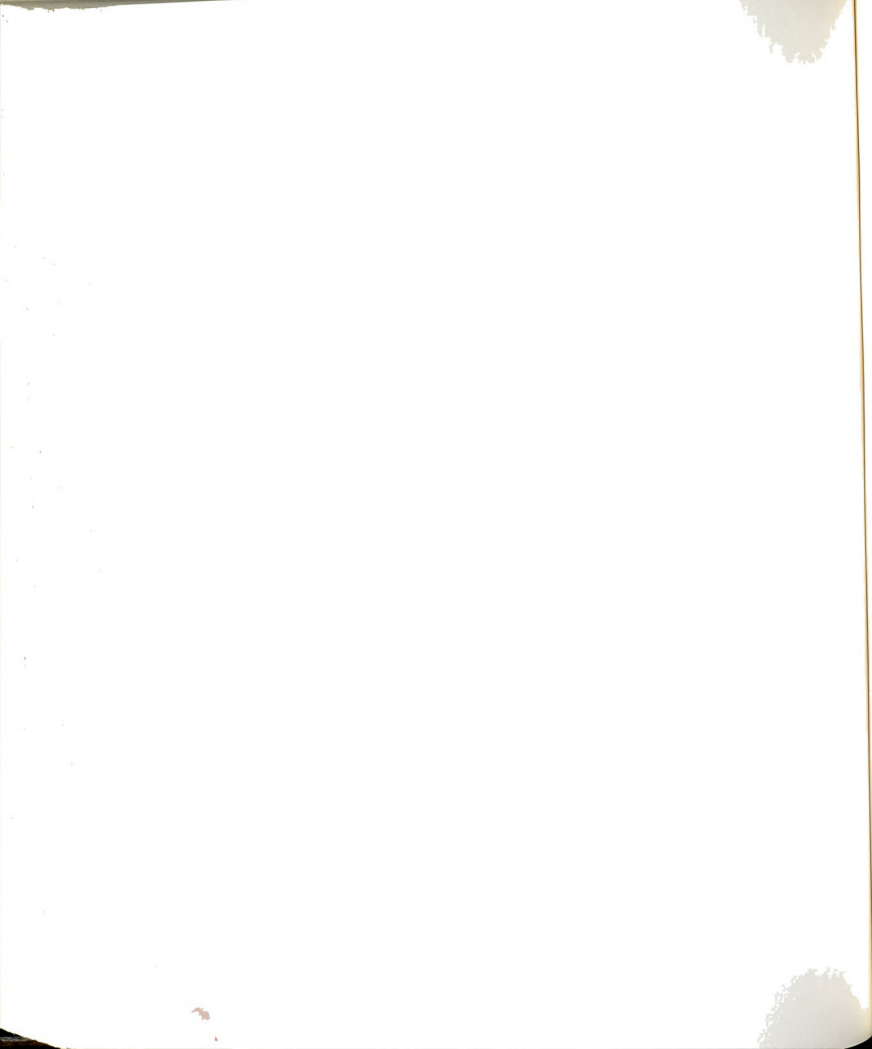


Figure 165. Nondimensional velocity time histories along the centerline of the jet at $Re=1527$ and $w=2.57$ cm.



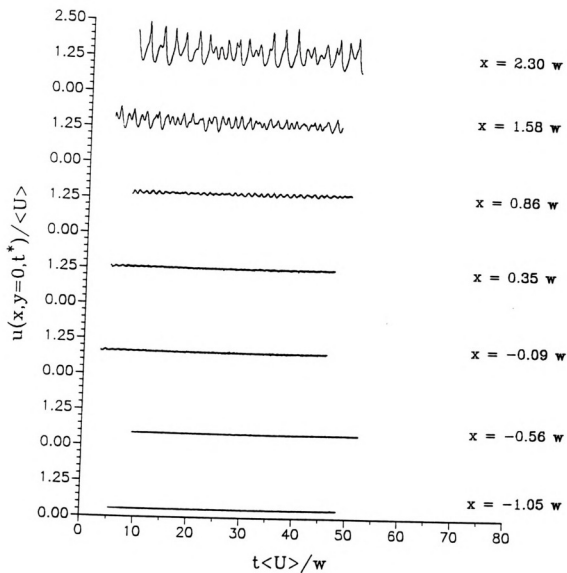
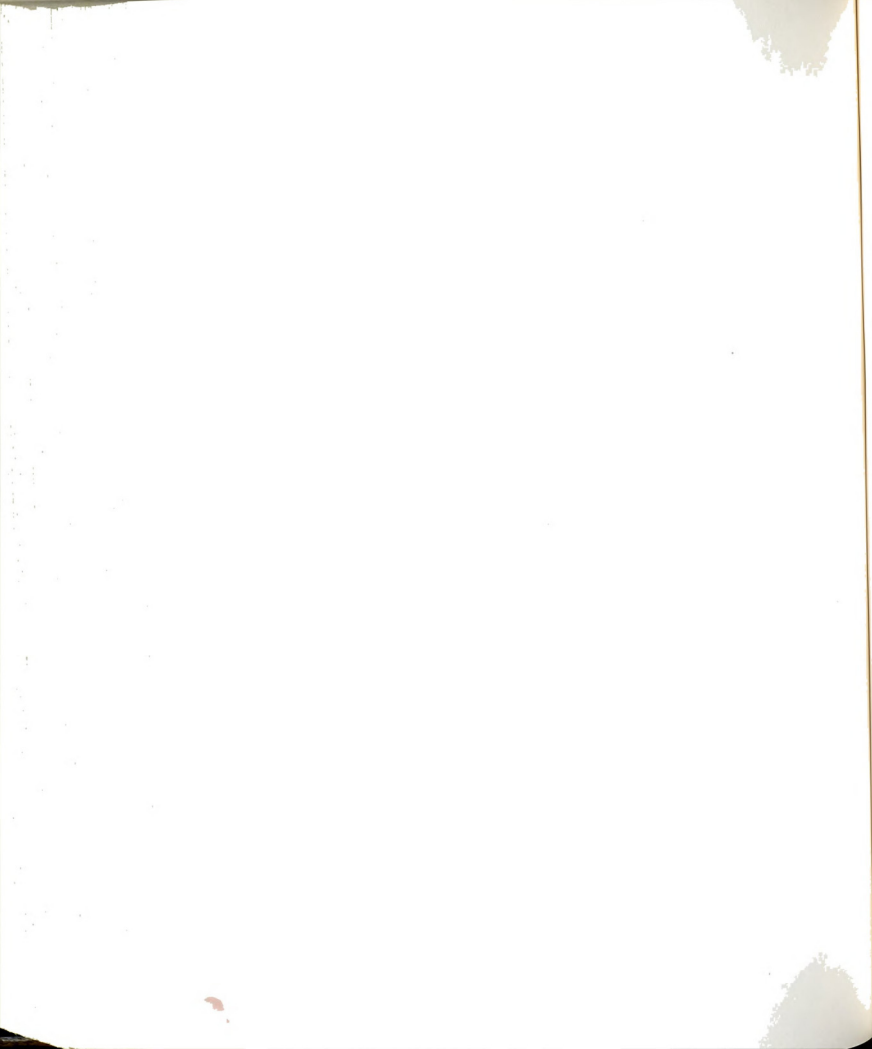


Figure 166. Nondimensional velocity time histories along the centerline of the jet at $Re=2308$ and $w=2.57$ cm.



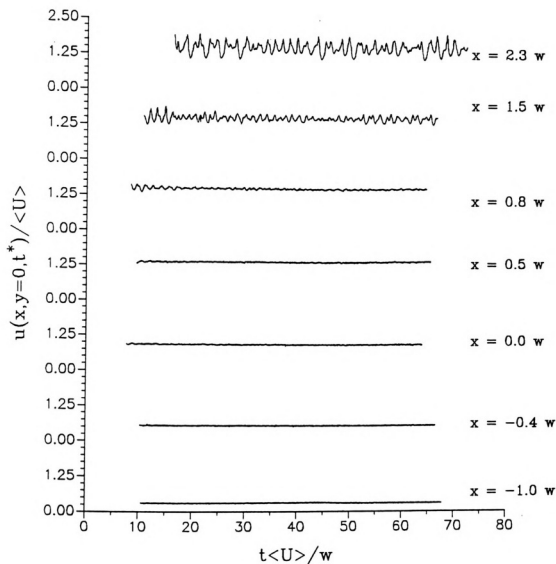
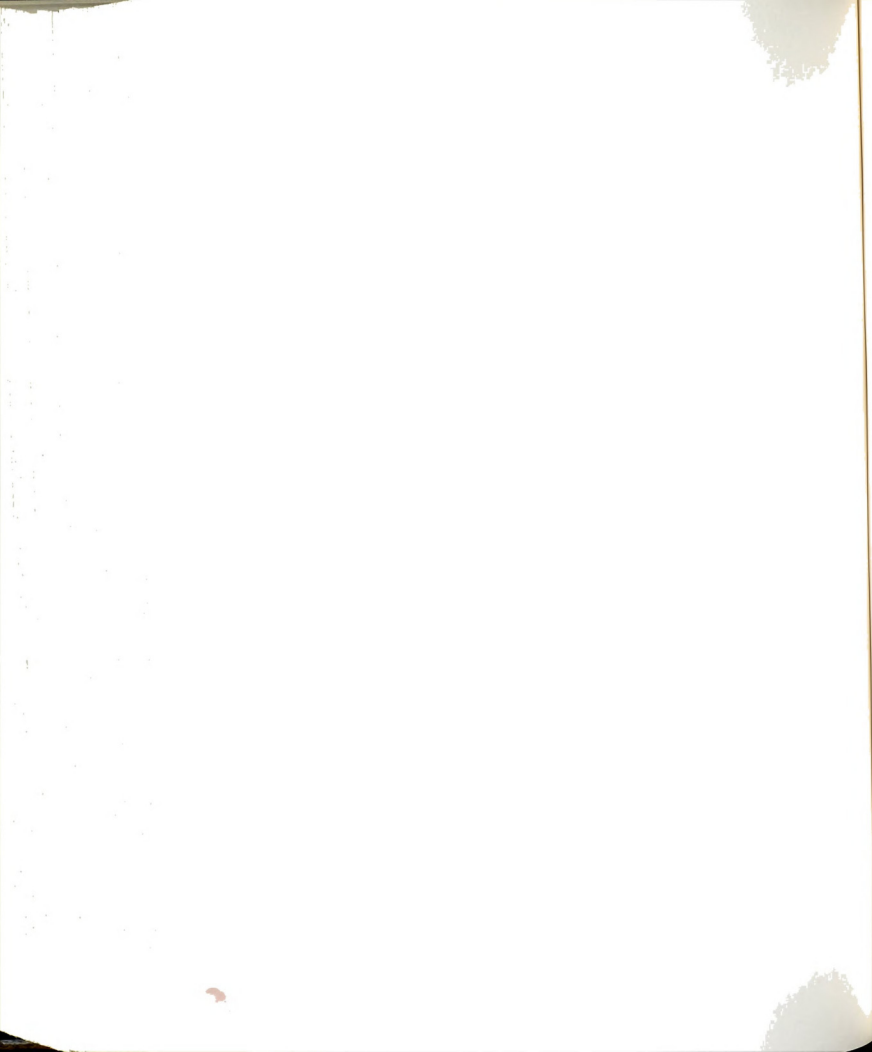


Figure 167. Nondimensional velocity time histories along the centerline of the jet at $Re=2854$ and $w=2.57$ cm.



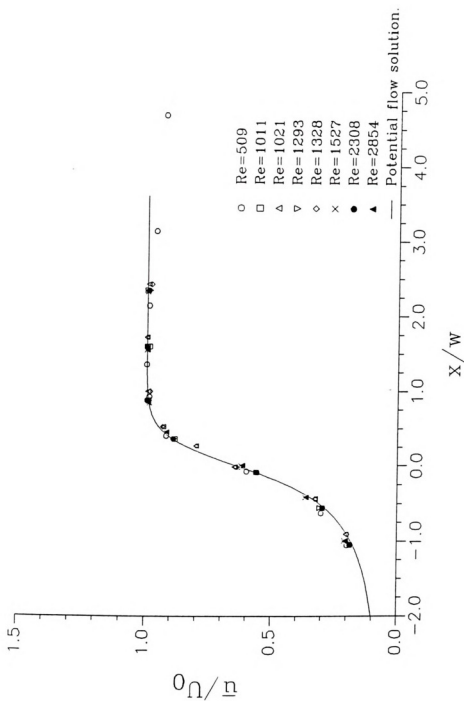
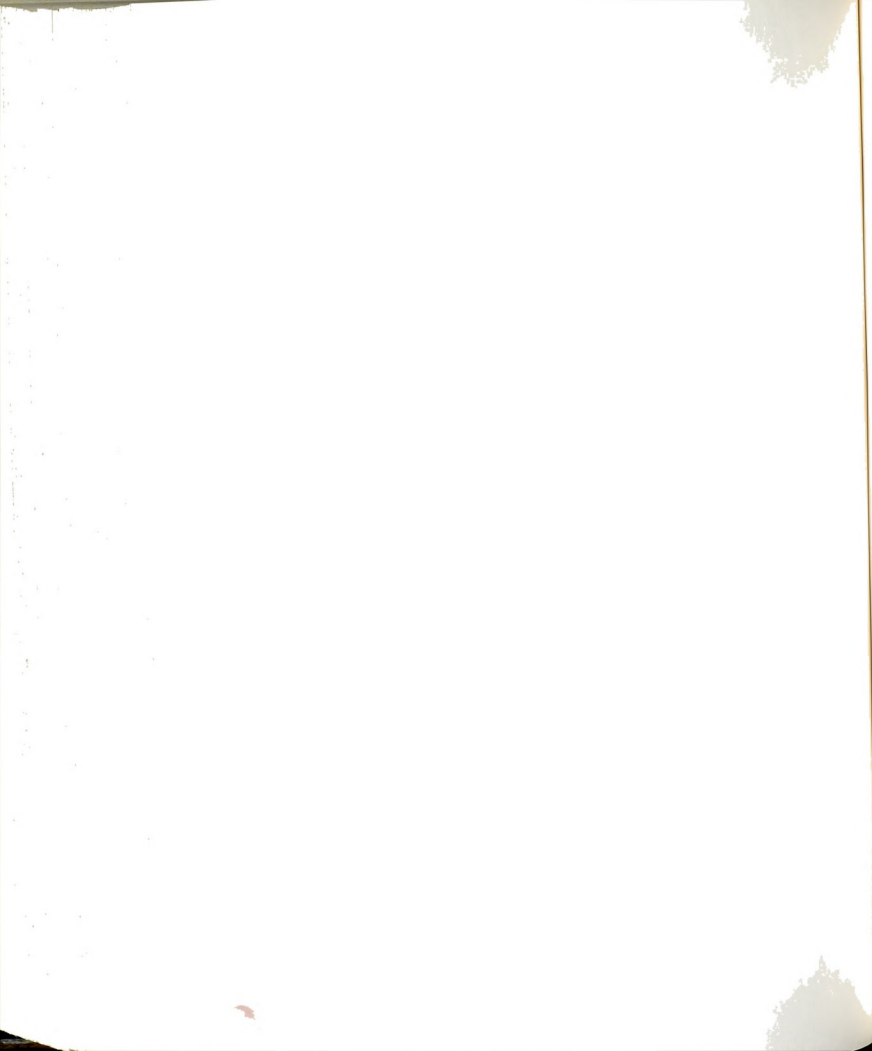


Figure 168. Normalized mean velocity distribution along the centerline of the jet. The solid line represents the inviscid velocity distribution.



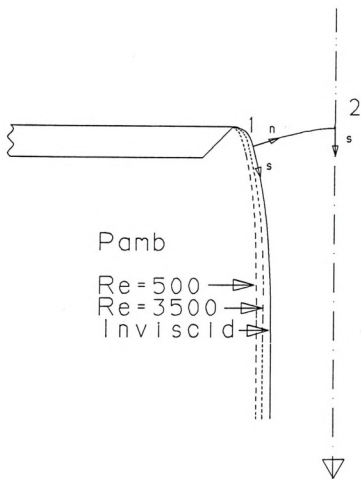
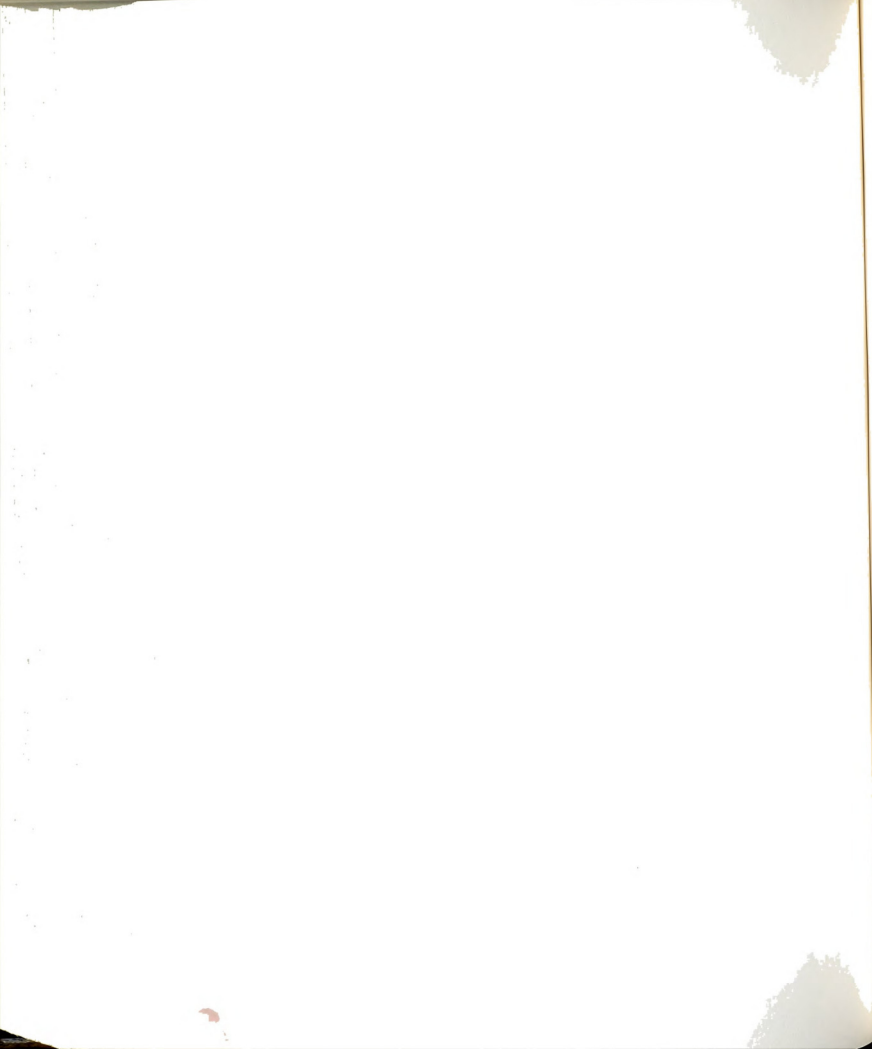


Figure 169. Schematic representation of the influence of Re on the trajectory of the separating streamline. The curve 1-2 represents the path of integration normal to the streamlines.



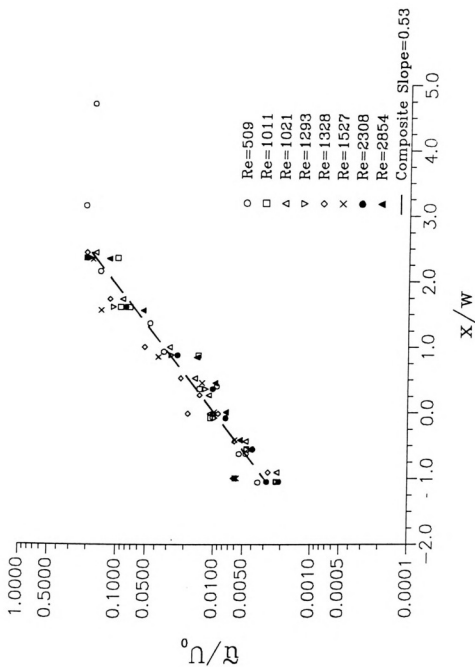
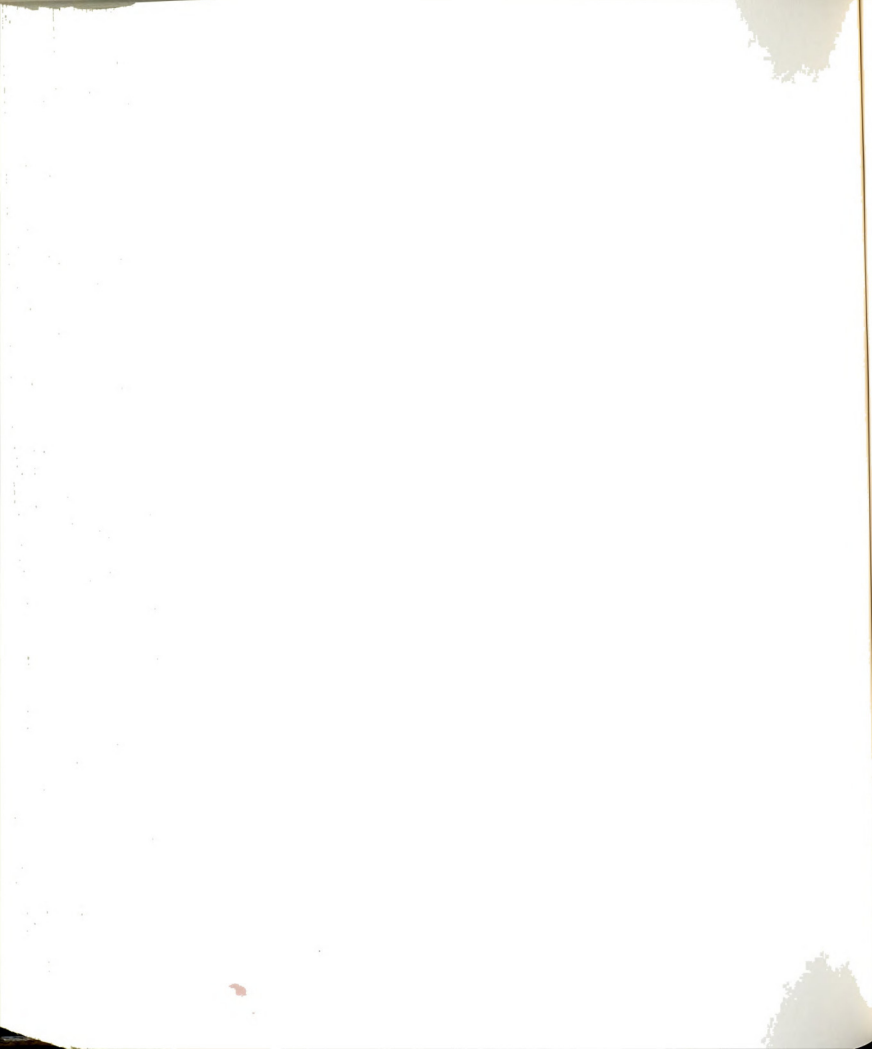


Figure 170. Distribution of the intensity of streamwise velocity fluctuations along the centerline of the jet on a logarithmic plot.



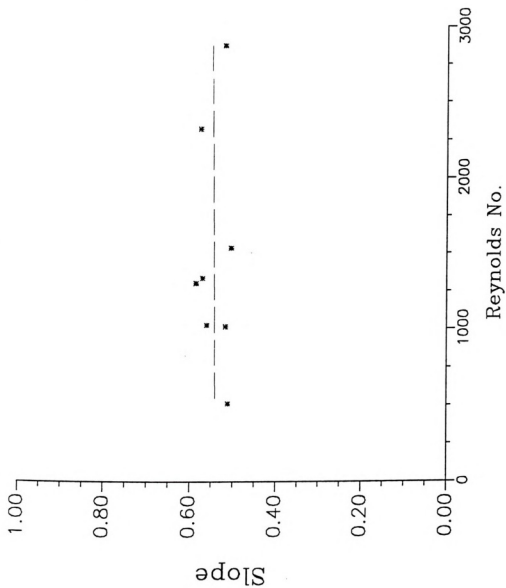
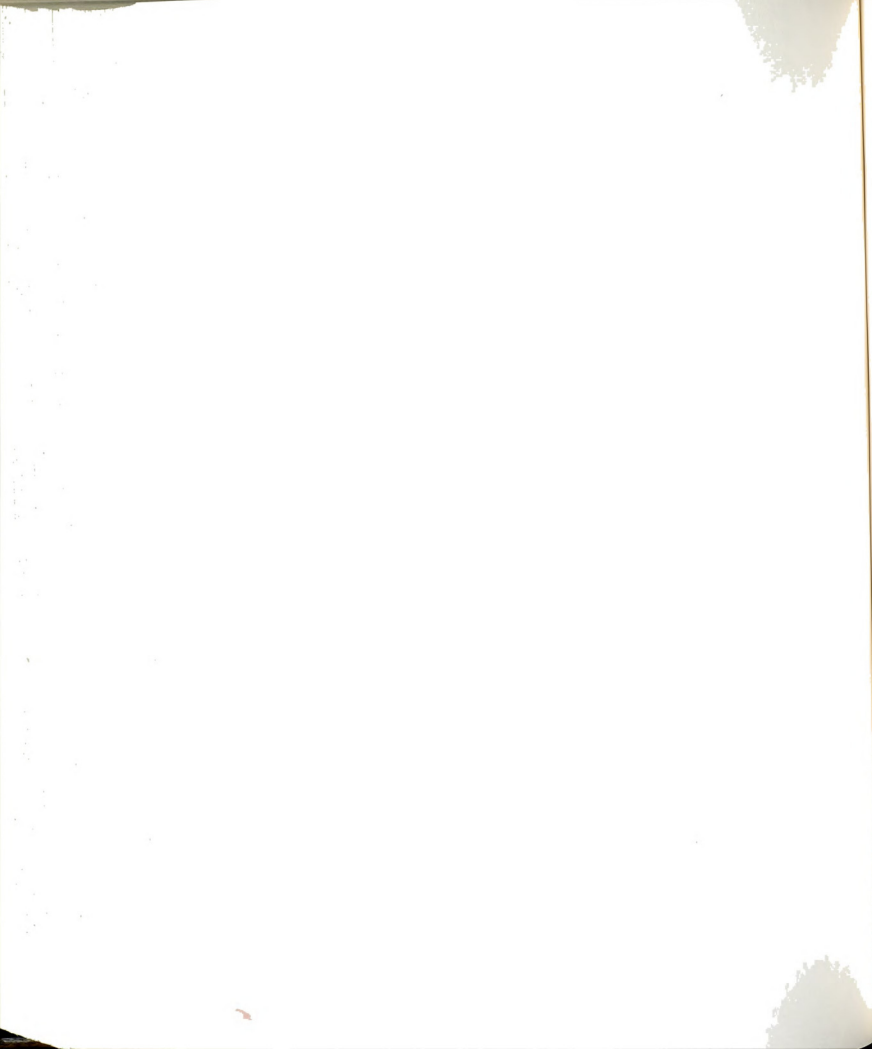


Figure 171. Dependence of the slope of streamwise distribution of $\log(\bar{u}(x,y=0)/U_0)$ on Reynolds number. Figure 170 presents the distribution at each value of Re .



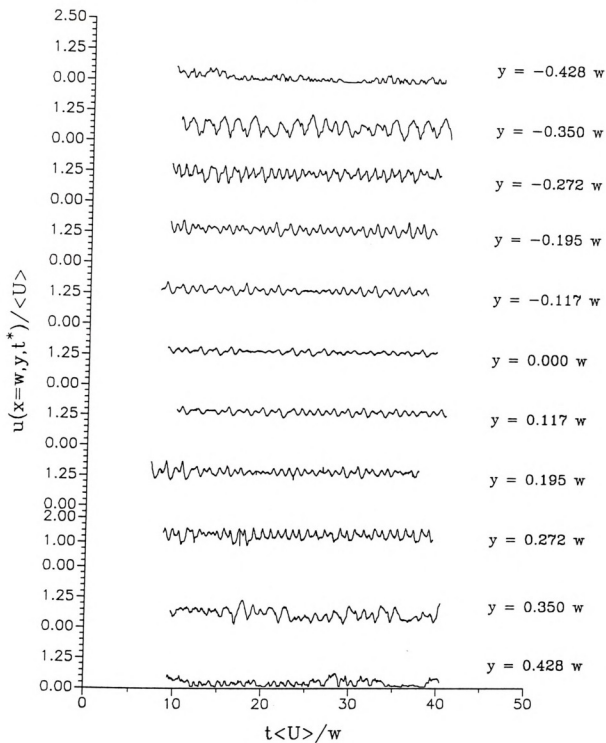
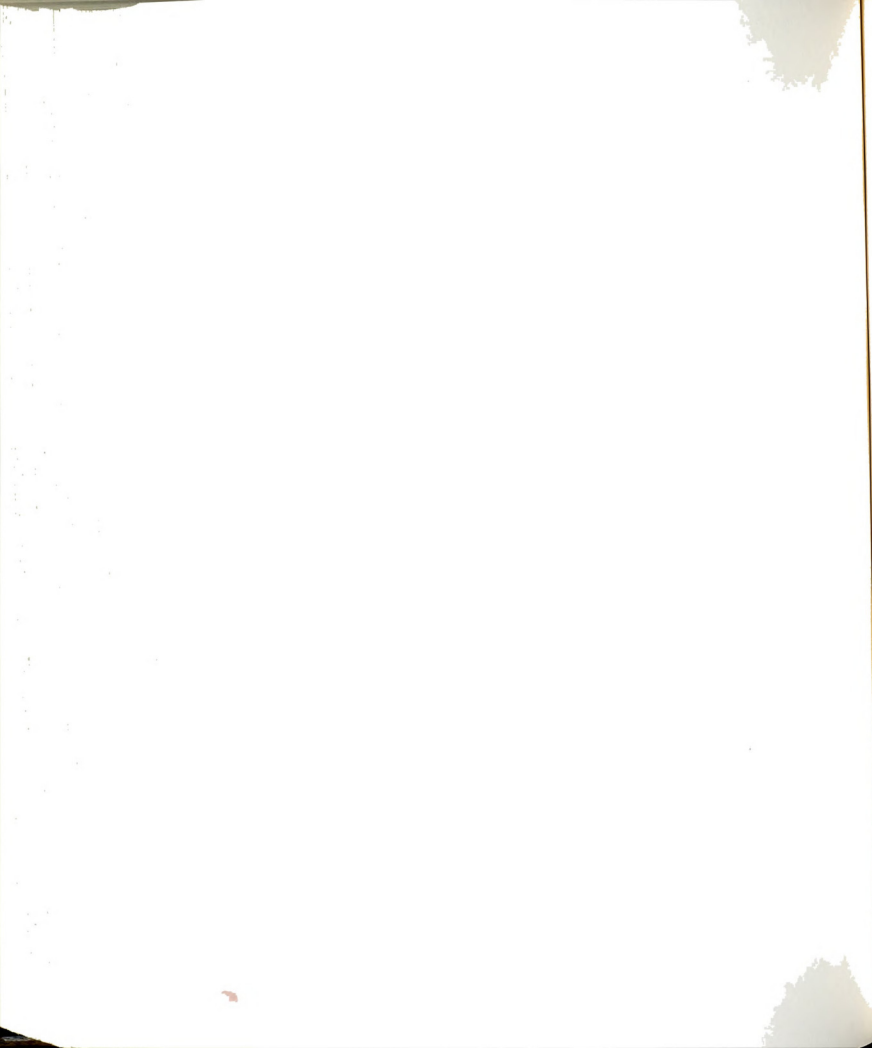


Figure 172. Nondimensional velocity time histories across the jet at $x/w=1$ and $Re=1600$.



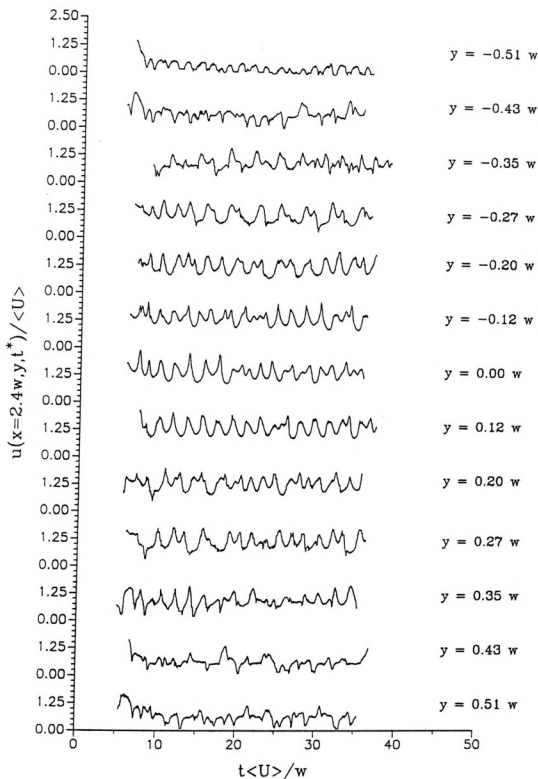
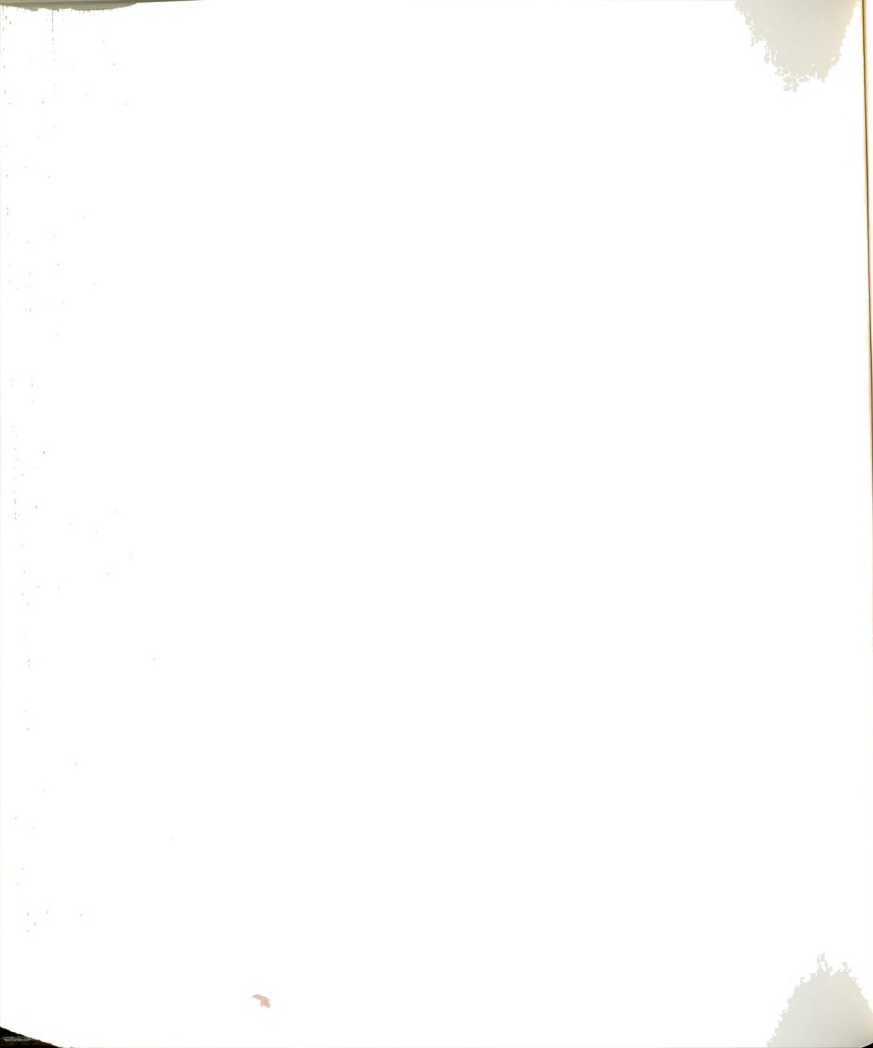


Figure 173. Nondimensional velocity time histories across the jet at $x/w=2.4$ and $Re=1600$.



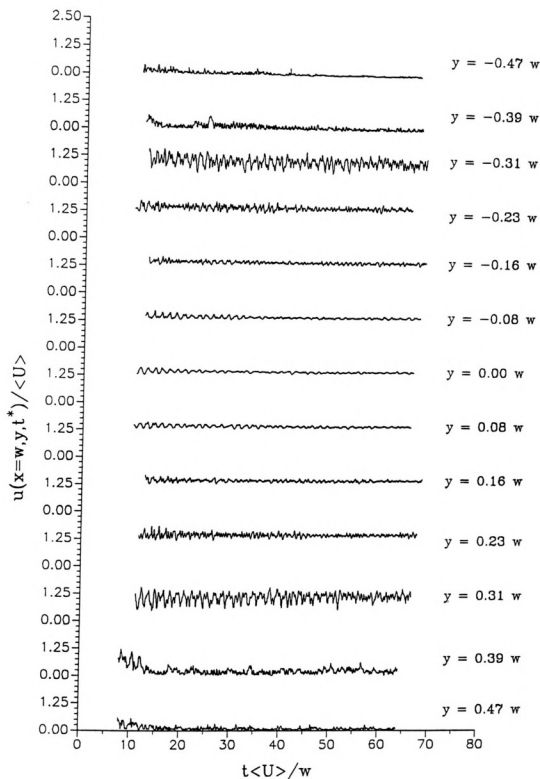


Figure 174. Nondimensional velocity time histories across the jet at $x/w=1$ and $Re=3000$.



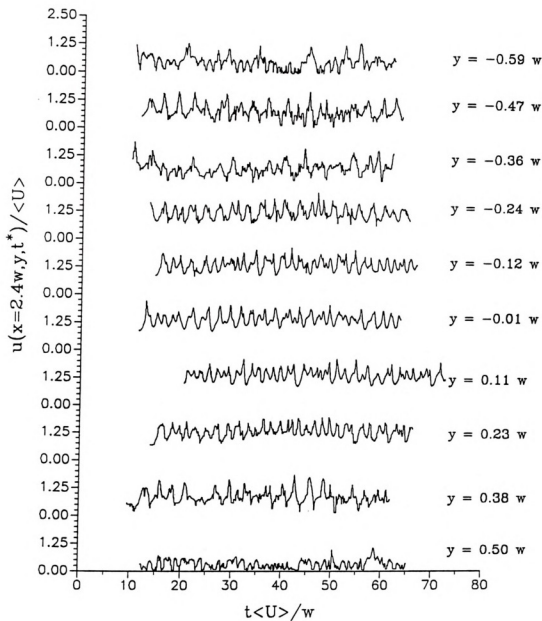
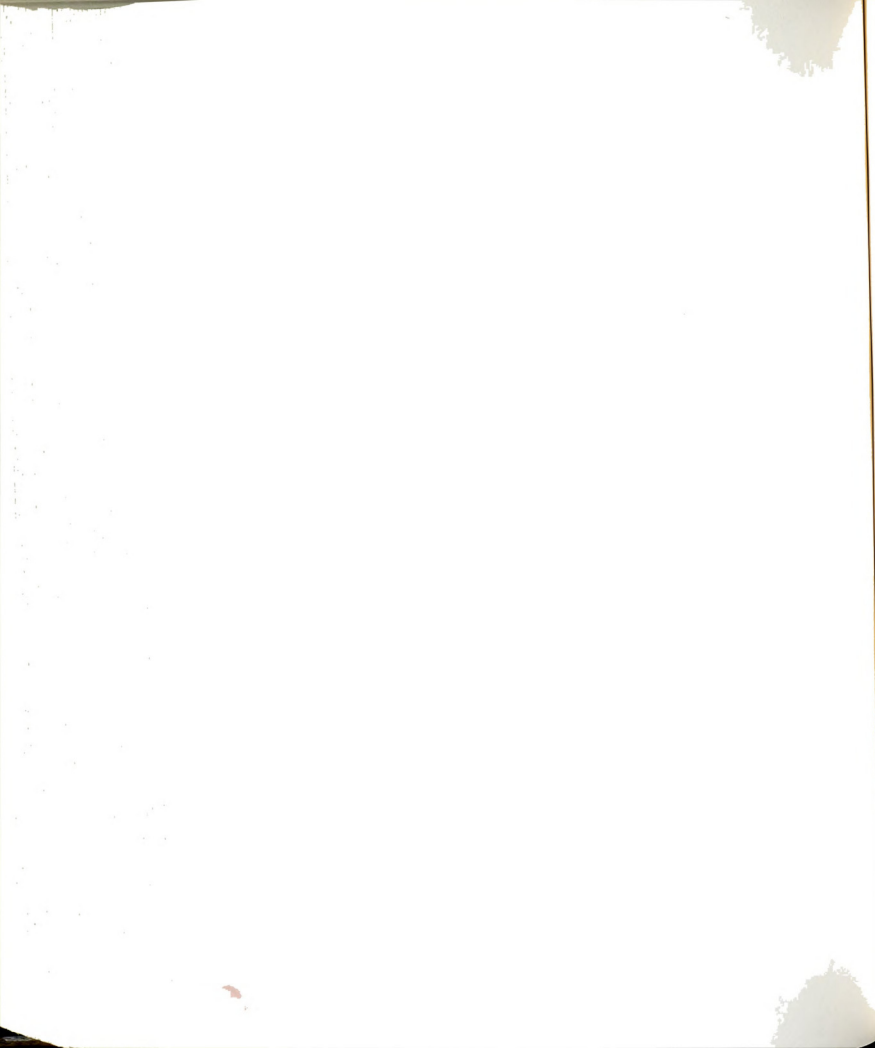


Figure 175. Nondimensional velocity time histories across the jet at $x/w=2.4$ and $Re=3000$.



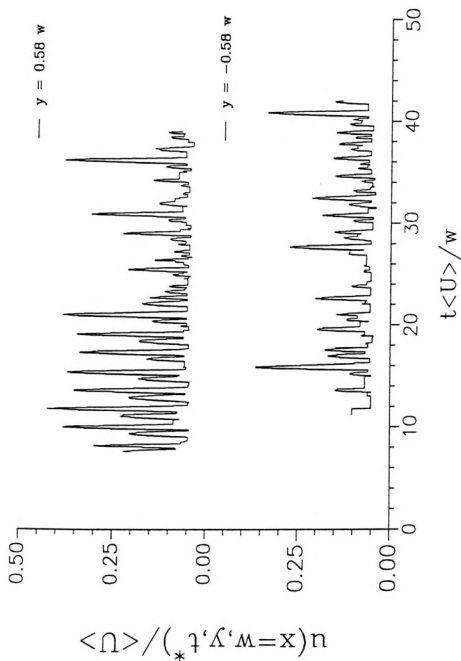
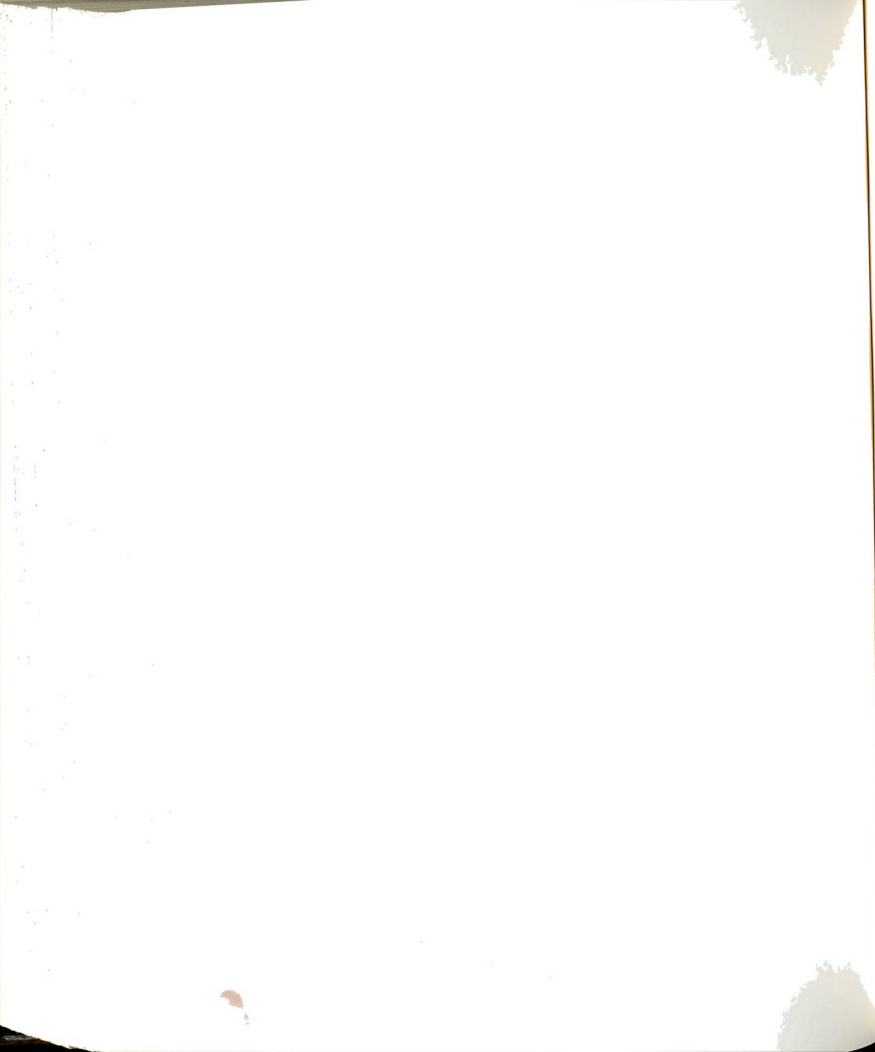


Figure 176. Samples of velocity time histories at $Re=1600$ and from two locations: $(x/w, y/w) = (1, \pm 0.58)$, at which flow reversals were inferred to have taken place.



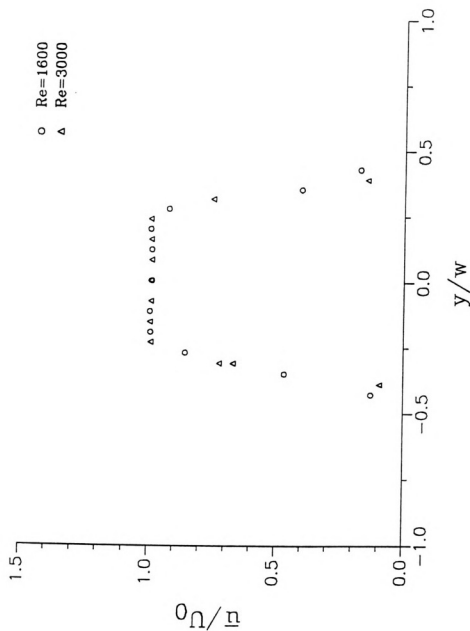
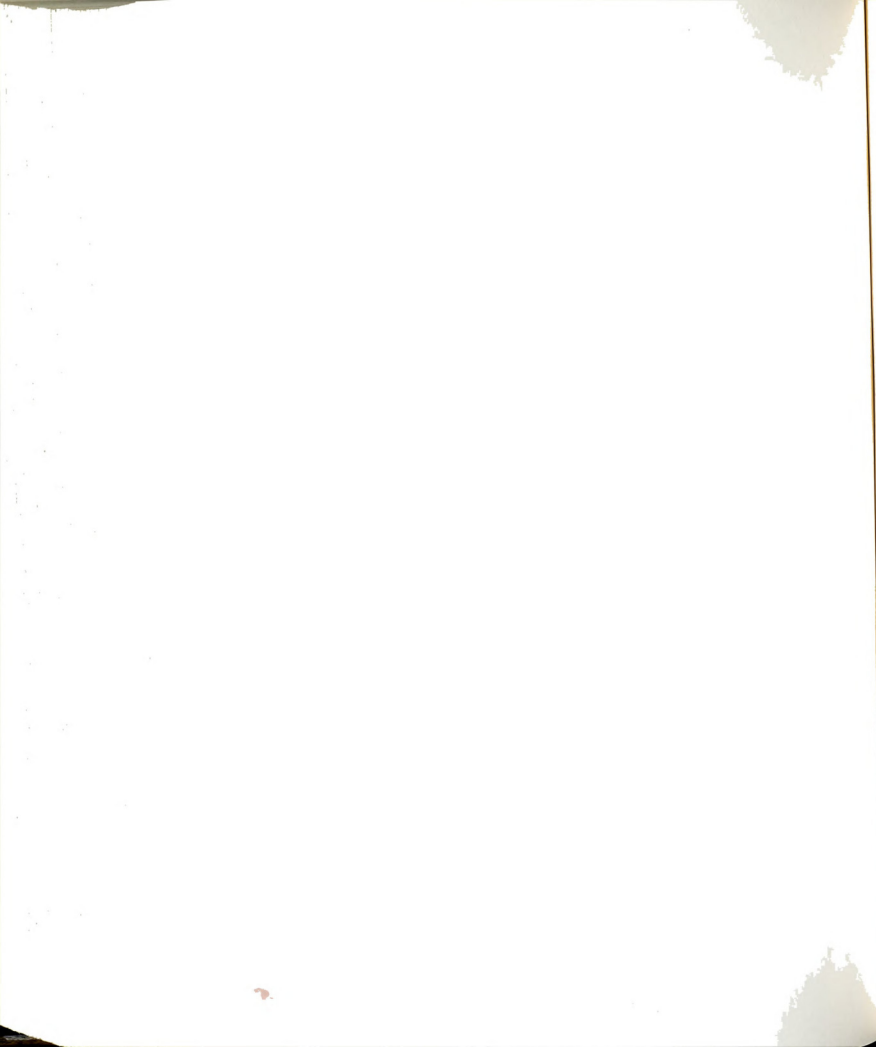


Figure 177. Mean velocity distribution across the jet at $x/w=1$ and two values of Re . The data from the regions where velocity reversals took place are not included here.



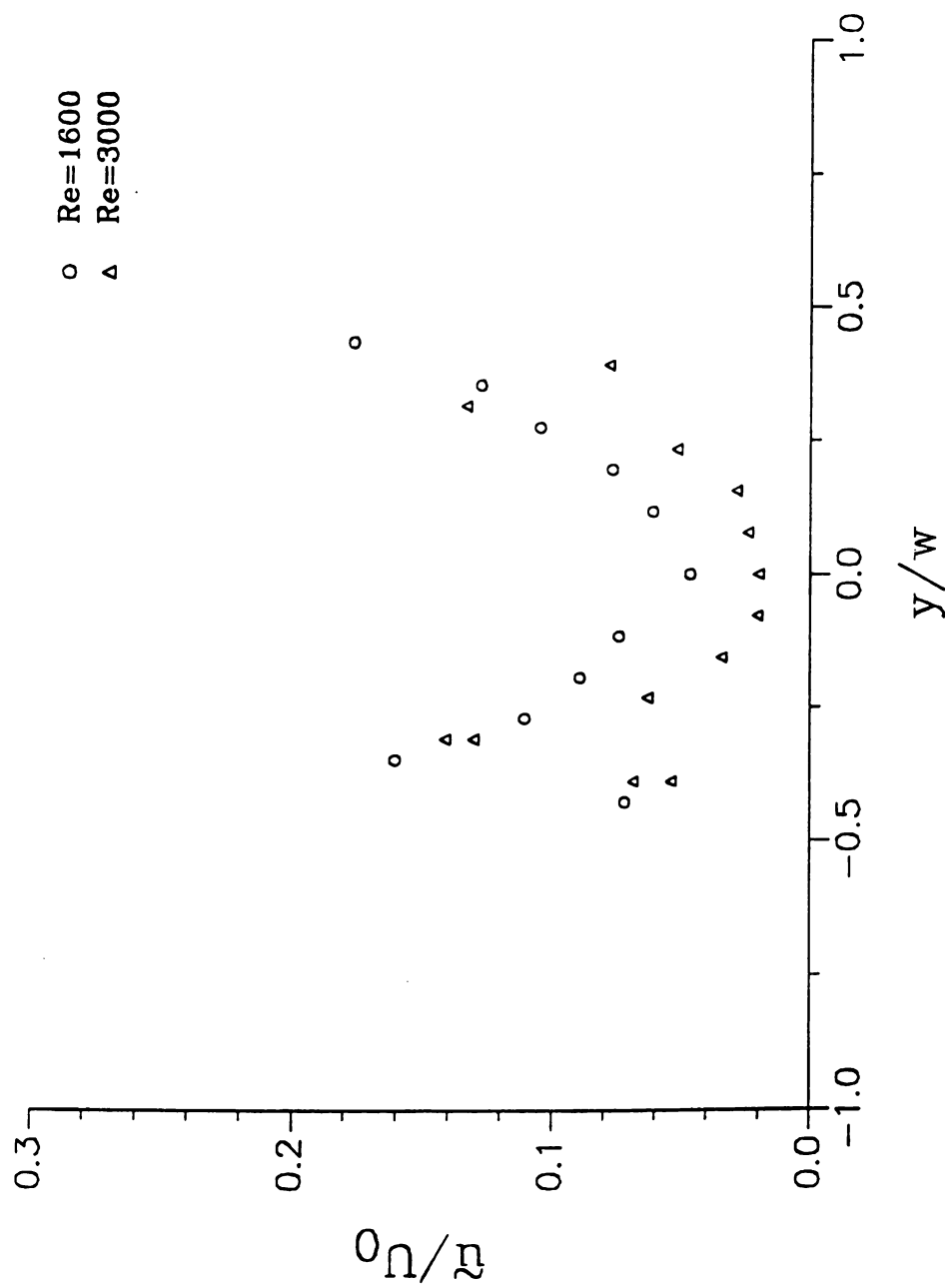
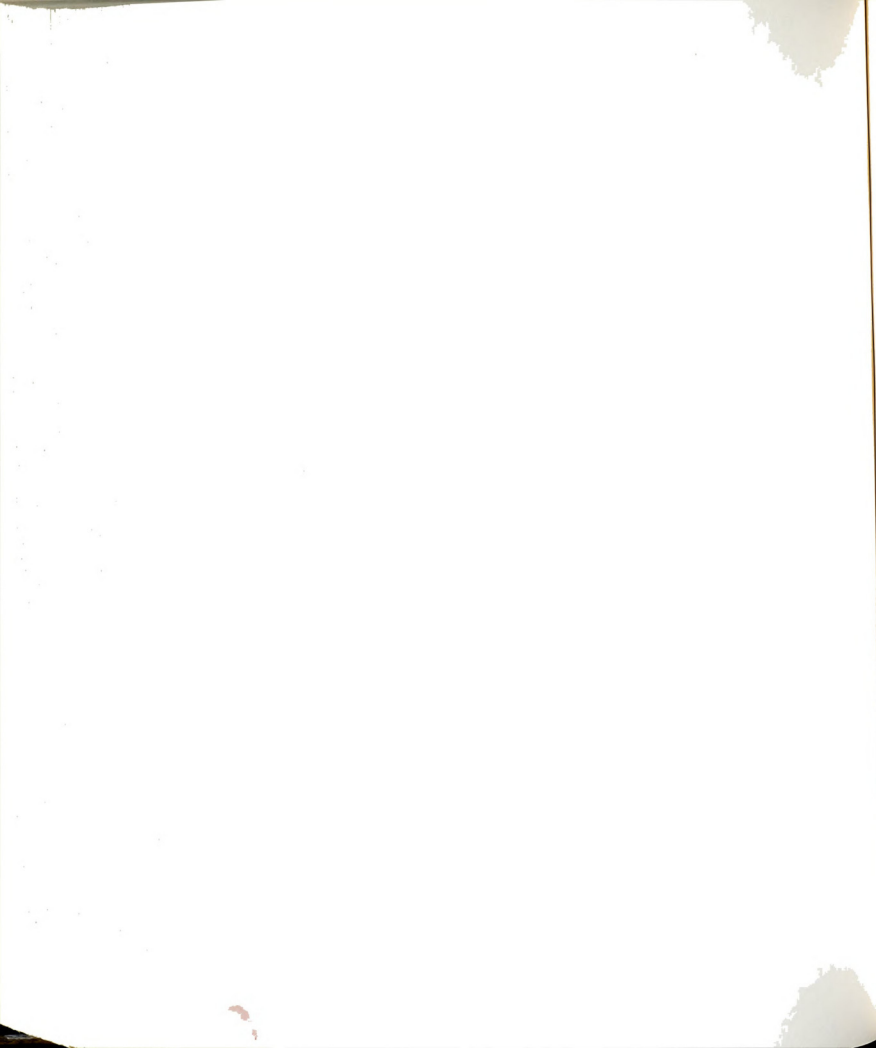


Figure 178. Distribution of the intensity of streamwise velocity fluctuations across the jet at $x/w=1$ and two values of Re .



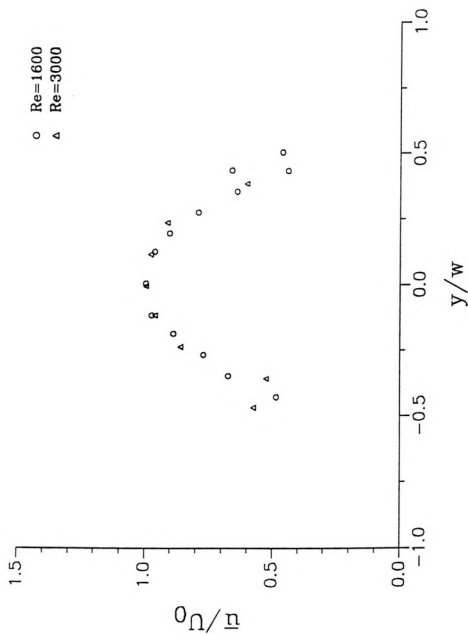
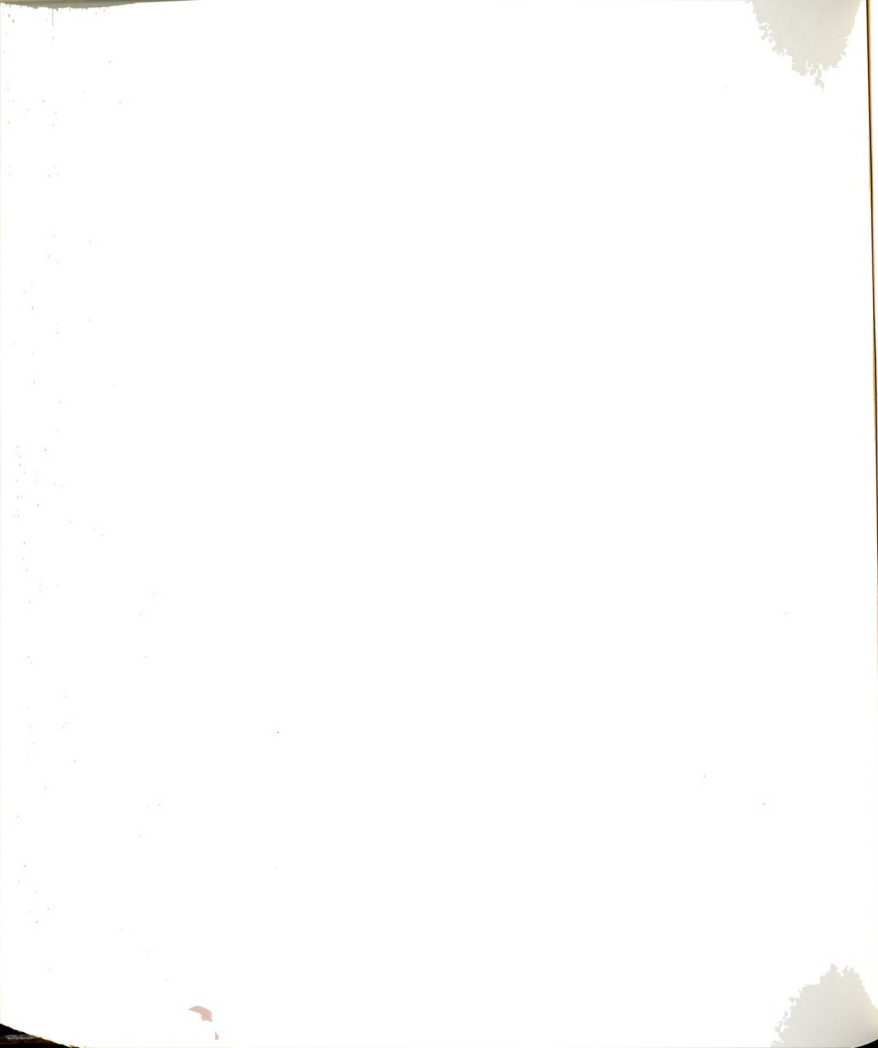


Figure 179. Mean velocity distribution across the jet at $x/w=2.4$ and two values of Re . The data from the regions where velocity reversals took place are not included here.



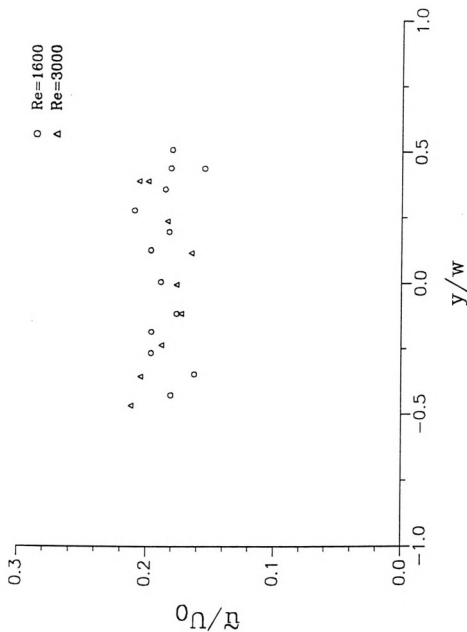
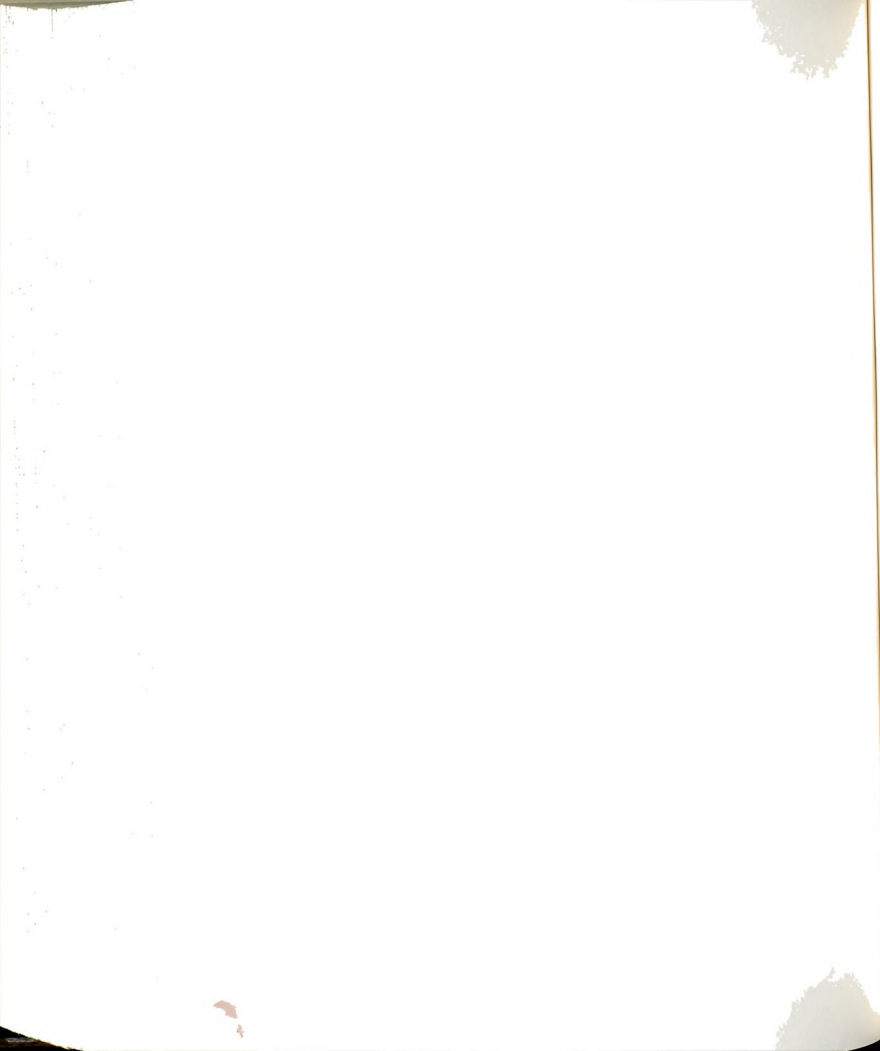


Figure 180. Distribution of the intensity of streamwise velocity fluctuations across the jet at $x/w=2.4$ and two values of Re .



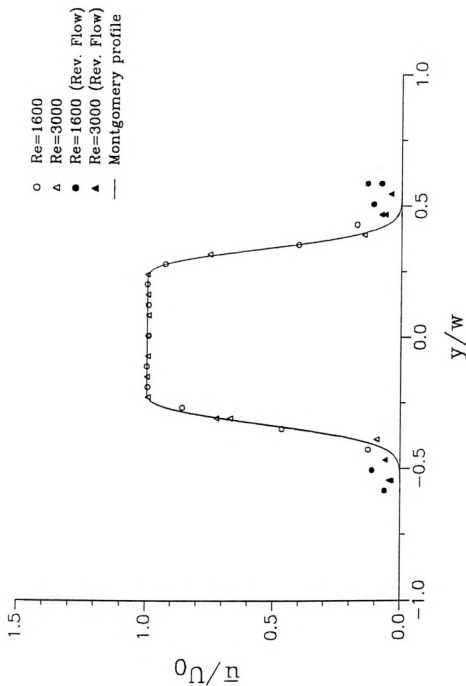
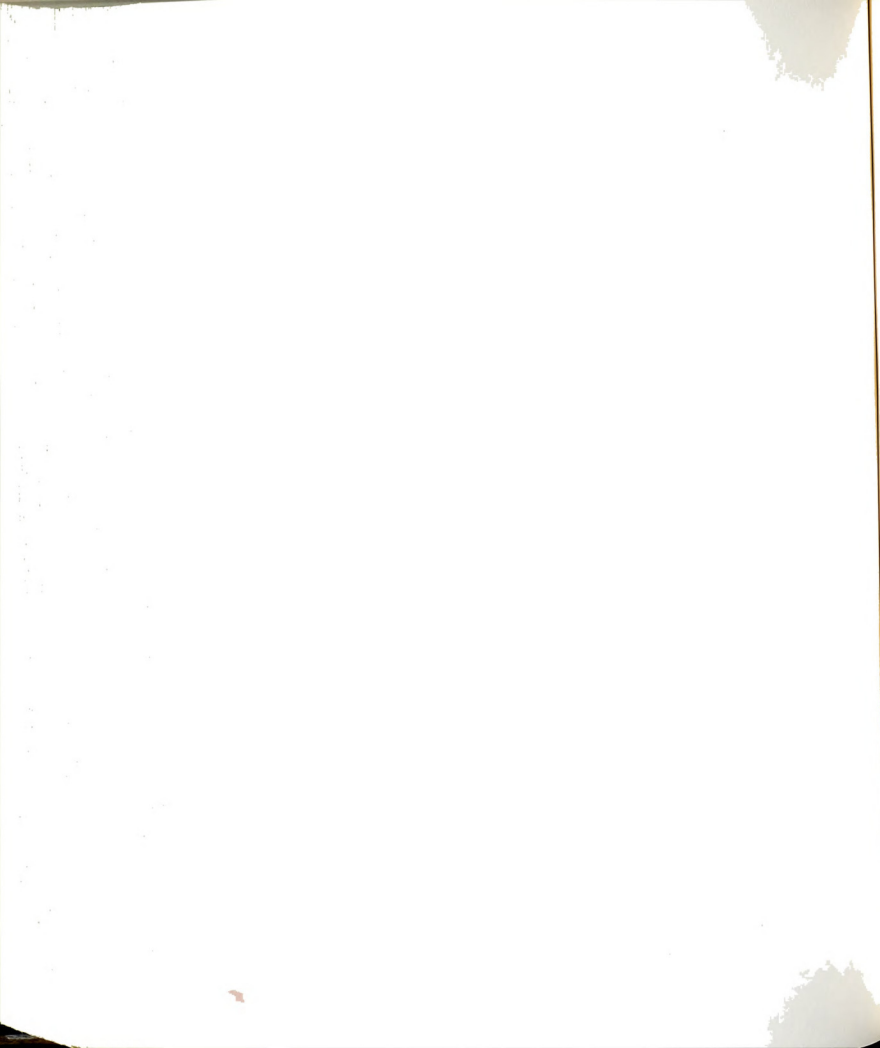


Figure 181. Normalized mean velocity profile at $x/w=1$. The solid line represents the Montgomery profile fitted to the measured data. The data in closed symbols were not included in determining the two parameters of the Montgomery profile.



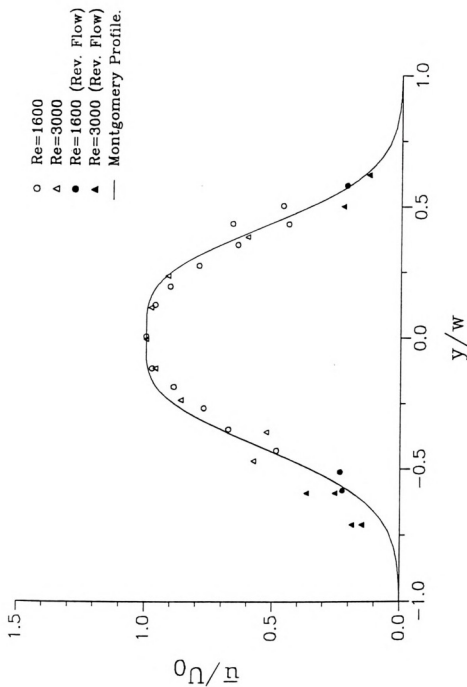
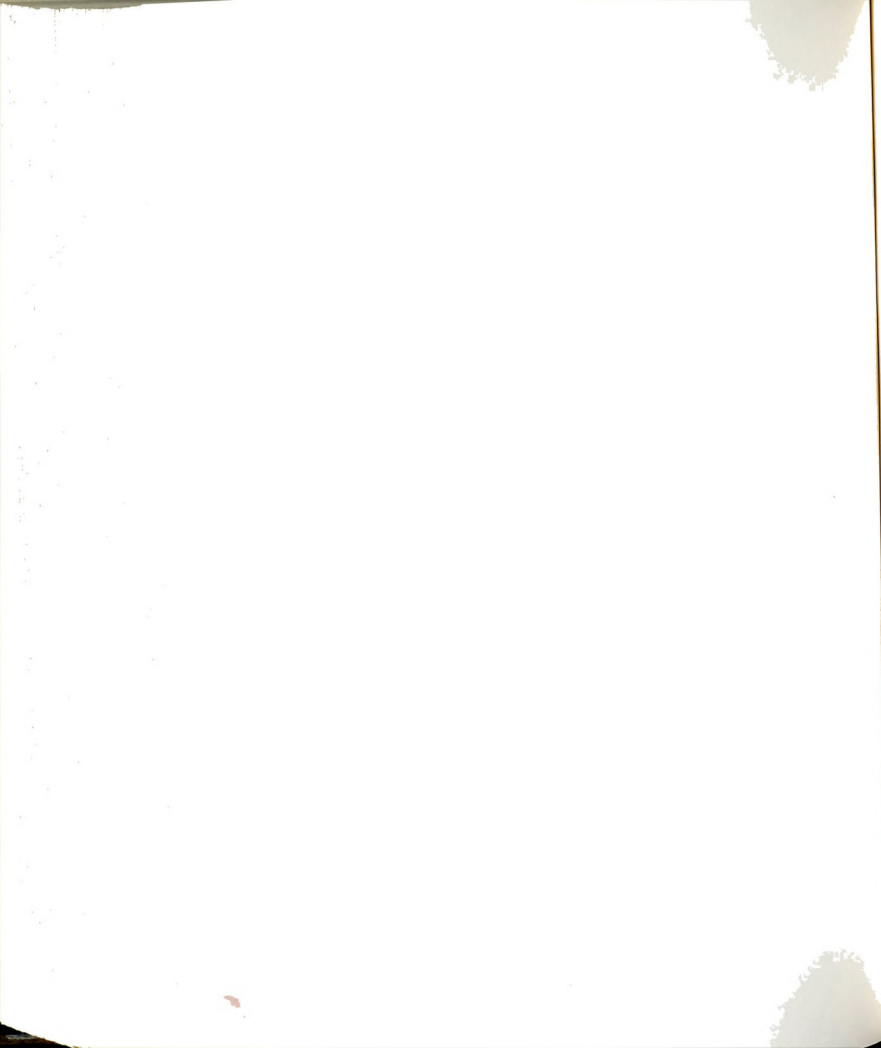


Figure 182. Normalized mean velocity profile at $x/w=2.4$. The solid line represents the Montgomery profile fitted to the measured data. The data in closed symbols were not included in determining the two parameters of the Montgomery profile.



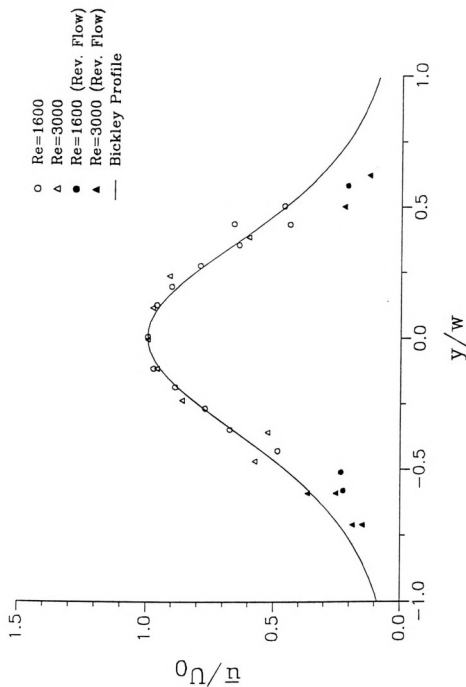
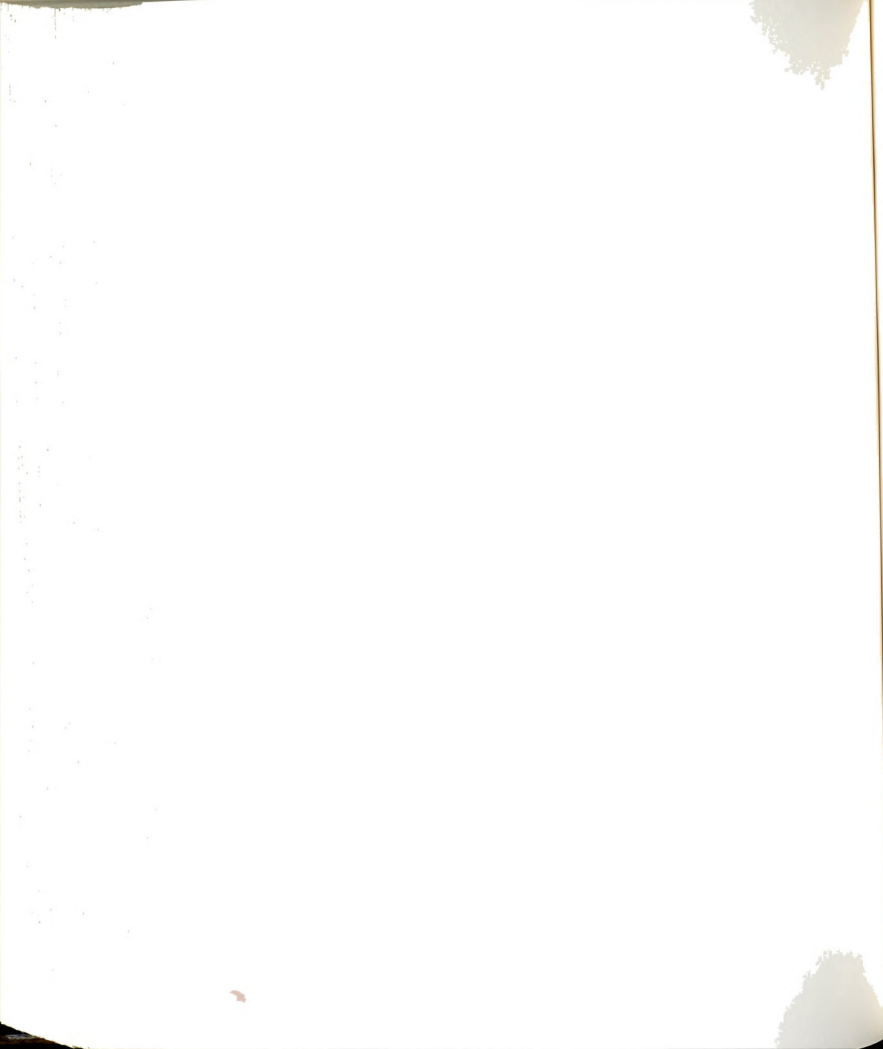


Figure 183. Normalized mean velocity profile at $x/w=2.4$. The solid line represents the Bickley profile fitted to the measured data. The data in closed symbols were not included in determining the parameter.



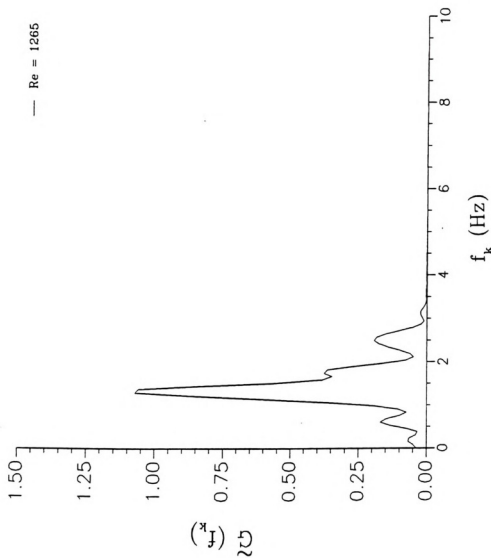
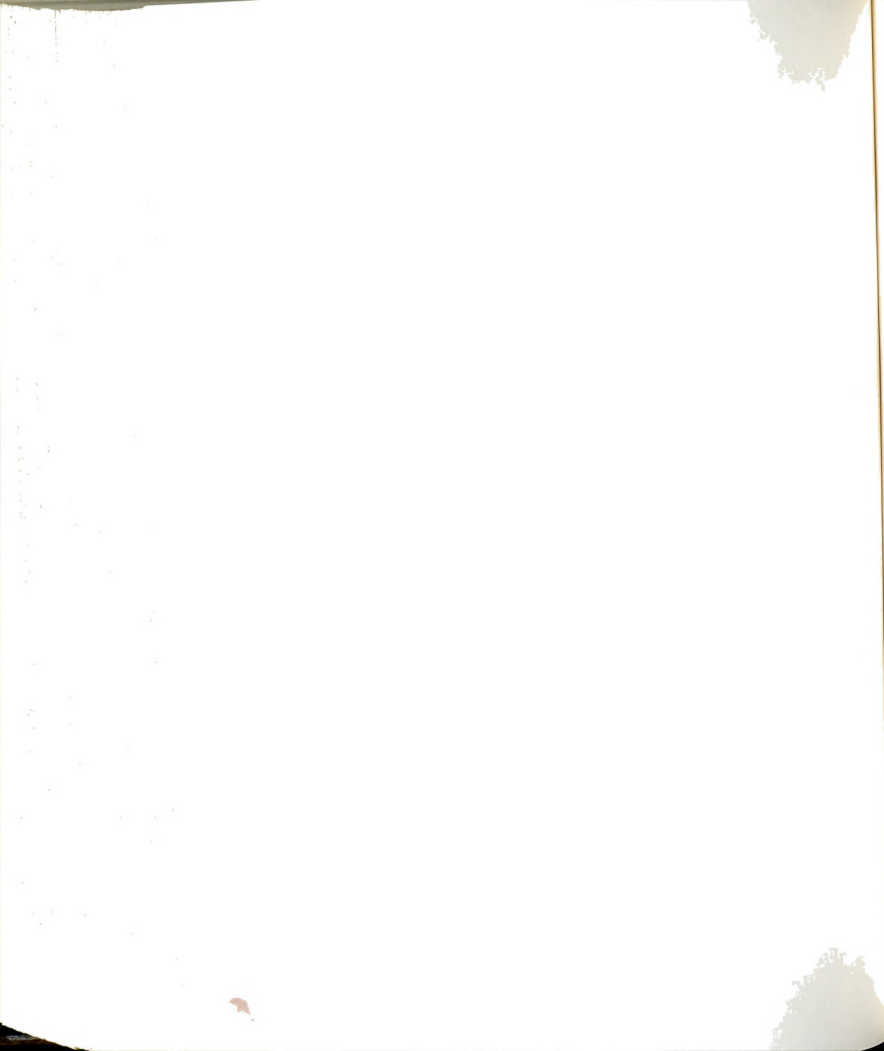


Figure 184. Power spectral density function of streamwise velocity at $(x/w, y/w) = (0.86, 0)$ and $Re \approx 1260$.



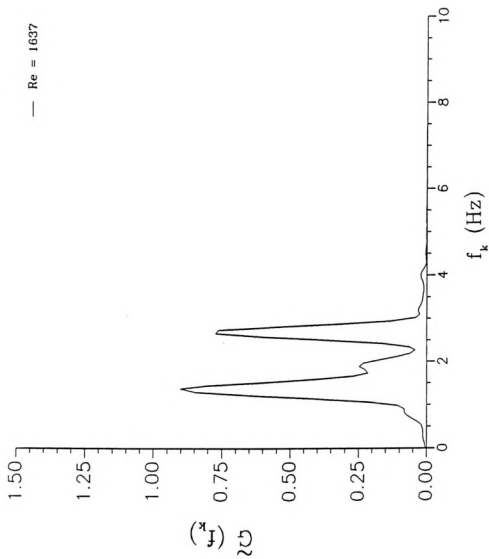
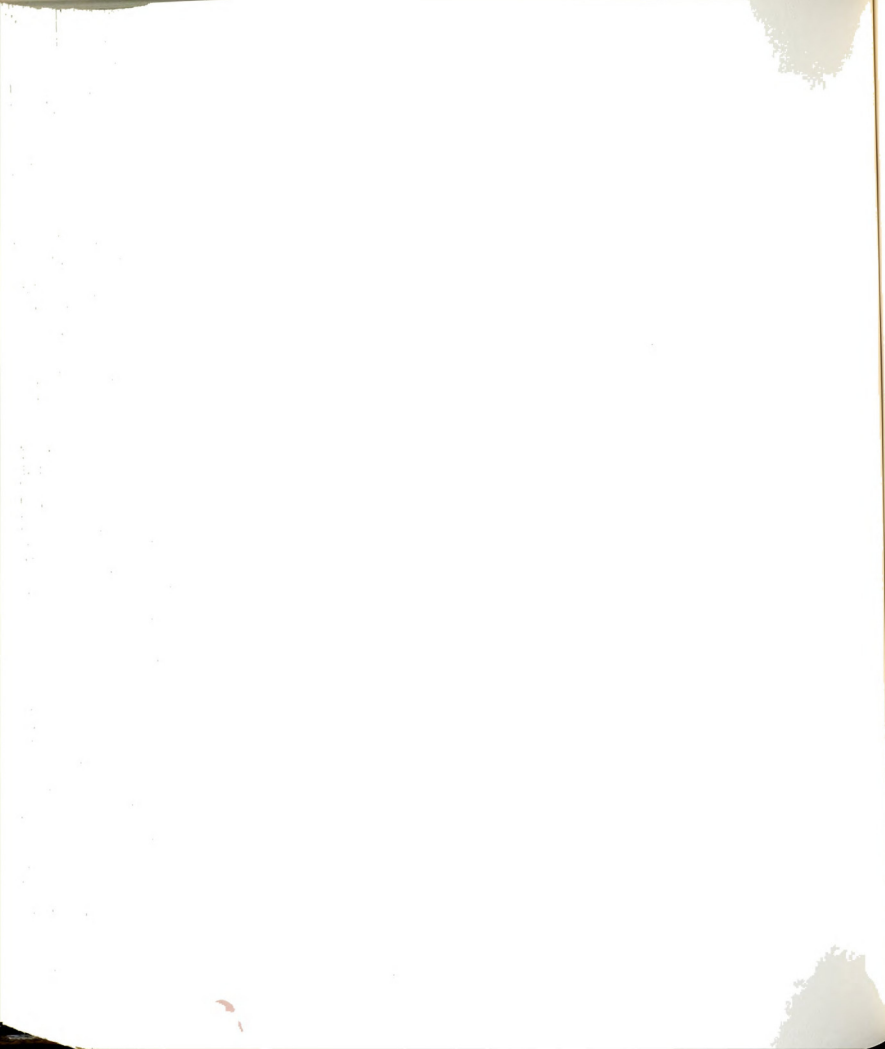


Figure 185. Power spectral density function of streamwise velocity at $(x/w, y/w) = (1, 0)$ and $Re \approx 1640$.



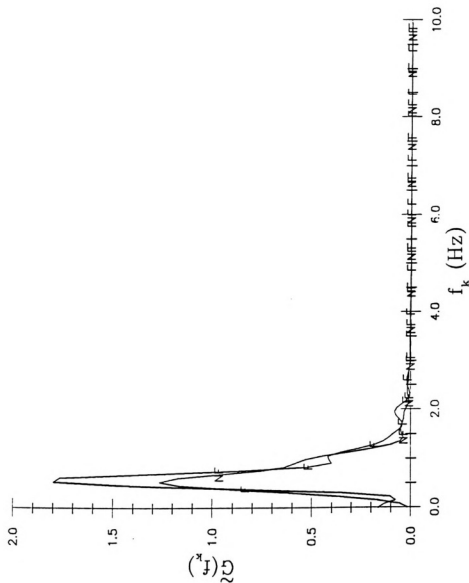
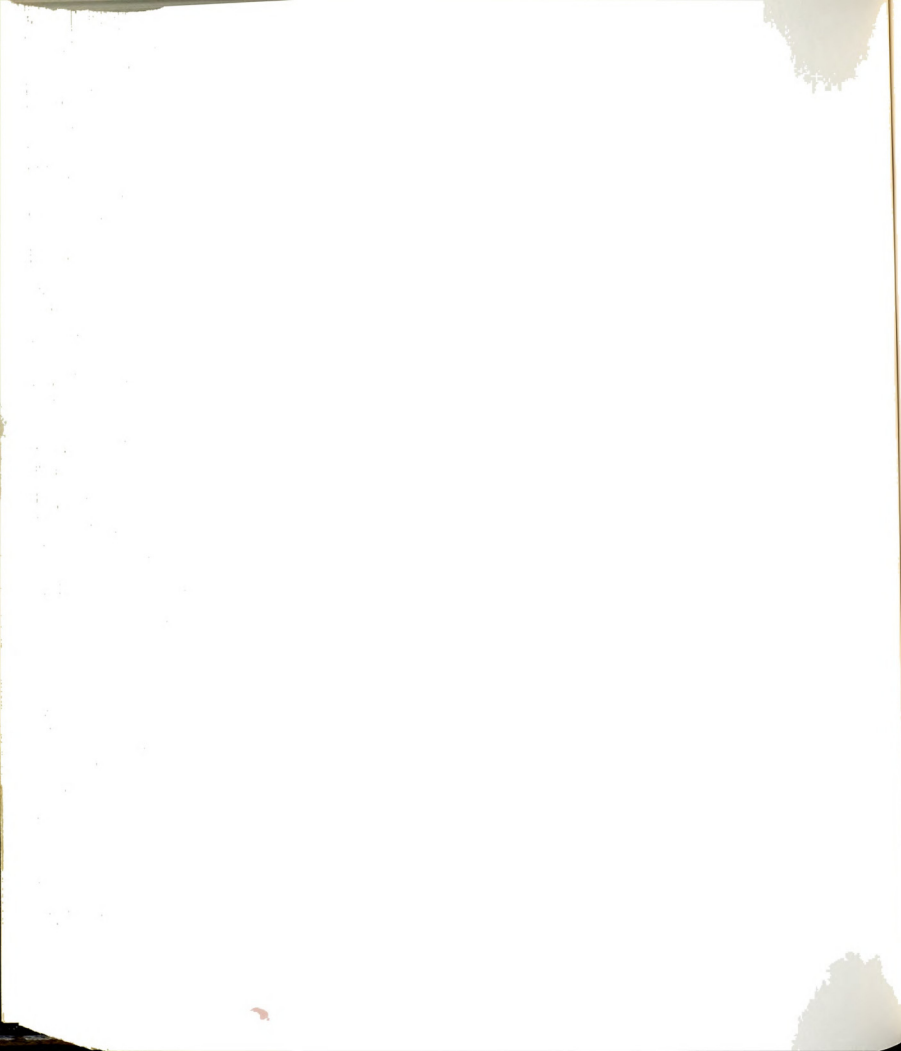


Figure 186. A comparison of the power spectral density function of the streamwise velocity at $Re=960$ and at $(x/w, y/w)=(2.2, 0)$ for two different filling conditions. The curve marked with F represents the case in which the filling device was used and NF indicates the case in which the filling device was not used.



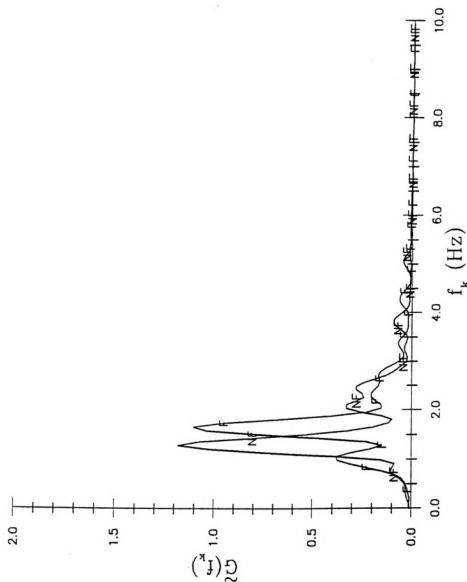
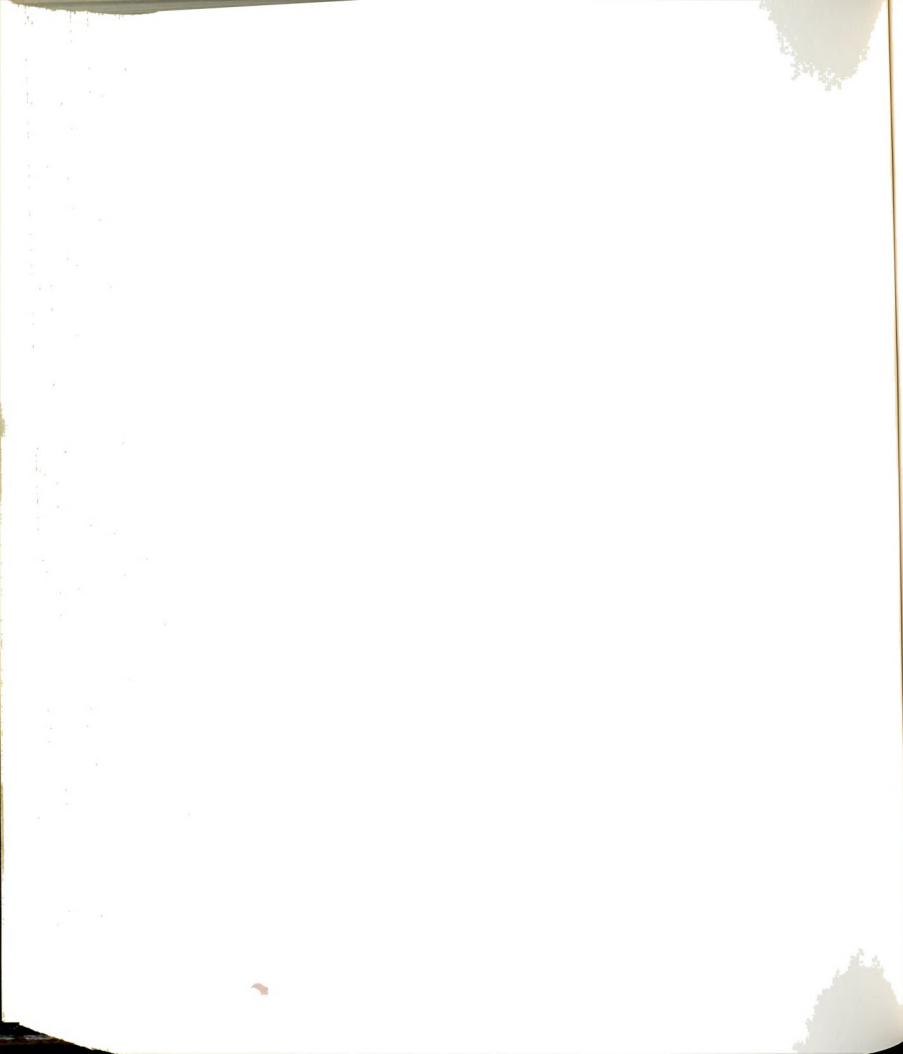


Figure 187. A comparison of the power spectral density function of the streamwise velocity at $Re=2000$ and at $(x/w, y/w)=(2.2, 0)$ for two different filling conditions. See Figure 186 for details.



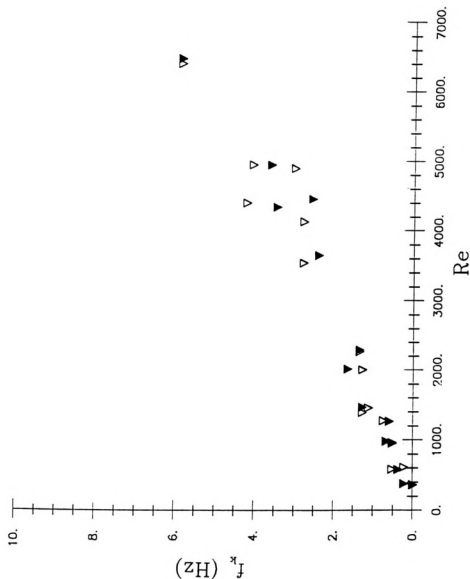
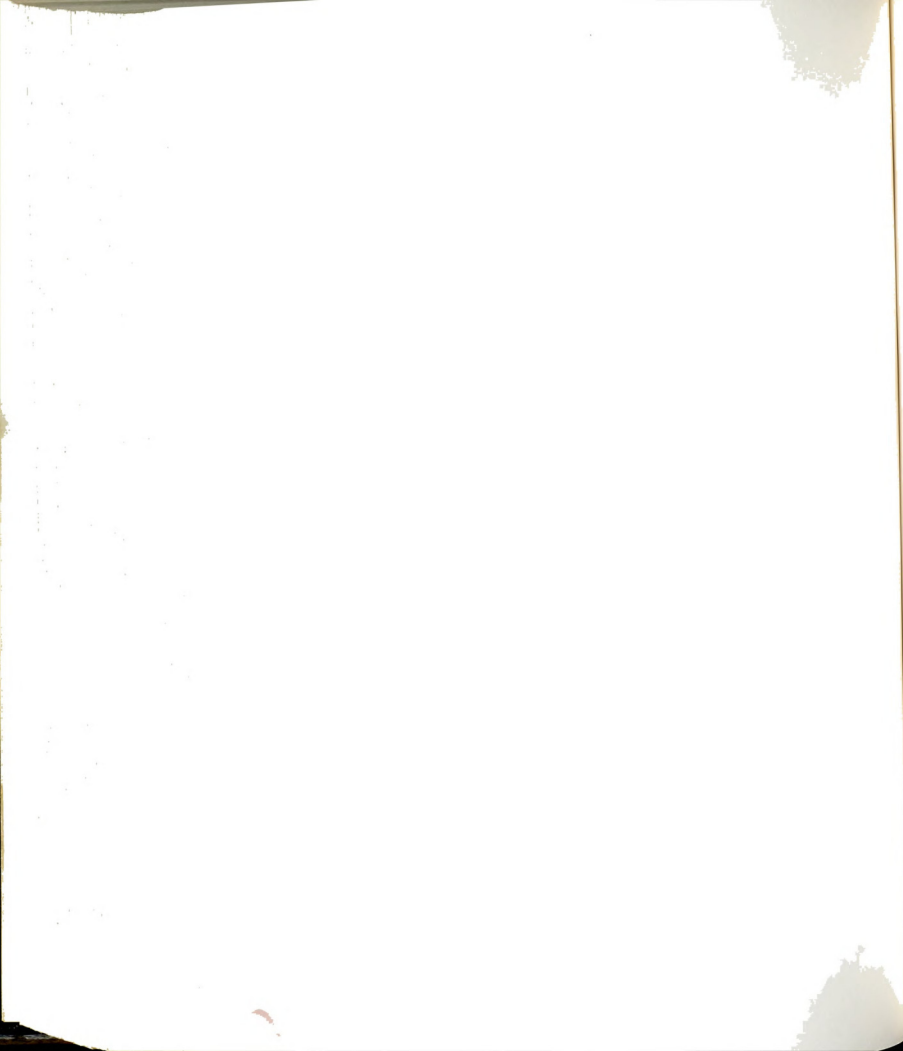


Figure 188. A comparison of the Re dependence of the frequency of dominant fluctuations in $u(t)$ for two different filling conditions. The closed symbols represent the case in which the filling device was used and the open symbols in which the filling device was not used.



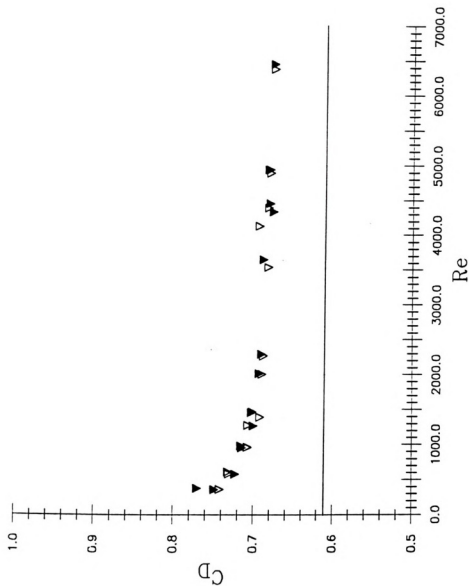
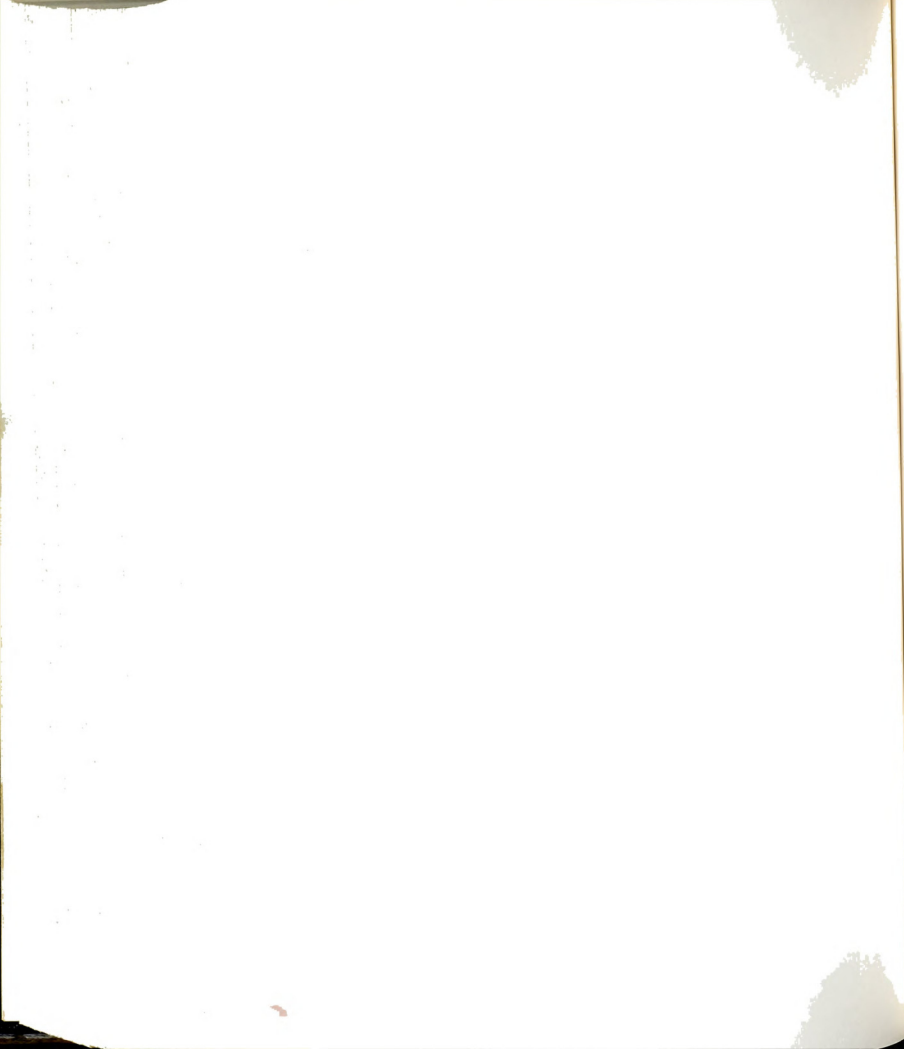


Figure 189. A comparison of the Re dependence of C_D for two different filling conditions. See Figure 188 for details.



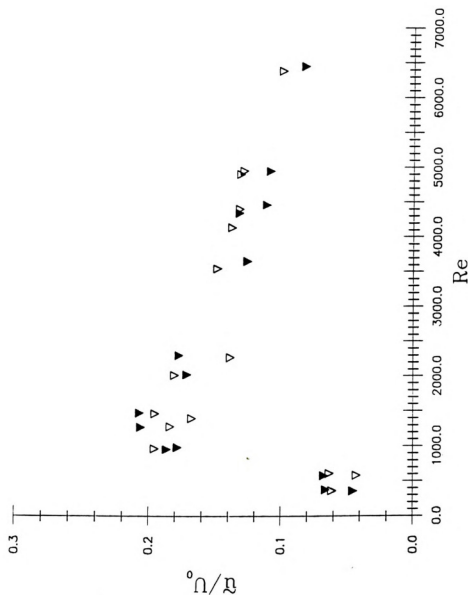
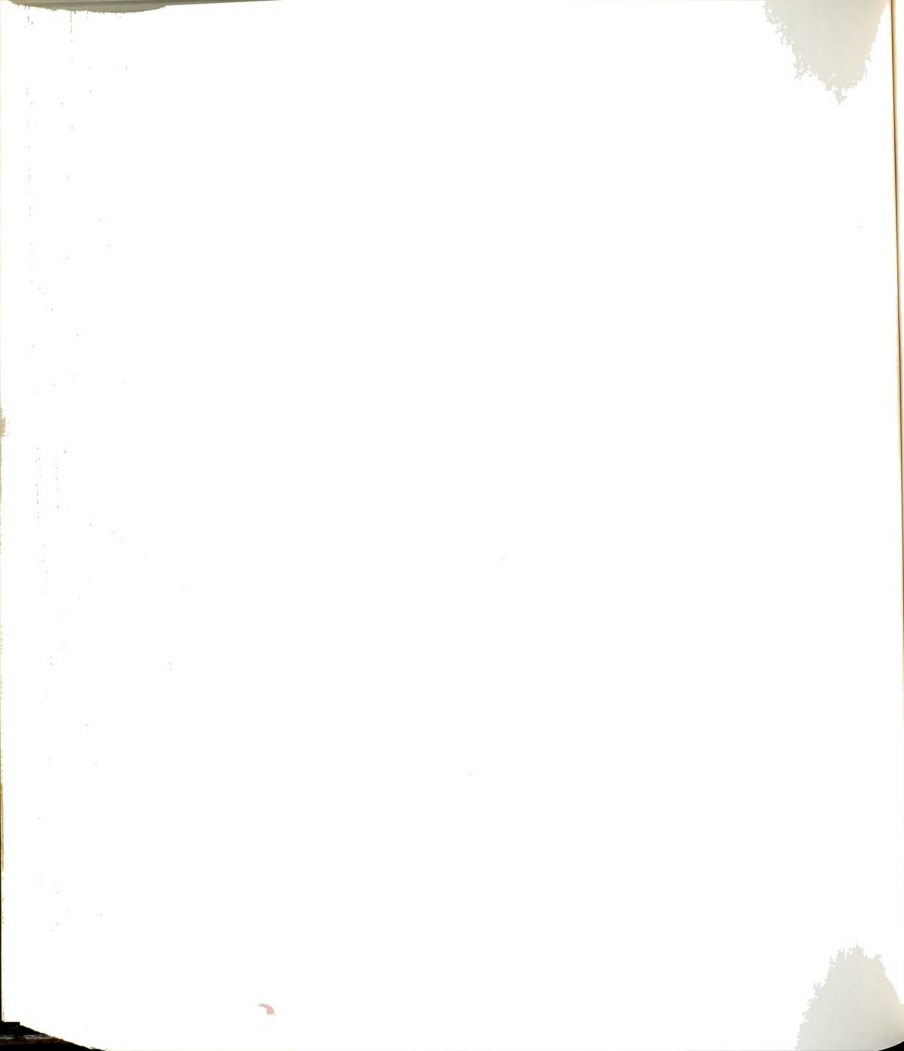


Figure 190. A comparison of the Re dependence of intensity of $u(t)$ for two different filling conditions. See Figure 188 for details.



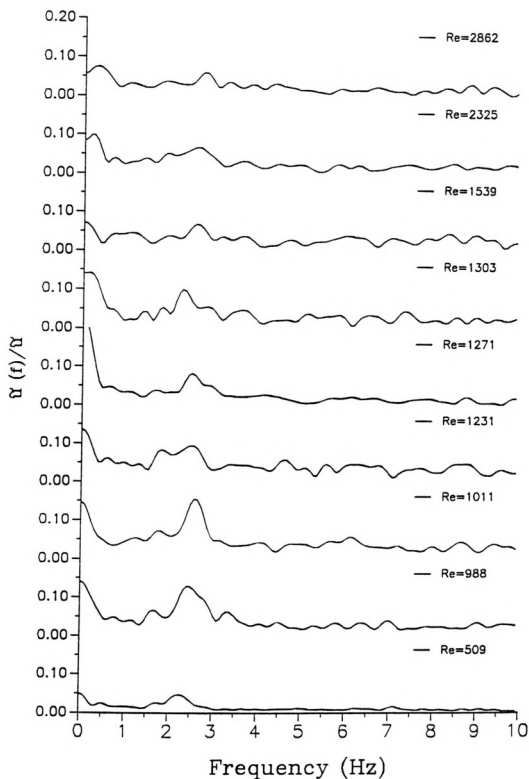
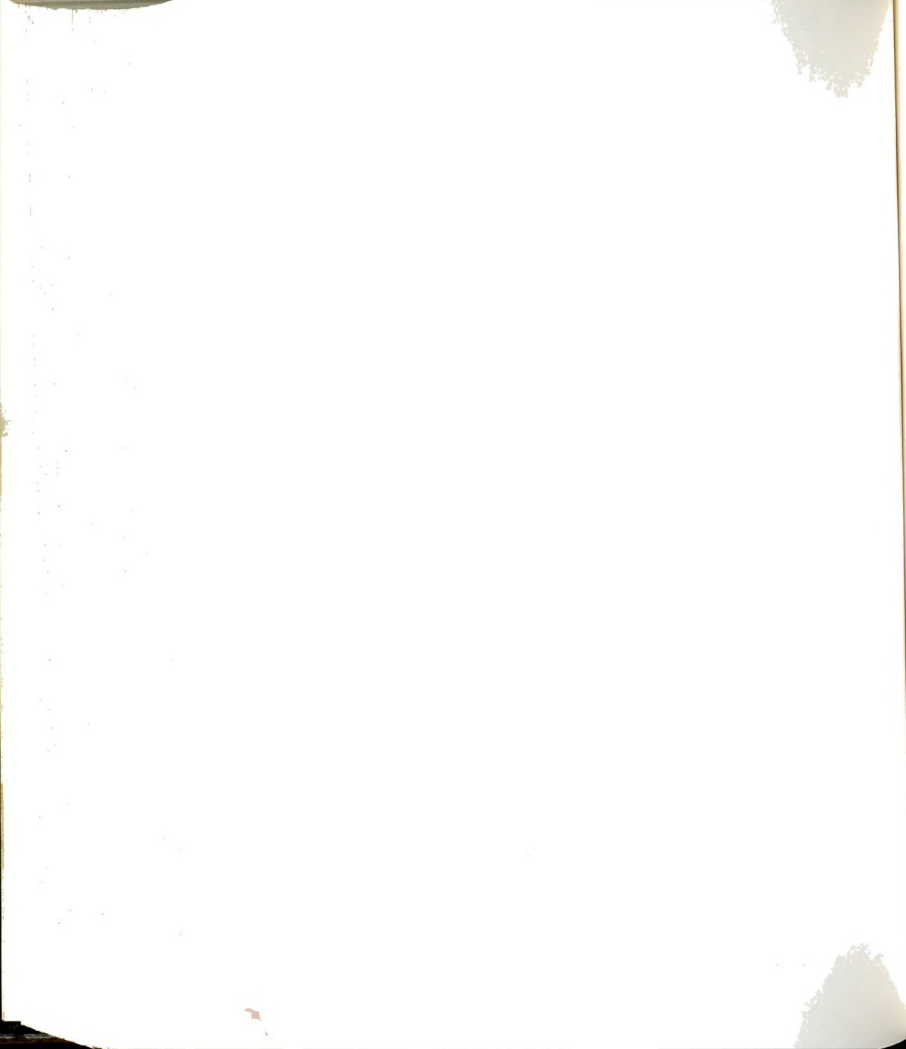


Figure 191. Plots of distribution of normalized intensity of streamwise velocity fluctuations as a function of frequency at $x/w=-1$ and over a wide range of Re.



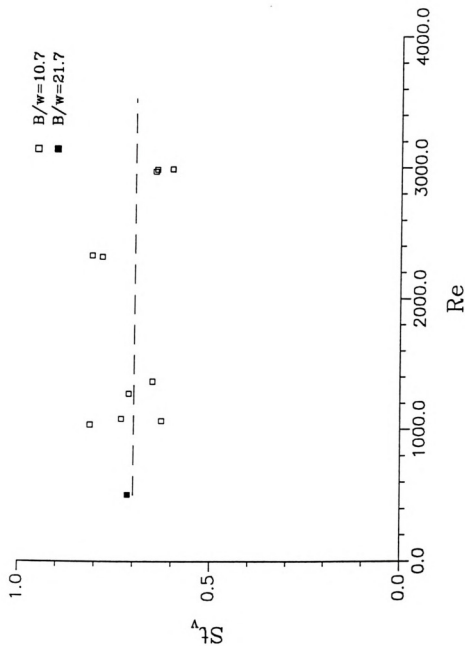
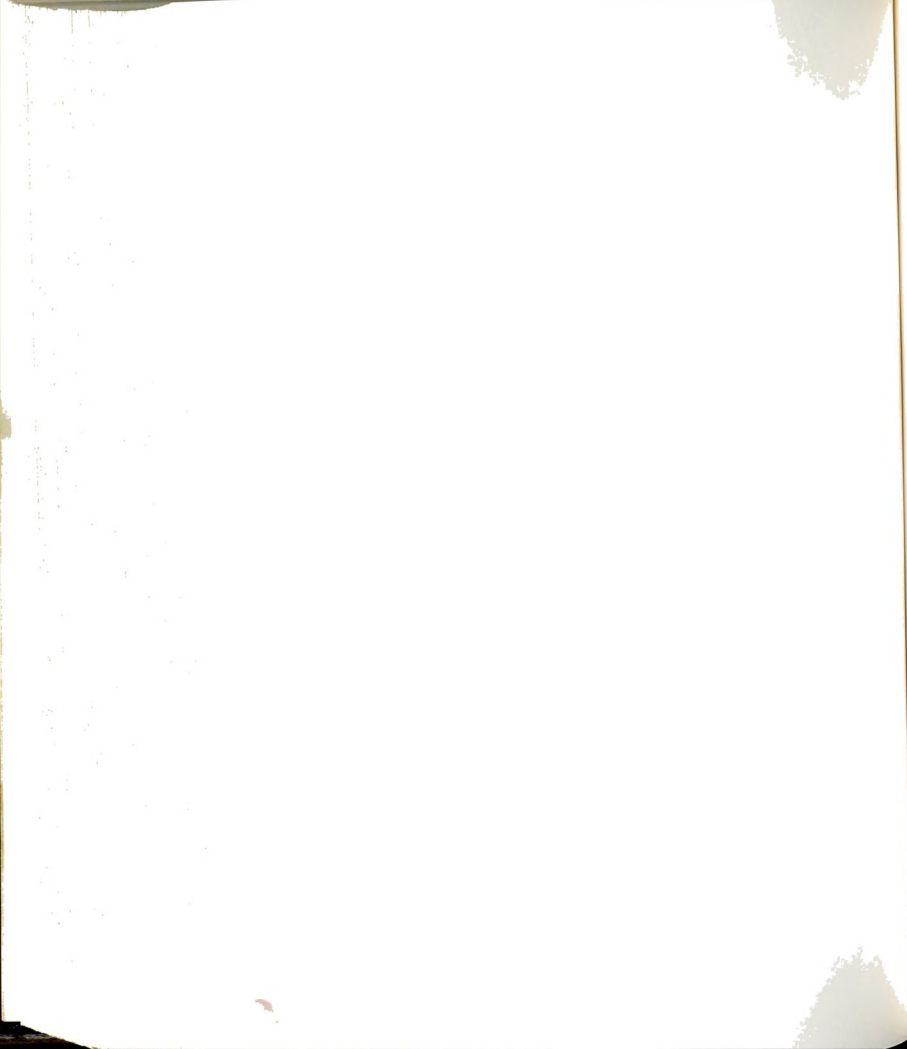


Figure 192. Distribution of St_v as a function of Re at $x/w=1$.
The dashed line represents the average value of $St_v=0.70$.



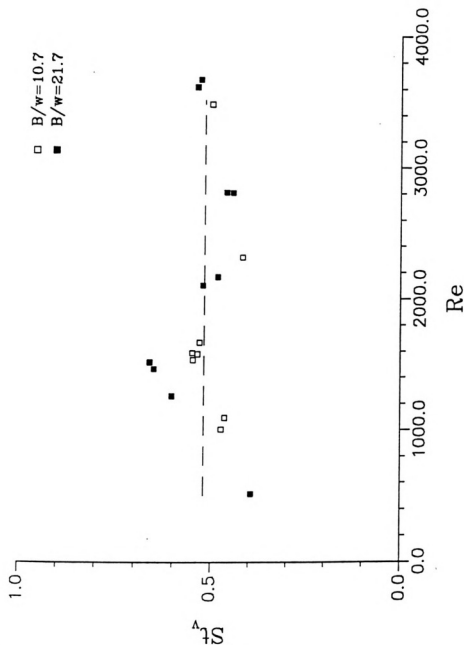
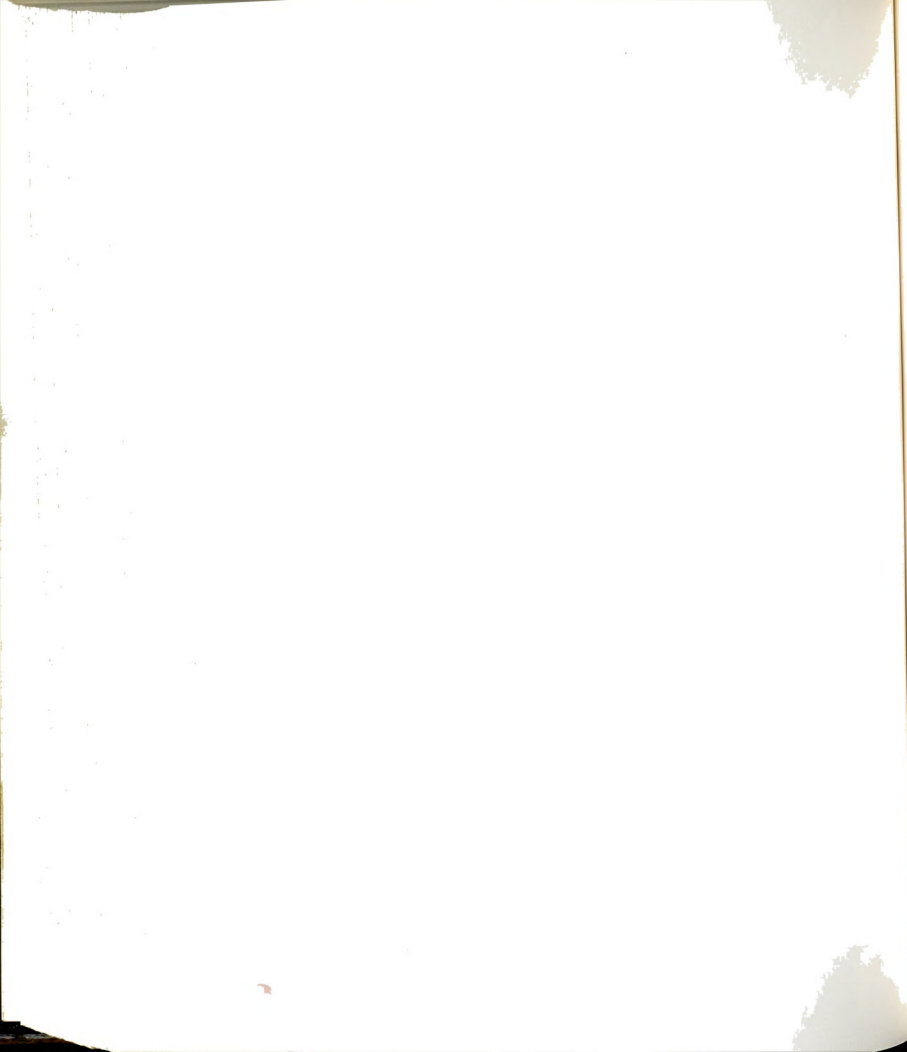


Figure 193. Distribution of St_v as a function of Re at $x/w=2.2$.
The dashed line represents the average value of $St_v=0.52$



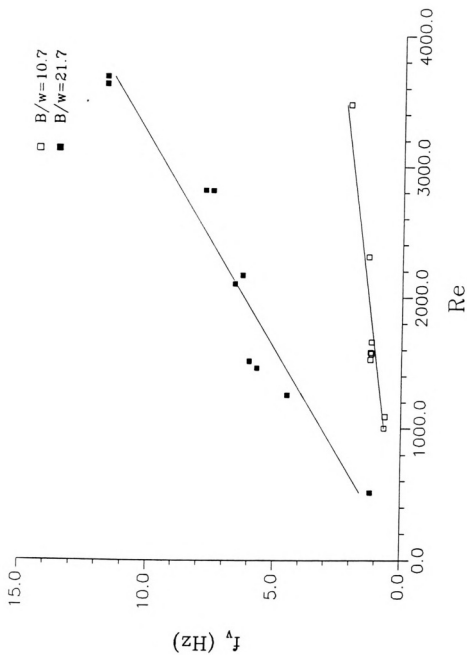
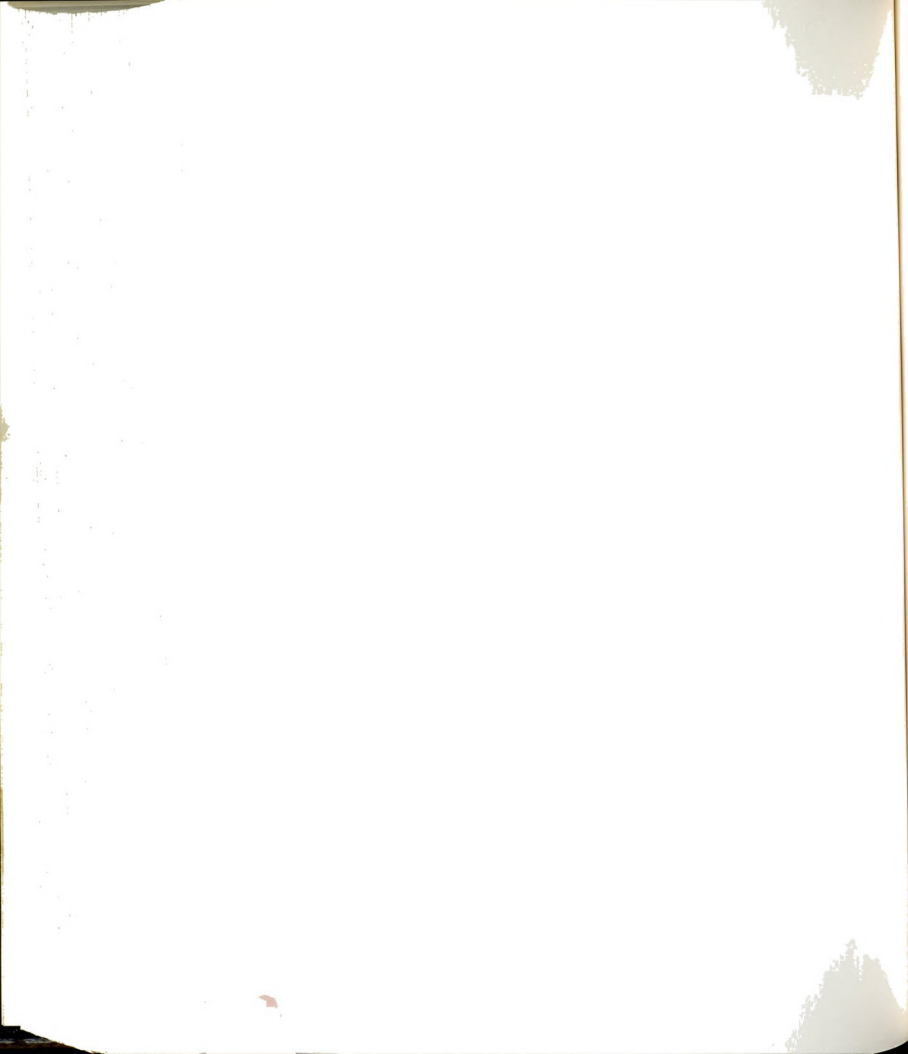


Figure 194. A comparison of the Re dependence of the frequency of dominant fluctuations of $u(t)$ for two jets with different slit widths at $x/w=2.2$.



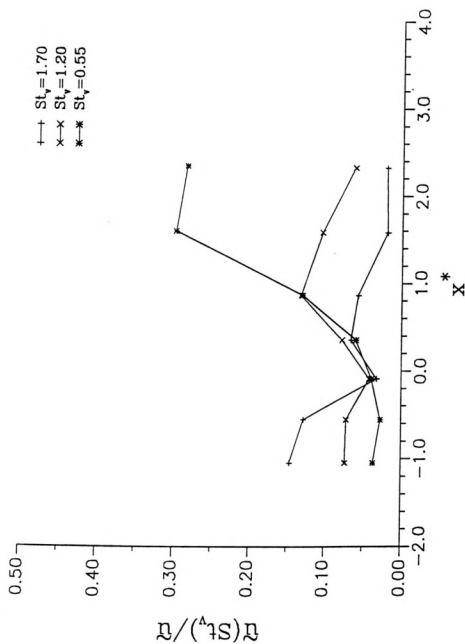
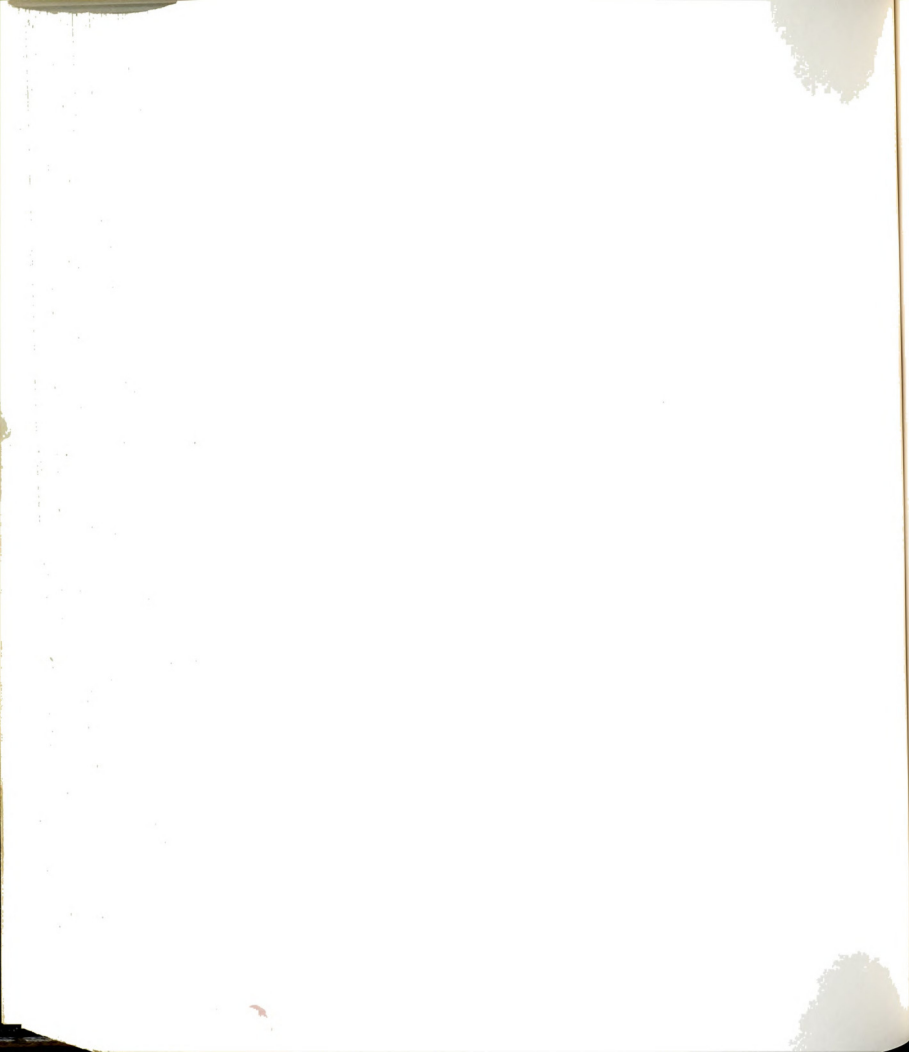


Figure 195. Streamwise distribution of the intensity of velocity fluctuations at $Re=1000$ and at three different values of St_v .



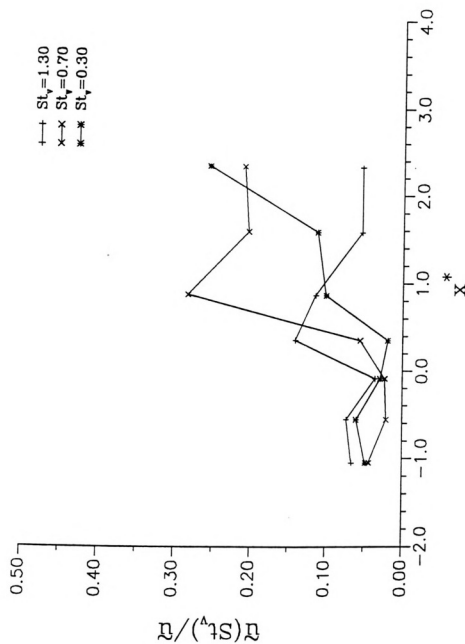
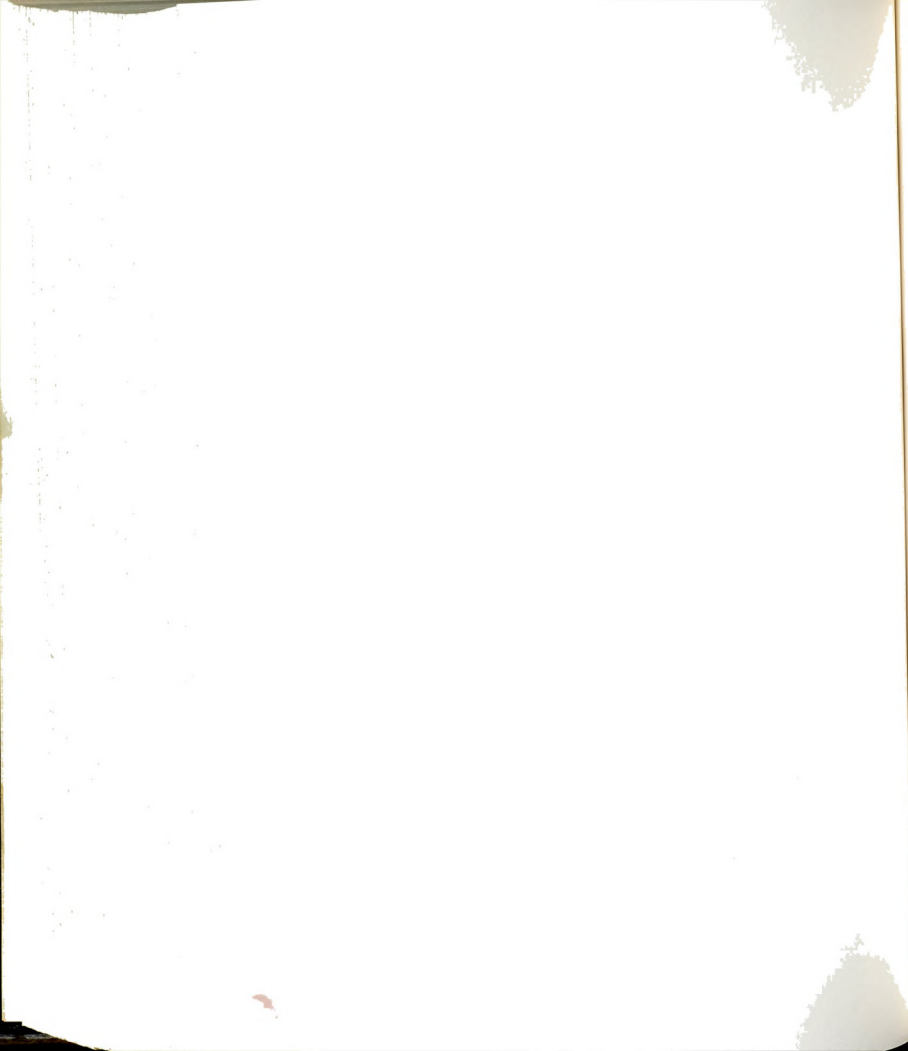


Figure 196. Streamwise distribution of the intensity of velocity fluctuations at $Re=1300$ and at three different values of St_v .



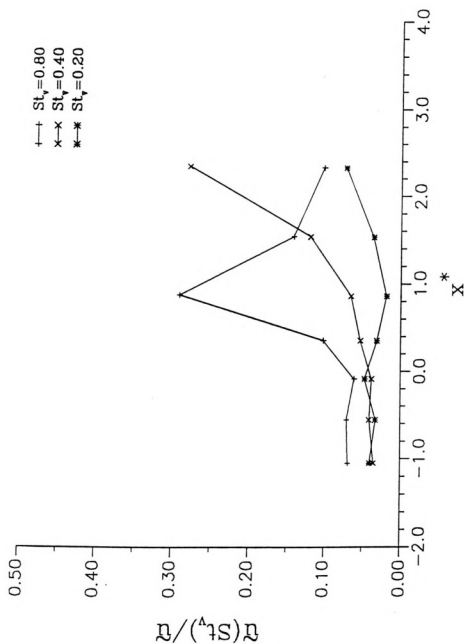
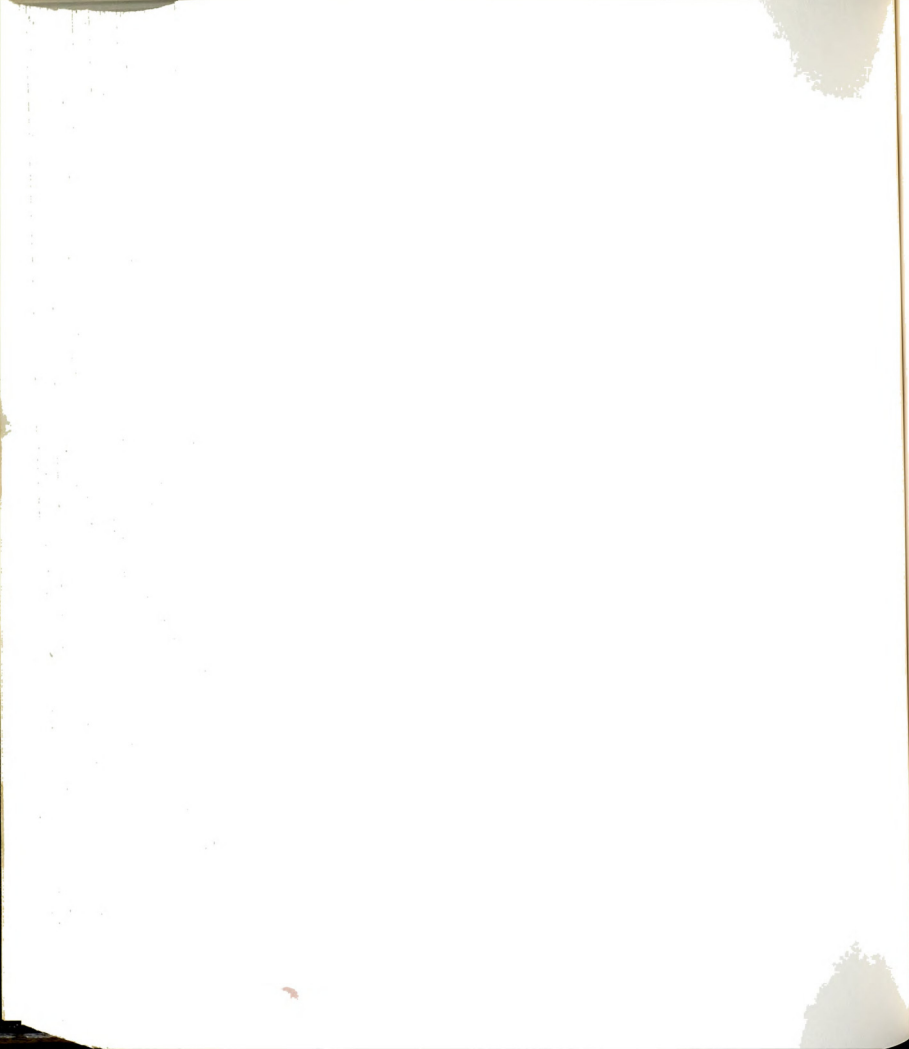


Figure 197. Streamwise distribution of the intensity of velocity fluctuations at $Re=2300$ and at three different values of St_v .



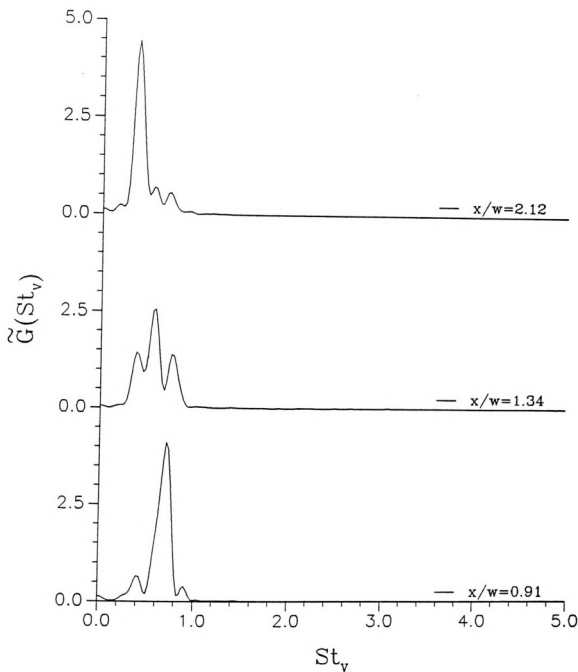
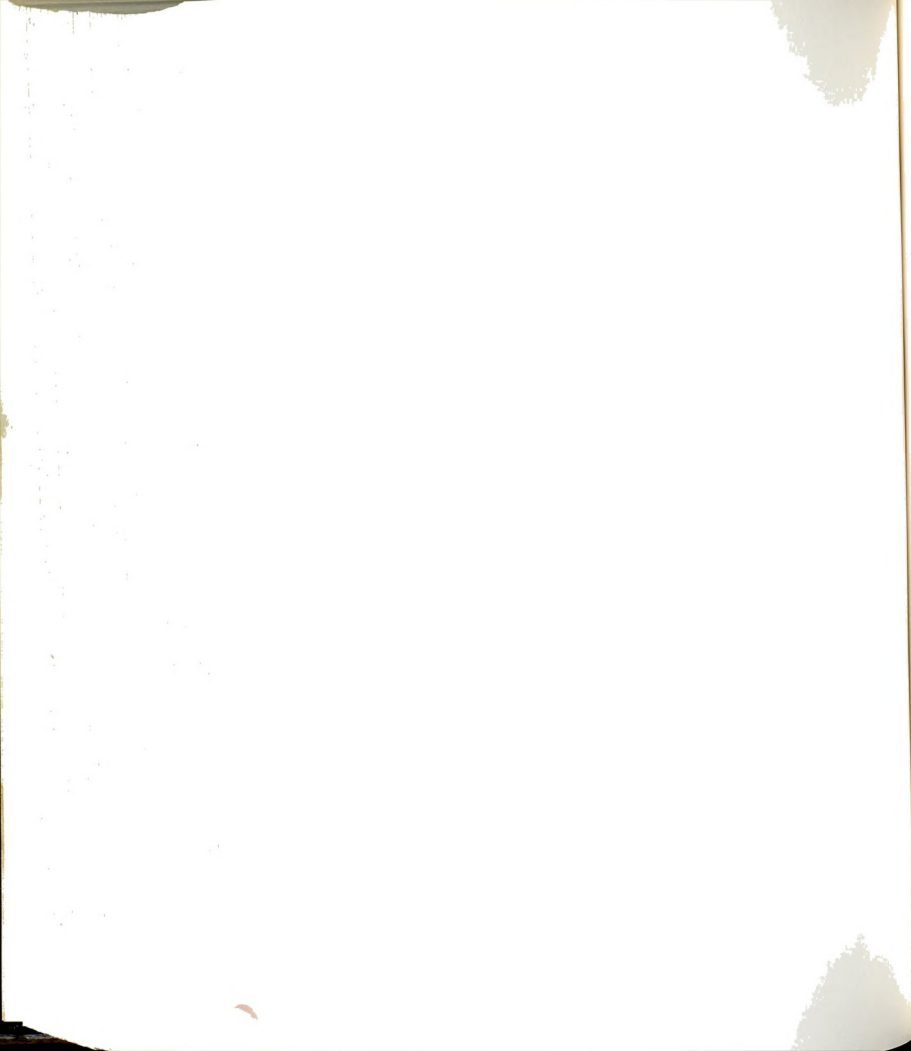


Figure 198. Autospectra of $u(t)$ in a jet with $w=1.27$ cm and $Re=510$. Note the transition in the neighborhood of $x/w=1.34$ - the "region of mutual interaction" - from $St_v=0.71$ at $x/w=0.9$ to $St_v=0.37$ at $x/w=2.12$.



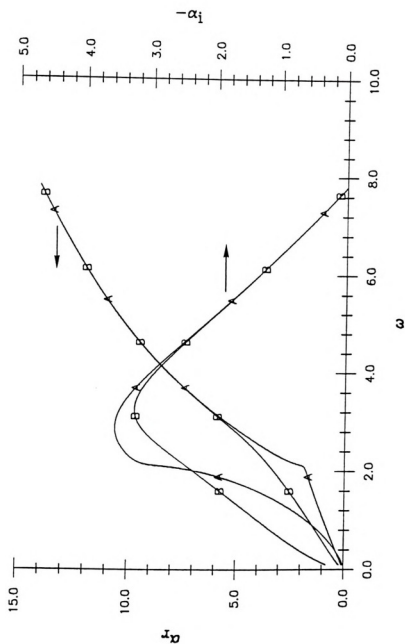
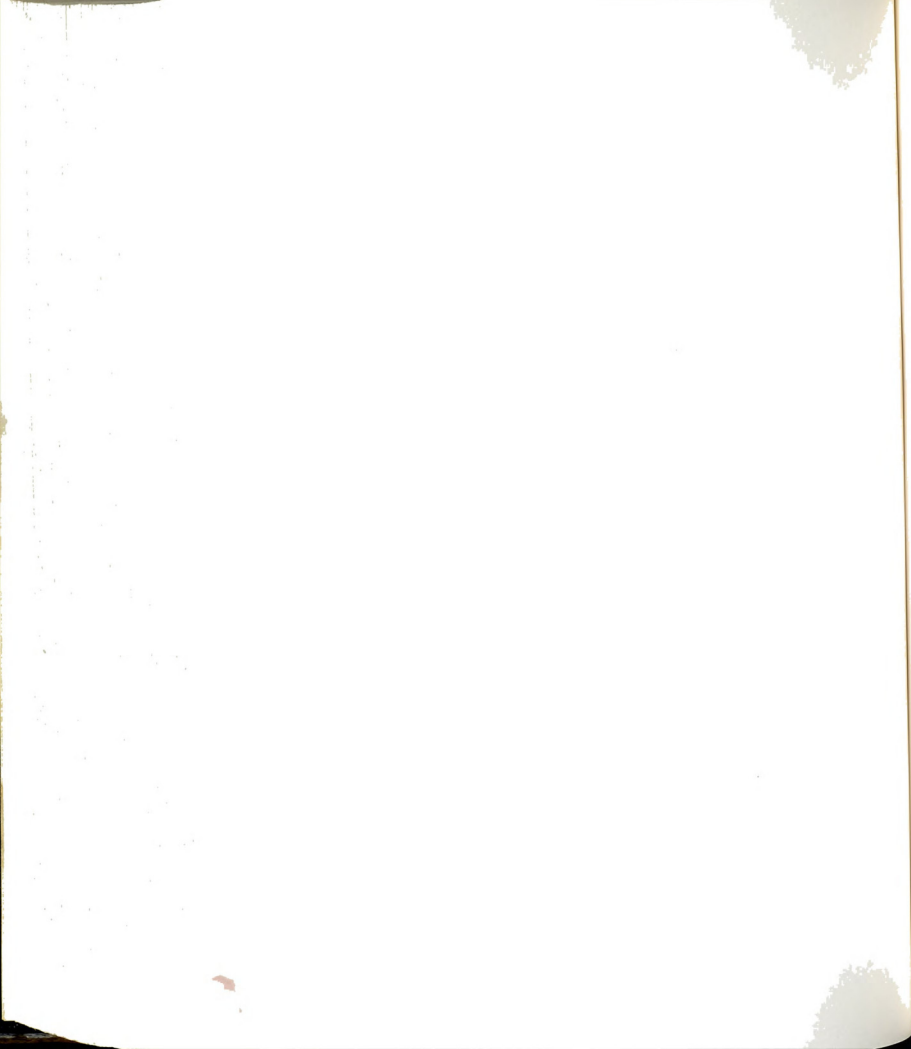


Figure 199. Eigenvalues for the Montgomery profile at $x/w=1$. A and B represent the symmetric and asymmetric solutions of the eigenvalue problem.



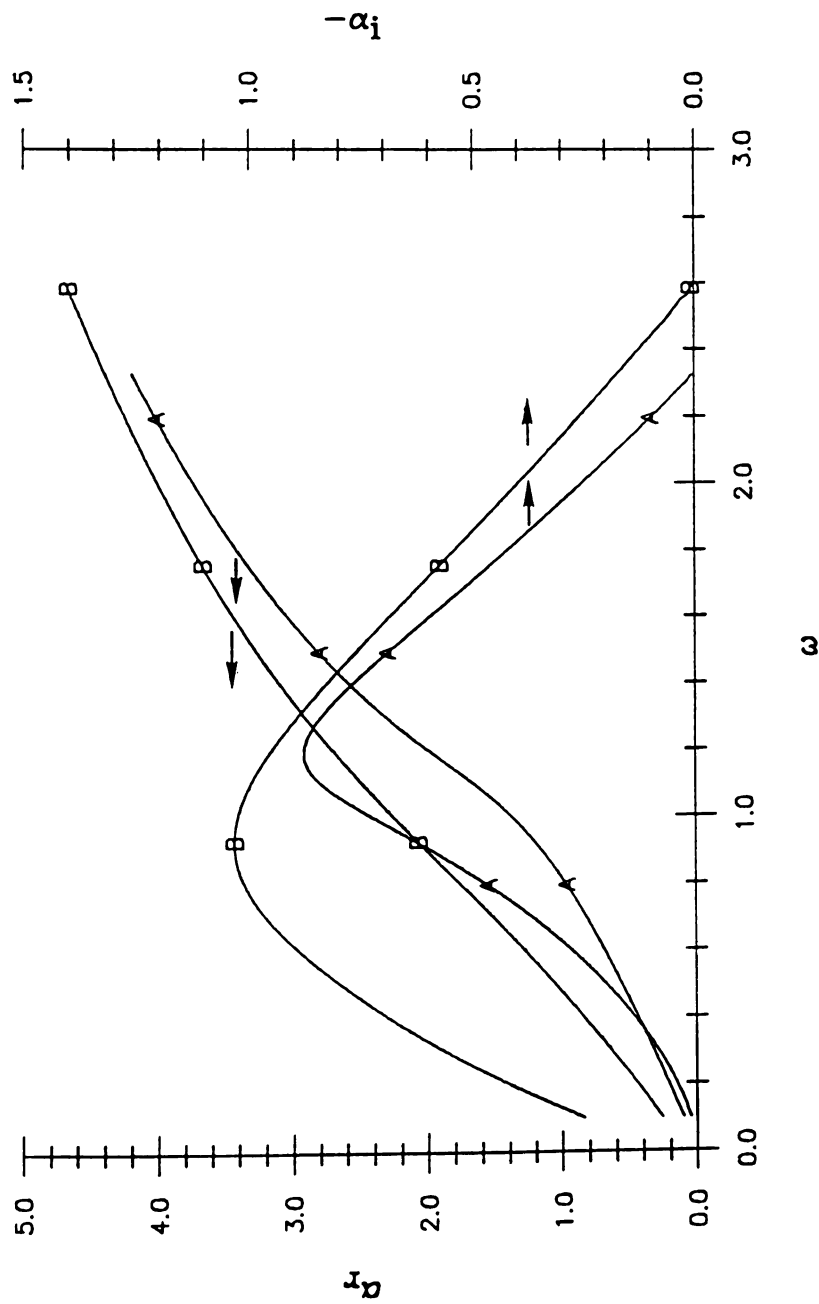
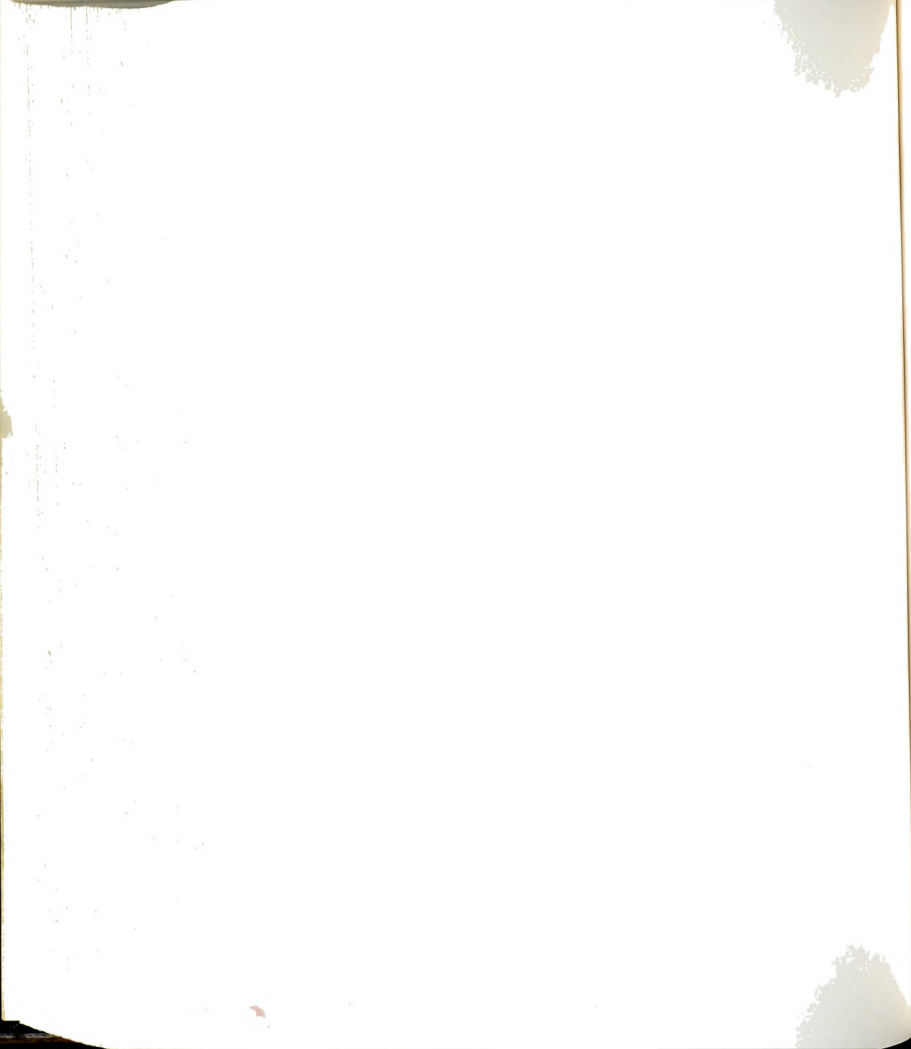


Figure 200. Eigenvalues of the Montgomery profile at $x/w=2.4$.
See Figure 199 for details.



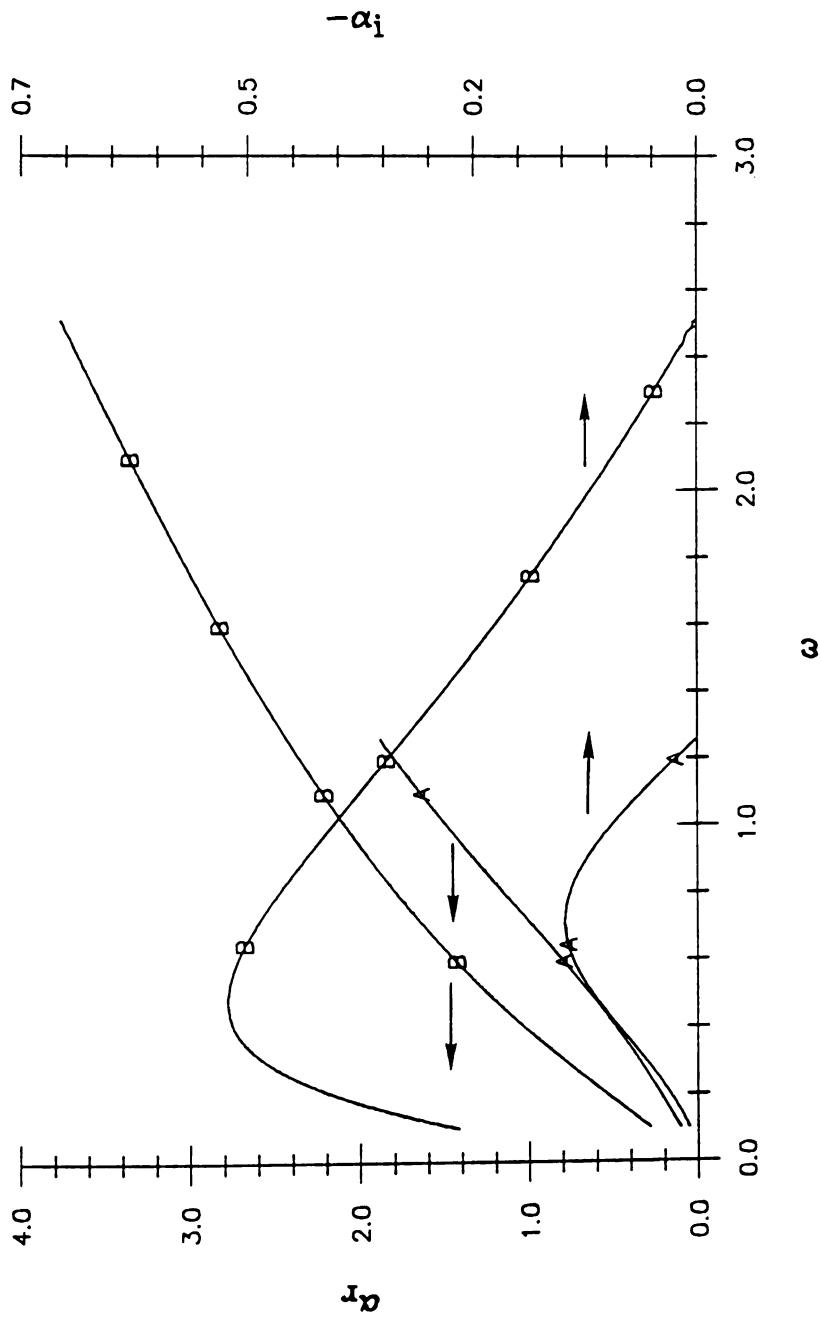


Figure 201. Eigenvalues of the Bickley profile at $x/w=2.4$.
See Figure 199 for details.



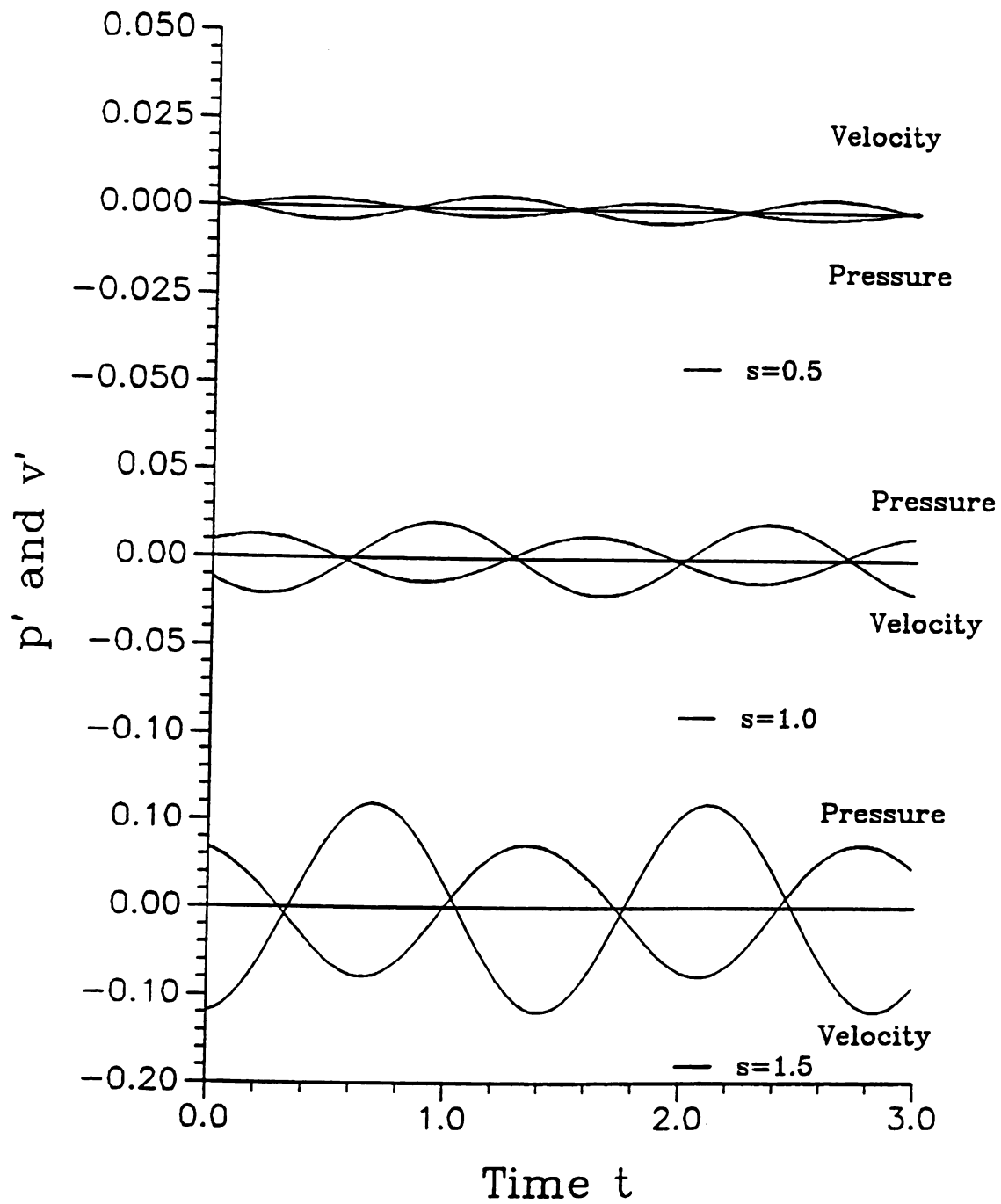
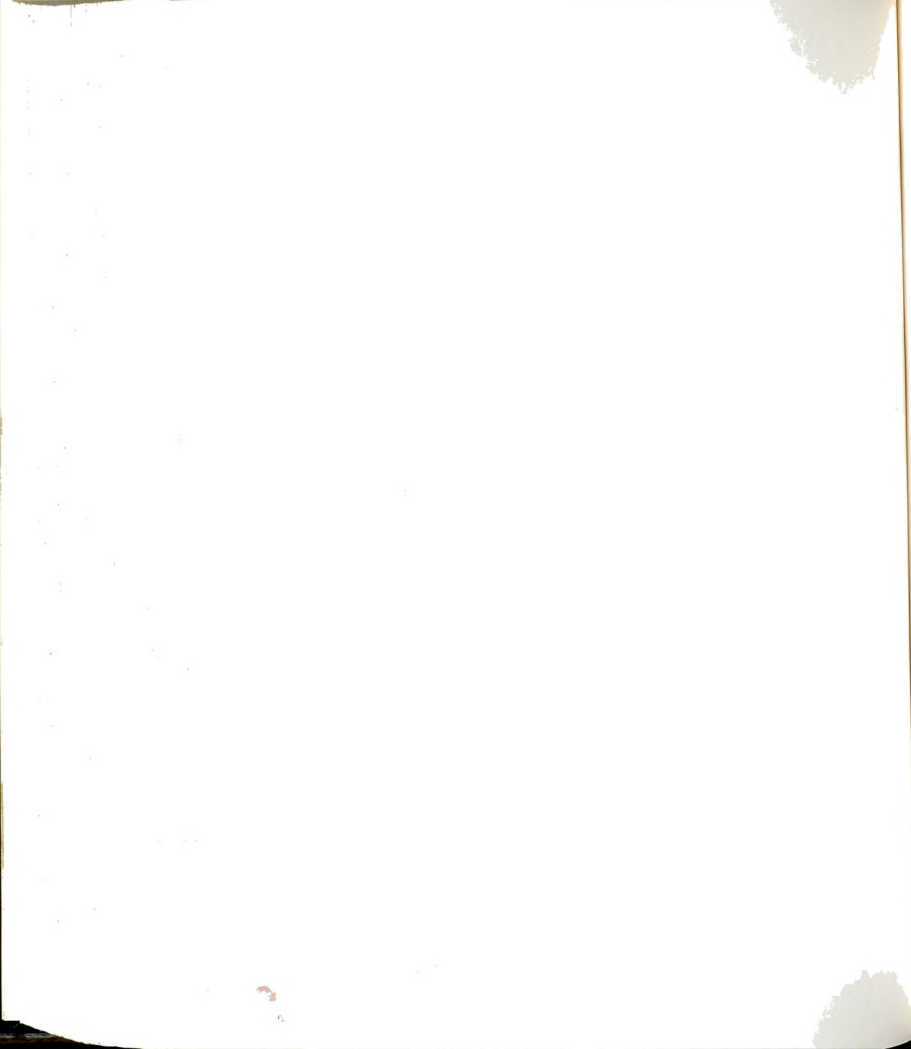
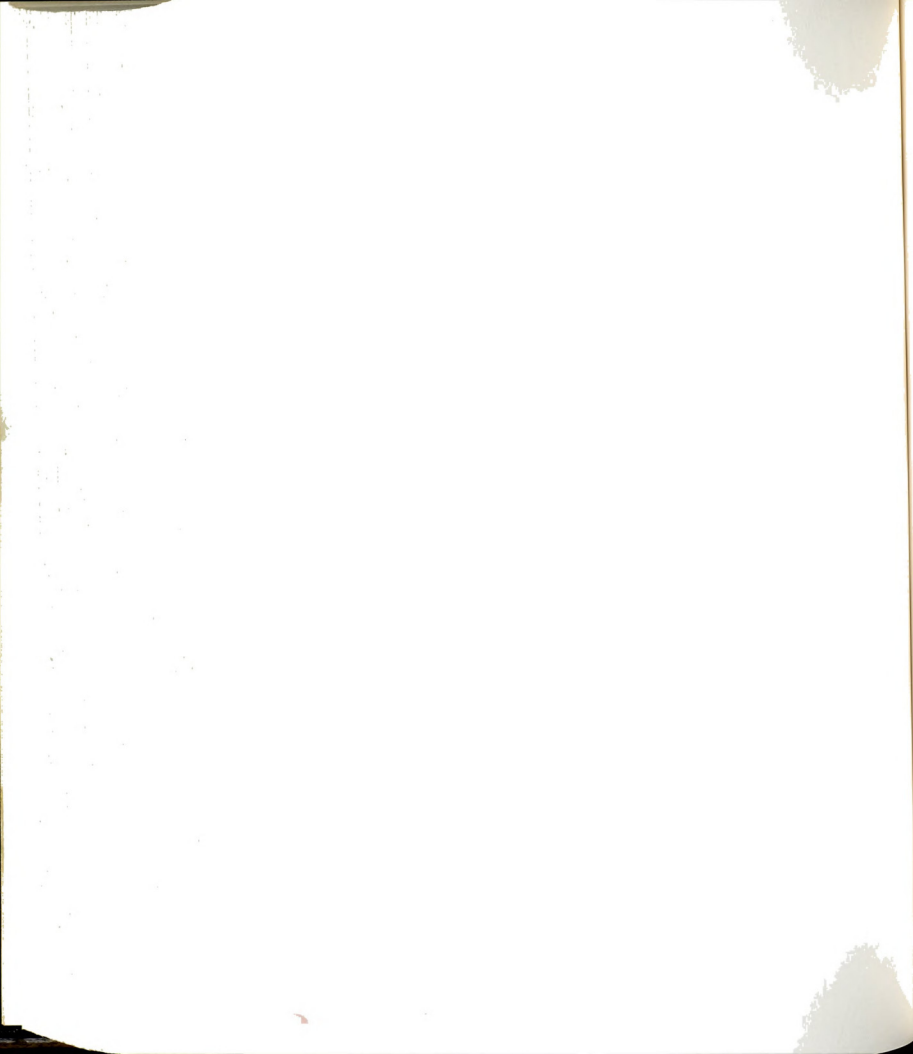


Figure 202. Normalized pressure and velocity fluctuations at three streamwise locations: $s=0.5$, 1.0 and 1.5 with $-\alpha_i=3.5$, $\alpha_r=10.4$, $\omega=4.4$ and $u_a=6.2 \times 10^{-4}$.



APPENDICES



APPENDIX A

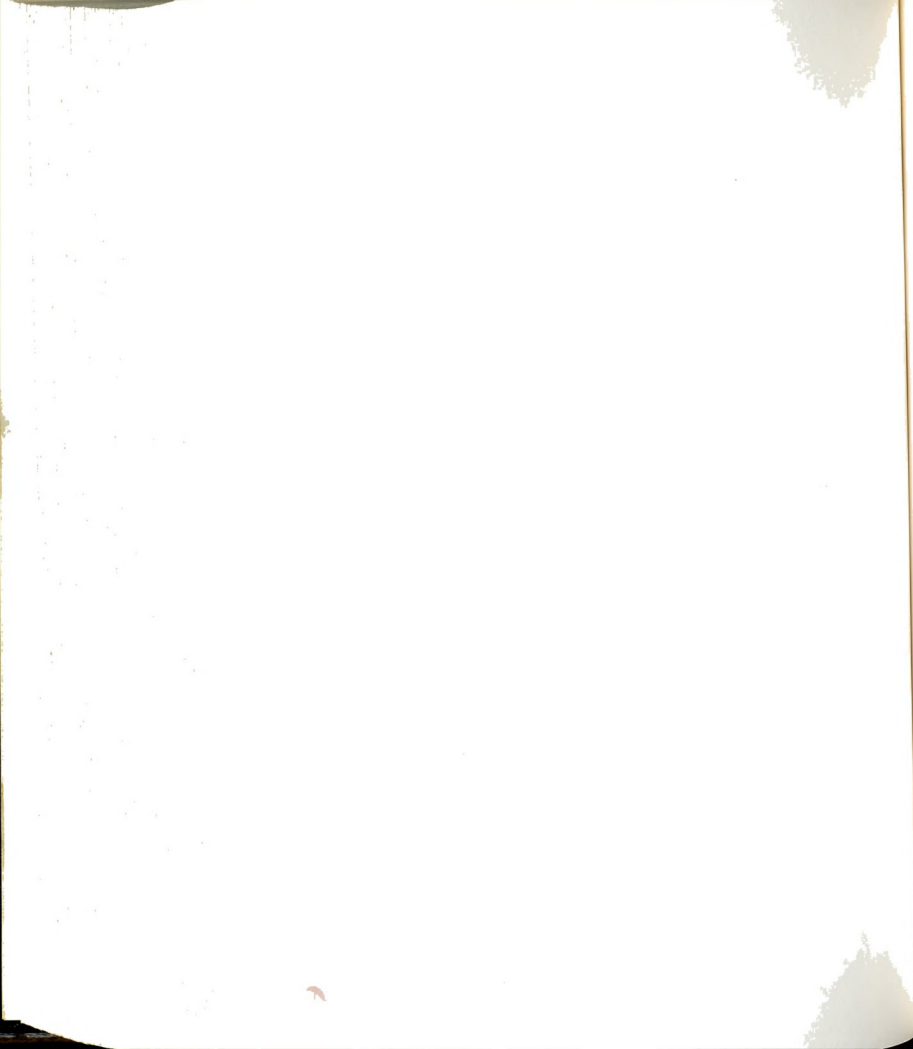
DESIGN OF FLOW FACILITY

A.1 General Requirements and Constraints

An idealized configuration of the experiment to study the stability characteristics of a slit-jet would involve an infinitely large plenum and a constant pressure differential Δp between the plenum and the receiver. In practice, however, a finite size plenum is either continuously supplied with the working fluid or some other arrangements are made to sustain a constant flow rate. The resulting pressure differential Δp will, in general, involve a finite level of fluctuations. The plenum pressure rise Δp can be described as a sum of Fourier modes as

$$\Delta p = \Delta p_0 + \sum [a_n \cos(\omega_n t) + b_n \sin(\omega_n t)] \quad (\text{A.1})$$

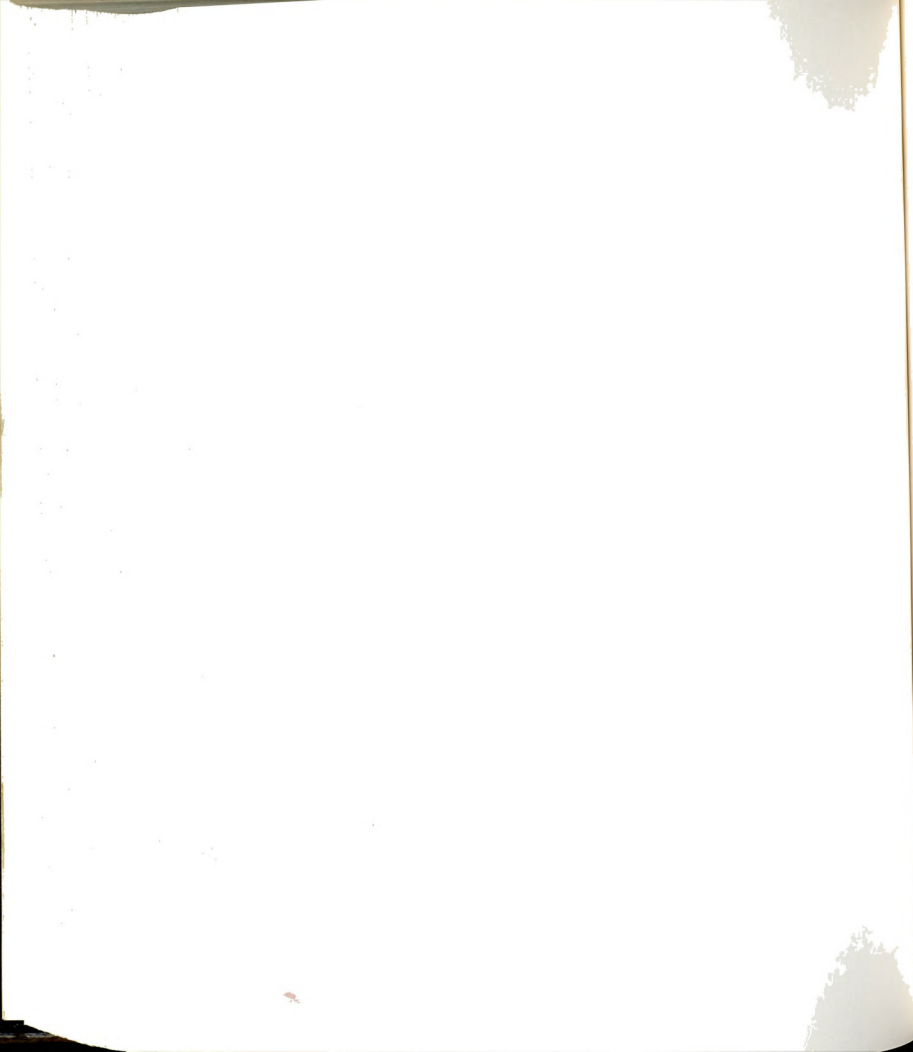
The Fourier coefficients a_n and b_n , would be zero for the ideal case.



In the case of a facility using liquid, like water, the use of a pump to maintain a constant head in the settling chamber would induce fluctuations in the flow; i.e., such a prime mover could introduce disturbances (a_n , b_n), that could have significant magnitudes at the frequencies of interest in the experiment itself. Beavers and Wilson (1970) report of such disturbances which prevented them from using the pump. A low disturbance level flow is thus the chief requirement for a flow which is to be investigated for stability considerations.

Other requirements are:

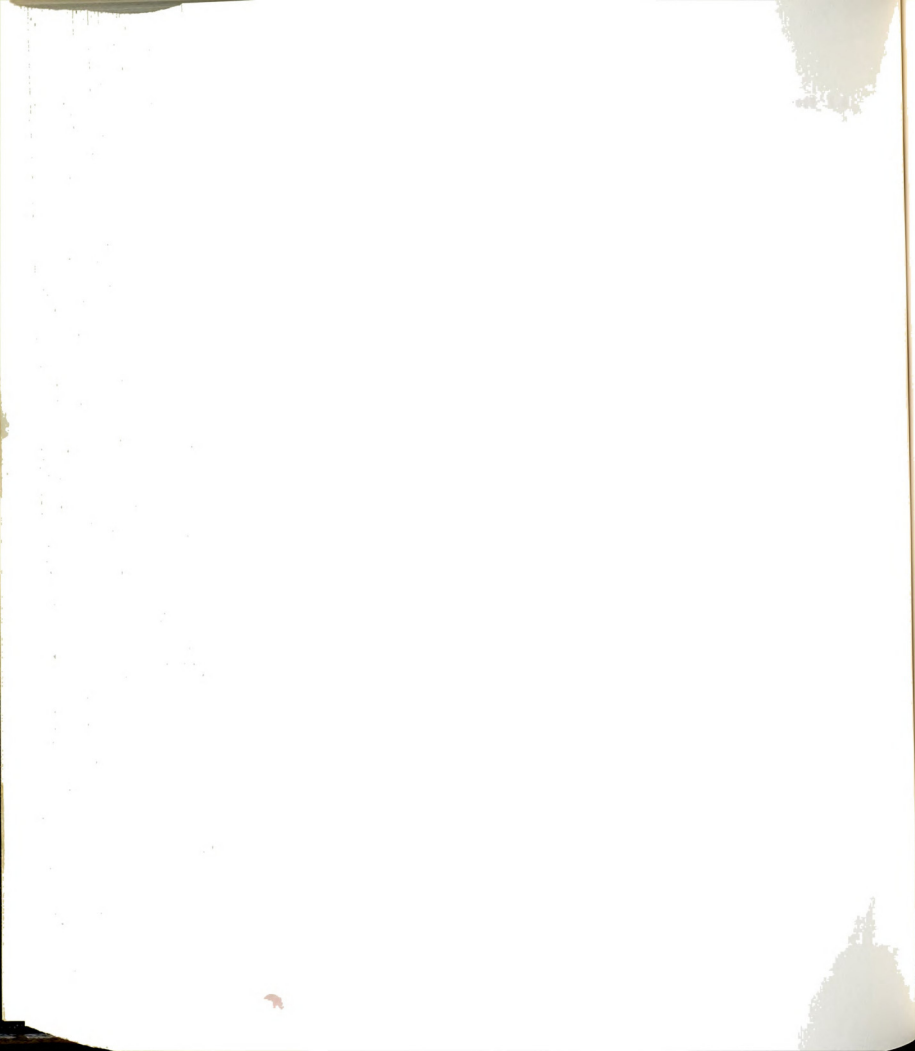
- i) Large aspect ratio, B/w . Beavers and Wilson (1970) [as reported by Foss (1980)] used $2.94 < B/w < 8$.
- ii) Variable slit width so that a wide range of Re could be covered with overlapping Re values.
- iii) Provision for carrying out flow visualization with good resolution.
- iv) Provision of establishing very small flow rate to execute experiments at low Re values.



A.2 Proposed Facility and Additional Constraints

Since it is easier to execute flow visualization in a facility which uses liquid as the working medium, it was decided to design and build a small, general purpose, gravity driven, finite duration liquid flow facility. A schematic of the facility is shown in Figure 16. It comprises of a 0.268 cubic meter (71 gallons) glass tank and a clear plastic insert called "Nozzle Housing (NH)". The NH has an airtight cover plate. The cover plate supports a bleed valve and has two additional openings: one for monitoring the pressure in the NH and the other for connecting the cavity to a vacuum line. Figure A.1 presents a schematic representation of the mechanism for actuating the bleed valve. The tapered valve slide is moved by the screw mounted on the computer controlled stepper motor. Note that, a variable width (aspect ratio) slit-jet forms as the bleed valve opens. When the NH is evacuated the liquid head is raised; a jet can thus be established with some flow rate, $q(t)$, by pressurizing the cavity. Some additional requirements arise because of this proposed configuration.

- v) Control of pressure in the cavity of the NH so that a time independent flow rate could be established.
- vi) Sufficient separation between the exit plane of the jet and the bottom wall of the tank, i.e., large h/w .



vii) No influence of the channel-like plenum on the flow field, specifically, due to the proximity of the lateral walls to the slit-jet, i.e., large H/w . The range of this ratio in Beavers and Wilson study [as reported by Foss (1980)] was $6.7 < H/w < 18.0$.

A.3 Design Strategies to Meet the Requirements

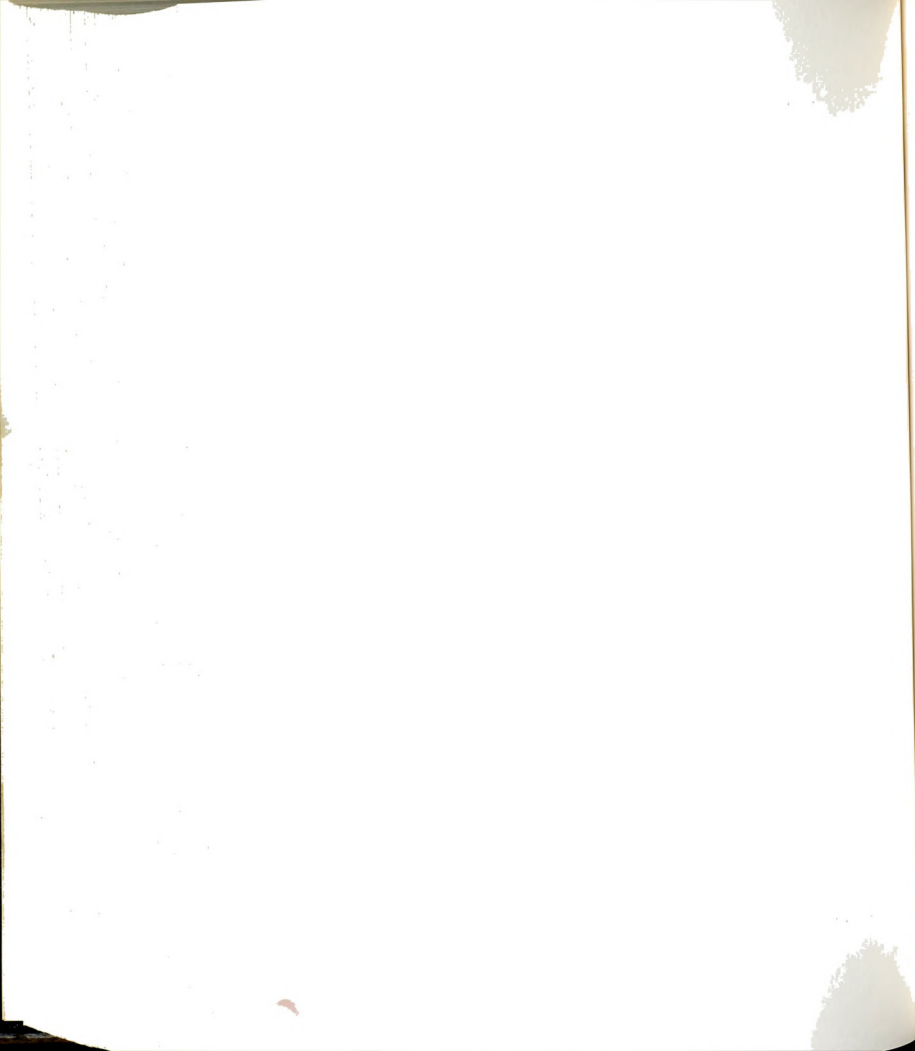
A.3.1 Dimensions and Range of Parameters

The glass tank is $120 \text{ cm} \times 30.5 \text{ cm}$ in cross section and 73.2 cm in height. The NH is $45.8 \text{ cm} \times 27.5 \text{ cm}$ in cross section and 89.3 cm high. The sides of the NH are partially open to allow working liquid discharged by the jet to redistribute in the receiver.

The two nozzle plates are $27.5 \text{ cm} \times 21.5 \text{ cm}$ each. The width = 21.5 cm allows a maximum jet width $w = 2.63 \text{ cm}$. Hence the smallest value of three geometrical ratios are:

- a) Aspect Ratio, $B/w = 10.5$
- b) Proximity Ratio, $H/w = 17.7$
- c) Height Ratio, $h/w = 14.5$

From the results of Beavers and Wilson (1970) it is expected that the smallest $B/w = 10.4$ would be adequate. The influence of the



lateral walls on the flow issuing from a channel-like plenum was investigated by using the potential flow methods; the results have been presented in Section 2.2. Based upon these results, it was concluded that the lateral walls will have a minimal influence on the development of the jet if the proximity ratio, H/w , is greater than 12.3. Regarding the influence of closeness of the bottom wall, an a posteriori check shows no adverse effects on the development of the jet.

A.3.2 Control of Flow Rate

A constant flow rate, i.e., a time independent jet velocity is established by pressurizing the air cavity in the NH at a controlled rate such that $\Delta p_k(t)$ remains constant. The bleed valve in the cover plate is opened under computer control to allow the ambient air to enter the cavity and thus cause the desired pressurization. This arrangement has produced satisfactory results. The modelling of the flow through the bleed valve is presented in Section 3.3.

A.3.3 Control of Disturbance Level

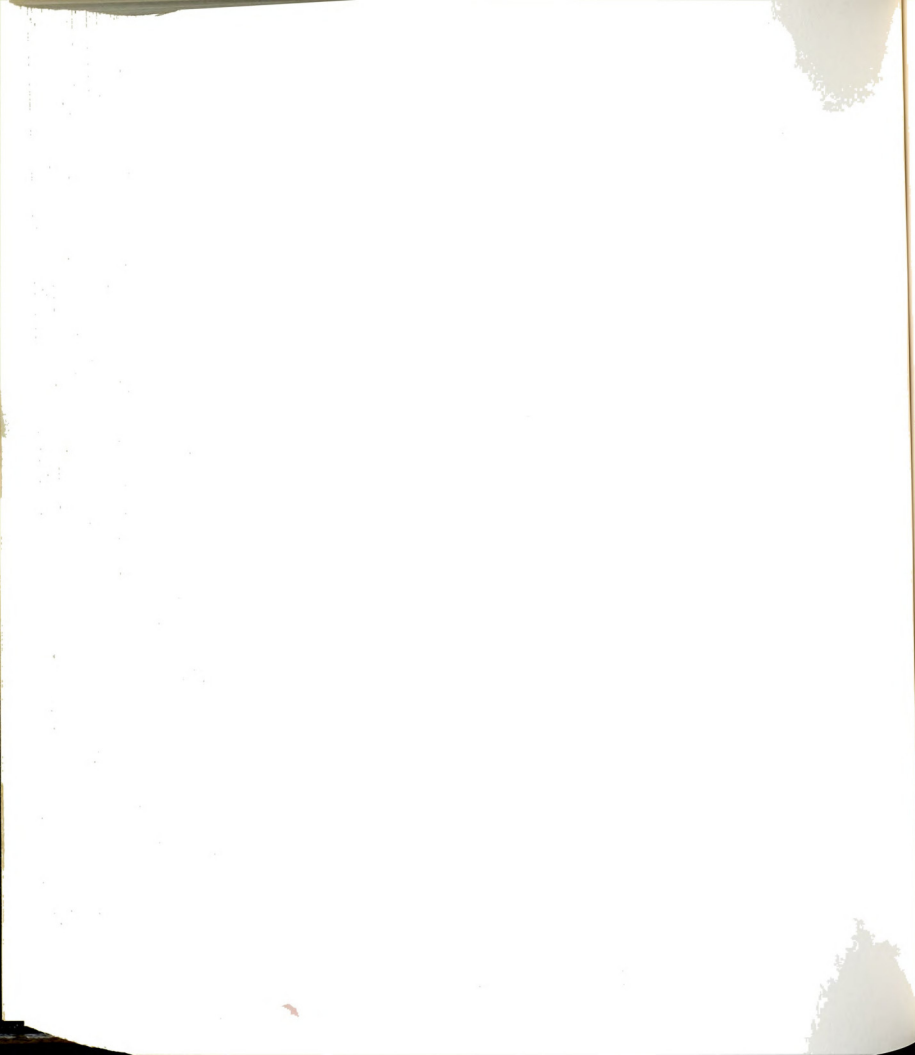
For the present configuration the disturbances can be induced in the flow from two sources:

- i) During the filling process when the liquid head is raised in the cavity.



- ii) During the execution of the experiment as the bleed valve is actuated by the stepper motor.

The disturbance due to the first source can be effectively controlled by allowing enough settling time after the filling of the NH. In the limit, the disturbance level would approach zero as the settling time becomes infinitely large. Regarding the second source of disturbance, i.e., the stepper motor which is mounted on the underside of the cover plate, no adverse effect of the continually increasing speed of the stepper has been found. In the case of a problem, a separate structure for supporting the stepper motor would have alleviated the problem.



APPENDIX B

SELECTION OF A REGRESSION MODEL FOR $E_I(T)$ DATA

B.1 Introduction

The voltage, $E_I(t)$, corresponding to the inverted cup pressure time history, $p_I(t)$, of the volume flow sensor (VFS) is expected to exhibit a linear time dependence. See Section 3.2.1 for the details of the VFS. The purpose of this appendix is to show that a linear model is adequate to describe the variation of $p_I(t)$ in the NH. A computer program was developed to check which order polynomial would best describe the $E_I(t)$ data in the least square sense. In other words, for the p th order model

$$\eta = \beta_0 + \sum_{i=1}^p \beta_i t_i \quad (B.1)$$

determine the value of p that will minimize the error

$$S_{LS} = (\bar{E}_I - \bar{\eta})^T (\bar{E}_I - \bar{\eta}) \quad (B.2)$$



where \bar{E}_I is the columnar matrix of the measured $E_I(t)$ data, $\bar{\eta}$ is the columnar matrix of the estimate of $E_I(t)$, and the superscript T indicates the transpose of the matrix $(\bar{E}_I - \bar{\eta})$.

The method described in Section 6.2 of Beck and Arnold (1977) was followed: the parameters $\bar{\beta}$ and the residual sum of squares, R, for p and (p-1) parameters for p=2,3,4,... are calculated. Using Theorem 6.2.4 of Beck and Arnold (1977), F test is performed on the statistic:

$$\frac{\frac{R_{p-1} - R_p}{p}}{\frac{R_p}{d.f.}} \quad (B.3)$$

where R_p is the residual sum of squares with p parameters and d.f.=(n-p) is the degree of freedom, n being the length of the data array $E_I(t)$. The hypothesis to be tested is $\beta_p^* = 0$. The ratio expressed in equation (B.3) is compared with $F_{1-\alpha}(1, d.f.)$ to check whether or not the hypothesis can be accepted at α % level of significance.

B.2 Example

The technique described in Section B.1 is applied to the $E_I(t)$ data from an experimental run at Re=1084. Figure B.1 presents a plot of the three signals recorded during the experiment; the sampling rate was 50 words/sec. The curve marked VAL14 represents the voltage $E_{NH}(t)$ corresponding to the pressure $p_{NH}(t)$ and the curve marked VAL5 represents the voltage $E_I(t)$ corresponding to the pressure $p_I(t)$. The curve marked LDV represents the output of the comparator circuit, C(t), (see Section 3.9) which marks the beginning and the end of the

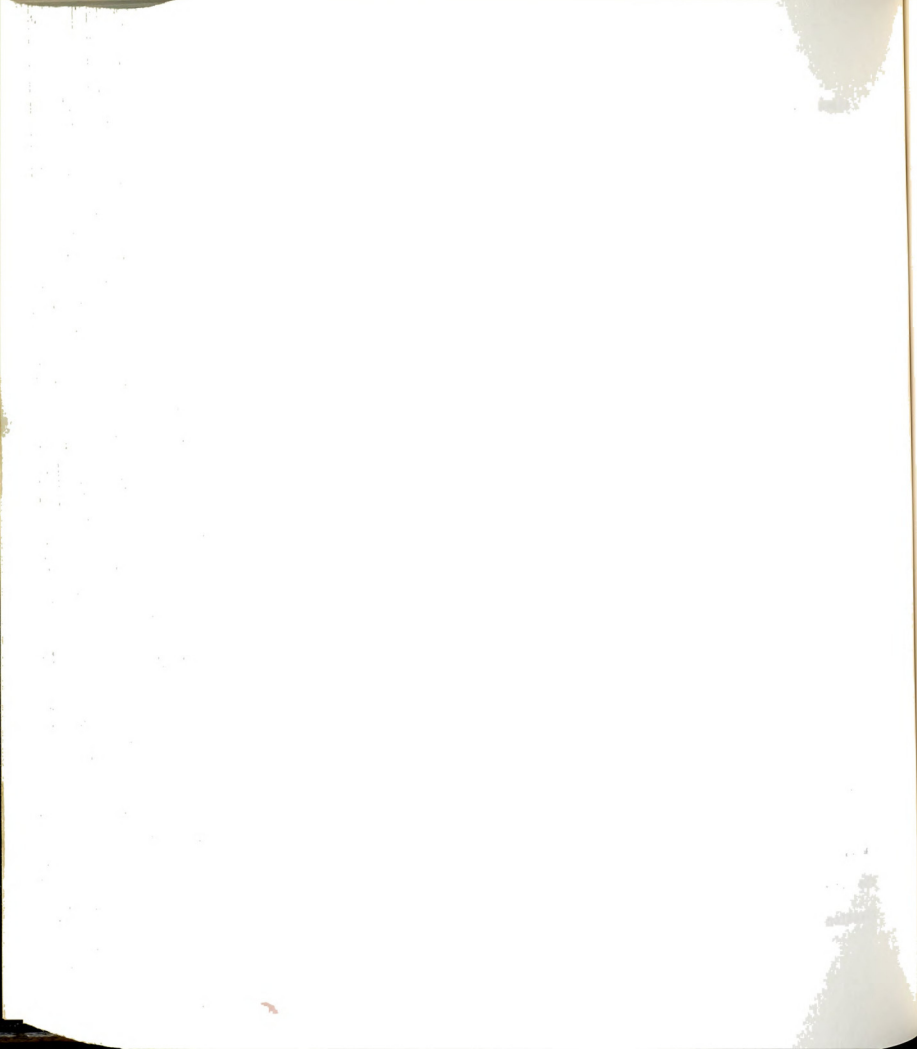


times during which the jet velocity, $u(t)$, was measured. In order to be consistent in using $u(t)$ along with the spatially averaged velocity $\langle U \rangle$ of the jet, only that portion of the $E_I(t)$ data were used in determining $\langle U \rangle$ which fell within the vertical lines of the $C(t)$ curve. Table B.1 presents the results of calculations.

Table B.1 - Sum of squares and F ratio

p	d.f. (n-p)	$R(\hat{\beta}_{LS})$	Mean Square ($s^2 = R/d.f.$)	ΔR ($R_{p-1} - R_p$)	F ($\Delta R/s^2$)
1	700	22.045	3.149 E-2	-	-
2	699	4.4703 E-2	6.395 E-5	3.143 E-2	491.44
3	698	4.4515 E-2	6.378 E-5	1.777 E-7	2.786 E-3
4	697	4.4494 E-2	6.384 E-5	-6.041 E-8	-9.464 E-4
5	696	4.4467 E-2	6.389 E-5	-5.328 E-8	-8.339 E-4

The ratio $F = \frac{\Delta R}{s^2}$, in the last column of Table B.1 is compared with $F_{0.95}(1, 77-p)$ which is between 3.92 and 3.84 for $(n-p) \approx 700$. The value of F for $p=2$ is much greater than 3.92 indicating that the second term in the model is needed; however, for $p=3$, the value of F is much smaller than 3.92 indicating that the hypothesis is accepted at 5% level of significance and that a third term in the model is not needed. Figure B.2 shows the voltage corresponding to the $p_I(t)$ data, a fitted straight line and the corresponding residual. The residual is about 8mV (or 6 least significant bits of the IFA200 A/D converter). Hence, apart from the transients in the beginning and end of the run, the head $h_{NH}(t)$ in the NH follows the model requirement (Section 3.3) and falls linearly yielding a constant velocity jet.



APPENDIX C

DETAILS OF EXPERIMENTAL RUNS AND SPACE-TIME PLOTS.

C.1 Introduction

This appendix presents in tabular form the details of all the flow visualisation experiments that were conducted during the course of this investigation. In addition it also presents the remainder of the space-time plots. The name under which the data file for a given run is stored is included in the table and is also indicated on the corresponding space-time plot.

C.2 Details of Experimental Runs

The details of experimental runs are presented in Table C.1. The information includes: file name, the Reynolds number of the jet, the width, w , of the jet in cm., the width, w_b , of the side bleed ports, the working liquid and whether or not the filling device was used. The Reynolds number is based upon the time mean of the spatially averaged velocity, $\langle U \rangle$, of the jet. In all the experiments in which



bleed ports were open the width w_b was same on the two sides, except for three experiments in which the width of the two side bleed ports were set differently. In the experiments whose file name begins with the letter U, the jet velocity, $u(x-c, y=0, t)$, was acquired using a laser Doppler anemometer together with the flow visualization records.

Table C.1 - Details of Experimental Runs

No.	File Name	Re	w (cm)	w_b (cm)	Work. Liq.	Fill. Dev.
1	R012A	86.3	1.99	0.32	Water-Sugar	Not Used
2	R015A	104.9	1.99	0.32	"	"
3	R020B	128.7	1.99	0.32	"	"
4	R022A	156.7	1.99	0.32	"	"
5	R020C	208.4	2.63	0.0	"	"
6	R040G	268.8	1.99	0.0	"	"
7	R040F	269.0	1.99	0.0	"	"
8	R040A	275.7	1.99	0.32	"	"
9	R040D	276.8	1.51	0.0	"	"
10	R040B	279.9	1.51	0.25	"	"
11	R040I	285.4	2.63	0.0	"	"
12	R060I	361.1	2.63	0.0	"	"
13	R060H	372.6	2.63	0.0	"	"
14	R090P	395.5	1.40	0.62	Water	"
15	R060E	406.8	1.51	0.56	Water-Sugar	"
16	R060G	407.7	2.63	0.0	"	"
17	R060B	411.7	1.51	0.25	"	"
18	R060D	421.2	1.51	0.0	"	"
19	R060A	422.8	1.99	0.32	"	"
20	R060F	425.6	1.99	0.0	"	"
21	R090V	509.5	1.40	0.62	Water	"
22	R090U	525.4	1.40	0.62	"	"
23	R090R	640.0	1.40	0.62	"	"
24	R090S	640.0	1.40	0.62	"	"
25	R090T	640.0	1.40	0.62	"	"
26	R100C	678.7	1.99	0.32	Water-Sugar	"
27	R100G	696.2	2.63	0.0	"	"
28	R100D	697.5	1.99	0.0	"	"
29	R180E	930.2	1.40	0.62	Water	"
30	R100H	980.1	2.63	0.0	Water-Sugar	"
31	U090A000	1001.3	2.57	0.0	Water	Used
32	U090A001	1004.3	2.57	0.0	"	"
33	U090C002	1026.7	2.57	0.0	"	"
34	R180D	1043.5	1.40	0.62	"	Not Used
35	U090C000	1063.1	2.57	0.0	"	Used
36	U090C001	1073.7	2.57	0.0	"	"

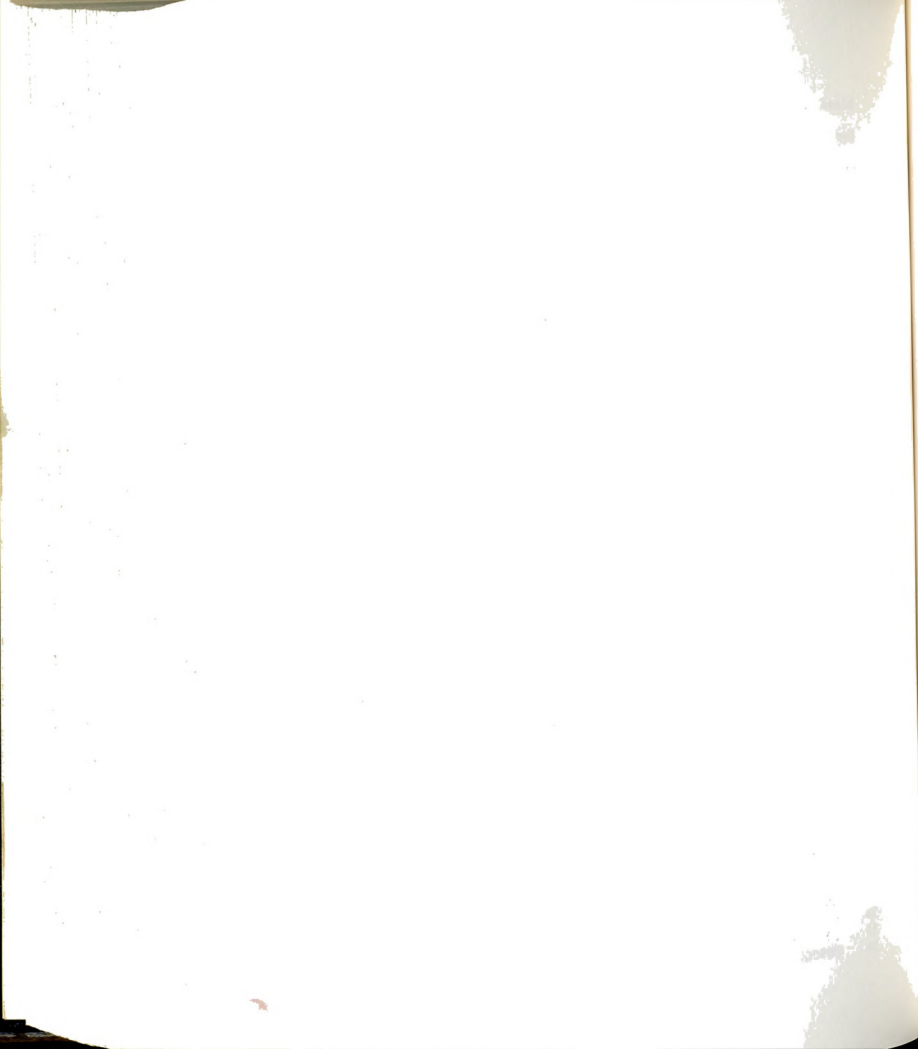
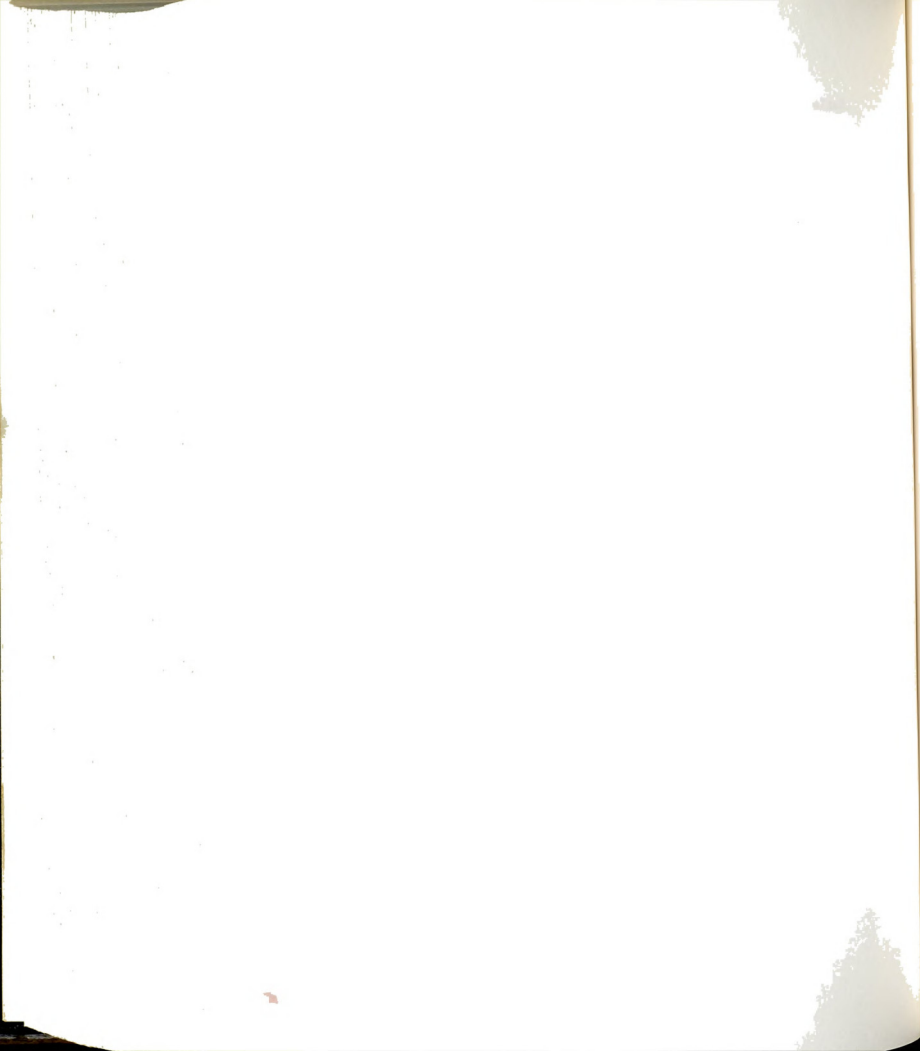


Table C.1 (cont'd.).

37	R180B	1268.8	1.40	0.3,0.9	"	Not Used
38	R180C	1256.8	1.40	0.3,0.9	"	"
39	R180A	1272.0	1.40	0.3,0.9	"	"
40	U150K001	1571.4	2.57	0.0	"	Used
41	U150K000	1579.7	2.57	0.0	"	"
42	U150L000	1685.3	2.57	0.0	"	"
43	U150L001	1697.2	2.57	0.0	"	"
44	U220C000	2298.8	2.57	0.0	"	"
45	U300I001	2949.4	2.57	0.0	"	"
46	U300I002	2964.2	2.57	0.0	"	"
47	U300G002	3389.4	2.57	0.0	"	"
48	U300G001	3400.7	2.57	0.0	"	"
49	U300G000	3469.1	2.57	0.0	"	"

C.3 Space-Time Plots

Six of the space-time plots have been presented in the main body of the thesis and the remainder are presented here. Note that for the first four cases ($Re < 268$) no space-time plots have been prepared, because, no large scale vortex motions were observed at these Re values.



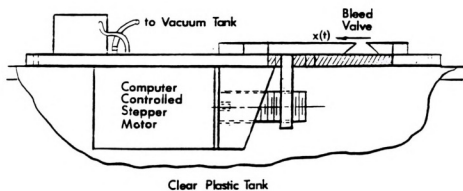
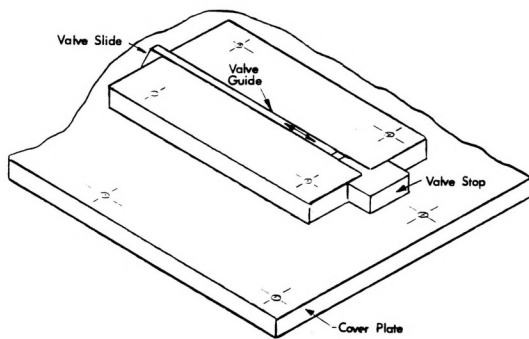
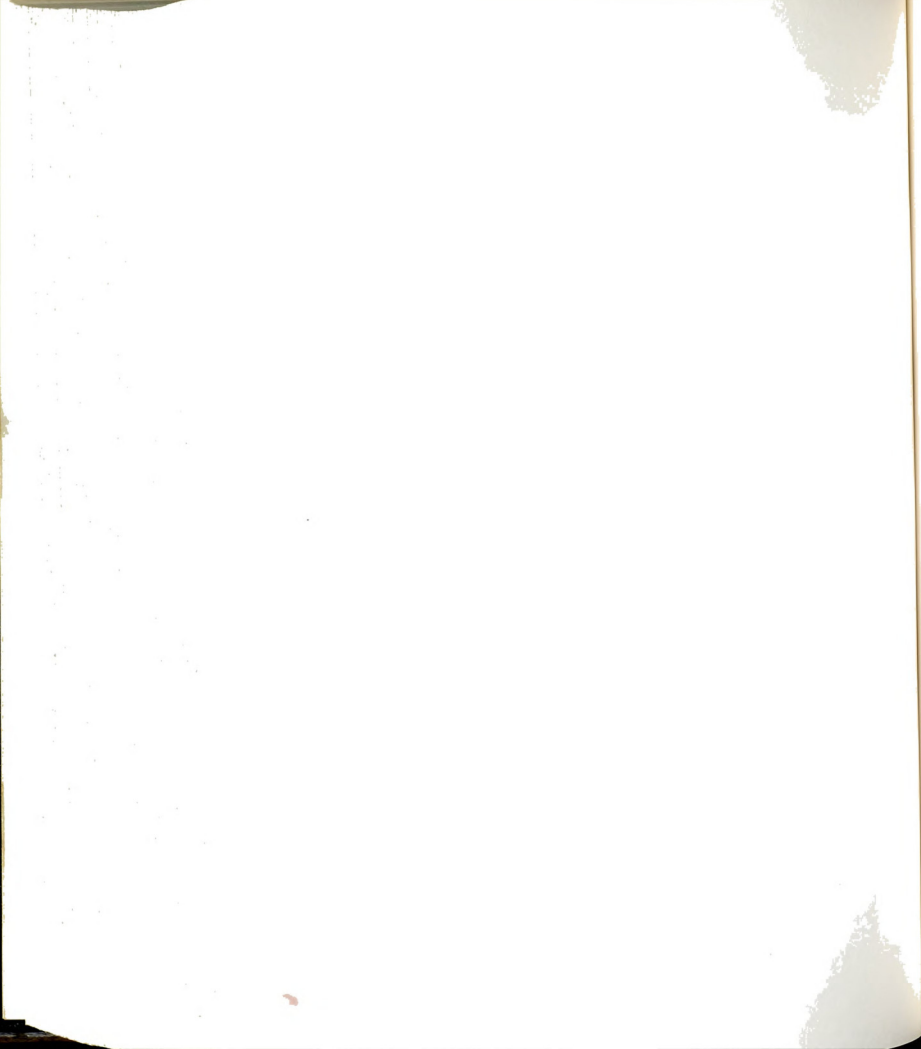


Figure A.1. Details of the mechanism for actuating the bleed valve.



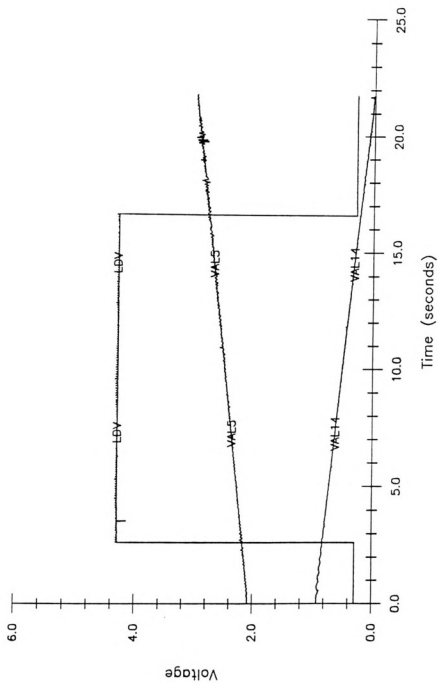
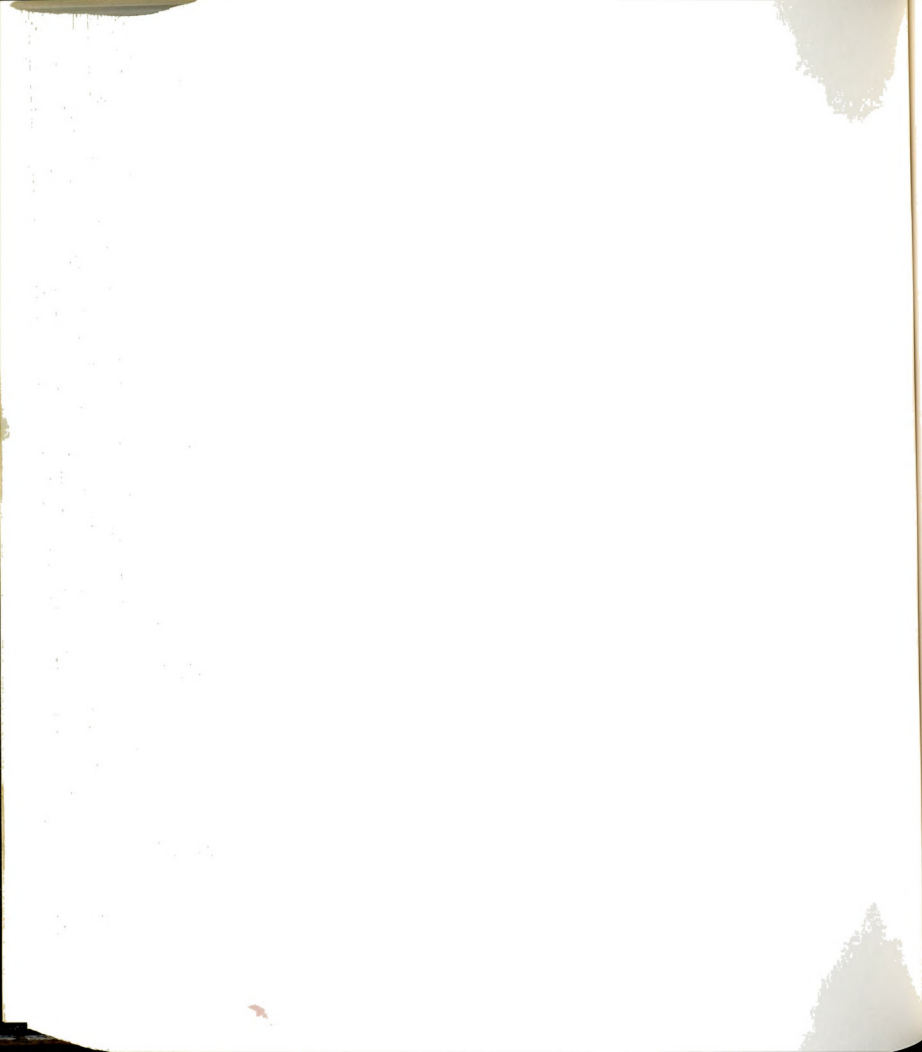


Figure B.1. Time histories of the voltages recorded during an experiment.



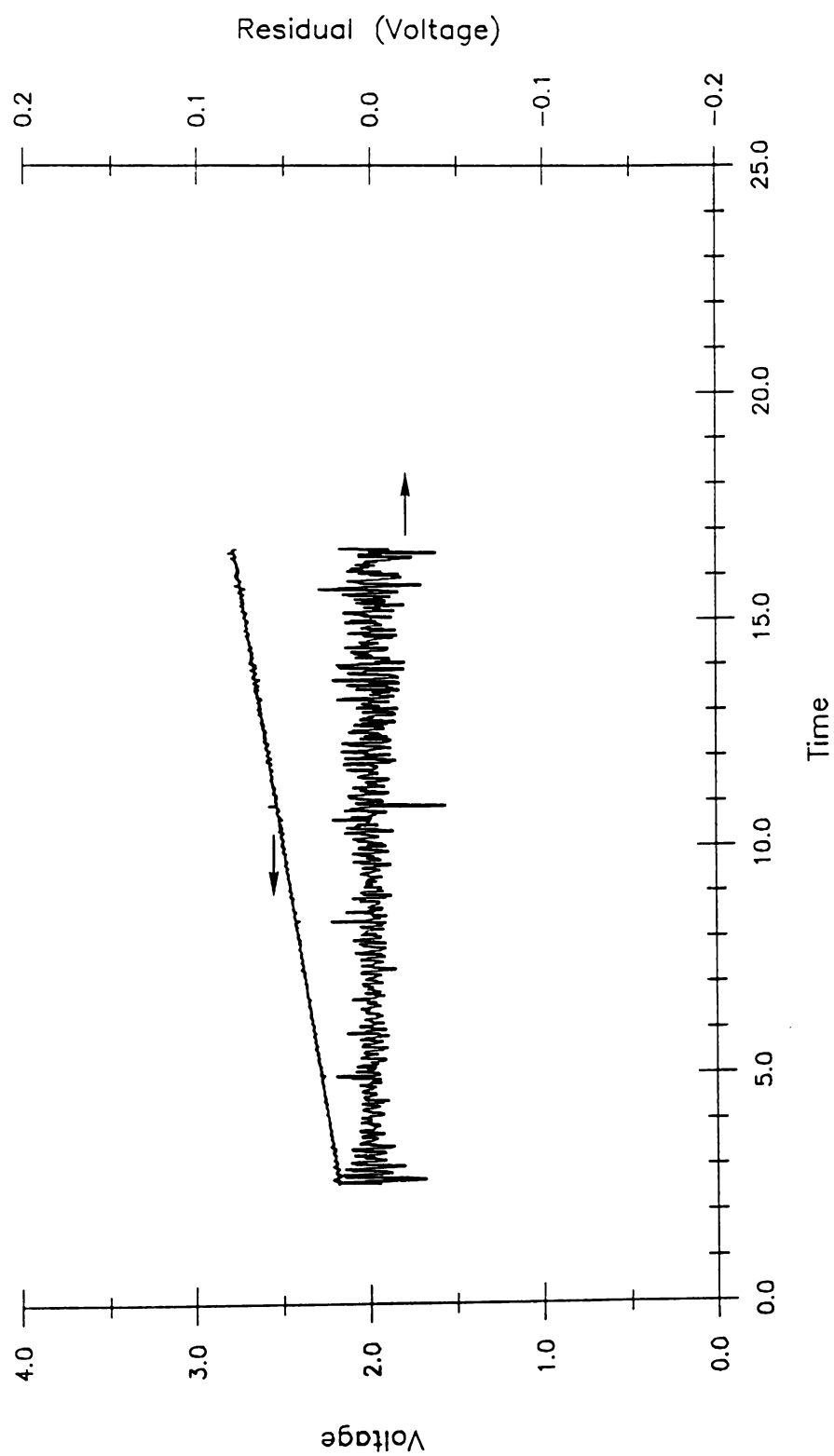


Figure B.2. An illustration of the regression of the measured voltage, $E_I(t)$, and the corresponding residual.



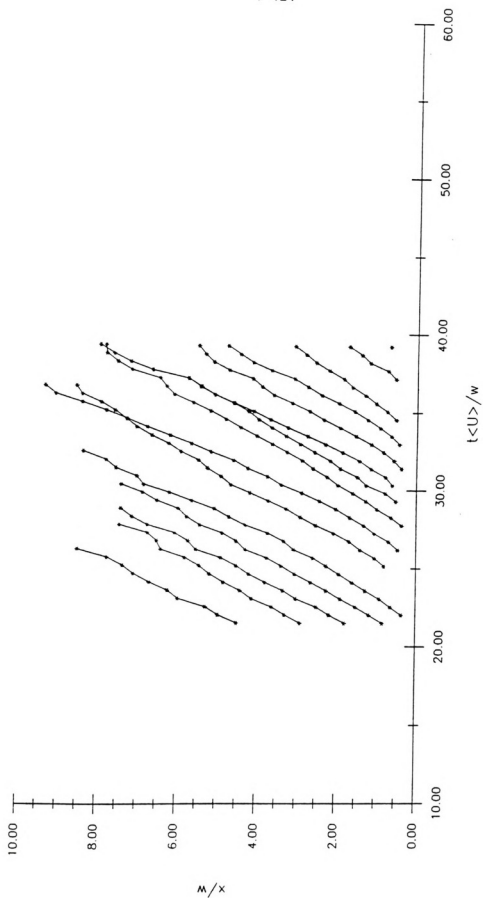
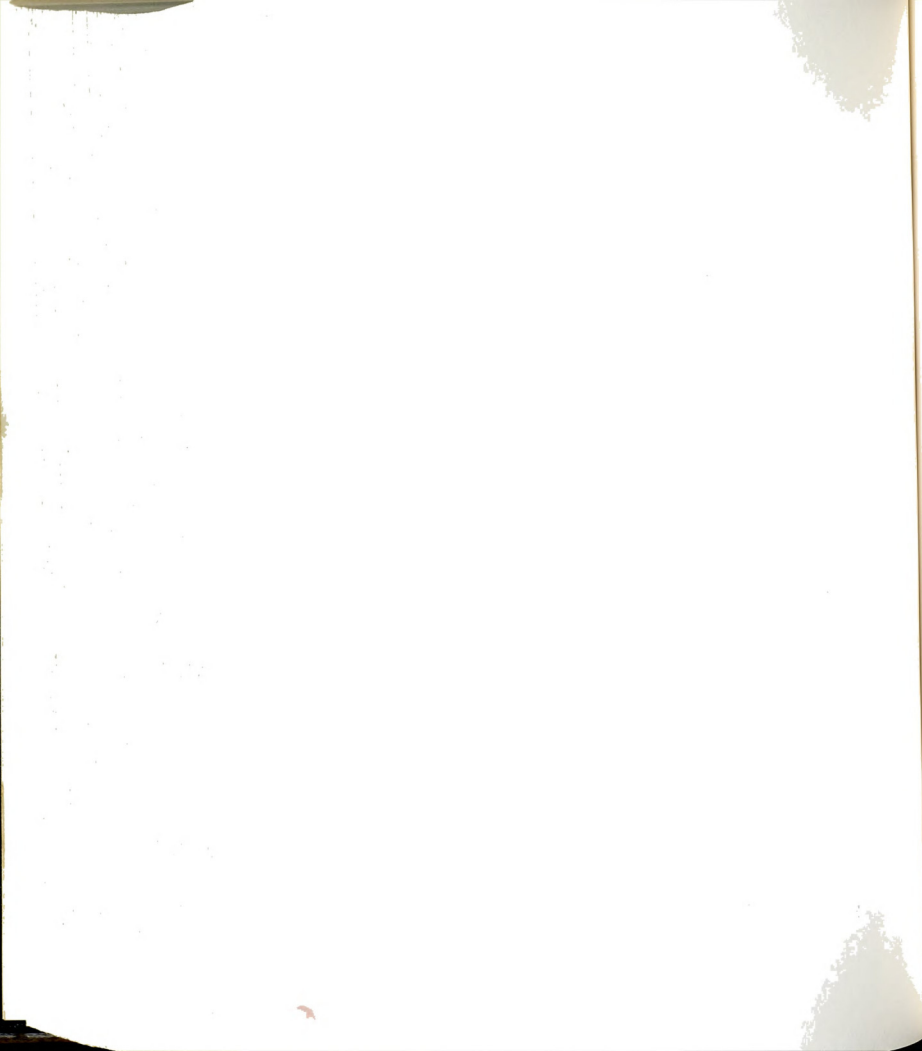


Figure C.1. Space-time plot of vortices (R040F) at $Re=269$ and $w=1.99$ cm.



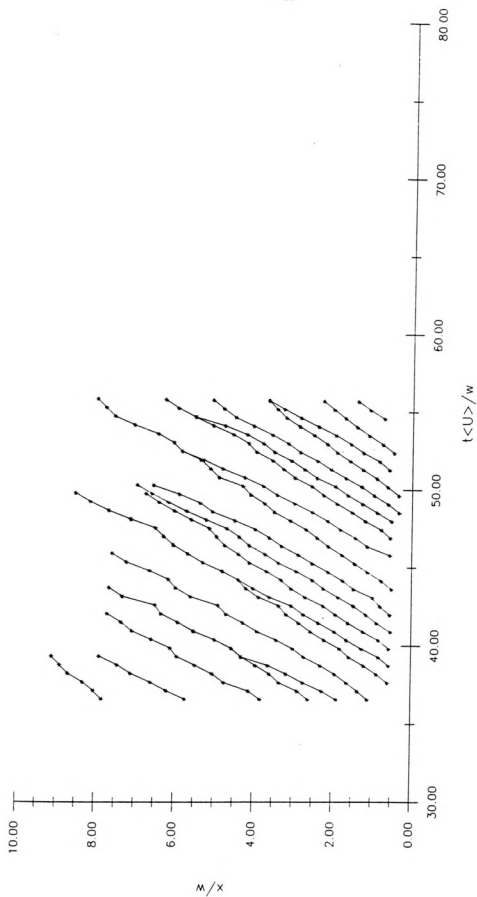
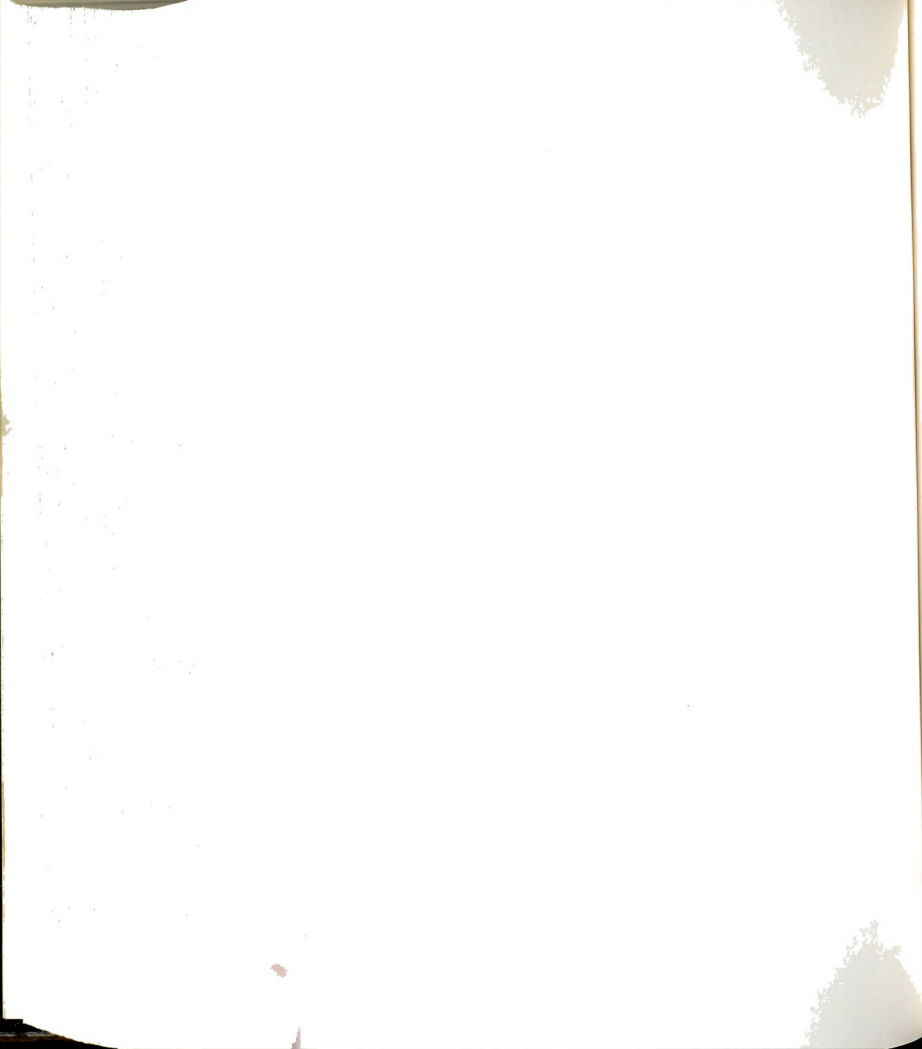


Figure C.2. Space-time plot of vortices (R040A) at $Re=276$ and $w=1.99$ cm.



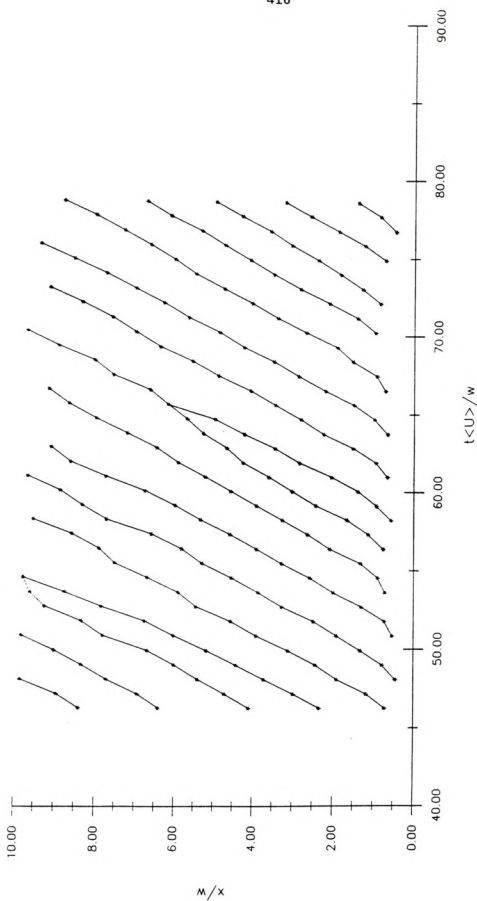
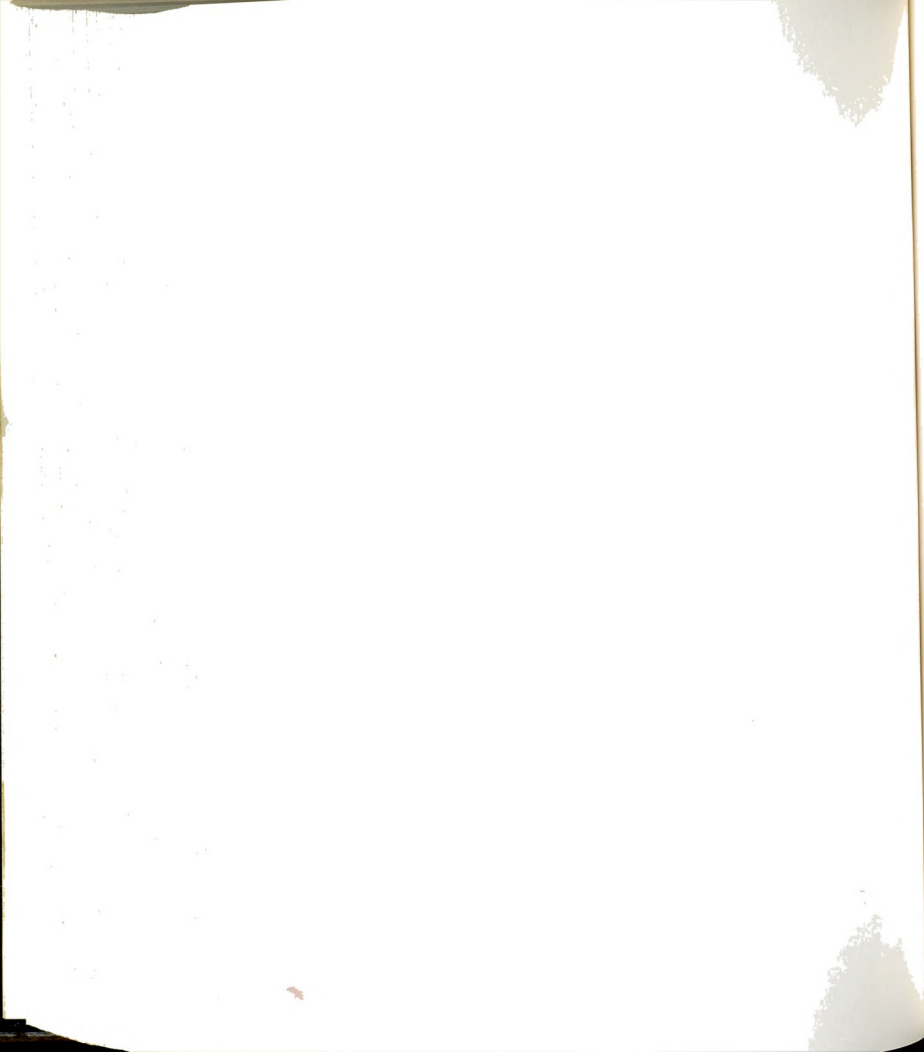


Figure C.3. Space-time plot of vortices (R040D) at $Re=277$ and $w=1.51$ cm.



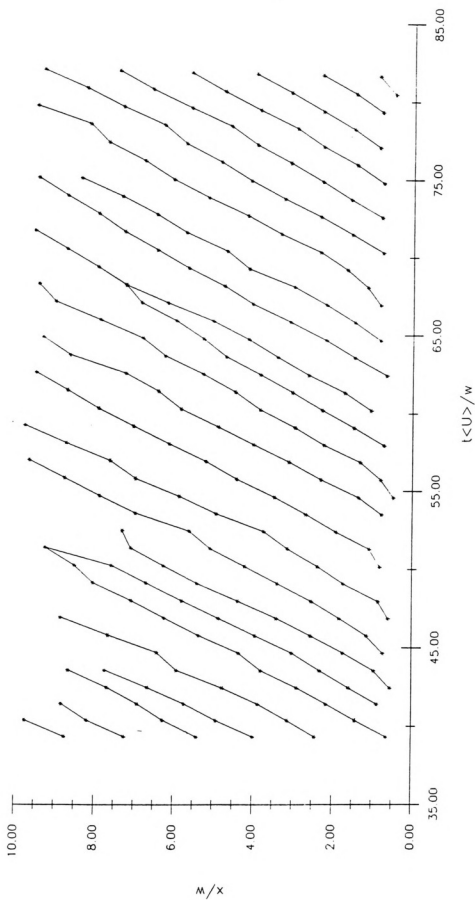


Figure C.4. Space-time plot of vortices (R040B) at Re=280 and $w=1.51$ cm.



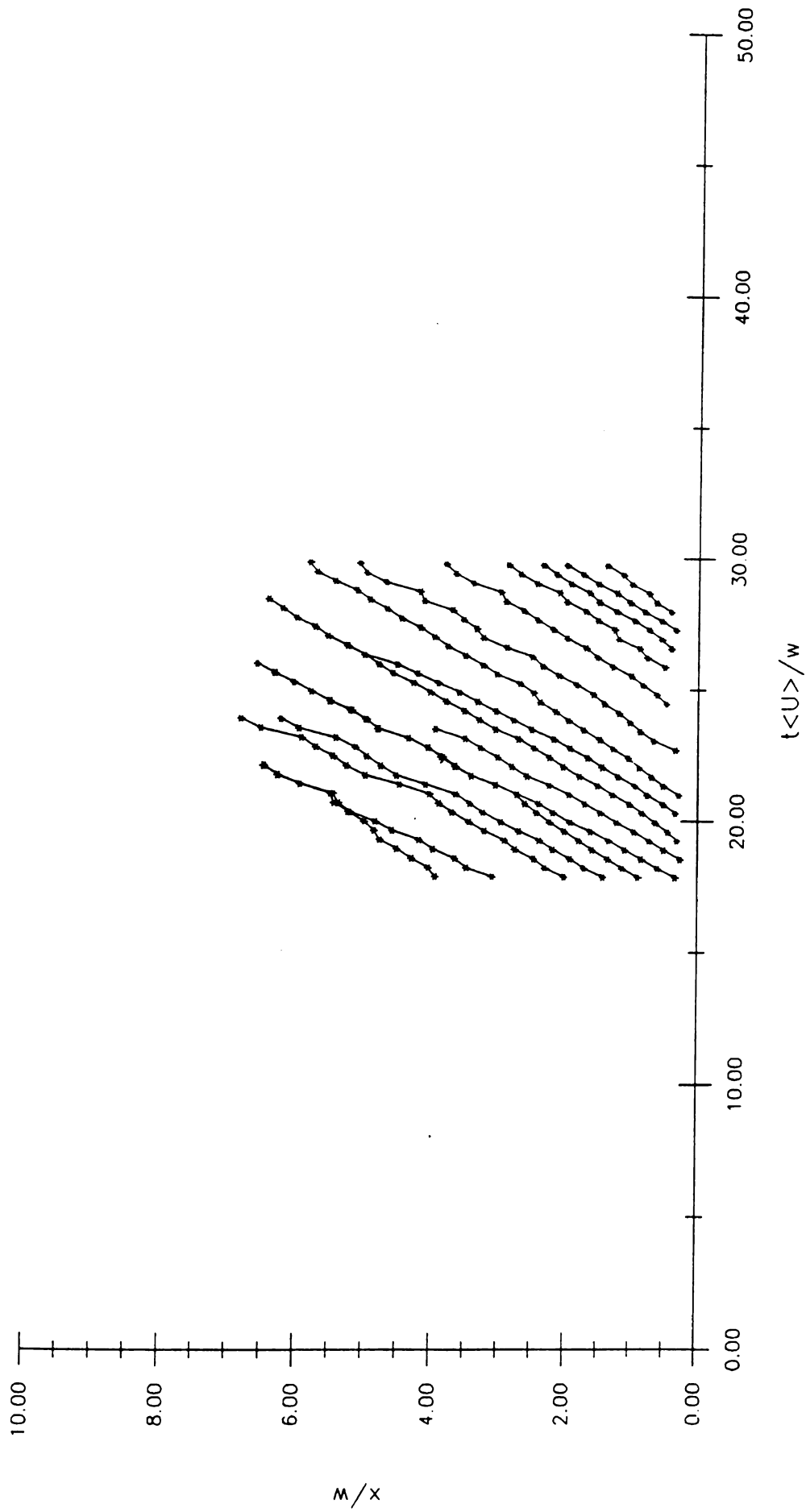
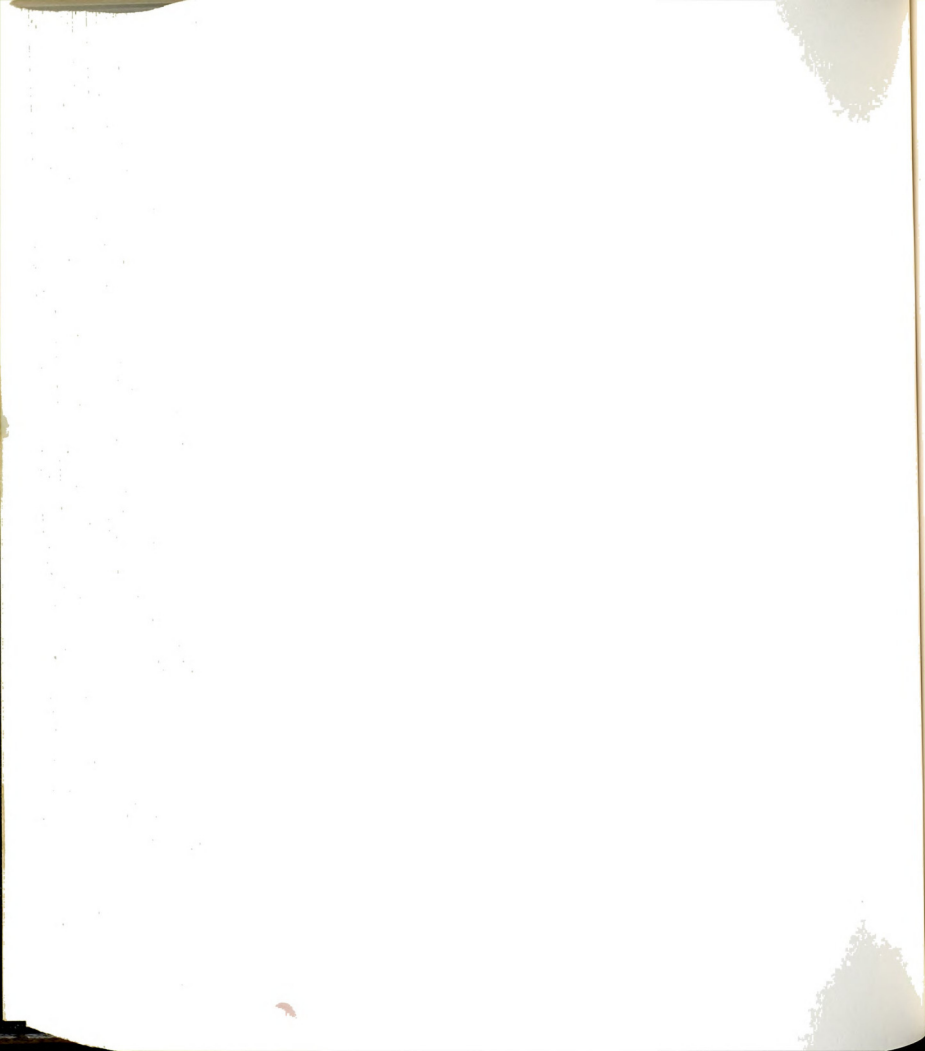


Figure C.5. Space-time plot of vortices (R040I) at $Re=285$ and $w=2.63$ cm.



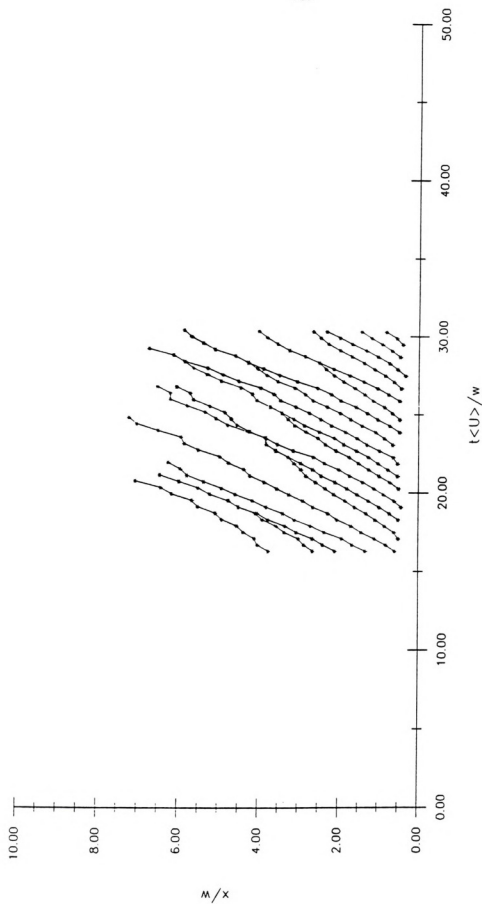


Figure C. 6. Space-time plot of vortices (R060I) at Re=361 and $w=2.63$ cm.



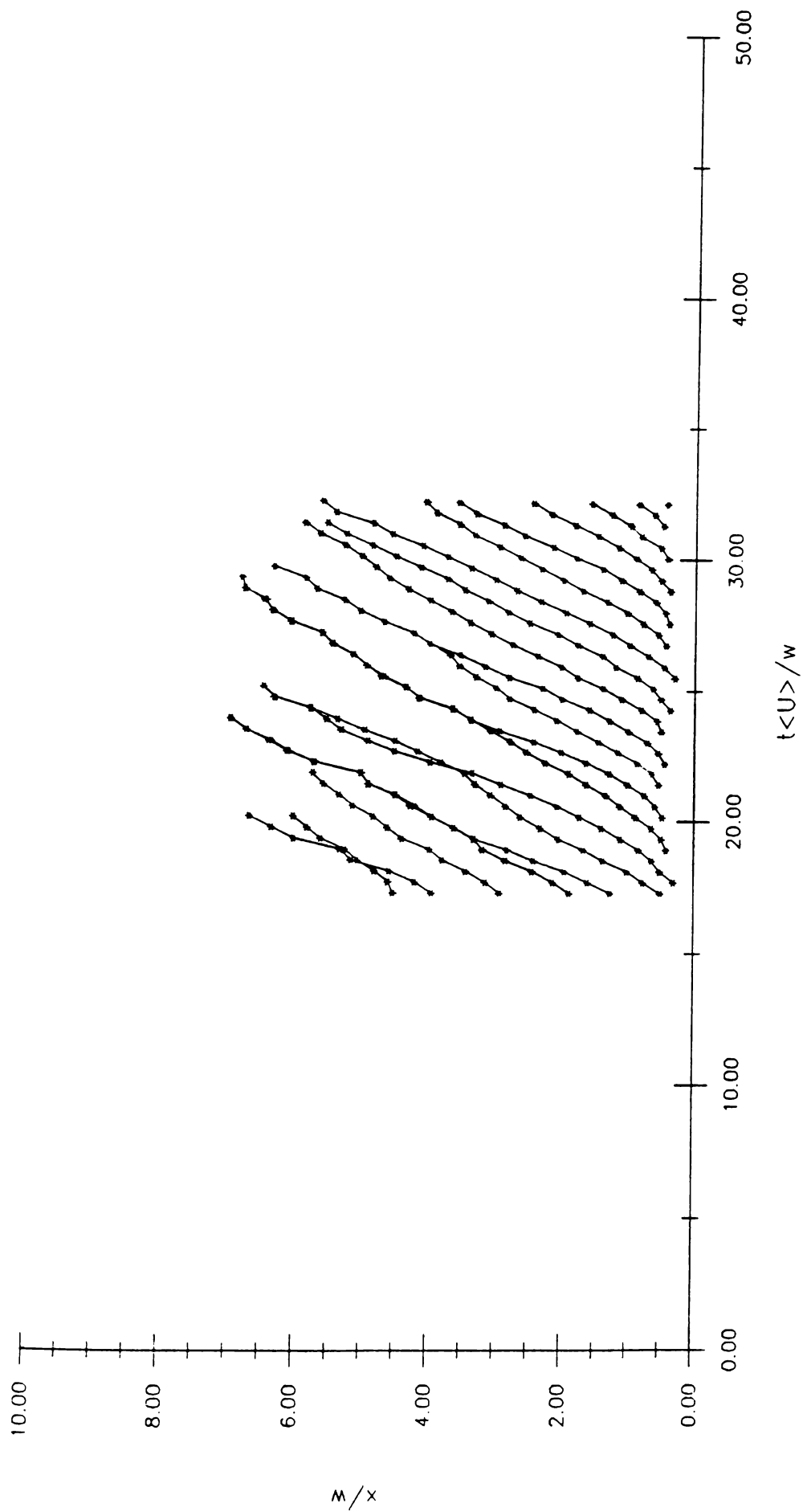
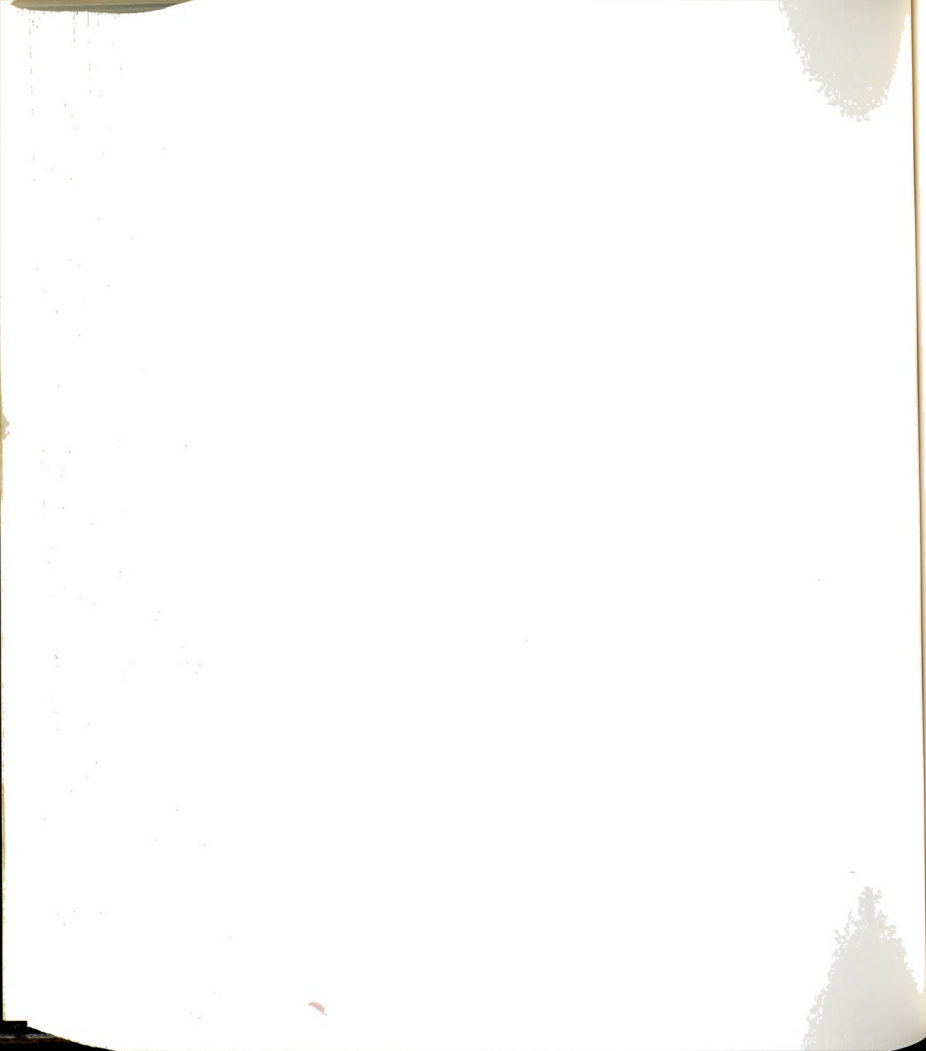


Figure C.7. Space-time plot of vortices (R060H) at $Re=373$ and $w=2.63$ cm.



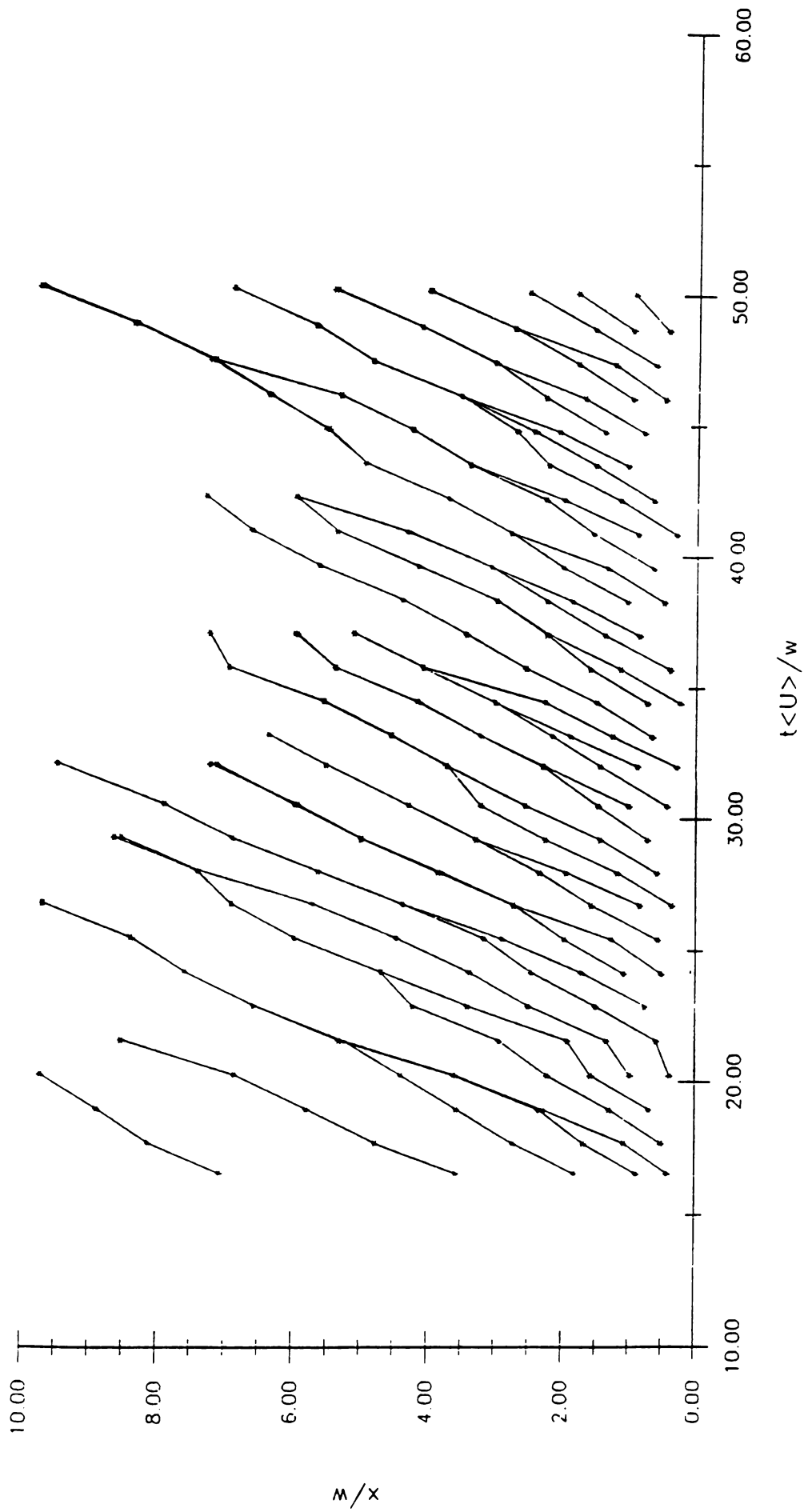
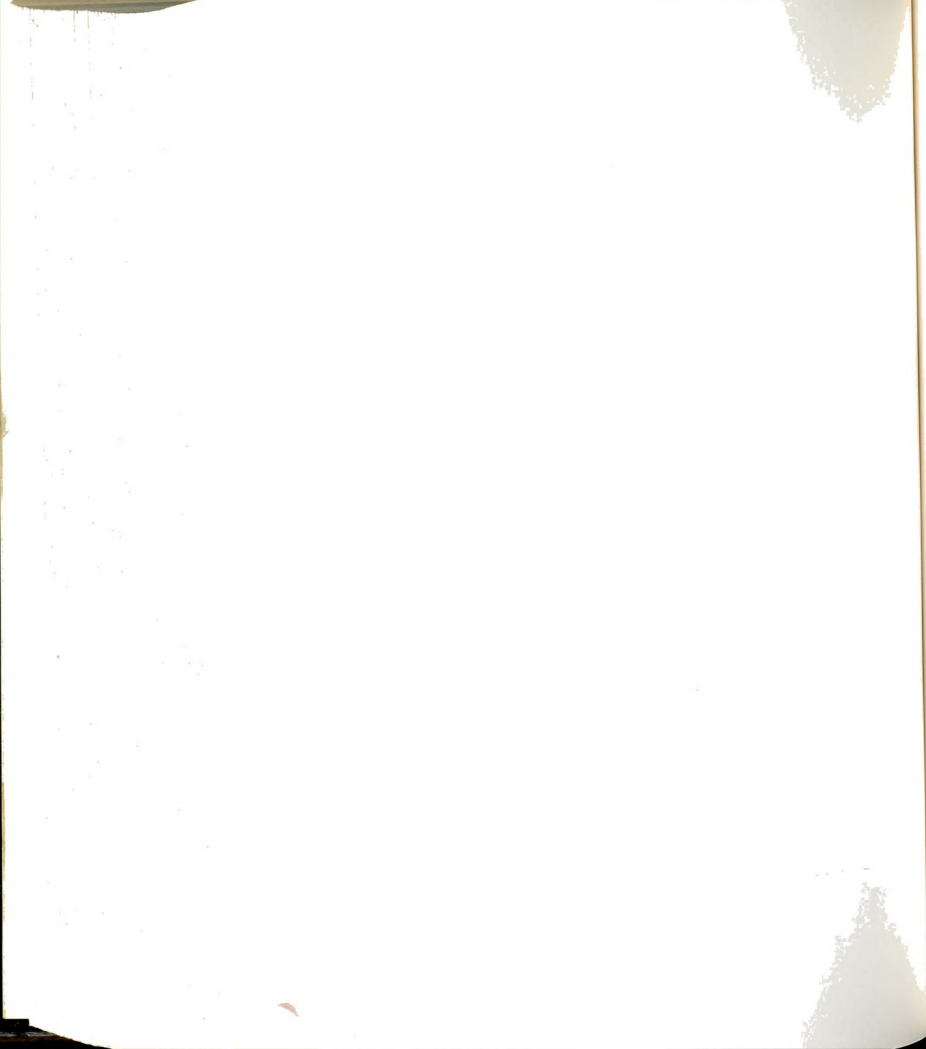


Figure C.8. Space-time plot of vortices (R090P) at $Re=396$ and $w=1.40$ cm.



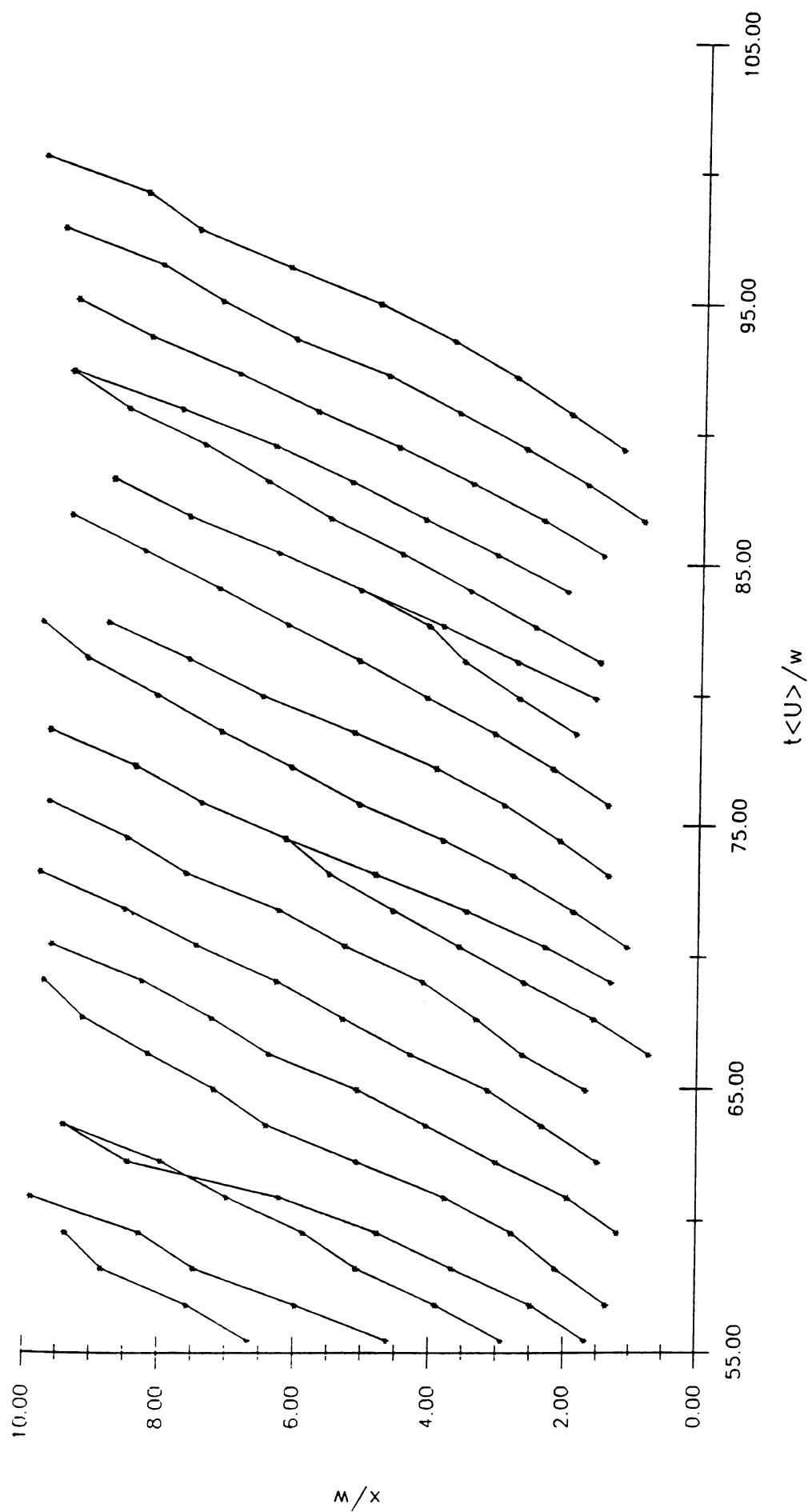


Figure C.9. Space-time plot of vortices (R060E) at $Re=407$ and $w=1.51$ cm.



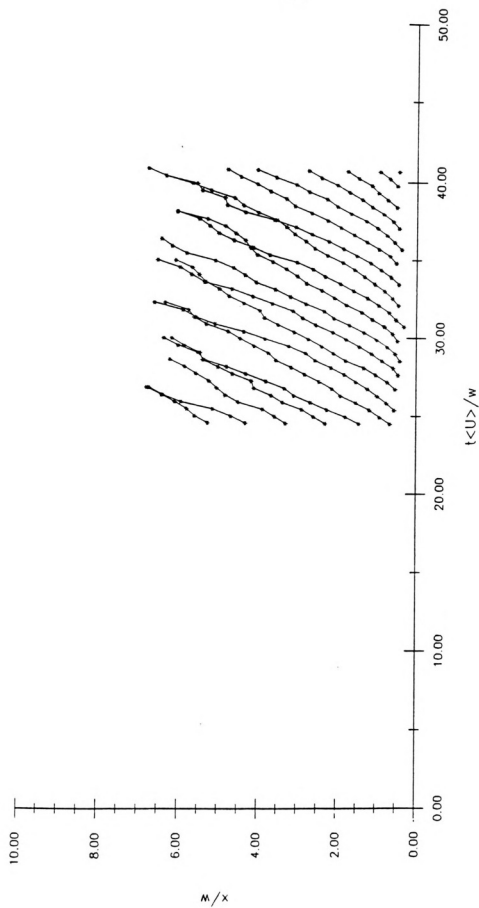


Figure C.10. Space-time plot of vortices (R060G) at $Re=408$ and $w=2.63$ cm.



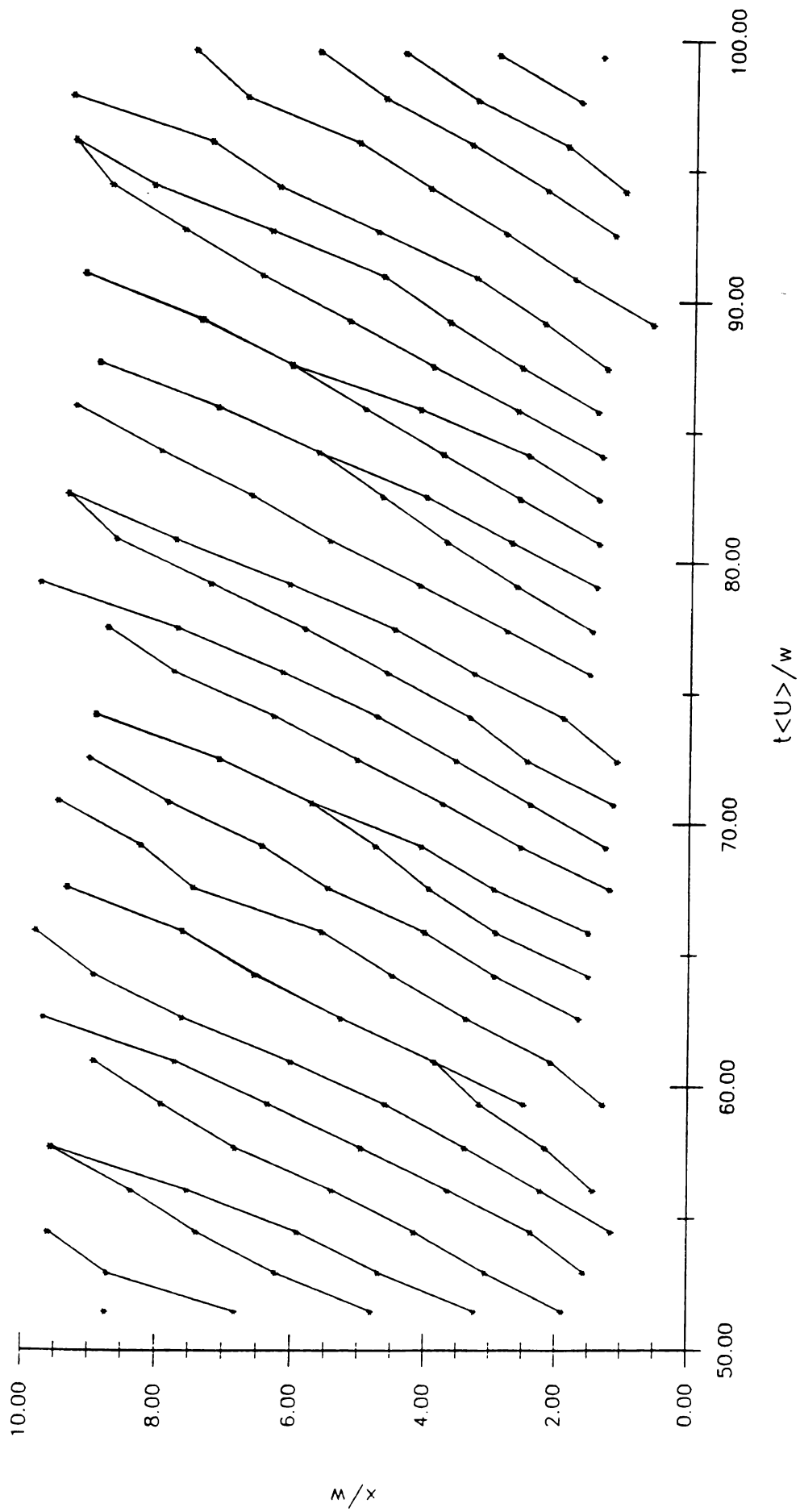


Figure C.11. Space-time plot of vortices (R060B) at $Re=412$ and $w=1.51$ cm.



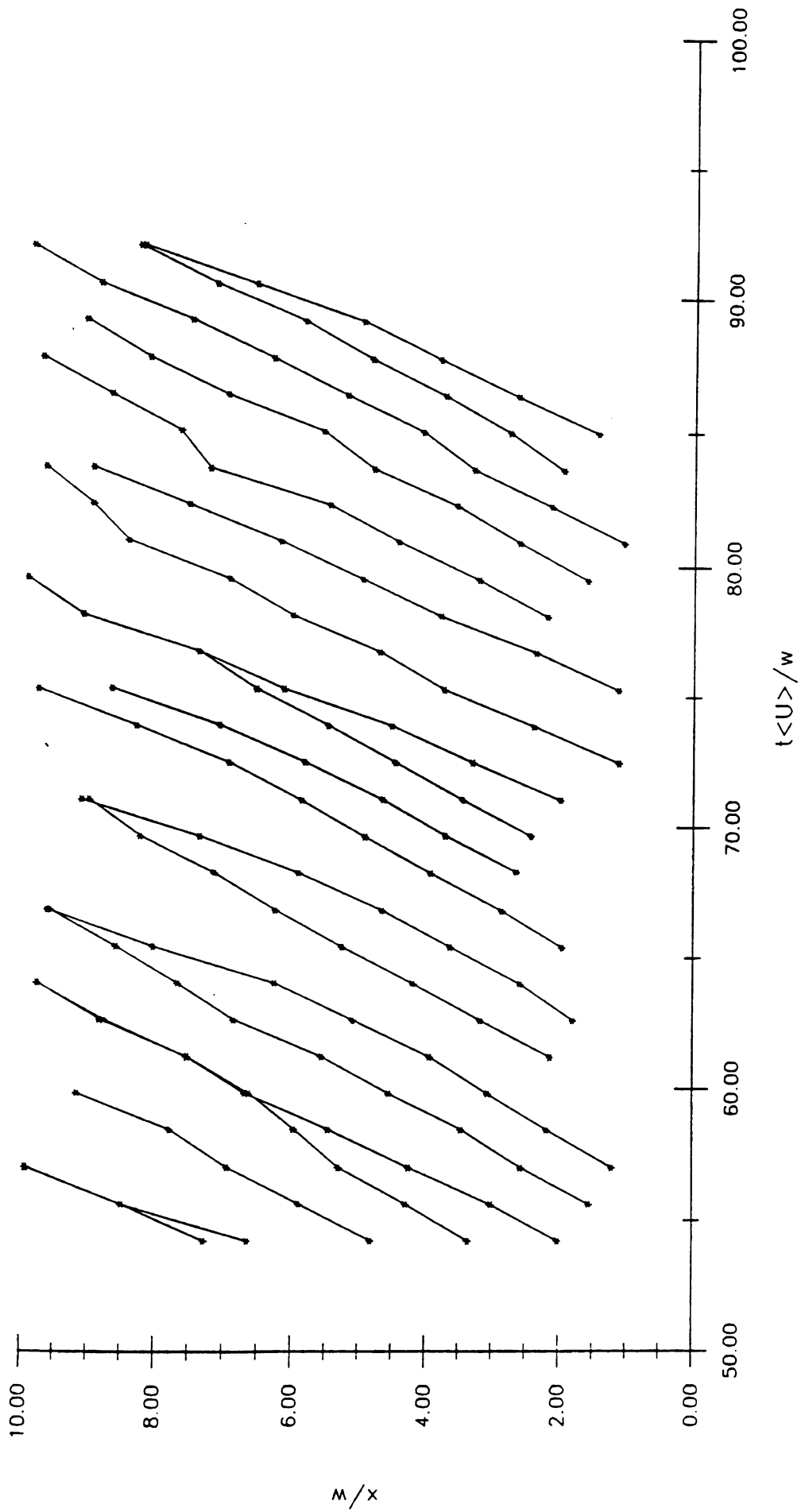
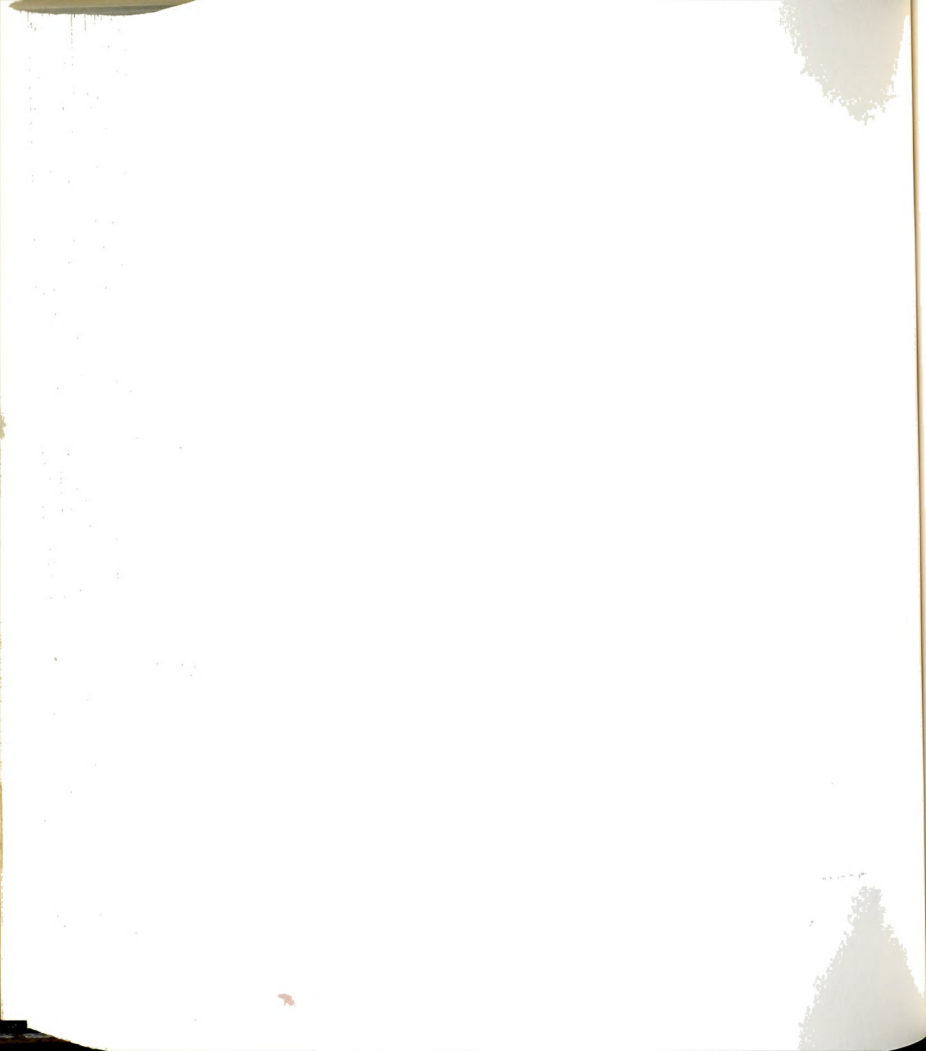


Figure C.12. Space-time plot of vortices (R060D) at $Re=421$ and $w=1.51$ cm.



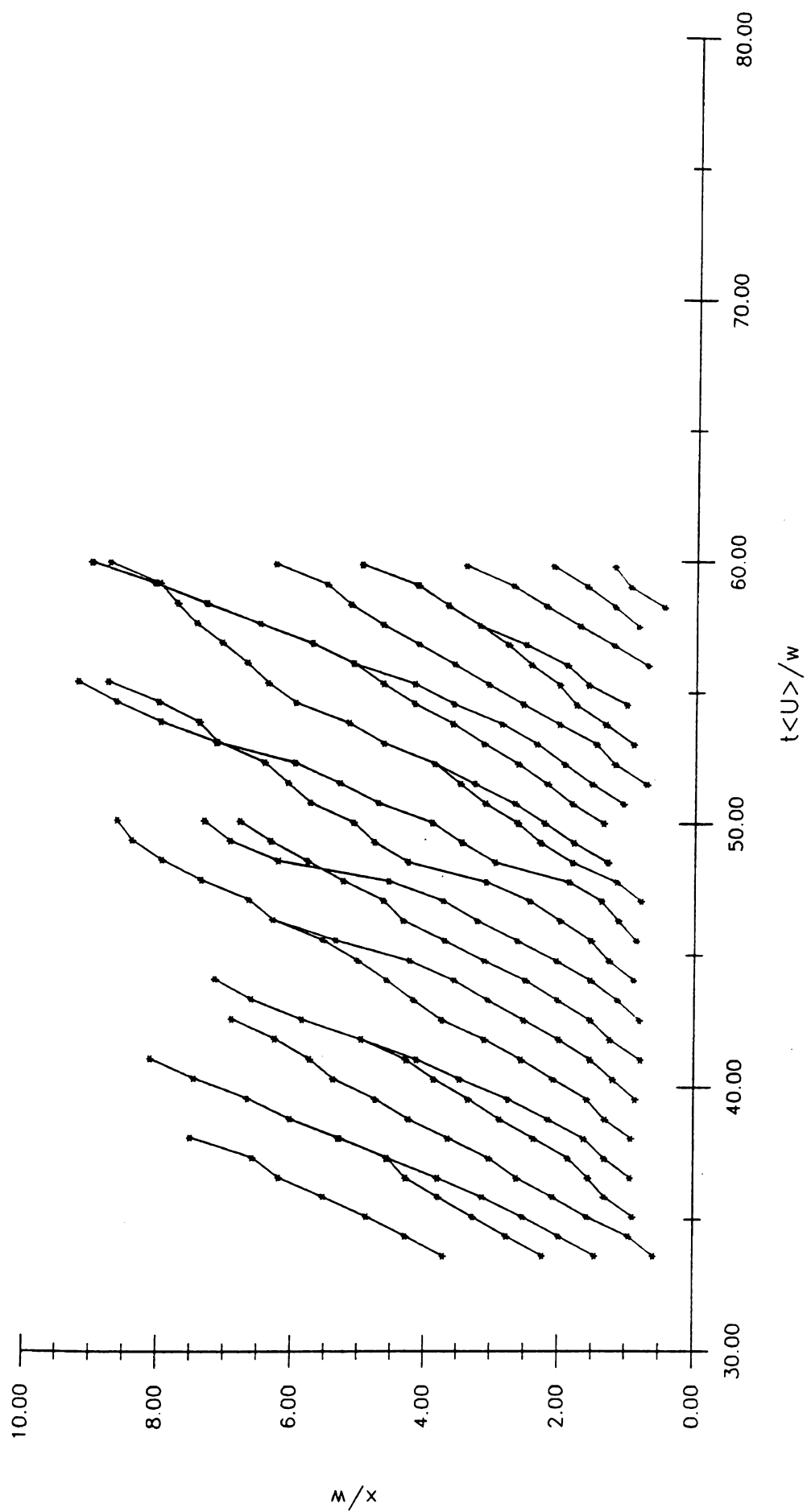


Figure C.13. Space-time plot of vortices (R060A) at $Re=423$ and $w=1.99$ cm.



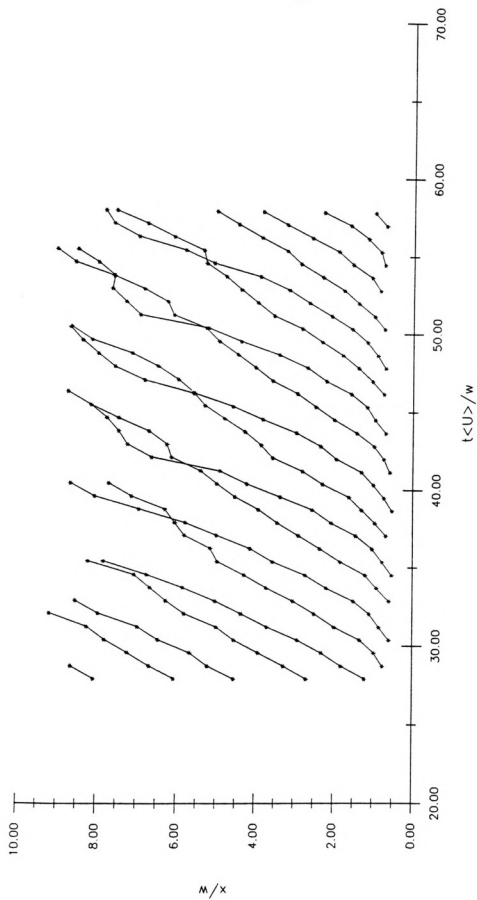


Figure C.14. Space-time plot of vortices (R060F) at $Re=426$ and $w=1.99$ cm.



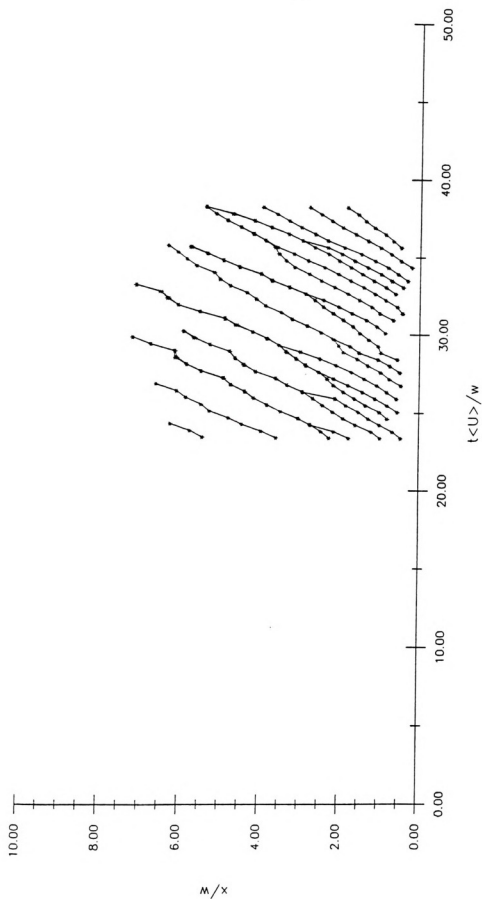
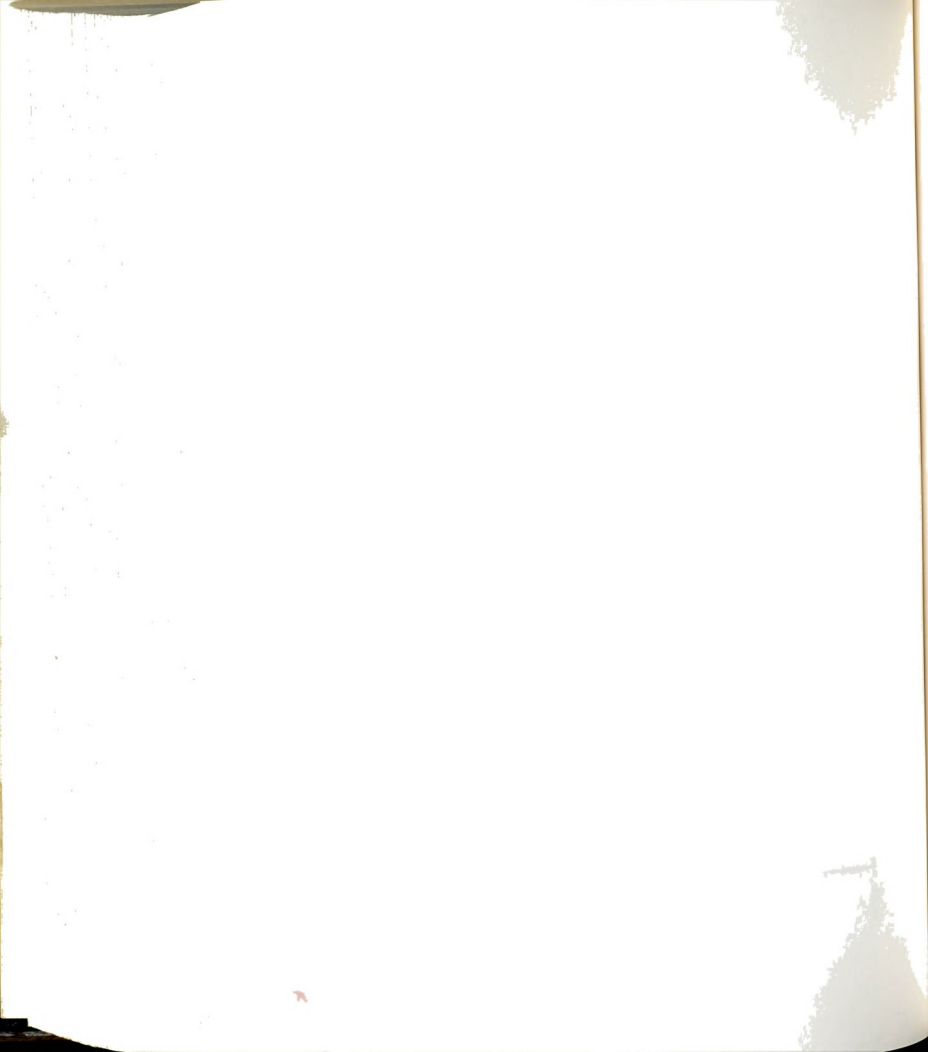


Figure C.15. Space-time plot of vortices (R090V) at Re=510 and $w=1.40$ cm.



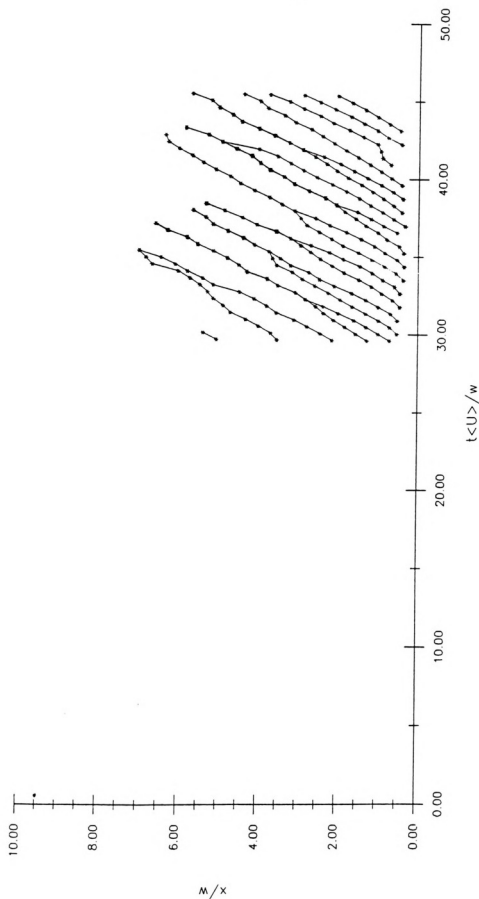
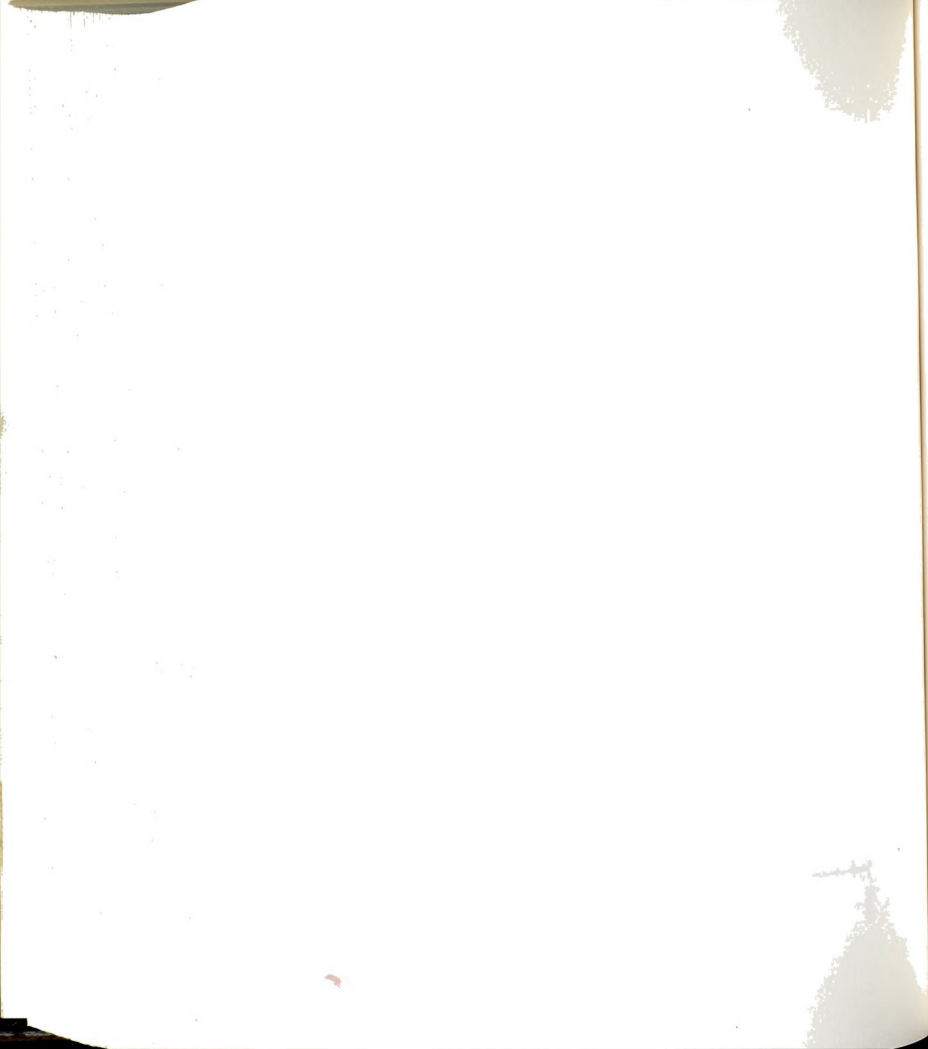


Figure C.16. Space-time plot of vortices (R090U) at $Re=525$ and $w=1.40$ cm.



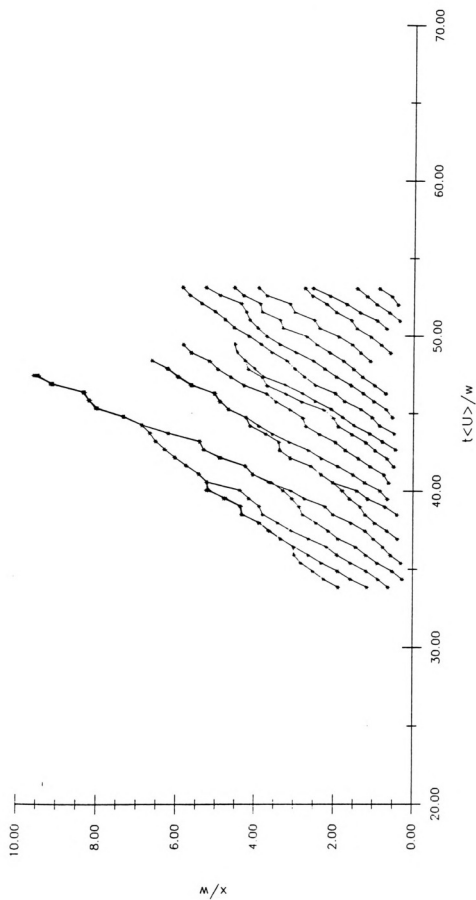
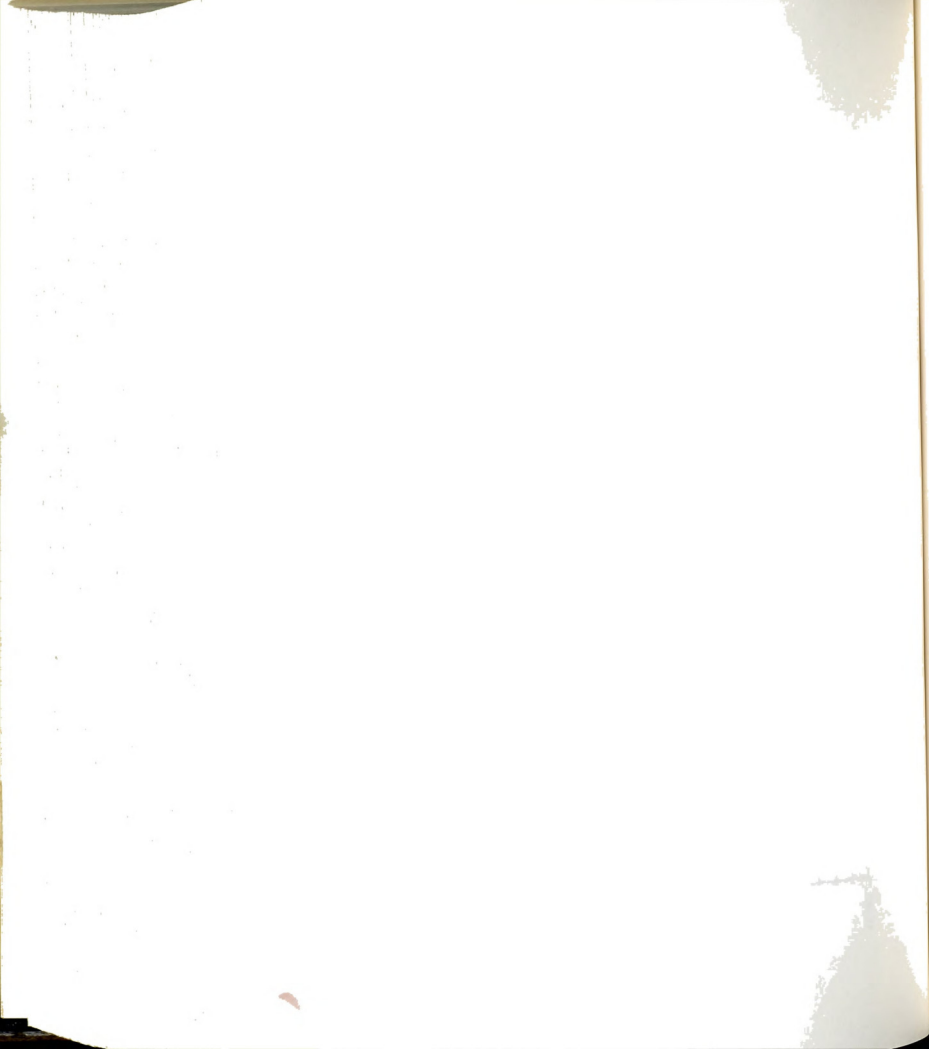


Figure C.17. Space-time plot of vortices (R090R) at $Re=640$ and $w=1.40$ cm.



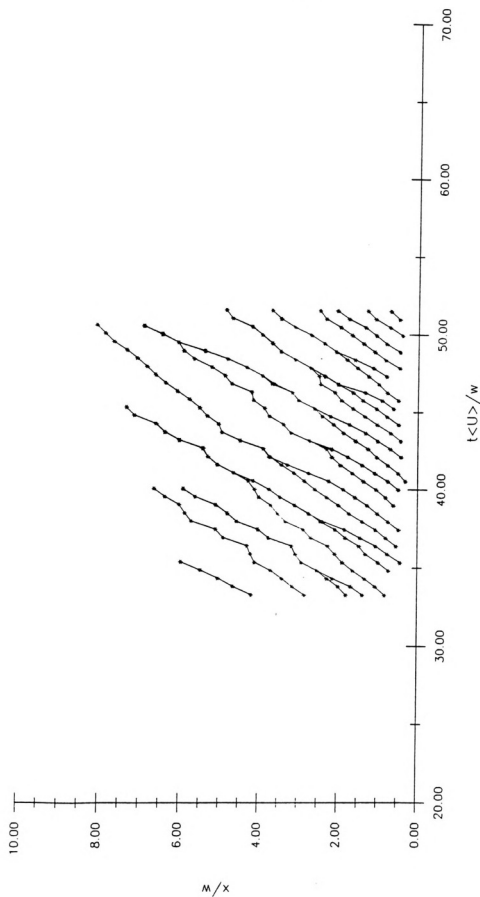
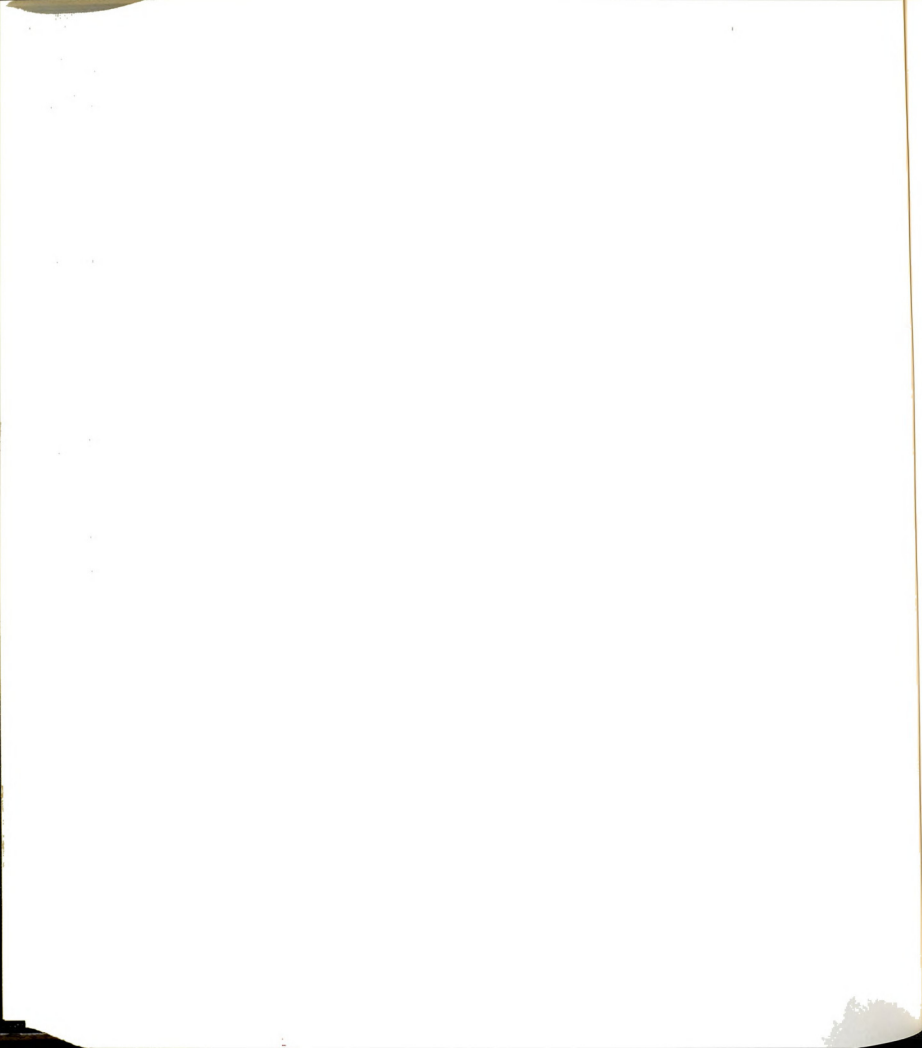


Figure C.18. Space-time plot of vortices (R090S) at $Re=640$ and $w=1.40$ cm.



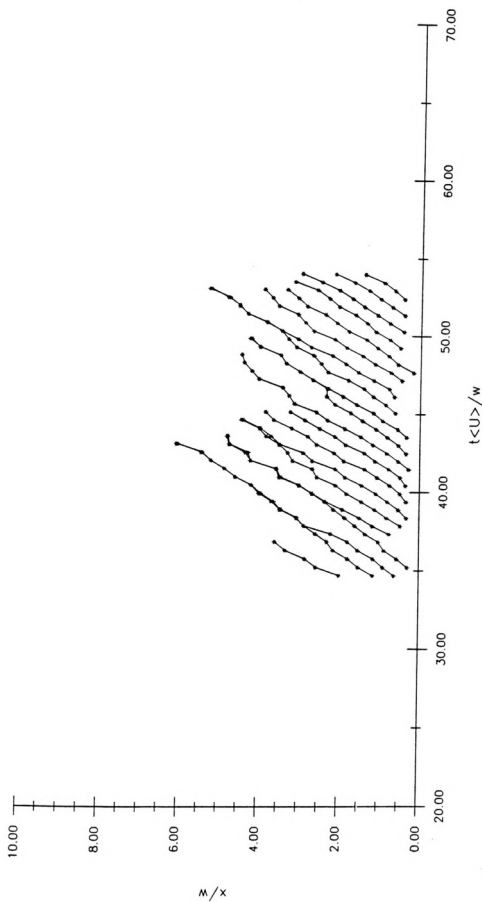
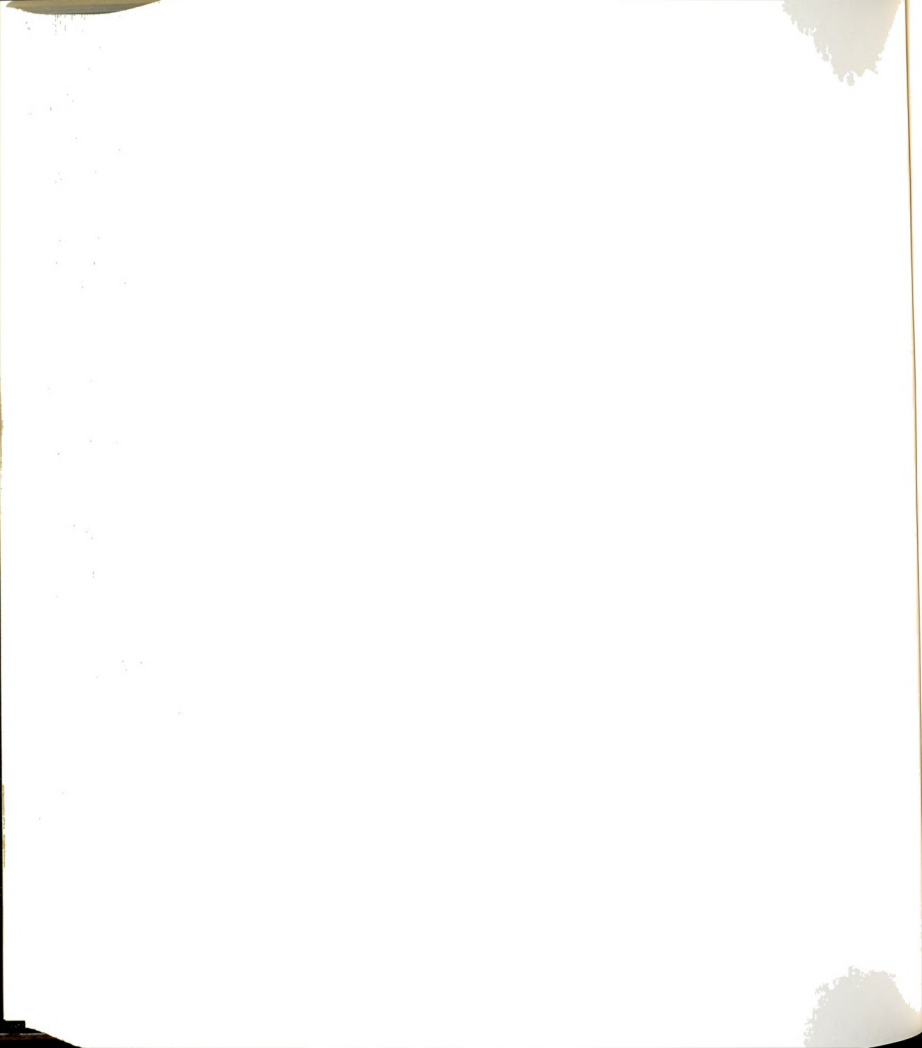


Figure C.19. Space-time plot of vortices (R090T) at $Re=640$ and $w=1.40$ cm.



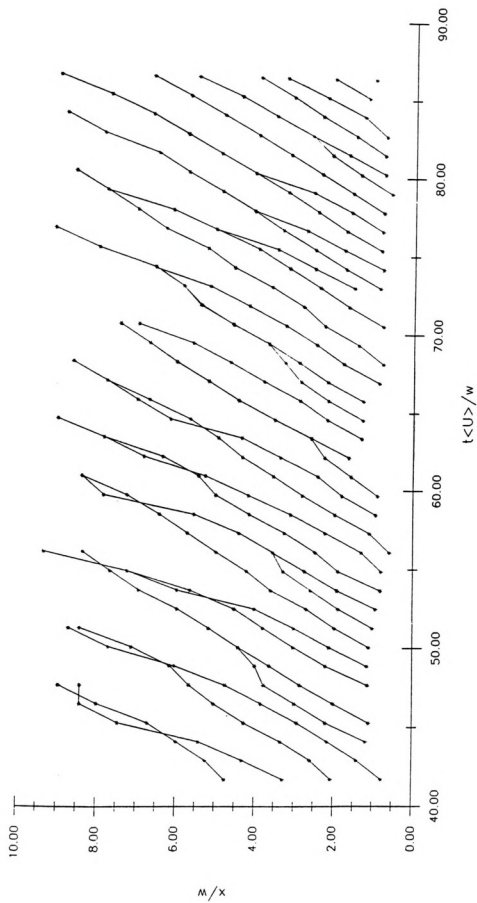
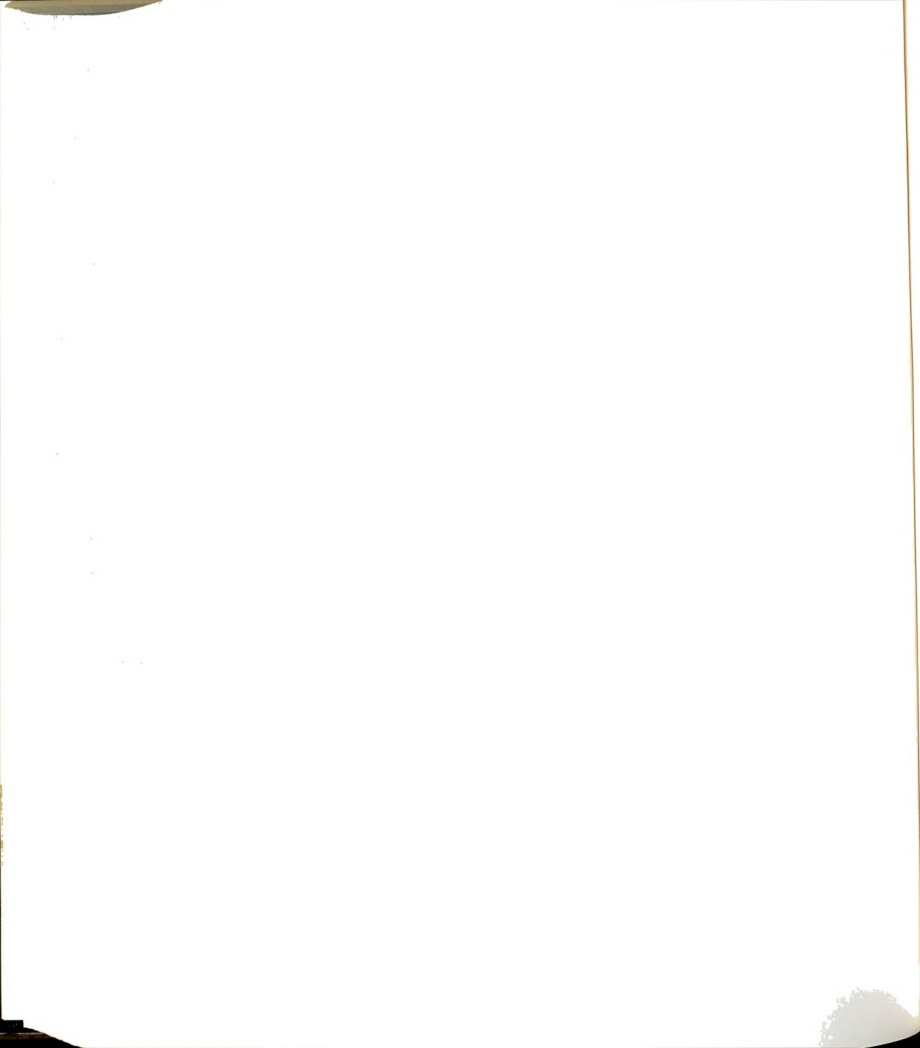


Figure C.20. Space-time plot of vortices (R100C) at $Re=679$ and $w=1.99$ cm.



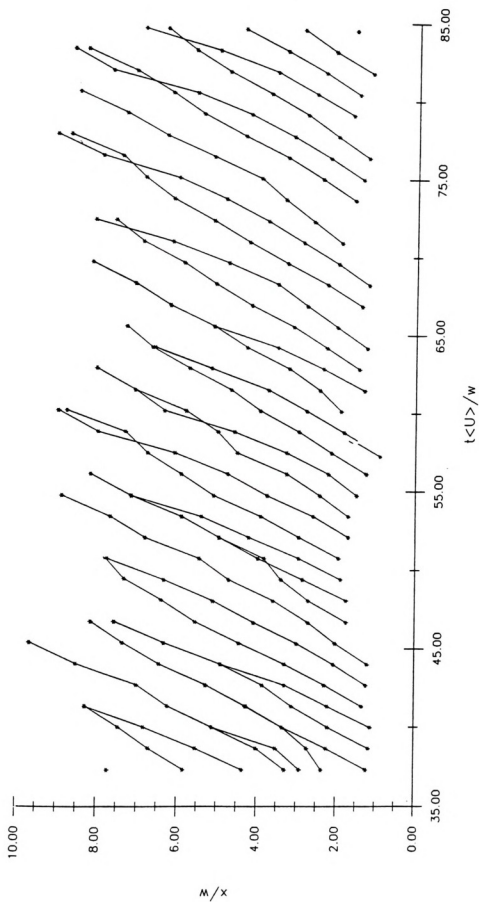
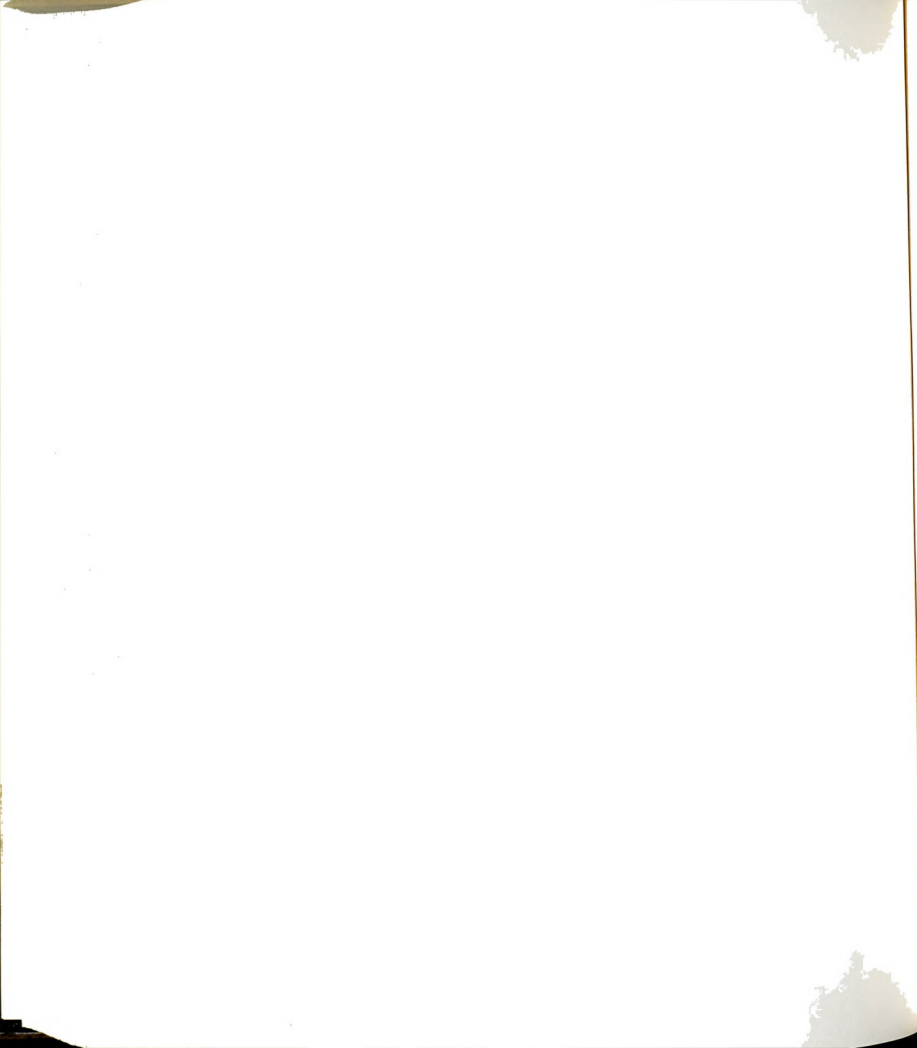


Figure C.21. Space-time plot of vortices (R100D) at $Re=698$ and $w=1.99$ cm.



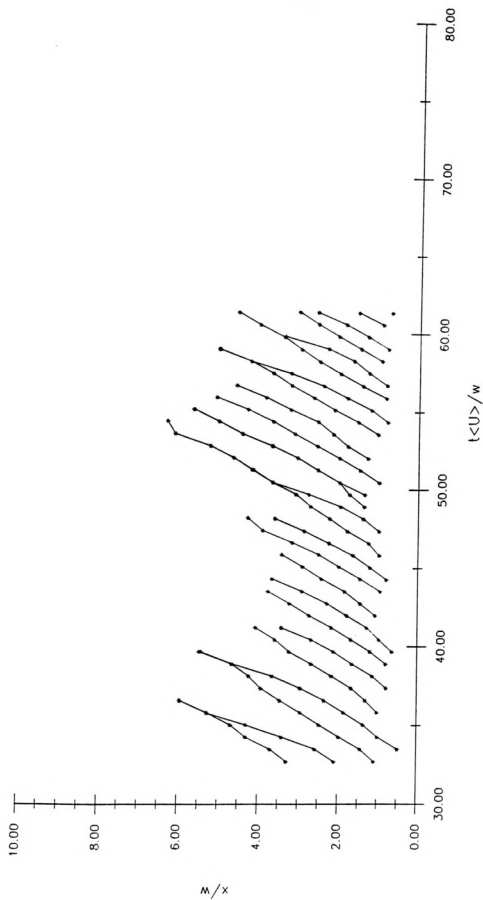
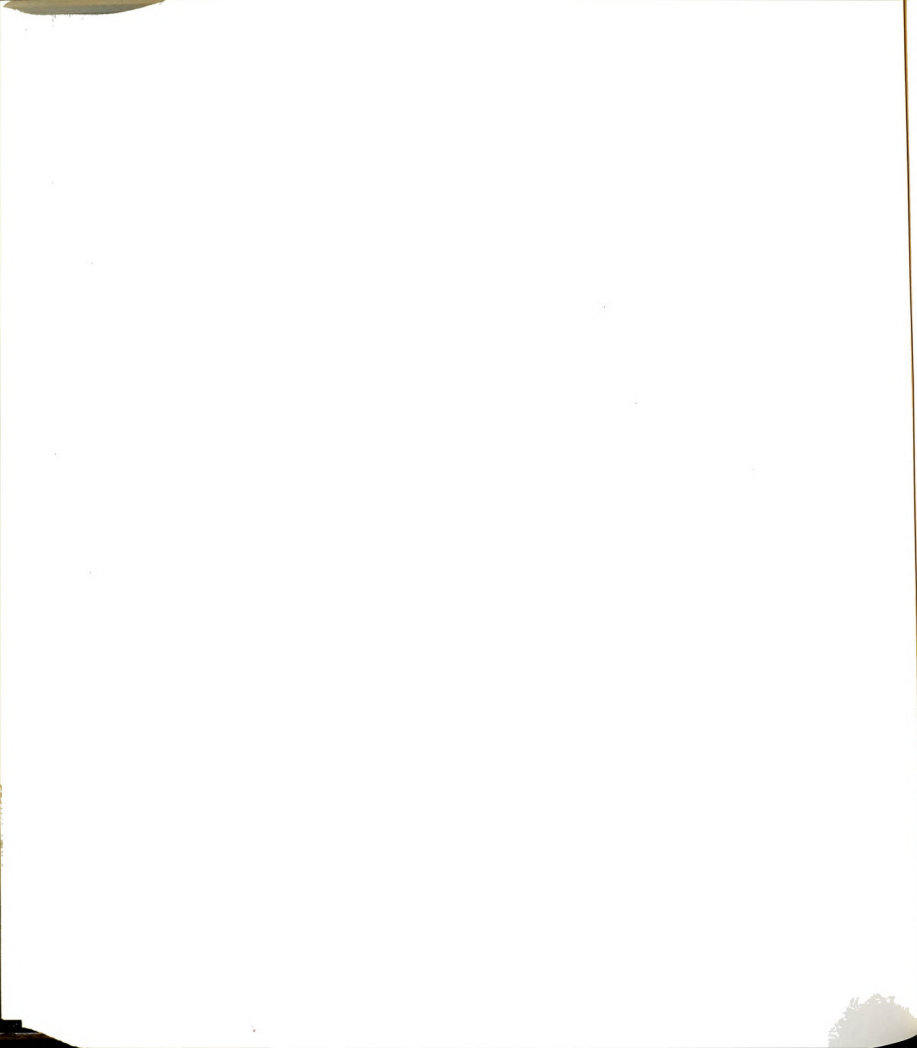


Figure C.22. Space-time plot of vortices (R180E) at $Re=930$ and $w=1.40$ cm.



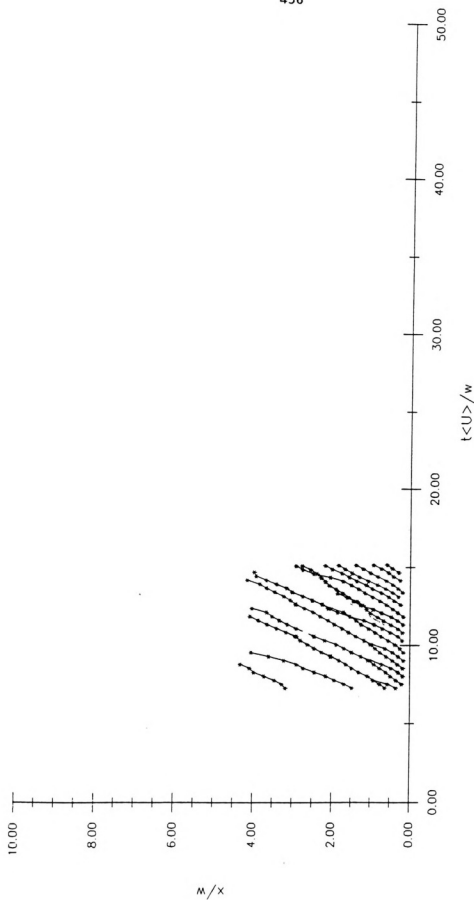
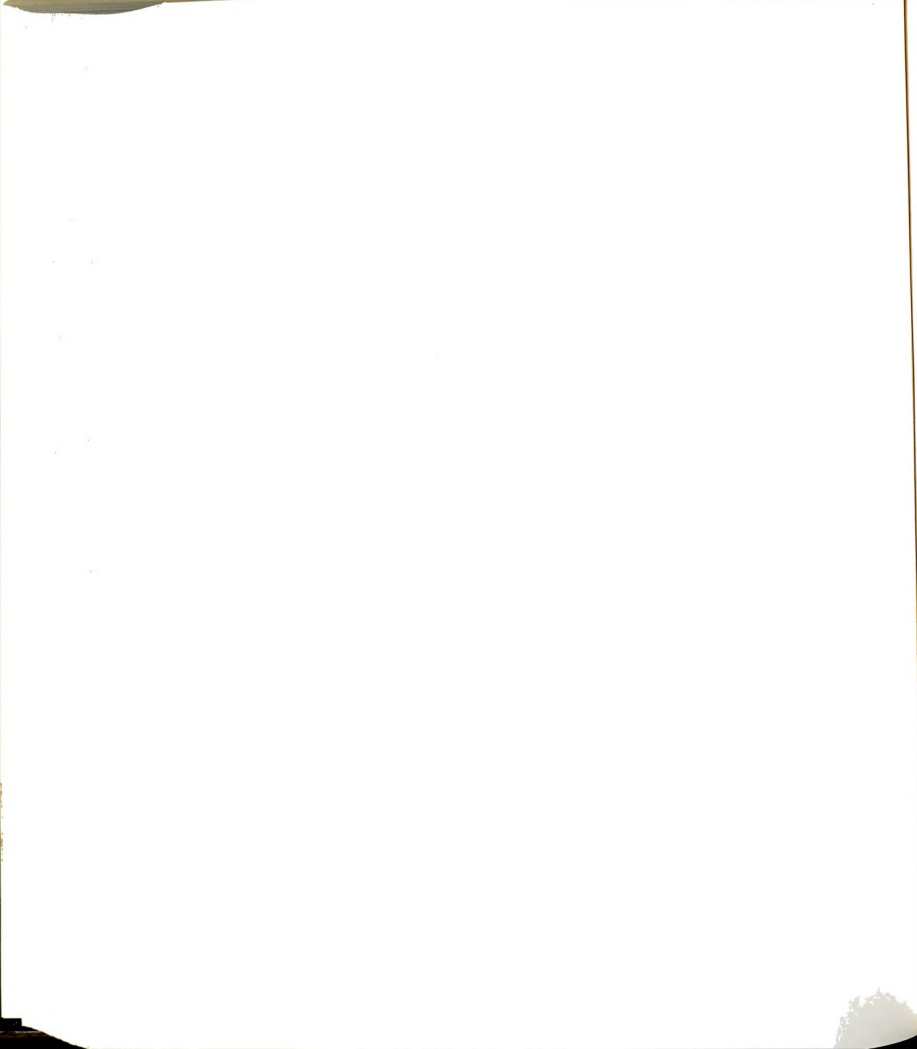


Figure C.23. Space-time plot of vortices (U090A000) at $Re=1001$ and $w=2.57$ cm.



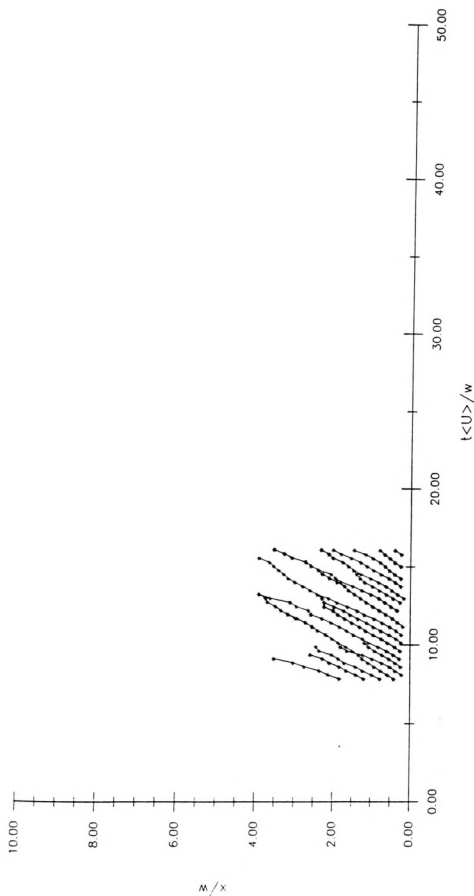
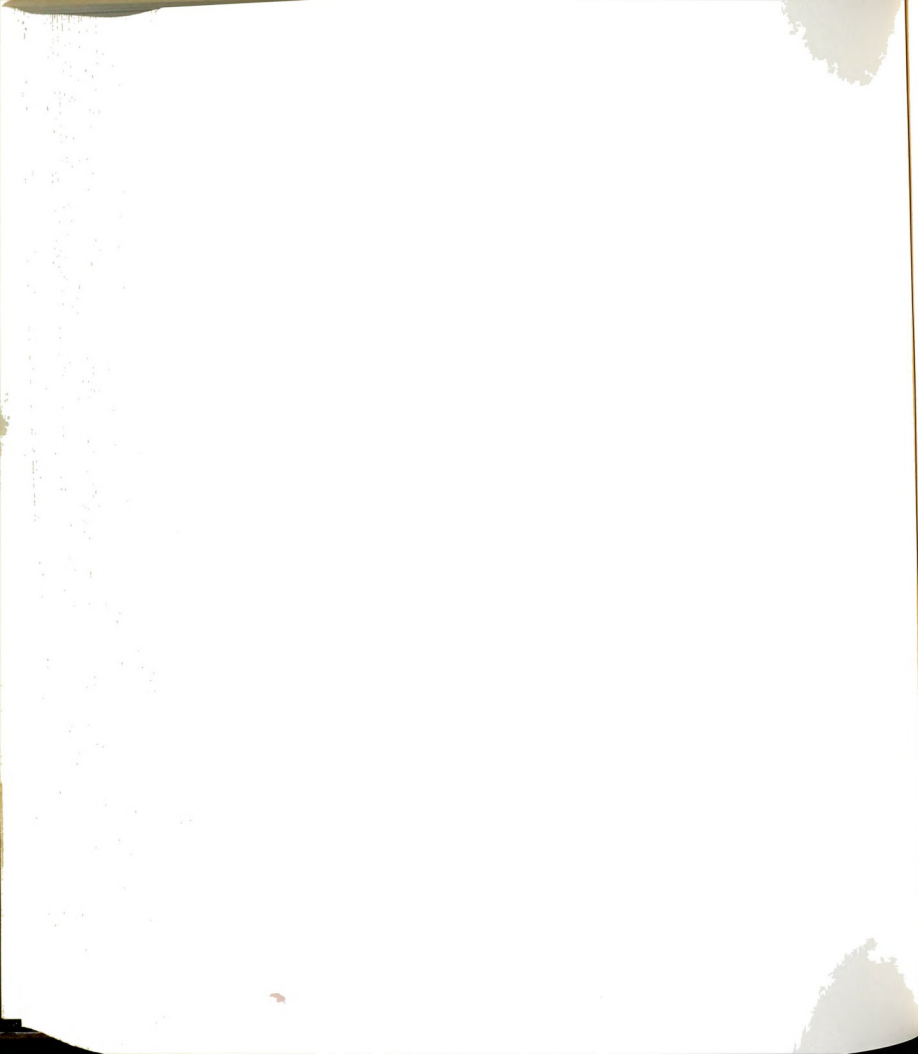


Figure C.24. Space-time plot of vortices (U090A001) at $Re=1004$ and $w=2.57$ cm.



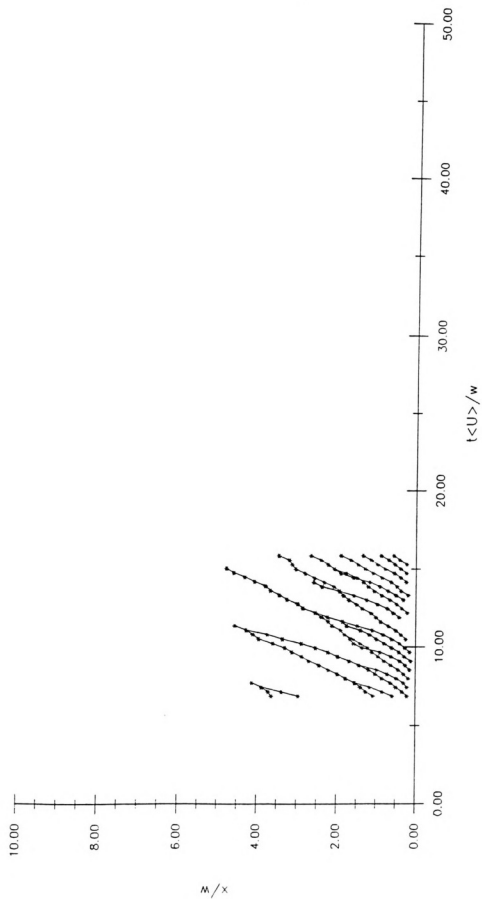


Figure C.25. Space-time plot of vortices (U090C002) at $Re=1027$ and $w=2.57$ cm.



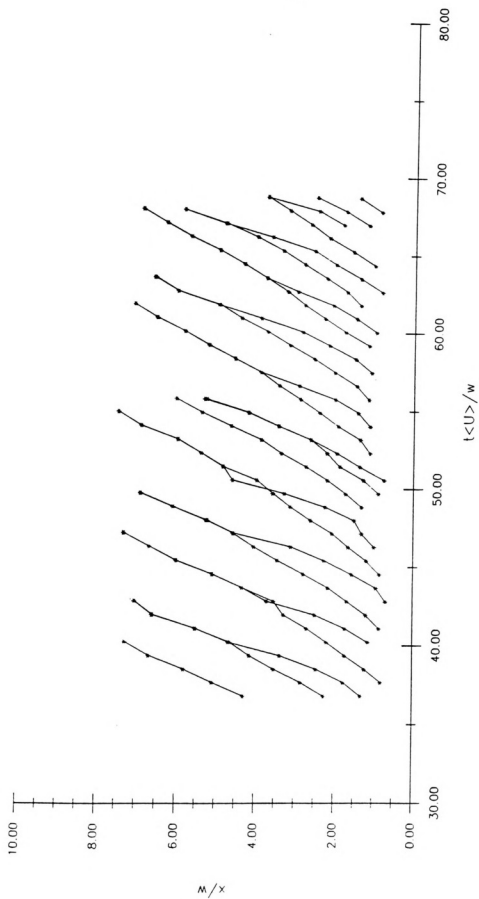
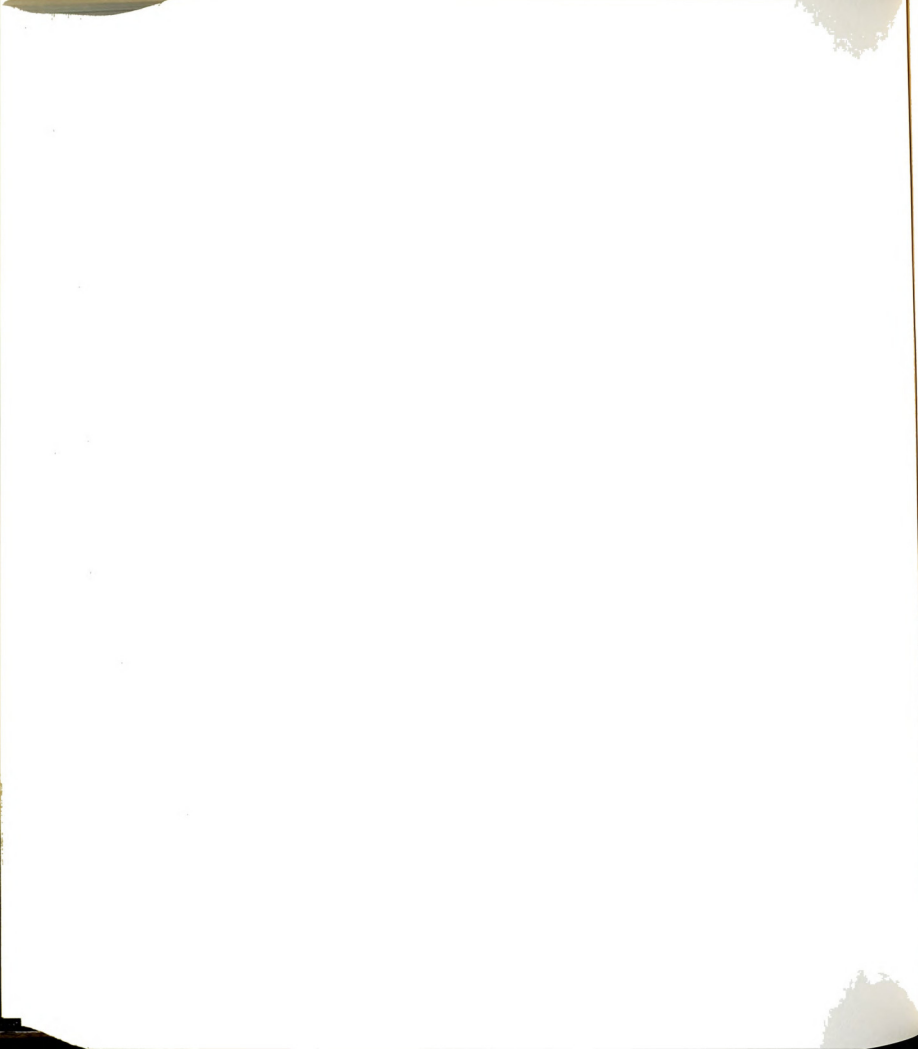


Figure C.26. Space-time plot of vortices (R180D) at $Re=1044$ and $w=1.40$ cm.



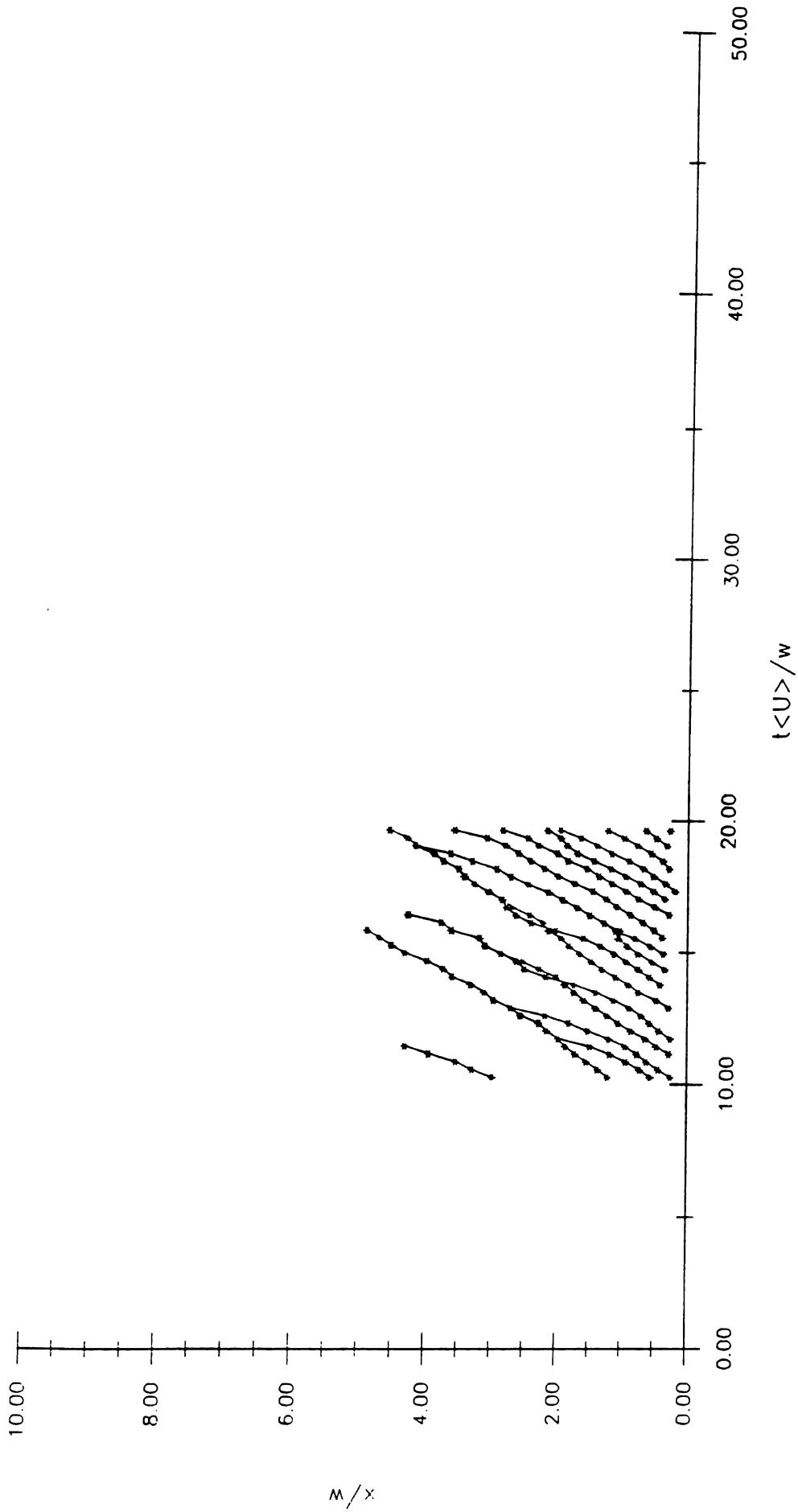
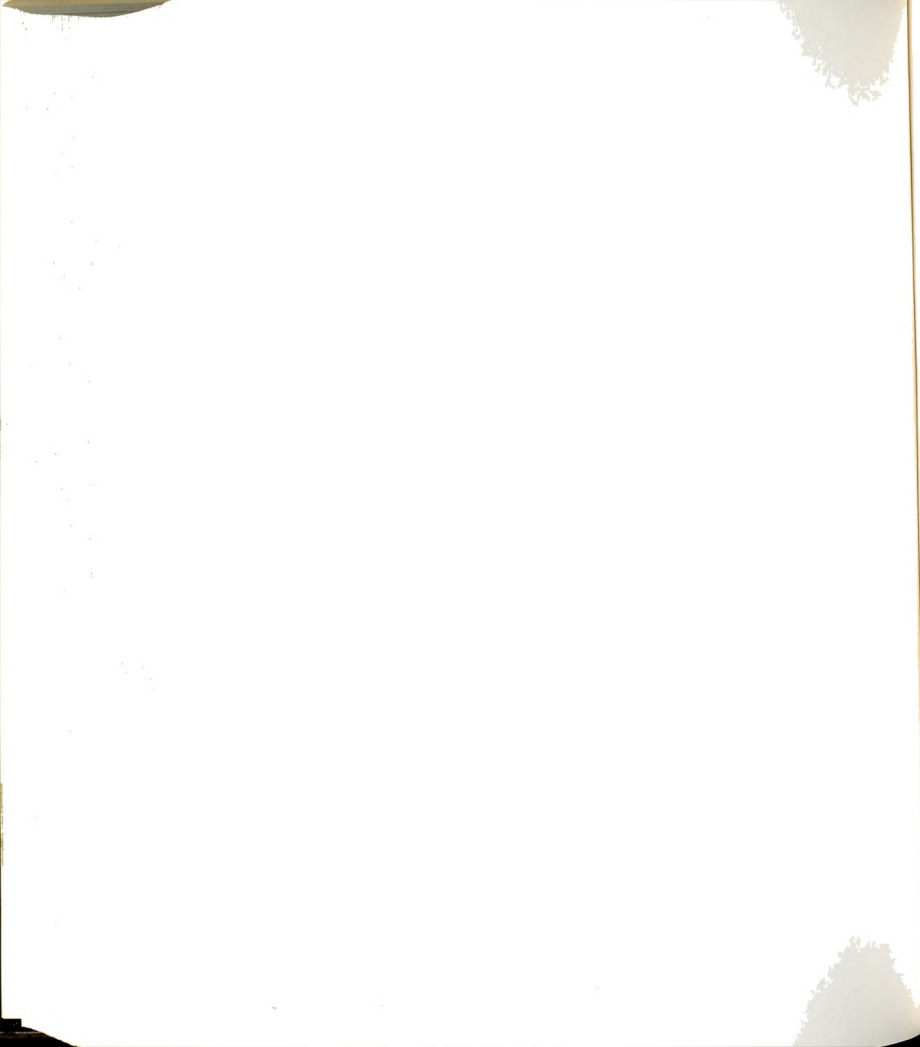


Figure C.27. Space-time plot of vortices (U090C000) at $Re=1063$ and $w=2.57$ cm.



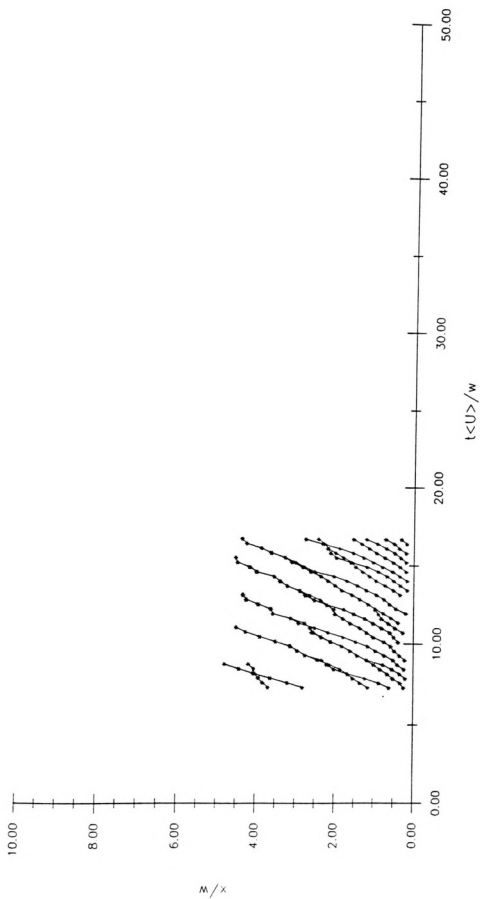


Figure C.28. Space-time plot of vortices (U090C001) at $Re=1074$ and $w=2.57$ cm.



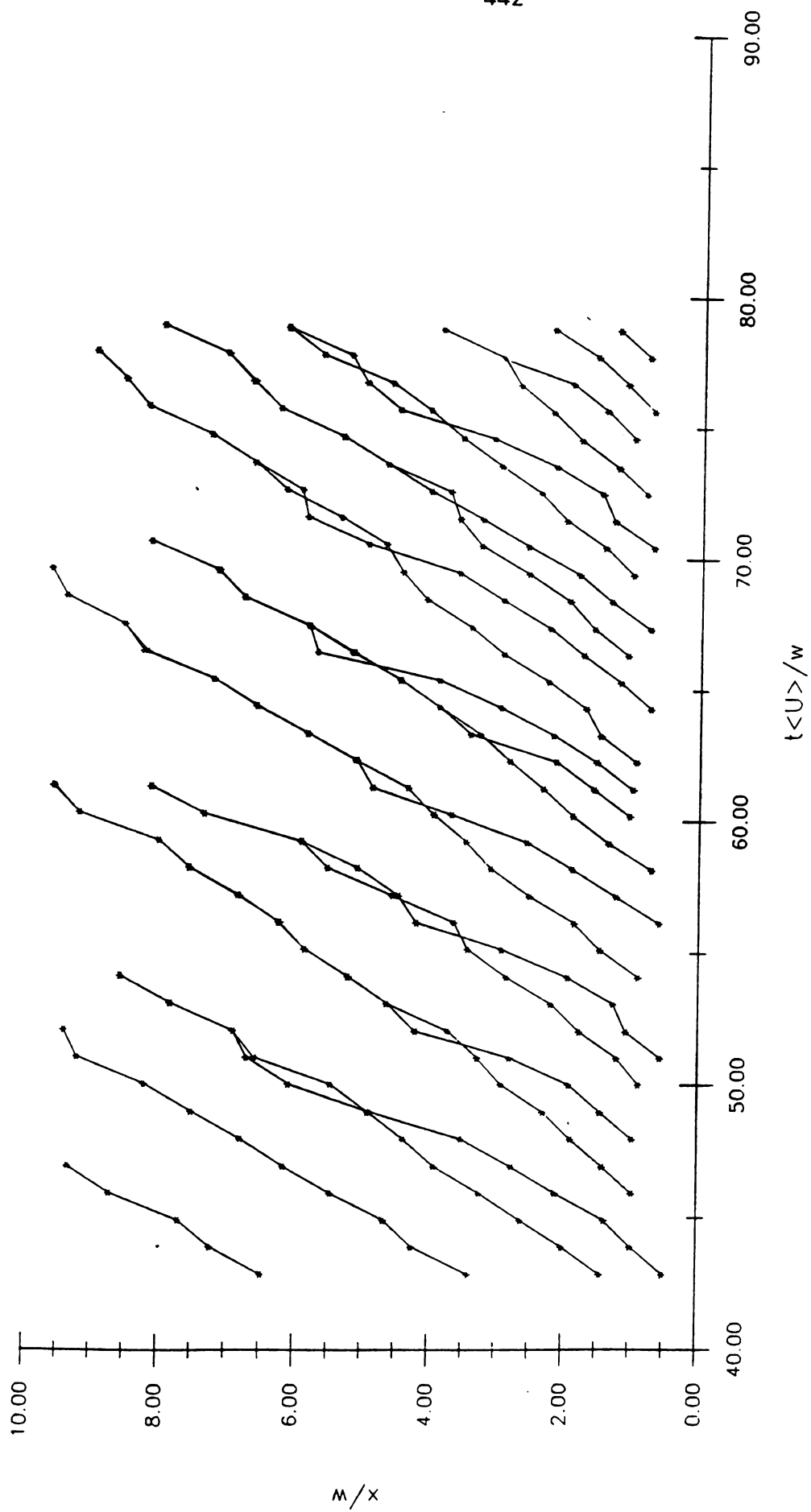


Figure C.29. Space-time plot of vortices (R180C) at $Re=1257$ and $w=1.40$ cm.



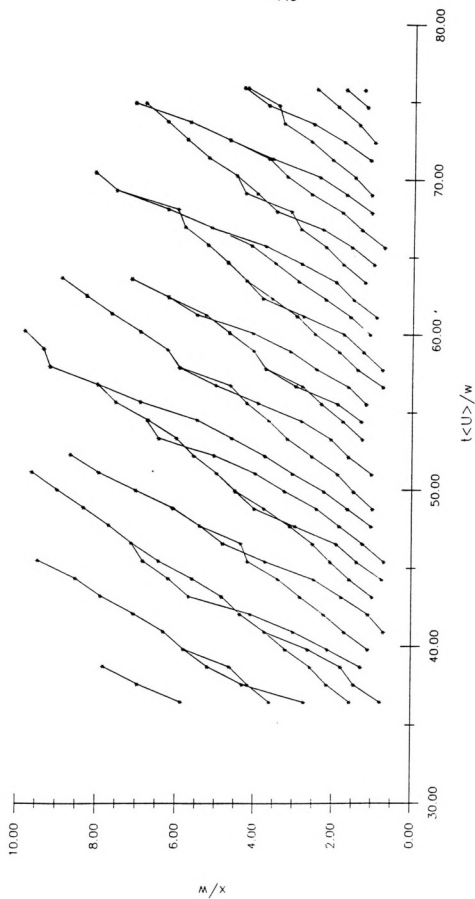
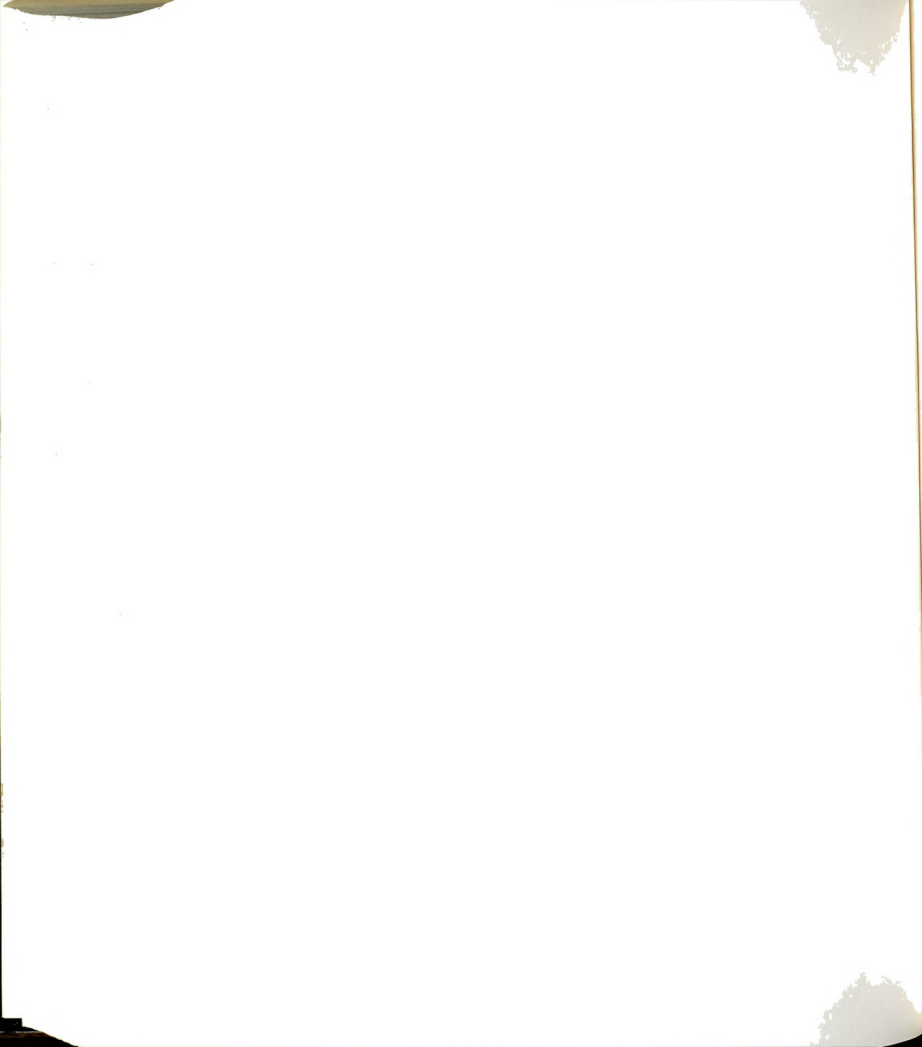


Figure C.30. Space-time plot of vortices (R180A) at $Re=1272$ and $w=1.40$ cm.



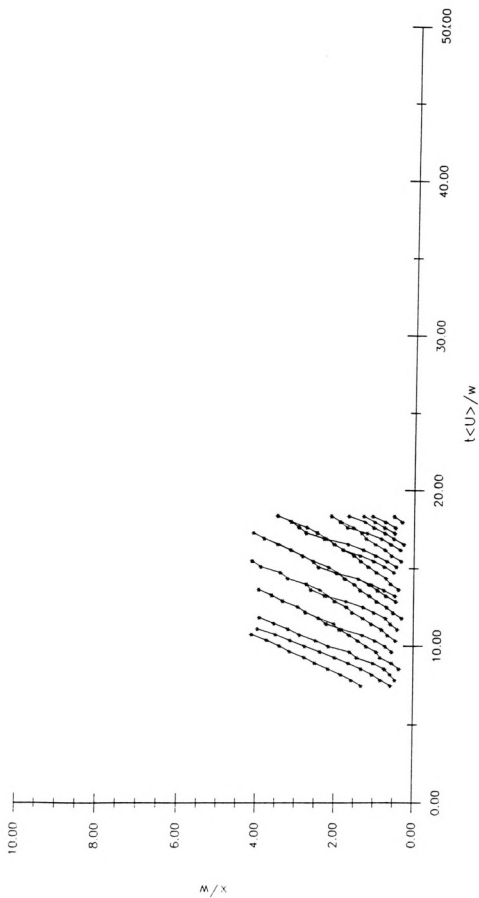


Figure C.31. Space-time plot of vortices (U150K001) at $Re=1571$ and $w=2.57$ cm.



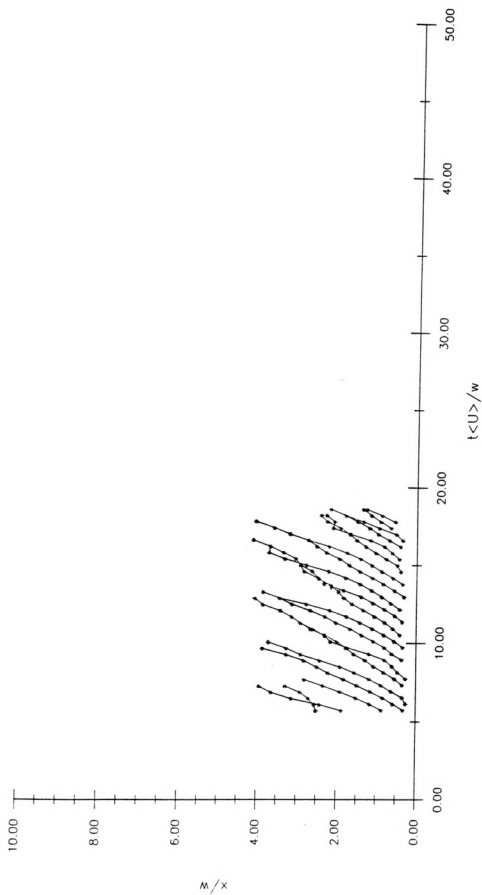


Figure C.32. Space-time plot of vortices (U150K000) at $Re=1580$ and $w=2.57$ cm.



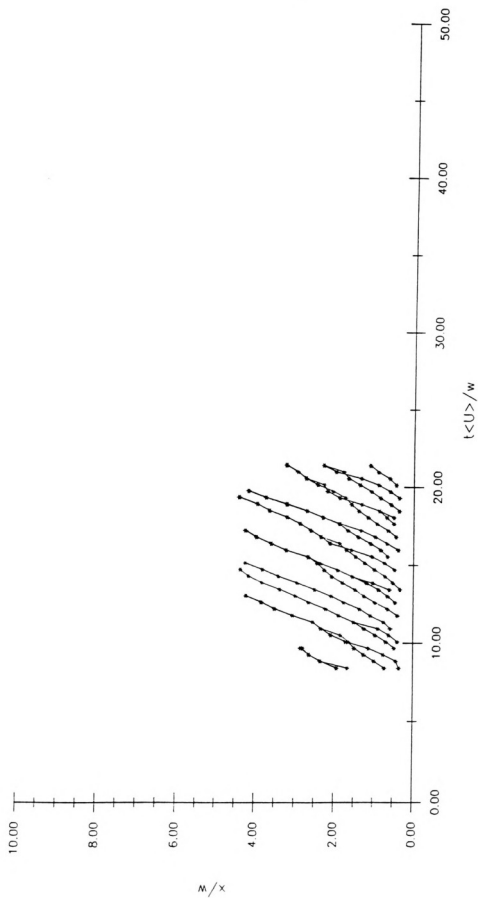


Figure C.33. Space-time plot of vortices (UI50L000) at $Re=1685$ and $w=2.57$ cm.



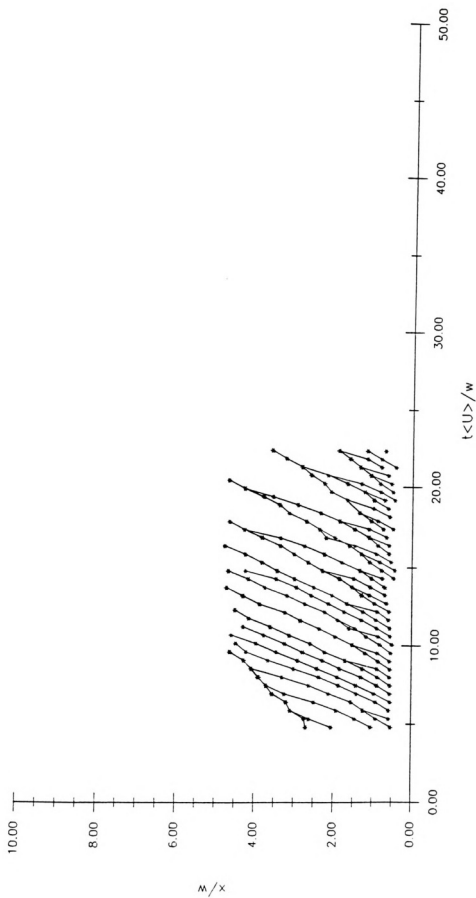
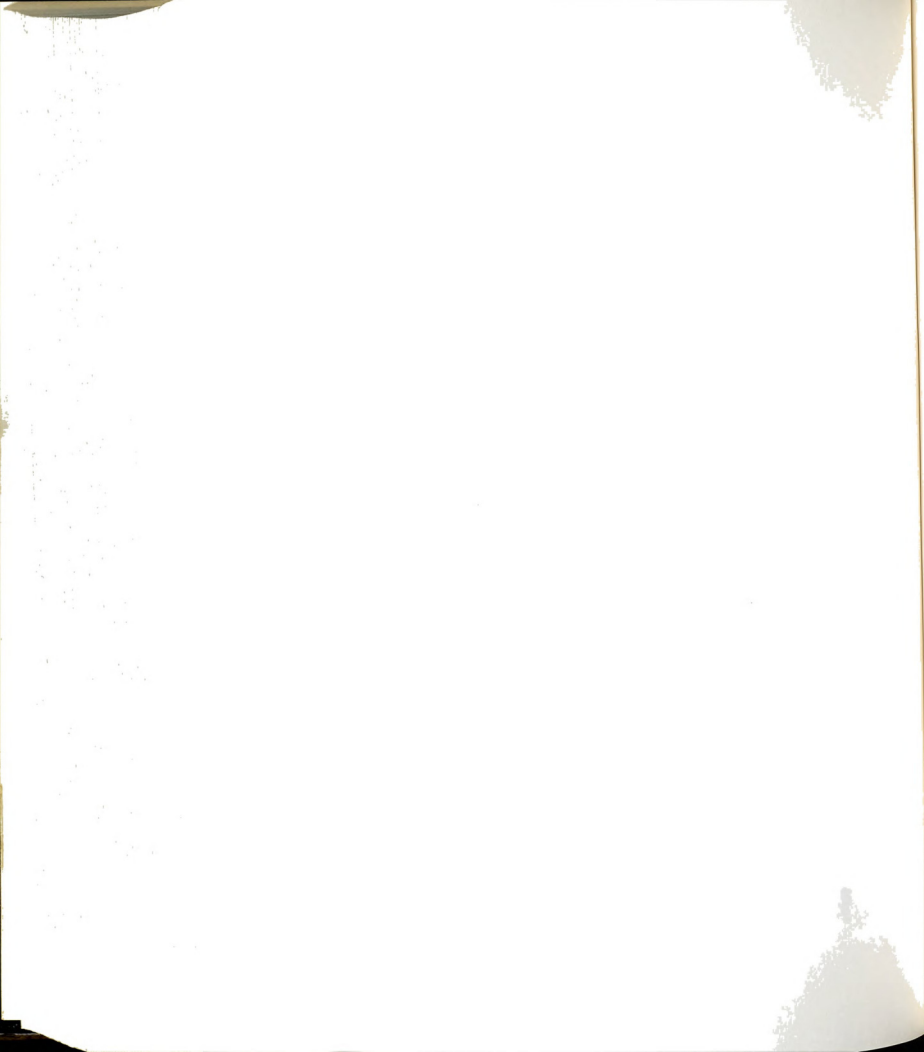


Figure C.34. Space-time plot of vortices (U220C000) at $Re=2299$ and $w=2.57$ cm.



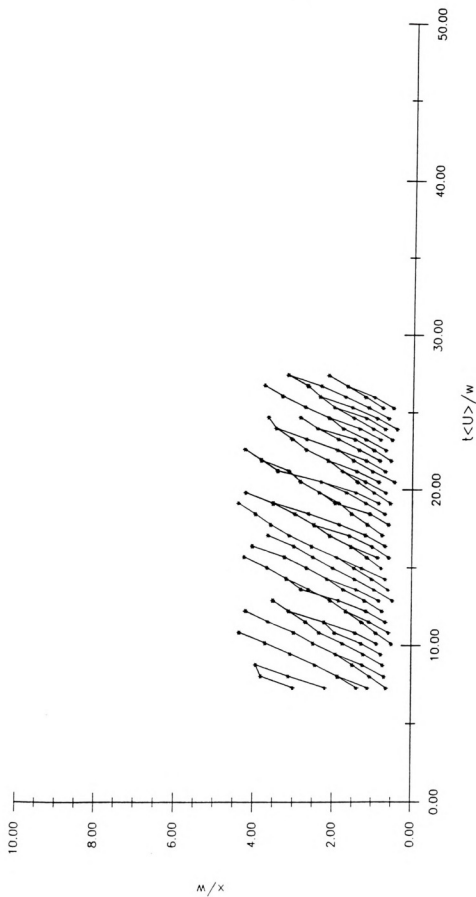


Figure C.35. Space-time plot of vortices (U300I001) at $Re=2949$ and $w=2.57$ cm.



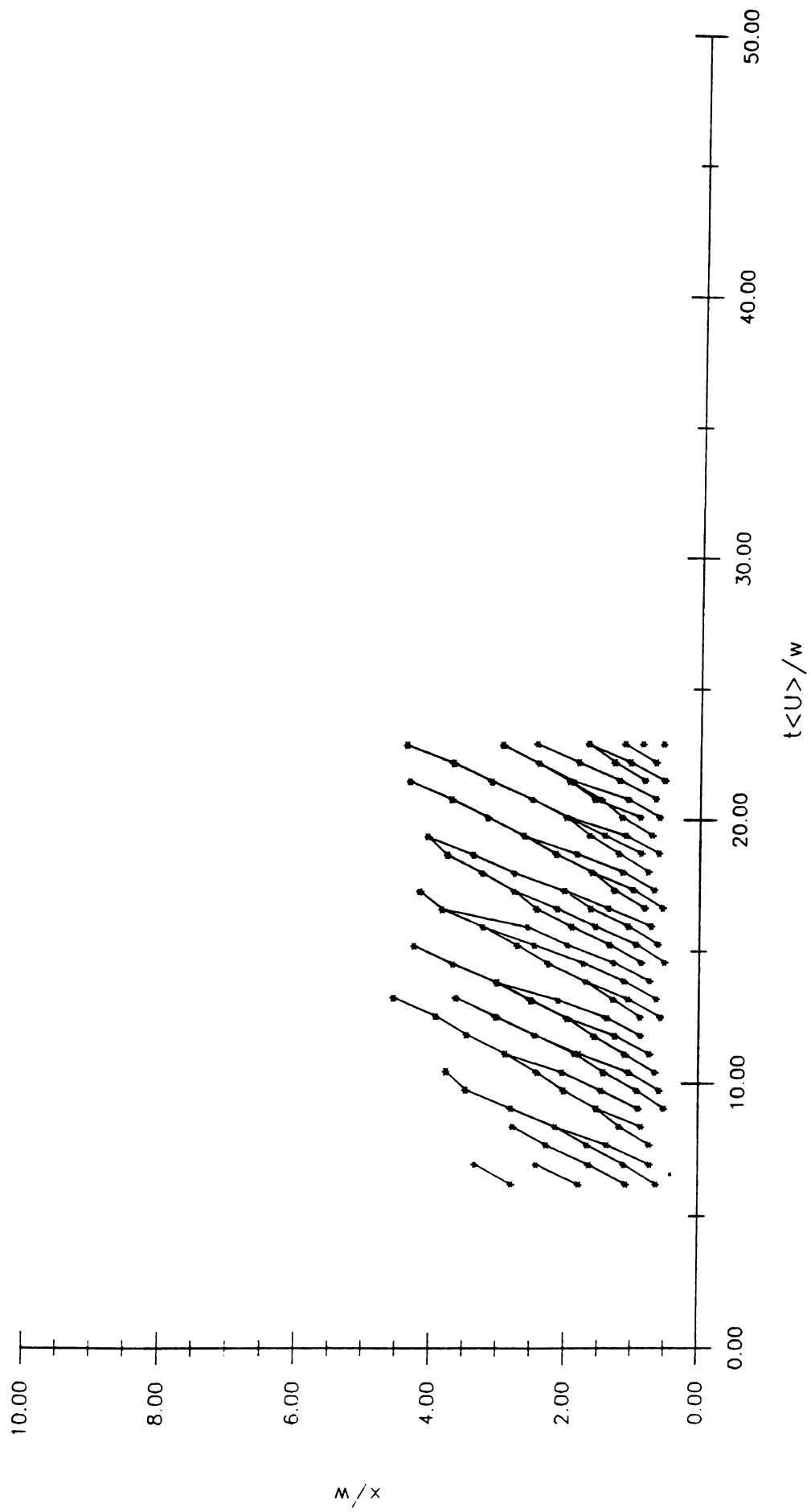
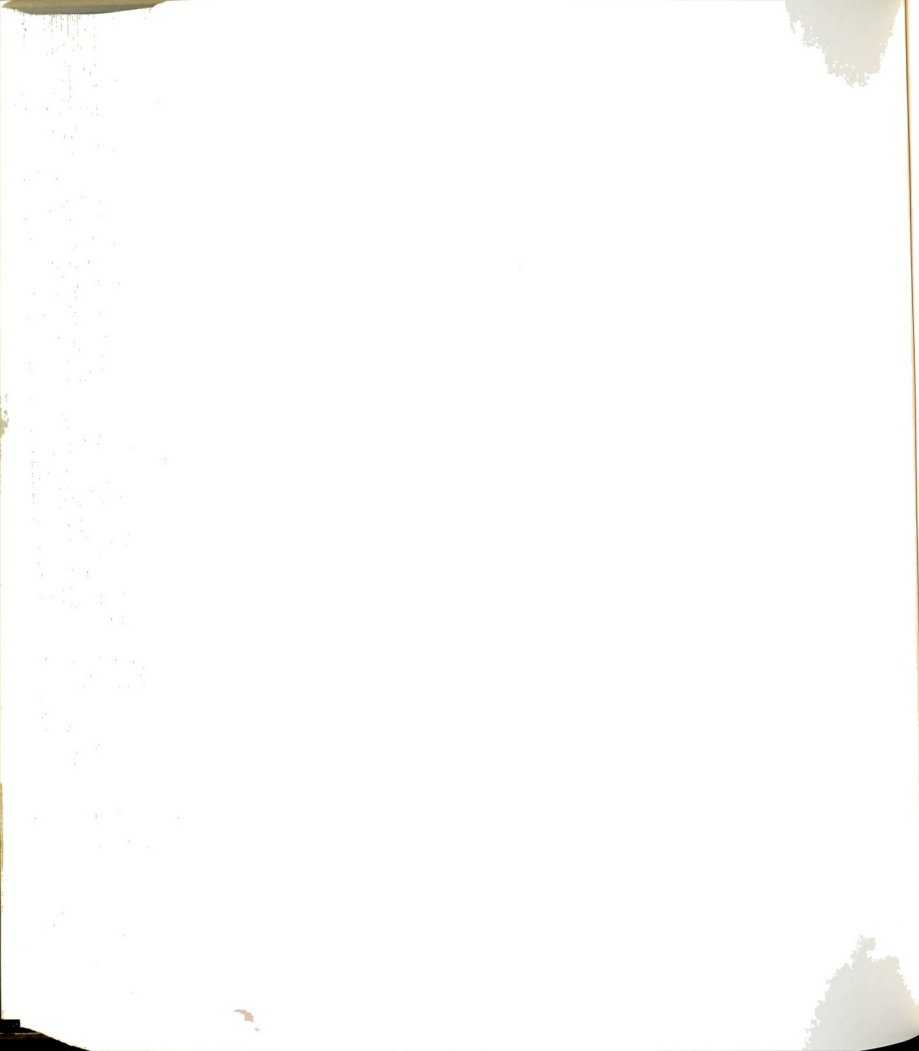


Figure C.36. Space-time plot of vortices (U300I002) at $Re=2964$ and $w=2.57$ cm.



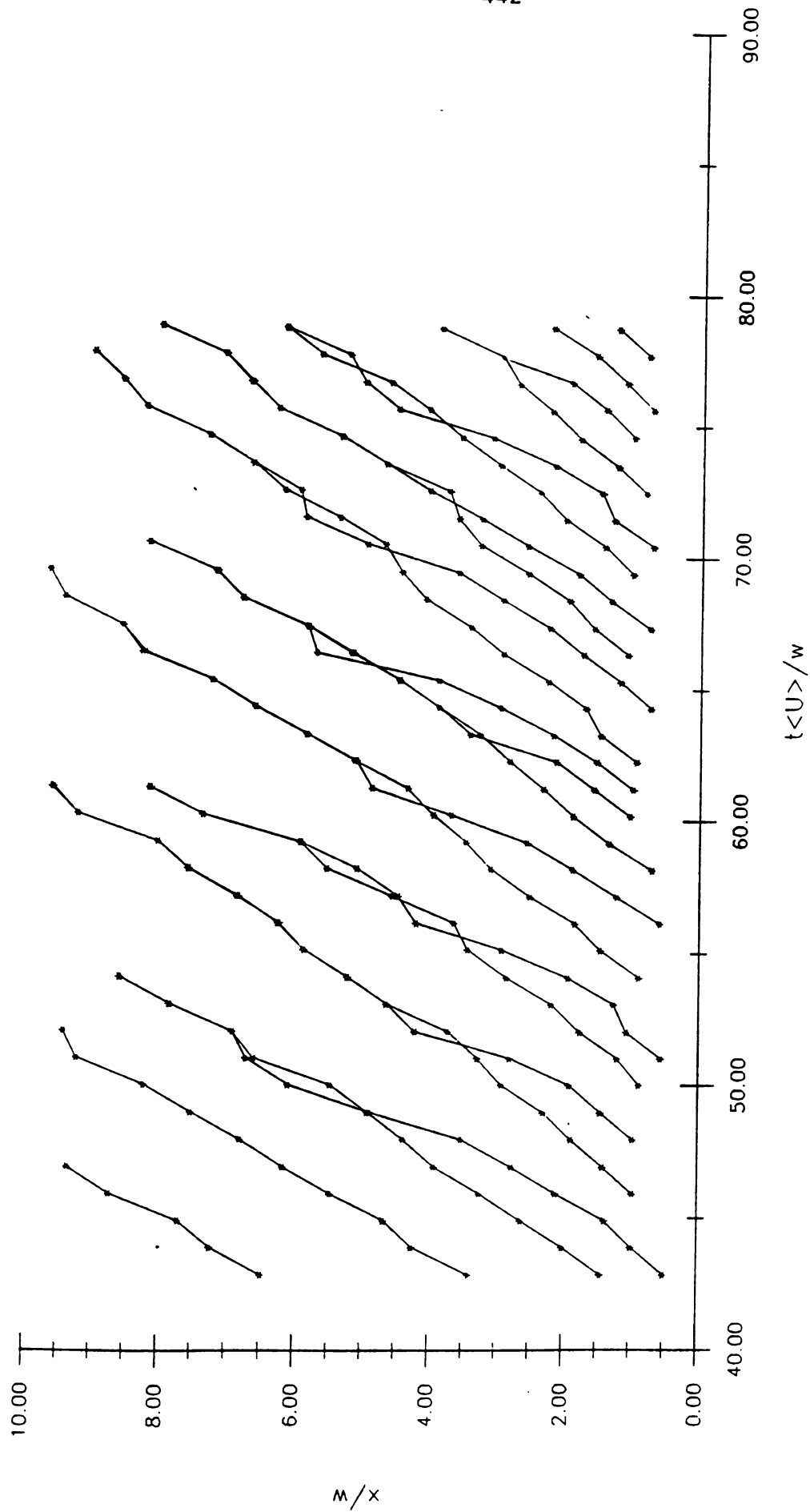
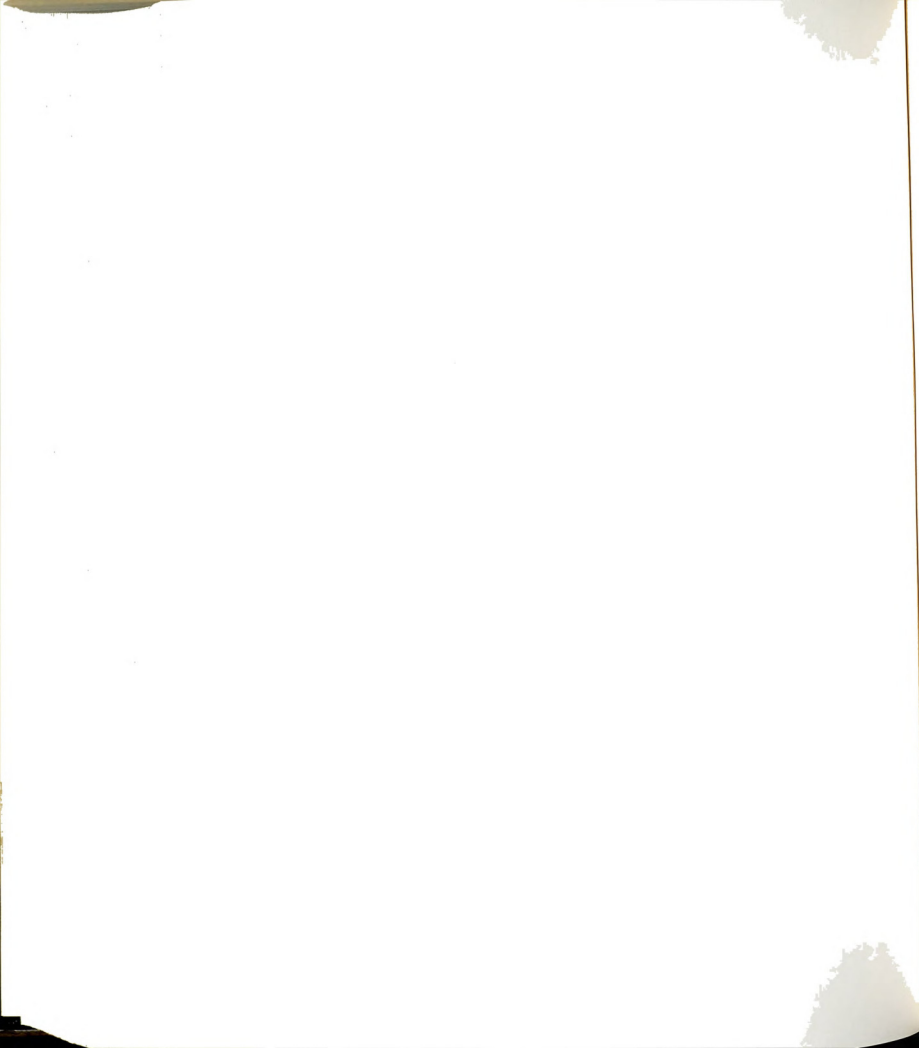


Figure C.29. Space-time plot of vortices (R180C) at $Re=1257$ and $w=1.40$ cm.



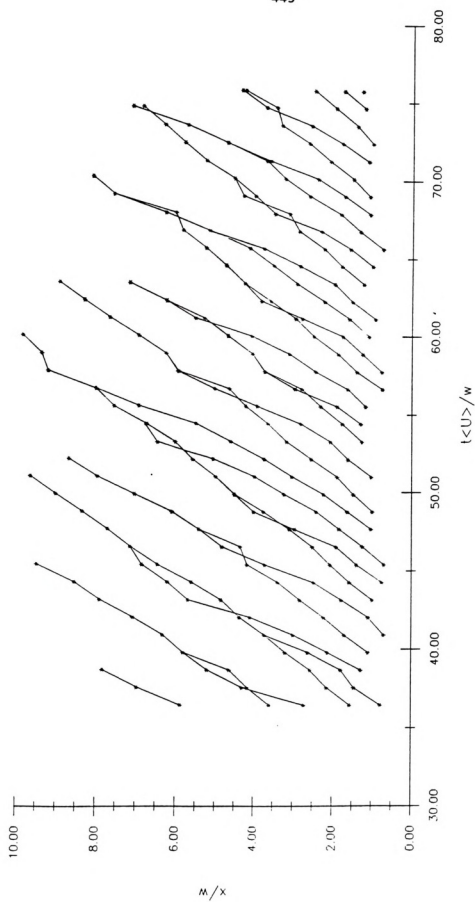
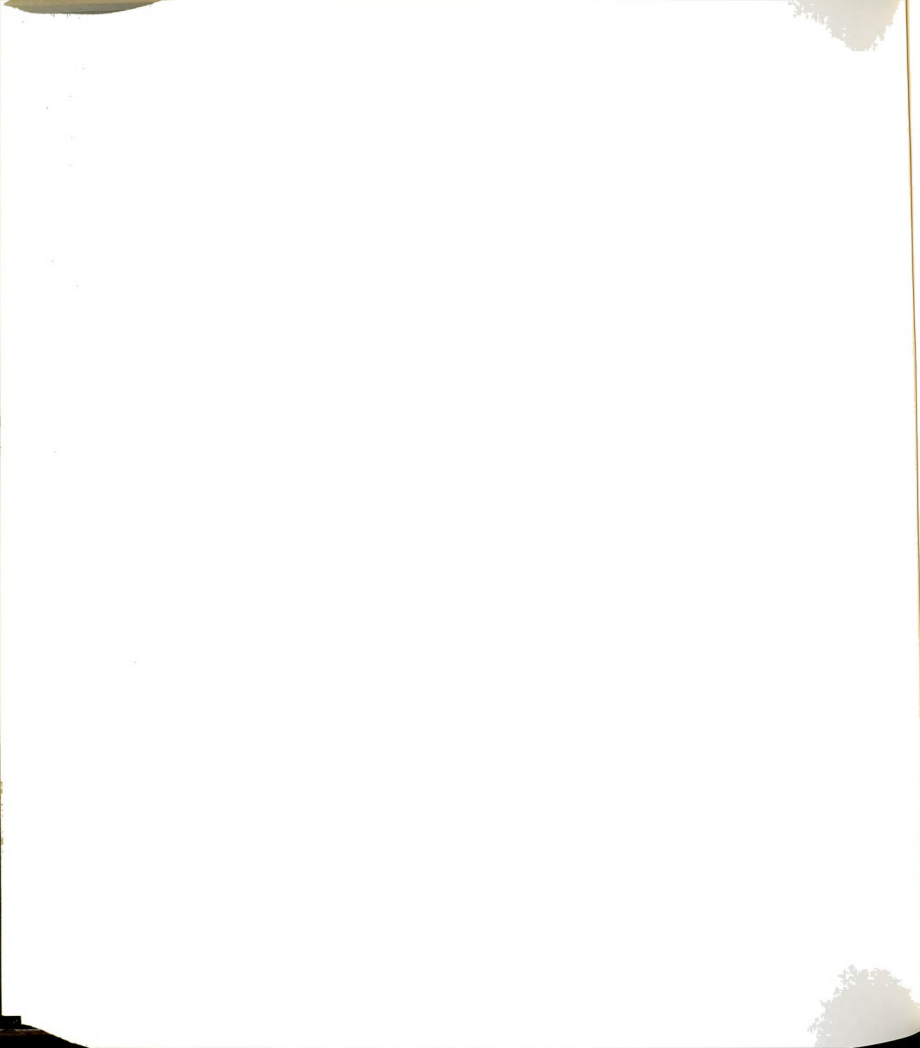


Figure C.30. Space-time plot of vortices (R180A) at $Re=1272$ and $w=1.40$ cm.



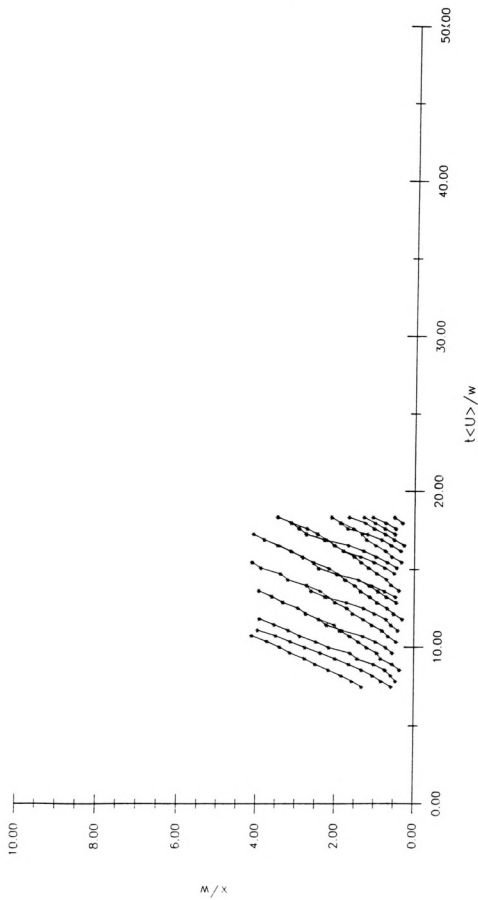
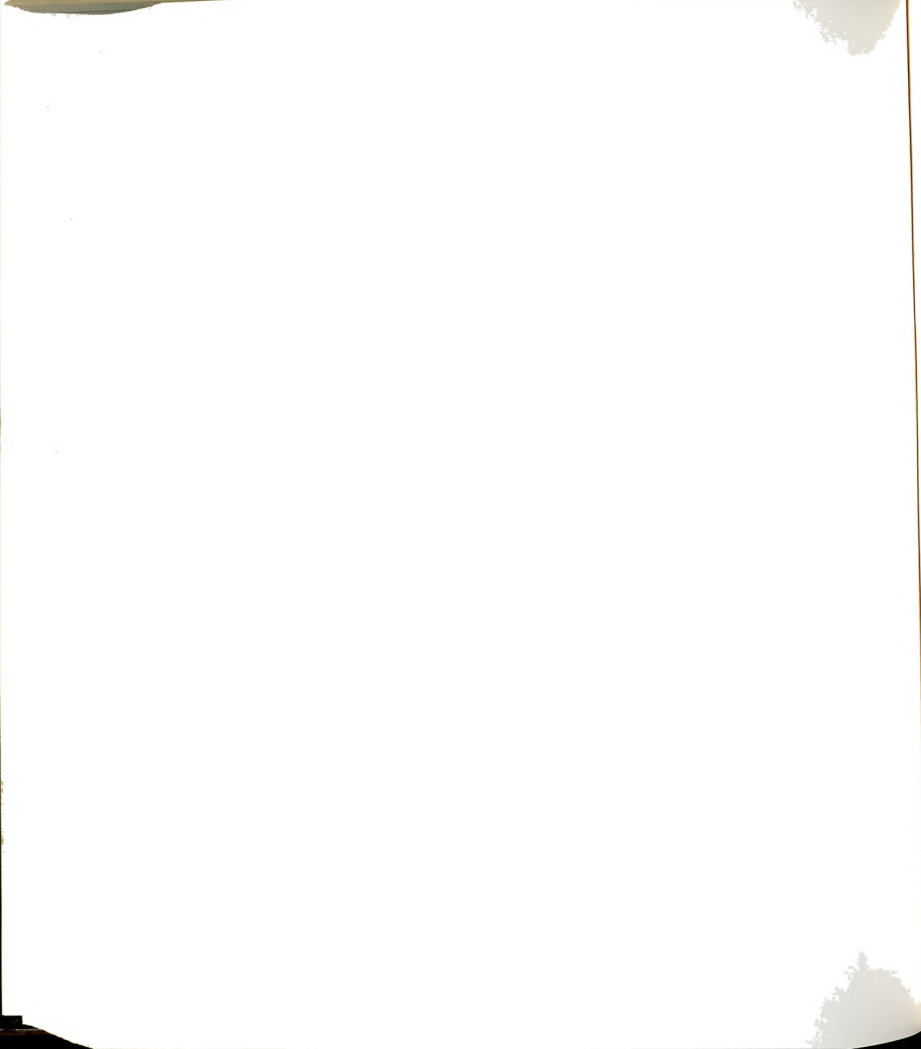


Figure C.31. Space-time plot of vortices (U150K001) at $Re=1571$ and $w=2.57$ cm.



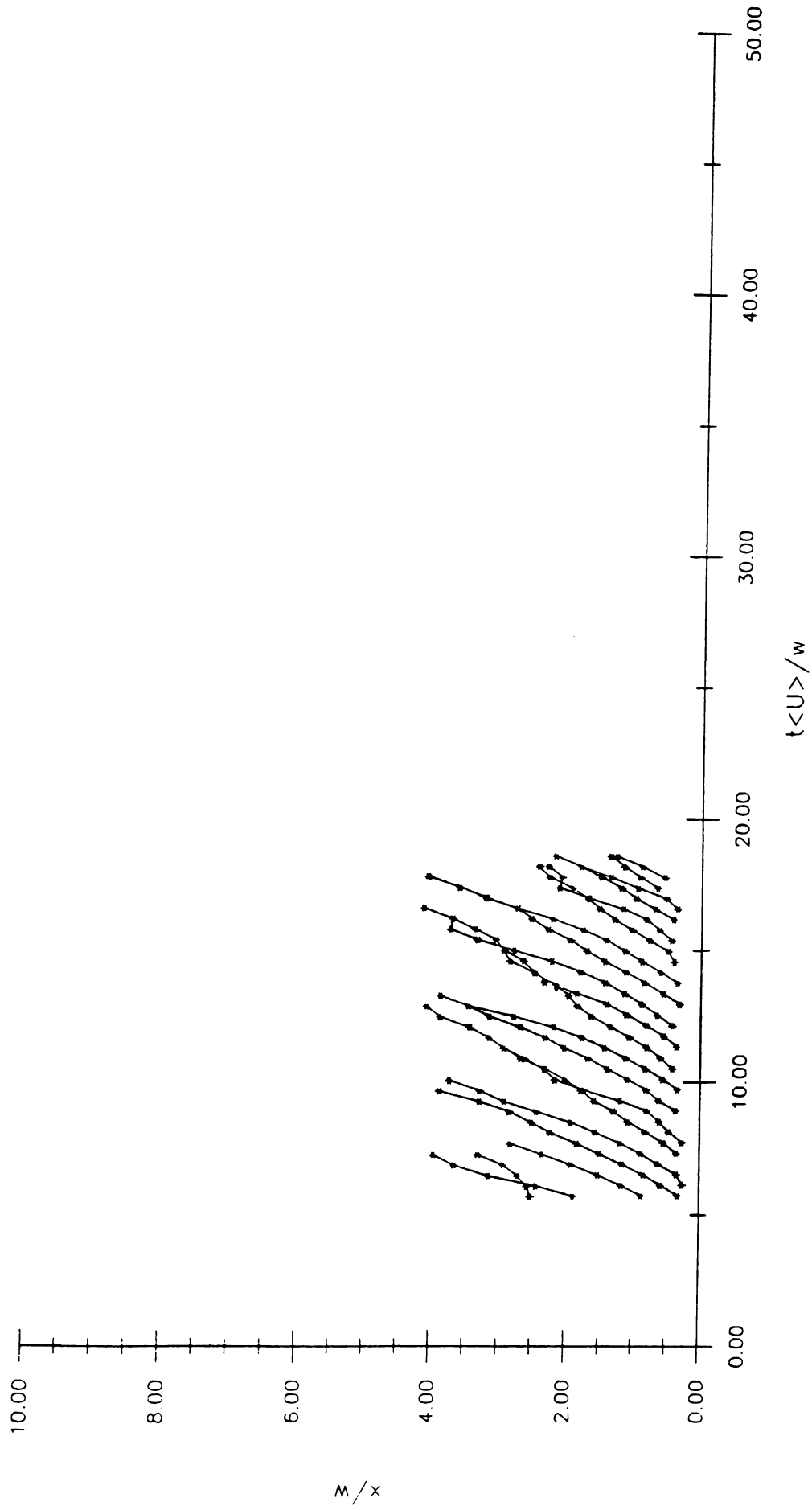
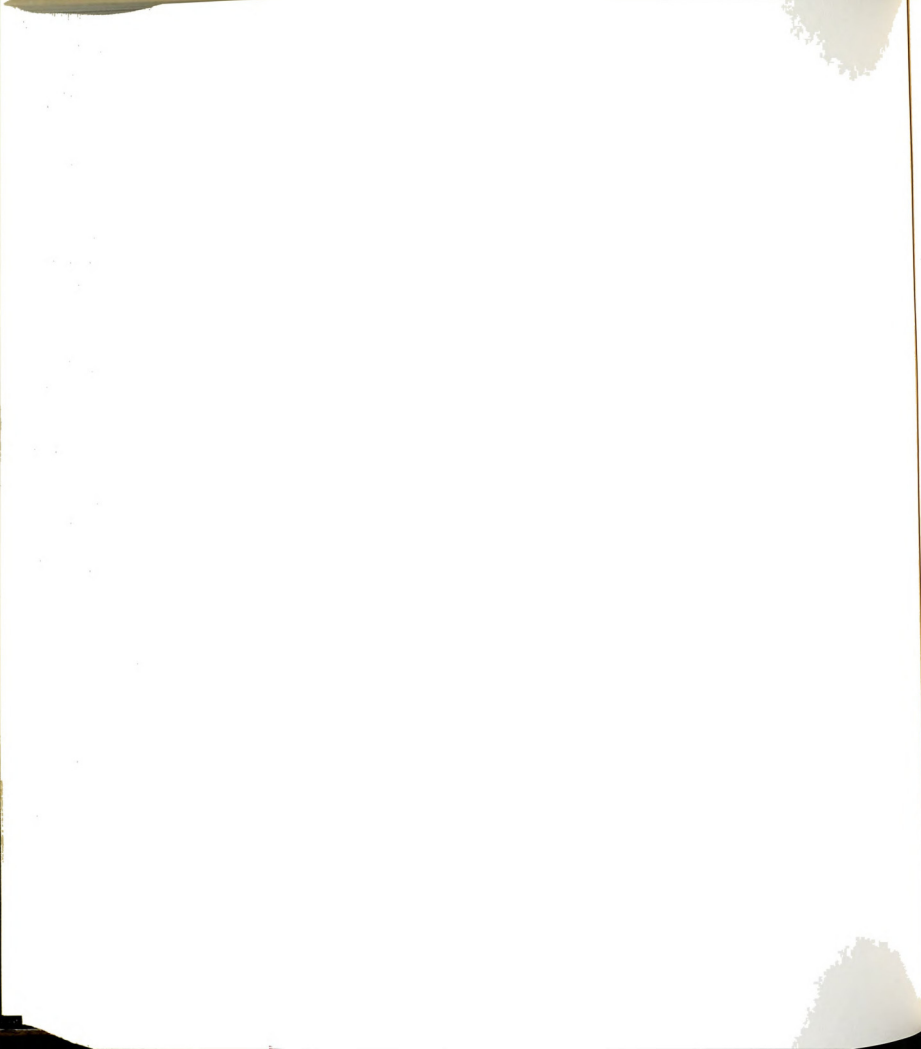


Figure C.32. Space-time plot of vortices (U150K000) at $Re=1580$ and $w=2.57$ cm.



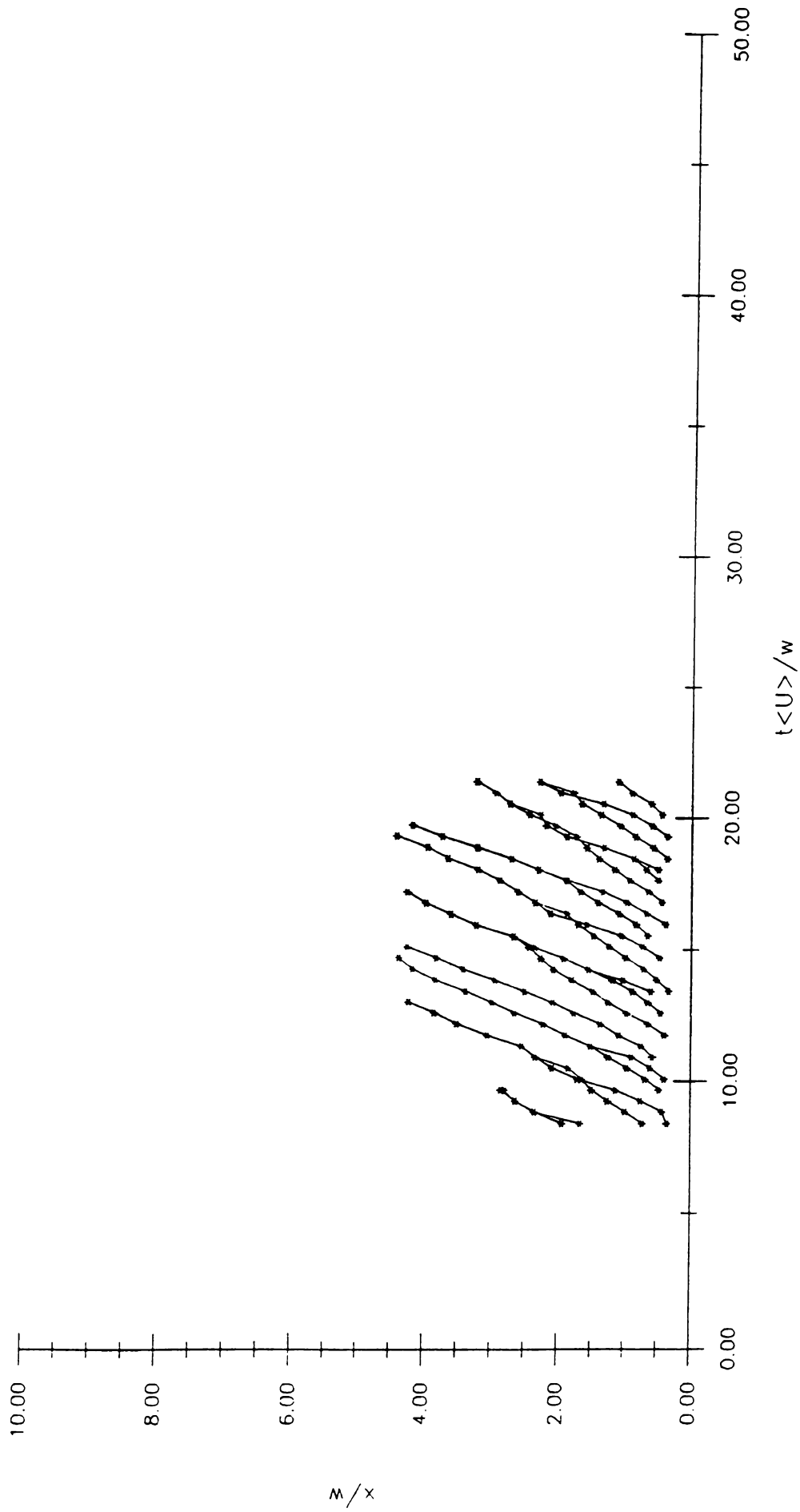


Figure C.33. Space-time plot of vortices (U150L000) at $Re=1685$ and $w=2.57$ cm.



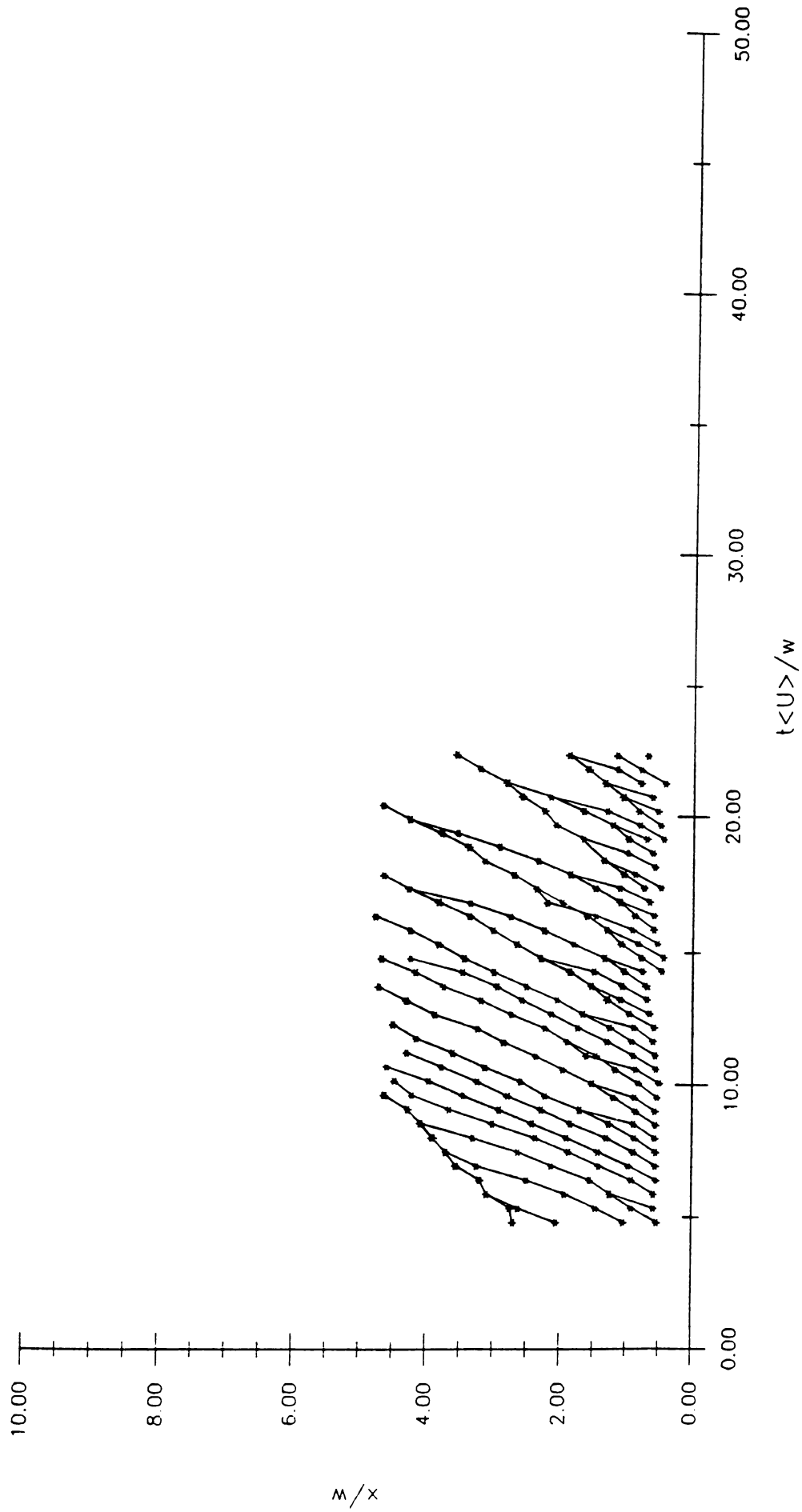
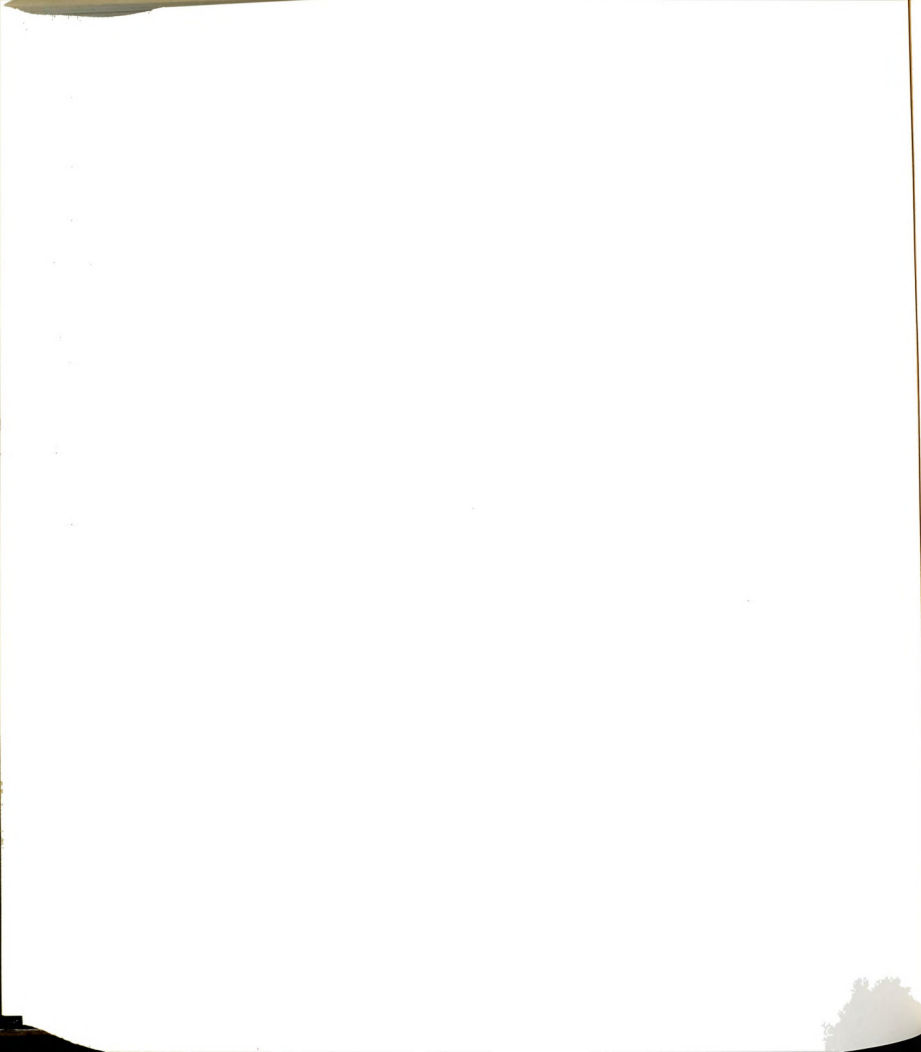


Figure C.34. Space-time plot of vortices (U220C000) at $Re=2299$ and $w=2.57$ cm.



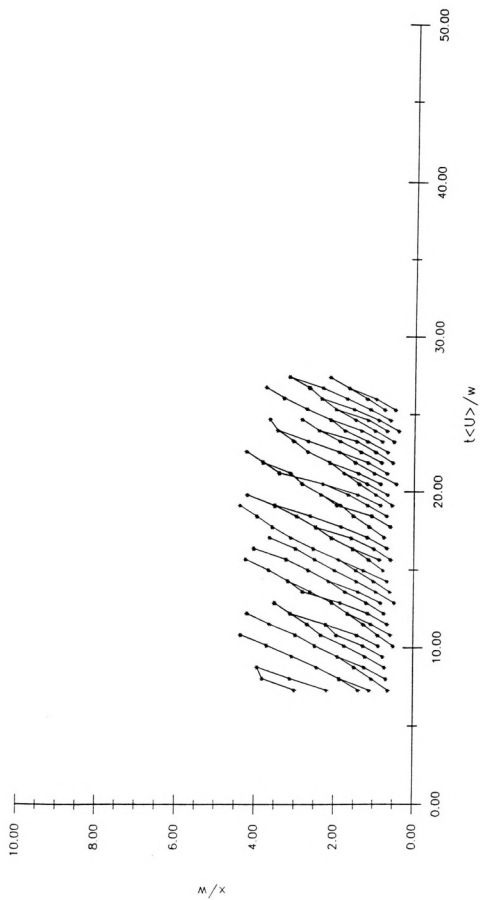
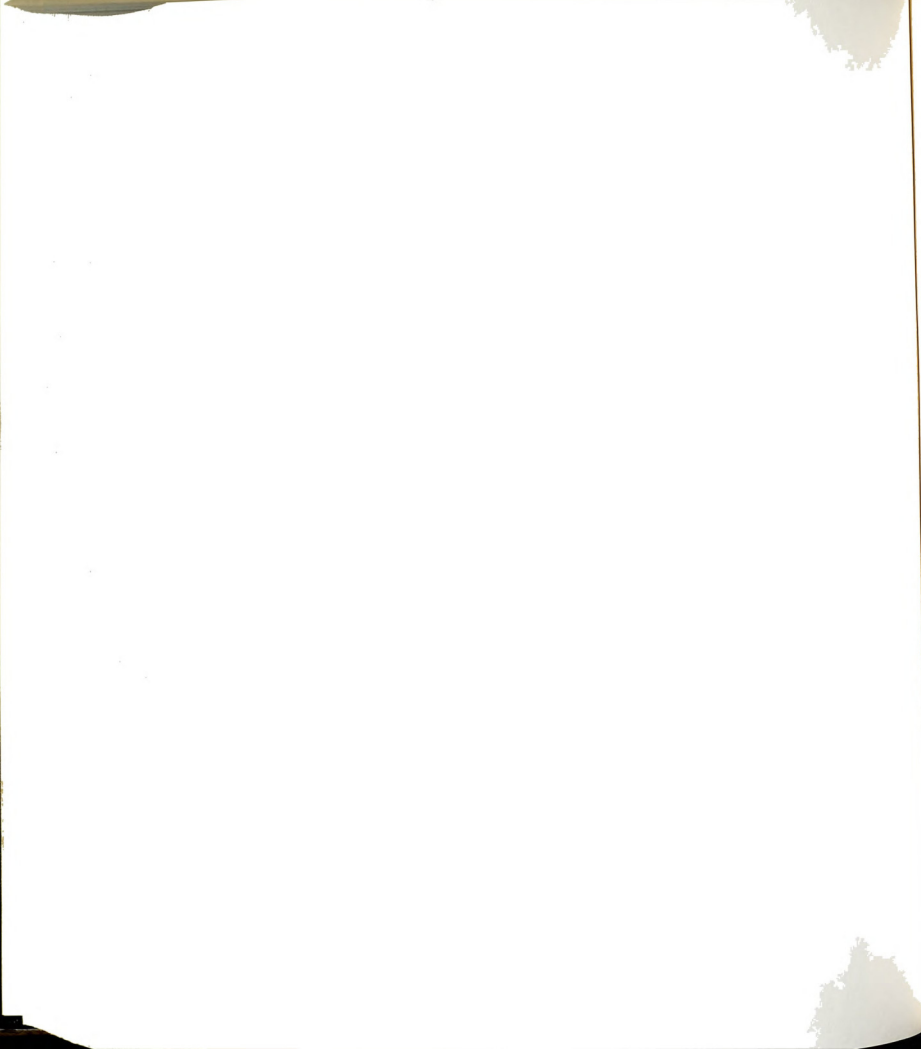


Figure C.35. Space-time plot of vortices (U300I001) at $Re=2949$ and $w=2.57$ cm.



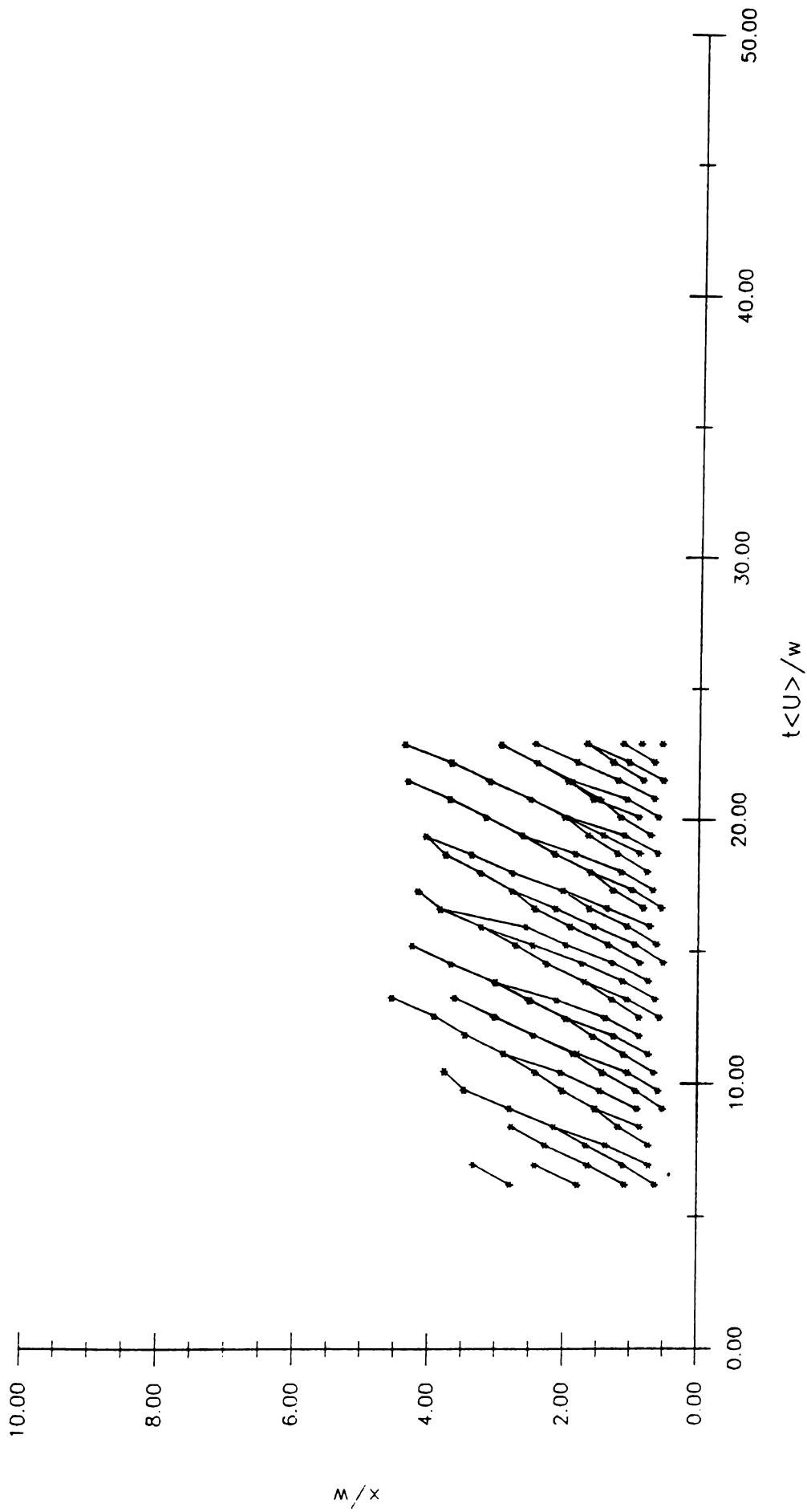
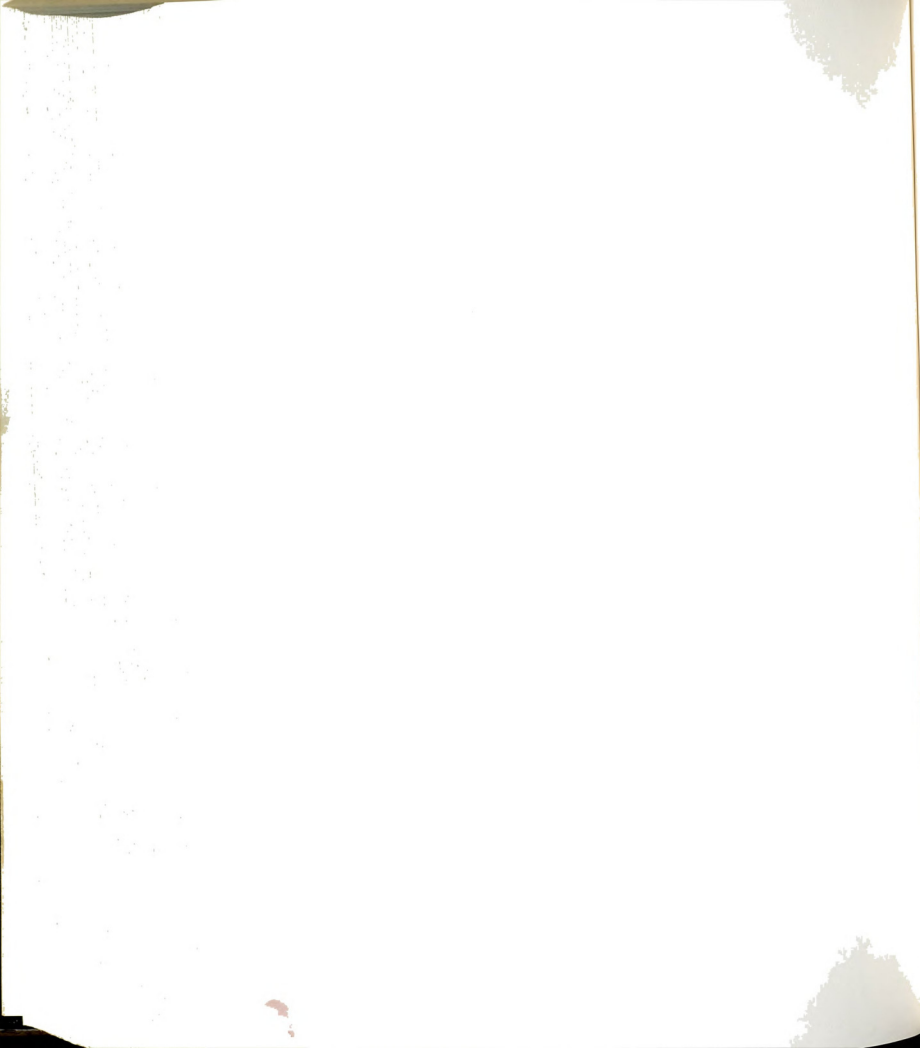


Figure C.36. Space-time plot of vortices (U300I002) at $Re=2964$ and $w=2.57$ cm.



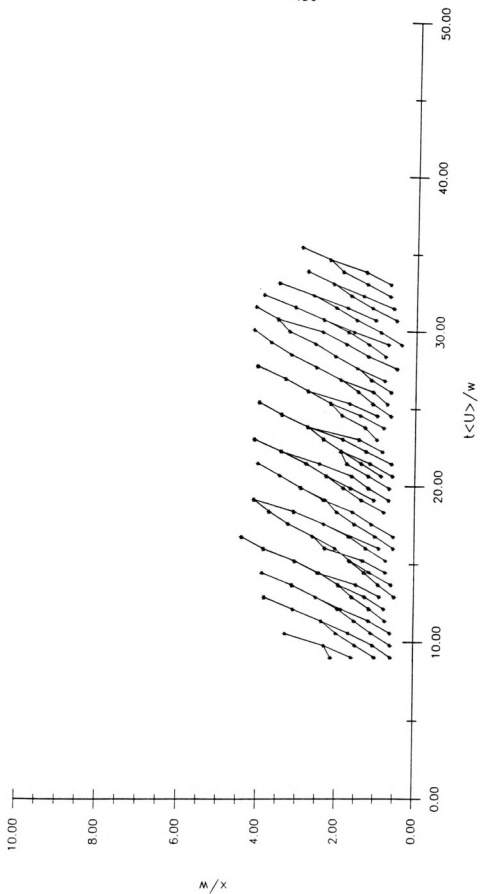
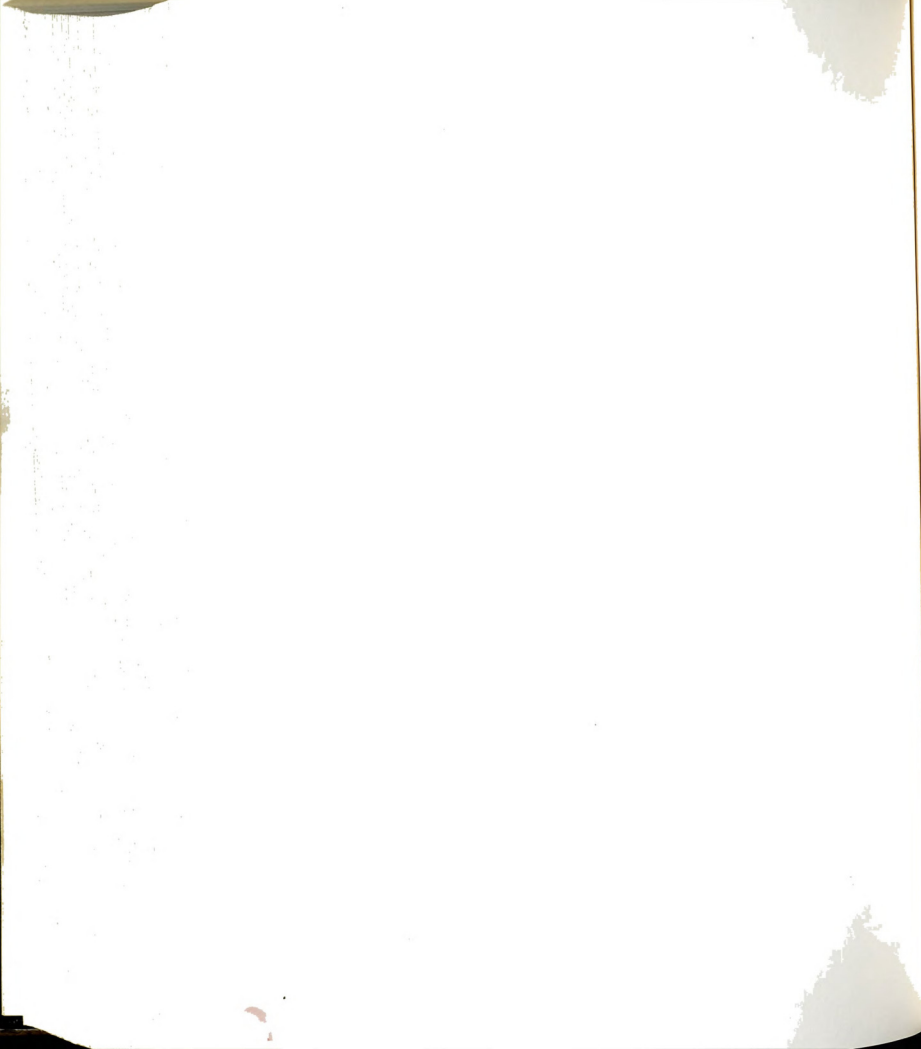


Figure C.37. Space-time plot of vortices (U300G002) at $Re=3389$ and $w=2.57$ cm.



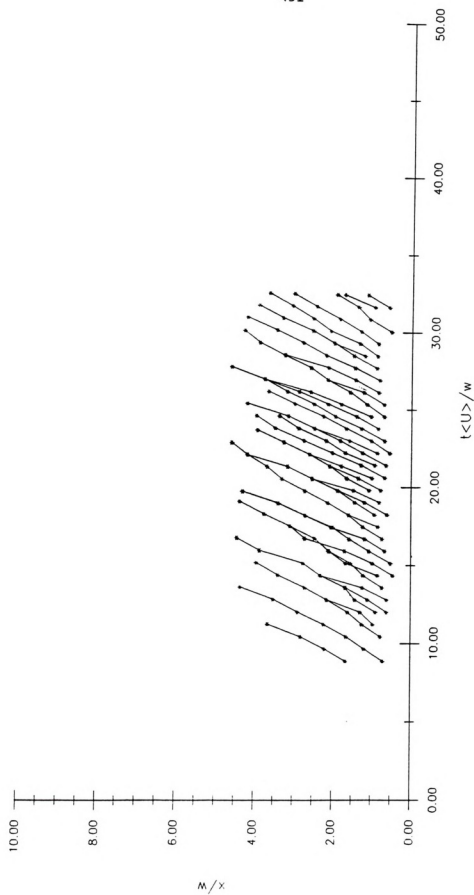
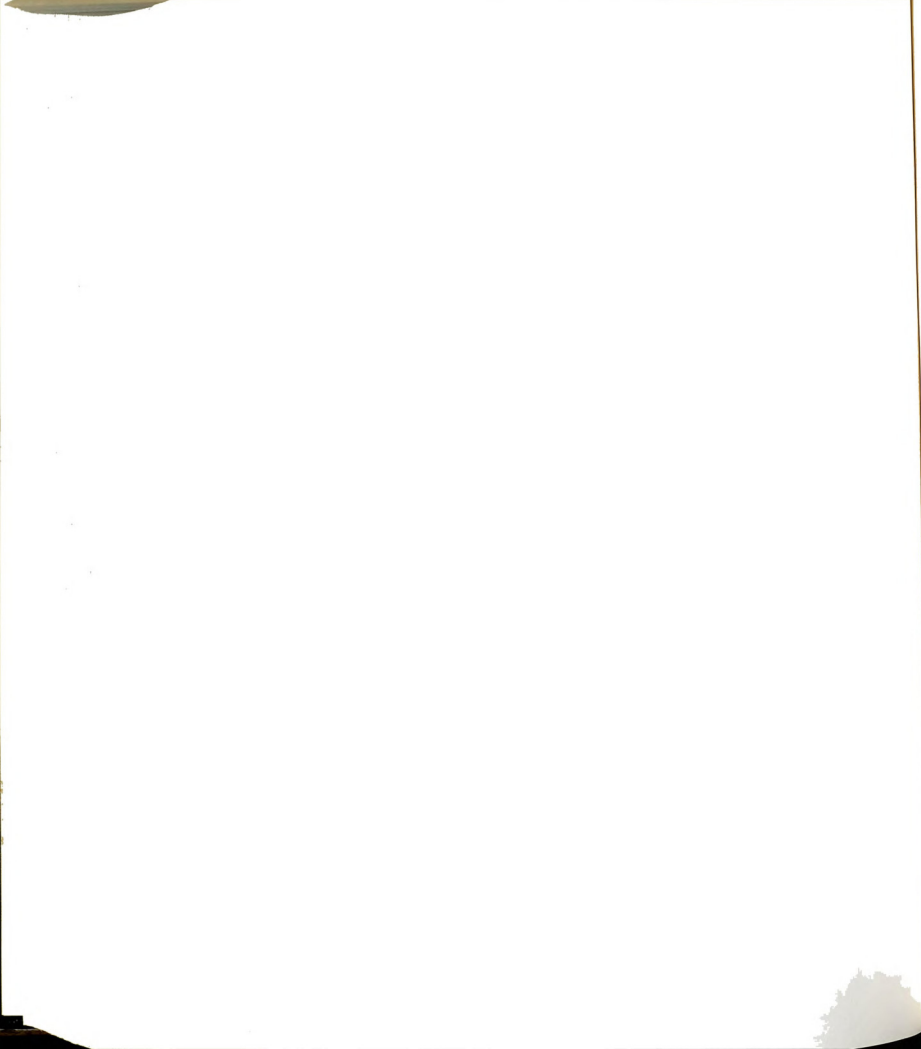


Figure C.38. Space-time plot of vortices (U300G000) at $Re=3469$ and $w=2.57$ cm.



REFERENCES

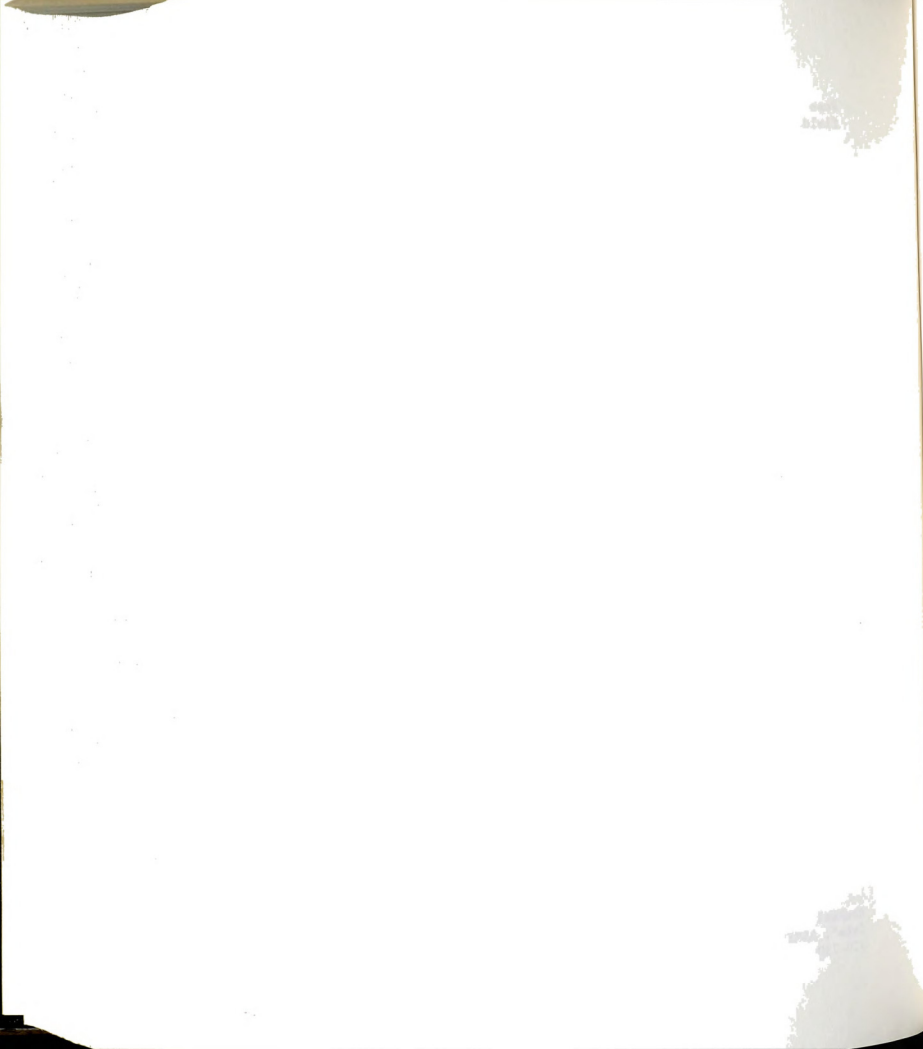


List of References

- Andrade, E. N. DA C., "The Velocity Distribution in a Liquid-into-Liquid Jet. Part 2: The Plane Jet", Proc. Physical Society of London, vol. 51, 1939, pp. 784-793.
- Antonia, R. A., Browne, L. W. B., Rajgopalan, S. and Chambers, A. J., "On the organized motion of a turbulent plane jet", J. Fluid Mech., vol. 134, 1983, pp. 49-66.
- Aref, H. and Siggia, E. D., "Evolution and breakdown of a vortex street in two dimensions", J. Fluid Mech., vol. 109, pp. 435-463.
- Beavers, G. S. and Wilson, T. A., "Vortex growth in jets", J. Fluid Mech., vol. 44, 1970, pp. 97-112.
- Becker, H. A. and Massaro, T. A., "Vortex evolution in a round jet", J. Fluid Mech., vol. 80, 1977, pp. 401-421.
- Beck, J. V. and Arnold, K. J., "Parameter Estimation in Engineering and Science", John Wiley and Sons, 1977.
- Bendat, J. S. and Piersol, A. G., "Random Data: Analysis and Measurement Procedures", Wiley-Interscience, 1971.
- Bickley, W. G., "The Plane Jet", London, Edinburgh and Dublin Philosophical Magazine and Journal of Science, 7th Series, vol. 23, 1937, pp. 727-731.
- Chambers, A. J., Antonia, R. A. and Browne, L. W. B., "Effect of symmetry and asymmetry of turbulent structures on the interaction region of a plane jet", Experiments in Fluids, vol. 3, 1985, pp. 343-348.
- Chambers, F. W. and Goldschmidt, V. W., "Acoustic Interaction with a Turbulent Plane Jet: Effects on Mean Flow", vol. 20, 1982, pp. 797-804.
- Clark, J. A. and Kit L., "Shear Layer Transition and the Sharp-Edged Orifice", ASME Journal of Fluids Engineering, vol. 102, 1980, pp. 219-225. (Discussion by Foss (1980).)
- Curle, N., "On Hydrodynamic Stability in Unlimited Fields of Viscous Flow", Proc. Royal Soc. of London Ser A, vol. 238, 1956-57, pp. 489-501.
- Durst, F., Schierholz, W. F. and Wunderlich, A. M., "Experimental and Numerical Investigations of Plane Duct Flows With Sudden Contraction", ASME Journal of Fluids Engineering, vol. 109, 1987, pp. 376-383.



- Foss, J. F. and Korschelt, D., "Instabilities in the slit-jet flow field", J. Fluid Mech., vol. 132, 1983, pp. 79-86.
- Freymuth, P., "On transition in a separated boundary layer", J. Fluid Mech., vol. 25, 1966, pp. 683-704.
- Gutmark, E. and Ho. C. M., "Preferred modes and the spreading rates of jets", Phys. Fluids, vol. 26, 1983, pp. 2932-2938.
- Husain, H. S. and Hussain, A. K. M. F., "Flow Visualization of the Coherent Structure Interactions in the Near Field of a Plane Jet", Flow Visualization III, Proc. of the 3rd Int. Symp. on Flow Visualization, Sep. 6-9 1983, Univ. of Michigan, Ann Arbor MI, pp. 510-513.
- Hussain, A. K. M. F. and Clark, A. R., "Upstream influence on the nearfield of a plane turbulent jet", Phys. Fluids, vol. 20, 1977, pp. 1416-1427.
- Ikeda, M., "Finite disturbances and growing vortices in a two-dimensional jet", J. Fluid Mech., vol. 80, 1977, pp. 401-421.
- Koochesfahani, M. M., Private Communication, 1989.
- Maroney, R. N., "Inviscid Shear Flow Analysis of Corner Eddies Ahead of a Channel Flow Contraction", ASME Journal of Fluids Engineering, vol. 107, 1985, pp. 212-217.
- Mattingly, G. E. and Criminale, W. O. Jr., "Disturbance Characteristics in a Plane Jet", Phys. Fluids, vol. 14, 1971, pp. 2258-2264.
- Michalke, A., "On spatially growing disturbances in an inviscid shear layer", J. Fluid Mech., vol. 23, 1965, pp. 521-544.
- Montgomery, M. T., "An Analytical Investigation of the Transition Flow from a Sharp-Edge Orifice Jet", M. S. Thesis, University of Washington, 1985.
- Namer, I. and Otugen, M. V., "Velocity measurements in a plane turbulent air jet at moderate Reynolds numbers", Experiments in Fluids, vol. 6, 1988, pp. 387-399.
- Page, W. M., "Two-dimensional problems in electrostatics and hydrodynamics", Proc. London Math. Soc. Ser II, vol. 11, 1912, page 321.
- Potter, M. C. and Foss, J. F., "Fluid Mechanics", Great Lakes Press, 1982.
- Rockwell, D. O. and Niccolls, W. O., "Natural Breakdown of Planar Jets", ASME Journal of Basic Engineering, vol. 94, Ser. D, 1972, pp. 720-730.



Sato, H., "The stability and transition of a two-dimensional jet", J. Fluid Mech., vol. 7, 1960, pp. 53-80.

Sato, H. and Sakao, F., "An experimental investigation of the instability of a two-dimensional jet at low Reynolds numbers", J. Fluid Mech., vol. 20, 1964, pp. 337-352.

Savic, P., "On Acoustically Effective Vortex Motion in Gaseous Jets", Phil. Mag. (7) 32, 1941, pp. 245-252.

Savic, P. and Murphy, J. W., "The Symmetrical Vortex Street in Sound Sensitive Plane Jets", Phil. Mag. (7), 34, 1943, pp. 139-144.

Schweiger, G., "Regular Structures in a Plane Triple Jet", ASME Journal of Fluids Engineering, vol. 105, 1983, pp. 42-46.

Shimizu, A. and Wada, T., "A Numerical Analysis of Vortex Growth in a Two-Dimensional Jet", Computers in Fluids, vol. 13, 1985, pp. 83-97.

Tatsumi, T. and Kakutani, T., "The stability of a two-dimensional laminar jet", J. Fluid Mech., vol. 4, 1958, pp. 261-275.

Thomas, F. O. and Goldschmidt, V. W., "Structural characteristics of a developing turbulent planar jet", J. Fluid Mech. vol. 163, pp. 227-256
Vallentine, H. R., "Applied Hydrodynamics", Second Edition, Plenum Press, 1967.

White, F. M., "Viscous Fluid Flow", McGraw Hill Inc, 1974.

Winant, C. D. and Browand, F. K., "Vortex Pairing: the mechanism of turbulent mixing layer growth at moderate Reynolds number", J. Fluid Mech., vol. 63, 1974, pp. 237-255.

Yih, C. S., "Two solutions for inviscid rotational flow with corner eddies", J. Fluid Mech., vol. 5, 1959, pp. 36-39.







31293008955837

